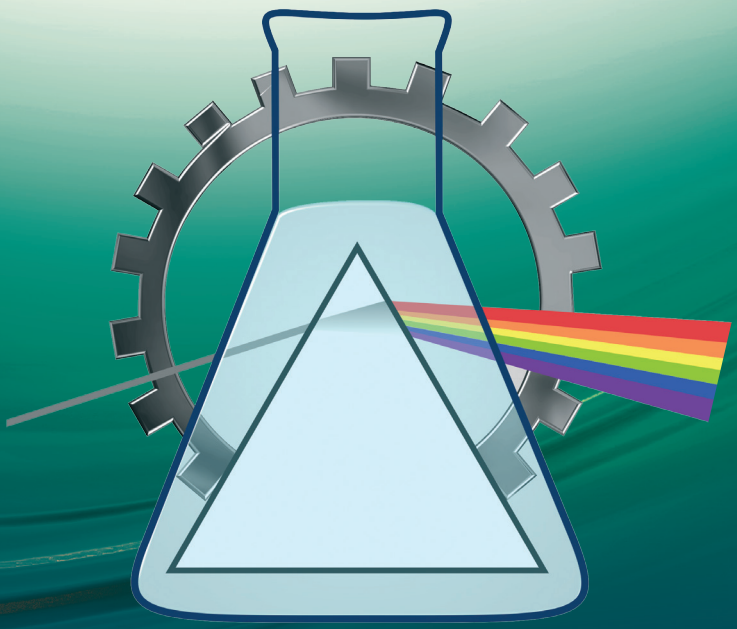
Maria Curie-Sklodowska University
Faculty of Chemistry

UMCS
UNIWERSYTET MARII CURIE-SKŁODOWSKIEJ

# SCIENCE AND INDUSTRY
## challenges and opportunities



WYDAWNICTWO UNIWERSYTETU MARII CURIE-SKŁODOWSKIEJ

**Maria Curie-Sklodowska University**
**Faculty of Chemistry**

# SCIENCE AND INDUSTRY
## challenges and opportunities

**Edited by:**
**prof. dr hab. Zbigniew Hubicki**

WYDAWNICTWO UNIWERSYTETU MARII CURIE-SKŁODOWSKIEJ
LUBLIN 2024

**Reviewers:**
Prof. dr hab. inż. Zygmunt Gontarz
Dr hab. Agata Jakóbik-Kolon, prof. PŚ
Dr hab. Monika Kalinowska, prof. PB
Dr hab. inż. Łukasz Klapiszewski, prof. PP
Dr hab. Joanna Kluczka, prof. PŚ
Dr hab. inż. Agnieszka Kołodziejczak-Radzimska
Dr hab. Urszula Kotowska
Prof. dr hab. Włodzimierz Lewandowski
Prof. dr hab. Joanna Matysiak
Dr hab. Piotr Nowicki, prof. UAM
Dr hab. inż. Magdalena Regel-Rosocka, prof. PP
Dr hab. inż. Katarzyna Siwińska-Ciesielczyk, prof. PP
Dr hab. inż. Katarzyna Staszak
Dr hab. Renata Świsłocka, prof. PB
Dr hab. inż. Karolina Wieszczycka, prof. PP
Prof. dr hab. Leszek Wachowski

**Technical editing, typesetting and proofreading:**
Dr hab. Monika Wawrzkiewicz, prof. UMCS

© Wydawnictwo UMCS, Lublin 2024

Artykuły są udostępniane na licencji
Creative Commons Attribution 4.0 International License (CC BY)

ISBN 978-83-227-9805-8

PUBLISHED BY WYDAWNICTWO UNIWERSYTETU MARII CURIE-SKŁODOWSKIEJ
20-031 Lublin, ul. Idziego Radziszewskiego 11
tel. (81) 537-53-04
www.wydawnictwo.umcs.eu
e-mail: sekretariat@wydawnictwo.umcs.lublin.pl

SALES DEPARTMENT:
tel./faks 81 537-53-02
Internet Bookstore: https://wydawnictwo.umcs.eu
e-mail: wydawnictwo@umcs.eu

Dear Sirs!

We are handing over to you the monograph “Science and industry - challenges and opportunities”, which is a continuation of the monograph “Science and industry - spectroscopic methods in practice, new challenges and opportunities”. It presents ongoing scientific research. The topics presented in its pages will help to disseminate information on research conducted by your scientific and research centers. We hope that it will contribute to the dissemination of knowledge transfer and new technologies being developed. It is in the interest of each university and research institute to establish an understanding and develop common areas of cooperation. Undoubtedly, these are mutually beneficial, both to scientists through integration with the economic and social environment, and to entrepreneurs adapting to changing market conditions. The joint implementation of utilitarian projects, the results of which can find application in industry, stimulates scientists to direct their activities towards the most desirable research topics. Universities and research units thus become a catalyst for economic development. Industry, on the other hand, thanks to such cooperation, gains access to the latest knowledge on the achievements of a given scientific field, supplemented by the knowledge and research experience of scientific partners. Undoubtedly, this cooperation is mutually beneficial. It is also associated with a number of challenges.

To meet the above expectations, we are pleased to present this monograph.

I wish you a fruitful reading experience!
Zbigniew Hubicki

## TABLE OF CONTENTS

**T. Banaszek, A. B. Nowicka, M. Szybowicz, R. Wichniarek, W. Kuczko, D. Tomczak, M. Wojtyłko, A. Froelich, B. Jadach, T. Osmałek** ..... 12
Raman spectroscopy in the study of active pharmaceutical ingredients

**J. Miętus, P. Tobiasz, I. Zdaniewicz, F. Borys, K. Wojciechowski, A. Susdorf, H. Krawczyk** ..... 16
Study of substituted chalcones combined with azobenzenes - new photoswitches

**B. Rojek, A. Bartyzel, A. Plenis** ..... 20
FTIR and TGA-FTIR in compatibility study of arbidol hydrochloride mixtures with excipients

**B. Rojek, A. Plenis** ..... 24
Piroxicam compatibility screening using spectroscopic techniques supported by thermal analysis

**L. Nosach, A. Chrzanowska, E. Skwarek** ..... 28
Formation of zinc sulfate and zinc acetate monolayers on nanosilica surface: modification and thermal transformations

**W. Korol, G. Bielecka, J. Rubaj, H. Nieściór** ..... 32
Determination of urea in high protein feed materials and compound and complementary feed by a spectrophotometric method

**J. Bąk, D. Kołodyńska** ..... 36
Hydrotalcite modified biochars (Zn/Al-LDH@BC, Co/Al-LDH@BC) as an example of effective sorbents for removing cerium(III) ions from aqueous media

**D. Paluch, A. Bazan-Woźniak, R. Pietrzak** ..... 40
X-ray photoelectron spectroscopy as an effective method for qualitative and quantitative surface analysis of carbon adsorbents derived from herbal materials

**R. Wolski, A. Bazan-Woźniak, R. Pietrzak** ..... 45
Activated carbons obtained from corn digest as adsorbents of pharmaceutical pollutants

**M. Wawrzkiewicz, B. Podkościelna, B. Tarasiuk** ..... 49
Synthesis, characterisation and application of new polymeric adsorbent containing starch for the removal of toxic dye

**D. Fila, Z. Hubicki, D. Kołodyńska** ..... 54
Influence of the type of crosslinking agents on the sorption properties of alginate hydrogel microspheres

**A. Wawruch, D. Fila, Z. Hubicki** ..... 58
Natural-based adsorbent in the sorption of critical raw materials

**A. Wawszczak, G. Józefaciuk, D. Kołodyńska** ..... 62
Optimization of cadmium ion sorption using bio-inspired matrices: experimental investigations

**B. Charmas, B. Wawrzaszek, K. Jedynak** ..... 66
Mechanochemical activation as an effective way of developing biocarbons surface and porosity

**B. Charmas, J. Skubiszewska-Zięba, K. Jedynak** ..... 70
Change in $SiO_2$ structure under hydrothermal conditions during mechanochemical milling

**B. Czech, A. Sokołowski** ..... 74
Phytotoxicity of biochars obtained from various raw materials

**B. Czech, A. Sokołowski** ..... 78
Phthalic acid esters in biochar-amended soil-vegetable system

**P. Radulski, B. Kaźmierczak, A. Kaczmarczyk** ..... 82
The use of spectroscopic methods for the analysis of biocarbon obtained from plant wastes

**B. Kaźmierczak, J. Drabik, P. Radulski, A. Kaczmarczyk, J. Molenda** ..... 86
The influence of pyrolysis temperature on qualitative changes in carbon materials obtained from tea bio-waste

**M. Wiśniewska, K. Tokarska, T. Urban, P. Nowicki** ..... 90
Production of activated biocarbons by microwave-assisted chemical activation of hardwood sawdust

**M. Wiśniewska, M. Gęca, P. Nowicki** ..... 94
Effect of the activation procedure on the adsorption properties of carbonaceous materials obtained from herbs towards ionic polymers

**S. Gustaw, J. Bąk, D. Kołodyńska** ..... 98
Biochar-based sorbents as materials in the sorption of arsenic(V) ions form aqueous solutions

**G. Wójcik, Z. Hubicki, K. Zinkowska** ..... 101
Sorption of nickel(II) ions on chelating ion exchanger

**A. Wołowicz, Z. Hubicki** ..... 105
Comparision of adsorptive removal of vanadium(V) ions from aqueous solutions by various ion exchange resins

**A. Gładysz-Płaska, A. Lipke, J. Padarz, M. Gajewska, E. Grabias-Blicharz, M. Majdan**..... 109
Studies of thorium sorption on functionalized mesoporous silica

**J. Bok-Badura, A. Jakóbik-Kolon, B. Sagan-Szendzielorz**..... 113
Sorption of cesium and strontium ions on hybrid pectin based sorbent

**M. Kalinowska, E. Gołębiewska, K. Koronkiewicz, M. Bieniek, A. Ziniewicz** ..... 116
Extraction of bioactive compounds from dandelion using modern extraction techniques

**M. Krystkowicz, M. Kalinowska, G. Kolenda, K. Koronkiewicz, E. Gołębiewska, R. Choińska, J. Skibicki**..... 120
Pressurized solvent extraction (PSE) of bioactive compounds from apple pomace

**H. Kuzmanenko, T. Okholina, W. Sofińska-Chmiel, U. Maciołek, M. Goliszek, M. Drewniak, J. Orzeł** ..... 124
Chemical analysis of kaolin from the Zhezheliv deposits from Vinnytsia region

**T. Okholina, H. Kuzmanenko, W. Sofińska-Chmiel, U. Maciołek, L. Gazda, E. Mendyk, K. Skrzypiec, J. Orzeł**..... 130
Spectroscopic characterization of amber from Ukrainian and Lublin deposits

**I. Pańczuk-Figura, W. Sofińska-Chmiel, U. Maciołek** ..... 134
Chemical analysis of coffee with the addition of cinnamon, ginger and cardamon

**K. Lewtak, W. Sofińska-Chmiel, J. Wydrych, B. Sidorska, M. J. Fiołka**..... 139
FTIR spectroscopy as a tool for analysing changes in the cell wall of the fungus *Candida Albicans* after the action of compounds of animal and plant origin

**M. Fiałek, C. Wardak, M. Wardak**..... 144
Potassium potentiometric sensors for testing the composition of pharmaceutical preparations

**M. Fiałek, M. Grabarczyk, M. Wardak** ..... 148
The influence of surfactive substances with different charge on the voltamperometric signal of gallium

**A. Pawlak, A. Nosal-Wiercińska** ..... 152
Research on the "cap-pair" effect for Bi(III) ions in aqueous-organic environments. Effect of selected ionic surfactants on the electrode process

**J. Lenik, C. Wardak**..... 156
Construction and properties of ion selective electrodes for chlorhexidine determination

**K. Morawska, C. Wardak, J. Lenik, M. Wardak** ..... 160
Nitrate ion-selective electrodes with nanocomposite-modified ion-sensitive membrane

**I. Gęca, M. Korolczuk** ..... 164
Application of cold vapour stripping voltammetry for determination of total mercury

**M. Ochab, I. Gęca** ..... 168
Determination of folic acid by adsorptive stripping voltammetry using a bismuth film-coated gold microelectrode arrays

**D. Gorylewski, K. Tyszczuk-Rotko, K. Staniec, A. Keller** ..... 171
State-of-art electrode materials in voltammetry ultratrace analysis of acyclovir

**D. Gorylewski, K. Tyszczuk-Rotko, A. Keller, K. Staniec** ..... 174
Fast, simple and sensitive voltammetric determination of curcumin via various sensors

**J. Baran, A. Drozd, A. Łassak, M. Kondracka, A. Watros** ..... 178
Determination of selected micronutrients in dried plants by X-ray fluorescence

**A. Drozd, M. Paluch, D. Kołodyńska** ..... 182
Application of TG and DCS analyses to evaluate thermal properties of polyacrylate-based hydrogels

**J. Kapelewska, U. Klekotka, A. Piotrowska-Niczyporuk, U. Czyżewska, M. Bartoszewicz, J. Karpińska** ..... 187
Abiotic and biotic degradation of polyethylene – physicochemical properties changes

**M. I. Bolińska, J. Piekutin, U. Kotowska** ..... 191
Selected emerging organic pollutants of the aquatic environment and the possibilities of their removal from the water

**M. Hryniewicka** ..... 195
Biosurfactants and their applications in sample preparation techniques

**M. Goliszek, A. Chabros, M. Drewniak, W. Sofińska-Chmiel** ..... 199
Exploring the versatility of xerogels based on agar and gelatin

**M. Goliszek, K. Skrzypiec, B. Podkościelna** ..... 203
Lignin as a sustainable additive for polymer protective materials

**B. Podkościelna, B. Tarasiuk, K. Młynarczyk, A. Puszka, K. Dawidek, A. Gryzińska** ..... 207
Synthesis and characterization of fire-resistant poly(urethane-methacrylate) materials

**K. Ciosmak, A. Puszka, A. Gryzińska, K. Dawidek, B. Podkościelna** ..... 211
Preparation and study of properties of soft poly(vinyl chloride) compositions with reduced flammability

**K. Dawidek, A. Gryzińska** ..... 215
The influence of screw rotation speed of extruder to gelation process of poly(vinyl chloride)

**M. Rogulska, M. Maciejewska** ..... 219
Studies on thermal and mechanical behavior of new biphenyl - derivative thermoplastic polyurethanes

**E. Krystkowiak** ..... 223
UV-VIS spectroscopy in the study of solute-solvent hydrogen bonding of donor and acceptor types

**B. Pawlak, K. Tyśkiewicz, M. Gruba, A. Wziątek, M. Konkol, G. Florkowski, Z. Fekner, V. M. Jiménez, J. Verspreet** ..... 227
Economical aspects of food by-products valorization by supercritical fluid extraction

**M. Groszek, R. Łyszczek, A. Ostasz** ..... 230
Spectroscopic characterization of cobalt(II) complexes with 4,4'-stilbenedicarboxylic acid and N-donor ligands

**K. Tyśkiewicz, M. Gruba, M. Kondracka, R. Tyśkiewicz, A. Wziątek, M. Konkol, R. Wiejak, R. Kowalski, A. Białek** ..... 234
Supercritical carbon dioxide extracts from clove buds with antifungal properties

**A. Sabitova, K. Akimzhanova, B. Mussabayeva** ..... 238
Chalcophile elements composition of north-east Kazakhstan Salt Lakes' mud

**A. Sabitova, A. Abdrakhmanova** ..... 241
The effect of the composition of electrolytes on the anode-free lithium-ion batteries

**A. Myka, R. Łyszczek, A. Bińczak** ..... 244
Polyhalite: what kind of fertilizer is it?

**Ł. Rusek** ..... 248
Technology for producing controlled-release mineral fertilizers (CRFs) using biodegradable materials in the coating process

**T. Michałek, M. Wojnicki** ..... 252
Improving the efficiency of palladium(II) cementation from dilute solutions by using silver-copper alloy powders

**M. Skrzetuszewski, Ł. Litwiniuk, M. Zajkowski, S. Górnik, K. Hovorov** ..... 256
Testing the spectral characteristics of reflective materials using a multi-angle attachment

**Z. Idrisheva, I. Ostolska, E. Sandybaev**, **E. Skwarek**, **G. Daumova, M. Wiśniewska** ..... 260
Migration of radioactive isotopes in soils at rare earth and thorium ore processing sites

**A. Skrzypek, B. Paw, J. Matysiak** ..... 265
Innovative methods for the extraction of bioactive compounds from plant sources

**P. Muszyński, J. Matysiak** ..... 271
Statistical analysis of fluorescence spectra in application to vegetable oil identification

**E. Skwarek,** K. **Misiołek, P. Skwarek** ..... 279
Synthesis and study of selected properties of the hydroxyapatite/$TiO_2$ composite

**E. Skwarek, O. Goncharuk, L. Nosach, P. Skwarek** ..... 284
Characterization of selected properties of hydroxyapatite-chitosan composites

**K. Wrzesińska, J. Czerwiński** ..... 288
Iodine contrast agents - fate and occurrence in the environment

**K. Wrzesińska, J. Czerwiński** ..... 290
Pharmacology and applications of iodine contrast agents

**A. Kustovska, V. Paientko, O. Pinchuk, Y. Buyan, A. Bryazun, E. Skwarek** ..... 293
Study of the release of chlorophylls of the *Lamiaceae* family by the spectrophotometric method

**R. Choińska, A. Dąbrowska, R. Świsłocka, W. Lewandowski** ..... 298
The influence of the biodegradation process on the antioxidant properties of polyphenols

**N. Kowalczyk, G. Świderski** ..... 303
Theoretical structural studies of picolinic acid - derived herbicides

**N. Kowalczyk, G. Tyniecka, E. Gołębiewska, G. Świderski** ..... 307
Metal complexes with hydroxypicolinic acid - spectroscopic studies and thermal analysis

**R. Świsłocka, A.I. Ziniewicz** ..... 311
Physicochemical and biological properties of methoxybenzoic acids and their complexes with Cr(III) and Fe(III)

**A. Golonko, A. Szklaruk, R. Świsłocka, W. Lewandowski** ..... 317
Application of flavonoid potential for metal complexing in food technology and nutrition

**M. Samsonowicz, A. Antoniuk, A. Dowbysz** ..... 322
Amylase inhibitory activities of matcha tea aqueous extract

**U. Maciołek, J. Matusiak, E. Grządka, W. Franus** ..... 327
Functionalization of zeolite with cellulose ethers of different ionic nature

**M. Kosińska-Pezda, U. Maciołek, A. Nowicka, M. Drewniak** ..... 331
Synthesis, spectral characterization, and fluorescent properties in the solid state and solution of dysprosium(III) ions complex with nalidixic acid

**K. Tyśkiewicz, M. Gruba, M. Kondracka, A. Wziątek, M. Konkol, R. Wiejak, R. Kowalski, A. Białek** ..... 335
Optimization of total cost of manufacturing of clove buds $scCO_2$ extracts

**M. Józwicki, K. Skrzypiec, W. Józwicka, P. Janusz, A. Kiczor, P. Mergo, W. Sofińska-Chmiel**..... 338
Spectroscopic and microscopic studies of UV filters in selected hair cosmetics

**E. Nalewajko-Sieliwoniuk, I. Wysocka, A. Kalinowska** ..... 343
Determination of antioxidants in edible oils using a flow system with chemiluminescence detection

**P. Kluczyński, M. Emmons-Burzyńska, E. Jędrzejczak, M. Wysokowski, M. Regel-Rosocka**..... 347
Green leaching agents for sustainable copper recovery from e-waste

**W. Stachowicz, M. Rzelewska-Piekut, W. Smułek, M. Regel-Rosocka** ..... 351
Bioorganic precipitation of platinum group metal nanoparticles

**H. Nikolaichuk, E. Fornal**..... 355
The effect of dietary flavonoids on proteins in Alzheimer disease

**H. Nikolaichuk, E. Fornal**..... 358
The effect of dietary flavonoids on post-translational modification of proteins in the context of degenerative diseases

**T. Wasilewski, A. Krzyszowska, Z. Hordyjewicz-Baran**..... 362
Coacervate as a form of hand wash cosmetic

**Z. Krupa, J. Nizioł, T. Ruman**..... 366
Laser ablation remote ionisation mass spectrometry imaging for detection of biomarkers and metabolites

**L. Senerovic, M. Atanaskovic, A. Djokic, N, Stankovic, L. Djokic, I. Moric**..... 369
Bioprospecting of microbial enzymes for industial application

**K. Karpińska-Wlizło, W. Gac, W. Zawadzki, G. Słowik** ..... 373
$CO_2$ hydrogenation in the presence of alumina and silica supported nickel catalysts

**S. Walczyński, W. Korol**..... 377
Near infrared reflectance spectrometry (NIRS) method in national and international feed comparative studies

**A. Žugić, J. Mudrić, N. Krgović, M. Tasić Kostov, V. M. Tadić** ..... 381
Encapsulation of green tea leaves extract by spray drying

**A. Žugić, S. Mirković, M. Tomović, M. Anđić, A. Petrović, I. Nešić, V. M. Tadić** ..... 383
Antiiflammatory activity of *Pinus Sp.* isolates

**N. Krgović, J. Mudrić, M. Martinović, A. Žugić, V. M. Tadić** ..... 385
Percolation vs ultrasound assisted extraction: impact on chemical composition and pharmacological activities of *Vaccinium myrtillus* fruit extracts

**O. Kapusta, M. Kaczmarczyk**, **M. Barczak** ..... 387
Synthesis of alginate hydrogels doped with iron microparticles: rheological and spectroscopic characterization

**A. Jakóbik-Kolon, J. Bok-Badura, B. Sagan-Szendzielorz** ..... 391
Ammonia equilibrium in aqueous solution: effect of pH, salinity and temperature

**S. Wójcik, K. Szarłowicz** ..... 395
Optymalization the methodology of $^{210}$Po determination in tobacco products

**M. V. Quynh Nguhen, A. K. Przybył** ..... 399
Synthesis and spectral analysis of new dapson squaramides

**D. Osypiuk, B. Cristóvão, A. Bartyzel** ..... 403
A comprehensive comparison of the spectroscopic properties of heteronuclear N,O-donor schiff base complexes

**D. Osypiuk, B. Cristóvão, A. Bartyzel** ..... 407
Analysis of selected properties of copper(II) and zinc homonuclear complexes

**A. Zdunek, D. Kołodyńska, K. Borowik** ..... 411
Removal of fluoride ions from ammonium sulphate(VI) solutions by ion exchange resin

**P. Tobiasz, M. Koźbiał, F. Borys, H. Krawczyk** ..... 415
Sposób otrzymywania pochodnych aminowych dihydrodibenzo[*b,f*]oksepin

**R. Sawczuk, N. Grodzka, J. Karpińska** ..... 419
Antioxidant activity of bee bread and drone brood homogenate in lipid peroxidation process and ferric(II) chelating assay

List of Authors ..... 423

# RAMAN SPECTROSCOPY IN THE STUDY OF ACTIVE PHARMACEUTICAL INGREDIENTS

**T. BANASZEK[1], A. B. NOWICKA[1], M. SZYBOWICZ[1], R. WICHNIAREK[2], W. KUCZKO[2], D. TOMCZAK[3], M. WOJTYŁKO[4], A. FROELICH[4], B. JADACH[4], T. OSMAŁEK[4]**, [1]Poznan University of Technology, Faculty of Materials Engineering and Technical Physics, Institute of Materials Research and Quantum Engineering, 3 Piotrowo Street, 60-965 Poznań, Poland, [2]Poznan University of Technology, Faculty of Mechanical Engineering, Institute of Materials Technology, 3 Piotrowo Street, 60-965 Poznań, Poland, [3]Poznan University of Technology, Faculty of Chemical Technology, Institute of Chemical Technology and Engineering, 4 Berdychowo Street, 60-965 Poznań, Poland, [4]Karol Marcinkowski University of Medical Sciences, Faculty of Pharmacy, Chair and Department of Pharmaceutical Technology, 6 Grunwaldzka Street, 60-780 Poznań, Poland.

**Abstract:** This work presents the results of Raman scattering study of an active pharmaceutical ingredients used for the treatment of depression and a biocompatible resin. As a result of the combination of the above-mentioned substances, new forms of 3D printing drug forms were obtained. The aim of the research was to characterize the changes occurring in the biocompatible resin containing active substance, before and after hardening, as well as determining the distribution of active substance on the surface of 3D printing microneedles

**Introduction:** By 'active pharmaceutical ingredients' (APIs) are meant chemical compounds that are intended to affect the body in order to prevent or fight disease. If the API(s) are combined with excipients, the result is a finished drug. These substances may have a different arrangement and/or conformation of the molecule in the crystallographic lattice. Consequently, the same substance may exhibit different properties [1]. Changing the parameters or production method influences which polymorphic form a substance will achieve. It is very important to determine the polymorphic form, as the physicochemical properties, bioavailability and even the efficacy profile of a drug may change with the form [2]. In order to ensure that the drug has the right properties, it is necessary to check which polymorphic form is being used at each production stage. According to studies, amorphous drug forms are the most beneficial in the pharmaceutical industry [3].

Agomelatine is an example of an API' used in the treatment of depression and anxiety disorders, with the structural formula $C_{15}H_{17}NO_2$. It is a potent agonist of melatonin $MT_1$ and $MT_2$ receptors and antagonist of the serotonin 5-$HT_{2C}$ receptor subtype [4]. According to the literature, agomelatine can exist in at least six polymorphic forms [5]. Raydent is a biocompatible resin that can be easily cured by ultraviolet light. Its properties include transparency and Class I biocompatibility, which translates into applications such as dental surgical templates. 3D printing is a technique widely used in both industry and pharmaceutical research. It offers the possibility of producing precisely designed and personalised components such as prostheses or implants, as well as printing drugs [6]. One method of 3D printing is Digital Light Processing (DLP),

which works by curing a photosensitive resins using a projected light source This method, compared to other 3D printing methods such as FFF (Fused Filament Fabrication), for example, is characterised by lower process temperatures and the precision of producing structures with a resolution of up to 200 μm [7].

**Experimental:** Raman spectra for the API powder and the biocompatible resin Raydent (Zortrax) for 3D printing, as well as cured mixtures of Raydent biocompatible resin and agomelatine, were performed using a Renishaw inVia micro-Raman system. In addition, a Leica DM200M optical microscope is attached to the spectroscope. A semiconductor laser with a wavelength of 785 nm was used for excitation light. The laser beam was focused on the sample using a x50 LWD long-distance working objective with a numerical aperture of NA=0.85. 3 weight percent agomelatine was added to the Raydent biocompatible resin, followed by mechanical mixing using ultrasonic scrubber. All measurements presented were performed using Raman spectroscopy. The solid active substance was obtained using the DLP method (Phrozen Sonic Mini 8K). The printing parameters include: layer height of 0.03 mm, bottom exposure time of 30 s, bottom layer count of 6, lifting distance of 5 mm and rest time after retract of 5 s. In addition, a Raman map of 30x30 μm with a step of 5 μm was made for the sample containing 3 wt.% agomelatine obtained by 3D printing.

**Results:** Figure 1 shows the spectra of pure agomelatine, uncured and cured Raydent biocompatible resin and cured and uncured Raydent biocompatible resin with 3 wt.% agomelatine. For the agomelatine powder, two distinct bands are observed at approximately 1370 $cm^{-1}$ and 1383 $cm^{-1}$. From the observations, it can be seen that the former has a higher intensity and is also observable in the composite with the biocompatible resin. It is assigned to the $CH_3$ deformation [8]. Raydent biocompatible resin has visible bands at 1407, 1455, 1636, 1721, 1764 $cm^{-1}$ and a doublet of bands in the range 1267-1314 $cm^{-1}$. As can be observed, the Raman spectrum of Raydent resin changes after curing. The C=C bond changes to a C-C bond during the curing process. In contrast, the C=O bond does not change its nature. In studies of the changes occurring in the sample during curing, the degree of conversion (DC) can be counted. This parameter tells what percentage of the substance has cross-linked during the curing process. The degree of conversion affects the mechanical properties (tensile strength, hardness, impact strength) as well as the physicochemical properties (characteristic temperatures, thermal stability, flame retardancy, viscosity). In order to calculate the degree of conversion, the formula was [9]:

$$DC(\%) = \frac{(A_{1407}/A_{1721})_0 - (A_{1407}/A_{1721})_t}{(A_{1407}/A_{1721})_0} \times 100$$

where $(A_{1407}/A_{1721})_0$ and $(A_{1407}/A_{1721})_t$ are integral intensities (peak-area ratio) of double bonds in the structure before curing and after curing in a given at time. In Figure 1, two areas are distinguished. The first at 1407 $cm^{-1}$ corresponding to the C=C vibration and the second at 1721 $cm^{-1}$ corresponding to the C=O vibration. This band does not change during curing. That is why it was chosen as the reference band. As can be observed the band associated with the C=C oscillation disappears during curing. It is these bands that were chosen to calculate the degree of conversion. The calculation shows that for the test

sample DC=55.5%. Figure 2 shows the results obtained by mapping the surface of a sample containing resin and 3 wt.% agomelatine. The band at 1370 $cm^{-1}$ was chosen as a marker band to illustrate the distribution of agomelatine in the 3D printed sample. It can be observed that agomelatine is distributed throughout the area studied.

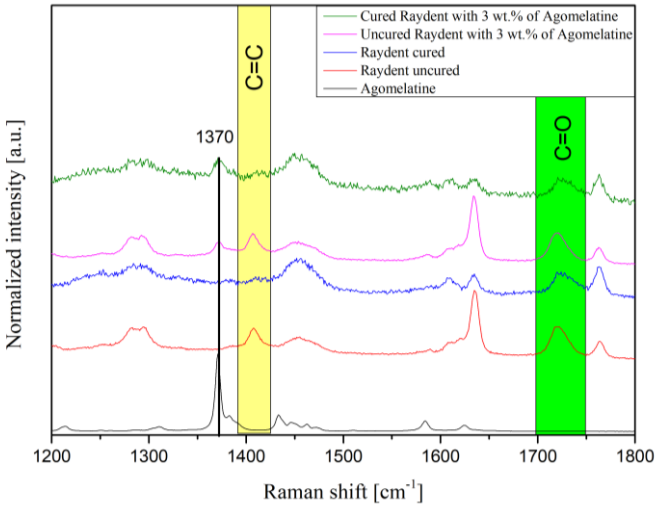



**Fig.1.** Normalized Raman scattering spectra for agomelatine powder, uncured and cured Raydent biocompatible resin and for uncured and cured resin containing 3 wt.% of agomelatine.

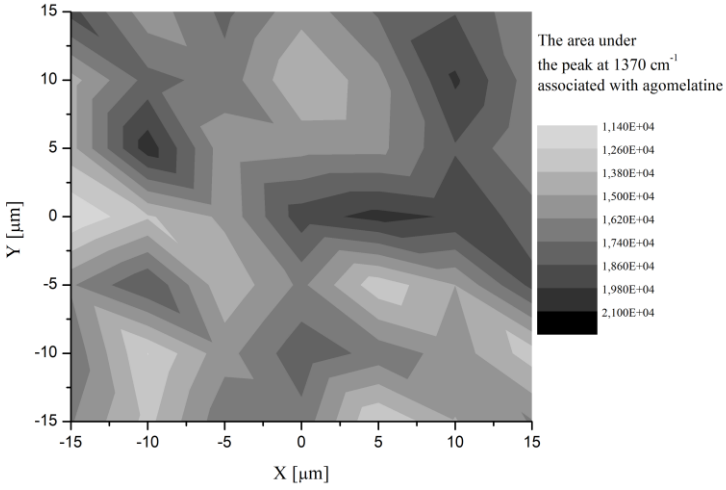



**Fig.2.** Raman map showing distribution of agomelatine on the surface of the composite.

**Conclusions:** Raman spectroscopy is a useful tool for research carried out in pharmaceuticals. It allows to determine the type of active substance, in our case agomelatine, its distribution in the resin and in the composite obtained by 3D printing (which may be a new form of drug administration in the future). In addition, it has been

shown that the degree of conversion, which changes during curing, can be studied using this method.

**Acknowledgements:** The work was performed as a result of the research project no. 2021/42/E/NZ7/00125 (ID: 526262) financed by the National Science Centre (Poland).

**References:**

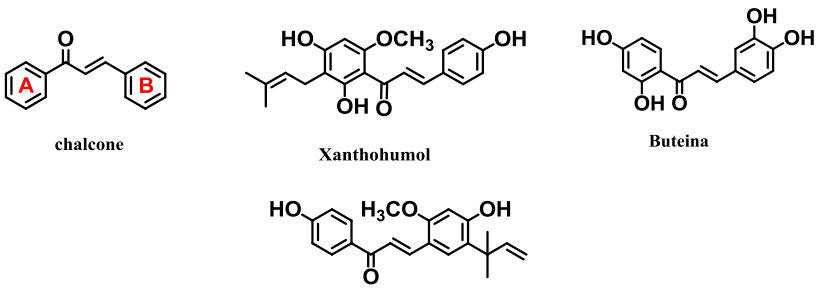
1. D. Giron, Journal of Thermal Analysis and Calorimetry, 64 (2001) 37.
2. I. Mirza, S. Saha, ACS Applied Bio Materials, 3 (2020) 8241.
3. K. J. Lee, J. Yoon, J. Lahaan, Current Opinion in Colloid & Interface Science, 16 (2011) 195.
4. M. Zupancic; C. Guilleminault, CNS drugs, 20 (2006) 981.
5. P. D. Crowley, H. C. Gallagher, Journal of Applied Microbiology, 117 (2014) 611.
6. E. B. Souto, J. C. Campos, Pharmaceutical Development and Technology, 24 (2019) 1044.
7. H. Li, J. Dai, Z. Wang, H. Zheng, W. Li, F. Cheng, Aggregate, 4 (2022) e270.
8.M. J. Lee, N. H. Chun, H. C. Kim, M. J. Kim, P. Kim, M. Y. Cho, G. J. Choi, Korean Journal of Chemical Engineering, 35 (2018) 984.
9. D. Tomczak, R. Wichniarek, W. Kuczko, F. Górski, Bulletin of the Polish Academy of Sciences. Technical Sciences, 71 (2023) e145936.

# STUDY OF SUBSTITUTED CHALCONES COMBINED WITH AZOBENZENES - NEW PHOTOSWITCHES

**J. MIĘTUS[1], P. TOBIASZ[1], I. ZDANIEWICZ[1], Filip BORYS[1,2], K. WOJCIECHOWSKI[1], A. SUSDORF[1], H. KRAWCZYK[1]**, [1]Department of Organic Chemistry, Faculty of Chemistry, Warsaw University of Technology, Noakowskiego 3, 00-664 Warsaw, Poland, [2]Nencki Institute of Experimental Biology, Polish Academy of Sciences, 3 Pasteur Street, 02-093 Warsaw, Poland.

**Abstract:** The article discusses the results of the synthesis of azochalcone derivatives. $^1$H NMR spectra and theoretical calculations were used to determine the structure of products in solution. The obtained molecules can be classified as a molecular switch because the *azo* bond present in the structure may, depending on the conditions, occur in the form of an isomer (*Z*) or (*E*).

**Introduction:** Chalcones consist of two aromatic rings (ring a and B) connected to a highly electrophilic three-carbon α, β-unsaturated carbonyl system (−CO – CH = CH–) in their structure (Fig.1). Due to their wide range of biological and chemical properties, chalcones are used in the treatment of various diseases [1]. The most known chalcones occurring in nature and having a beneficial effect on human health include Xanthohumol, Buteine, and Licochalcone (Fig.1) [2]. They occur in nature in the plants Toxicodendron vernicifluum, Humulus lupulus, and Glycyrrhiza glabra. The literature on anticancer chalcones highlights the use of three strategies: structural manipulation of both aryl rings, replacement of aryl rings with heteroaryl scaffolds, and "molecular hybridization" by conjugation with other pharmacologically interesting scaffolds to enhance anticancer properties. From a biological point of view, chalcones of various structures are important natural and synthetic compounds that are used in many fields of science and technology. A wide spectrum of biological activity is observed [1] i.e. antileishmanial activity [3], antituberculosis [4], antipyretic, antibacterial, antifungal [5], against HIV [6], *anti*-inflammatory [7], and anticancer [8]. The health benefits of natural chalcones can be attributed to their redox properties and their ability to scavenge radical oxygen species [9].




chalcone Xanthohumol Buteina

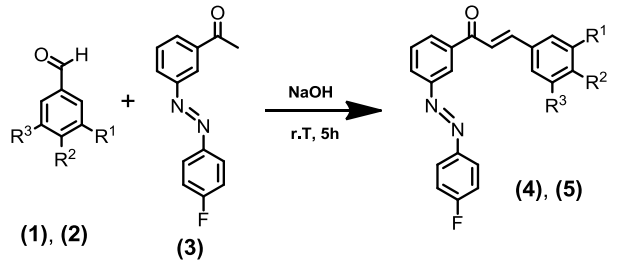
Likochalkon A

**Fig.1.** Structure of chalcone, Xanthohumol, Buteina and Likochalkon A.

The combination of chalcone derivatives and fragments containing an *azo* bond and fluorine substituents can be classified as molecular switches. Photochromic molecular switches are molecules used, among others, in photopharmacology. They undergo reversible 'switching' between permanent thermodynamic states after exposure to electromagnetic radiation in the visible range. Structural changes accompanying photoinduced and reversible transformations can be used, for example, to absorb or release molecules. In our work, we investigated such hybrid compounds.

**Experimental:** Aldehydes (**1**) or (**2**) were placed in a flask. Then methanol was added. Mixing enabled. Then ethanone (**3**) in the appropriate amount of 6 molar sodium hydroxide solution was added to the solution. The reactions were carried out for 5 hours at room temperature. The obtained precipitate was crystallized from methanol. The yield of products (**4**) or (**5**) is approximately 30%.

**Results:** Figure 2 shows the synthesis of products (**4**) and (**5**). In the aldol condensation of the appropriate aldehyde (**1**) or (**2**) with (*E*)-1-(3-((4-fluorophenyl) diazenyl)phenyl)ethanone (**3**) the products were obtained.




**(1)**, **(4)**: $R^1$= $OCH_3$, $R^2$ = $OCH_3$, $R^3$ = H
**(2)**, **(5)**: $R^1$= $OCH_3$, $R^2$ = H, $R^3$ = $OCH_3$

**Fig.2.** Synthesis of *azo*-chalcones (**5**) and (**6**).

Based on the measured $^1$H NMR spectra (Figs.3 and 4) and the calculations of the optimal geometry (the Gaussian 03 program -DFT[B3LYP in the 6.316* database) (Figs.5 and 6), the structure of compounds (**4**), and (**5**) in solution were identified. The products (**4**), and (**5**) have *azo* bonds. They can change their configuration from *E* to *Z* under the influence of different wavelengths.

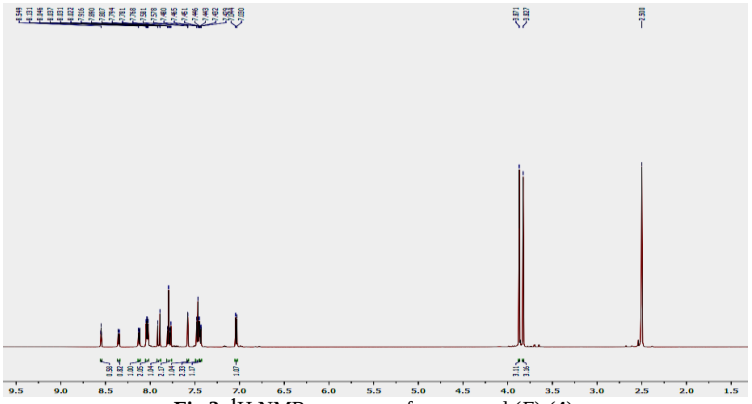


**Fig 3.** $^{1}$H NMR spectrum of compound (*E*)-(**4**).

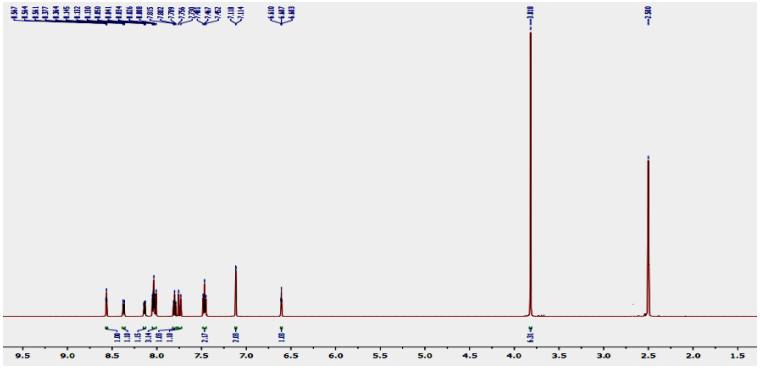


**Fig.4.** $^{1}$H NMR spectrum of compound (*E*)-(**5**).

**a)** **b)**

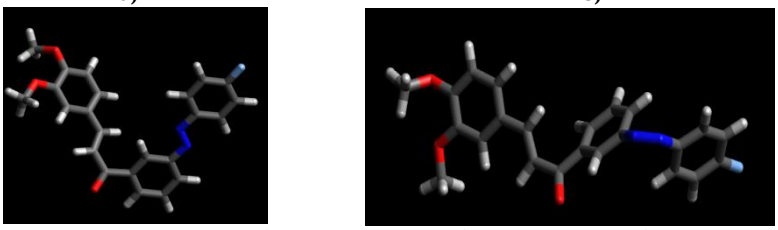


**Fig.5.** Calculated structure of compound (**4**): a) configuration (*E*), b) configuration (*Z*).

**a)** **b)**

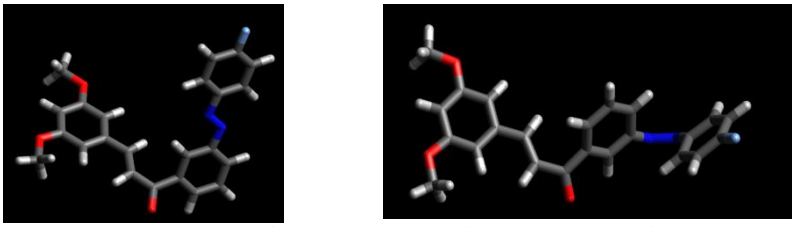


**Fig.6.** Calculated structure of compound (**5**): a) configuration (*E*), b) configuration (*Z*).

**Conclusions:** As a result of the synthesis of the appropriate aldehyde (**1**) or (**2**) with (*E*)-1-(3-((4-fluorophenyl)diazenyl)phenyl)ethanone (**3**), two chalcone derivatives with one *azo* bond (*E*)-(**4**) and (*E*)-(**5**) are formed. The resulting compounds act as photochromic switches due to the presence of double bonds between nitrogen atoms. It is possible to change their configuration from *E* to *Z* under the influence of different wavelengths.

**Acknowledgments:** The project was financed by the Faculty of Chemistry of the Warsaw University of Technology and NChem 5 IDUB program.

**References:**

1. Z. Nowakowska, European Journal of Medicinal Chemistry, 42 (2007) 125.
2. C. Karthikeyan, N.S.H. Narayana Moorthy, S. Ramasamy, U. Vanam, E. Manivannan, D. Karunagaran, P. Trivedi, Recent Patents on Anti-Cancer Drug Discovery, 10 (2015) 97.
3. S.F. Nielsen, S.B. Christensen, G. Cruciani, A. Kharazmi, T. Liljefors, Journal of Medicinal Chemistry, 41 (1998), 4819; L. Zhai, M. Chen, J. Blom, T.G. Theander, A. Kharazmi, Journal of Antimicrobial Chemotherapy, 43 (1999) 793.
4. Y. Lin, Y. Zhou, M.T. Flavin, L. Zhou, W. Nie, F. Chen, Bioorganic & Medicinal Chemistry, 10 (2002) 2795.
5. K.L. Lahtchev, D.I. Batovska, S.P. Parushev, V.M. Ubiyvovk, A.A. Sibirny, European Journal of Medicinal Chemistry, 43 (2008), 2220; P.M. Sivakumar, Chemical Biology & Drug Design, 74 (2009) 68.
6. A.L Cole, S. Hossain, A.M Cole, O. Phanstiel, Bioorganic & Medicinal Chemistry, 24 (2016) 2768.
7. Y.H. Kim, J. Kim, H. Park, H.P. Kim, Biological and Pharmaceutical Bulletin, 30 (2007) 1450.
8. A. Boumendjel, X. Ronot, J. Boutonnat, Current Drug Targets, 10 (2009) 363.
9. P.W. Snijman, E. Joubert, D. Ferreira, X.C. Li, Y. Ding, I.R. Green, W.C.A. Gelderblom, Journal of Agricultural and Food Chemistry, 57 (2009) 6678.

# FTIR AND TGA-FTIR IN COMPATIBILITY STUDY OF ARBIDOL HYDROCHLORIDE MIXTURES WITH EXCIPIENTS

**B. ROJEK[1], A. BARTYZEL[2], A. PLENIS[1]**, [1]Medical University of Gdansk, Faculty of Pharmacy, Department of Analytical Chemistry, Gen. Hallera Ave. 107, 80-416 Gdansk, Poland, [2]Maria Curie-Sklodowska University, Faculty of Chemistry, Institute of Chemical Sciences, Department of General, Coordination Chemistry and Crystallography, M. Curie--Sklodowska Sq. 3, 20-031 Lublin, Poland.

**Abstract:** Recently, arbidol hydrochloride, a drug produced in Russia with a broad spectrum of antiviral activity and, in the light of recent studies, also effective against Covid-19, has been enjoying great interest. However, there is little information about its physicochemical properties and behavior in the presence of various excipients. For this reason, studies on the compatibility of arbidol hydrochloride with excipients have been carried out. The most frequently used analytical tools in compatibility study, apart from thermal analysis techniques, are spectroscopic and thermal coupled with spectroscopic ones. Therefore, the aim of the work was to investigate the compatibility of arbidol hydrochloride with selected excipients (accacia, glucose and sucrose) using Fourier transform infrared (FTIR) and thermogravimetry coupled with FTIR (TGA-FTIR). Differential scanning calorimetry (DSC) was used to confirm the results of the above analyses. The obtained results indicated that among the used excipients, sucrose was the most compatible with arbidol hydrochloride.

**Introduction:** Spectroscopic techniques and thermal coupled with spectroscopic ones have become a reliable tool for pharmaceutical analysis, compatibility assessment of preformulation ingredients and quality control [1]. Although it should be noted that to date, there is no generally accepted protocol for assessing the compatibility of the active pharmaceutical ingredient (API) with other ingredients [2]. Fourier transform infrared spectroscopy (FTIR) is primarily a fast, non-sample-destructive method and sensitive to the structure of organic compounds and the environment, which is reflected in the detection of incompatibilities between pharmaceutical ingredients. Detection of potential incompatibilities occurring between the ingredients of pharmaceutical mixtures is based on the comparison of the spectra of the mixtures with those of the unmixed ingredients [3]. Compatibility between ingredients occurs when the spectrum of the mixture is the sum of the absorption bands coming from the components of the mixture. In turn, incompatibilities between ingredients in the spectra of mixtures are indicated by shifts, spectral changes, the appearance of new bands as a result of the interaction of components, or the disappearance of ingredient bands. Thermoanalytical techniques such as differential scanning calorimetry (DSC) and thermogravimetric analysis (TGA), alongside spectroscopic ones, play an important role in the early detection of API incompatibilities with the excipient. The combination of thermoanalytical and spectroscopic techniques allows for accurate characterization of occurring incompatibilities, and thus allows for the selection of appropriate excipients for APIs in order to obtain a stable, effective and safe solid dosage form. Concomitant, the use of

thermal and spectroscopic methods avoids costly material losses and significantly reduces the time needed to develop the pre-formulation of an appropriate preparation [1].

**Experimental:** Arbidol hydrochloride was purchased from LGC Standards (Toronto, Ontario, Canada), accacia from Pol-Aura (Gdansk, Poland), glucose and sucrose from Sigma-Aldrich (Steinhem, Germany). Two-component mixtures of arbidol hydrochloride with excipients were prepared by mixing components in a porcelain mortar with a plastic spatula. FTIR spectra of samples pelleted with KBr were recorded in the mid-infrared range with a resolution of 4 $cm^{-1}$ using a Nicolet 380 spectrometer (Thermo Fischer Scientific, Madison, USA). TGA-FTIR measurements were performed using a TG Q5000 thermogravimetric analyzer (TA Instruments, New Castle, Delaware, USA) coupled with a Nicolet 6700 spectrometer (Thermo Fischer Scientific, Madison, USA) in the range of 25-700 °C, at a heating rate of 20 °C/min and in a nitrogen atmosphere. Additionally, DSC was used to confirm the FTIR and TGA-FTIR results, where sample analyzes were carried out in the temperature range of 25-400°C in a nitrogen atmosphere with a purity of 99.9997 % and a heating rate of 10°C/min using an 822e differential scanning calorimeter (Mettler Toledo, Schwerzenbach, Switzerland).

**Results:** Figure 1A presents the spectra of arbidol hydrochloride, its mixtures and excipients. Arbidol hydrochloride spectrum (Fig. 1A) shows at 3407 $cm^{-1}$ a strong, wide band for OH stretch, at 3126 $cm^{-1}$ a band both of aromatic CH stretch and NH stretch, at 3056 $cm^{-1}$ a band of aromatic CH stretch and at 2980 $cm^{-1}$, 2926 $cm^{-1}$, 2853 $cm^{-1}$ and 2708 $cm^{-1}$ bands of $CH_3$ and $CH_2$ stretch and also at 1682 $cm^{-1}$ band of C=O stretch [4-6]. The spectra of carbohydrate excipients reveal OH and CH stretch in the range of 3600-2800 $cm^{-1}$, HCH and $CH_2OH$ in the are of 1500-1200 $cm^{-1}$, CO stretch in the range of 1200-950 $cm^{-1}$, COH, CCH and OCH deformation in the area of 950-700 $cm^{-1}$, exocyclic (CCO) deformation in range of 700-500 $cm^{-1}$ and below 500 $cm^{-1}$ endocyclic (CCO, CCC) deformation [7,8]. In the spectrum of the mixture of arbidol hydrochloride with accacia (Fig. 1A), an increase in the intensity of the NH band coming from arbidol hydrochloride at 3126 $cm^{-1}$ can be observed, which may indicate the formation of hydrogen bonds. In turn, the intensity of the CO vibration band at 1682 $cm^{-1}$ increased, but the width of this band decreased. Changes in the 1682 $cm^{-1}$ band are also visible in the spectra of mixtures with glucose. TGA-FTIR analysis of arbidol hydrochloride (Fig. 1B) revealed its stability up to about 90 °C in a nitrogen atmosphere, but above this temperature it decomposes. First, the ester bond is broken, which is reflected in the FTIR spectrum of gaseous products (Fig. 1E) in the bands characteristic of water (3450–4000 $cm^{-1}$ and 1300–1950 $cm^{-1}$) and carbon dioxide (2240–2400 $cm^{-1}$). Next, defragmentation and pyrolysis take place by releasing water molecules and carbon dioxide. In turn, at a temperature of approx. around 155 °C, weak bands characteristic of methanol appear (3150–2750 $cm^{-1}$ and1100–950 $cm^{-1}$). Above a temperature of 180°C, bands appear at 3069, 2965, 1270, 1179, 1066, 1026, 739, 692, 669 and 650 $cm^{-1}$ probably related to thiophenol molecules, aliphatic amines and benzene. However, at a temperature of about 310 °C, the intensity of these bands decreases and they are characteristic of ammonia vibrations (double 965 and 929 $cm^{-1}$), and above 380 °C occur bands for methane in the range of 3150–2700 $cm^{-1}$ with a maximum at 3015 $cm^{-1}$. Further, at a temperature of 530 °C, CO and HCl vibration bands are visible in the range of 2650–3100 $cm^{-1}$.

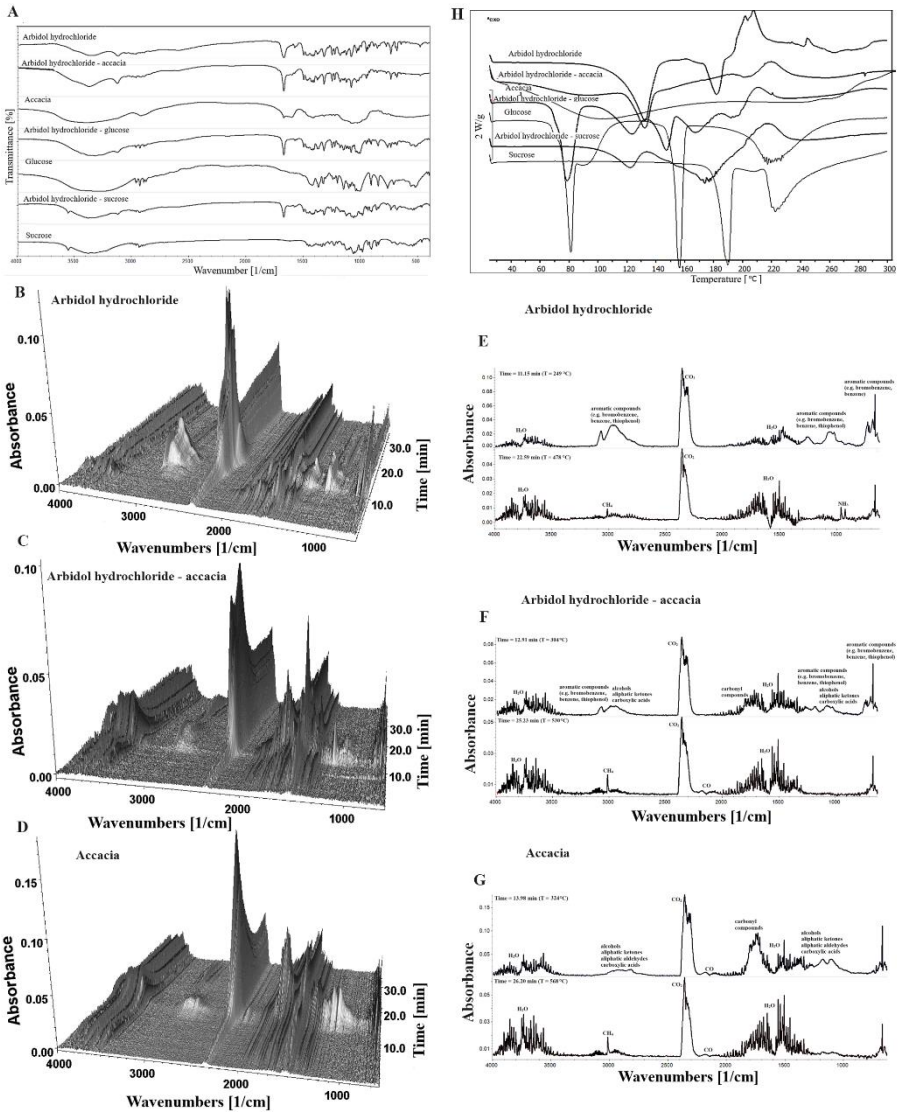



**Fig.1.** A) FTIR spectra and B), C), D) 3D surface plot for TGA-FTIR spectra of the evolved gaseous products, E), F), G) FTIR spectra of decomposition for arbidol hydrochloride, arbidol hydrochloride-accacia mixture and accacia and H) DSC curves of arbidol hydrochloride, excipients and their mixtures.

Thermal decomposition of excipients, e.g. accacia (Fig. 1D) begins with a weight loss of several percent due to dehydration. In the next stage, thermal decomposition occurs, resulting in the formation of intermediate products (Fig. 1G), and then the carbonization residues are burned. In the case of the decomposition of the arbidol hydrochloride - accacia mixture (Figs. 1C and 1F), an overlap of some processes related to the decomposition of arbidol hydrochloride and some related to the decomposition of accacia was observed. The least changes are noticed in the spectrum of the mixture of

arbidol hydrochloride and sucrose (data not shown), which may indicate the compatibility of these two ingredients. The results of FTIR and TGA-FTIR analyzes confirm the DSC analyses (Fig. 1H). The characteristic peaks of arbidol hydrochloride in the DSC curves of the mixtures are slightly shifted towards lower temperatures and broadened. However, in the case of the mixture with accacia, there is no peak at a temperature of approx. 180 °C.

**Conclusions:** Compatibility studies using FTIR and TGA-FTIR spectroscopy revealed changes in the structure of arbidol hydrochloride in its binary mixtures with accacia and glucose, which can indicate incompatibilities between arbidol hydrochloride and these two excipients. The above results were confirmed by DSC analyses.

**References:**

1. R. Chadha, S. Bhandari, Journal of Pharmaceutical and Biomedical Analysis, 87 (2014) 82.
2. M.Ch. Adeyeye, H.G. Brittain, Preformulation in Solid Dosage Form Development. Informa Healthcare, New York, 2008.
3. B. Rojek, M. Wesolowski, Spectrochimica Acta Part A: Molecular and Biomolecular Spectroscopy, 208 (2019) 285.
4. M.K. Anwer, M. Iqbal, M.M. Ahmed, M.F. Aldawsari, M.N. Ansari, E. Ezzeldin, N.Y. Khalil, R. Ali, Pharmaceuticals, 14 (2021) 411.
5. X. Li, X. Wang, Q. Jiang, F. Chi, Q. Liu, T. Zhang, Drug Development and Industrial Pharmacy, 43 (2017) 123.
6. R.M. Silverstein, F.X. Webster, D.J. Kiemle, Spektroskopowe metody identyfikacji związków organicznych. PWN, Warszawa, 2007.
7. E. Wiercigroch, E. Szafraniec, K. Czamara, M.Z. Pacia, K. Majzner, K. Kochan, A. Kaczor, M. Baranska, K. Malek, Spectrochimica Acta Part A: Molecular and Biomolecular Spectroscopy, 185 (2017) 317.
8. M. Kačuráková, R.H. Wilson, Carbohydrate Polymers, 44 (2001) 291.

# PIROXICAM COMPATIBILITY SCREENING USING SPECTROSCOPIC TECHNIQUES SUPPORTED BY THERMAL ANALYSIS

**B. ROJEK, A. PLENIS**, Medical University of Gdansk, Faculty of Pharmacy, Department of Analytical Chemistry, Gen. Hallera Ave. 107, 80-416 Gdansk, Poland.

**Abstract:** Compatibility screening between the ingredients of pharmaceutical preparations is a crucial step at the pre-formulation stage, which enables the rapid detection of excipients causing incompatibilities with the active pharmaceutical ingredient (API). The use of spectroscopic techniques, mainly Fourier transform infrared spectroscopy (FTIR) and Raman spectroscopy, significantly contributes to the early prediction of potential incompatibilities. It should be noted that the compatibility between the components indicate by the presence of all they absorption bands in the spectrum of the mixture. Any changes in the spectra of mixtures related to the shift, change in intensity or disappearance of characteristic bands of components or the appearance of other bands indicate incompatibilities between the ingredients. However, difficulties in interpreting the spectra of mixtures, caused by the overlapping of component bands, can be avoided by using chemometric methods. In connection with the above, the aim of the study was to use spectroscopic techniques in the compatibility screening of piroxicam with excipients (chitosan, methylcellulose and magnesium stearate) mixed at the ratios 7:3, 1:1 and 3:7. The results of spectroscopic study revealed the incompatibility of piroxicam with magnesium stearate, which was confirmed by thermal analysis, i.e. differential scanning calorimetry (DSC) and thermogravimetric analysis (TGA).

**Introduction:** Commonly used analytical techniques in prospective compatibility screening between active pharmaceutical ingredient (API) and excipients include thermal methods, such as differential scanning calorimetry (DSC), thermogravimetric analysis (TGA), and spectroscopic analytical methods, namely, Fourier transform infrared spectroscopy (FTIR), Raman spectroscopy, and powder X-ray diffraction (PXRD) [1]. In general, spectroscopic techniques are responsive to the structure as well as the environment of organic compounds. These techniques focus on the solid-state behavior of APIs and their formulations and thus enable compatibility screening, because the vibrational alterations as a probe indicate the existence of potential intermolecular interactions between the ingredients. Hence, pharmaceutical interactions that during pharmaceutical processing result from dehydration, hydrate/solvate formation, desalting, transformations crystalline to amorphous form and vice versa or polymorphic changes can be detected using these techniques [2]. Primarily, spectroscopic techniques offer a unique fingerprint of APIs and excipients based on their physicochemical properties. The high sensitivity of these techniques allows for easy and quick detection of any subtle deviations in the physicochemical properties of APIs caused by interactions with excipients. Therefore, the advantage of these techniques is rapid analysis, which involves fast and easy detection of incompatibilities due to shifts spectral changes, the appearance of new bands of interaction products or the

disappearance of bands of ingredients [3]. Unfortunately, an inconvenience in interpreting the results is the overlapping bands in the spectra, which may make it difficult to predicting incompatibility [2]. To solve this problem, the interpretation of spectra can be aided by chemometric methods, e.g. principal component analysis (PCA) or hierarchical cluster analysis (HCA) or others. By reducing the dimensionality of huge data sets, which involves only minimal loss of information, PCA aims to increase the interpretability of the data. In turn, in the case of HCA, there is a noticeable tendency to create clusters of samples, i.e. groups of samples with similar characteristics [4]. In addition, thermal analysis can be used to confirm incompatibility detected by spectroscopic techniques. For this reason, the aim of this study was to use spectroscopic techniques (FTIR and Raman) supported by thermal analysis (DSC, TGA) in the compatibility screening of piroxicam, which was mixed with chitosan, methylcellulose and magnesium stearate at the ratios of 7:3, 1:1 and 3:7.

**Experimental:** Piroxicam was obtained from GlaxoSmithKline Pharmaceuticals (Mumbai, Maharashtra, India), chitosan low-viscous from Fluka (Siegen, Germany), methylcelullose from Shin-Etsu Chemical Co. (Tokio, Japan) and magnesium stearate from Faci (Carasco Genoa, Italy). Binary mixtures were prepared by mixing appropriately weighed piroxicam and excipients with a plastic spatula in a porcelain mortar. FTIR spectra of the KBr-pressed samples were recorded using an FTIR spectrophotometer, Nicolet 380 (Thermo Fischer Scientific, Madison, USA) in the spectral range of 4000-400 $cm^{-1}$ with resolution of 4 $cm^{-1}$. In turn, Raman spectra were recorded using a DXR SmartRaman spectrometer (Thermo Fisher Scientific, Madison, USA) at a DXR laser wavelength of 780 nm and a power of 15 mW in the range of 3414–400 $cm^{-1}$ at a resolution of 2 $cm^{-1}$. Calculations in the area of multivariate statistics based on FTIR and Raman data were performed in the TIBCO Statistica 13.3 program (StatSoft Inc., Tulsa, OK, USA). Thermal analyzes of approx. 4 mg samples were performed using an 822e DSC calorimeter (Mettler Toledo, Schwerzenbach, Switzerland) in the range of 25-300 °C with a 10 °C/min heating rate, in a 70 ml/min flow of nitrogen, while TGA /DTG analysis of 200 mg samples were carried out using a derivatograph, model OD-103 (MOM, Budapest, Hungary) in the air at a rate of 5 °C $min^{-1}$ up to a final temperature of 700 °C. Indium and zinc were used to calibrate the DSC instrument, and $\alpha$-$Al_2O_3$ was used for the derivatograph.

**Results:** Figs. 1A and 1B shows the FTIR spectra of piroxicam, magnesium stearate and their mixtures at the ratios of 7:3, 1:1 and 3:7. Piroxicam revealed characteristic stretching vibration bands at 3338 $cm^{-1}$ (pyridin-2-yl-amino), 1629 $cm^{-1}$ (-NH-CO), 1577 $cm^{-1}$ (C=C) and 1528 $cm^{-1}$ (secondary -NH). The next bands representing bending vibrations are located at 1435 $cm^{-1}$ (asymmetric C-H) and 1351 $cm^{-1}$ (symmetric C-H). Moreover, stretching vibration bands can be noticed at 1299 $cm^{-1}$ (symmetric S=O), 1216 $cm^{-1}$ (C-C) and 1148 $cm^{-1}$ (-$SO_2$-N-), while the band at 769 $cm^{-1}$ belongs to ortho-disubstituted phenyl group. This is consistent with the literature data [5]. Characteristic vibrational bands of magnesium stearate occur in the range of 2918 - 2850 $cm^{-1}$, attributed to $CH_2$–$CH_3$ stretching vibrations, while the asymmetric stretching vibration bands of $COO^-$ are located at 1567 $cm^{-1}$ and 1464 $cm^{-1}$ [6]. In the case of the spectra of mixtures of piroxicam with magnesium stearate, changes in the shape of the bands can be observed in the range of 2950 - 2800 $cm^{-1}$ and 1700 - 1500 $cm^{-1}$. The low intensity of

the OH and NH group bands can indicate a possible interaction with hydrogen present in magnesium stearate by forming a hydrogen bond [7]. However, the use of PCA and HCA chemometric analysis allows for a clear statement of incompatibilities between piroxicam and magnesium stearate. Since the first two principal components PC1 and PC2 together explain more than 90% of the total variance, the results of the PCA analysis are presented using a biplot.

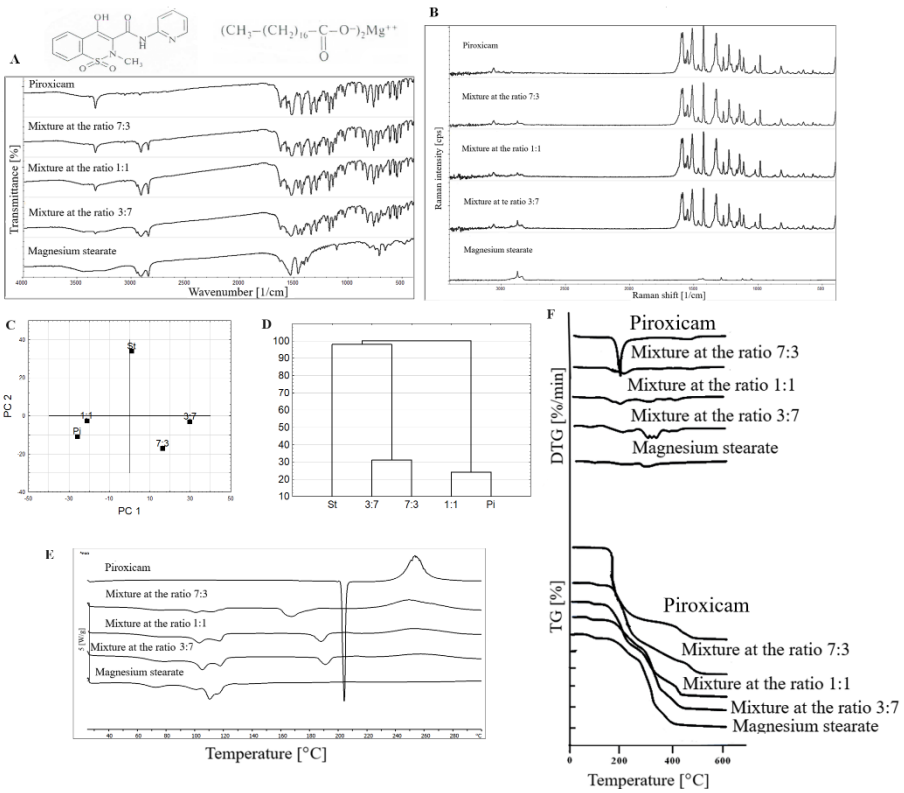



**Fig.1.** A) FTIR spectra, B) Raman spectra, C) PCA biplot, D) HCA dendrogram, E) DSC curves and F) TG/DTG curves of piroxicam (Pi), magnesium stearate (St) and their mixtures at the ratio 7:3, 1:1, 3:7.

The values for the first three principal components of PCs for mixtures of piroxicam with all excipients are listed in Table 1. The PCA biplot and HCA dendrogram for arbidol hydrochloride-magnesium stearate mixture and ingredients (Figs. 1C and 1D) show three distinct clusters. One cluster contains piroxicam and its mixture with magnesium stearate at a 1:1 ratio, and the next cluster contains two mixtures of piroxicam with magnesium stearate at a 7:3 and 3:7 ratio. In turn, the last cluster is formed only by magnesium stearate. This distribution of these samples indicates the existence of incompatibility of piroxicam with magnesium stearate. The detected incompatibility are confirmed by thermal analyses, i.e. DSC and TGA (Figs. 1E and 1F). DSC and TG curves of piroxicam - magnesium stearate mixtures reveal the absence of the characteristic peak of piroxicam at 203 °C. It should be mentioned that at a temperature of 203 °C (Fig. 1E), piroxicam melts and then decomposes. The course of

decomposition in the TG curves (Fig. 1F) of the mixtures also differs from that for piroxicam. On the other hand, in the case of the mixtures of piroxicam with chtosan or methycellulose the PCA and HCA results based on FTIR and Raman data confirmed the compatibility of these mixtures. Therefore, there were two clusters, one of piroxicam with its mixtures with excipient at a ratio of 7:3 and 1:1, and the other cluster was formed by excipient and a mixture at a ratio of 3:7 (data not shown).

**Table 1.** PCA calculations for binary mixtures of piroxicam with excipients.

| Excipient | PC1, Variance [%] | PC2, Variance [%] | PC3, Variance [%] |
|---|---|---|---|
| Chitosan | 92.8 | 5.6 | 0.8 |
| Methylcellulose | 76.5 | 20.4 | 1.9 |
| Magnesium stearate | 52.8 | 38.4 | 4.8 |

**Conclusions:** The results of spectroscopic studies supported by chemometric analysis (PCA and HCA) for mixtures of piroxicam with three excipients (chitosan, methylcellulose and magnesium stearate) at the ratios 7:3, 1:1 and 3:7 showed that one of these excipients, i.e. magnesium stearate was incompatible with piroxicam. Thermal analysis using DSC and TGA confirmed the FTIR and Raman spectroscopy results**.**

## References:

1. M.Ch. Adeyeye, H.G. Brittain, Preformulation in Solid Dosage Form Development. Informa Healthcare, New York, 2008.
2. R. Chadha, S. Bhandari, Journal of Pharmaceutical and Biomedical Analysis, 87 (2014) 82.
3. S.S. Bharate, S.B. Bharate, A.N. Bajaj, Journal of Excipients and Food Chemicals, 1 (2010) 3.
4. J.N. Miller, J.C. Miller, Statistics and Chemometrics for Analytical Chemistry, 6th ed., Pearson Education: Essex, UK, 2010.
5. S. Suresh, S. Gunasekaran, S. Srinivasan, Spectrochimica Acta Part A: Molecular and Biomolecular Spectroscopy, 138 (2015) 447.
6. A. Gumieniczek, A. Berecka-Rycerz, H. Trębacz, A. Barzycka, E. Leyk, M. Wesolowski, Molecules 27 (2022) 4283.
7. H.K. Stulzer, M.P. Tagliari, A.P. Cruz, M.A.S. Silva, M.C.M. Laranjeira, Pharmaceutical Chemistry Journal, 42 (2008) 215.

# FORMATION OF ZINC SULFATE AND ZINC ACETATE MONOLAYERS ON NANOSILICA SURFACE: MODIFICATION AND THERMAL TRANSFORMATIONS

**L. NOSACH[1], A. CHRZANOWSKA[2], E. SKWAREK[3]**, [1]Chuiko Institute of Surface Chemistry, NAS of Ukraine, Department of Amorphous and Structurally Ordered Oxides, Gen. Naumov Str. 17, 03164 Kyiv, Ukraine, [2]Maria Curie-Sklodowska University, Faculty of Chemistry, Institute of Chemical Sciences, Department of Physical Chemistry, M. Curie-Sklodowska Sq. 3, 20-031 Lublin, Poland, [3]Maria Curie-Sklodowska University, Faculty of Chemistry, Institute of Chemical Sciences, Department of Radiochemistry and Environmental Chemistry, M. Curie-Sklodowska Sq. 3, 20-031 Lublin, Poland.

**Abstract:** Nanotechnology has rapidly advanced, leading to the creation of novel structures and systems with diverse applications. Among nanomaterials, zinc oxide (ZnO) nanoparticles stand out for their versatility and low toxicity with extensive utility in gas sensing, biosensing, drug delivery, and more. Leveraging the unique properties of nanoscale fumed silica (nanosilica), the study investigates the formation of zinc sulfate and zinc acetate monolayers on nanosilica surface using the gas-phase solvate-stimulated mechanosorption modification method. Furthermore, the feasibility of achieving zinc oxide formation on the nanosilica surface through thermal transformations of zinc salts is examined, offering valuable insights into potential biomedical applications.

**Introduction:** The distinct physicochemical characteristics of nanomaterials have paved the way for the creation of novel structures, systems, and devices with vast potential applications. Notably, among these nanomaterials, metal oxide nanoparticles have demonstrated exceptional versatility, owing to their diverse properties and functionalities. Among the plethora of metal oxide nanoparticles, zinc oxide (ZnO) nanoparticles hold a prominent position due to their extensive range of applications. These applications span across fields such as gas sensing, chemical sensing, biosensing, cosmetics, optical and electrical devices, drug delivery, as well as in the treatment and prevention of dermatitis, diaper rash, bedsores, and skin damage [1-4].
Leveraging the advantageous properties of nanoscale fumed silica (nanosilica), innovative sorption-detoxication preparation such as ‘Silics’ have been developed [5]. To enhance its antimicrobial, anti-inflammatory, and regenerative properties, investigations have been conducted to explore the formation of zinc oxide on the surface of nanosilica.
Thus, the objective of this study was to investigate the formation of zinc sulfate and zinc acetate monolayers on the nanosilica surface using the gas-phase solvate-stimulated mechanosorption modification method. Furthermore, we aimed to explore the feasibility of zinc oxide formation on the nanosilica surface through thermal transformations of dispersed zinc salts.

**Experimental:** Initial fumed silica (nanosilica) with specific surface area ($S_{BET}$) of 342 $m^2/g$, was supplied from a pilot plant of the Chuiko Institute of Surface Chemistry,

Kalush, Ukraine. Zinc sulfate monohydrate ($ZnSO_4 \cdot H_2O$) and zinc acetate dihydrate ($Zn(CH_3COO)_2 \cdot 2H_2O$) were purchased from Merck KGaA, Darmstadt, Germany and used as modificators.

Nanocomposites comprising nanosilica and zinc salts were synthesized using the gas-phase solvate-stimulated mechanosorption modification (GSSMSM) method, a technique developed at the Chuiko Institute of Surface Chemistry of NAS of Ukraine in recent years [6]. This method involves subjecting the nanosilica/salt mixture to low-intensity mechanical activation within a controlled atmosphere. The mechanosorption modification of nanosilica with $ZnSO_4 \cdot H_2O$ and $Zn(CH_3COO)_2 \cdot 2H_2O$ was carried out in quantities corresponding to the amount of free silanol groups on the nanosilica surface (0.8 mmol of salt per 1 g of nanosilica). This process took place in a 0.5 L ceramic ball mill (ball size 2–3 cm, speed of 60 $min^{-1}$), under both dry and moist (500 mg water per 1 g of nanosilica) atmospheres for 5 h. Subsequently, all samples were air-dried at a temperature of 80 °C for 2 h.

IR spectral studies were conducted using a Thermo-Nicolet Fourier transform spectrometer (Nicolet Instrument Corporation, USA) in the reflection mode. Thermogravimetric studies were conducted using a Q-1500 D derivatograph (Paulik and Paulik, Hungary). X-ray diffraction patterns of the nanocomposites were obtained using a DRON-4-07 diffractometer (Russia) equipped with Cu Ka radiation and a Ni filter, following the Bragg-Brentano geometry for reflected rays.

**Results:** The mechanical treatment of a mixture of nanosilica and zinc sulfate in a dry atmosphere, similar to other salts [7-9], does not result in the formation of a nanocomposite. Instead, the sample contains salt in crystalline form.

The IR spectra of the silica-zinc sulfate nanocomposite obtained in a moist atmosphere indicates the perturbation of all free silanol groups (Fig.1a). Upon heating this nanocomposite in air at 300 °C, an absorption band of free silanol groups at 3750 $cm^{-1}$ emerges in the IR spectra (Fig.1b), suggesting the removal of water molecules that constitute a hydrate shell around salt ions. Following heating in air at 800 °C for 3 hours, the salt decomposes, yielding zinc oxide according to the scheme: $ZnSO_4 \rightarrow ZnO + SO_3$. Simultaneously, the intensity of the absorption band of free silanol groups in the range of 3750 $cm^{-1}$ increases in the IR spectra (Fig.1c).

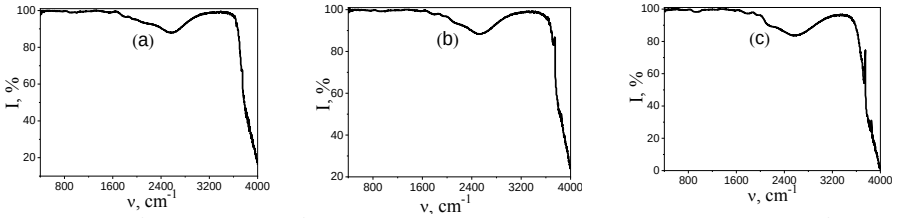



**Fig.1.** IR spectra of the silica-zinc sulfate nanocomposites obtained by the GSSMSM method (a), after heating in air at 300 °C (b) and at 800 °C (c).

X-ray diffraction patterns revealed that upon thermolysis of the salt at 800°C, the silica-zinc sulfate nanocomposite formed in a moist atmosphere produces not only zinc oxide but also a zinc silicate phase (Fig.2).

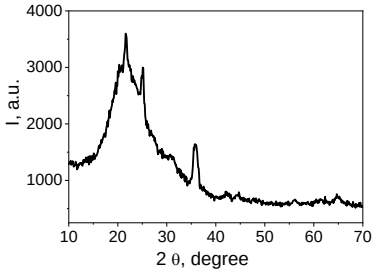



**Fig.2.** XRD patterns of the silica-zinc sulfate nanocomposite obtained by the GSSMSM method after heating in air at 800 $^{o}$C.

Zinc oxide can be obtained under milder conditions through the thermal decomposition of its another salt, zinc acetate. Thus, to create a silica-zinc oxide nanocomposite, we explored the formation process of a zinc acetate layer, following a similar approach used for zinc sulfate. However, mechanical treatment of a mixture of nanosilica and zinc acetate in a dry atmosphere does not result in the formation of a monolayer of salt on the nanosilica surface. In such a sample, the salt remains in the form of small crystals or clusters (Fig.3a).

In contrast, the nanosilica sample with zinc acetate, obtained under conditions of moist atmosphere, exhibits an absence of crystalline structure (Fig.3b) and perturbation of the absorption band at 3750 cm$^{-1}$ in the IR spectra. However, upon heating the silica-zinc acetate nanocomposite in air at temperatures of 550 and 800 $^{o}$C, the absorption band at 3750 cm$^{-1}$ in the IR spectra becomes more clearly visible, similar to the observations in silica-zinc sulfate nanocomposites.

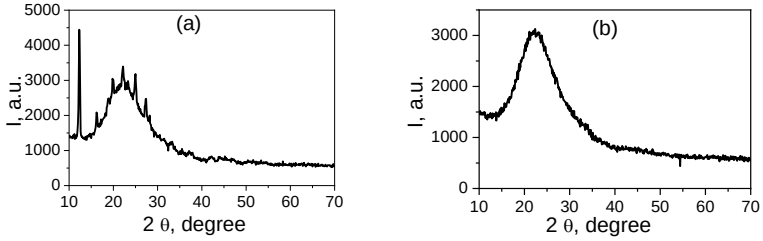



**Fig.3.** XRD patterns of nanosilica with zinc acetate after mechanical treatment in a dry (a) and moist (b) atmosphere.

The thermogravimetric analysis curves of a mechanical mixture of nanosilica with zinc acetate exhibit three peaks (Fig.4a). The initial peak at 89 °C signifies the desorption of physically sorbed water, primarily bound to the silica surface. The second peak at 171.8 °C corresponds to the water molecules from the crystal hydrate of the salt, while the third peak at 384 °C results from the thermolysis of acetate groups. Contrarily, on the thermogravimetric analysis curves of the silica-zinc acetate nanocomposite, the peak at 171.8 °C, indicative of crystal hydrate water molecules, is absent (Fig.4b). This suggests a distinct structural configuration of zinc acetate in this sample. The significant amount of water released within the 20-300 °C range (25% by mass) signifies the highly hydrated state of salt ions in the silica-zinc acetate nanocomposite, with approximately 8-10 water molecules per ion.

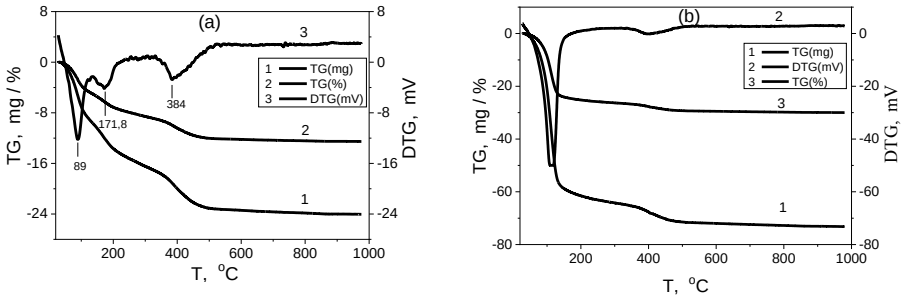



**Fig.4.** Thermogravimetric analysis curves of nanosilica with zinc acetate after mechanical treatment in a dry (a) and moist (b) atmosphere.

During the gas-phase solvate-stimulated mechanosorption modification of nanosilica, water molecules act as solvating agents for the salt. This process weakens the interactions between the ions of the salt. The high surface adsorption potential further facilitates the interaction of ions with the surface, leading to the formation of a monolayer coating. Due to the high activity of ions and their extensive hydration, they can exist in a nanodispersed state, forming a monolayer on the surface of a silica nanoparticle.

**Conclusions:** The application of the GSSMSM method demonstrates the ability to achieve monolayer coverage on the surface of silica nanoparticles, comprising highly hydrated ions from the salt, as indicated by: 1) the absence of peaks on the XRD patterns of the samples, 2) the perturbation of free silanol groups in the IR spectra, and 3) significant desorption of water observed during thermal analysis. Furthermore, under low-intensity mechanical activation in a dry atmosphere, clusters or particles of salts are formed rather than separated ions.

To achieve the formation of the zinc oxide phase, it is advisable to select zinc salts with the lowest decomposition temperature. This is necessary as the process may be complicated by the potential formation of the zinc silicate phase.

**Acknowledgements:** This work was supported by the International Visegrad Fund (ID 52300028). I wish to express my deep gratitude to the Doctor of Sciences E. Voronin for the statement of the problem and for his constant interest in my work. Thanks are due to E. Pakhlov for the help in carrying out this study.

**References:**

1. A. Umar, Y.-B. Hahn, Metal Oxide Nanostructures and Their Applications, American Scientific Publishers, 2015.
2. Y. Zhang, T.R. Nayak, H. Hong, W. Cai, Current Molecular Medicine, 13 (2013) 1633.
3. European Pharmacopoeia 5th ed., Council of Europe, Strasbourg, 2005.
4. The Merck index: An Encyclopedia of chemicals, drugs and biological, 2001.
5. O.O. Chuiko, O.O. Pentyuk, V. K. Pogorelyi, Enterosorbent Silics: Properties and Clinical Application, in Colloidal silica: fundamentals and applications, Taylor & Francis Group, Boca Raton London New York, 2006.
6. Patent №87126 UA 2009.
7. L. Nosach, E. Voronin, O. Oranska, E. Pakhlov, Metallofizika i Noveishie Tekhnologii, 33 (2011) 31.
8. E.F. Voronin, L.V. Nosach, V.M. Gun'ko, B. Charmas, Journal Physics and Chemistry of Solid State, 20 (2019) 22.
9. L. Nosach, H. Bodnar Yankovych, E. Skwarek, I. Melnyk, European Journal of Chemical Physics and Physical Chemistry, 25 (2024) e202300820.

# DETERMINATION OF UREA IN HIGH PROTEIN FEED MATERIALS AND COMPOUND AND COMPLEMENTARY FEED BY A SPECTROPHOTOMETRIC METHOD

**W. KOROL, G. BIELECKA, J. RUBAJ, H. NIEŚCIÓR**, National Research Institute of Animal Production in Kraków, National Laboratory for Feedingstuffs, Chmielna St. 2, 20-079 Lublin, Poland.

**Abstract:** The aim of the paper was to present the results of high protein feed materials (HPFM) and compound and complementary feed monitoring in the scope of the content of urea determined by the spectrophotometric method according to the Commission Regulation No 152/2009 [1]. In the years 2021-2023 total number of 157 samples, mainly feed yeast, soybean products, fish meal and compound and complementary feed were investigated in the feed monitoring program carried out by NRIAP [2]. Polish regulation allows to trace levels of urea in HPFM equal to 5 g/kg. In 69 samples of feed yeast urea content ranged from 0.2 g/kg to 24.6 g/kg in one sample urea exceeding 5 g/kg. In the rest HPFM urea levels were below 5 g/kg. For HPFM, non-compliant samples accounted for 0.8% of total samples tested.

**Introduction:** Urea ($CH_4N_2O$) is a feed additive used in ruminant feeding, category 'nutritional additives', functional group 'urea and its derivatives'. Maximum urea content in feed mixtures for ruminants equals 8.8 g/kg. Urea contains 46.6% of nitrogen, where 1% of urea in feed responds to the content of 2.92% of crude protein tested by Kjeldahl method (N x 6.25). Cases of adulteration of feed materials with urea were found in 2012, especially in the feed yeast and fish meal, in the scope of the feed monitoring programme carried out by National Research Institute of Animal Production (NRIAP). Urea has been tested in the Polish Feed Control Programme (PFCP) from 2013 and about 160 samples per year are investigated. The presence of urea in high protein feed materials (HPFM) exceeding the limit of quantification is unacceptable, taking into account measurement uncertainty. The limit of quantification (LOQ) was stated at 4 g/kg (the highest LOQ calculated in Veterinary Hygiene Establishments VHE) and measurement uncertainty of urea at the level of LOQ as 1 g/kg. According to PFCP the content of urea in HPFM exceeding 5 g/kg (LOQ plus uncertainty) is regarded as inconsistent with the requirements, yet only in case when urea has not been declared on the label. The legal basis to undertake action can be found in Regulation (EC) no 767/2009 of the European Parliament and of the Council [1], article 4, item 2a, according to which business operators placing feed on the market shall ensure that the feed is sound, genuine, unadulterated, fit for its purpose and of merchantable quality. In the years 2012-2018 high levels of urea cases in HPFM were found [3]. The aim of the paper was to present the test results of monitoring high-protein feed materials (HPFM), performed by NRIAP in the years 2021-2023, in the scope of the content of urea. Moreover the results of urea testing in compound and complementary feed, mainly for ruminant, were presented.

**Experimental:** The tests were carried out in the years 2021-2023 in National Laboratory for Feedingstuffs in Lublin. Total number of 131 samples of HPFM were tested, mainly feed yeast, soybean meal and cake and fish meal. Investigated samples (26) also included complete and complementary feeds. Urea was tested by the official spectrophotometric method with 4-dimethyloaminobenzaldehyde (4-DMAB) at λ=435 nm, given in the Commission Regulation No 152/2009 [1]. The limit of quantification (LOQ) of the method equals 2 g/kg. Expanded measurement uncertainty U (k=2, P=95%) on the level of less than 10 g/kg equals ±1 g/kg and ±10% (R) for the content ≥10 g/kg. Recovery of the method calculated on the base of collaborative study organized lately by JRC ranged from 102% to 111% (ruminant feed). Crude protein equivalent for urea was calculated multiplying the urea content by the coefficient of 2.92.

**Results:** Table 1 presents the results of testing urea content in HPFM during the implementation of feedingstuff monitoring programme in the years 2021-2023. The study including 131 HPFM samples. In one sample of feed yeast, revealed urea adulteration amounting to more than 5 g/kg, which was equivalent to 1.4% of the analyzed yeast samples and to 0.8% of total HPFM. In the samples of soybean meal, fish meal and meat meal the mean content of urea was lower than the method's LOQ (2.0 g/kg) and amounted, respectively, to 0.93 g/kg, 1.77 g/kg and 0.99 g/kg. The samples of these materials and other HPFM did not reveal any adulteration with urea exceeding 5 g/kg. The mean values calculated amounted 1,50 g/kg. Urea content in the samples not exceeding the accepted level of 5.0 g/kg (131 samples) ranged between 0.2 g/kg and 4.8 g/kg, with mean value of 1.50 g/kg and standard deviation of 0.90 g/kg. The median was generally lower than the mean value, suggesting the dominating effect of samples with trace content of urea, below the method's LOQ.

**Table 1.** Results of urea testing in the samples of HPFM during monitoring programme in 2021-2023.

| Item | n, total /positive | from – to g/kg | mean value, g/kg | SD g/kg | median g/kg | crude protein Equivalent, g/kg |
|---|---|---|---|---|---|---|
| Feed yeast | 69/11 | 0.2-24.6 | 1.84 | 2.87 | 1.90 | 0.5-71.8 |
| Soybean meal | 29/0 | 0.2-2.0 | 0.93 | 0.69 | 0.80 | 0.6-5.8 |
| Meat meal | 7/0 | 0.5-1.4 | 0.99 | 0.35 | 1.00 | 1.5-4.1 |
| Fish meal | 19/2 | 0.6-2.4 | 1.77 | 0.57 | 2.00 | 1.7-7.0 |
| Other HPFM | 7/2 | 0.3-4.8 | 1.98 | 1.44 | 2.00 | 0.9-14.0 |
| Total | 131/15 | 0.2-24.6 | 1.50 | 0.80 | 1.65 | 0.5-71.8 |

n – number of samples; positive sample contains urea ≥ 0.2 g/kg

Table 2 demonstrates the results of testing urea content in 26 compound feed and complementary feed samples. Urea levels in complementary feed for cattle ranged from 14.3 to 35.4 g/kg with mean value 26.6 g/kg and were typical contents consistent with the product labels. Complementary feed contain higher levels of nutrients and feed additives including urea then compound feed and are not directly fed to animals but after mixing with feed materials. Several samples of compound feed for cattle were investigated and in none of them the urea content exceeds the maximum content of 8.8 g/kg. Trace amounts of urea, ranging from 0.2 to 0.4 g/kg, were found in compound feed for pigs, below LOQ of the method.

**Table 2.** Results of urea testing in compound feed and complementary feed during monitoring programme in 2021-2023.

| Item | n, total /positive | from – to g/kg | mean value, g/kg | SD g/kg | median g/kg | crude protein Equivalent, g/kg |
|---|---|---|---|---|---|---|
| Complementary feed for cattle | 17/17 | 14.3-35.4 | 26.6 | 5.29 | 25.8 | 41.8-103 |
| Compound feed for cattle | 6/6 | 2.0-8.4 | 4.6 | 2.82 | 4.25 | 5.8-24.5 |
| Compound feed for pigs | 3/1 | 0.2-0.4 | 0.27 | 0.11 | 0.20 | 0.6-1.2 |
| Total | 26/24 | 0.2-35.4 | 4.39 | 8.24 | 20.0 | 0.6-103 |

n – number of samples

Incompliant samples of HPFM during Polish feed supervision in the scope of urea testing in the years 2020-2023 are presented in Table 3. Total number of 160 samples were tested yearly. Number of adulteration cases has been decreasing, from 8 cases in 2020 (5.3%) to no case in 2022 and 2023 (0%), with 2.4% on average. However, in 2023 cases of non-compliance were identified for compound feed for ruminants.

**Table 3.** Non-compliance of HPFM samples during Polish feed supervision in the scope of urea.

| Item/year | 2020 | 2021 | 2022 | 2023 | 2023* |
|---|---|---|---|---|---|
| Urea, non-compliance, n | 8 | 6 | 0 | 0 | 4* |
| Urea, non-compliance, % | 5.3 | 4.1 | 0 | 0 | 2.8* |

n – number of incompliant samples; * concerns compound feed for ruminants

**Conclusions:** In the case of monogastric animals urea is an useless substance which causes redundant burden to the organism. Polish regulation accepts urea content in HPFM no higher than 5 g/kg. Samples with higher urea level are considered as incompliant, but only if urea is not declared on the label. The labeling of feed should not mislead the user. Mean degree of adulteration by urea in high risk HPFM in the last years tested in the Institute (NRIAP) monitoring program (2016-2020) was higher than in Polish feed supervision and equals to 15.0% in five years period (3.0% per year ). A higher degree of urea adulteration found in HPFM samples used in the monitoring programme implemented by the Institute may have resulted from the sampling method. The programme of the Institute took into account signals sent by the users, such as a low price of standard HPFM, some doubts concerning the origin of the samples or their quality, a potentially higher quality (e.g. higher content of crude protein) at a standard price. Within the official supervision feed samples are taken at the amounts proportional to the manufacturing capacity in a given area (e.g. in the area of a voivodship), and the risk analysis carried out in the general form referred to individual cases of adulteration to a lower degree. Still, potential sources of threats have been determined, which are being efficiently controlled within the official supervision, e.g. border checkpoints. It has been noted on the basis of long-standing observations that in some countries urea or ammonium compounds are used as a substrate for manufacturing feed yeast and their remains may be left in the end product in case of incomplete purifying process.
In such a case there is a problem with a lacking claim stating the content of urea on the label rather than intentional adulteration with urea. Feed yeast contaminated with urea

may be used in feeding ruminants (taking into account the urea content) yet it should not be served to monogastric animals.

This would lead to improved protection of the HPFM market and have a positive effect on health and, indirectly, on the quality of animal products; it would also enhance product integrity and reduce problems related to customer loss, sale reduction and recalls of products (Feed Fraud Information, 2017 [2]). HPFM contaminated with urea reveal a lower content of amino acids, as compared with standard feed materials. The degree of reducing amino acid content depends on the level of urea adulteration [3].

In the presented example urea adulteration would result in animals' insufficient demand coverage for amino acids found in a feed mixture manufactured with the use of this type of material. The results of our studies suggested that in case of feed mixture analyses the measurement of absorbance with the wave length of $\lambda$=435 nm let us obtain lower results regarding the urea content, from 0.4 g/kg to 2 g/kg. The differences were as a rule lower than quantification limit (2 g/kg) and did not affect significantly the assessment of results. Different results were obtained by Pibarot and Pilard [4], who used the spectrophotometric method with 4-DMAB while testing pet-food and observed urea content higher than 2 g/kg to 1.1 g/kg as compared to the results of studies using the enzymatic and LC/MS methods. However, in case of pet-food products rich in fat and subjected to pressure and thermal processing (extrusion) there may occur a problem with obtaining clear extracts, and even their slight cloudiness may lead to noting increased, erroneous test results. Our experience suggests that it is useful to centrifuge the cloudy solution after evoking the color. The aim of the implemented analyses was to detect the presence of urea in HPFM amounting to more than 5 g/kg and the spectrophotometric method used in the tests proved to be adequate to this purpose. Presented data confirmed the need of testing HPFM for urea. The challenge for official control, apart from covering possibly representative feed samples for urea monitoring, is the need of testing of ammonium compounds in HPFM contaminated with urea [5,6].

## References:

1. Commission Regulation (EC) no 152/2009 of 27 January 2009 laying down the methods of sampling and analysis for the official control of feed, O.J. L 54/1, 26.02.2009.
2. Feed Fraud Information document, GMP+ D 1.3, January 2017, GMP+ International, The Netherlands.
3. H. Nieściór, M. Majewska, W. Korol, G. Bielecka, J. Rubaj, S. Walczyński**.** Metody spektrofotometryczne w kontroli zafałszowań wysokobiałkowych materiałów paszowych. Rozdział w monografii, red. prof. dr hab. Z. Hubicki pt. „Nauka i przemysł - metody spektroskopowe w praktyce, nowe wyzwania i możliwości". UMCS Lublin 2019, 511.
4. P. Pibarot, S. Pilard, American Journal of Analytical Chemistry, 3 (2012) 613.
5. Regulation (EC) no 1831/2003 of the European Parliament and of the Council of 22. September 2003 on additives for use in animal nutrition, O.J. L 268/29, 18.10.2003.
6. Regulation (EC) no 767/2009 of the European Parliament and of the Council of 13 July 2009 on the placing on the market and use of feed, O.J. L 229/1, 1.9.2009.

# HYDROTALCITE MODIFIED BIOCHARS (Zn/Al-LDH@BC, Co/Al-LDH@BC) AS AN EXAMPLE OF EFFECTIVE SORBENTS FOR REMOVING CERIUM(III) IONS FROM AQUEOUS MEDIA

**J. BĄK, D. KOŁODYŃSKA**, Department of Inorganic Chemistry, Institute of Chemical Sciences, Faculty of Chemistry, Maria Curie-Skłodowska University, Maria Curie-Skłodowska Sq. 2, 20-031, Lublin, Poland.

**Abstract:** To determine the effectiveness of using hydrotalcite modified biochars (Zn/Al-LDH@BC and Co/Al-LDH@BC) in the sorption process of cerium(III) ions, studies were performed on the effects of: pH, phase contact time, initial solution concentration and temperature. The results were used to determine the optimal conditions for the sorption process, for which the removal of Ce(III) ions was the most effective.

**Introduction:** The demand for rare earth elements (REE) increases in all types of industries, resulting in the resources depletion. Ecological solutions for their recovery and reuse are imperative. Other methods such as co-precipitation, ion exchange, and solvent extraction are used however, they face challenges like secondary pollution and high costs, prompting the search for better alternatives. Adsorption emerges as a promising method due to its non-toxicity, reusability, and abundance of natural adsorbents. The research focuses on finding sorbents, like biochars, capable of efficient removal of REE ions from aqueous solutions. Biochars, derived from waste materials, offer homogeneous composition and high adsorption capacity due to such surface functional groups as hydroxyl and carboxyl ones [1-4].
Hydrotalcite was used as an example of a biochar modifier. Hydrotalcite is a mixed layered magnesium hydroxide aluminum with the summary formula: $Mg_6Al_2(OH)_{16}CO_3{\cdot}4H_2O$, a naturally occurring mineral. In hydrotalcite, divalent cations ($Mg^{2+}$) are substituted by cations of higher valence ($Al^{3+}$), which leads to the appearance of a positive charge on layers. This charge is compensated by the hydrated anions found in the interlayer space. The name "hydrotalcite" is more and more often used to describe the synthetic group equivalents or compounds mimicking a characteristic structure so-called layer double hydroxides (LDH) of the general formula of $[M^{2+}_{1-x}\ M^{3+}_{x}\ (OH)_2]^{x+}\ (A^{n-})^{x/n}{\cdot}mH_2O$, where $M^{2+}$ and $M^{3+}$ are the divalent and trivalent metal cations located on the sheets, x ($M^{3+}/M^{2+}+M^{3+}$) is the molar fraction of trivalent metals, n is the valence of anion in the interlayer space and m is the number of hydrated water molecules. The condition for formation of the proper hydrotalcite structure is the use of metal cations with similar ionic radii, e.g. $Mg^{2+}$, $Ni^{2+}$, $Cu^{2+}$, $Zn^{2+}$, $Mn^{2+}$ and $Fe^{3+}$, $Al^{3+}$, $Cr^{3+}$. In addition, the appropriate proportions of di- and trivalent metals must be maintained, which is determined by the mole fraction x ranging from 0.2 to 0.33. One of the most commonly used methods of LDH synthesis is co-precipitation at constant pH. It consists in slow addition of the solution containing di- and trivalent metal salts to the reactor containing water (aqueous sodium carbonate solution is also often used). At the same time, an alkaline solution (usually NaOH) is also added to the reactor to maintain a constant pH. The pH range in which the synthesis takes place should be selected so that both metals precipitate in the form of hydroxides [5-7].

**Experimental:** The preparation of hydrotalcite modified biochars: Zn/Al-LDH@BC and Co/Al-LDH@BC, was conducted with a molar ratio of 3/1 for $M^{2+}/M^{3+}$. Metal nitrates in the second oxidation state were weighed into a 200 mL volumetric flask to obtain a solution concentration of 0.45 mol/L. Additionally, an appropriate amount of hydrated aluminum nitrate, equivalent to a concentration of 0.15 mol/L (solution 1), was weighed into the same flask. Subsequently, 10 g of biochar was added to the prepared solution. Layered double hydroxides were precipitated by gradually adding a solution of 2 mol/L NaOH and 1 mol/L $Na_2CO_3$ (solution 2) until the pH reached 10-11. After stirring for 30 minutes and aging for 24 hours, the suspension was washed, filtered, and dried at 343 K for 20 hours before grinding. The investigations on cerium(III) ions sorption efficiency from the aqueous media were carried out using the static method in the 100 mL conical flasks by adding 0.04 g of hydrotalcite modified biochars (Zn/Al-LDH@BC and Co/Al-LDH@BC) and shaking with 20 mL of the solution at 293 K. Examining the impact of pH in the range of 2 to 6 was the first stage in identifying the process conditions. The effects of the phase contact time, which ranged from 1 to 360 minutes, and the starting solution concentration, which ranged from 50 to 200 mg/L, were determined in the following step.

**Results:** The study of the effects of solution pH on the sorption process of Ce(III) ions on Zn/Al-LDH@BC and Co/Al-LDH@BC is shown in Figure 1. Table 1 presents the obtained values of equilibrium capacities of Ce(III) ions along with the leaching values of hydrotalcite building ions (presented in the form of concentrations).

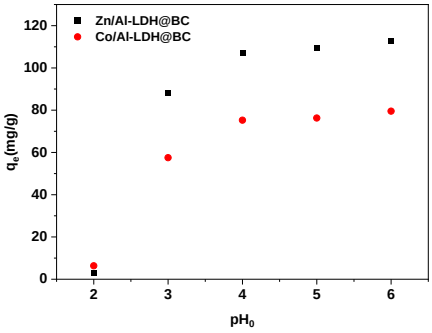



**Fig.1.** Dependence of the equilibrium capacity on the initial pH for the cerium(III) ions sorption on Zn/Al-LDH@BC and Co/Al-LDH@BC (t 360 min., $C_0$ 200 mg/L, 180 rpm, 293 K).

**Table 1.** Equilibrium capacitance values for Ce(III) ions sorption on Zn/Al-LDH@BC and Co/Al-LDH@BC.

| $pH_0$ | Zn/Al-LDH@BC | | | | Co/Al-LDH@BC | | | |
|---|---|---|---|---|---|---|---|---|
| | $pH_k$ | $q_e$ [mg/g] | Leaching of | | $pH_k$ | $q_e$ [mg/g] | Leaching of | |
| | | | Al [mg/L] | Zn [mg/L] | | | Al [mg/L] | Co [mg/L] |
| 2 | 4.01 | 2.99 | 173.69 | 436.38 | 3.80 | 6.37 | 149.74 | 460.95 |
| 3 | 5.55 | 88.39 | 2.28 | 97.32 | 5.24 | 57.52 | 1.77 | 23.92 |
| 4 | 5.78 | 106.87 | 0.57 | 35.53 | 5.26 | 75.25 | 0.20 | 14.76 |
| 5 | 5.94 | 109.54 | 0.39 | 35.28 | 5.48 | 76.28 | 0.16 | 15.20 |
| 6 | 5.96 | 112.79 | 0.50 | 27.96 | 5.58 | 79.53 | 0.03 | 15.06 |

The sorption process with the greatest efficiency occurs at pH 6 and this pH value was selected for further research. Under this condition the $q_e$ values are: 112.79 mg/g for Zn/Al-LDH@BC and 79.53 mg/g for Co/Al-LDH@BC. The lowest values of equilibrium capacities were obtained for pH 2. Moreover, strongly acidic reaction environment (pH 2) favours leaching aluminum ions and elements building hydrotalcite.
After choosing pH 6 as optimum, the dependence of phase contact time and initial concentration of solution was investigated, as illustrated in Fig.2.

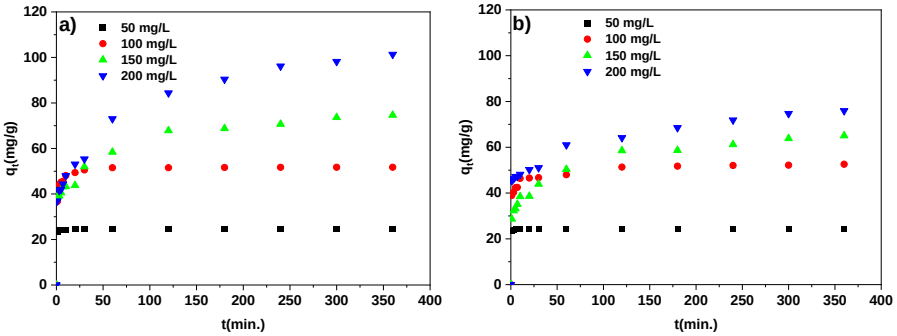



**Fig.2.** Dependence of the phase contact time and initial concentration of solution on Ce(III) ions sorption on a) Zn/Al-LDH@BC and b) Co/Al-LDH@BC (t 1-360 min., $C_0$ 50-200 mg/L, pH 6, 180 rpm, 293 K).

Based on the data it can be stated that the amount of adsorbed ions increases with the increasing phase contact time and initial concentration of solution and the lower the initial concentration, the faster it is equilibrated. For Zn/Al-LDH@BC the amounts of adsorbed Ce(III) ions were equal to: 24.58, 51.75, 74.67 and 102.31 mg/g for the concentrations: 50, 100, 150 and 200 mg/L, respectively. For the same initial concentrations, the sorption capacities for Co/Al-LDH@BC were: 24.51, 52.57, 65.06 and 75.93 mg/g. Comparing the amount of adsorbed cerium(III) ions, a greater efficiency of zinc-aluminum hydrotalcite modified biochar was found.
Temperature is another significant parameter in the adsorption process (Fig.3.).

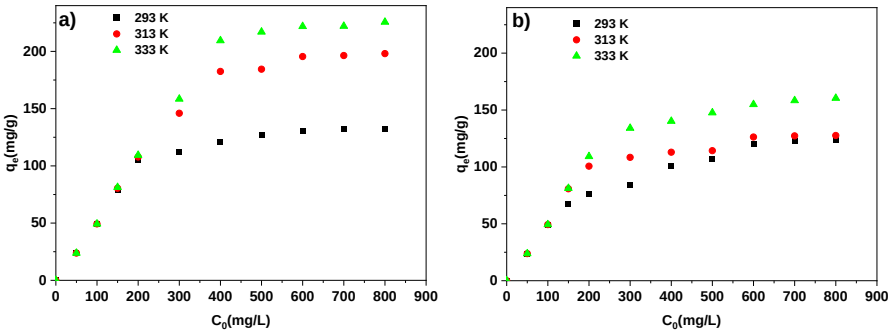



**Fig.3.** Effect of temperature of Ce(III) ions sorption on a) Zn/Al-LDH@BC and b) Co/Al-LDH@BC (t 360 min., pH 6, 180 rpm).

The increase in the cerium(III) sorption with the increasing temperature indicates that the Ce(III) sorption on the hydrotalcite modified biochars is encouraged at high temperatures. Nevertheless, for real wastewaters, the preferred increase in the cerium(III) ions removal efficiency with temperature is not practical. It would result in higher processing expenses. Even at room temperature, the attained high equilibrium capacities indicate satisfactory results.

**Conclusions:** The obtained satisfactory amounts of adsorbed cerium(III) ions on the hydrotalcite modified biochars confirm that these sorbents can be used for waters and wastewaters treatment.

**Funding:** This paper was financially supported by the National Science Centre in accordance with decision No. 2023/07/X/ST5/00784.

**References:**

1. F. Zhao, E. Repo, Y. Meng, X. Wang, D. Yin, M. Sillanpää, Journal of Colloid and Interface Science, 465 (2016) 215.
2. D. Fila, Z. Hubicki, D. Kołodyńska, Chemical Engineering Journal, 446 (2022) 137245.
3. Y. Chen, X. Zhang, W. Chen, H. Yang, H. Chen, Bioresource Technology, 246 (2017) 101.
4. J. Bąk, S. Gustaw, D. Kołodyńska, Chemical Engineering Journal, 470 (2023) 144309.
5. L. Dong, S. Li, Y. Jin, B. Hu, G. Sheng, Applied Surface Science, 567 (2021) 150794.
6. W. Liao, X. Zhang, S. Jingai, H. Yang, S. Zhang, H. Chen, Fuel Processing Technology, 235 (2022) 107389.
7. T. Wang, C. Li, C. Wang, H. Wang, Colloids and Surfaces A, 538 (2018) 443.

# X-RAY PHOTOELECTRON SPECTROSCOPY AS AN EFFECTIVE METHOD FOR QUALITATIVE AND QUANTITATIVE SURFACE ANALYSIS OF CARBON ADSORBENTS DERIVED FROM HERBAL MATERIALS

**D. PALUCH, A. BAZAN-WOŹNIAK, R. PIETRZAK**, Adam Mickiewicz University in Poznań, Faculty of Chemistry, Department of Applied Chemistry, Uniwersytetu Poznańskiego 8 Str., 61-614 Poznań, Poland.

**Abstract:** In this study, two carbon adsorbents were obtained through chemical activation of fennel seeds using sodium carbonate (Na-AC) and potassium carbonate (K-AC). The surface composition of the carbon adsorbents was determined using X-ray photoelectron spectroscopy. The tests carried out indicate that the activated carbon produced by chemically activating fennel seeds with potassium carbonate had a higher elemental carbon content (94.64%) than the adsorbent produced in a similar manner using sodium carbonate as an activator (92.62%). Additionally, the K-AC adsorbent exhibits a greater variety of both carbon and oxygen bonds on its surface.

**Introduction:** Activated carbon is a highly porous adsorbent that is widely used due to its expansive surface area and potent surface reactivity. It has applications in various industries, including drinking water purification, air and gas filtration, and the food industry. The effectiveness of activated carbon in removing contaminants from drinking water, such as organic substances, colorants, and trace chemicals, is widely acknowledged [1]. Utilizing bio-waste in production of sorptive materials has a beneficial effect on environmental conservation by decreasing solid waste and simultaneously generating cost-effective activated carbons with the ability to eliminate pollutants [2]. Carbon materials have been extensively researched and utilised. X-ray photoelectron spectroscopy (XPS) is a highly effective method for measuring surface properties, making it an ideal tool for chemical imaging of carbon materials [3].
X-Ray Photoelectron Spectroscopy is a key surface analytical technique in which X-rays are directed at the surface of a material, allowing the kinetic energy of the emitted electrons to be measured. Its power as an analytical method lies in two key features: its surface sensitivity and its ability to reveal the chemical state of the elements within the sample [4]. With the exception of hydrogen and helium, XPS can detect all elements, facilitating its widespread application in the study of materials ranging from plastics to textiles, soil to semiconductors. As surfaces determine interactions with other materials, factors such as surface wettability, adhesion, corrosion, charge transfer and catalysis are dependent on surface properties [5].
The aim of this study was to produce activated carbons from fennel seeds biomass through chemical activation using sodium and potassium carbonate. Subsequently, an X-ray photoelectron spectroscopy for qualitive and quantitive analysis of surface was conducted for the resulting activated carbons.

**Experimental:** The precursor material used for producing activated carbons was fennel seeds, which did not met the quality control standards and were therefore considered

waste from the herbal industry. The initial characterization of the fennel seeds showed a volatile matter content of 7.9 wt.%, a moisture content of 5.3 wt.%, and an ash content of 5.8 wt.%. The precursor material underwent a 24-hour drying period and was then divided into two parts for further processing. The fennel seeds were initially divided into three parts and each part was impregnated with either $Na_2CO_3$ (Na-AC) or $K_2CO_3$ (K-AC) as an activator, in a 1:2 precursor to impregnator ratio.The impregnated precursors were then heated in a tube furnace to 750 ºC and maintained at that temperature for 45 minutes. The process of chemical activation took place in a nitrogen atmosphere flowing at a rate of 330 mL/min. The samples were washed with a hot 5% hydrochloric acid solution and then neutralized with approximately 10 liters of boiling distilled water until a neutralized filtrate was obtained. Finally, the activated products were dried until a constant mass was achieved.
X-ray photoelectron spectroscopy (XPS) was carried out using an ultrahigh vacuum photoelectron spectrometer based on a Phoibos150 NAP analyzer (Specs). The analytical chamber was operated in vacuum at a pressure close to $5\times10^{-9}$ mbar, and the sample was irradiated with nonmonochromatic Al Kα radiation (1486.6 eV). Any charge that occurred during the measurements (due to incomplete neutralization of ejected surface electrons) was compensated for by rigidly shifting the entire spectrum by the distance needed to set the C 1s binding energy assigned to the random carbon to an assumed value of 284.8 eV.

**Results:** The XPS analysis of the resulting adsorbents revealed a surface composed entirely of carbon and oxygen. Figures 1 and 2 show the high-resolution XPS spectra of C 1s and O 1s. The analysis revealed that the chemical activation of fennel seeds with potassium carbonate resulted in a material with a higher elemental carbon content (94.64%) compared to activation with sodium carbonate under the same conditions (92.62%). Additionally, the K-AC adsorbent had a lower oxygen content (5.36%) than the Na-AC sample (7.38%). Figure 3 shows an example of the surface structure of activated carbon.

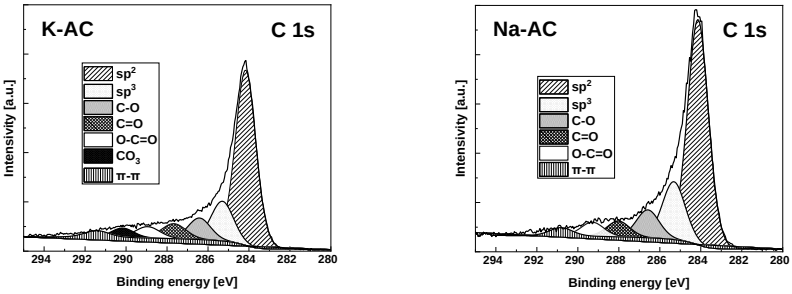



**Fig.1.** The XPS carbon (C 1s) spectra of obtained activated carbon samples.

As shown in Fig.1, the C 1s spectra could be resolved into five to six peaks at binding energy about 284.2, 285.3, 286.5, 287.9, 289.4, 290.2 and 291.5 eV, assigned to $sp^3$, $sp^2$, aromatic C-O, ketone C=O, carboxylic O-C=O, carbonate $CO_3$ and π-π bond,

respectively [6]. The O1s spectra could be resolved into two to three peaks. The peaks at the lowest binding energy - about 531 eV are attributed to oxygen double bonded with carbon in carbonyl groups (C=O), those at 532.6 eV are related to C-O groups and those at 535.7-536.5 eV are related to hydroxyl groups (C-OH) [3].

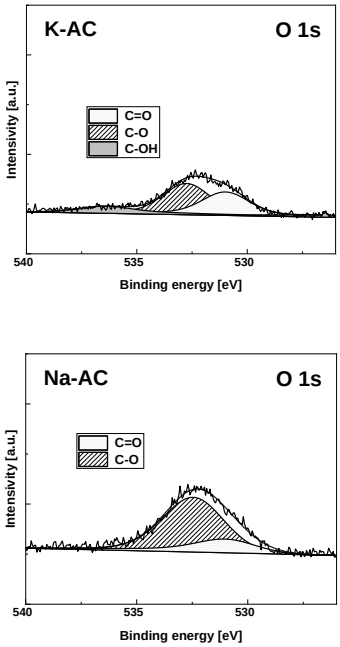



**Fig.2.** The XPS oxygen (O 1s) spectra of obtained activated carbon samples.

During the activation stage, the potassium or sodium compound generated would permeate the internal structure of the char matrix, expanding pre-existing pores and generating new porosities [7]. The study shown that potassium carbonate contributed to the formation of a greater variety of carbon and oxygen atoms on the surface of the resulting sorption material. The XPS C 1s spectra of the K-AC sample has a peak originating from carbon dioxide ($CO_3$), which is absent in the spectrum of the Na-AC sample. Upon analysing Figure 2, it is evident that the NA-AC sample lacks a peak from the C-OH group. However, the C 1s spectrum of this sample shows peaks from the C-O and O-C=O groups, indicating the presence of these groupings in the carbonaceous material. This phenomenon is likely due to the high intensity of the C-O peak, which overlaps the C-OH band and prevents its isolation.

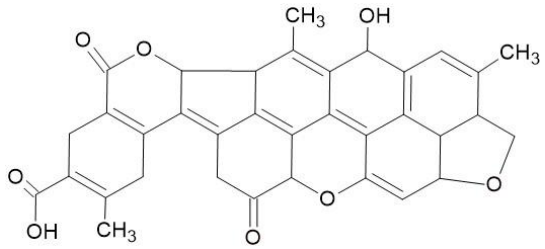



**Fig.3.** Example of the surface structure of activated carbon.

After analysing the results presented in Table 1, it is clear that the obtained samples exhibit a greater total peak area of carbon atoms bonding with carbon or hydrogen ($sp^2$, $sp^3$) than those bonding with oxygen (C-O, C=O, O-C=O and CO3). Meanwhile, upon analysing the results obtained for the Na-AC adsorbent, it can be observed that this material has a higher content of $sp^2$ and $sp^3$ bonds on the material surface than the other sample.

**Table 1.** The C 1s and O 1s deconvolutions of obtained samples.

| Spectra | Type of atom | Binding energy [eV] | K-AC % At | Na-AC % At |
|---|---|---|---|---|
| C 1s | C=C $sp^2$ | 284.16 | 59.88 | 62.19 |
| | C-C $sp^3$ | 285.34 | 14.95 | 17.50 |
| | C-O | 286.51 | 8.17 | 8.44 |
| | C=O | 287.90 | 6.48 | 5.00 |
| | O-C=O | 289.39 | 5.08 | 4.23 |
| | $CO_3$ | 290.22 | 4.50 | - |
| | π-π | 291.47 | 1.94 | 2.64 |
| O 1s | C=O | 531.02 | 38.21 | 21.12 |
| | C-O | 532.66 | 50.64 | 78.88 |
| | C-OH | 536.49 | 11.16 | - |

**Conclusions**: XPS is a helpful analysis tool to study the surface of carbon materials. The study showed that the surface of sorption materials obtained by chemical activation of herbal residues - fennel seeds with sodium and potassium carbonate, was primarily composed of carbon, with a minor oxygen content ranging from 5.36% to 7.38%. XPS analysis revealed the presence of six to seven different types of carbon atoms and two to three types of oxygen atoms on the surface of the materials obtained. The samples obtained showed a higher total peak area of carbon atoms bonding with carbon or hydrogen than those bonding with oxygen. Furthermore, the peak intensity obtained from the analysis confirmed that the K-AC sample had a higher carbon content, while the Na-AC sample had a higher oxygen content.

## References:

1. M.S. Reza, , C.S. Yun, S. Afroze, N. Radenahmad, M.S.A Bakar, R. Saidur, A.K. Azad, Arab Journal of Basic and Applied Sciences, 27 (2020) 208.
2. M.F. Hassan, M.A. Sabri, H. Fazal, A. Hafeez, N. Shezad, M. Hussain, Journal of Analytical and Applied Pyrolysis, 145 (2020) 104715.
3. X. Chen, X. Wang, D. Fang, Fullerenes, Nanotubes and Carbon Nanostructures, 28 (2020) 1048.
4. F.A. Stevie, C.L. Donley, Journal of Vacuum Science & Technology A, 38 (2020).
5. M. Aziz, A.F. Ismail, Membrane Characterization, Elsevier, 2017.
6. G. Simões dos Reis, C. Mayandi Subramaniyam, A. D. Cárdenas, S. H. Larsson, M. Thyrel, U. Lassi, F. Garcia-Alvarado, ACS omega, 7 (2022) 42570.
7. M. Sevilla, N. Díez, A.B. Fuertes, ChemSusChem, 14 (2021) 94.

# ACTIVATED CARBONS OBTAINED FROM CORN DIGEST AS ADSORBENTS OF PHARMACEUTICAL POLLUTANTS

**R. WOLSKI**, **A. BAZAN-WOŹNIAK, R. PIETRZAK**, Adam Mickiewicz University in Poznań, Faculty of Chemistry, Department of Applied Chemistry, Uniwersytetu Poznańskiego St. 8, 61-614 Poznań, Poland.

**Abstract:** Activated carbons were obtained from the waste material that is corn digest and their adsorption capacities were tested against diclofenac as an example of contamination by pharmaceutical compounds. Activated carbons were obtained by a two-step process. In the first stage, carbonizate was obtained by pyrolysis and then physical activation of the material was performed under a $CO_2$ atmosphere. Microporous materials with specific surface areas of 456 and 732 $m^2/g$ and a predominance of acid groups on their surface were obtained. Adsorption studies have shown that the activated carbons obtained from corn digest can be successfully used in the processes of removing iodine and diclofenac from aqueous solutions.

**Introduction:** Pharmaceutical production is a profitable and rapidly growing industry. At the same time, there is a global increase in the consumption of pharmaceuticals. Estimates show that global consumption of pharmacologically active substances is currently more than 100,000 tons and is on an upward trend. After use, some of the active substances from drugs are excreted from the body. This results in the transfer of active substances and their metabolites into the environment, which poses a potential threat to aquatic ecosystems as well as public health. Long-term exposure of aquatic organisms to these substances can have adverse effects such as endocrine disruption, toxicity and also causes significant disruption of ecological systems. It is therefore necessary to treat wastewater containing residues of pharmaceutical substances [1].
The use of activated carbon in the removal of pharmaceutical organic contaminants is currently one of the most effective purification methods compared to other adsorbents [2]. Activated carbons are made from a material characterized by a high elemental carbon content. The manufacturing process is directed to obtain: good affinity for various groups of chemical compounds, large surface area, well-developed micro and mesoporous structure and regeneration ability [3]. Currently, the development of research has been directed towards obtaining activated carbon from renewable resources. These include biomass, natural materials and even organic waste [4].

**Experimental:** The precursor of activated carbons was the residue from the fermentation process of corn (*Zea mays*) stalks and leaves, which was used to obtain methane. The residue was obtained from the biogas plant in granular form with different grain sizes. The precursor was sieved and a fraction with a granulation of 2-3 mm, dried at 110 °C for 24 hours to a solid mass, was taken for further studies.
In the first step, the precursor was subjected to pyrolysis. The process was carried out in a conventional furnace at 500 °C for 60 minutes, equipped with a tubular quartz reactor, under a nitrogen atmosphere. The gas flow rate was 170 ml/min and the temperature rise was 10 °C/min.

The resulting biochar was subjected to activation with carbon dioxide. The sample was placed in a tube furnace heated to 700 °C or 800 °C and activated for 60 min at a $CO_2$ flow rate of 250 ml/min. The sample was then removed from the heating zone and cooled to room temperature in a $CO_2$ atmosphere. After activation, the samples were washed several times with portions of distilled water and dried at 110 °C. The obtained active biocarbon was determined for 700 °C - PC7 and for 800 °C - PC8, respectively.

Elemental analysis was performed for the corn digest, biochar and activated carbons using a Vario EL III elemental analyzer. To determine the ash content, samples of the materials were burned in a microwave muffle furnace in accordance with PN.

Textural characterization was performed using an ASAP 2020 sorptometer. The analysis was based on adsorption-nitrogen desorption isotherms measured at -196 °C. Samples were degassed at 250 °C for 24 hours to remove substances adsorbed on the surface of active biocarbon. BET specific surface area ($S_{BET}$) was evaluated in the relative pressure range $p/p_0$ 0.05-0.30.

The Boehm method was used to determine the content of acidic and basic functional groups. The procedure is described in the paper. Standard solutions of 0.1 mol/dm$^3$ NaOH and 0.1 mol/dm$^3$ HCl were used for titration.

The pH of the aqueous extracts was tested by weighing 0.5 g of each material as a fine powder and then adding 25 cm$^3$ of distilled water. The suspension was shaken on a shaker for 12 hours to establish equilibrium. The pH of the suspension was measured using a Hanna HI-9126 device equipped with a BlueLine 25 pH polymer electrode.

The $pH_{pzc}$ (point zero charge) was determined by the salt addition technique. A 40-ml NaCl solution of 0.1 mol/dm$^3$ was added to a series of 100 ml flasks. Then 0.2 g of a previously powdered activated carbon sample was added. The flasks were placed on a shaker. After 24 hours, the $pH_f$ value was measured. The $pH_{pzc}$ value was obtained from graphs of the dependence of $pH_i$ on $pH_f$.

Determination of the iodine number, i.e. the sorption capacity of the tested activated biocarbons with respect to iodine, was performed in accordance with PN-83/C-97555.04.

The sorption capacity of activated carbons against diclofenac was determined by measuring the absorbance of the test solution after the adsorption process at 276 nm using a Waters 2690 liquid chromatograph equipped with a Waters 2487 UV-Vis detector. For adsorption tests, a 25 mg weight of activated carbon was used, which was poured into 50 ml of an aqueous solution of diclofenac in the concentration range from 10 to 200 mg/L. The adsorption process was carried out for 24 hours.

**Results:** Activated carbons were obtained with yields for formulation PC7 of about 52% and PC8 of about 37% relative to the starting material used. The moisture content of the precursor was 10.3%. Both the precursor and the obtained activated carbons are characterized by a high ash content (Table 1). The results of elemental analysis indicate a decrease in hydrogen and oxygen content during the process of obtaining activated carbons. However, the content of elemental carbon increases.

**Table 1.** Elemental and proximate analysis of prepared activated carbon.

| Sample | $C^{daf}$ | $H^{daf}$ | $N^{daf}$ | $S^{daf}$ | $O^{daf}$ | Technical analysis | | |
|---|---|---|---|---|---|---|---|---|
| | | | | | | Ash | Moisture | Yield |
| prekursor | 35.6 | 4.5 | 4.4 | 1.8 | 53.7 | 35.4 | 10,3 | - |
| PC7 | 56.3 | 2.6 | 4.6 | 1.1 | 35.4 | 42.4 | | 51.8 |
| PC8 | 62.6 | 2.4 | 4.8 | 1.7 | 28.5 | 49.1 | | 36.9 |

Textural analysis showed that the obtained activated carbons have a medium specific surface area (Table 2). Both activated carbons are characterized by a well-developed micro-pore area, for PC7 385 $m^2/g$ and for PC8 536 $m^2/g$, which may suggest their good adsorption capacity. The average pore size is 3.862 nm for PC7 and 3.583 nm for PC8, respectively. The obtained iodine number values indicate good adsorption of small molecules of inorganic compounds.

**Table 2.** Textural parameters obtained from $N_2$ adsorption isotherm of activated carbons.

| Sample | Total | | Micropore | | | | |
|---|---|---|---|---|---|---|---|
| | Surface Area [$m^2/g$] | Pore Volume [$cm^3/g$] | Area [$m^2/g$] | Volume [$cm^3/g$] | Micropore Contribution | Mean Pore Size [nm] | Iodine numer [mg/g] |
| PC7 | 456 | 0.362 | 385 | 0.276 | 0.863 | 3.862 | 476 |
| PC8 | 732 | 0.568 | 536 | 0.487 | 0.852 | 3.583 | 704 |

Analysis of oxygen groups (Table 3) showed that there are about twice as many groups of acidic nature as of basic nature in the obtained activated carbons. This is consistent with the method used to obtain activated carbons. Activation in a $CO_2$ atmosphere promotes the formation of oxygen groups of an acidic nature.

**Table 3.** Textural parameters obtained from $N_2$ adsorption isotherm of activated carbons.

| Sample | Acidic Groups Content [mmol/g] | Basic Groups Content [mmol/g] | Total Content of Surface Groups [mmol/g] | pH of Aqueous Extracts |
|---|---|---|---|---|
| prekursor | 1.25 | 0.45 | 1.70 | 4.49 |
| PC7 | 0.77 | 0.38 | 1.15 | 5.78 |
| PC8 | 0.86 | 0.39 | 1.25 | 5.56 |

The pH values of the aqueous extracts have very similar values and indicate the slightly acidic character of the surface of the obtained materials, which is characteristic of carbons with a predominance of acidic oxygen groups. In contrast, the pH value of the aqueous extract from the precursor is one unit lower than that of the obtained activated carbons. The pHpzc values are close to the pH values of the aqueous extracts and indicate that the surfaces of the carbons are positively charged (Fig.1).

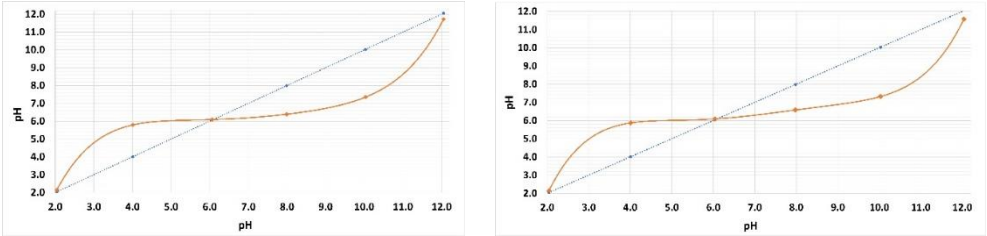



**Fig.1.** Determination of the point of zero charge ($pH_{pzc}$) of activation carbon.

**Table 4.** Linear isotherm models of diclofenac adsorption by activated carbons.

| Sample | $q_e$ [mg/g] | Langmuir model | | | Freundlich model | | |
|---|---|---|---|---|---|---|---|
| | | $R^2$ | $q_{max}$ [mg/g] | $K_L$ [l/mg] | $R^2$ | $K_F$ [mg/g(L/mg)$^{1/n}$] | 1/n |
| PC7 | 55 | 0.972 | 54 | 0.010 | 0.999 | 2.78 | 0.485 |
| PC8 | 128 | 0.977 | 129 | 0.614 | 0.999 | 46.62 | 0.229 |

The results obtained from the adsorption of diclofenac (Table 4) determined from Langmuir and Freundlich models indicate that there is multilayer adsorption and adsorption described by physical phenomena. The values of the maximum adsorption capacity determined experimentally coincide with those determined theoretically.

**Conclusions:** Waste material from biogas plants is a good starting material for obtaining activated carbons. The results obtained indicate good sorption properties against pharmaceutical impurities of which diclofenac is an example. However, further research is needed that takes into account the optimization of the parameters for obtaining activated carbons in order to increase their sorption properties.

**References:**

1. L. Lonappan, S.K. Brar, R.K. Das, M. Verma, R.Y. Surampalli, Environment International, 96 (2016) 127.
2. S. De Gisi, G. Lofrano, M. Grassi, M. Notarnicola, Sustainable Materials and Technologies, 9 (2016) 10.
3. M.A.M. Salleh, D.K. Mahmoud, A.K. Wan, A. Wan, A. Idris, Desalination, 280 (2011) 1.
4. A.A. Spagnoli, D.A. Giannakoudakis, S. Bashkova, Journal of Molecular Liquids, 229 (2017) 465.

# SYNTHESIS, CHARACTERISATION AND APPLICATION OF NEW POLYMERIC ADSORBENT CONTAINING STARCH FOR THE REMOVAL OF TOXIC DYE

**M. WAWRZKIEWICZ[1], B. PODKOŚCIELNA[2], B. TARASIUK[2]**, [1]Maria Curie-Sklodowska University, Faculty of Chemistry, Institute of Chemical Sciences, Department of Inorganic Chemistry, M. Curie-Sklodowska Sq. 3, 20-031 Lublin, Poland, [2]Maria Curie-Sklodowska University, Faculty of Chemistry, Institute of Chemical Sciences, Department of Polymer Chemistry, Gliniana St. 33/51, 20-614 Lublin, Poland.

**Abstract:** This study aimed to synthesis an environmentally friendly adsorbent based on poly(ethylene glycol dimethacrylate-co-vinyl acetate) (EGDMA-VA) and 40 wt. % of soluble starch (St). The adsorbent (EGDMA-VA-St) was characterized by ATR/FT-IR and SEM/EDX. The porous structure and particle size distribution were evaluated, as well as the $pH_{pzc}$ was determined. The application potential of the adsorbent was then assessed towards the cationic dye C.I. Basic Yellow 2 (BY2).

**Introduction:** Adsorption techniques as one of the physical methods of dyes removal from industrial effluents and are considered as simple and effective, with significant efficiencies in the range of 86.8-99% [1]. They are thought to be highly economical due to the ease of handling, as well as the possibility of reusing the adsorbents in subsequent sorption-desorption cycles. It has been estimated that the average cost of wastewater treatment by adsorption is US$ 5.0-200/$m^3$, while other technologies are in the range of US$10.0-450/$m^3$ [2]. It is therefore particularly important to obtain new adsorbents, especially those containing biocomponents in their composition, making them more biodegradable and low-cost materials. In recent years, adsorbents containing such biodegradable additives as lignin [3], cellulose [4] or starch [5] have attracted great interest in wastewater treatment technologies. Starch belongs to the group of polysaccharides of plant origin. It is composed of glucose mers linked by α-glycosidic bonds and acts as an energy store in plants. Starch is a very interesting biopolymer, the possibilities for its use in sorption processes being created by its very interesting structure resulting from the presence of hydroxyl groups. The undoubted advantages of using starch are its very wide availability, low price and hydrophilic nature. Poor mechanical resistance and partial solubility in hot water limits its usage. The use of starch as an additive or modificator in the synthesis of polymeric microspheres can significantly improve the aforementioned properties and broaden the range of potential applications of this biopolymer [6,7].

**Experimental:** The synthesis of adsorbent was performed by the suspension-polymerization method in the aqueous medium [8]. 150 mL of redistilled water, 1.00 g of PVA, and 1.20 g $CaCl_2$ were stirred (0.5 h at 80 $^oC$) in a three-necked flask fitted with a thermometer, a water condenser, and a mechanical stirrer. 5.75 g (40 % wt. on monomers) of starch (St) was previously dissolved in 20 mL of benzyl alcohol (2 h at 60 $^oC$). Then, the solution containing: 10.00 g of the EGDMA and 4.30 g of VA (in molar mass 1:1), 1% wt. of initiator AIBN, and the mixture of benzyl alcohol with starch was

added to the aqueous medium. Above mentioned chemicals were obtained from Sigma-Aldrich (Germany). Copolymerization was completed for 10 h at 80-85 $^{o}$C. The obtained microspheres were washed with distilled water (2000 mL) and acetone (200 mL). The adsorbent was dried at 80 $^{o}$C to a constant weight.

The batch adsorption technique was used to determine the equilibrium adsorption parameters for BY2 removal. 0.05 g of the starch-based adsorbent was weighed out into Erlenmeyer flasks, and then 20 mL of BY2 (Fig.1, Sigma-Aldrich, Germany) solution at the specified initial concentration ranging from 1 to 25 mg/L was poured in. According to preliminary studies, maximum dye removal with bioadsorbent was recorded at pH=8.3 (pH-meter CPC-411, Elmetron, Poland). The flasks were placed in a mechanical shaker Elpin +358S (Elpin, Poland) with a constant oscillation amplitude (A=8, 170 cycle/min), and the contents were shaken for 24 h at 25 $^{o}$C. BY2 content after sorption was determined spectrophotometrically against distilled water as a reference using a Cary 60 UV–vis spectrophotometer (Agilent Technologies, USA) at 431 nm.

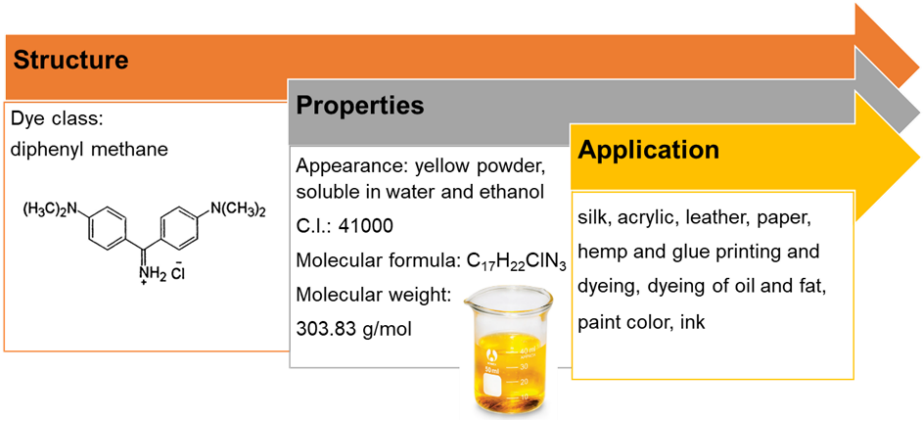



**Fig.1.** C.I. Basic Yellow 2 characteristics.

The adsorbent was characterized by the following methods: ATR/FT-IR (Fourier transform infrared (FT-IR) spectroscopy with the attenuated total reflectance (ATR) technique; Bruker Tensor 27 FTIR spectrometer, Germany), SEM/EDX (scanning electron microscope (SEM) Quanta 3D FEG with energy dispersive X-ray spectroscopy (EDX); FEI, USA), porous structure (ASAP 2405 adsorption analyzer, Micrometrics Inc., USA), and particle size distribution (laser particle size analyzer Mastersizer 2000; Malvern Instruments, UK).

**Results:** Analysing the ATR-FT-IR spectra of the obtained starch microspheres, it can be observed the increase in the intensity of bands originating from oxygen-containing groups, i.e. O-H hydroxyl groups (approximately 3400 cm$^{-1}$) and -C-OH and C-O-C groups (approximately 1050 cm$^{-1}$). The signal around 2980-2940 cm$^{-1}$ is qualified to stretching vibrations in aliphatic C-H. The characteristic sharp signal around 1720 cm$^{-1}$ is attributed to C=O stretching vibrations mainly from EGDMA.

The surface morphology of starch-based adsorbent was illustrated using SEM/EDX microscopy and is presented in Fig. 2. By equipping the SEM with an EDX device, it was also possible to determine the elemental composition of the adsorbent (in weight

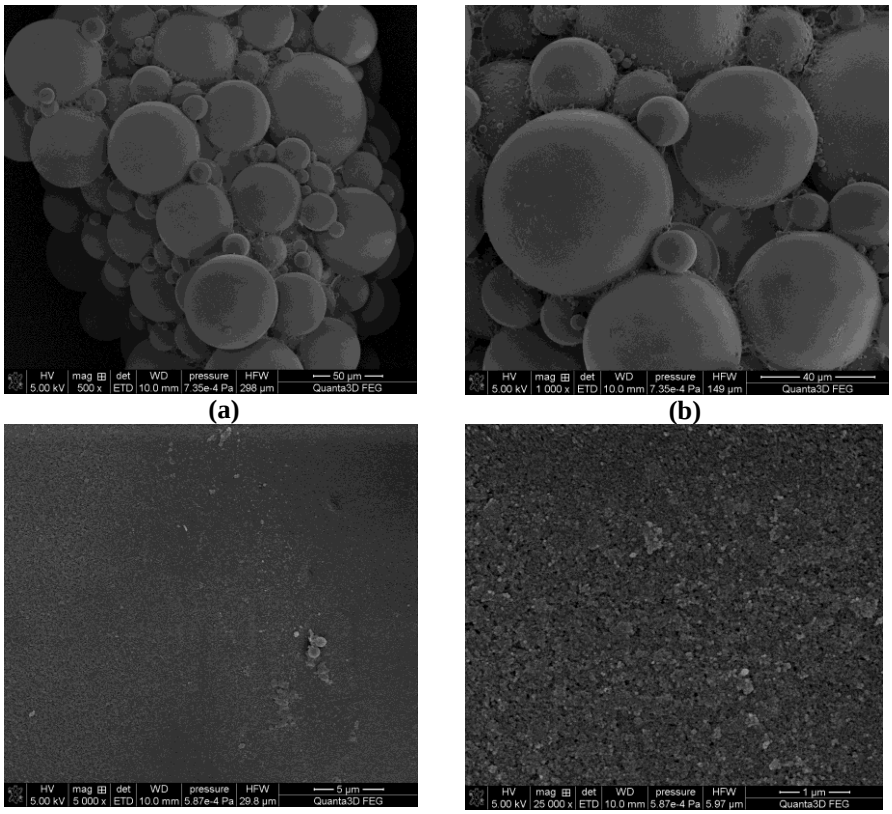



**Fig.2.** Starch modified microspheres visualization by the SEM analysis at (a) 500×, (b) 1000×, (c) 5000× and (d) 25000× magnification.

percent), which is as follows: 73.6% C, 26.33% O, 0.04%Al, 0.03% Si. The EGDMA-VA-St synthesized in our study has a BET surface area of 111 $m^2/g$, a total pore volume of 0.150 $cm^3/g$ and an average pore size of 5.50 nm. It was shown that the EGDMA-VA-St was characterized by heterodispersity, 10% of adsorbent beads is smaller than 73.9 µm and 116.02 µm, 50% is smaller than 105.34 µm and 173.37 µm, and 90% is smaller than 145 µm and 221.41 µm, respectively. The $pH_{pzc}$ of the EGDMA-VA-St was found to 7.21.

To determine the adsorption capacity of the EGDMA-VA-St the correlation between the initial BY2 dye concentration and its equilibrium concentration was investigated. The experimental data were fitted to Langmuir, Freundlich, Temkin and Dubinin-Raduschkevich isotherm models. The equilibrium parameters were calculated using linear forms of the isotherm models and the plots $C_e/q_e$ vs $C_e$, log $q_e$ vs log $C_e$, $q_e$ vs ln $C_e$ and ln $q_e$ vs $\varepsilon^2$:

$$\frac{C_e}{q_e} = \frac{1}{Q_0 k_L} + \frac{C_e}{Q_0}$$

$$\log q_e = \log k_F + \frac{1}{n}\log C_e$$

$$q_e = \left(\frac{RT}{b_T}\right)\ln A + \left(\frac{RT}{b_T}\right)\ln C_e$$

$$lnq_e = lnq_m - k_{DR}\varepsilon^2$$

where: $q_e$ - adsorption capacity (mg/g), $C_e$ - equilibrium concentration of BY2 in solutions (mg/L), $Q_0$ - the monolayer adsorption capacity (mg/g), $k_L$ - the Langmuir constant (relating to the free energy of adsorption) (L/mg), $k_F$ ($mg^{1-1/n}\ L^{1/n}/g$) and 1/n - the Freundlich constants regarding to adsorption capacity and the surface heterogeneity, respectively, R -gas constant (8.314 J/mol K), T - temperature (K), a (L/mg) and $b_T$ (J/mol g/mg) - the Temkin constants, $q_m$ (mg/g) - maximum adsorption capacity, $k_{DR}$ ($mol^2/J^2$) - constant concerning the adsorption energy, ε (J/mol) - adsorption potential [9].

Analysis of the parameters presented in Table 1 and the distribution of experimental points with fitting of isotherm models (Fig.3) allows us to conclude that the most suitable model for describing the adsorption of BY2 on EGDMA-VA-St is the Langmuir model ($R^2$=0.923) rather than Temkin ($R^2$=0.979). According to Langmuir isotherm model, the formation of monolayer coverage of BY2 dye molecules on the surface of starch modified adsorbents should be occured. The monolayer adsorption capacity of EGDMA-VA-St/ was equalled to 11.1 mg/g.

**Table 1.** Isotherm parameters for BY2 sorption on EGDMA-VA-St.

| Isotherm | Parameters | EGDMA-VA-St |
|---|---|---|
| Freundlich | $k_F$ ($mg^{1-1/n}\ L^{1/n}/g$) | 5.95 |
| | 1/n | 0.629 |
| | $R^2$ | 0.859 |
| Langmuir | $k_L$ (L/mg) | 1.37 |
| | $Q_0$ (mg/g) | 11.1 |
| | $R^2$ | 0.923 |
| Temkin | $b_T$ (J g/mol mg) | 1253 |
| | A (L/mg) | 25.8 |
| | $R^2$ | 0.979 |
| Dubinin-Radushkevich | $q_m$ (mg/g) | 7.59 |
| | $k_{DR} \times 10^{-8}$ ($mol^2/J^2$) | 4.35 |
| | E (kJ/mol) | 3.39 |
| | $R^2$ | 0.917 |

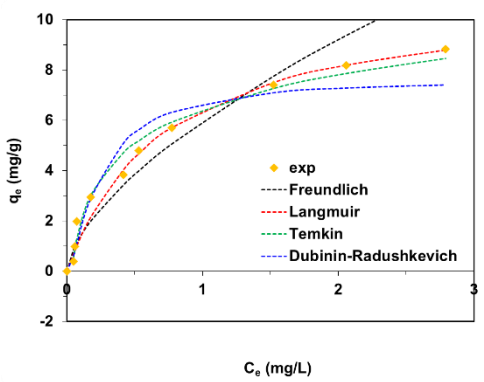



**Fig.3.** Fitting of isotherm models to experimental equilibrium data of BY2 sorption on EGDMA-VA-St.

**Conclusions:** In the study, the new bioadsorbent based on poly(ethylene glycol dimethacrylate-co-vinyl acetate) with an addition of 40 wt. % of soluble starch was successfully fabricated as a spherical bead shape by suspension polymerization method and applied for BY toxic dye removal. The beads showed a tendency to agglomerate. The chemical structure of microspheres was confirmed by ATR-FTIR spectroscopy. The specific surface areas and total pore volumes of the obtained adsorbents were 111 $m^2/g$ and 0.150 $cm^3/g$, respectively. The $pH_{pzc}$ of the polymer was found to be 7.21. The equilibrium studies revealed that the adsorbent can be applied for the removal of toxic basic dye BY2.

## References:

1. V. Katheresan, J. Kansedo, S. Y. Lau, Journal of Environmental Chemical Engineering, 6 (2018) 4676.
2. G. L. Dotto, J. M. N. Santos, I. L. Rodrigues, R. Rosa, F. A. Pavan, E. C. Lima, Journal of Colloid and Interface Science, 446 (2015) 133.
3. M. Jiang, Y. Ma, T. Wang, N. Niu, L. Chen, International Journal of Biological Macromolecules, 238 (2023) e124080.
4. A. Ali Aslam, S. Ul Hassan, M. Haris Saeed, O. Kokab, Z. Ali, M. Shahid Nazir, W. Siddiqi, A. Ali Aslam, Journal of Cleaner Production, 421 (2023) e138555.
5. K. Fang, L. Deng, J. Yin, T. Yang, J. Li, W. He, International Journal of Biological Macromolecules, 218 (2022) 909.
6. J.I. Enrione, S.E. Hill, J.R. Mitchell, Journal of Agricultural and Food Chemistry, 55 (2007) 2956.
7. T. Oniszczuk, S. Muszyński, A. Kwaśniewska, Przemysł Chemiczny, 94 (2015) 1752.
8. M. Wawrzkiewicz, B. Podkościelna, P. Podkościelny, Molecules, 25 (2020) e5247.
9. M. Mozaffari Majd, V. Kordzadeh-Kermani, V. Ghalandari , A. Askari , M. Sillanpää, Science of the Total Environment, 812 (2022) e151334.

# INFLUENCE OF THE TYPE OF CROSSLINKING AGENTS ON THE SORPTION PROPERTIES OF ALGINATE HYDROGEL MICROSPHERES

**D. FILA, Z. HUBICKI, D. KOŁODYŃSKA**, Maria Curie-Sklodowska University, Faculty of Chemistry, Institute of Chemical Sciences, Department of Inorganic Chemistry, M. Curie-Sklodowska Sq. 2, 20-031 Lublin, Poland.

**Abstract:** In the presented work, the cross-linked alginate hydrogel microspheres were obtained by ionic crosslinking. The sorption process of Ho(III) ions on alginate sorbents synthesized by ion crosslinking with calcium, zinc, aluminum, and iron ions was studied. The influence of several factors on the sorption process of Ho(III) ions was discussed. The maximum sorption capacities of the synthesized alginate adsorbents were determined. ATR/FT-IR spectra of the microspheres before and after the sorption of Ho(III) ions were recorded.

**Introduction:** Alginate is a common anionic polysaccharide found in the natural environment. Its polymer chain consists of linearly linked β-D-mannuronic acid (M) and α-L-guluronic acid (G) mers. Alginate shows great potential in a variety of industrial applications in all aspects of food, wound dressing, drug delivery, tissue engineering, and wastewater treatment [1]. One significant disadvantage of alginate is its poor stability in aqueous environments and the difficulty in controlling the degradation rate. Crosslinking is the primary means of modifying alginate. Crosslinking methods include ionic, covalent, enzymatic, and photo-crosslinking ones. Very often, a combination of these methods is also used. The choice of the appropriate crosslinking method depends on the applications for which the materials are to be used [2,3].

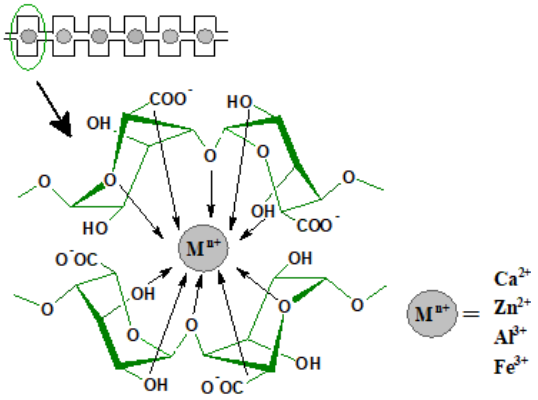



**Fig.1.** Scheme of ionic crosslinking of alginate.

Ionic crosslinking is one of the simplest methods of crosslinking alginate (Fig.1). This method has been used to formulate beads, alginate films, fibers, hydrogels, nanoparticles, and microparticles. The ease of bead preparation and mild conditions for

the production of alginate metal complexes make it unique compared to other polysaccharides. Ionic cross-linking of the alginate hydrogel is possible through the interaction of metals on the +II/+III oxidation state with the alginate carboxyl groups present in the guluronic residues (G). The M/G ratio, the chain length of the G-block, and the sequence of the G- and M-blocks are the most important factors influencing the alginate complexes obtained. An alginate gel can be readily formed by ionic interaction in an aqueous medium – gel beads are usually obtained by dropping sodium alginate solution into a chloride solution of metal ions [4].

**Experimental:** Four alginate sorbents were synthesized using the ionic cross-linking method and named according to the cross-linking agent used: calcium alginate (ALG@Ca), zinc alginate (ALG@Zn), aluminum alginate (ALG@Al), and iron alginate (ALG@Fe). The alginate microspheres were subjected to sorption property tests using a static method analyzing the effects of pH, contact time, concentration, and temperature. Based on the kinetic and equilibrium models, parameters characterizing the sorption process were determined.

**Results:** Figure 2 shows the ATR/FT-IR spectra of alginate microspheres before and after Ho(III) sorption.

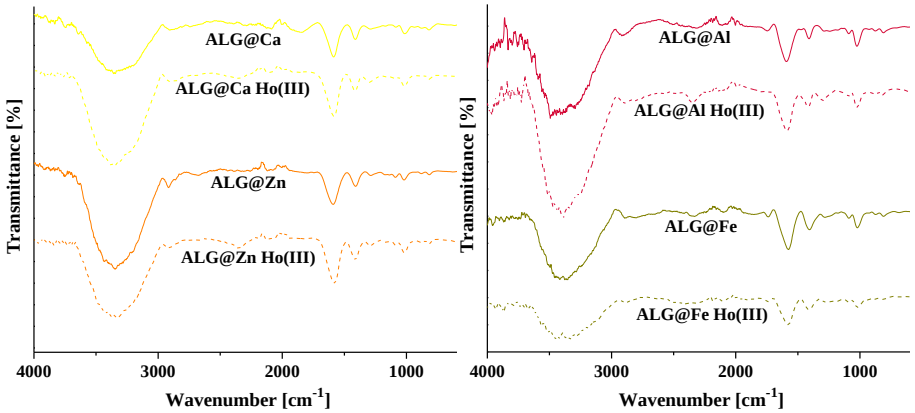



**Fig.2.** ATR/FT-IR spectra of ALG@Ca, ALG@Zn, ALG@Al, and ALG@Fe before and after loading of Ho(III) ions.

The bands characteristic of the alginate structure in the range of 3200-3600 $cm^{-1}$ (νOH) and the range of 1100-1400 $cm^{-1}$ (νC-O-C, νC=O, νC-O) were noted. Shifts of characteristic alginate bands in the 1100-1400 $cm^{-1}$ range indicate a different crosslinking mechanism with the metal ions used. After Ho(III) sorption, the peak movements were also noticed confirming the ions exchange process during metal sorption. In the first step, the effect of solution pH on the sorption of Ho(III) ions on ALG@Ca, ALG@Zn, ALG@Al, and ALG@Fe sorbents was evaluated (Fig.3A). At pH 5, the highest sorption capacity values were achieved for ALG@Ca, ALG@Zn, and ALG@Al and were 40.31 mg/g, 40.34 mg/g, and 33.37 mg/g, respectively. For the sorbent ALG@Fe, the highest sorption capacity was achieved at pH 4, which equals

11.51 mg/g. Holmium(III) binding kinetics from solutions by ALG@Ca, ALG@Zn, ALG@Al, and ALG@Fe show that adsorbed Ho(III) increased with time (fig.3B). The primary objective of the kinetic investigations was to find the amount of time it takes for the studied systems to achieve adsorption equilibrium.

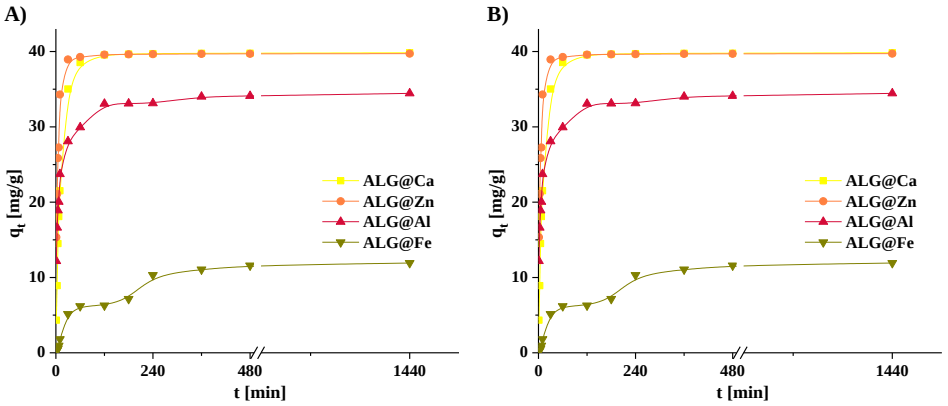



**Fig.3.** Adsorption of holmium(III) ions by alginate microspheres cross-linked with $Ca^{2+}$, $Zn^{2+}$, $Al^{3+}$, and $Fe^{3+}$ ions: A) pH tests, B) kinetics.

In the examined systems, the kinetic process rate depends on the synthesized alginate microspheres. The equilibrium was established after 120 minutes for ALG@Ca, 60 minutes for ALG@Zn, 120 minutes for ALG@Al, and 360 minutes for ALG@Fe, after which 99.14%, 99.59%, 82.92%, and 31.03% Ho(III) ions were removed from the alginate microspheres, respectively. Kinetics experiments indicated that the pseudo-second order model displayed the best correlation with holmium(III) adsorption kinetics data for all the tested systems. The adjusted determination coefficients for the linear $t/q_t$ dependence as a function of time ranged from 0.999 to 1.000 (Table 1). Values of Ho(III) adsorption ($q_{exp}$) at an equilibrium state for 100 mg/dm$^3$ solutions are consistent with the theoretical adsorption capacities ($q_2$) obtained from the Ho(III) adsorption kinetic presented in this study. The value of $k_2$ calculated for the PSO model describing Ho(III) adsorption solutions from ALG@Zn was higher compared to $k_2$ values calculated for ALG@Ca, ALG@Al, and ALG@Fe.

**Table 1**. Estimated kinetic model parameters for holmium(III) adsorption by alginate beads cross-linked with $Ca^{2+}$, $Zn^{2+}$, $Al^{3+}$, and $Fe^{3+}$ ions ($C_0$= 100 mg/dm$^3$).

| Kinetic models | Parameters | ALG-Ca | ALG-Zn | ALG-Al | ALG-Fe |
|---|---|---|---|---|---|
| | $q_{exp}$ [mg/g] | 39.84 | 39.72 | 34.44 | 11.92 |
| PFO | $q_1$ [mg/g] | 11.24 | 4.88 | 11.31 | 11.18 |
| | $k_1 \times 10^{-2}$ [1/min] | 1.45 | 1.43 | 0.87 | 0.72 |
| | $R^2$ | 0.792 | 0.741 | 0.884 | 0.972 |
| PSO | $q_2$ [mg/g] | 40.07 | 39.78 | 34.55 | 12.67 |
| | $k_2 \times 10^{-2}$ [g/mg·min] | 0.45 | 1.71 | 0.50 | 0.10 |
| | h [mg/g·min] | 7.30 | 27.08 | 5.99 | 0.16 |
| | $R^2$ | 1.000 | 1.000 | 1.000 | 0.999 |

Adsorption isotherm analysis showed that for the ALG@Ca and ALG@Zn microspheres, the Langmuir model was the most suitable isotherm model to describe the equilibrium data of the Ho(III) ion sorption process, for the ALG@Al the Langmuir and Freundlich model, and the ALG@Fe the Freundlich model. The maximum monolayer coverage values for the Ho(III) ions sorption under the most optimal conditions determined from the Langmuir model were: 202.07 mg/g for the ALG@Ca, 241.20 mg/g for the ALG@Zn, 118.49 mg/g for the ALG@Al, and 42.88 mg/g for the ALG@Fe. For ALG@Ca and ALG@Zn sorbents, an increase in temperature contributed to an increase in equilibrium adsorption capacities, while for ALG@Al and ALG@Fe sorbents, an increase in temperature caused a decrease in adsorption capacities during sorption of Ho(III) ions.

**Conclusions:** Alginate hydrogel microspheres were successfully synthesized by ionic crosslinking using $Ca^{2+}$, $Zn^{2+}$, $Al^{3+}$, and $Fe^{3+}$ salts. The sorption properties of alginate microspheres were strongly influenced by the crosslinking agent used. Crosslinking agents on the +II oxidation state, i.e. $Ca^{2+}$ and $Zn^{2+}$, proved to have better exchange capacities with holmium ions, while crosslinking agents on the +III oxidation state, i.e. $Al^{3+}$ and $Fe^{3+}$, performed worse. Based on the obtained results alginate hydrogel microspheres were ranked according to increasing affinity for Ho(III) ions: ALG@Zn > ALG@Ca > ALG@Al > ALG@Fe.

**Acknowledgments:** The National Science Centre (Poland) provided financial support for this study under decision No. 2019/35/N/ST8/01390.

**References:**

1. K. Zdiri, A. Cayla, A. Elamri, A. Erard, F. Salaun, Journal of Functional Biomaterials, 13 (2022) 117.
2. D. Nataraj, N. Reddy, International Journal of Chemistry Research, 4 (2020) 1.
3. D. M. Roquero, A. Othman, A. Melman, E. Katz, Materials Advances, 3 (2022) 1849.
4. G. Alkhayer, Properties and Applications of Alginates, Intechopen, 2022.

# NATURAL-BASED ADSORBENT IN THE SORPTION OF CRITICAL RAW MATERIALS

**A. WAWRUCH, D. FILA, Z. HUBICKI**, Maria Curie-Sklodowska University, Faculty of Chemistry, Institute of Chemical Sciences, Department of Inorganic Chemistry, M. Curie-Sklodowska Sq. 2, 20-031 Lublin, Poland.

**Abstract:** The primary objective of this study was to elucidate the potential of natural-based adsorbents, i.e., calcium alginate, in the sorption of critical raw materials such as Ce(III), Pr(III), Nd(III), and Sm(III). Specifically, it includes exploring the various factors influencing adsorption, such as pH, temperature, and contact time. Two kinetic models, i.e., pseudo-first and pseudo-second order as well as three equilibrium isotherm models, i.e., Langmuir, Freundlich, and Temkin, have been applied to describe the characteristics of adsorption.

**Introduction:** In recent years, exploring sustainable and environmentally friendly solutions has become imperative, particularly in industries reliant on critical raw materials. Critical raw materials, i.e., rare earth elements, are essential components in various industries, such as electronics, renewable energy, and healthcare. Moreover, they are characterized by scarcity, high economic value, and strategic importance [1]. As the global demand for these materials continues to rise, finding efficient and eco-conscious methods for their extraction and recovery has become paramount. Chemical methods for recycling rare earth elements (REEs) produce significant hazardous waste, contradicting green development strategies. One promising avenue of research lies in utilizing natural-based adsorbents for the sorption of these critical raw materials [2,3]. Introducing biopolymers offers an environmentally friendly approach to REE recovery. Research has explored utilizing biomass such as bacteria, algae, fungi, and plants to create biosorbents for recovering REEs. Among these, employing sodium alginate gel shows promising application potential. The use of alginate in most applications consists in its ability to form heat-stable strong gels which can develop and set at room temperature. The gel strength depends on the guluronic content and also the average number of G-units in the G-blocks of alginate. The binding zone between the G-blocks is often described as the so-called 'egg-box model'. Moreover, sodium alginate, a natural anionic polysaccharide abundant in -OH and -COOH functional groups, serves as an effective ligand due to its ability to coordinate with REE(III) ions, which are hard Lewis acids [4].
Alginate gel formation with $Ca^{2+}$ ions is of interest in most applications. So this study used sodium alginate, a natural polymer, to synthesize adsorbent gels, aiming to assess their selectivity for rare earth elements such as Ce(III), Pr(III), Nd(III), and Sm(III). Thorough evaluations of the adsorption kinetics and isotherms were carried out to clarify the fundamental process of REE adsorption onto the produced alginate gels.

**Experimental:** a study of the sorption process of rare earth metal ions such as Ce(III), Pr(III), Nd(III), and Sm(III) on calcium alginate with 0.6 mm grain size was conducted. 0.05 g of sorbent was weighed into 100 ml conical flasks and 20 ml of the test solution about defined concentration was added. The effects of the following parameters were investigated: pH in the range of 2-6, phase contact time in the range of 1-1440 minutes,

and temperature in the range of 293-333 K. To test the pH a series of solutions with an ion concentration of 100 mg/dm$^3$ and pH of 2, 3, 4, 5, 6 were prepared. Sorption was carried out for 480 min and the concentration of the solutions after sorption was measured. In the case of studying the effect of contact time, studies were also conducted for a solution concentration of 100 mg/ dm$^3$, at the designated optimal pH. The effect of temperature was studied by conducting sorption at 293 K, 313 K, and 333 K for 480 minutes and solution concentration from 25 to 1000 mg/dm$^3$. The ICP-OES spectrometer was used to determine the concentration of metal ions after the sorption process. Based on the results obtained, the characteristic parameters of the sorption process, as well as kinetic and equilibrium parameters, were determined.

**Results:** The first parameter tested was the solution pH. For all 4 tested ions, similar dependencies of the sorption process were obtained, as shown in Fig.1. The weakest sorption occurred at a pH of 2, but for pH between 3 and 6 much better results were obtained, similar to each other. The percentage of metal ions adsorbed on the sorbent was highest for pH = 5 and equal to nearly 100%, so further studies were conducted at this pH.

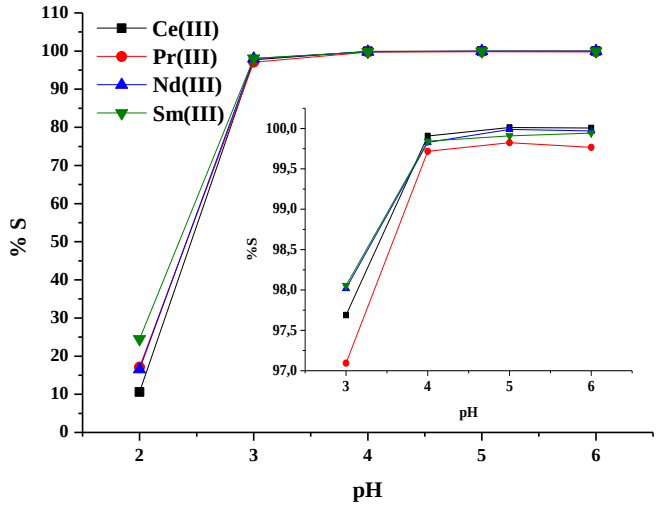



**Fig.1.** Dependence of the percentage of adsorbed metal ions on solution pH.

Analysis of the kinetics of ion sorption showed that as the time of phase contact time, the amount of adsorbed metal ions increases until sorption equilibrium is established. Figure 2 shows the obtained dependence of sorption capacity on time. The time to reach the plateau is similar for the studied ions and was about 120 min. Based on the determined kinetic parameters, it was found that the process of sorption of rare earth ions on calcium alginate is best described by a pseudo-second order kinetic model. The obtained correlation coefficients $R^2$ for Ce(III), Pr(III), Nd(III), and Sm(III) are 1.000 in each case.

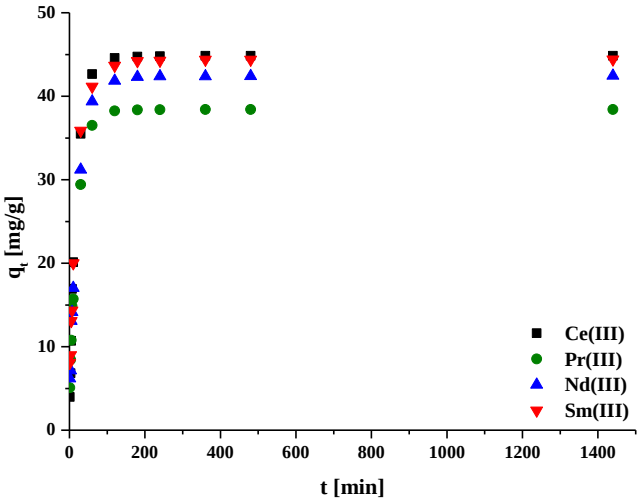



**Fig.2.** Time dependence of sorption capacity.

The effect of temperature was also investigated. Figure 3 shows the $q_e/C_e$ relationships for the ions studied. It has been shown that for each ion, an increase in temperature causes an increase in sorption capacity. The best adsorption performance was obtained at 333 K.

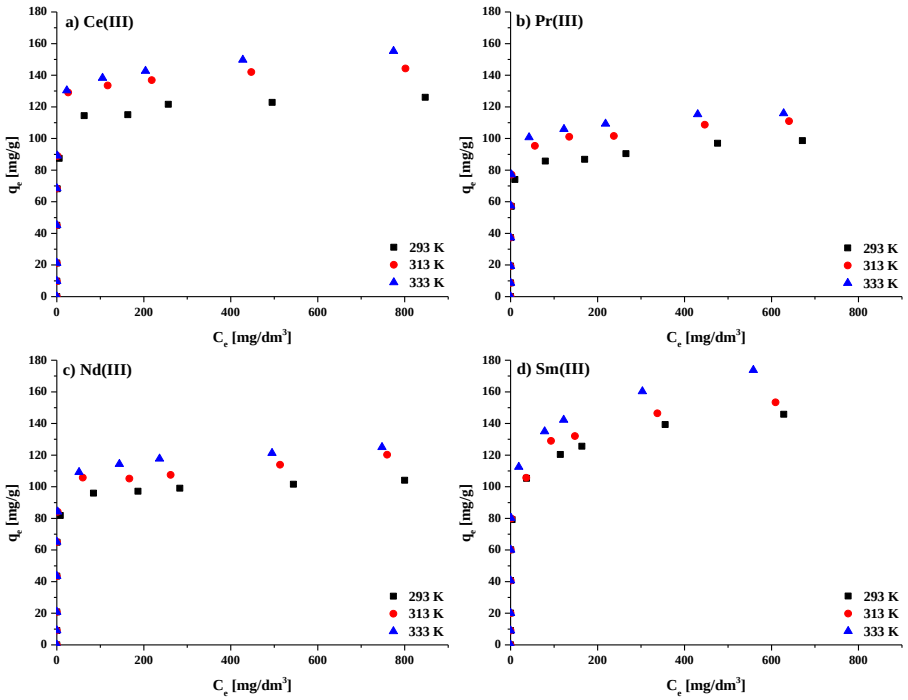



**Fig. 3.** The $q_e/C_e$ relationships for (a) Ce(III), (b) Pr(III), (c) Nd(III), and (d) Sm(III) at different temperatures.

The obtained experimental data were fitted using linear forms of Langmuir, Freundlich, and Temkin isotherm models. The estimated values of the parameters characterizing these models are shown in Table 1. Based on the obtained correlation coefficients, it can be concluded that the studied sorption process is best described by the Langmuir model.

**Table 1.** Calculated isotherms parameters at temperature 333 K.

| Isotherm model | Parameter | Ce(III) | Pr(III) | Nd(III) | Sm(III) |
|---|---|---|---|---|---|
| Langmuir | $q_{0,cal}$ [mg/g] | 154.18 | 115.70 | 123.93 | 171.48 |
| | $K_L$ [L/mg] | 0.26 | 0.31 | 0.28 | 0.15 |
| | $R^2$ | 0.999 | 0.999 | 0.999 | 0.996 |
| Freundlich | $K_F$ [$mg^{1-1/n}L^{1/n}g^{-1}$] | 50.49 | 38.01 | 46.88 | 49.44 |
| | n | 4.69 | 4.79 | 5.73 | 4.43 |
| | $R^2$ | 0.805 | 0.719 | 0.658 | 0.751 |
| Temkin | A [L/g] | 202.74 | 118.00 | 590.71 | 102.30 |
| | B [J/mol] | 13.70 | 11.00 | 10.02 | 15.45 |
| | $R^2$ | 0.963 | 0.925 | 0.898 | 0.964 |

**Conclusions:** Studies have shown that the natural-based adsorbent calcium alginate has a high sorption capacity for Ce(III), Pr(III), Nd(III), and Sm(Ⅲ) ions. The sorption efficiency depends on solution pH, phase contact time, initial solution concentration, and temperature. The sorption occurred most efficiently for pH 5 and temperature 333 K with a minimum time required to establish equilibrium of 120 min. According to the kinetic and equilibrium studies, the sorption process followed the pseudo-second order kinetic model and the Langmuir isotherm model. Based on the obtained results the affinity of calcium alginate for the tested rare earth metal ions was as follows: Sm(III) > Ce(III) > Nd(III) > Pr(III).

**Acknowledgments:** The National Science Centre (Poland) provided financial support for this study under decision No. 2019/35/N/ST8/01390.

**References:**

1. D. A. Atwood, The Rare Earth Elements: Fundamentals and Applications, Wiley, New York, 2012.
2. M. Asadollahzadeh, R. Torkaman, M. Torab-Mostaedi, Separation & Purification Reviews, 50 (2020) 417.
3. R. M. Brown, A. Mirkouei, D. Reed, V. Thompson, Renewable and Sustainable Energy Reviews, 173 (2023) 113099.
4. O. Levy Ontman, S. Nagar, O. Paz Tal, A. Wolfson, Journal of Polymers and the Environment, (2024), https://doi.org/10.1007/s10924-024-03196-7.

# OPTIMIZATION OF CADMIUM ION SORPTION USING BIO-INSPIRED MATRICES: EXPERIMENTAL INVESTIGATIONS

**A. WAWSZCZAK[1], G. JÓZEFACIUK[2], D. KOŁODYŃSKA[1]**, [1]Maria Curie-Sklodowska University, Faculty of Chemistry, Institute of Chemical Sciences, Department of Inorganic Chemistry, M. Curie-Sklodowska Sq. 3, 20-031 Lublin, Poland, [2]Institute of Agrophysics, Polish Academy of Sciences, Doświadczalna 4 St., 20-290 Lublin, Poland.

**Abstract:** With increasing regulations on industrial practices related to environmental protection, the significance of utilizing natural sorbents is becoming paramount. Alginates, as a representatives of natural polymers, are a potential candidate for synthesizing such sorbents. Due to their unique properties such as nontoxicity and their ability to form gel structures through interaction with calcium ions, alginates represent promising candidates for diverse applications, especially in the sorption of heavy metal ions. Based on the above, research was undertaken on the optimization of cadmium sorption on synthesized calcium alginate matrices. The study included the analysis of equilibrium and kinetic parameters as well as the degree of release of calcium ions from the matrix during Cd(II) sorption. Furthermore, structural characterization of the synthesized matrices was conducted utilizing mercury porosimetry methodology.

**Introduction:** In recent years, the increasing issue of heavy metal pollution has garnered significant attention because of its adverse impacts on both ecosystems and human health. One notable focus has been on addressing cadmium ion contamination in water sources as a potential mitigation strategy. Numerous studies have concentrated on developing efficient sorbent materials capable of removing cadmium ions from aqueous solutions, with synthetic sorbents commonly utilized for this purpose [1,2]. However, despite their efficacy, challenges persist concerning the storage and recycling of synthetic sorbents after use, prompting researchers to explore sorbents derived from natural compounds. Polysaccharides of natural origin, particularly alginates, have emerged as promising candidates in recent years. Renowned for their biodegradability, nontoxicity, cost-effectiveness, biocompatibility, and ease of crosslinking with calcium ions, alginates offer versatile advantages for sorption applications [3,4]. Recent studies have demonstrated the effectiveness of calcium alginate-based sorbents in removing heavy metal ions from water, highlighting their potential for practical applications [5,6]. Because alginates are derived from various species of seaweed found throughout the world, their initial composition, and consequently the material obtained from these alginates, may vary. Therefore, there is a need for optimization of sorption processes, particularly for heavy metals. On the basis of this premise, research was conducted aimed at optimising cadmium sorption onto synthesized calcium alginate matrices, with a focus on exploring equilibrium and kinetic parameters, alongside examining calcium ion release during Cd(II) sorption. Structural characterization of the matrices conducted using mercury porosimetry. These efforts aim to advance the development of effective, environmentally friendly sorbents for the Cd(II) removal.

**Experimental:** Sodium alginate, calcium chloride, ethanol and demineralized water were used to synthesize biopolymer matrices. Aqueous solutions of sodium alginate were prepared with a mass concentration of 3%. During the process of dissolving sodium alginate in water, a small amount of ethanol was used in the initial mixing phase. The addition of ethanol was used to facilitate the homogenization of sodium alginate aqueous solutions. The mixture was then left to deaerate and then poured into previously prepared round moulds. The moulds with sodium alginate prepared in this way were frozen at a temperature of 245 K and then freeze-dried for two days at a temperature of 213 K and a pressure of 0.1 mBar. Freeze-dried sodium alginate solutions were poured with a previously prepared solution of 3% calcium chloride (1:1 v/v). After two 12 hours, the obtained matrices were washed until the chloride ions were washed out. The matrices were then frozen and freeze-dried again. The dried matrices were subjected to sorption tests in model Cd(II) solutions at pH 4. The sorption isotherm of Cd(II) ions was tested in solutions with an initial concentration of 10-500 mg/dm$^3$, while the kinetics was performed in a solution with a Cd(II) concentration of 50 mg/dm$^3$. The solution concentrations after the Cd(II) sorption experiments were analyzed using atomic absorption spectroscopy (AAS) method. In turn, the concentration of calcium ions was analyzed using the ICP-OES spectrometer.

**Results:** Utilizing mercury porosimetry, the average pore size and volume were determined to be 7.2 µm and 0.0073 cm³/g, respectively. The Figure 1 illustrates the influence of contact time between matrix phases on Cd(II) sorption efficiency and the concentration of released Ca(II) ions as well as the solution pH following Cd(II) sorption.

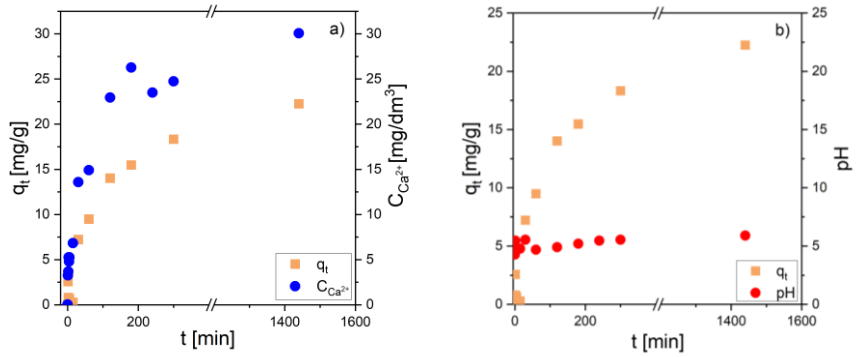



**Fig.1.** The influence of contact time on the matrix phases on: a) the efficiency of Cd(II) sorption and the concentration of Ca(II) ions released from the matrix, b) the efficiency of Cd(II) sorption and the pH solutions.

Analysis of the $q_t=f(t)$ curve revealed two discernible stages in the sorption of Cd(II) ions on matrices: an initial rapid adsorption phase followed by a period of kinetic equilibrium formation. Furthermore, an increase in phase contact time corresponded with higher levels of Ca(II) released into the solution, indicating sorption occurred via ion exchange. A subtle rise in solution pH observed during Cd(II) sorption also validates the release of Ca(II) ions. To identify the most suitable model for Cd(II) ion adsorption isotherm, equilibrium parameters for the Langmuir, Freundlich, and Temkin models were determined and are summarized in Table 1.

**Table 1.** Equilibrium parameters for the sorption process of Cd(II) ions onto the matrix at pH 4 solutions.

| Model | Parameter | ALG |
|---|---|---|
| Langmuir | $q_{e,\,exp}$ [mg/g] | 269.54 |
| | $q_0$ [mg/g] | 225.70 |
| | $K_L$ [dm$^3$/mg] | 0.008 |
| | $R^2$ | 0.934 |
| Freundlich | $K_F$ [mg/g] | 2.10 |
| | n | 1.13 |
| | $R^2$ | 0.984 |
| Temkin | B [dm$^3$/g] | 48.85 |
| | A [J/mol] | 0.22 |
| | $R^2$ | 0.645 |

The higher fitting of the Freundlich model to the data suggests that the cadmium ion sorption process onto matrices may be more complex and heterogeneous than assumed by the Langmuir model.

**Table 2.** Kinetic parameters of Cd(II) ion sorption on the matrix at pH 4 solutions utilizing pseudo-first-order (PFO) and pseudo-second-order (PSO) models.

| Model | Parameter | ALG |
|---|---|---|
| PFO | $q_{exp}$ [mg/g] | 22.25 |
| | $q_1$ [mg/g] | 23.11 |
| | $k_1$ [1/min] | 0.006 |
| | $R^2$ | 0.954 |
| PSO | $q_2$ [mg/g] | 7.15 |
| | $k_2$ [g/mg min] | 0.006 |
| | $R^2$ | 0.739 |

Analysis of the correlation coefficient $R^2$ (Table 2) indicated that the pseudo-first-order kinetic model better describes the adsorption kinetics compared to the pseudo-second-order kinetic model.

**Conclusions:** Based on the conducted research, it was observed that the sorption process of Cd(II) ions onto matrices is influenced by the contact time between matrix phases. The increase in phase contact time led to higher levels of calcium ions released into the solution, suggesting sorption occurred via ion exchange. The Freundlich model exhibited superior fitting to the experimental data, implying that the sorption process may be more complex and heterogeneous. The pseudo-first order kinetic model suggests an adsorption process primarily governed by physical forces, such as Van der Waals or electrostatic interactions, rather than chemisorption. These findings contribute to a better understanding of Cd(II) ion sorption mechanisms and provide valuable insights for environmental remediation strategies.

## References:

1. S. Elfeghe, S. Anwar, Y. Zhang, Canad. Journal of Chemical Engineering, 100 (2022) 3006.
2. H. Thrikkykkal, R. Antu, P.S. Harikumar, Water Science and Technology, 87 (2023) 2277.
3. A. Cano-Vicent, A. Martínez-Agut, A. Tuñón-Molina, H. Bakshi, R.S. Serra, European Polymer Journal, 197 (2023) 1.

4. Y. S. Chen, S. W. Phang, A. S. Shuib, and J. L. Tee, Asia-Pacific Journal of Chemical Engineering, 18 (2023) 1.
5. X. Gao, C. Guo, J. Hao, Z. Zhao, H. Long, M. Li, International Journal of Biological Macromolecules, 164 (2020) 4423.
6. M. Kuczajowska-Zadrożna, U. Filipkowska, T. Jóźwiak, Journal of Environmental Chemical Engineering, 8 (2020) 103878.

# MECHANOCHEMICAL ACTIVATION AS AN EFFECTIVE WAY OF DEVELOPING BIOCARBONS SURFACE AND POROSITY

**B. CHARMAS[1], B. WAWRZASZEK[1], K. JEDYNAK[2]**, [1]Maria Curie-Sklodowska University, Faculty of Chemistry, Institute of Chemical Sciences, Department of Chromatography, M. Curie-Sklodowska Sq. 3, 20-031 Lublin, Poland, [2]Jan Kochanowski University, Faculty of Natural Sciences, Institute of Chemistry, Uniwersytecka St. 7, 25-406 Kielce, Poland.

**Abstract:** Biomass is the most abundant renewable resource on the Earth. This waste material is one of the most promising raw materials for replacing fossil resources. However, biomass valorization poses a significant challenge due to environmental sustainability concerns and low conversion efficiency. The mechanical ball milling technology is a promising alternative to the traditional methods of biomass thermal conversion. This method proved to be efficient and environmentally friendly for processing biomass and activating the resulting biochar products. The mechanical energy during the ball milling process can induce transformation of biomass and biocarbons under the solvent-free conditions. The paper presents the results of research on the possibility of using mechanochemical processes to activate the structure and surface of biochars in terms of their use as effective adsorbents in water purification processes.

**Introduction:** Nowadays, most chemicals, fuels, and materials used by humans are made of non-renewable fossil resources such as oil, natural gas and coal. The amount of non-renewable resources on the Earth is decreasing, while the world demand for energy, chemicals, and materials continues to grow. The consumption of fossil resources can lead to severe environmental pollution and global climate change as a result of the release of large amounts of greenhouse gases and potentially toxic elements [1]. Therefore an intensive search for renewable alternatives to fossil resources for production of chemicals, fuels and materials is ongoing.

It is estimated that global biomass production is around 130 billion tons per year. Applying biological, physicochemical or thermochemical technologies, biomass resources can be converted into sustainable chemicals, fuels and other materials. Biomass processing has a mild effect for the environment due to its carbon neutrality [1]. Waste biomass can be also used to produce biochar, which has become an eco-friendly and sustainable material used for soil improvement, chemical synthesis, energy recovery/storage as well as water and wastewater treatment processes. However, biochars have limited adsorption capacity, low porosity and heterogeneous surface functionality. To improve the properties of biochars, they can be modified physically or chemically applying various techniques. Currently, only a small amount of biomass is used for commercial purposes, as the compact structure of biomass confines its conversion. A helpful alternative is the use of mechanochemical activation processes. Mechanochemical processes take place under the influence of direct absorption of mechanical energy, causing impact, compression, shear, friction and stretching [2]. Mechanochemical activation leads to reduction in particle size, an increase in the specific surface area, formation of pores and introduction of functional groups onto the

surface of biochars. There are formed new surfaces with new active sites and numerous defects desirable for the potential use of activated biochars as adsorbents. Activated biochars show a better ability to remove organic and inorganic contaminants from water and soil. Therefore, mechanochemical activation is more efficient, greener and more durable than the conventional (physical, chemical activation) biochar activation methods. The aim of the study was to analyze in detail the influence of pyrolysis temperature as well as milling parameters and time on the activation efficiency of biochars in terms of their potential use as adsorbents in water purification.

**Experimental:** Sawdust from mixed trees was used as the starting biomass. After drying (105°C, 24 h), the biomass was pyrolyzed (atm. $N_2$, flow rate 150 $cm^3$/min) from 20°C to 500°C and 800°C. The biocarbons were then subjected to mechanochemical activation (MChA) in a planetary mill (Pulverisette 7, Fritsch, Germany) at the rotation rates of 300 rpm and 800 rpm for 1 and 3 hours. The activated biocarbons were designated with 3 digits, e.g. for sample *531*: the first digit (*5*) indicates the pyrolysis temperature of the biochar (here: 500°C), the second digit (*3*) indicates the rotation speed during activation (for sample 531 the rotation was 300 rpm) and the last digit indicates the activation time (for sample 531 it was 1 h). The structural parameters of the materials were determined using the nitrogen adsorption/desorption method at -196°C (Micromeritics ASAP 2405N, USA). The specific surface area $S_{BET}$ was calculated from the BET equation at $p/p_0$ between 0.06 and 0.2. The desorption isotherm data were used for determination of the pore size distributions ($fV(R) \sim dV_p/dR$, PSD) using the self-consistent regularization procedure (SCR) [3]. The pore volume as well as the surface area of the micro ($V_{mi}$, $S_{mi}$) and mesopores ($V_{me}$, $S_{me}$) as well as the macropores ($V_{ma}$, $S_{ma}$) were calculated using the differential function (Table 1). Thermal properties of the biocarbons were determined using a Derivatograph C (Paulik, Paulik & Erdey, MOM, Budapest). The analysis was made in air atmosphere in the temperature range from 20 to 1000°C (heating rate 10°C $min^{-1}$ ) [4].

**Results:** The purpose of materials activating that are to act as effective adsorbents is to develop surface and porosity as well as to introduce surface functionalities. For the method to be environmentally friendly, it is necessary to optimize the pyrolysis and activation conditions. The initial biocarbons were obtained in the process of pyrolysis at 500°C and 800°C, however, it is known that a more effective surface development is obtained using higher activation temperatures. In the case of tested biocarbons, it was $S_{BET}$ = 29.5 $m^2$/g (sample 500) vs. 277.5 $m^2$/g (sample 800) (Table 1). Microporous biocarbons with poorly developed surface area and porosity were obtained. Mechanochemical activation (MChA) was performed under different conditions of time and speed of mill rotation. The study showed that the most intense structural changes occurred after the MChA of the 500 series biocarbons: after 1 hour of grinding (sample 531) a 14-fold increase in $S_{BET}$ was observed (Fig.1a, yellow line), and the extension of the grinding time to 3 hours (sample 533) did not cause significant changes (Fig.1). Increasing the rotation rate to 800 rpm proved to be more effective, with a ~16-fold increase in the surface area compared to the original biocarbon (sample 500), especially after milling for 3 hours. MChA caused about a 7-fold increase in the micropore volume which determines the efficiency of adsorption (Fig.1b).

The surface and porosity development in the 800 series biocarbons was much less intense (Fig.1a). There was observed a ~2-fold increase in $S_{BET}$ and an almost 2-fold increase in the micropore volume (Fig.2b) compared to the initial biocarbon 800.

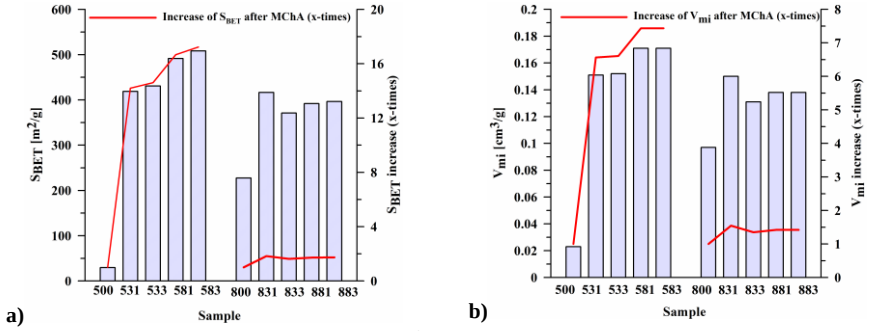



**Fig.1.** Changes in $S_{BET}$ (a) and $V_{mi}$ (b) of initial and activated by MChA biocarbons.

These changes are confirmed by the pore size distribution curves (Fig.2a). The visible maximum indicates an intensive increase in the volume of micropores with a dominant radius of $R_{dom}$~0.8 nm after MChA (Fig.a) and the formation of a meso/macroporous structure (Fig.2a), which increases the value of $R_{av}$ (Table1) for materials after MChA. The greatest changes in the meso- and macroporous structure occur after activation at a higher rotation speed (biocarbons 581 and 583, Table 1).

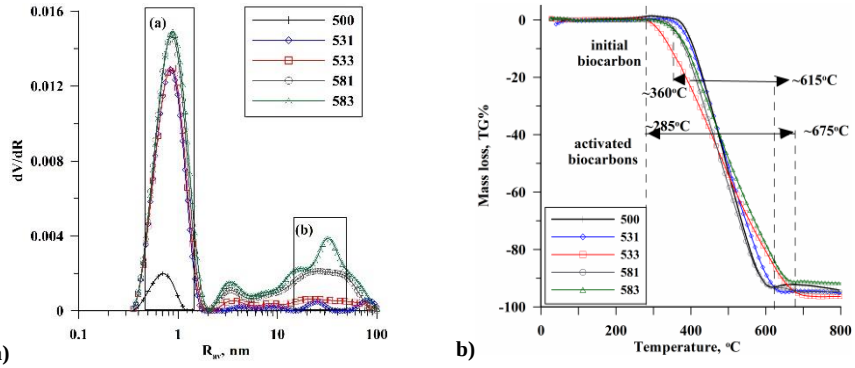



**Fig.2.** Pore size distribution (a) and TG% (b) curves for biocarbons of series 500.

The results of thermal analysis (Fig.2b) indicate that activated biocarbons undergo thermal degradation over a temperature range wider than that for non-activated biocarbon 500. The lower temperature of the onset of degradation (~285 °C) may result from a significant reduction in biocarbon particles due to MChA, such particles are more easily thermally degraded. The widening of the degradation area towards higher temperatures may be due to the better ordering of the structure of activated biocarbons and the presence of surface functional groups that are sure to be formed on the surface of the biocarbon during the activation process.

**Table 1.** The structural characteristics of the exemplary activated biocarbons.

| Carbon | $S_{BET}$ [$m^2/g$] | $S_{mi}$ [$m^2/g$] | $S_{me}$ [$m^2/g$] | $V_{mi}$ [$cm^3/g$] | $V_{me}$ [$cm^3/g$] | $R_{av}$ [nm] |
|---|---|---|---|---|---|---|
| 500 | 29.5 | 29.2 | 0.2 | 0.023 | 0.001 | 0.68 |
| 531 | 419.0 | 370.2 | 48.7 | 0.151 | 0.039 | 2.95 |
| 533 | 430.9 | 372.0 | 58.5 | 0.152 | 0.055 | 3.87 |
| 581 | 491.7 | 413.8 | 76.5 | 0.171 | 0.095 | 7.15 |
| 583 | 508.3 | 414.5 | 91.6 | 0.171 | 0.118 | 9.18 |
| 800 | 227.5 | 215.6 | 11.9 | 0.097 | 0.009 | 0.75 |
| 831 | 416.5 | 373.1 | 43.3 | 0.15 | 0.030 | 2.35 |
| 833 | 371.1 | 330.8 | 40.1 | 0.131 | 0.032 | 3.71 |
| 881 | 392.0 | 344.5 | 47.1 | 0.138 | 0.045 | 5.04 |
| 883 | 396.4 | 343.1 | 52.3 | 0.138 | 0.059 | 6.62 |

**Conclusions:** In this paper, a detailed analysis of the influence of pyrolysis conditions and mechanochemical activation on the structural and thermal properties of biochars obtained from sawdust of mixed trees was performed. It was shown that the increase in the pyrolysis temperature is very effective in development of the biochar surface, however, the obtained materials have a very poorly developed porosity. The proposed method of mechanochemical activation proved to be an effective and environmentally friendly for developing surface and porosity of materials. It was proved that the MChA of biocarbon is most effective when it is obtained in the pyrolysis at a lower temperature (500 °C, not 800 °C) and when milling proceeds at a higher mill speed (800 rpm, not 300 rpm). It was concluded that there was no justification for conducting the MChA for 3 hours. In the case of biocarbons obtained from sawdust, their activation is recommended from economical and ecological point of view to obtain biochars at a lower temperature (e.g. 500 °C) and then their 1-hour MChA without additional activating factors.

## References:

1. M. Naghdi, M. Taheran, S.K. Brar, T. Rouissi, M. Verma, R.Y. Surampalli, J.R. Valero, Journal of Cleaner Production, 164 (2017) 1394.
2. J.F. Fernandez-Bertrn, Pure Applied Chemistry, 71 (1999) 581.
3. V.M. Gun'ko, S.V. Mikhalovsky, Carbon, 42 (2004) 843.
4. B. Charmas, Journal of Thermal Analysis and Calorimetry, 120 (2015) 1347.

# CHANGE IN $SiO_2$ STRUCTURE UNDER HYDROTHERMAL CONDITIONS DURING MECHANOCHEMICAL MILLING

**B. CHARMAS[1], J. SKUBISZEWSKA-ZIĘBA[1], K. JEDYNAK[2]**, [1]Maria Curie-Sklodowska University, Faculty of Chemistry, Institute of Chemical Sciences, Department of Chromatography, M. Curie-Sklodowska Sq. 3, 20-031 Lublin, Poland, [2]Jan Kochanowski University, Faculty of Natural Sciences, Institute of Chemistry, Uniwersytecka Str. 7, 25-406 Kielce, Poland.

**Abstract:** There are many threats for the environment caused by human activities, including air and water pollution, overextraction and consumption of natural resources, climate changes and degradation of ecosystems. In response to these threats, it is necessary to develop and implement new pro-ecological technologies that can eliminate or limit the changes taking place. One way is to modify existing materials to expand their use. A good example is $SiO_2$, an available and low-cost material with a great application potential. To improve the properties of commercial $SiO_2$ for specific applications (e.g. adsorption properties), eco-friendly hydrothermal modification (HTT) can be used applying mechanochemical procedures (MChT). The paper showed that as a result of HTT application with the use of MChT, there was an intensive reconstruction of porous structure and change in the size of silica gel globules, which translates into the possibility of their potential use in adsorption processes.

**Introduction:** Nowadays as a result of large human interference in the natural environment, civilization is approaching a critical state. It is sufficient to mention the greenhouse effect, the ozone hole, acid rain and its impact on climate change to realize how enormous the impact of this interference is. It is believed that further reckless, even robbery activity of the society in relation to nature can make the Earth incapable of self-regeneration and existence, for both the animals and plants as well as people. Currently, the most important aspects are protection of the environment, human health and life. The most appropriate way for further progress in civilization is a new approach to environmental protection issues – the search for more ecological and sustainable methods of production, processing and chemical synthesis.

One of the pro-ecological solutions for the synthesis and modification of materials is mechanochemistry. This is a branch of chemistry exploiting mechanical energy, such as friction, impact, or abrasion, to conduct chemical reactions. The method is an alternative to the traditional solvent-based methods, which can be harmful to the environment. Mechanochemistry makes processes more efficient eliminating the need for large amounts of solvents, which at the same time leads to reduction in chemical waste and greenhouse gas emissions.

Porous silica gels are widely applied in many fields of science and modern technology as adsorbents, catalyst carriers, fillers and fillings for chromatographic columns. The wide range of applications is due to its high mechanical and thermal strength, developed specific surface area and well-defined pore structure [1]. The wide range of applications of $SiO_2$ necessitates the development of new materials with modified surfaces. One of the most commonly used and effective methods of regulating the textural and structural

parameters of adsorbent and catalyst surfaces is hydrothermal modification (HTT) [2]. The essence of hydrothermal modification is to subject the tested material to water (in the liquid form or the water vapor form) at a temperature above 100$^{o}$C, at a pressure higher than the atmospheric one. Silica gels are particularly susceptible to water vapor in such a system [3]. Under these conditions, water changes its physicochemical properties, causing the silica mass to be transported: depolymerization of small silica particles to form orthosilicic acid, followed by its re-condensation on larger particles. The efficiency of HTT process depends on the structure of the output adsorbent, temperature, time and conditions of the process (in the gas phase or the liquid phase) and pH of the medium. As a result of such modification, among others, specific surface area, pore size and structure, chemical nature of the surface, etc., are changed. An in-depth analysis of the effects of hydrothermal modification is extremely important because it facilitates prediction of changes in the properties of adsorbents and catalysts that occur during numerous technological processes carried out at high temperatures, often in the presence of water.

Hydrothermal activation can be carried out using mechanochemical processes. The process involves the dispersion of solids and their plastic deformation, leading to structural changes. High temperature of the system, resulting from generation of heat during inelastic collisions between grinding balls and their collisions with the vessel wall, allows hydrothermal processes to take place.

The study aimed at analyzing the effects of mechanochemical grinding of silica gel with different water content on changes in the porous structure of the obtained ground silica.

**Experimental:** The starting material was silica gel Si-60 (Merck, d = 0.2-0.5 mm, $S_{BET}$ = 433 $m^2/g$). Milling was carried out in Planetary mill Pulverisette 7 (FRITSCH, Germany) equipped with a Radio sensor (Easy GTM software, FRITSCH) used to record the temperature and pressure values formed during milling. The vessel (80 ml) and spheres (Ø = 5 mm) were made of $ZrO_2$ (250 spheres, rotation speed: 1000 rpm, milling time: 15 or 30 minutes, water quantity: from 0 to 15 ml/10g silica gel).

The structural parameters of the materials were determined based on the low-temperature (77.4 K) nitrogen adsorption-desorption isotherms (Micromeritics ASAP 2405N, USA). The particle size distribution was determined using MASTERSIZER 2000 (Malvern Instruments Ltd., UK) apparatus. The surface morphology was determined using Atomic Forces Microscopy (NanoScope III, USA).

**Results:** Mechanochemical reactions of solids in the presence of water can be considered hydrothermal. The hydrothermal method is based on the ability of water to dissolve substances at elevated temperatures and pressures. The use of water as a solvent is based on its self-ionization according to the equation:

$$2H_2O \longleftrightarrow H_3O^+ + OH^-$$

The basic element of the structure of $SiO_2$ are globules, which are made of $SiO_4$ tetrahedrons, and these are arranged in a spatially disordered network. Globules are formed during the condensation of orthosilicic acid. Active hydroxyl groups are present on the surface of the globules, which give surface reactivity to the silica gel. This makes it easy to modify the surface properties of the gel, both in terms of its chemical nature and pore structure. During silica HTT, the depolymerization (decondensation) of small particles to orthosilicic acid occurs according to the following reaction:

$$(SiO_2)_n + 2H_2O \longleftrightarrow (SiO_2)_{n-1} + Si(OH)_4$$

This is followed by acid deposition (recondensation) processes on large silica particles. Mechanochemical milling allows such reactions to take place due to the increased pressure and temperature. The silica gel globules clump or fuse at the contact points to form a skeleton with a modified internal surface. The size of the free spaces (pores) between the globules depends on the size of the globules and their packing. During hydrothermal modification, the amount and nature of surface hydroxyl groups (isolated, twin, etc.) also change [4] causing changes in the adsorption properties of modified silica, which is in line with the trend towards greener and more sustainable procedures.

The AFM analysis (Fig.1) showed that grinding Si-60 increased the original size of $SiO_2$ globules (Fig.1a,b). A large amount of water and a longer grinding time result in more complex structures (Fig.1c,d).

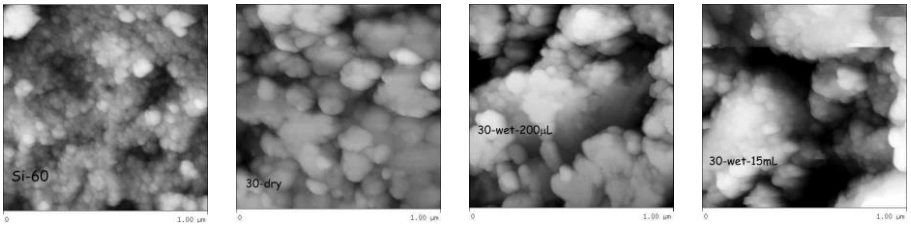



**Fig.1.** AFM images of the samples: Si-60, 30-dry, 30-wet-200µl and 30-wet-15ml.

The analysis of $N_2$ adsorption data shows that the largest change in the specific surface area of the samples after the mechanochemical modification compared to the starting material occurs for the samples obtained with small amounts of water present in the system (microliters, Fig.2a). A longer machining time results in greater changes in the specific surface area value. This is related to the titer of the size of the globules (Fig.2b), the largest globule sizes were observed for the ground gel with the addition of water ~ 1 ml (Fig.2b).

The change in the porous structure is evidenced by changes in the shape of the $N_2$ adsorption/desorption isotherms and the pore size distribution curves (Fig.3). Depending on the water content in the system during MChT, the hysteresis loops acquired different shapes (Fig.3a,b). A longer modification time results in larger changes. It was found that the initial Si-60 is characterized by a monomodal and ground silica by a bimodal pore distribution.

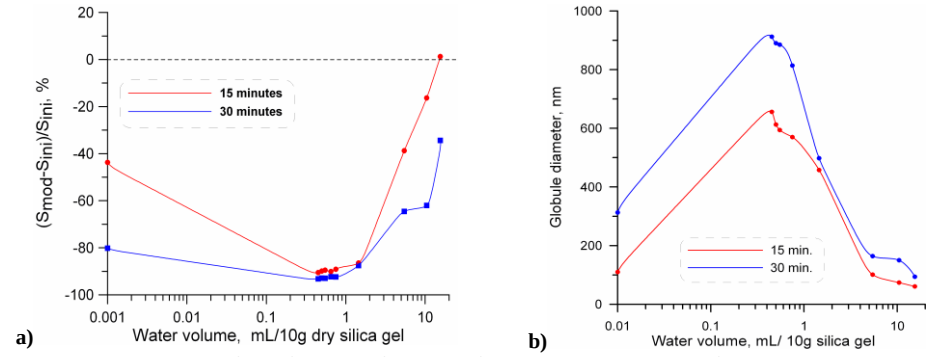



**Fig.2.** Changes in the specific surface area of samples after mechanochemical modification (a) and changes in the size of silica-modified globules (b) depending on the volume of added water.

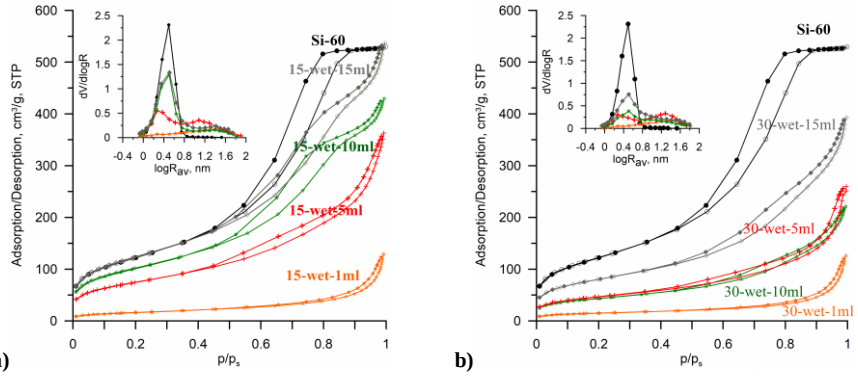



**Fig.3.** $N_2$ adsorption/desorption isotherms and pore size distribution curves (insets) of 15 min (a) and 30 min (b) milled silica.

**Conclusions:** It was proved that mechanochemical grinding of $SiO_2$ in the presence of water is a hydrothermal process in which the structure of materials is intensively restructured. The intensity of the changes depends largely on the water content in the system. The greatest changes in $S_{BET}$ correspond to small quantities of water (microliters).

## References:

1. R.K. Iler, The Chemistry of Silica, Wiley, New York, 1979.
2. R. Leboda, V.A. Tertykh, V.V. Sidorchuk, J. Skubiszewska-Zięba, Colloids and Surfaces A, 135 (1998) 253.
3. J. Skubiszewska-Zięba, Adsorption, 16 (2010) 485.
4. B. Charmas, K. Kucio, V. Sydorchuk, S. Khalameida, M. Zięzio, A. Nowicka, Colloids Interfaces, 3 (2019) 6.

# PHYTOTOXICITY OF BIOCHARS OBTAINED FROM VARIOUS RAW MATERIALS

**B. CZECH, A. SOKOŁOWSKI**, Maria Curie-Sklodowska University, Faculty of Chemistry, Institute of Chemical Sciences, Department of Radiochemistry and Environmental Chemistry, M. Curie-Sklodowska Sq. 3, 20-031 Lublin, Poland.

**Abstract:** Biochar (BC) may be successfully used in sustainable agriculture and environmental remediation. It may be derived from various types of feedstocks. The type of raw material used determines the physicochemical properties of the obtained biochar. Also, the toxicity of the final product corresponds with the applied feedstock. The effect of biochar addition to the soil depends on the composition of biochar and its physicochemical properties. Some compounds present in biochar such as polycyclic aromatic hydrocarbons and heavy metals may affect plants and soil microflora in the BC-amended soil. Therefore, the key point nowadays is assessing the ecotoxicity of various biochars before using them as soil amendments on a large scale. The presented results show the effect of different types of biochar, added to the soil at 1wt.%, obtained from different feedstocks on the germination and growth of *Lepidium sativum L.*

**Introduction:** Biochar, a carbon-rich material derived from the pyrolysis of organic biomass in an oxygen-limited environment, is a promising tool in sustainable agriculture and environmental remediation. Produced at high temperatures and in the absence of oxygen, biochar retains a stable carbon structure, making it resistant to decomposition and capable of sequestering carbon from the atmosphere for extended periods [1]. The feedstock for biochar production varies widely and includes sewage sludge, agricultural wastes, forestry residues, and other organic materials. This diversity in feedstock contributes to the variability in biochar properties, influencing its potential applications and efficiency as a soil amendment. The properties of biochar obtained from different feedstocks exhibit significant variations, impacting its chemical composition, surface area, pore structure, and nutrient content [2]. Biochar's application as a soil amendment has garnered considerable attention due to its ability to enhance soil fertility. Studies have shown that biochar amendments can positively influence soil pH, increase the availability of essential nutrients, such as phosphorus and potassium, and promote the proliferation of beneficial soil microorganisms. Additionally, biochar amendments have been associated with improved soil structure, water retention, and cation exchange capacity (CEC) [3]. However, the effects of biochar on soil properties and plant growth depend not only on its inherent physicochemical properties but also on its interactions with soil components and microbial communities [4]. Despite the potential benefits of biochar, concerns regarding its safety and potential toxicity persist. The interactions between biochar properties, soil conditions, and plant responses underscore the importance of testing to assess the safety of biochar amendments. Evaluating the impact of biochar on plant growth, nutrient uptake, and overall ecosystem health is essential. The toxicity of biochar may result from its composition, especially the presence of heavy metals and polycyclic aromatic hydrocarbons (PAHs). PAHs are products of incomplete combustion of organic matter, so it is a group of compounds that are produced in the

pyrolysis process [5]. Heavy metals are the main inorganic contaminants of biochar. They may be present in biochar only when the feedstock contains heavy metals. Additionally, due to the decomposition of organic matter, the concentration of metals in obtained biochar is greater than in raw material [6]. For this purpose, it is necessary to perform ecotoxicity tests, determining the effect of biochar on plants and microorganisms. Phytotox is a test, that examines the impact of biochar addition on germination and growth of seeds of *Lepidium sativum L.* It is conducted in the solid phase. The biochar is added to certified soil and results are compared with the results obtained for control.

**Experimental:** The experiment was divided into the following stages:
- biochar production – different types of biochar were obtained from waste materials: sewage sludge from a wastewater treatment plant Częstochowa (50°49′04″N 19°08′18″E) (Ss-BC) and residues from biogas production (Przypisówka 51°32′42″N 22°33′49″E) (Bg-BC), and two agricultural wastes: corn straw (*Zea mays L.*) (Cr-BC) and sunflower straw (*Helianthus L.*) (Sf-BC). All materials were pyrolyzed at 600 ˚C in a nitrogen atmosphere for 3 hours.
- testing of physicochemical properties – the physicochemical properties of all obtained biochars were examined. The physical properties such as specific surface area, porosity, and surface morphology were determined. To determine the composition of tested biochars the content of carbon, hydrogen, nitrogen, and oxygen, total organic carbon (TOC) content, and ash content were analyzed. To assess the concentrations of various metals in tested materials, biochar samples underwent microwave mineralization. Subsequently, the resulting solutions were analyzed using the Thermo Scientific iCAP™ 7000 ICP-OES. The pH of the tested biochars was measured.
- Phytotoxkit test – in this stage, based on the procedure [7] phytotoxicity tests of the obtained biochars were carried out to assess their impact on vegetation. In the test, *Lepidium sativum L.* seeds were used. The growth, development, and general condition of plants were observed in the presence of 1% biochar and controls without biochar. The test plates were placed in a laboratory dryer at 25˚C. After 72 hours, the root length of the germinated seeds was measured. The results of this research helped to assess the potential environmental risks associated with the use of biochar.

**Results:** All tested biochars were prepared at 600 ˚C so that the differences in properties result only from the type of raw material used for pyrolysis. The results of the physicochemical test are presented in Table 1. All tested biochars differ significantly in their elemental composition. Biochar obtained from sewage sludge possessed the greatest oxygen content (9.5%) and the lowest carbon content (23.49%) among all tested materials. Sunflower-derived biochar was characterized by the greatest carbon content (86.71%) and the lowest oxygen content (3.96%). Sewage sludge-derived biochar was enriched in ash content – mineral fraction (62.78%) whereas biochar obtained from sunflower straw has the lowest ash content (6.7%). Plant waste-derived biochars had a similar TOC content: 878.52 mg/g in Sf-BC, and 818.42 mg/g in Cr-BC. However, they differed significantly in the extent of their specific surface area <2 $m^2$/g in Sf-BC, 90.104 $m^2$/g in Cr-BC, the lowest and the highest values for tested biochars. All prepared biochars had an alkaline pH, ranging from 8.06 for Ss-BC to 10.66 for Bg-BC.

**Table 1.** Physicochemical properties of obtained biochars

| Material | Feedstock | pH | ash (%) | C (%) | H (%) | N (%) | O (%) | TOC (mg/g) | $S_{BET}$ ($m^2$/g) |
|---|---|---|---|---|---|---|---|---|---|
| Ss-BC | Sewage sludge | 8.06 | 62.78 | 23.49 | 0.57 | 3.66 | 9.5 | 328.05 | 26.05 |
| Bg-BC | Biogas residues | 10.66 | 25.93 | 62.88 | 1.2 | 2.57 | 7.43 | 630.99 | <2 |
| Sf-BC | Sunflower | 9.26 | 6.7 | 86.71 | 1.67 | 0.96 | 3.96 | 878.52 | <2 |
| Cr-BC | Corn | 9.6 | 14.12 | 76.68 | 2.71 | 1.3 | 5.18 | 818.42 | 90.104 |

The concentration of heavy metals in biochars was strongly correlated with the type of feedstock used in the pyrolysis process. In the experiment, the concentrations of various metals were determined (Table 2). Some of them are necessary for plants to grow such as copper, zinc, manganese, and iron. The greatest content of dangerous heavy metals was noted in Ss-BC. This material contained significant amounts of lead and cobalt, and it was the only biochar that contained cadmium. Biochars obtained from plant materials had much lower metal concentrations compared to those obtained from other organic wastes. All biochars meet heavy metal content standards, established by International Biochar Initiative (IBI).

**Table 2.** Concentration of various metals in tested biochars

| Metal | Ss-BC | Bg-BC | Sf-BC | Cr-BC |
|---|---|---|---|---|
| [mg/kg] | | | | |
| Cr | 768.005 | 6.161 | 1.109 | 0.985 |
| Cu | 459.611 | 20.946 | 22.055 | 7.632 |
| Fe | 26227.129 | 2783.391 | 349.803 | 476.98 |
| Mn | 929.075 | 632.085 | 22.425 | 45.421 |
| Ni | 226.886 | 2.464 | 0.986 | 0.492 |
| Zn | 3396.959 | 86.249 | 26.861 | 85.55 |
| Co | 15.815 | 1.232 | ND | 0.123 |
| Cd | 0.973 | ND | ND | ND |
| Pb | 75.061 | 1.232 | ND | 2.339 |

ND-not detected

Results of the Phytotoxkit test showed that all prepared materials had a positive effect on the seeds of *Lepidium sativum L.* germination and growth (Figure 1). After three days the roots of plants from samples with biochar addition were longer than the roots of plants from the control sample. The most stimulating effect revealed biochar obtained from sewage sludge. Roots of tested plants from samples with Ss-Bc additive were 127.34% longer than in the control, probably due to the high Fe rather than TOC content. The least stimulation of the growth of roots was observed in the sample with biochar obtained from sunflower residues (105.52%) even though this BC was characterized by the highest C and TOC content. These results were confirmed when the Pearson test was performed. O% content in biochar significantly ($p<0.001$) affected the growth of the tested plant. A slightly lower impact revealed the presence of inorganics (the correlation between root length and ash content was at $p<0.1$). However, at higher TOC content in biochar, the growth of *L. sativum* was hindered ($p<0.005$).

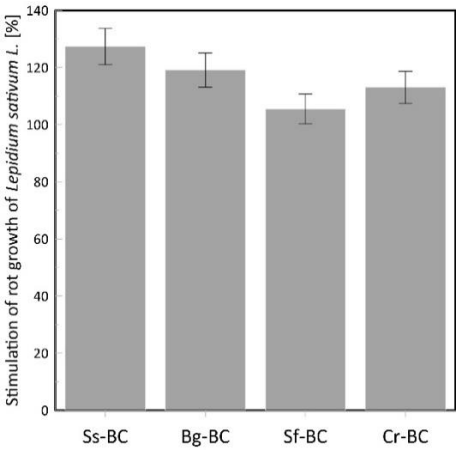



**Fig.1.** Phytotoxkit test results

**Conclusions:** The study investigated the effects of four different biochars derived from various raw materials on seed germination and plant growth. The findings revealed that all tested biochars have a positive impact on seed germination and root growth, thereby stimulating overall plant growth. These results suggest that biochar additives have the potential to enhance soil fertility and promote plant development. Moreover, their safety for use as soil amendments was demonstrated, indicating their suitability for widespread application in agricultural practices. Overall, the study underscores the promising role of biochar in sustainable agriculture, offering a natural and effective solution for improving soil health and optimizing plant growth. Further research should focus on examining their long-term impact on soil fertility and ecosystem sustainability.

**Acknowledgements:** This study was supported by grant No. 2021/40/Q/NZ8/00006 from the National Science Centre, Poland.

**References:**

1. W. Xiang, X. Zhang, J. Chen, W. Zou, F. He, X. Hu, D.C.W. Tsang, Y.S. Ok, B. Gao, Chemosphere, 252 (2020) 126539.
2. S. Joseph, A.L. Cowie, L. Van Zwieten, N. Bolan, A. Budai, W. Buss, M.L. Cayuela, E.R. Graber, J. A. Ippolito, Y. Kuzyakow, Y. Luo, Y.S. Ok, K. N. Palasooriya, J. Shepherd, S. Stephens, Z. Weng, J. Lehmann, GCB Bioenergy, 13 (2021) 1731.
3. M.W. Kang, M. Yibeltal, Y.H. Kim, S.J. Oh, J.C. Lee, E.E. Kwon, S.S. Lee, Science of the Total Environment, 836 (2022) 155746.
4. S. Adhikari, W. Timms, M.A. Parvez Mahmud, Science of the Total Environment, 851 (2022) 158043.
5. E. Reizer, B. Viskolcz, B. Fiser, Chemosphere, 291 (2022) 132793.
6. I. Hilber, A.C. Bastos, S. Loureiro, G. Soja, A. Marsz, G. Cornelissen, T.D. Bucheli, Journal of Environmental Engineering and Landscape Management, 25 (2017) 86.
7. A. Baran, M. Tarnawski, Ecotoxicology and Environmental Safety, 98 (2013) 19.

# PHTHALIC ACID ESTERS IN BIOCHAR-AMENDED SOIL-VEGETABLE SYSTEM

**B. CZECH, A. SOKOŁOWSKI**, Maria Curie-Sklodowska University, Faculty of Chemistry, Institute of Chemical Sciences, Department of Radiochemistry and Environmental Chemistry, M. Curie-Sklodowska Sq. 3, 20-031 Lublin, Poland.

**Abstract:** Soil contamination with phthalates (PAEs) is currently a serious problem in large-scale agriculture. PAEs may be taken up by plants and introduced into the food chain. It is the main route of human exposure to PAEs. Phthalates are known endocrine disruptors and it is necessary to remove them effectively from the environment. Biochar can be used for this purpose. It has a porous structure on which phthalates may be immobilized. At the same time, biochar has a beneficial effect on soil microflora and may promote the proliferation of various bacteria that degrade phthalates. Other advantages of biochar are its low price, and the possibility of obtaining it from many different raw materials.

**Introduction:** Biochar (BC) is produced by heating carbon-rich materials in an oxygen-free atmosphere. A characteristic feature of this material is its porous structure and abundance of various surface groups. Types of those groups and other properties of obtained biochars are strongly related to the raw material used. Change in the feedstock, can influence the final product causing it to differ in specific surface area, porosity, pH, and chemical composition. Various types of organic residues like agricultural and forestry residues, wood, but also sewage sludge from wastewater treatment plants [1] may be used as feedstock. BC can be successfully used in environmental remediation as a sorbent for removing pollutants from soils and waters [2]. Biochar has also been used as a soil additive for many years. It improves soil properties such as soil pH, increases the availability of essential nutrients, like K, P, Mg, N, Ca, and Cu by improving their retention, and improves soil structure, soil's water-holding capacity, and cation exchange capacity (CEC) [3]. The porous structure of biochar is a great habitat for soil bacteria and fungi that also improve soil fertility [4]. These two properties make biochar a promising tool for removing various contaminants from agricultural soil, which may be contaminated with various dangerous organic and inorganic compounds. Examples of the organic pollutants present in agricultural soils are phthalic acid esters (PAEs). It is a group of compounds commonly used in industry. PAEs may be divided into two groups with different applications. Low molecular weight (LMW) phthalates are mainly used as solvents in cosmetics and high molecular weight (HMW) phthalates are the main plasticizers used in the polymer industry [5]. Phthalates are present in all soil types but their presence in agricultural soil is the most dangerous for people. Soil contamination with phthalates is a huge problem, especially in fields where various types of agricultural films are used. Phthalates are not chemically bonded to the polymer matrix, and they may be easily washed out to the environment. This process is accelerated by variable weather conditions such as rain, snow, frost, and UV radiation [6]. Phthalates present in soil may be taken up by plants, accumulated in different plants' parts, and then introduced into the food chain. Food contaminated with phthalates is the main route of

human exposure to them [7]. Due to the recognition of phthalates as endocrine disruptors, which may block the action of endogenous hormones, the United States Environmental Protection Agency (US EPA) added some phthalates (dimethyl phthalate (DMP), diethyl phthalate (DEP), dibutyl phthalate (DBP), butyl benzyl phthalate (BBP), di-(2-ethyl hexyl) phthalate (DEHP), and di-n-octyl phthalate (DNOP)) to the list of pollutants requiring priority control, whereas DEHP was classified as a probable human carcinogen [8]. Different crops have different tendencies to uptake and accumulate phthalates in various parts like roots, leaves, and fruits. The process of phthalates distribution in the plant is influenced by their properties. For example, HMW phthalates are more difficult to transport, and they are accumulated in parts where they are taken up [9]. The composition of plant tissues also has an impact on the transport of phthalates between different parts of the plant. Higher fat content in tissue promotes a higher accumulation of phthalates [6]. Phthalates may be removed from soils by adding the biochar, which may also act as a fertilizer and improve the soil properties.

**Experimental:** In this experiment, various types of biochar were added to the soil and their impact on the fate of phthalates (DMP, DEP, DBP, BBP, DEHP, and DNOP) in the soil-vegetable system was tested. Two different types of vegetables were chosen: radish (*Raphanus sativus L.*) and lettuce (*Lactuca sativa L.*). Both vegetables can be eaten raw and are very popular in many countries. Additionally, they represent different types of crops. Radish is a root vegetable and lettuce is a leafy vegetable. The biochars used in the experiment were obtained by subjecting raw material, sunflower stalks (*Helianthus L.*), to a temperature of 600 ˚C, in a nitrogen atmosphere for 3 hours. As a raw material, were used. Physicochemical properties of all biochars were determined. Some important properties for efficient sorption like specific surface area were determined in ASAP 2420 Analyzer (Micromeritics, USA), and the types of functional groups present on the surface of biochars were determined via FT-IR spectroscopy and X-ray photoelectron spectroscopy (XPS). Also, the composition of tested biochars: the content of carbon, hydrogen, nitrogen, and oxygen, total organic carbon (TOC) content, and ash content were analyzed. Plants in the experiment were cultivated on agricultural soil whose basic properties were determined. 340 g of soil in glass containers was mixed with 3.4 g (1% additive) of biochar, spiked with 1mL of PAEs mix containing 1 µg/mL of each tested compound, and was watered to achieve 65% hydration. Seeds were germinated by keeping them wet, in the dark in the Petri dish. After 48 h of germination three sprouted radish seeds, and after 72 h five sprouted lettuce seeds were added to the soil. The containers were placed in Conviron GEN100 and exposed to light/dark cycles (12:12 h), temperature 22°C/18°C day/night, and constant humidity 65%. All samples were watered three times a week to keep the 65% water-holding capacity of the soil. After 6 weeks plants were harvested and roots were separated from leaves. All the subparts were washed in distilled water and air-dried, frozen in the freezer (-20 °C, Liebherr), and freeze-dried in Alpha 1-2 LDplus (Christ) for GC-MS/MS according to the procedure [10].

**Results:** The biochar used in the experiment was characterized by alkaline pH. Biochar obtained from sunflowers contained 82.39% of C, 1.35% of H, and 7.46% of ash. The FT-IR and XPS analysis results confirmed that very common forms of carbon on biochar were carbon bonded to hydrogen and C=C $sp^2$. The surface of tested biochar was

abundant in carbonyl and carboxyl groups. Concentrations of tested compounds in roots and leaves of tested vegetables and in soil after cultivation are presented in Table 1. Phthalates concentrations in samples without PAEs mix addition were <LOD.

**Table 1.** Phthalates concentrations in the soil, and in different parts of plants in samples with PAEs, and samples with PAEs and sunflower-derived biochar.

| Sample | | DMP | DEP | DBP | BBP | DEHP | DNOP |
|---|---|---|---|---|---|---|---|
| | | ng/L | | | | | |
| Soil + PAEs + lettuce | Roots | 1.078 | 3.368 | 0.608 | 1.014 | 0.738 | 1.629 |
| | Leaves | 5.506 | 3.207 | 7.596 | 5.085 | 7.17 | 2.941 |
| | Soil | 23.06 | 23.07 | 21.461 | 23.535 | 21.75 | 25.039 |
| Soil + PAEs + BC+lettuce | Roots | 0.787 | 2.172 | 0.586 | 0.808 | 1.558 | 1.619 |
| | Leaves | 3.941 | 3.208 | 8.135 | 6.41 | 5.331 | 4.857 |
| | Soil | 18.001 | 17.54 | 15.16 | 16.23 | 16.46 | 16.756 |
| Soil + PAEs + radish | Roots | 0.623 | 2.054 | 0.254 | 0.176 | 1.457 | 0.486 |
| | Leaves | 2.682 | 2.627 | 7.426 | 3.738 | 6.307 | 2.517 |
| | Soil | 26.19 | 24.84 | 21.90 | 25.60 | 21.82 | 23.491 |
| Soil + PAEs + BC + radish | Roots | 0.677 | 2.172 | 0.267 | 0.181 | 1.483 | 0.547 |
| | Leaves | 2.626 | 2.573 | 7.214 | 3.671 | 6.26 | 2.842 |
| | Soil | 20.69 | 19.57 | 17.45 | 20.26 | 17.25 | 20.622 |

**Conclusions:** In this experiment, the fate of phthalates in a soil-vegetable system was investigated, following the addition of various types of biochar obtained from various organic residues to the soil. The tested vegetables, lettuce (a leafy vegetable) and radish (a root vegetable) were found to accumulate phthalates, with higher concentrations detected in the leaves compared to the roots. This finding is particularly significant for lettuce, as its leaves are consumed directly by humans. The presence of sunflower-derived biochar in the soil decreases concentrations of LMW phthalates (DMP, DEP, DBP, and BBP) in the lettuce roots. This material also decreases the concentrations of DMP, and DEHP in lettuce leaves. In the case of radish, the addition of this biochar does not have a significant effect on the concentration of phthalates in both leaves and roots. The concentration of all six tested phthalates in the soil after cultivation both lettuce and radish are much lower in samples with biochar additions. This may suggest that phthalates have been strongly immobilized on the biochar surface or have been decomposed. There are known soil bacteria, such as *Agromyces*, that can decompose phthalates. These bacteria revealed a high PAEs degradation efficiency [11]. The porous structure of biochar can be a great habitat for these bacteria and favor their multiplication. Obtained results suggest that biochar may play a crucial role in reducing the bioavailability and uptake of phthalates by plants, thereby potentially decreasing human exposure to these harmful compounds through the consumption of contaminated vegetables. Phthalates are known to pose serious health risks to humans, including endocrine disruption, reproductive toxicity, and carcinogenicity. Therefore, strategies aimed at reducing phthalate contamination in agricultural systems, such as the incorporation of biochar, hold promise for safeguarding human health and promoting food safety. Overall, this study underscores the potential of biochar as a sustainable and effective tool for mitigating phthalate contamination in agricultural environments. Additionally, further research into the long-term effects of biochar additives on soil phthalate fate is necessary to fully understand the efficacy and sustainability of this approach. Long-term studies will provide valuable insights into the stability of biochar-

phthalate interactions, potential leaching or accumulation of phthalates in the soil over time, and the overall impact on soil health, plant growth, and ecosystem dynamics.

**Acknowledgments:** This study was supported by grant No. 2021/40/Q/NZ8/00006 from the National Science Centre, Poland.

**References:**

1. Y. Li, R. Gupta, Q. Zhang, S. You, Bioresource Technology, 369 (2023) 128423.
2. M. Kamali, N. Sweygers, S. Al-Salem, L. Appels, T.M. Aminabhavi, R. Dewil, Chemical Engineering Journal, 428 (2022) 131189.
3. M. Ginebra, C. Muñoz, R. Calvelo-Pereira, M. Doussoulin, E. Zagal, Science of The Total Environment, 806 (2022) 150465.
4. Z. Dai, X. Xiong, H. Zhu, H. Xu, P. Leng, J. Li, C. Tang, J. Xu, Biochar, 3 (2021) 239.
5. R.-K. Poopal, J. Zhang, R. Zhao, M. Ramesh, Z. Ren, Chemosphere, 252 (2020) 126498.
6. A. Giuliani, M. Zuccarini, A. Cichelli, H. Khan, M. Reale, International Journal of Environmental Research and Public Health, 17 (2020) 5655.
7. J. Eales, A. Bethel, T. Galloway, P. Hopkinson, K. Morrisey, R.E. Short, R. Garside, Environmental International, 158 (2022) 106903.
8. S. Ghosh, M. Sahu, Journal of Hazardous Materials Advances, 6 (2022) 100065.
9. F. Zhao, Z. Ma, H. Ping, Z. He, B. Li, Y. Gao, C. Li, Environmental Pollution, 292 (2022) 118391.
10. A. Sokołowski, M.P. Dybowski, P. Oleszczuk, Y. Gao, B. Czech, Food Chemistry, 440 (2024) 138222.
11. F. Chen, X. Li, Y. Dong, J. Li, Y. Li, H. Li, L. Chen, M. Zhou, H. Hou, Chemosphere, 266 (2021) 129061.

# THE USE OF SPECTROSCOPIC METHODS FOR THE ANALYSIS OF BIOCARBON OBTAINED FROM PLANT WASTES

**P. RADULSKI, B. KAŹMIERCZAK, A. KACZMARCZYK**, Łukasiewicz Research Network - Institute of Exploitation Technologies, Center for Bioeconomy and Eco-innovation, Proecological Technologies Research Group, K. Pułaskiego St. 6/10, 26-600 Radom, Poland.

**Abstract:** The subject of this study was to determine the changes occurring in the structure of biocarbon produced from waste biomass during the pyrolysis process conducted at 500°C and 700°C. Apple waste biomass was used for the study. Raman spectroscopy was used to identify bands indicative of the ordering of the structure of the obtained carbon materials. Infrared spectroscopy (FTIR) enabled the identification of functional groups. By using the Raman and FTIR methods, a comprehensive evaluation of the changes in the biocarbon materials resulting from pyrolysis processes was made and their applicability was determined.

**Introduction:** Poland is considered the third largest producer of apples in the world. The large accumulation of orchards, as well as the need to cut trees, creates a significant amount of waste biomass [1]. Biomass is currently the most widespread form of renewable energy, and its use is increasing due to concerns about the devastating impact of fossil fuel consumption, i.e. climate change, global warming and their negative impact on human health [2,3]. Biomass can be divided into woody biomass, herbaceous biomass, aquatic biomass (algae), biomass from animal and human waste, and biomass mixtures. Herbaceous biomass can include: grasses (alfalfa, bamboo, cane), straws (beans, flax, corn, canola), other residues (fruits, hulls, husks, seeds, coconut fiber, stalks, cobs) [4,5]. Due to the European Union's regulations on the principles of sustainable development and limiting coal production, scientists are looking for technologies to process biomass and obtain environmentally friendly materials that meet the criteria set for activated carbons [3]. One way of processing biomass is pyrolysis, which produces biocarbon. Pyrolysis is the process of converting specific biomass into liquid (bio-oil), solid (charcoal) and gaseous (combustible gas) products through partial combustion at temperatures above 400 °C and in the absence of oxygen [6]. There are different ways to conduct the pyrolytic process affecting the production of bio-oil, syngas and carbon residues. Carbonization occurs at temperatures between 300 and 500 °C. Slow or conventional pyrolysis occurs at moderate temperatures around 500 °C. Fast pyrolysis occurs at moderately low temperatures (500 to 650 °C). Flash pyrolysis is carried out at temperatures higher than 650 °C and favors the production of a gaseous fraction [7]. Cascade pyrolysis, on the other hand, is a slow pyrolysis, due to which the effect of thermal inertia of the furnace is reduced, and it increases the sorption area of biocarbon, as well as increases the amount of solid fraction obtained. The pyrolysis process is carried out with the participation of an inert gas, such as nitrogen, carbon dioxide [8]. Activated carbon has a similar structure to biocarbon. Activated carbons contain an ordered phase composed of graphite-like crystals, a disordered phase

composed of complex aromatic-aliphatic structures, and a porous phase composed of micro-, meso- and macropores [9]. According to the literature [3], biocarbon has similar properties. To determine the possibility of using biocarbons as, for example, lubricant additives or metal sorbents from aqueous solutions, a number of physicochemical analyses are required. Among these analyses are spectroscopic methods. Spectroscopic methods play an important role in determining the structure of biocarbons. With Raman spectroscopy, bands indicating the ordering of carbon structures can be found. Infrared spectroscopy is used to identify functional groups, as well as changes in chemical composition resulting from pyrolysis in carbon materials, dependent on thermal conditions. Hydroxyl groups, for example, can positively influence the sorption properties of metal ions, such as chromium (III) [3]. Biocarbon can also be added to lubricants, instead of graphite additives [10]. The purpose of this study was to determine what changes occur in biocarbon obtained from apple waste biomass under the temperature of the pyrolysis process.

**Experimental:** The apple pomace was processed by pyrolysis at 500 °C and 700 °C. The inert gas used was CO2. Carbonization was carried out under cascade conditions. Pyrolysis was carried out in a Czylok muffle furnace, type FCF-V12RM, with an inert gas flow of 5 l/min, and then after the process was completed, the biocarbon was seasoned for 22 hours. The material obtained by pyrolysis, was crushed, and then FTIR and Raman studies were carried out. Fourier spectroscopy spectra were performed with a Jasco FTIR 6200 spectrometer, in reflectance mode, using a Pike attachment with a diamond crystal. Raman spectroscopy spectra were performed at room temperature with an NRS-5100 spectrometer, from Jasco (Japan), using laser excitation at 532 nm, an objective of 100, an exposure time of 1 spectrum of 100 seconds, an accumulation count of 20, and a measurement range of 100 $cm^{-1}$ to 4000 $cm^{-1}$ during the study.

**Results:** The studies carried out by FTIR technique showed the changes occurring in the biocarbon obtained from apple waste at different temperatures (Fig.1). On the presented spectra, bands located in the range of 2000-1500 $cm^{-1}$ were observed. They correspond to valence vibrations of double bonds, e.g. -C=C=C-, -C=O and O-H [11]. The bands in the 1500-650 $cm^{-1}$ range correspond to the dactyloscopic region and are difficult to interpret [12]. The 2100 $cm^{-1}$ and 2097 $cm^{-1}$ bands indicate the appearance of the -C≡C- grouping. The presence of the C=O stretching vibration of cellulose and hemicellulose can be associated with the appearance of the peak 1701 $cm^{-1}$ and 1689 $cm^{-1}$. The -C=O and aromatic C=C stretching bonds are characteristic of the peak 1553 $cm^{-1}$ and occur through the presence of lignin in the studied material. The band 1060 $cm^{-1}$, corresponds to C-O-H stretching bonds of cellulose and hemicellulose. In contrast, the 743 $cm^{-1}$ peak was caused by aromatic C-H atoms [13].

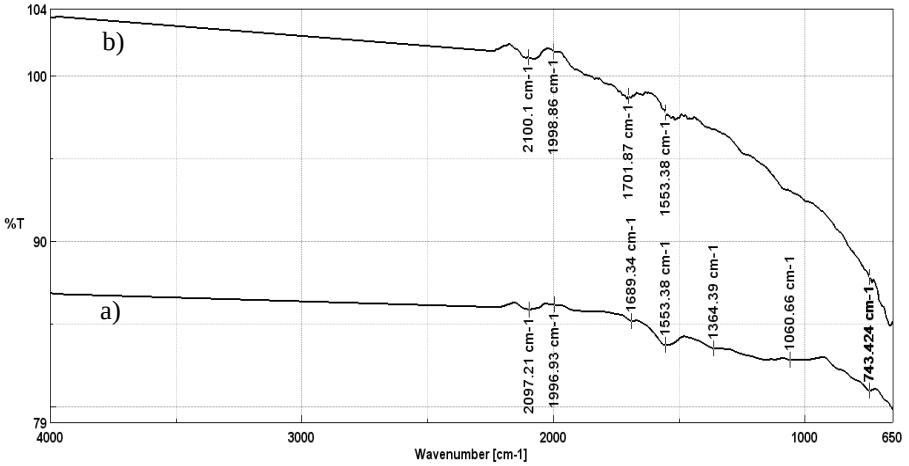



**Fig.1.** Comparison of spectra of natural carbon materials obtained pyrolytically from apple waste at a) 500 ºC and b) 700 ºC.

These studies conducted by Raman technique showed the presence of two bands in the biocarbon indicating the ordering and disordering of carbon structures (Fig.2). The spectra of the biocarbon studied contain bands directly related to the vibration of carbon and hydrocarbon structures. In the case of analysis of Raman spectra obtained for biocarbon in the process of pyrolysis at 500°C and 700°C, bands 1590 $cm^{-1}$, 1588 $cm^{-1}$, otherwise known as G-bands, was observed. This band corresponds to stretching vibrations with E2g symmetry. This band occurs in the case of graphite with an ordered structure. Bands located at 1338 $cm^{-1}$, 1354 $cm^{-1}$, characterize the level of amorphousness of carbon structures and indicate a highly disordered biocarbon structure. This band is usually referred to as the D1 defect band. It corresponds to A1g symmetry and is associated with plane imperfections, such as defects and heteroatoms [14].

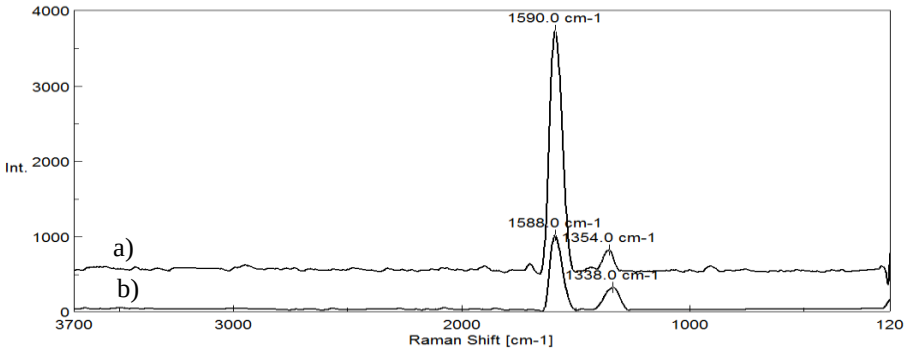



**Fig.2**. Natural carbon materials obtained pyrolytically from apple waste at a) 500ºC and b) 700ºC

**Conclusions:** Raman spectroscopy, like infrared spectroscopy (FTIR), provides information about the structure of a molecule and the interatomic bonds that form it. Therefore, it can be concluded that Raman spectroscopy is complementary to FTIR

spectroscopy and vice versa [3]. The biocarbons obtained by apple pyrolysis were studied by both methods. Using Raman spectra, the resulting biocarbon was observed to have a structure similar to that of activated carbon, making it a potential replacement as, for example, an anti-wear additive for lubricants. The FTIR method, on the other hand, makes it possible to observe what functional groups are on the surface of the biocarbon. The resulting biocarbon has more oxygen groups, which may result in greater sorption capacity for metal ions than activated carbon.

**Acknowledgements:** This study performed under statutory grants 03.951, 03.017 and 03.055 in 2021-2024.

**References:**

1. A. Dyjakon, J. Boer, A. Szumny, E. Boer, Sustainability, 11 (2019) 1604.
2. A. Turs, Biofuel Research Journal, 22 (2019) 962.
3. B. Kaźmierczak, J. Molenda, M. Swat, Environmental Technology & Innovation, 23 (2021) 101737.
4. H. Chum, A. Faaij, J. Moreira, IPCC Special Report on Renewable Energy Sources and Climate Change Mitigation, Cambridge University Press, Cambridge, 2011.
5. S. Vassilev, D. Baster, L. Andersen, Ch. Vassileva, T. Morga, Fuel, 94 (2012) 1.
6. N.D. Kaushika, K.S. Reddy, K. Kaushik, Sustainable Energy and the Environment: a Clean Technology Approach, 1 (2016) 123.
7. M. Kaltschmitt, Renewable energy from biomass, Introduction, Renewable Energy Systems, Springer, New York, 2013.
8. A. Bieniek , W. Jerzak, M. Sieradzka, Ł. Mika, K. Sztekler, A. Magdziarz, Energies, 15 (2022) 2491.
9. S. Błazewicz, A. Świątkowski, B.J. Trznadel, Carbon, 37 (1999) 693.
10. J. Molenda, Z. Pawelec, E. Pawelec, B. Kaźmierczak, Tribologia, 2 (2020) 47.
11. W. Zieliński, A. Rajca, Metody spektroskopowe i ich zastosowanie do identyfikacji związków organicznych – praca zbiorowa, Wydawnictwo Naukowo-Techniczne, Warszawa, 1995.
12. E. Ahmed, H.M. Abdulla, A.H. Mohamed, A.D. El–Bassuony, Process Safety and Environmental Protection, 104 (2016) 1.
13. E. Behazin, E. Ogunsona, A. Rodriguez-Uribe, A. Mohanty, M. Misra, A. Anyia, BioResources, 11 (2016) 1334.
14. K. Grodecki, Materiały Elektroniczne, 41 (2013) 47.

# THE INFLUENCE OF PYROLYSIS TEMPERATURE ON QUALITATIVE CHANGES IN CARBON MATERIALS OBTAINED FROM TEA BIO-WASTE

**B. KAŹMIERCZAK, J. DRABIK, P. RADULSKI, A. KACZMARCZYK, J. MOLENDA**, Łukasiewicz Research Network - Institute of Exploitation Technologies, Center for Bioeconomy and Eco-innovation, Proecological Technologies Research Group, K. Pułaskiego St. 6/10, 26 – 600 Radom, Poland.

**Abstract:** This study presents the use of FTIR spectrophotometry and Raman spectroscopy to assess changes occurring in biocarbon obtained from tea leaves under the influence of the temperature of the pyrolysis process. The FTIR spectrophotometry allowed the identification of the structure of biocarbon. The Raman spectroscopy allowed for the assessment of the degree of order of structures in biocarbon. Studies carried out using the Raman technique have shown that biocarbon have an ordered structure characteristic of graphite.

**Introduction:** Tea, next to water and coffee, is one of the most popular drinks in the world. The largest producer of tea is Asia (84.5%), then Africa (12.9%). The least amount of tea is produced in the countries of America (2%), Europe (0.3%) and Oceania (0.2%) [1]. Approximately 20 billion cups of tea are consumed every day in the world. In Poland, tea consumption amounts to approximately 1.5 kg/person annually [2]. World tea production in 2019 was approximately 7.5 million tons [1]. Such quantities of tea are a source of bio-waste, generated mainly by cafes and households. The tea bio-waste is one of the components of municipal waste. This type of waste can be used to produce biocarbon, materials with a wide range of applications. Pyrolysis of bio-based food waste is beneficial for the environment because it contributes to waste management and processing. The transformation of bio-waste into a valuable resource used in the bioeconomy is the added value of the circular economy. The biocarbon can be used as sorbents of metals from water solutions, materials for water treatment, absorbing unpleasant odors, soil improver or as an addition for lubricants. The pyrolysis of tea bio-waste, depending on the process conditions, can lead to the formation of bio-oil, which enables the production of renewable fuels [3]. For example, chemically reduced biocarbon from tea waste can effectively remove 98.31% of fluoride from fluoride-containing wastewater [4]. The current intense increase in scientists' interest in biocarbon products requires the use of specialized research methods, including: to evaluate the changes occurring in them as a result of the pyrolysis process. For this purpose, spectroscopic methods are used, such as: FTIR infrared spectrophotometry and Raman spectroscopy. The use of infrared spectrophotometry (FTIR) enables the identification of the types of bonds and vibrations of molecules in crystal lattices in the tested material. The FTIR spectrophotometry allows the analysis of the following functional groups occurring on the surface of biocarbon: carbonyl groups, –OH, C–H, C=C, C≡C groups [5,6]. The Raman spectroscopy allows you to determine the crystalline form, chemical composition, intermolecular interactions, degree of order and spatial distribution of stresses in the tested material [5,7].

The aim of this study was to determine the changes occurring in biocabon obtained from tea bio-waste under the influence of the temperature of the pyrolysis process.

**Experimental:** The subject of the research was biocarbon obtained from plant biomass, i.e. from tea bio-waste. The biocarbon was produced in the pyrolysis process carried out at temperatures of 500 °C, 600 °C and 700 °C. The pyrolysis processes were carried out in laboratory conditions, on a station equipped with a Czylok muffle furnace, type FCF-V12RM. Then, the changes occurring in the structure of biocarbon under the influence of the set temperature of the pyrolysis process were assessed using a Raman and FTIR spectrometer. The Raman spectra were taken using the NRS-5100 spectrometer from Jasco, using laser excitation with a wavelength of 532 nm and an exposure time of 100 seconds. The FTIR spectrometer was used to identify the structure of biocarbon. The spectra were taken using a Jasco FTIR 6200 spectrometer, in the reflection mode, using a Pike attachment with a diamond crystal.

**Results:** Biocarbon obtained from tea leaves was analyzed using FTIR infrared spectrophotometry. There are three key ranges in the biocarbon spectra, i.e. 2500–2000 $cm^{-1}$, in which valence vibrations of the C=C=C system and C≡C triple bonds occur; 2000–1500 $cm^{-1}$, which includes valence vibrations of C=C, C=O double bonds, deformation vibrations of O–H bonds and 1500–650 $cm^{-1}$ is the fingerprint area, difficult to interpret, mainly valence vibrations of C–C, C–O bonds and C–H deformation vibrations occur here [5,8]. In the spectra presented (Fig.1), changes were observed in the form of the disappearance of the 1601 $cm^{-1}$ and 1576 $cm^{-1}$ bands with the increase in the temperature of the pyrolysis process. The bands mentioned indicate the presence of –C=O groups. In biocarbon obtained at temperatures of 600 °C and 700 °C, the appearance of a band of 2114 $cm^{-1}$ is observed, indicating the presence of –C≡C– groups. The bands 1411 $cm^{-1}$, 1414 $cm^{-1}$ and 1425 $cm^{-1}$ correspond to the plane deformation vibrations of CH in –C=C–H [9,10].

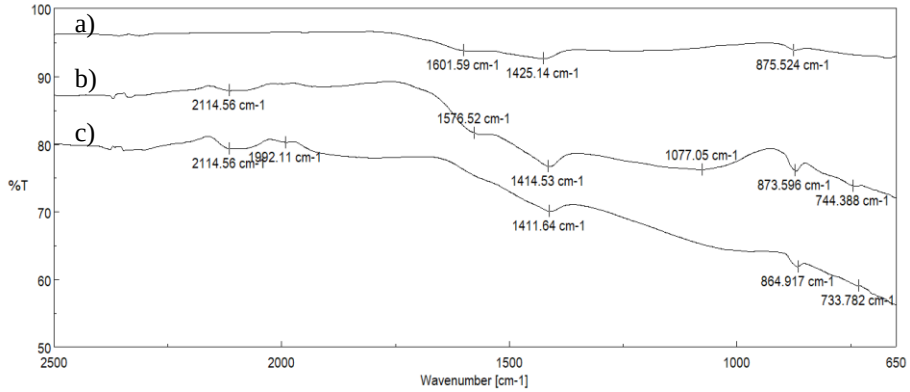



**Fig.1.** The FTIR spectra of biocarbon obtained from tea biowaste in the pyrolysis process carried out at a) 500 °C, b) 600 °C, c) 700 °C.

The Raman spectra excited by green laser light at 532 nm of three tested biocarbon samples from tea bio-waste are shown in Figure 2. As you can see, in all three cases two

types of peaks can be observed: D, G occurring for graphite in the range of 1200–1500 $cm^{-1}$, 1500–1800 $cm^{-1}$, respectively [1,7]. The peak D appears at approximately 1380 $cm^{-1}$, suggesting the presence of defects attached to the ground plane of the graphite crystal structure. The peak G appears in the samples at 1594 $cm^{-1}$ and results from the vibrational stretching of C–C bonds, which is characteristic of $sp^2$ hybridized structures, which proves the graphitic nature of the tested biochar samples.

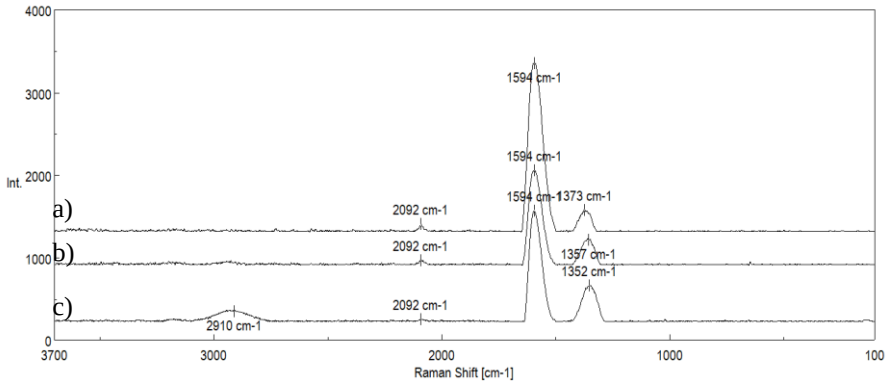



**Fig.2.** The Raman spectra of biocarbon obtained from tea waste in the pyrolysis process carried out at a) 500 °C, b) 600 °C, c) 700 °C.

In biocarbon obtained at temperatures of 500 °C and 600 °C, the occurrence of a band of 2092 $cm^{-1}$ was observed, indicating the occurrence of C=O structures. Carrying out pyrolysis at a temperature of 700 °C, the appearance of a peak at approximately 2700 $cm^{-1}$ was additionally confirmed, which indicates the presence of a 2D graphite phase in the sample [11]. It should be noted that the Raman spectra of biocarbon samples obtained from tea bio-waste are very similar to those in literature sources examining biocarbon materials. In the spectra presented, changes in the intensity of peaks assigned to the G and D bands were observed. The $I_D/I_G$ band ratio for biocarbon obtained from tea bio-waste at 500 °C was found to be 0.120. For biocarbon obtained at a temperature of 600 °C the ratio is 0.275. However, for biocarbon obtained at a temperature of 700 °C, the $I_D/I_G$ ratio is 0.310. The based on the conducted analyses, it was observed that biocarbon obtained from tea bio-waste exhibit an ordered structure attributed to the graphite structure with increasing pyrolysis temperature [12].

**Conclusions:** The use of spectroscopic methods allowed for the determination of changes occurring in the structure of biocarbon obtained from tea bio-waste under the influence of the temperature of the pyrolysis process. The FTIR infrared spectrophotometry allowed the identification of the structure of biocarbon. The biocarbon is characterized by a D band indicating a disordered structure and a G band indicating ordered structures. The degree of structure order in biocarbon increases as the temperature of the pyrolysis process increases. The analytical methods used confirmed that biocarbon was obtained from tea waste with a structure comparable to that of graphite.

**Acknowledgements:** The research was realized under statutory grants No. 03.951, 03.017 and 03.055 in the years 2021-2024.

## References:

1. H. Nguyen-Thi-Lan, S. Fahad, N. Ho-Ngoc, T. Nguyen-Anh, D. Pham-Van, H. Nguyen-Thi-Viet, P. Do-Hoang, Ch. Do-Kim, N. To-The, Journal of the Saudi Society of Agricultural Sciences, 22 (2023) 158.
2. L. Polechońska, M. Dambiec, A. Klink, A.Rudecki, Journal of Food and Drug Analysis, 23 (2015) 486.
3. B. Rijo, A. Dias, M. Ramos, N. Jesus, J. Puna, Energy, 235 (2021) 121252.
4. S. Roy, S. Sengupta, S. Manna, P. Das, Process Safety and Environmental Protection, 116 (2018) 553.
5. B. Kaźmierczak, J. Molenda, M. Swat, Environmental Technology & Innovation, 23 (2021) 101737.
6. S. Yang, L. Li, Z. Pei, C. Li, J. Lv, J. Xie, B. Wen, S. Zhang, Colloids and Surfaces A, 457 (2014) 100.
7. A. Merlen, J.G. Buijnsters, C. Pardanaud, Coatings, 7 (2017) 2.
8. M. Dudkiewicz, J. Berłowska, D. Kręgiel, Laboratorium Przemysłowe, 9-10 (2015) 44.
9. Z. Xu, Z. Sun, Y. Zhou, W. Chen, T. Zhang, Y. Huang, D. Zhang, Colloids and Surfaces A, 582 (2019) 12393.
10. S. Huang, Q. Liang, J. Geng, H. Luo, Q. Wei, Materials Chemistry and Physics, 238 (2019) 121919.
11. K. Plenča, S. Cvetnić, H. Prskalo, M. Kovačić, M. Cvetnić, H. Kušić, Z. Matusinović, M. Kraljić Roković, B. Genorio, U. Lavrenčič Štangar, A. Lončarić Božić, Materials, 16 (2023) 7658.
12. F. Wang, X. Yu, M. Ge, S. Wu, J. Guan, J. Tang, X. Wu, R.O. Ritchie, Environmental Pollution, 248 (2019) 229.

# PRODUCTION OF ACTIVATED BIOCARBONS BY MICROWAVE-ASSISTED CHEMICAL ACTIVATION OF HARDWOOD SAWDUST

**M. WIŚNIEWSKA[1], K. TOKARSKA[1], T. URBAN[1], P. NOWICKI[2]**, [1]Maria Curie-Skłodowska University in Lublin, Faculty of Chemistry, Institute of Chemical Science, Department of Radiochemistry and Environmental Chemistry, Maria Curie-Skłodowska Sq. 3, 20-031 Lublin, [2]Adam Mickiewicz University, Faculty of Chemistry, Department of Applied Chemistry, Uniwersytetu Poznańskiego 8, 61-614 Poznań.

**Abstract:** Sawdust of deciduous trees was used as a raw material for the preparation of carbonaceous adsorbents. Two variants of chemical activation were applied, i.e. impregnation with $K_2CO_3$ and $H_3PO_4$ reagents. Additionally, the microwave heating was involved. The obtained acivtated biocarbons were characterized in terms of their porous structure, as well as surface and electrokinetic properties. The sorption abilities of both materials towards synthetic and natural polymers in the process of their removal from aqueous systems were also determined.

**Introduction:** Wood processing, especially on an industrial scale, generates large amounts of sawdust. This type of waste biomass is an extremely valuable raw material with numerous applications. Over the years, the use of sawdust has changed, but its properties have always been appreciated. In the past, they were used primarily as a cheap type of fuel. Currently, there are many more ways to sawdust management, and technological development constantly enables new applications of this material. The most obvious seems to be their use in the production of fuel materials - briquettes and pellets. Both fuels can be used in coal furnaces, in modern ecological central heating boilers and fireplaces. High-quality fuel requires the application of dry material from trees, which naturally have a high lignin content in the wood. For this reason, both briquettes and pellets are produced primarily from pine, spruce, fir, beech, as well as birch and aspen sawdust [1].

Other ways of using sawdust include fertilizing and mulching the soil [2]. Their great advantage is natural origin and high humus content. However, first the sawdust must be subjected to a composting process, which guarantees the removal of substances dangerous to plants, such as tannins and polyphenols. To shorten the long composting process, nitrogen source substances, such as calcium-nitrogen nitrate or manure, are often added.

Due to the fact that burning sawdust generates large amounts of smoke, it is also worth using it in home smokehouses. Oak, beech, alder or birch sawdust allow to obtain the extremely desirable natural smell of cold cuts. It is worth mentioning the use of sawdust as a wall decoration material. It is often mixed with paints, which allows to achieve spectacular and unique aesthetic effects.

An interesting way of sawdust management is the production of activated carbons [3]. This is primarily due to the relatively high carbon content and low ash contribution for sawdust precursor [4]. Activated carbons are mainly produced from natural organic raw materials with a polymeric structure) through thermochemical processes including

physical or chemical activation [5]. This first method predominantes, which includes two processing stages: carbonization (pyrolysis) of the organic raw material and subsequent activation using a gaseous oxidizing agent (steam, carbon dioxide or their mixture). In chemical activation, used on a smaller scale, the precursor is impregnated or mixed with an appropriate chemical reagent (zinc chloride, phosphoric acid, sodium or potassium hydroxide) and subjected to a one-step heat treatment. The greater reactivity of these activating agents allows to eliminate the carbonization stage and reduce the temperature and time of the process. Moreover, the advantage of this activation variant is the high yield of the final product, characterized by a significantly developed specific surface area, well-defined porous structure and very low ash content.
The main goal of the presented studies was to produce a series of new activated biocarbons by means of chemical activation of common oak sawdust as well as to assess their usefulness in removing polymer impurities from aqueous solutions. Two activating reagents were applied, namely potassium carbonate and phosphoric acid. Moreover, conventional heating was abandoned in favor of the use of microwave energy. Such solution allows the sample to be heated from its interior, therefore the final process temperature is reached faster and energy consumption is lower. In addition, the resulting carbonaceous material has a more uniform porous structure.

**Experimental:** The starting material (S) was impregnated with a $H_3PO_4$ or $K_2CO_3$ solution (weight ratio of reagents 1:2) for 24 h and then subjected to a one-stage heating procedure. The impregnated samples were heated to the final activation temperature of 550 °C (for sample SM_P) or 800 °C (for sample SM_K) at the rate of 10 °C/min in a nitrogen atmosphere (flow rate 20 L/h). Finally, the samples were cooled to room temperature and subjected to a post-activation washing procedure.
Low-temperature (77 K) nitrogen adsorption-desorption isotherms, measured with an automatic ASAP 2020 apparatus (Micromeritics Instrument Corporation) were used to determine the textural parameters of carbonaceous materials. In turn, the potentiometric titration method was applied to obtain the surface charge density as a function of solution pH and points of zero charge (pzc) of both activated biocarbons [6]. Additionally, the electrokinetic characterization of carbonaceous materials was performed using microelectrophoresis technique, enabling the determination of the zeta potential vs. solution pH and isoelectric points (iep) of examined suspensions.
For the adsorption studies, two water-soluble polymers were selected. There were: synthetic poly(acrylic acid) – PAA (Fluka) and natural protein lysozyme (LSZ) (Sigma-Aldrich). The poly(acrylic acid) (PAA) is a weak polyelectrolyte with the anionic character (originating from the carboxyl groups present in its molecules). The average molecular weight of applied PAA is equal to 2 kDa and its $pK_a$ value is about 4.5. The lysozyme with the molecular weight 14.3 kDa and pI value 11, belongs to the group of proteins with high internal stability (hard proteins). These proteins are 'rigid' and they have the ability to assume their native conformation over the wide range of solution pH due to high denaturation energy.
The amounts of polymers adsorbed on the surface of activated biocarbons were determined based on the decrease in their concentration in the solution as a result of the adsorption. Quantification of macromolecular compounds in the solution was performed using the spectrophotometric method. Polymer concentration was measured applying UV/Vis spectrophotometer Cary 100 (Varian). In the case of poly(acrylic acid), its

complexation reactions with hyamine 1622, giving white coloured complex absorbing the light at wavelength 500 nm [7] was applied. In turn, the lysozyme concentration was determined directly at the wavelength 280 nm (aromatic amino acids present in the polypeptide chains, mainly tryptophan and tyrosine, are responsible for light absorption at this wavelength) [8]. The adsorption process was carried out at 25 °C, for 24 h, at pH 3, 6 and 11 in the polymer concentration range 10-400 ppm.

**Results:** Both activated biocarbons obtained via the microwave-assisted chemical activation of hardwood sawdust have a well-developed surface area and a porous structure composed of significant amounts of micropores and mesopores. The specific surface area of SM_P biocarbon is as much as 1777 $m^2$/g, while for the SM_K sample it is 1093 $m^2$/g. The mean pore size reaches values 3.04 and 1.72 nm, respectively. The carbonaceous materials show acidic properties of the surface, evidence of which is the location of points of zero charge and isoelectric points within the acidic range of solution pH (Table 1). The $pH_{pzc}$ values changes from 5.9 to 6.5, while $pH_{iep}$ are located within the pH range from 3.6 to 4.2, for SM_K and SM_P activated carbons, respectively. The sign and magnitude of electric charge occurring on the activated biocarbons surface defines electrostatic conditions for the adsorption of ionic polymers. Favourable electrostatic attraction will occur between the solid surface and anionic poly(acrylic acid) in the pH range 3-6, while for lysozyme (which is positively charged with a wide pH range up to its pI value) it will take place from pH 3 to 11.

**Table 1.** Surface and electrokinetic parameters of activated biocarbons.

| Adsorbent | pH | Surface charge density [μC/$cm^2$] | $pH_{pzc}$ | Zeta potential [mV] | $pH_{iep}$ |
|---|---|---|---|---|---|
| SM_K | 3 | 1.54 | 5.9 | 20.02 | 3.6 |
| | 6 | -1.73 | | -37.28 | |
| | 11 | -33.72 | | -42.04 | |
| SM_P | 3 | 3.42 | 4.5 | 24.42 | 4.2 |
| | 6 | -0.95 | | -24.02 | |
| | 11 | -28.12 | | -27.14 | |

As can be seen in Fig.1 the polymer adsorbed amounts depend considerably on solution pH. It is obvious, because changes in this parameter cause not only changes in the solid surface groups ionization, but also dissociation of PAA carboxyl groups and protonation/deprotonation of LSZ amine and carboxyl ones. As a result, the polymeric macromolecules assume the specific conformation in the bulk solution, which usually undergo changes during their adsorption process at the solid/liquid interface. Poly(acrylic acid) chains are absorbed in larger amounts on the surface of biocarbon obtained with the application of $H_3PO_4$ as an activating agent, especially at pH 3. Under such conditions, PAA adsorption reaches level of 194 mg/g. Minimal dissociation of the PAA functional groups at pH 3 causes the most coiled conformation of this synthetic polymer, which enables dense packing of adsorbed coils, also in the solid pores with an average size of about 3 nm. In turn, the lysozyme adsorption is the most effective at pH 11 on the surface of carbonaceous material obtained via chemical activation with $K_2CO_3$. In such a case the maximal adsorbed amount of LSZ is 142 mg/g. Literature data

confirm that protein adsorption is the highest at pH conditions corresponding to the isoelectric point of a given natural polymer [9].

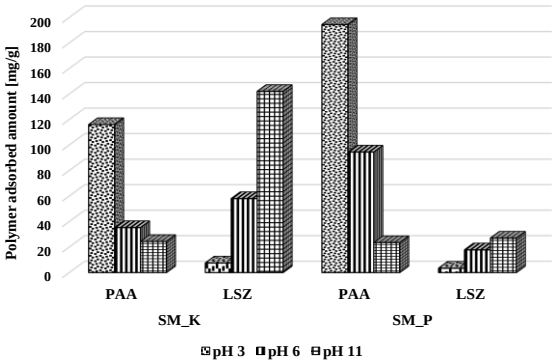



**Fig.1.** Adsorbed amounts of ionic polymers on the surface of examined activated biocarbons from the aqueous solutions with initial concentration 200 ppm, at pH 3, 6 and 11.

**Conclusions:** The activated biocarbons obtained by microwave-assisted chemical activation of hardwood sawdust are effective materials for removing synthetic and natural polymers from their aqueous solutions. Their good adsorption properties towards macromolecular compounds, such as poly(acrylic acid) and lysozyme result from favourable textural parameters (well-developed specific surface area, up to 1800 $m^2/g$ and appropriate pore size up to 3 nm) as well as the presence of surface oxygen groups with acidic-basic nature. The latter ones participate in electrostatic and chemical (formation of bonds) interactions with the functional groups of ionic polymers. The solution pH is an important parameter in the studied systems, which influences significantly polymeric chains conformation and their affinity to the activated biocarbon surface. The maximal adsorption of PAA was observed at pH 3 for the SM_P sample (194 mg/g), whereas LSZ was adsorbed in the greatest amount at pH 11 on the SM_K material (142 mg/g).

## References:

1. D. Kwaśniewski, Agricultural Engineering, 23 (2019) 5.
2. H.J. Park, H.S. Heo, J.K. Jeon, J. Kim, R. Ryoo, K.E. Jeong, Y.K. Park, Applied Catalysis B Environmental, 95 (2010) 365.
3. T. Kalak, M. Kaczmarek, P. Nowicki, R. Pietrzak, Y. Tachibana, R. Cierpiszewski, Wood Science and Technology, 56 (2022) 1721.
4. F.B. Elehinafe, O.B. Okedere, O.A. Odunlami, A.O. Mamudu, S. F. Bamidele, International Journal of Civil Engineering and Technology, 10 (2019) 51.
5. P. Nowicki, J. Kazmierczak, R. Pietrzak, Powder Technology, 269 (2015) 312.
6. M. Medykowska, M. Wiśniewska, K. Szewczuk-Karpisz, R. Panek, Applied Nanoscience, 13 (2023) 6737.
7. W.B. Crummett, R.A. Hummel, Journal of American Water Works Association, 55 (1963) 209.
8. A. Aitken, M.P. Learmonth, The Protein Protocols Handbook, 2nd Edition, Humana Press Inc., Totowa, NJ, 2002.
9. K. Szewczuk-Karpisz, M. Wiśniewska, Soft Materials, 12 (2014) 268.

# EFFECT OF THE ACTIVATION PROCEDURE ON THE ADSORPTION PROPERTIES OF CARBONACEOUS MATERIALS OBTAINED FROM HERBS TOWARDS IONIC POLYMERS

**M. WIŚNIEWSKA[1], M. GĘCA[1], P. NOWICKI[2]**, [1]Maria Curie-Skłodowska University in Lublin, Faculty of Chemistry, Institute of Chemical Science, Department of Radiochemistry and Environmental Chemistry, Maria Curie-Skłodowska Sq. 3, 20-031 Lublin; [2]Adam Mickiewicz University, Faculty of Chemistry, Department of Applied Chemistry, Uniwersytetu Poznańskiego 8, 61-614 Poznań.

**Abstract:** The nettle, sage, mint and lemon balm herbs were used to prepare carbonaceous adsorbents using chemical and direct activation methods. It has been shown that the activation procedure has decisive impact on the type of porous structure generated and the acidic-basic nature of adsorbents' surface. It has been proven that the textural and surface properties of activated biocarbons significantly affect their sorption capacity in relation to anionic and cationic polymers (both in the case of systems containing one or two adsorbates with different ionic nature/character).

**Introduction:** Activated carbons, traditionally derived from non-renewable fossil fuels such as lignite or bituminous coal, have long been an important material in various industries, including wastewater treatment, air and drinking water purification as well as pharmaceuticals or food production. However, the limited nature of fossil resources and their associated environmental impacts have prompted the search for alternative precursors for activated carbon production. Biomass, covering a wide range of organic materials derived from plants, agricultural residues or food industry waste, can be an attractive and sustainable alternative to conventional resources. The conversion of biomass into activated carbons involves a series of pyrolytic and activation processes. This procedure not only allows the production of activated carbons with the desired porous structure or surface chemistry, but also offers proper waste management and promotes the principles of a circular economy. Moreover, the utilization of biomass-derived activated carbons aligns with the concept of carbon sequestration, contributing to the reduction of greenhouse gas emissions by diverting carbon from the atmosphere into stable carbonaceous materials. This dual benefit of mitigating both environmental pollution and climate change emphasizes the significance of biomass-derived activated carbons in the current global scenario.

Chemical and physical (thermal) activation are two main processes of carbonaceous materials preparation, each offering distinct pathways for engineering the structure and surface chemistry of activated carbons. Chemical activation, characterized by the use of activating agents such as alkali metal hydroxides, phosphoric acid or zinc chloride, induces the activation of carbonaceous materials through chemical reactions (e.g. oxidation, dehydration, dehydrogenation and aromatisation), that modify their molecular structure. This method typically involves impregnation of the precursor with an activating agent followed by carbonization, resulting in the development of porous networks with well-defined pore structures and enhanced surface functionalities [1].

Chemical activation offers precise control over pore size distribution and surface chemistry, making it particularly suitable for applications that require tailored adsorption properties and catalytic performance. In turn, the thermal activation method involves the conversion of carbon-containing materials as a result of their partial decomposition and gasification in the presence of activating agents such as steam or carbon dioxide. Unlike the chemical method, physical activation does not involve the use of corrosive and harmful chemical agents, thus offering a cleaner and more environmentally friendly way [2]. Through the controlled use of temperature and activation gases, the physical variant facilitates the formation of porous networks with a wide range of pore sizes, promoting better accessibility and diffusion kinetics of adsorbates or reactants.

**Experimental:** Stems of nettle (NE), sage (SA), mint (MT) and lemon balm (LB) herbs were cut into pieces 1.5-2.0 cm long and dried at 100 °C. For chemical activation, the samples were impregnated with a 50 % $H_3PO_4$ solution (precursor:activating agent weight ratio 1:2) for 24 h. After this time the materials were dried, placed in the quartz boats and heated in a nitrogen atmosphere (flow rate 200 $cm^3$/min). First, the samples were heated to a temperature of 200 °C (rate 5 °C/min) and annealed for 30 min. Then, the samples were heated to the final activation temperature of 500 °C (rate 5 °C/min) and annealed again for 30 min. After this time, the materials were cooled down in the nitrogen atmosphere at room temperature. The obtained biocarbons were washed with 10 $dm^3$ of hot distilled water in a vacuum filtration funnel with a glass sintered disc and dried to a constant mass at 110 °C. The products of chemical activation were denoted as NE_AC, SA_AC, MT_AC and LB_AC. On the other hand, for the physical activation, the samples were subjected to simultaneous pyrolysis and activation in the $CO_2$ atmosphere (flow rate 250 $cm^3$/min). The starting materials were placed in a laboratory furnace preheated to 800 °C and annealed under these conditions for a period of 30 min. The samples were then cooled down to room temperature and denoted as NE_AP, SA_AP, MT_AP and LB_AP.
The textural parameters of activated biocarbons were examined by nitrogen adsorption-desorption measured at −196 °C using ASAP 2420 (Micrometrics). The content of surface functional groups was determined acc. to the Boehm method.
Two water-soluble polymers (anionic poly(acrylic acid) - PAA and cationic polyethylenimine - PEI) were used for adsorption tests. The adsorption procedure was carried out at 25 °C, for 24 h, at pH 3 in single and binary adsorbate systems. For this purpose, the activated carbons were added to the 10 $cm^3$ of the solution containing 200 ppm of appropriate polymer and 0.001 mol/$dm^3$ of NaCl (acting as a supporting electrolyte). The mass of AC samples was 0.01 g, whereas that of AP samples 0.02 g. The amount of adsorbed macromolecular substances was determined using the static method based on the difference in adsorbate concentration in the solution before and after the process. The absorbance of the solution was measured applying the Carry 100 UV/Vis spectrophotometer (Varian). Due to the fact that none of the polymers absorb the light on their own, they were complexed with special substances. PAA reacts with hyamine 1622 giving a white-coloured complex absorbing the light at the wavelength of 500 nm. In the case of PEI, its reaction with $CuCl_2$ was applied. The product of this reaction is blue and absorbs the light at the wavelength of 285 nm.

**Results:** The textural parameters of the prepared adsorbents are presented in Table 1. Carbonaceous materials obtained by chemical activation of herb stems are characterized by much more developed specific surface area and porous structure than analogous ones prepared via direct activation. Additionally, the structure of $H_3PO_4$-activated samples is dominated by mesopores (mean pore size ~4-5 nm), while $CO_2$-treated materials are characterized by a better developed microporous structure. The greatest surface area (S) of 1145 $m^2/g$ and the greatest pore volume (V) of 1.47 $cm^3/g$ has MT_AC sample obtained from mint herb. In turn, the least favourable textural parameters (S = 368 $m^2/g$, V = 0.20 $cm^3/g$) are demonstrated by NE_AP sample prepared from the nettle herb.

**Table 1.** Textural parameters of biocarbons obtained by chemical and direct activation of herb stems.

| Adsorbent | Specific surface area [$m^2/g$] | | Pore volume [$cm^3/g$] | | Mean pore size [nm] | Micropore contribution |
|---|---|---|---|---|---|---|
| | total | micropore | total | micropore | | |
| NE_AC | 801 | 157 | 0.85 | 0.07 | 4.23 | 0.09 |
| SA_AC | 842 | 155 | 0.83 | 0.07 | 3.93 | 0.09 |
| LB_AC | 950 | 149 | 1.10 | 0.07 | 4.63 | 0.06 |
| MT_AC | 1145 | 184 | 1.47 | 0.07 | 5.12 | 0.05 |
| NE_AP | 368 | 248 | 0.20 | 0.10 | 2.26 | 0.50 |
| SA_AP | 399 | 327 | 0.21 | 0.13 | 1.96 | 0.62 |
| LB_AP | 547 | 430 | 0.26 | 0.17 | 1.92 | 0.65 |
| MT_AP | 666 | 535 | 0.32 | 0.21 | 1.91 | 0.66 |

The analysis of the data presented in Fig. 1 indicates that the prepared carbonaceous materials also differ significantly in the content and type of surface functional groups. Samples activated with $CO_2$ are characterized by a clear predominance of basic functional groups, which can be related to the high content of mineral substances in their structure and the high processing temperature (800 °C). In the case of materials activated with orthophosphoric acid, the content of functional species is significantly lower, and acidic groups predominate on their surface.

Table 2 presents the amounts of the poly(acrylic acid) and polyethylenimine adsorbed on the surface of activated biocarbons in the case of one- and two-component polymer solutions. Anionic PAA is better adsorbed on the surface of all carbonaceous materials than cationic PEI. It is related to the specific conformation of polymeric chains, that they assume at pH 3. PAA containing carboxyl functional groups, dissociates only to a small extent, which results in a more coiled structure of its macromolecules. In turn, PEI with amine functional groups dissociates completely at acidic pH and its chains assume a significantly developed conformation. In binary adsorbate systems, the affinity of PAA to the surface of AC materials decreases. The dominance of acidic groups on the surface of these adsorbents results in parallel adsorption of PEI, which blocks active sites for PAA adsorption. On the other hand, the basic functional groups present on the surface of AP adsorbents cause a more perpendicular adsorption of polyethylenimine and an increase in the amount of adsorbed poly(acrylic acid) due to the slight electrostatic attraction between both polymers. In the case of PEI, the adsorbed amounts from single and binary solutions are at a similar level.

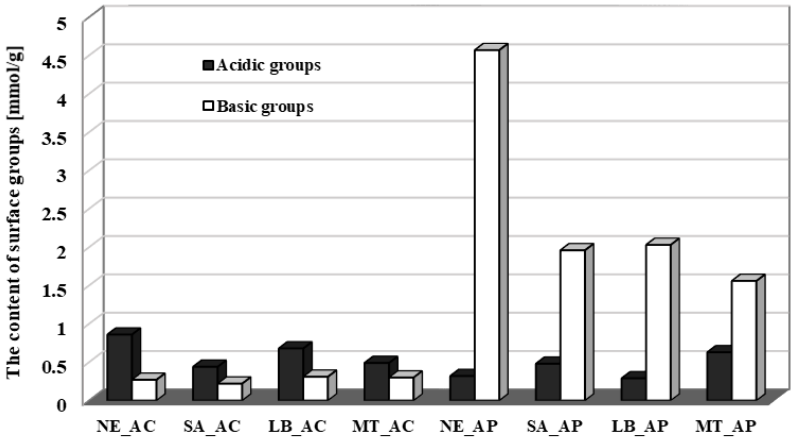



**Fig. 1.** Acid-base properties of activated biocarbons obtained from herb stems.

**Table 2.** The adsorbed amounts of PAA and PEI on the surface of prepared activated biocarbons.

| Adsorbent | PAA adsorbed amount [mg/g] | | PEI adsorbed amount [mg/g] | |
|---|---|---|---|---|
| | PAA | PAA + PEI | PEI | PEI + PAA |
| NE_AC | 198.12 | 128.02 | 48.73 | 55.42 |
| SA_AC | 137.81 | 125.17 | 51.61 | 50.79 |
| LB_AC | 195.71 | 141.87 | 79.99 | 61.74 |
| MT_AC | 187.13 | 119.01 | 84.27 | 62.12 |
| NE_AP | 61.39 | 94.32 | 21.88 | 50.39 |
| SA_AP | 25.21 | 42.26 | 24.73 | 21.45 |
| LB_AP | 24.95 | 62.13 | 27.84 | 27.64 |
| MT_AP | 30.39 | 44.16 | 30.54 | 25.31 |

**Conclusions:** The conducted studies have shown that waste biomass can be successfully used as a cheap and renewable precursor for the production of activated biocarbons. The physicochemical parameters of carbonaceous materials obtained from herb stems are significantly determined by the variant of the thermochemical conversion used. Samples activated with orthophosphoric acid are characterised by a well-developed surface area and mesoporous structure, thanks to which they demonstrate high adsorption efficiency towards poly(acrylic acid) and polyethylenimine (both from one- and two-component systems). In the case of analogous materials obtained by direct activation of plant precursors, less favourable textural parameters and sorption properties are observed.

## References:

1. D. Angin, E. Altintig, T.E Köse, Bioresources Technology, 148 (2013) 542.
2. Y. Ding, J. Qi, R. Hou, B. Liu, S. Yao, J. Lang, J. Chen, B. Yang, Energy & Fuels, 36(10) (2022) 5456-5464.

# BIOCHAR-BASED SORBENTS AS MATERIALS IN THE SORPTION OF ARSENIC(V) IONS FORM AQUEOUS SOLUTIONS

**S. GUSTAW, J. BĄK, D. KOŁODYŃSKA**, Maria Curie-Sklodowska University, Faculty of Chemistry, Institute of Chemical Sciences, Department of Inorganic Chemistry, M. Curie-Sklodowska Sq. 2, 20-031 Lublin, Poland.

**Abstract:** The efficiency of the sorption process of arsenic(V) ions on the surface of iron(III) ion-modified and unmodified biochars was investigated. The next stage of the study was to evaluate the efficiency of the sorption process of arsenic(V) ions and ions contained in mine water on biochars modified with iron(III) ions at different pH.

**Introduction:** An increasing number of inorganic pollutants are appearing in the environment under the influence of human activities, and arsenic has been identified as a potentially hazardous pollutant in the same class as lead, mercury, and vanadium. Arsenic has high mobility in the environment. Modification of such materials with, for example, iron(III) ions, can lead to an improvement in their sorption properties. Research has shown that modified biochars are proving to be an effective and economical solution for environmental remediation. Biochars a and B used in the study were obtained from Ecochar and were derived from dairy cattle manure and farmed fowl manure. They were obtained by a gasification process.

**Experimental:** An iron(III) solution of 50 mg/L was prepared at pH 2. Biochars a and B were placed in 100 mL conical flasks of 0.1 g per flask. The samples were then shaken in the presence of iron(III) ions for 4 hours (50 mL of solution per 0.1 g of biochar). The resulting product was filtered, dried and subjected to sorption of arsenic(V) ions. The concentration of arsenic(V) ions and mine water in the solution after the sorption process was determined using an optical emission spectrometer with inductively coupled plasma excitation (ICP-OES 720 ES, Varian). The amounts of ions adsorbed were calculated from the expression:

$$q_t = \frac{(C_0 - C_t)V}{m}$$

where: $C_0$ - initial concentration of the solution (mg/L), $C_t$ - concentration of the solution after time t (mg/L), V - volume of solution (L), m - sorbent mass (g).

**Results:** Figure 1 shows the effect of pH on the sorption efficiency of As(V) ions on the surface of unmodified biochars. The adsorption efficiency of As(V) ions on biochars modified with iron(III) ions was investigated as a function of pH and the results are presented in Fig.2. Table 1 shows the concentration of iron(III) ions on the surface of modified biochars after adsorption of ions of As(V). The results of testing the concentrations of selected metal ions in mine water at different pH as well as in the presence of As(V) ions, and the concentrations of these ions after sorption on biochar

modified with iron(III) ions are shown in Table 2. Amount of adsorbed ions after sorption of As(V) ions on biochars modified with iron(III) ions are shown in Table 3.

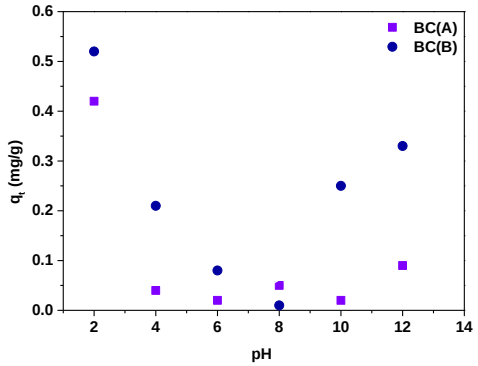



**Fig.1.** Values of adsorption of As(V) ions as a function of pH on biochars unmodified with iron(III) ions (15 mg/L As(V) solution).

For the sorption of As(V) ions on unmodified biochars, the highest $q_t$ values were obtained at pH 2 and they are equal to 0.42 mg/g for BC(A) and 0.52 mg/g for C(B).

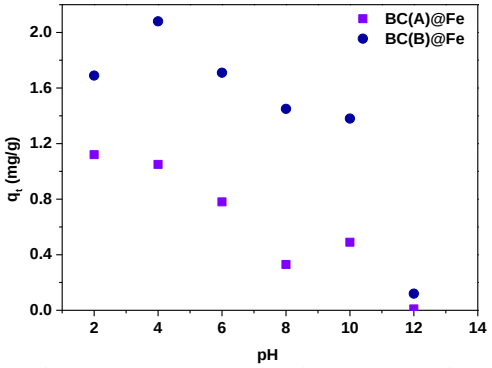



**Fig.2.** Adsorption efficiency of As(V) ions on iron(III) modified biochar as a function of pH (for BC(A)@Fe and BC(B)@Fe, 15 mg/L As(V) ion solution).

**Table 1.** Concentration of iron(III) on the surface of modified biochars after adsorption of As(V).

| | BC(A)@Fe | | | BC(B)@Fe | | |
|---|---|---|---|---|---|---|
| pH | $pH_k$ | $q_t$ [mg/g] | $C_{Fe}$ | $pH_k$ | $q_t$ [mg/g] | $C_{Fe}$ |
| 2 | 2.30 | 1.12 | 3.36 | 2.40 | 1.69 | 1.06 |
| 4 | 5.10 | 1.05 | 0.00 | 5.25 | 2.08 | 0.03 |
| 6 | 5.54 | 0.78 | 0.00 | 5.68 | 1.71 | 0.11 |
| 8 | 6.38 | 0.33 | 0.46 | 6.19 | 1.45 | 0.23 |
| 10 | 6.69 | 0.49 | 0.03 | 6.49 | 1.38 | 0.20 |
| 12 | 11.59 | 0.01 | 1.33 | 11.43 | 0.12 | 1.46 |

Based on the data obtained, it was found that for BC(A)@Fe the highest $q_t$ values occurred at pH 2 equal to 1.12 mg/g and for BC(B)@Fe at pH 4 equal to 2.08 mg/g. Unmodified biochars BC(A) and BC(B) showed lower $q_t$ values compared to biochars

modified with Fe(III) ions: BC(A)@Fe and BC(B)@Fe, hence it can be concluded that the modification slightly improves the efficiency of the sorption process of As(V) ions. For BC(A), BC(B), BC(A)@Fe the highest $q_t$ values were obtained at pH 2, for BC(B)@Fe at pH 4.

**Table 2.** Concentrations of selected metal ions in mine water at different pH as well as in the presence of As(V) ions and the concentrations of these ions after sorption on biochars modified with iron(III) ions.

| System | Ca [mg/L] | Fe [mg/L] | K [mg/L] | Mg [mg/L] | Na [mg/L] | As [mg/L] | $pH_k$ |
|---|---|---|---|---|---|---|---|
| Mine water | 11.43 | 0.00 | 21.02 | 7.46 | 116.66 | 0.00 | 8.42 |
| Mine water pH4 + As(V) | 12.20 | 0.00 | 20.88 | 7.61 | 123.41 | 13.44 | 4.00 |
| Mine water pH8 + As(V) | 11.23 | 0.00 | 20.98 | 7.50 | 125.77 | 12.83 | 8.12 |
| BC(A)@Fe-mine water pH4 | 14.26 | 0.00 | 22.51 | 9.06 | 116.84 | 11.29 | 6.40 |
| BC(A)@Fe-mine water pH8 | 8.77 | 0.00 | 22.19 | 7.68 | 116.71 | 11.53 | 7.95 |
| BC(B)@Fe-mine water pH4 | 14.79 | 0.05 | 24.22 | 8.13 | 116.36 | 9.31 | 6.60 |
| BC(B)@Fe-mine water pH8 | 5.70 | 0.11 | 23.56 | 5.38 | 116.96 | 9.65 | 8.15 |

Iron(III) ion modified biochars were used to test the removal efficiency of As(V) ions and ions present in mine waters: BC(A)@Fe and BC(B)@Fe. The table shows the concentrations of As(V) ions and other ions present in the mine water.

**Table 3.** Amount of adsorbed ions after sorption of As(V) ions on biochars modified with iron(III) ions: BC(A)@Fe, BC(B)@Fe at pH 4 and 8 after a time of 240 min.

| Biochar | $q_t$ [mg/g] |
|---|---|
| BC(A)@Fe-pH4 | 1.08 |
| BC(A)@Fe-pH8 | 0.65 |
| BC(B)@Fe-pH4 | 2.07 |
| BC(B)@Fe-pH8 | 1.59 |

Better results of As(V) sorption (added to the mine water) were obtained for BC(B)@Fe, where the calculated $q_t$ values were 2.07 mg/g for pH 4 and 1.59 mg/g for pH 8. The following metal ions are present in mine waters: Na, K, Mg and Ca. At the highest concentration: 116 mg/L there are Na ions, which are not sorbed by the iron-modified biochars, as evidenced by the same concentration of Na ions after the sorption process. K ions are also not sorbed by the obtained sorbents. A slight reduction in the concentration of Mg ions from 7.46 mg/L to 5.38 mg/L was observed with BC(B)@Fe at pH 8, indicating that these ions are slightly sorbed under these conditions. The sorbents show the highest ability to remove Ca ions at pH 8 - a reduction in the concentration from 11.43 mg/L to 8.77 mg/L for BC(A)@Fe and to 5.70 mg/L for BC(B)@Fe was observed. For pH 4, even higher concentrations of metal ions were sometimes obtained, which is related to the establishment of the appropriate pH as a result of the addition of water with acid.

**Conclusions:** The studies conducted show that biochars modified with iron(III) ions can be used as a sorbent in the treatment of water from arsenic(V) ions.

## References:

1. W. Li, X. Chen, M. Yao, B. Sun, K. Zhu, W. Wang, A. Zhang, Ecotoxicology and Environmental Safety, 274 (2024) 116183.

# SORPTION OF NICKEL(II) IONS ON CHELATING ION EXCHANGER

**G. WÓJCIK, Z. HUBICKI, K. ZINKOWSKA**, Maria Curie-Sklodowska University, Faculty of Chemistry, Institute of Chemical Sciences, Department of Inorganic Chemistry, M. Curie-Sklodowska Sq. 2, 20-031 Lublin, Poland.

**Abstract:** Nickel is an environmental pollutant and should be removed from waste water, moreover it belongs to critical elements. The sorption methods are used for nickel removal. Lewatit MonoPlus TP 220 was used for nickel(II) ions sorption from water in the pH range from 1 to 8 and in the acidic solution of 0.1 M to 3M HCl. The studies have proved a decrease in the recovery percentage of Lewatit MonoPlus TP 220 for Ni(II) with the increasing acid concentration. The maximum nickel(II) ions removal was obtained in the pH range 3-7.

**Introduction:** Besides cobalt, lithium and RRE nickel belongs to critical elements. These elements are essential to for manufacturing batteries, computers, TV sets, electric vehicles. The main producers of nickel are Indonesia, China, Russia, Japan and Canada. Nickel and chromium are used for stainless steel production. Stainless steel is applied for chemical installation and household devices production. Nickel is becoming increasingly common in clean energy technology products such as electric vehicles, wind turbines and battery storage [1]. Electric vehicles and battery storage are expected to overcome stainless steel as the largest user of nickel by 2040 [2]. Nickel salts like chloride, nitrate and sulphate as well as organic salts are readily water-soluble, whereas, nickel sulfides and nickel oxides are poorly water-soluble. Nickel is extensively distributed in the environment as it originates from the anthropogenic activity. Toxic and carcinogenic effects of nickel are related to the way of consumption into the organism. Water-soluble nickel compounds are absorbed by lungs and removed by kidneys. Insoluble nickel compounds remain in the lungs for a longer time, and they are the forms of nickel responsible for cancer [3,4]. The nervous system is one of the main target organs for Ni toxicity. In fact, it can be accumulated in the brain. The molecular mechanisms of Ni induced neurotoxicity are still not clear, but the researchers think that oxidative stress and mitochondrial dysfunctions have a primary and important role [4]. For this reason nickel should be removed from water and waste water. Ion exchange is often used for removal of toxic metals from waste waters or industrial streams. The Lewatit MonoPlus TP 220 was used for sorption of nickel(II) ions from hydrochloric acid of 0.1-6M [5]. The chelating bis-picolylamine groups should also sorb nickel ions in slightly acidic and neutral solutions. For this reason the sorption of nickel ions by Lewatit MonoPlus TP 220 was tested in the pH range 1-8.

**Experimental:** The nickel(II) stock solution was prepared by dissolution of $NiCl_2 \cdot 6H_2O$ purchased from the POCh S.A. company (Gliwice, Poland). 1000 mg/L nickel stock solution was diluted to 50 mg/L. The 0.1 M HCl and 0.1 M NaOH solution were used for pH adjustment. Lewatit MonoPlus TP 220 is a macroporous, cross linked polystyrene,

weakly basic resin with chelating bis-picolylamine groups. Its appearance is presented in Fig.1.

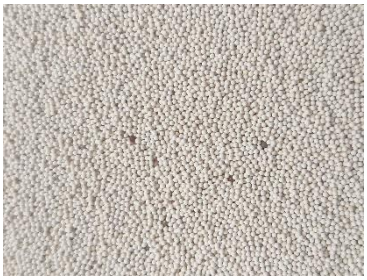


**Fig.1.** Lewatit MonoPlus TP 220.

The physical and chemical properties of Lewatit MonoPlus are presented in Table 1.

**Table 1.** The physical and chemical properties of Lewatit MonoPlus TP 220.

| | |
|---|---|
| Uniformity Coefficient | 1.1 |
| Mean bead size | 0.62(+/- 0.05) mm |
| Bulk density | 690 g/L |
| Density | 1.1 g/ml |
| Water retention | 48-60% |

The Ni(II) ions concentration in the samples was determined using the Atomic Absorption Spectroscopy spectrometer Varian AA240FS. The measurement parameters were: wavelength 232.0 nm, lamp current 7 mA, air:acetylene flow 13.5:2 L/min. The calibration curve was in the range 0-5mg/L.

**Results:** The adsorption of Ni(II) ions (50 mg/L) from the hydrochloric acid solution (0.1 - 3 M) and pH range 1-8 using 0.05 g of Lewatit MonoPlus TP 220 was investigated at the contact time 1440 min. The recovery percentage (%R) of nickel(II) ions was calculated using the equation:

$$\%R=(C/C_0)\times 100\%$$

where: $C_0$ is the initial concentration of nickel(II) ions, C is the concentration of Ni(II) ions calculated from the difference in the solution concentration before and after the sorption process.

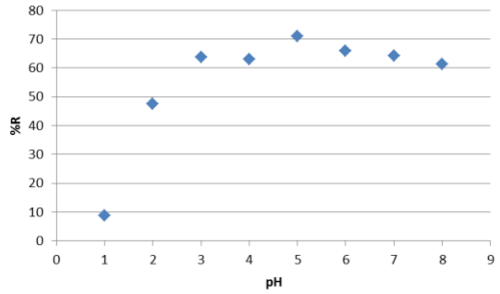



**Fig.2.** Influence of pH values on %R nickel(II) ions on Lewatit MonoPlus TP 220.

The influence of pH values on nickel ions removal on Lewatit MonoPlus TP 220 is presented in Fig.2. The removal percentage of nickel(II) ions on Lewatit MonoPlus TP 220 depends on pH values. The %R values increase sharply from pH 1 to 4. The maximum value of %R is estimated at pH 5.

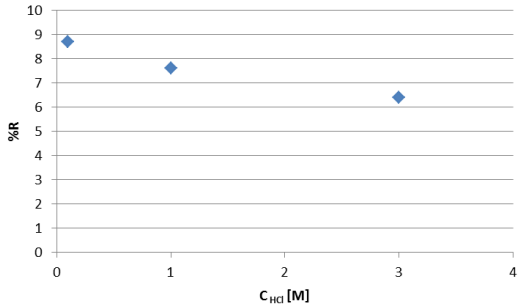



**Fig.3.** Influence of HCl concentration on %R nickel(II) ions on Lewatit MonoPlus TP 220.

The influence of hydrochloric acid on nickel ions removal on Lewatit MonoPlus TP 220 is presented in Fig.3. The removal percentage of nickel(II) ions on Lewatit MonoPlus TP 220 depends on the HCl concentration. The removal percentage of nickel(II) on Lewatit MonoPlus TP 220 ions decrease slightly in the HCl concentration range 0.1-3 M.

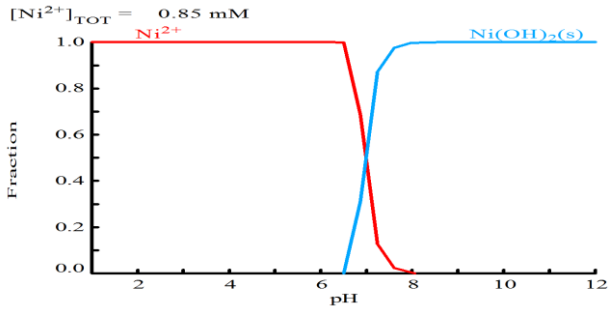



**Fig.4.** Influence of pH values on the nickel(II) ions fraction.

The investigations show that removal of nickel(II) ions on Lewatit MonoPlus TP 220 is more effective in the pH range 2-8 than in the hydrochloric solution of 0.1-3 M. In the neutral and slightly acidic solutions (Fig.4) nickel ions exist in one form as $Ni^{2+}$. Thus the changes in the removal percentage of nickel ions in the pH range 1-8 depend on chemical properties of bis-picolylamine groups.

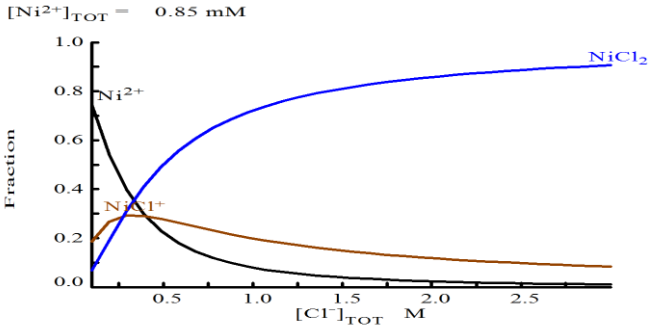



**Fig.5.** Influence of HCl concentration on the nickel(II) ions fraction.

The bis-picolylamine groups have chelating properties and can chelate nickel(II) ions. In the acidic media (0.1M-3M HCl) nickel(II) ions exist as the cation $Ni^{2+}$ and as the cationic chlorocomplex $NiCl^{+}$ (Fig.5). Moreover, donor nitrogen atom in the bis-picolylamine groups is protonated in the hydrochloric acid solutions. Protonated nitrogen atom attracts chloride anions more strongly than nickel(II) ions which is positively charged.

**Conclusions:** The investigations of nickel(II) ions sorption proved that nickel(II) ions can be removed by the chelating ion exchanger Lewatit MonoPlus TP 220. The best results of nickel ions sorption were obtained in the pH range 3-7. This pH range indicates the possibility of its use for sorption of nickel(II) ions from water and wastewater solutions.

**Acknowledgements:** We would like to thank Agnieszka Lipke Ph.D. for her help in performing nickel(II) ions sorption measurements.

**References:**

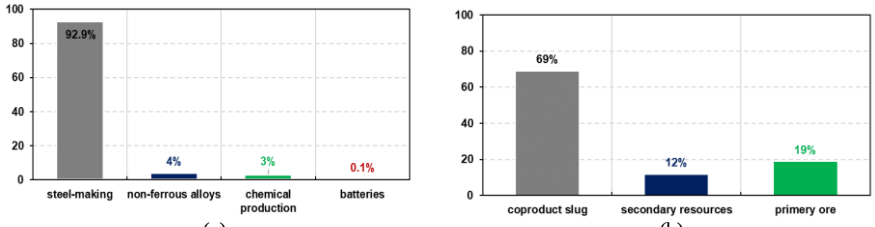
1. https://nickelinstitute.org/en/blog/2021/september/wind-and-water-nickel-in-clean-energy, (access 04.2024).
2. https://www.iea.org/reports/the-role-of-critical-minerals-in-clean-energy-transitions/executive-summa-ry, (access 04.2024).
3. S.K. Seilkop, A.R. Oller, Regulatory Toxicology and Pharmacology, 37 (2003) 173.
4. G. Genchi, A. Carocci, G. Lauria, M.S. Sinicropi, A. Catalano, International Journal of Environmental Research and Public Health, 17 (2020) 679.
5. A. Wołowicz, M. Wawrzkiewicz, Processes, 9 (2021) 285.

# COMPARISION OF ADSORPTIVE REMOVAL OF VANADIUM(V) IONS FROM AQUEOUS SOLUTIONS BY VARIOUS ION EXCHANGE RESINS

**A. WOŁOWICZ, Z. HUBICKI**, Maria Curie-Sklodowska University, Faculty of Chemistry, Institute of Chemical Sciences, Department of Inorganic Chemistry, M. Curie-Sklodowska Sq. 2, 20-031 Lublin, Poland.

**Abstract:** The critical applications of vanadium in different fields, its increasing concentration in water and wastewaters and its toxicity of this element have led to intensitive study in the field of development of new and efficient methods of its elimination and treatment. Vanadium(V) ions removal from aqueous solutions by different types of ion exchangers were discussed here. The chelating ion exchangers and the anionic ones with different basicity of their functional groups as well as the sorbent Lewatit AF5 without functional groups were taken into account. The optimization of the sorption process were made with particular consideration of the influence of the pH, the sorbent mass, the phases contact time, the initial concentration. The study was carried out using the batch and the column methods and the sorption and the working ion exchange capacities were compared. Moreover, the posibility of V(V) desorption and ion exchanger reuse were presented. Different ablicability of the ion exchangers for vanadium(V) ions removal was proved both in the model and real solutions but the ion exchangers Purolite S984 and Lewatit MonoPlus TP220 were the higest potential for V(V) removal.

**Introduction:** Vanadium(V) as a critical strategic resource is widely used in many fields (production of steel, chemicals, non-ferrous metal alloys and batteries) due to due to its excellent properties and is named the ‘vitamins of the modern industry‘ (Fig.1a) [1-3]. Annually production of vanadium being approximately 110,000 metric tons from which about 69% is a co-product formed during steel manufacturing, 19% derives from primary production and 12% is from secondary sources (vanadium recovery from spent catalysts, fly ash or petroleum residues etc.) (Fig.1b) [4,5].




(a) (b)

**Fig.1.** Main branches of industry using vanadium (a) and its sources in production (b).

In recent years the increase in vanadium and its compunds global use was observed. Since 2011, there has been an approximately 45% increase in the global use of vanadium and its compounds, and forecasts show that this upward trend will continue [5]. The high

consumption of vanadium generates a huge amount of wastewater containing high concentrations of vanadium e.g. wastewater from mining, industrial production, fertilizer or pesticide use, which is discharged into the environment, resulting in increased concentrations of vanadium in soils and natural waters. Depending on the concentration, vanadium is essential for proper cell growth (in trace amounts 0.05 μM) or be harmful and toxic in excess to humans, animals and plants at high concentrations (>10 μM) [6]. The permissible concentration threshold for vanadium in drinking water in China is 0.05 mg/l [7]. The German Federal Environmental Agency has established a guidance value of vanadium in drinking waters 4 μg/L and a maximum value of 20 μg/L whereas the WHO guidelines do not contain a limit value for vanadium. Moreover, vanadium is not regulated in the United States, despite it is listed on the US-EPA Contaminant Candidate as a contaminant of concern. On the other hand, the California Office of Environmental Health Hazard Assessment (OEHHA) has established vanadium level should not be higer than 15 μg/L in drinking water [8]. High concentrations of vanadium pose a threat to human health because vanadium damages organs such as the heart, kidneys, gastrointestinal tract and central nervous system. Compared to other heavy metals, vanadium is more toxic and causes severe oxidative damage to cells. The toxicity of V is dependent on many different factors such as the diet, type of compound, valence, route of entry into the organism, duration of exposure or individual species sensitivity dose [6]. Due to increase in laws and regulations concerning the vanadium concentration in various area of environment the development of novel cost-effective methods of its removal has been in progress. Adsorption technology has developed rapidly in recent years, so it has found wide application in the treatment of vanadium-containing wastewater due to its high efficiency, low energy consumption and environmental friendliness [9].

In the present study, an effort has been made to adsorptive vanadium removal from aqueous solutions using the commercially available ion exchange resins of different types such as Purolite, Lewatit and Dowex and sorbent Lewatit AF5. The ability of ion exchangers of various functional groups towards V(V) ion removal from the model's and real wastewater were determined. These results fill the gap in developing knowledge about vanadium ions removal. The optimization of vanadium adsorption process, comparision of the adsorption capacities obtained in the batch and column studies, and the desorption efficiency as well as the ion exchangers posibility to reuse were presented. In this paper a possible adsorption mechanism was also proposed.

**Experimental:** The ASAP, %CHNS, SEM, ATR-FTIR, XPS analyses were applied to characterize the ion exchange resins porous structure, functional groups, morphology, BET surface area, average pore diameter and to describe the adsorption mechanism. Adsorption and desorption experiments were performed using the batch technique (the temperature 295 K, 20 $cm^3$ of V(V) solutions, the mass of the ion exchanger 0.01-0.5 g, the initial concentration $C_{0=}$50-2000 $mg/dm^3$, the agitation speed 170 rpm, the amplitude 8, the phases contact time 1 min-24 h) using the laboratory mechanical shaker (type 358A, Elpin Plus, Poland). After proper period of time the phases were separated by filtration and the V(V) concentration was determined by means of the graphite furnace atomic absorption spectrometry (GFAAS). The effects of pH, ion exchanger dose, contact time, initial V(V) concentration, desorption and reusability of ion exchangers which characteristic is presented in Table 1 were investigated. The V(V) removal were

carried out from the model and real solutions ($V_2O_5$ spent catalyst using for sulfuric acid production after digestion by HCl or $H_2SO_4$ and NaOH or KOH solutions).
The fixed-bed column method was also applied (the glass columns of diameter 1 cm filled with 10 mL of swollen ion exchange resins, flow rate of 0.4 mL/min) for V(V) removal from the aqueous solutions of the initial vanadium concentration: 50, 100 or 200 mg/L at pH 4 or 6. The V(V) ion breakthrough curves, the weight ($D_w$), bed ($D_b$) distribution coefficients and the working ion exchange capacity ($C_w$) were determined:

- working ion exchange capacity ($C_w$) (g/mL) $$C_w = \frac{U_p \times C_0}{V_j} \quad (1)$$

- weight distribution coefficient ($D_w$) $$D_w = \frac{U^{"} - U_0 - V_f}{m_j} \quad (2)$$

- bed distribution coefficient ($D_b$) $$D_b = D_w \times d_z \quad (3)$$

where $U_p$ - the volume of eluate to the break through the column (L), $C_0$ - the initial, concentration of V(V) in the water phase (mg/L), $V_j$ - the volume of the sorbent in the column, U", $U_0$ - the eluate volume for $C/C_0$ = 0.5 (mL) and the dead column volume (2 mL); $V_f$ - the free volume of the sorbent bed (4 mL), $m_j$ - the mass of dry sorbent in the column (g), $d_z$ - the sorbent density (g/mL).

**Table 1.** Properties of ion exchangers and carbonaceous sorbent applied for V(V) removal.

| Ion exchanger | Matrix | Structure | Functional Groups | Types |
|---|---|---|---|---|
| Lewatit MonoPlus TP220 | cross-linked PS | macroporous | bis-picolylamine, bis(2-pyridyl-methyl)amine | ChIE/ WBA |
| Dowex M4195 | DVB cross-linked PS | macroporous | | ChIE |
| Lewatit MonoPlus SR7 | cross-linked PS | macroporous | quaternary ammonium, type 3 | SBA |
| Purolite A400TL | cross-linked PS | microporous | quaternary ammonium, type 1 | SBA |
| Dowex PSR2 | cross-linked PS | microporous | quaternary ammonium, tri-n-butyl amine | SBA |
| Dowex PSR3 | DVB cross-linked PS | macroporous | | SBA |
| Purolite A830 | DVB cross-linked PAc | macroporous | complex amine | WBA |
| Purolite S984 | DVB cross-linked PAc | macroporous | polyamine | ChIE |
| Lewatit AF5 | carbonaceous | microporous | without functional groups | sorbent |

DVB – divinylbenzene, PS – polystyrene, PAc – polyacrylic, WBA – the weakly basic and SBA – the strongly basic anion exchanger, ChIE – the chelating ion exchanger.

**Results:** The ion exchangers characteristic is presented in our previously published papers [10-11]. The effects of the adsorbent dose (0.01 to 0.1 ± 0.0005 g) studies on the vanadium(V) adsorption (the initial concentration of V(V) ions $C_0$=50 mg/L, temperature T=295 K, the agitation speed $A_s$=170 rpm, the amplitude a = 8, the phases contact time, t = 4h) shows that the percentage removal (%R) of V(V) values increased whereas the adsorption capacities decreased with the increase in the sorbent mass from 0.01 to 0.1 g. The optimal sorbent mass selected for further research was 0.1 g. The effects of solutions pH (2–10) on the vanadium(V) removal efficiency on the SR7, A400TL, PSR2, PSR3, A830, S984, M4195, TP220 and AF5 sorbents (0.1 g, $C_0$ = 50 mg/L, T = 295 K, 170 rpm, a = 8, t = 4 h) shows that most sorbents exhibit the great sorption capacities at pH 3-9, and the highest values were observed at pH 4 for ion exchangers with the bispicolylamine functional groups (TP220, M4195) and pH 6 for the other one; therefore, this pH were chosen in further studies. The smallest adsorption

capacities at pH<3 is a result of the electrostatic repulsion between $VO_2^+$ species and the positive charges of the sorbent surface and is a concequence of the competition effect of $H^+$ ions with $VO_2^+$ for the active site. Additionally, the amount of V(V) ions adsorbed and the adsorption capacities usually increase with the increasing phase contact time. With the higher V(V) concentration, the %R is smaller and the time required for equilibrium establishment increase with the initial V(V) concentration increse from 50 to 200 mg/L. The suitability of the commercial ion exchangers and the sorbent of the carbonaceous matrix was confirmed by the following series: Lewatit MonoPlus TP220 ($q_{e,exp}$=244.4 mg/g) >> Purolite S984 ($q_{e,exp}$=221.4 mg/g) >> Dowex M4195 ($q_{e,exp}$=205.4 mg/g) > Purolite A830 ($q_{e,exp}$=202.4 mg/g) ≈ Purolite A400TL ($q_{e,exp}$=200.4 mg/g) > Lewatit MonoPlus SR7 ($q_{e,exp}$=30.8 mg/g) ≈ Dowex PSR3 ($q_{e,exp}$=29.12 mg/g) ≈ Dowex PSR2 ($q_{e,exp}$=29.28 mg/g) > Lewatit AF5 ($q_{e,exp}$=27.76 mg/g) [10-11]. The column tests and the obtained selectivity series coincide with those obtained by the static method and indicate the great application potential of the chelating ion exchangers and the weakly basic anion exchange resin Purolite A830. The breakthrough curves resembled the typical "S" shape and the $D_w$ and $D_b$ parameters decrease with the initial concentration increase. The desorption yield is changeable and depends on the eluting agents concentration (0.1; 0.25; 0.5; 1 mol/L HCl and 0.1; 0.25; 0.5; 1 mol/L NaOH). The most effective agents for the V(V) ions desorption from the ion exchanger/sorbent phase include the NaOH solutions and in the case of the Purolite S984 ion exchanger also the HCl one. For Purolite S984 and Purolite A830 the quantitative desorption (%D=100%) was obtained using NaOH solutions. The applicability of ion exchangers toward V(V) was also confirmed by the sorption from the real solutions. The spent catalyst for the sulfuric acid production containing vanadium can be effectively leached and V(V) ions can be removed with high efficiency by the resin wih bis-picolylamine functional groups and Purolite S984. Moreover, co-precipitation of iron and vanadium ions was observed.

**Conclusions:** Lewatit MonoPlus TP220 and Purolite S984 can be promising in practical applications for wastewater treatment containing V(V) on a larger scale.

## References:

1. M.H. Anjass, K. Kastner, F. Nagele, M. Ringenberg, J.F. Boas, J. Zhang, A.M. Bond, T. Jacob, C. Streb, Angewandte Chemie International Edition England, 56 (2017) 14749.
2. R. Gilligan, A.N. Nikoloski, Mineral Engineging, 146 (2020) 106106.
3. G. Rahimi, S.O. Rastegar, F.R. Chianeha, RSC Advances, 10 (2020) 1685.
4. D.A. Santos, M.K. Dixit, P.P. Kumar, S. Banerjee, iScience, 24 (2021) 103277.
5. A. Wołowicz, Z. Hubicki, Molecules, 27 (2022) 5432.
6. A. Ścibiora, Ł. Pietrzyka, Z. Plewac, A. Skibad, Journal of Trace Elements in Medicine and Biology, 61 (2020) 126508.
7. S. Wang, B. Zhang, M. Diao, J. Shi, Y. Jiang, Y. Cheng, H. Liu, Environmental Pollution, 242 (2018) 249.
8. Q. Huang, S. Fu, H. Zhu, H. Song, Z. Yang, X. Zhang, J. Bie, J. Lu, M. Shi, B. Liu, Water, 14 (2022) 2867.
9. V.R. Gurjar, P.S. Koujalagi, H.N. Revankar, R.M. Kulkarni, Emergent Materials, 5 (2022)1543.
10. A.Wołowicz, Z. Hubicki, Hydrometallurgy, 211 (2022) 105871.
11. A.Wołowicz, Z. Hubicki, Molecules, 27 (2022) 5432.

# STUDIES OF THORIUM SORPTION ON FUNCTIONALIZED MESOPOROUS SILICA

**A. GŁADYSZ-PŁASKA[1], A. LIPKE[1], J. PADARZ[1], M. GAJEWSKA[1], E. GRABIAS-BLICHARZ[2], M. MAJDAN[1]**, [1]Maria Curie-Sklodowska University, Faculty of Chemistry, Institute of Chemical Sciences, Department of Inorganic Chemistry, M. Curie-Sklodowska Sq. 2, 20-031 Lublin, Poland; [2]Medical University of Lublin, Faculty of Pharmacy, Department of Analytical Chemistry, Chodzki 4a, 20-093 Lublin.

**Abstract:** Studies were carried out to assess the sorption capacity towards thorium ions for adsorbents obtained on the basis of silica. One of them was modified with a component of natural origin and the other with a ligand containing phosphorus(III).During the adsorption tests, the optimal conditions for the removal process from model water systems were determined. The kinetic, equilibrium and thermodynamic parameters of the adsorption process were estimated. The fundamental stage of the research was the regeneration of the applied adsorbents enabling the assessment of the possible reuse of these materials.

**Introduction:** The rapid development of civilization, associated with a large demand for electricity, resulted in the energy crisis that becomes threatening. To prevent this, there is a constant search for new energy sources. One way to obtain electricity are nuclear power plants, which use uranium as reactor fuel, or it is also possible to use thorium. Unfortunately, both of these elements pose a threat to the natural environment due to their radioactive nature. Thorium is a radioactive element that occurs in large quantities all over the globe, and monazite is the most common source of its extraction. Owing to its properties, it is worth using its potential in nuclear energy, in line with the idea of sustainable development. Unlike uranium, thorium used as nuclear fuel can be completely consumed. At the same time, the natural radioactivity of thorium should be taken into account, which has negative effects on human health. The consequences of contact with this nuclide are experienced after many years. Removing thorium ions from the aquatic environment can contribute to the protection of people and animals against excessive doses of radiation and consumption of compounds of this element. For this reason, waste and sewage from nuclear power plants pose a great threat to the natural environment and living organisms. Therefore, it is important to reduce their negative impact through disposal or complete neutralization. The currently used methods are: precipitation process, membrane techniques, ion exchange, extraction and adsorption. Adsorption is considered one of the most effective and economical methods of removing contaminants from water systems. It is a very flexible process in both design and implementation. When choosing adsorption as an effective method for removing pollutants, the possibility of re-regeneration of sorbents seems to be important. The adsorption process is largely based on the selection of an appropriate adsorbent. In recent years, adsorbents of natural origin have become increasingly common. Attempts are being made to obtain materials that are cheap and effective in removing contaminants from water systems. In particular, biomass possesses very favourable adsorption properties. The most commonly used adsorbents of natural origin include: clay, peat,

chitin, lignin, compounds contained in numerous minerals and microorganisms (bacteria, fungi and yeast). Due to the great availability and low costs of obtaining these materials, they are included in the group called low-cost adsorbents.

**Experimental:** Two types of sorbents were used in the work: $SiO_2$-BIO and $SiO_2$-P(III). In order to obtain these sorbents, a simple and cheap sol-gel method from TEOS was used. The BIO-component was natural mycelium obtained from Polish forests, which had been previously dried and freeze-dried. $H_3PO_3$ was used as a phosphorus(III)-containing ligand.

**Results:** The obtained adsorbents have been tested to assess their properties sorption to thorium ions. The first step was checking the minimum sample size that can be used. For this purpose, weighs ranging from 0.05 to 0.25 g were prepared and contacted with solutions containing thorium ions at a concentration of 0.5 mmol/dm$^3$. Based on the obtained results, a 0.05 g sample was selected for further testing. The next step was to examine the influence of time on the sorption process. The results are presented in Fig.1. It is clearly visible that the sorption process occurs most quickly on the $SiO_2$-BIO sorbent. Then, the influence of the dependence of the sorption amount on the initial concentration of thorium ions in the solution was examined. For this purpose, solutions were prepared with initial concentrations ranging from 0.1 to 1 mmol/dm$^3$. The tests were carried out at two temperatures: 293 K and 313 K. The obtained results are presented in Fig.2. In order to analyze and determine the adsorption properties of the sorbents, the data obtained from the adsorption isotherms were fit using the two most popular models of adsorption isotherms: the Freundlich model and the Langmuir model. As a result of modeling the experimental data, the adsorption parameters were obtained: $Q_{max}$ = 0.002 mol/g for a temperature of 293 K and 0.003 mol/g for a temperature of 313 K.

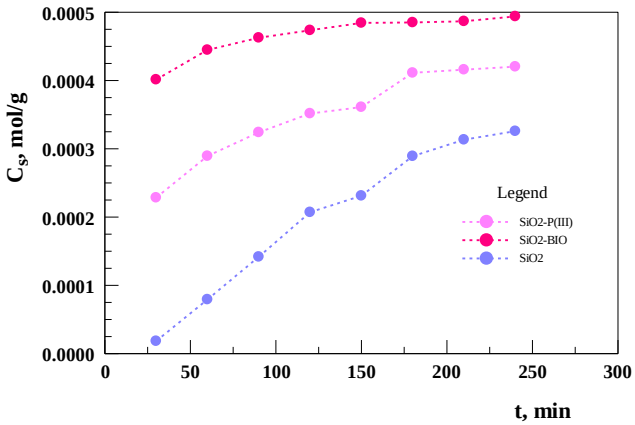



**Fig.1.** Time influence on thorium sorption on sorbents: $SiO_2$-BIO, $SiO_2$-P(III), $SiO_2$ ($C_s$ – concentration of thorium on sorbent phase in mol/g).

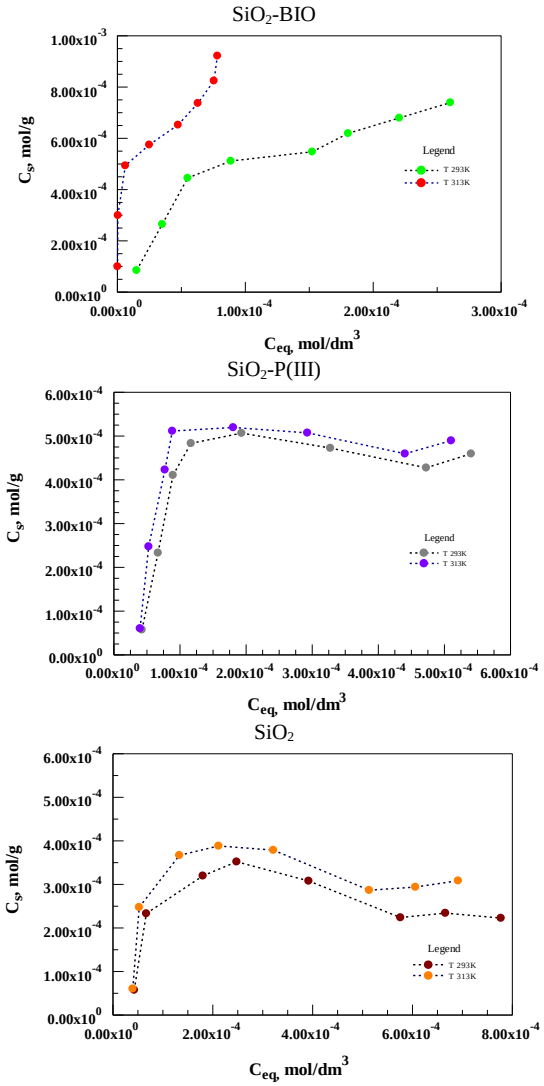



**Fig. 2**. Adsorption isotherms of thorium on sorbents: $SiO_2$-BIO, $SiO_2$-P(III), $SiO_2$ at various temperatures: 293K and 313K ($C_s$ – concentration of thorium on the sorbent phase in mol/g, $C_{eq}$ – concentration of thorium in the equilibrium solution).

The surface heterogeneity parameter was above 1, i.e. the value of $1/n$ was lower from unity, which indicates a relatively large energetic heterogeneity of the surface these two tested sorbents. The fit of the models to the obtained experimental data was above than 90%, both the Freundlich model and the Langmuir model (Table 1). This may indicate that the adsorption mechanism is largely a physical adsorption based on van der Waals-type interactions of the adsorbent with thorium ions. In research on the preparation and use of adsorbents, an important factor, also from an economic point of view, is

determining the possibility of re-use the adsorbent. For this purpose, the desorption of ions previously deposited on the surface of the tested adsorbent is examined.

**Table 1.** Fitting parameters of the isotherms adsorption of thorium ions on silica based adsorbents according to Freundlich and Langmuir models.

| Parameter | $SiO_2$-BIO | | $SiO_2$-P(III) | | $SiO_2$ | |
|---|---|---|---|---|---|---|
| Freundlich model | 293 K | 313 K | 293 K | 313 K | 293 K | 313 K |
| $Q_{max}$, mol/g | 0.001 | 0.003 | 0.0008 | 0.001 | 0.0008 | 0.001 |
| $K_F$, mol·dm$^3$/g | 6.6 | 5.55 | 11.6 | 8.8 | 10.1 | 9.8 |
| 1/n | 0.68 | 0.69 | 1.05 | 1.02 | 0.95 | 1.2 |
| $R^2$ | 0.96 | 0.98 | 0.78 | 0.73 | 0.72 | 0.67 |
| Langmuir model | | | | | | |
| $Q_{max}$, mol/g | 0.0012 | 0.001 | 0.0005 | 0.00055 | 0.00032 | 0.0004 |
| $K_L$, dm$^3$/mol | 15.5 | 7.8 | 13.3 | 14.5 | 5.5 | 6.7 |
| $R^2$ | 0.85 | 0.80 | 0.98 | 0.97 | 0.95 | 0.95 |

Weights of 0.1 g of $SiO_2$-BIO or $SiO_2$-P(III) or $SiO_2$ were prepared and filled with thorium ions in the amount 0.6 mmol/g. Then they were exposed to various solutions. Received results are included in Table 2. The presented numerical data show that the percentage of desorption is small, maximum 55%, therefore multiple the use of these sorbents is very limited. They can therefore be used to permanently immobilize thorium in storage areas or to build earth barriers preventing the penetration and spread of water contaminated with thorium ions over a larger area.

**Table 2.** Effect of desorption agent on the recovery of thorium ions (S – percentage of thorium ions recovery).

| Sample | S, % | | | |
|---|---|---|---|---|
| | $H_2O$ | 0.01mol/dm$^3$ $Na_2CO_3$ | 0.001mol/dm$^3$ HCl | 0.01mol/dm$^3$ $Na_2SO_4$ |
| $SiO_2$-BIO_Th | 2 | 5 | 55 | 3 |
| $SiO_2$_P(III)_Th | 0 | 0 | 34 | 0 |
| $SiO_2$_Th | 3 | 3 | 40 | 3 |

**Conclusions:** The $SiO_2$-BIO sorbent turned out to be the best among the three tested. The highest sorption capacity for this material was obtained. Additionally, this sorbent had the highest regenerative capacity. It is also important that this sorbent was obtained from natural materials, which was forest mycelium.

## References:

1. S. Yusan, C. Gok, S. Erenturk, S. Aytas, Appllied Clay Science, 12 (2012) 67.
2. M. Żukowski, Wykorzystanie pustaków szczelinowych wypełnionych ekspandowanym perlitem w technologiach energooszczędnych, Materiały Ceramiczne, 63 (2011) 195.
3. Z. Talip, M. Eral, Ü. Hiçsoönmez, Journal of Environmental Radioactivity, 100 (2009) 33.

# SORPTION OF CESIUM AND STRONTIUM IONS ON HYBRID PECTIN BASED SORBENT

**J. BOK-BADURA, A. JAKÓBIK-KOLON, B. SAGAN-SZENDZIELORZ**, Silesian University of Technology, Faculty of Chemistry, Department of Inorganic, Analytical Chemistry and Electrochemistry, B. Krzywoustego 6, 44-100 Gliwice, Poland.

**Abstract:** In this paper the use of a hybrid sorbent consisting of copper(II) hexacyanoferrate(II) (CuHCF) and pectin for simultaneous removal of cesium and strontium ions was proposed. It has been proven that proposed sorbent exhibit very good sorption properties over a wide pH range (4-10). The maximum sorption capacities of the hybrid pectin-CuHCF sorbent were $q_{Cs}$ = 0.69 mmol/g and $q_{Sr}$ = 0.33 mmol/g. Comparing the obtained results with literature data, it was concluded that the proposed sorbent can be successfully used for simultaneous removal of cesium and strontium ions.

**Introduction:** Cesium and strontium are byproducts of various industrial processes, including nuclear power plants, medical imaging and industrial manufacturing [1,2]. The radioactive isotopes of cesium (Cs-137) and strontium (Sr-90) are products of nuclear fission reactions. These isotopes exhibit prolonged radioactive decay periods, rendering them hazardous to ecosystems and human health. Inadequate containment or mishandling of radioactive waste can lead to the release of cesium and strontium ions into water sources and wastewater. Moreover, the solubility of cesium and strontium compounds in water facilitates their dispersion in aquatic environments [3]. Therefore, the development of effective methods for the removal and disposal of cesium and strontium ions is a challenge. Several methods have been developed to remove cesium and strontium ions from wastewater. These methods vary in terms of efficiency, cost-effectiveness and applicability to different wastewater. Some of the commonly used techniques, include precipitation, membrane filtration, ion exchange and adsorption [4,5]. Among these methods, ion exchange and adsorption have many advantages and are often proposed for the disposal of waste containing radioactive isotopes. In this work, we propose the use of hybrid inorganic-pectin sorbents for simultaneous removal of cesium and strontium ions. The inorganic part of the sorbent, copper(II) hexacyanoferrate (CuHCF), has a high affinity for cesium ions while the cross-linked pectin (P) has an affinity for divalent ions and will therefore traps strontium ions.

**Experimental:** In this study a hybrid sorbent composed of copper(II) hexacyanoferrate (CuHCF) immobilized in a pectin matrix cross-linked with calcium ions was used. The method of preparation of the sorbent and its characteristics were presented in a previous paper [6]. Sorption studies were conducted using the batch method. An appropriate amount of sorbent was added to a mixed solution of cesium (1 mmol/L) and strontium (1 mmol/L) ions. The solutions were prepared from solid $CsNO_3$ and $Sr(NO_3)_2$ (Sigma-Aldrich, Darmstadt, Germany). The pH of the solutions was adjusted with NaOH (Avantor, Gliwice, Poland) and $HNO_3$ (‘Suprapur’ from Merck, Darmstadt, Germany). The sorbents were shaken with solutions for 24 hours at constant temperature (22 ± 1 °C). After this time the solution was filtered. The concentration of cesium and

strontium ions before and after sorption was determined by inductively coupled plasma atomic emission spectrometer (ICP-AES) – Varian, Palo Alto, CA, USA. For all experiments, demineralized water purified with a Millipore Elix 10 system (Milipore SAS, Molsheim, France) was used.

**Results:** The sorbent used was in the shape of beads with a diameter of 1-2 mm in dry form. A detailed characterization of the sorbent was presented in a previous paper, in which it was proven that the sorbent shows very good sorption properties towards cesium ions [6]. The inorganic part of the sorbent, CuHCF, is responsible for cesium sorption. On the other hand, pectin cross-linked with calcium ions is known to have an affinity for divalent ions. Therefore, the proposed sorbent can also retain strontium ions, which can occur in wastewater together with cesium ions. Fig.1 shows the effect of pH on the hybrid pectin-CuHCF sorption capacity against cesium and strontium ions.

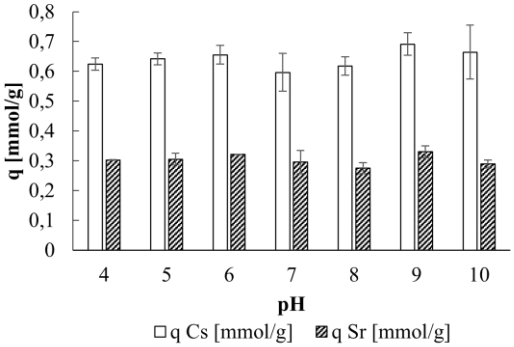



**Fig. 1.** Effect of pH on simultaneous sorption of cesium and strontium on hybrid pectin-CuHCF sorbent (sorbent dose = 1 g/L, $C_{Cs}$ = 1 mmol/L, $C_{Sr}$ = 1 mmol/L, temp. = 22 ± 1 °C, t = 48 h).

The sorption capacity of hybrid pectin-CuHCF sorbent was in the range of 0.62-0.69 mmol/g, and 0.27-0.33 mmol/g for cesium and strontium, respectively. However, the sorbent dose used in the study was selected for cesium sorption. Therefore, the maximum removal rates were 75% and 33% for cesium and strontium, respectively. It was also shown that the sorption capacity of the hybrid pectin-CuHCF sorbent against both cesium and strontium did not differ significantly (student t-test, $v = 2$, $\alpha = 0.05$) in the pH range of 4 to 10. The sorption capacities of the proposed sorbent and other sorbents proposed in the literature were also compared (Table 1). The sorption capacities of the materials are in the range from 0.006 to 1.6 mmol/g and 0.02 to 2.8 mmol/g for cesium and strontium ions, respectively. So, there are sorbents with better, but also definitely worse sorption properties than the proposed hybrid pectin-CuHCF sorbent.

**Table 1.** Cesium and strontium adsorption capacities in some literature studies.

| Adsorbent | Adsorption capacity [mmol/g] | References |
|---|---|---|
| Prussian blue-embedded alginate aerogel | $q_{Cs}$ = 0.15, $q_{Sr}$ = 0.23 | [7] |
| Magnetic potassium zinc hexacyanoferrate(II) | $q_{Sr}$ = 0.036 | [8] |
| Mucilaginous seeds of Ocimum basilicum | $q_{Cs}$ = 1.2, $q_{Sr}$ = 2.8 | [9] |

| | | |
|---|---|---|
| Coconut shell activated carbon | $q_{Cs} = 0.006$, $q_{Sr} = 0.02$ | [10] |
| Prussian blue analog caged in chitosan surface-decorated carbon nanotubes | $q_{Cs} = 1.6$, $q_{Sr} = 2.3$ | [11] |
| Sodium cobalt hexacyanoferrate (CoFC)-encapsulating alginate beads | $q_{Cs} = 0.91$, $q_{Sr} = 0.80$ | [12] |
| Sodium cobalt hexacyanoferrate (CoFC)-encapsulating alginate beads reinforced with highly dispersed multiwalled carbon nanotubes | $q_{Cs} = 1.00$, $q_{Sr} = 0.82$ | [12] |
| hybrid pectin-CuHCF sorbent | $q_{Cs} = 0.69$, $q_{Sr} = 0.33$ | This study |

However, it should be noted that the choice of a suitable sorbent is not determined only by its sorption capacity, but primarily by its functional properties. It should be easily used in a flow system, so it should not frm a clumped sludge that clogs the column. The proposed hybrid sorbent has a suitable grain shape by which it is easily separated from the purified solution. It has also been successfully applied in a flow system for the removal of cesium ions [6]. In order to confirm its utility for simultaneous removal of cesium and strontium ions, additional studies should be conducted.

**Conclusions:** The preliminary studies concerning sorption of cesium and strontium ions on hybrid pectin based sorbent have been performed. The results indicate that the materials used to be promising for simultaneous removal of cesium and strontium ions in wide pH range, therefore further studies are recommended.

**Acknowledgements:** This research was funded by the Polish Ministry of Science and Higher Education, grant number BK-04/010/BK_24/1080.

**References:**

1. N. Evangeliou, Y. Balkanski, A. Cozic, A.P. Møller, Environment International, 64 (2014) 17.
2. B. Is¸ık, A. E. Kurto˘glu, G. Gürda˘g, G. Keçeli, Journal of Hazardous Materials, 403 (2021) 123652.
3. Toxicological Profile for Cesium, Agency for Toxic Substances and Disease Registry, 2004.
4. T. Vincent, C. Vincent, Y. Barré, Y Guari, G. Le Saout, E. Guibal, Journal of Materials Chemistry A, 2 (2014) 10007.
5. J. R. Wiley, Industrial & Engineering Chemistry Process Design and Development, 17 (1978) 67.
6. J. Bok-Badura, A. Kazek-Kęsik, K. Karoń, A. Jakóbik-Kolon, Water Resources and Industry, 28 (2022) 100190.
7. S. Eun, J. Ryu, H. Kim, H. J. Hong, S. Kim, Journal of Environmental Management, 297 (2021) 113389.
8. G. N. Pshinko, L. N. Puzyrnaya, V. S. Shunkov, A. A. Kosorukov, V. Ya. Demchenko, Radiochemistry, 58 (2016) 491.
9. D. Chakraborty, S. Maji, A. Bandyopadhyay, S. Basu, Bioresource Technology, 98 (2007) 2949.
10. M. Caccin, F. Giacobbo, M. Da Ros, L. Besozzi, M. Mariani, Journal of Radioanalytical and Nuclear Chemistry, 297 (2012) 9.
11. T. Li, F. He, Y.D. Dai, Journal of Radioanalytical and Nuclear Chemistry, 310 (2016) 1139.
12. A. K. Vipin, S. Ling, B. Fugetsu, Carbohydrate Polymers, 111 (2014) 477.

# EXTRACTION OF BIOACTIVE COMPOUNDS FROM DANDELION USING MODERN EXTRACTION TECHNIQUES

**M. KALINOWSKA**, **E. GOŁĘBIEWSKA, K. KORONKIEWICZ, M. BIENIEK**, **A. ZINIEWICZ**, Bialystok University of Technology, Faculty of Construction and Environmental Sciences, Department of Chemistry, Biology and Biotechnology, Wiejska 45 E St., 15-351 Bialystok, Poland.

**Abstract:** Common dandelion (*Taraxacum officinale*) is a plant from the *Asteraceae* family. It is a source of many valuable bioactive compounds, such as flavonoids, phenolic acids, vitamins, and minerals. The properties of common dandelion have been known and widely used in folk medicine for many centuries. The natural compounds contained in common dandelion exhibit a wide spectrum of health-promoting effects, including antioxidant, anti-inflammatory, antibacterial, and antiviral activities. In this study, the influence of selected modern extraction methods (pressure extraction and ultrasound-assisted extraction) on the properties of extracts obtained from common dandelion petals was investigated. The antioxidant activity (DPPH$^{\bullet}$ radical scavenging assay (2,2-diphenyl-1-picrylhydrazyl), FRAP assay (Ferric Reducing Antioxidant Power), as well as pro-oxidant activity, of the extracts were analyzed, and their qualitative and quantitative composition was determined using chromatographic methods.

**Introduction**: Common dandelion (*Taraxacum officinale*) belongs to the *Asteraceae* family and is a pharmacopoeial and edible plant. It probably originates from Europe, gradually spreading to Asia, later to North America, and some countries in South America. In many European countries, it is a common weed growing along roadsides, meadows, and lawns [1]. Pharmacopoeial raw materials include roots, herbs, and flowers. Traditionally, common dandelion has been used as a medicinal remedy for kidney diseases, diabetes, bacterial infections, as a diuretic, in liver, kidney, and spleen diseases, as well as an anti-inflammatory agent. Selected parts of this plant are also used as food. Young leaves are added to salads, while dandelion roots are rich in inulin, and a brew from it can serve as a substitute for coffee or tea [2]. Extract from dandelion petals can be used as a food additive, such as in desserts, sweets, cakes, puddings, and similar products [3]. The medicinal properties of common dandelion are attributed to the bioactive compounds it contains, including carotenoids, flavonoids (e.g., quercetin, 7-glucoside of luteolin), phenolic acids (e.g., caffeic acid, chlorogenic acid, ferulic acid), polysaccharides, sterols, and triterpenes [4]. Extraction is one of the methods enabling the isolation of these valuable components from plant material. However, classical extraction methods usually involve a high consumption of solvents and energy, which is not environmentally friendly. Modern extraction technologies utilizing high pressure, microwaves, and ultrasound come to the rescue, increasing the efficiency of the extraction process, reducing the consumption of harmful chemicals and energy, and decreasing the amount of generated waste [5]. Therefore, in this study, the effectiveness of pressure extraction and ultrasound-assisted extraction on the antioxidant and pro-

oxidant properties, as well as the content of bioactive compounds in ethanol extracts from common dandelion flowers, was compared.

**Experimental**: The research material consisted of dried common dandelion flowers. To conduct high pressure extraction, three portions of common dandelion flowers weighing approximately 0.5 g were weighed out. A SpeedExtractor E-916 was used for extraction. 100% ethanol was used as the solvent. The ratio of fat-free quartz sand to biological material should be 1:1, so approximately 0.5 g of sand was weighed out and mixed with the common dandelion flowers. The prepared biological material was then carefully transferred to metal cells. Extraction was carried out at a temperature of 100°C and a pressure of 100 bar in three cycles. The total volume of the obtained extract was 37.5 ml ($m_{material}/v_{solvent}$=1/75). To conduct ultrasound-assisted extraction, three portions of common dandelion flowers weighing approximately 2 g were weighed out into dark screw-capped bottles, and then 50 ml of 100% ethanol was added ($m_{material}/v_{solvent}$ =1/75). Extraction was performed three times in an ultrasonic bath (50 Hz; 3x30 min; T=60°C), each time filtering the residues under reduced pressure and adding a fresh portion of the solvent. The total volume of the obtained extract was 150 ml.

The determination of the total content of phenolic compounds was carried out using the Folin-Ciocalteu (F-C) reagent method. Before the analysis, a standard curve of gallic acid was prepared. To each test tube, 0.25 ml of diluted F-C reagent (v:v; 1:1) was added, along with 0.5 ml of 14% sodium carbonate solution and 4 ml of deionized water. In the case of the blank sample, 0.25 ml of solvent (100% ethanol) was added to the test tube instead of the extract. After an hour of incubation, the absorbance of the samples was measured at a wavelength of λ=760 nm (against the blank sample). Then, the total content of phenolic compounds per 1 g of research material was calculated using the formula below.

$$CZZF = \frac{C_{zf} \cdot V_r}{m_m}$$

where: CZZF - total phenolic compounds content [mg/g], $C_{zf}$ - phenolic compounds content [ml], $V_r$ - solvent volume [ml], $m_m$ – material weight [g].

Antioxidant activity (DPPH assay, FRAP assay) and pro-oxidant activity of the obtained extracts from common dandelion were measured according to the methodology described in [5].

**Results**: The results of determining the total content of phenolic compounds illustrate the beneficial effect of increased pressure on the polyphenol content in the tested extracts (Fig.1). The content of phenolic compounds in extracts obtained using elevated pressure was over twice as high (14.086±0.380 mg/g dry weight), compared to extracts obtained using ultrasound-assisted extraction (5.867±0.324 mg/g dry weight).
Extracts obtained using pressure extraction showed a higher percentage of DPPH• radical inhibition (25.32%) and exhibited a higher capacity for reducing Fe(II) ions (0.984 μmol $Fe^{2+}$/L) compared to extracts obtained using ultrasound (corresponding to 13.83% and 0.733 μmol $Fe^{2+/}$L, respectively) (Fig.2).

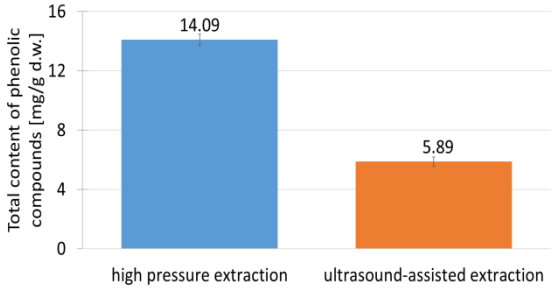



**Fig.1.** Comparison of the total content of phenolic compounds in extracts depending on the extraction method used.

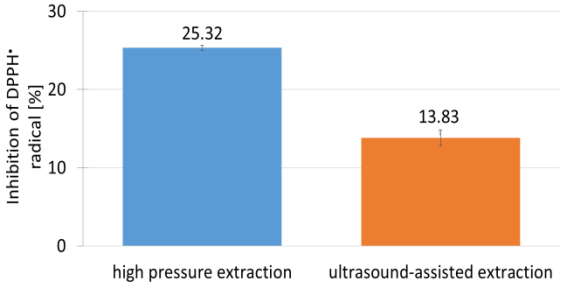



**Fig.2.** Comparison of the ability to inhibit the DPPH- radical [%] by extracts depending on the extraction method used.

Figure 3 presents the results of the pro-oxidant activity assay conducted for the obtained extracts. Extracts obtained through ultrasound-assisted extraction showed an increase in the trolox oxidation level ranging from 1.55% to 11.55% compared to the control sample without extract. In contrast, extracts obtained through high-pressure assisted extraction exhibited a significantly higher trolox oxidation level, ranging from 1.99% to 27.95%.

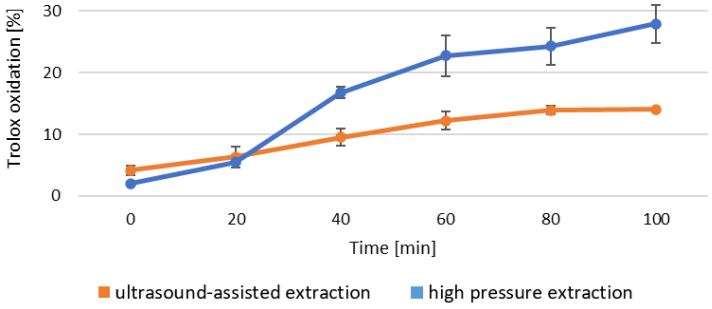



**Fig.3.** Comparison of pro-oxidation properties of the tested extracts expressed as the degree of trolox oxidation [%].

HPLC analysis revealed that the main phenolic compounds present in extracts from common dandelion flowers were procyanidin A2 (pressure extraction: 4211.80±82.52 µg/g dry weight; ultrasound-assisted extraction: 1790.28±17.42 µg/g dry weight), catechin, rutin, chlorogenic acid, phloridzin, kaempferol, and ferulic acid

(Fig.4). The highest amounts of these compounds were identified in extracts obtained using accelerated pressure extraction.

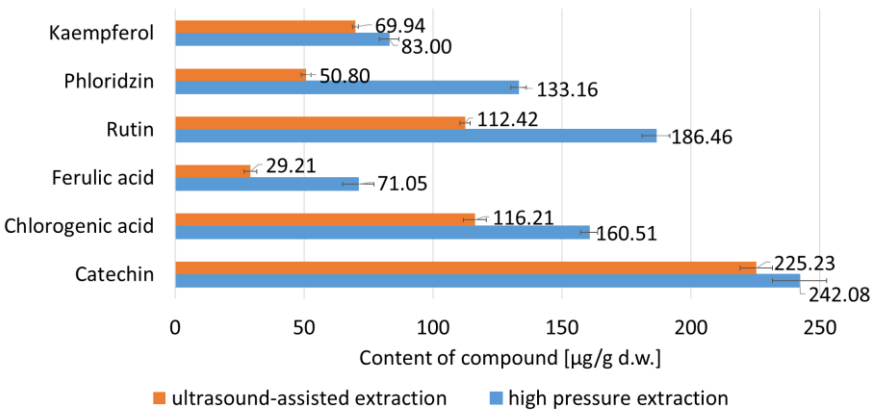



**Fig.4.** Comparison of the content of selected phenolic compounds [µg/g dry weight] in the obtained extracts depending on the extraction method used.

**Conclusions**: The use of pressure extraction enables the extraction of phenolic compounds from dandelion flowers to be more efficient compared to ultrasound-assisted extraction. HPLC analysis revealed that the main phenolic compounds present in the obtained extracts included procyanidin A2, catechin, rutin, and chlorogenic acid, among others. Extracts obtained using high pressure extraction exhibited over two times higher total phenolic compounds content and higher antioxidant and pro-oxidant properties than extracts obtained using ultrasound-assisted extraction.

**Acknowledgements:** This research was funded by the National Science Centre, Poland, Grant No. 2021/43/B/NZ9/03102.

**References:**

1. C. Jalili, M. Taghadosi, M. Pazhouhi, F. Bahrehmand, S.S. Miraghaee, D. Pourmand, I. Rashidi, World Cancer Research Journal (WCRJ), 7 (2020) e1679.
2. D. Esiyok, S. Ötles, E. Akcicek, Asian Pacific Journal of Cancer Prevention, 5 (2004) 334.
3. M. Gonzalez-Castejon, F. Visioli, A. Rodriguez-Casado, Nutrition Reviews, 70 (2012) 534.
4. A. Di Napoli, P. Zucchetti, Bulletin of the National Research Centre, 45 (2021) 110.
5. E. Gołębiewska, M. Kalinowska, G. Yildiz, Materials, 15 (2022) 1788.
6. M. Kalinowska, K. Gryko, A.M. Wróblewska, A. Jabłońska-Trypuć, D. Karpowicz, Scientific Reports, 10 (2020) e14951.

# PRESSURIZED SOLVENT EXTRACTION (PSE) OF BIOACTIVE COMPOUNDS FROM APPLE POMACE

**M. KRYSTKOWICZ[1], M. KALINOWSKA[1], G. KOLENDA[1], K. KORON-KIEWICZ[1], E. GOŁĘBIEWSKA[1], R. CHOIŃSKA[2], J. SKIBICKI[3]**, [1]Bialystok University of Technology, Faculty of Construction and Environmental Sciences, Department of Chemistry, Biology and Biotechnology, Wiejska 45 E St., 15-351 Bialystok, Poland, [2]Prof. Waclaw Dabrowski Institute of Agricultural and Food Biotechnology–State Research Institute (IBPRS-PIB), Department of Fermentation Technology, Rakowiecka 36 St., 02-532 Warsaw, Poland, [3] SAJSAD Jan Skibicki, Gminna 105 St., 15-587 Kuriany, Poland.

**Abstract:** The research was aimed at examining pomace from the Polish Gold Milenium apple variety in terms of the content of antioxidants (including phenolic compounds) and antioxidant properties. The pressurized solvent extraction (PSE) was used to obtain methanolic and ethanolic extracts from apple pomace. The extracts were tested for antioxidant activity using the following methods: DPPH$^{\bullet}$ (2,2-diphenyl-1-picrylhydrazyl), CUPRAC (*Cupric Reducing Antioxidant Capacity*). Quantitative and qualitative analysis of phenolic compounds and triterpenoids was performed using HPLC.

**Introduction**: One of the by-products in apple processing is pomace, which accounts for as much as 25-30% [1]. It is rich in water, with a moisture content ranging between 70% and 85%, making apple pomace susceptible to microbiological contamination [2]. Moreover, apple pomace contains dietary fiber, starch, mono- and disaccharides, volatile compounds, triterpenoids, non-volatile acids, and polyphenols - natural bioactive substances with health-promoting properties [3]. Food supplementation with compounds present in recovered agri-food waste can be a significant strategy to increase the intake of these compounds [4]. Utilizing apple pomace in bakery or meat products can mitigate the deficiency of dietary fiber while improving the taste and consistency of the final products [1]. Natural antioxidants aid in preventing chronic diseases and slowing aging processes, making their consumption highly valuable [5]. There is increasing research confirming the prevention of cancer risk, particularly lung cancer [6]. Additionally, consuming apples may offer numerous benefits in preventing other civilization diseases, including cardiovascular diseases, asthma, and type II diabetes [7]. Different types of extraction techniques are employed to recover valuable health-promoting compounds from plant material. Conventional extraction methods require a large amount of solvents and labor input. Consequently, modern technologies utilizing high pressures, ultrasound, or microwaves and consuming fewer harmful chemicals and less energy are increasingly being used. This work presents the results of antioxidant study of extracts from apple pomace obtained by PSE. Phenolic compounds and triterpenoids were quantitatively and qualitatively determined using highly efficient High Performance Liquid Chromatography (HPLC).

**Experimental**: The material for the study consisted of dried micronized apples pomace from Gold Milenium variety obtained from SAJSAD company which is well known producer of biopreparation from Gold Milenium apples. The apple pomace was measured using 3D optical profilograph VR-6000 (Keyence) (Fig.1.). The PSE extraction was carried out using the SpeedExtraction E-916 apparatus. 2.5g of apple pomace was extracted using methanol (99.8%, MeOH) and ethanol (96%, EtOH) in three cycles at a pressure of 100 bar and temperatures of 80 °C (MeOH) or 100°C (EtOH). The volume of solvent used in each sample was 30 $cm^3$.

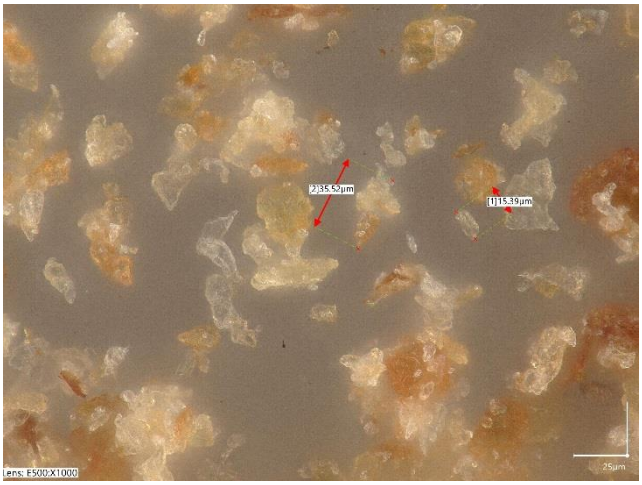



**Fig.1.** The micronized apple pomace surface.

Chromatographic separation of phenolic compounds and triterpenoids from the evaporated extracts was performed using an Agilent 1260 Infinity liquid chromatograph with a DAD spectrophotometric detector (Zorbax Eclipse Plus C18 Analytical 4.6x250mm pre-column; 5µm) according to the methodology described in [8]. The determination of antioxidant activity ($DPPH^{\bullet}$ and CUPRAC assay) of Gold Milenium apple pomace was performed based on the methodology described in [8].

**Results**: The extracts from apple pomace obtained by pressurized solvent extraction using methanol as solvent showed a slightly higher percentage of $DPPH^{\bullet}$ radical inhibition (72.57% ± 3.275) than the ethanolic extract (67,20% ± 0,906). The results presented in the form of a graph (Fig.2). Methanolic extract showed a higher ability to reduce Cu(II) ions (0.439 ± 0.015 $\mu mol_{Trolox}/dm^3$), than ethanolic extract (0.330 ± 0,011 $\mu mol_{troloks}/dm^3$) (Fig.3).
The total content of phenolic compounds was higher in methanolic extracts (3.073 mg/g $_{d.m.\ extract}$) than in ethanolic extracts (2.741 mg/g $_{d.m.\ extract}$). The content of particular compounds in the extracts differed taking into account the type of solvent, e.g. one of the triterpenoids - betulinic acid was detected with a much higher content in the ethanolic extract (29.927± 0.019 mg/g $_{d.m\ extract}$) compared the methanolic one (17.797 ± 0.313 mg/g $_{d.m.\ extract}$). The content of phenolic compounds in the examined extracts is presented in Fig.4.

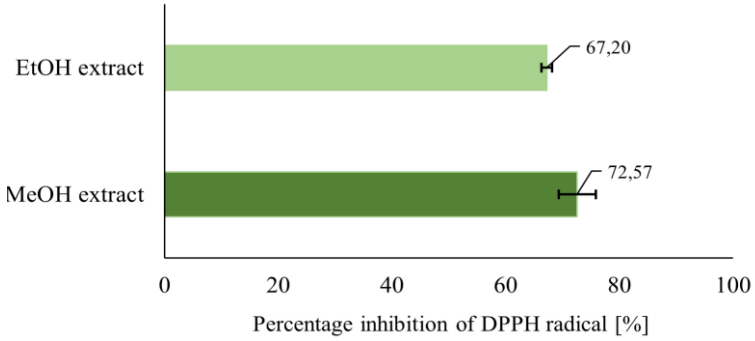



**Fig.2.** Comparison of the ability to inhibit the DPPH$^{\bullet}$- radical [%] by MeOH and EtOH extracts.

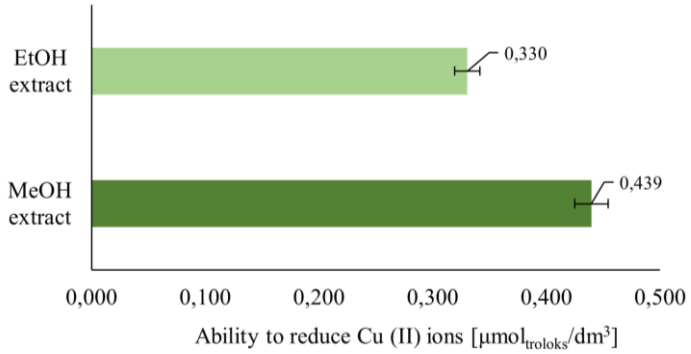



**Fig.3.** Antioxidant activity by MeOH and EtOH extracts in CUPRAC assay – Trolox equivalents [µmol/dm$^3$].

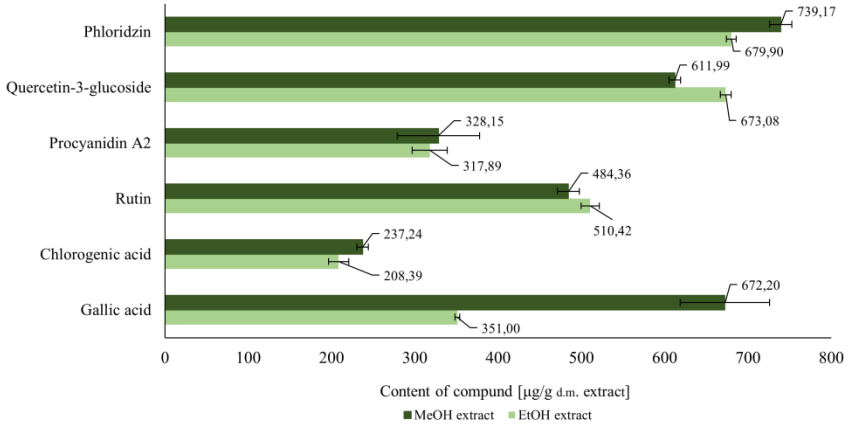



**Fig.4.** Content of phenolic compounds in MeOH and EtOH extracts from apple pomace.

**Conclusions**: The Gold Milenium apple pomace extracts obtained by the PSE showed high antioxidant properties and revealed high content of phenolic compounds. Methanolic extracts exhibit higher antioxidant properties than ethanolic extracts in the DPPH$^{\bullet}$ and CUPRAC tests, and they also showed higher phenolic compound content in

the HPLC analysis. The phenolic compounds detected during HPLC analysis are: phloridzin, quercetin-3-glucoside, procyanidin A2, rutin, chlorogenic acid and gallic acid.

**Acknowledgements:** This research was funded by the National Science Centre, Poland, Grant No. 2021/43/B/NZ9/03102.

**References:**

1. F. Lyu, S.F. Luiz, D.R.P. Azeredo, A.G. Cruz, S. Ajlouni, C.S. Ranadheera, Processes, 8 (2020) 319.
2. K. Waldbauer, R. McKinnon, B. Kopp, Planta Medica, 83 (2017) 994.
3. M. Kalinowska, E. Gołębiewska, M. Zawadzka, R. Choińska, K. Koronkiewicz, K. Piasecka-Jóźwiak, M. Bujak, Scientific Reports, 13 (2023) 19310.
4. P.A. Fernandes, S.S. Ferreira, R. Bastos, I. Ferreira, M.T. Cruz, A. Pinto, D.F. Wessel, Antioxidants, 8 (2019) 189.
5. J. Boyer, R. H. Liu, Nutrition Journal, 3 (2004) 1.
6. D. Feskanich, R.G. Ziegler, D.S. Michaud, E.L. Giovannucci, F.E. Speizer, W.C. Willett, G.A. Colditz, Journal of the National Cancer Institute, 92 (2000) 1812.
7. M. Kalinowska, Prozdrowotne właściwości jabłek oraz metody izolacji i identyfikacji związków biologicznie czynnych z jabłek. Aparatura badawcza i dydaktyczna. Biblioteka Nauki. ABiD3 (2012) 38-42.
8. M. Kalinowska, K. Gryko, A.M. Wróblewska, A. Jabłońska-Trypuć, D. Karpowicz, Scientific Reports, 10 (2020) 14951.

# CHEMICAL ANALYSIS OF KAOLIN FROM THE ZHEZHELIV DEPOSITS FROM VINNYTSIA REGION

**H. KUZMANENKO[1], T. OKHOLINA[1], W. SOFIŃSKA-CHMIEL[2], U. MACIOŁEK[2], M. GOLISZEK[2], M. DREWNIAK[2], J. ORZEŁ[3]**, [1]Institute of Geological Sciences of NAS of Ukraine, Olesya Honchara St., 55B, Kyiv, 01054, Ukraine, [2]Maria Curie-Sklodowska University, Faculty of Chemistry, Institute of Chemical Sciences, Analytical Laboratory, M. Curie-Sklodowska Sq. 3, 20-031 Lublin, Poland, [3]Maria Curie-Sklodowska University, Faculty of Chemistry, Institute of Chemical Sciences, M. Curie-Sklodowska Sq. 3, 20-031 Lublin, Poland.

**Abstract:** The aim of the research was the chemical characterization of kaolin of the Zhezheliv deposit of the Vinnytsia region. The powder X-ray diffraction studies, FTIR-ATR spectroscopic studies and elemental composition analysis using the WD XRF technique were presented. The research enabled for determination of main crystalline components of the tested materials and accompanying elements.

**Introduction:** Kaolin is a clayey, white or yellowish main rock, the main component of which is mineral kaolinite. It is formed in the processes of weathering or hydrothermal decomposition of igneous and metamorphic rocks rich in feldspar. In terms of origin, kaolin is divided into residual (primary – formed on the site of the original rock) and sedimentary (secondary – formed by washing away the weathered primary rock and transporting the rock material and its accumulation another place) [1-2].
Deposits of kaolins (mainly primary and epigenetic ones) are widely distributed within the Ukrainian crystalline shield. In terms of size recognized kaolin resources, currently Ukraine ranks first in the world. In Poland kaolin occurs only in Lower Silesia [3-4].
It is used in production of fine and construction ceramics (it is added to clay in production of ceramic roof tiles), in the chemical and paper industries. It also finds used application in production of casting molds in flexographic printing. It is sometimes used in chemical laboratories to ensure even boiling of a solution. In medicine, it is used as an antidiarrheal agent and a base for preparing ointments. Finely ground kaolin is used to purify water, sewage and clarify drinks – contaminants are adsorbed in the micropores on its surface. It is a valuable raw material employed in the production of building materials as well as faience, ceramics, porcelain, paper, cosmetics and chemical products. Kaolin is used to produce metakaolin, a material produced in the process of dehydration at high temperatures. Its addition to cement increases resistance to chemical corrosion, especially sulphate corrosion, and improve significantly the properties, such as resistance to low temperatures and tightness of mortars and concretes. The addition of prepared kaolin changes the structure of pores in concrete, while reducing possibile diffusion of aggressive solutions, carbon dioxide and water. The result is a material with increased strength parameters. Kaolin also gives building materials and ceramics refractory properties and improves their application capabilities [5-6].
The Zhezheliv deposit of primary kaolin is located in the Vinnytsia region. It has a complex geological structure of both the crystalline basement and the weathered crust

itself. It is located within the tectonic contact zone of crystalline complexes of different ages, which differ in origin, mineral composition and textural and structural features.
For the experiment, samples of primary kaolin were selected on four ledges of the quarry. Sample 5/1 was taken on the lower ledge of the quarry at an altitude of 252.3 m above sea level (Baltic Sea vertical datum). Sample 5/2 – at an altitude of 257.3 m; sample 5/3 – at an altitude of 261.3 m; sample 5/4 – at a height of 264.3 m (Fig.1).

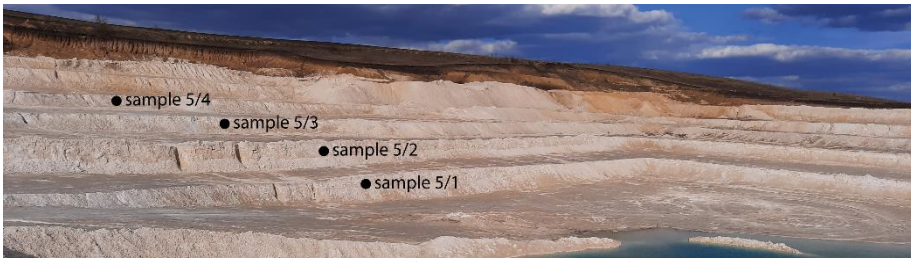



**Fig.1.** The quarry of the Zhezheliv deposit of primary kaolin.

**Experimental:** In order to characterize kaolin of the Zhezheliv deposit of the Vinnytsia region chemically, powder X-ray diffraction tests, FTIR-ATR spectroscopic tests and analysis of the elemental composition using the XRF technique were performed.
The XRD diffraction studies were carrird out using an Empyrean, PANalytical X-ray diffractometer. Kaolin samples were ground in an agate mortar to obtain powder. The slides were transferred to a cuvette and their area was levelid using a slight pressure. The analyzed samples were placed in the goniometer holder and the measurement was performed. The obtained diffraction patterns were compared with the ICDD PDF4+2023 diffraction database. FTIR spectra were obtained using the ATR technique with a diamond crystal. A Nicolet 8700A FTIR spectrometer was used for the research. The tests were carried out directly from the sample surface in the wave number range of 4000-400 $cm^{-1}$ and with a spectral resolution of 4 $cm^{-1}$. A DTGS detector was used in the research. The obtained spectra were subjected to ATR correction, baseline correction, and normalization using the Omnic SpectaTM software. The analysis of the elemental composition was performed using an ED-XRF Epsilon 5 spectrometer from Panalytical. After weighing, the samples were placed in measuring cups with the supporting foil (Myler foil). All measurements were performed using the Auto Quantify method without a standard using the Genie 2000 software, the measurement was performed twice.

**Results:** In order to identify the crystalline phases in the tested kaolin samples, XRD diffraction studies were carried out. The test results are presented in Figs. 2-5 and Tables 1-4.

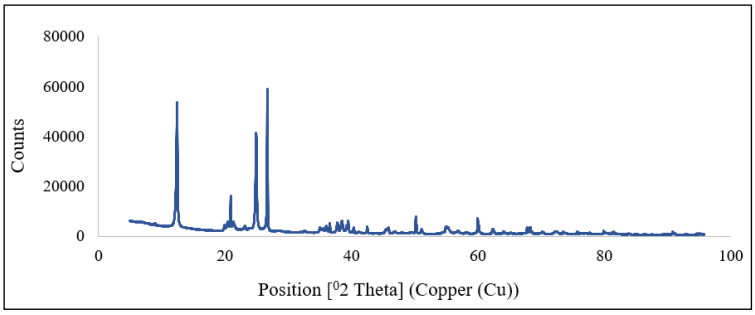



**Fig.2.** XRD diffractograms of sample 5/1.

**Table 1.** Comparison of the obtained diffraction pattern of sample 5/1 with the ICDD PDF4+2023 diffraction database.

| No. | Ref. Code | Compound Name | Chemical Formula | SemiQuant [%] |
|---|---|---|---|---|
| 1 | 04-007-9911 | Silicon Oxide | $SiO_2$ | 29.2(3) |
| 2 | 04-013-2830 | Aluminum Silicate Hydroxide | $Al_2Si_2O_5(OH)_4$ | 71(1) |

The XRD examination showed the following composition of the crystalline phases of the sample 5/1: 29.2% of $SiO_2$ and 71.0% of $Al_2Si_2O_5(OH)_4$.

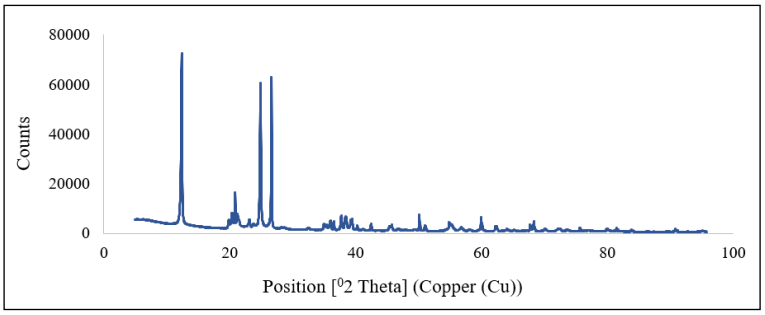



**Fig.3.** XRD diffractograms of sample 5/2.

**Table 2.** Comparison of the obtained diffraction pattern of sample 5/2 with the ICDD PDF4+2023 diffraction database.

| No. | Ref. Code | Compound Name | Chemical Formula | SemiQuant [%] |
|---|---|---|---|---|
| 1 | 04-007-9911 | Silicon Oxide | $SiO_2$ | 26.6(3) |
| 2 | 04-013-2830 | Aluminum Silicate Hydroxide | $Al_2Si_2O_5(OH)_4$ | 73(1) |

The examination of the composition of the crystalline phases showed 26.6% of $SiO_2$ and 73.0% of $Al_2Si_2O_5(OH)_4$ in sample 5/2.

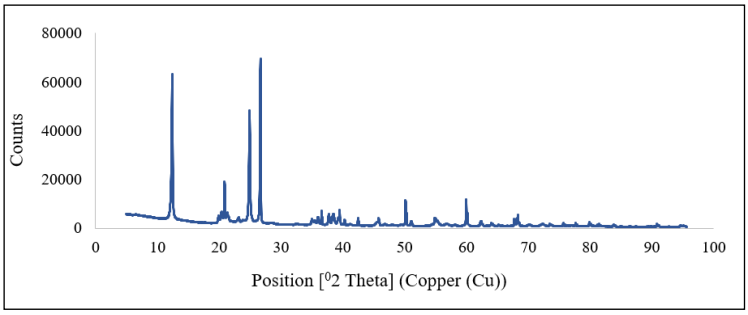



**Figure 4.** XRD diffractograms of sample 5/3.

**Table 3.** Comparison of the obtained diffraction pattern of sample 5/3 with the ICDD PDF4+2023 diffraction database.

| No. | Ref. Code | Compound Name | Chemical Formula | SemiQuant [%] |
|---|---|---|---|---|
| 1 | 04-007-9911 | Silicon Oxide | $SiO_2$ | 35.1(3) |
| 2 | 04-013-2830 | Aluminum Silicate Hydroxide | $Al_2Si_2O_5(OH)_4$ | 65(1) |

The XRD tests showed the following composition of crystalline phases of sample 5/3:35.0% of $SiO_2$ and 65.0% of $Al_2Si_2O_5(OH)_4$.

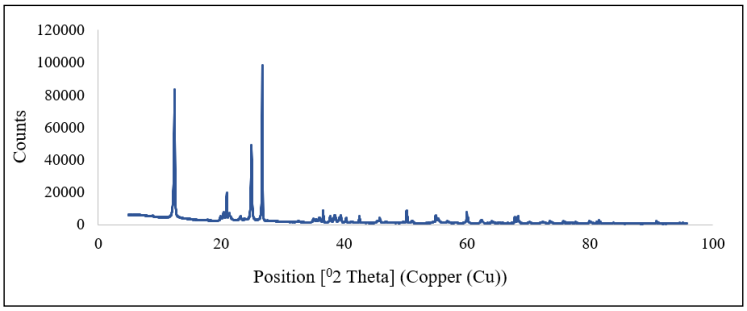



**Fig.5.** XRD diffractograms of sample 5/4.

**Table 4.** Comparison of the obtained diffraction pattern of sample 5/4 with the ICDD PDF4+2023 diffraction database.

| No. | Ref. Code | Compound Name | Chemical Formula | SemiQuant [%] |
|---|---|---|---|---|
| 1 | 04-007-9911 | Silicon Oxide | $SiO_2$ | 37.3(3) |
| 2 | 04-013-2830 | Aluminum Silicate Hydroxide | $Al_2Si_2O_5(OH)_4$ | 63(1) |

The examination of the composition of crystalline phases using the XRD method showed: 37.3% of $SiO_2$ and 63.0% of $Al_2Si_2O_5(OH)_4$ in sample 5/4.
In order to identify the non-crystalline components of the tested samples, FTIR spectroscopy was performed. The research results are presented in Fig.6.

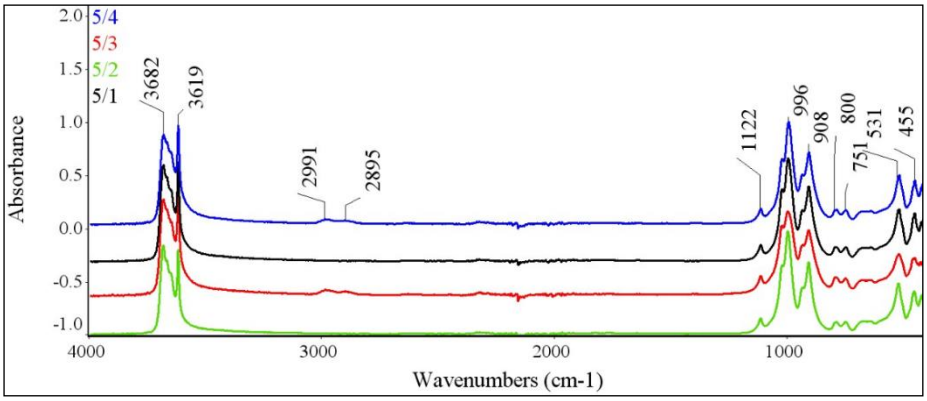



**Fig.6.** FTIR-ATR spectra of sample 5/1, 5/2, 5/3 and 5/4 with marked bands.

The tests carried out using infrared spectroscopy showed the presence of bands characteristic of both aluminum silicate hydroxide and silicon oxide. The presence of stretching vibrations of the O-H groups was found at positions 3682 and 3619 $cm^{-1}$. The FTIR-ATR spectra showed also bands characteristic of Si-O bonds at 1122 $cm^{-1}$ and 455 $cm^{-1}$ and a band characteristic of Al-OH bonds at 908 $cm^{-1}$. Peaks corresponding to Si-O-Al bonds were also observed in the FTIR spectra at 800 $cm^{-1}$, 751 $cm^{-1}$ and 531 $cm^{-1}$ [1]. Moreover, in samples 5/3 and 5/4, the presence of the bands corresponding to the stretching vibrations of CH groups were observed [2]. This may indicate the presence of organic matter in the tested samples.
In order to determine the elemental composition of the tested samples, tests using XRF spectrometry were also carried out. The test results are presented in Table 5. The table shows the components whose contents were above 0.1%.

**Table 5**. WD-XRF analysis results converted into oxides.

| Compound | Concentration % | | | |
|---|---|---|---|---|
| | Sample 5/1 | Sample 5/2 | Sample 5/3 | Sample 5/4 |
| $Al_2O_3$ | 12.580 | 16.478 | 16.359 | 12.224 |
| $SiO_2$ | 20.380 | 27.509 | 27.928 | 22.584 |
| $P_2O_5$ | 0.266 | 0.318 | 0.313 | 0.291 |
| $K_2O$ | 0.160 | <0.1 | 0.131 | 0.179 |
| CaO | 0.131 | 0.156 | 0.199 | 0.149 |
| $TiO_2$ | 0.256 | 0.730 | 1.265 | 0.445 |
| $Fe_2O_3$ | 0.131 | 0.145 | 0.132 | 0.178 |
| $Tl_2O_3$ | <0.1 | 0.536 | <0.1 | <0.1 |

The WD-XRF tests showed the presence of elements characteristic of crystalline phases identified by powder X-ray diffraction. The presence of silicon and clay was confirmed. The tests also showed the presence of phosphorus, potassium, calcium, titanium and iron. In the case of sample 5/2, WD-XRF also exhibited the presence of tellurium.

**Conclusions:** The applied research methods enabled chemical characterization of kaolin samples from the Zhezheliv deposit of primary kaolin in the Vinnytsia region. The XRD tests showed composition of the crystal phases of the tested material. The main components of all tested samples are aluminum silicate hydroxide and silicon oxide.

Their presence was also confirmed by infrared spectroscopy. The FTIR spectra showed all the characteristics of both $Al_2Si_2O_5(OH)_4$ and $SiO_2$. The C-H bonds in samples 5/3 and 5/4 was proved by the spectroscopic tests. This may indicate the presence of organic matter. Moreover, the WD-XRF tests confirmed the presence of elements in aluminum silicate hydroxide and silicon oxide. The elements accompanying these phases were also observed.

**Acknowledgements:** The research was carried out using the apparatus maintained based on the project INFRASTARt.

**References:**

1. M.S. Prasad, K.J. Reid, H.H. Murray, Applied Clay Science, 6 (1991) 87.
2. M.A. El-Aal, A.E.A. Said, M.H. Abdallah, M.N. Goda, Scientific Reports, 12 (2022) 9407.
3. M. Magomedova, E. Galanova, I. Davidov, M. Afokin, A. Maximov, Catalysts, 9 (2019) 485.
4. D.P. Kgabi, A.A. Ambushe, Sustainability, 15 (2023) 12679.
5. L. Diko-Makia, R. Ligege, Minerals, 10 (2020) 700.
6. A. Kumar, P. Lingfa, Materials Today: Proceedings, 22 (2020) 737.
7. A. Tironia, M.A. Trezzaa, E.F. Irassara, A.N. Scianb, Procedia Materials Science, 1 (2012) 343.
8. M. Silverstein, F.X. Webster, D.J. Kiemle, Spektroskopowe metody identyfikacji związków organicznych, PWN Warszawa 2007.

# SPECTROSCOPIC CHARACTERIZATION OF AMBER FROM UKRAINIAN AND LUBLIN DEPOSITS

**T. OKHOLINA[1], H. KUZMANENKO[1], W. SOFIŃSKA-CHMIEL[2], U. MACIOŁEK[2], L. GAZDA[3], E. MENDYK[2], K. SKRZYPIEC[2], J. ORZEŁ[4],** [1]National Academy of Sciences of Ukraine, Institute of Geological Sciences, Volodymyrska St., 54, 01030 Kyiv, Ukraina, , [2]Maria Curie-Sklodowska University, Faculty of Chemistry, Institute of Chemical Sciences, Analytical Laboratory, M. Curie-Sklodowska Sq. 3, 20-031 Lublin, Poland, [3]The University College of Applied Sciences in Chelm, Institute of Technical Sciences and Aviation, Pocztowa St. 54, 22-100 Chełm, Poland, [4]Maria Curie-Sklodowska University, Faculty of Chemistry, Institute of Chemical Sciences, M. Curie-Sklodowska Sq. 3, 20-031 Lublin, Poland.

**Abstract:** In the presented study, spectroscopic and microscopic analyses were conducted using atomic force microscopy (AFM) on ambers sourced from Lublin and Ukrainian deposits. A comparison of FTIR-ATR spectra was made to assess the degree of polymerization. Surface structure analyses at the nanometric level were performed using AFM. Maps of surface microgeometry were generated, and nanomechanical parameters (Young's modulus) were determined. The FTIR-ATR analyses revealed a lower intensity of signals originating from the C=C bonds in the Lublin amber sample, indicating a smaler degree of polymerization. This amber also exhibited a lower value of longitudinal elasticity modulus.

**Introduction:** The occurrence of amber in the Lublin region, as well as in Samland, Polesia, and Volhynia (Ukraine), is associated with the deposits of the Paleogene marine transgression, which reached its maximum in the late Eocene. Thus, the primary resin accumulations in these regions are approximately contemporaneous. In these primary accumulations, amber was deposited in the coastal zone of the basin, in shallow-water, coastal-marine, and lagoon-deltaic sandy and sandy-muddy deposits with glauconite. In Volhynia, amber-bearing deposits also occur in secondary deposits in the Lower Oligocene formations [1,2]. Furthermore, in these regions, amber is found in younger Neogene, Pleistocene, and Holocene sediments. It should be assumed that differences in the constitution (degree of polymerization and hardness) of amber from these regions will depend less on the time of their formation (moment of resinification) since they are approximately contemporaneous and more on the type of original resin (tree species), the time and conditions of exposure on land, the physicochemistry of the deposition basin of these resins, and subsequent geological processes. The research aimed at comparisone and evaluation of the a degree of polymerization of amber from the Lublin region and Ukraine, as well as their physical characteristics, such as Young's modulus. A necessary condition for the natural transformation of resin into amber is the presence of polymerization precursors. This group includes, among others, bicyclic diterpenes - chemical compounds from the labdanoid group. The main component of resins from the Araucariaceae species of trees is the isomer of ozolic acid. Baltic amber and identical Lublin anad Ukrainian amber originate from the resins of these trees. The presence of carboxyl groups in diterpenoids is characteristic of resins whereas Baltic amber contains

mainly esters. The most important gemmologically is the exocyclic methylene group $=CH_2$- involved in the processes of polycondensation and polymer cross-linking - i.e., the processes of the final transformation of resins into amber and C=C bonds.

**Experimental:** The research was carried out using two samples of amber originating from the Lublin deposit (Górka Lubartowska) and the Ukrainian deposit. FTIR spectroscopic analyses were performed using the ATR technique. Spectra were recorded by means of a Thermo Nicolet 8700 FTIR spectrometer equipped with a Smart Orbit™ diamond ATR accessory and a DTGS detector. To ensure good contact between the sample and the diamond crystal, the amber samples were ground in an agate mortar. Spectra were obtained in the wavenumber range of 4000 – 400 $cm^{-1}$, with a spectral resolution of 4 $cm^{-1}$. The obtained FTIR-ATR spectra were subjected to the ATR correction, baseline correction, and scaled normalization operations.
In the further part of the study, surface microgeometry maps were generated using an atomic force microscope (AFM): MultiMode™8, NanoScope® V from Bruker-Veeco, employing the PeakForce QNM technique. Before AFM microscopy, the samples of Lublin and Ukrainian amber were mechanically processed (polished) to obtain a smooth surface. The Young's modulus was also determined for the samples.

**Results:** The FTIR-ATR spectra of the samples of amber are presented in Figs.1-3.

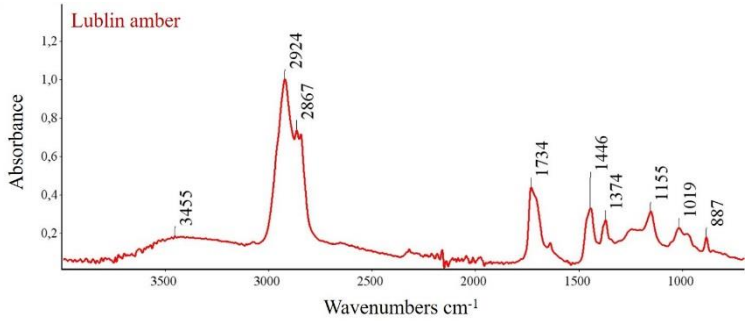



**Fig.1.** FTIR-ATR spectrum of the Lublin amber sample with the spectral bands values.

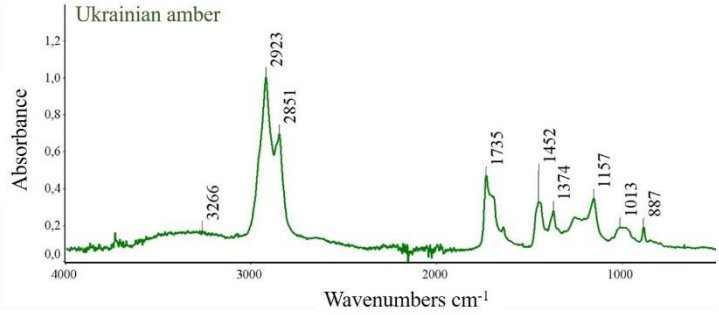



**Fig.2.** FTIR-ATR spectrum of the Ukrainian amber sample with the spectral bands values.

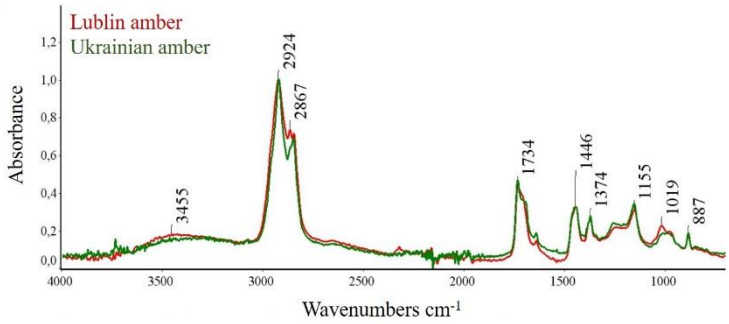



**Fig.3.** Comparison of FTIR-ATR spectra of the Lublin and Ukrainian amber samples.

The FTIR-ATR analysis of Lublin and Ukrainian amber did not reveal significant differences in the positions of spectral bands. No differences were observed in the intensities of signals in the range of 2900–2850 $cm^{-1}$ corresponding to the stretching vibrations of groups: $CH_3$, $CH_2$, and CH, as well as in the range of 1735–1695 $cm^{-1}$ corresponding to the stretching vibrations of C=O in carbonyl groups in esters, ketones, and carboxylic acids. Additionally, no differences in the signal intensity at 1640 $cm^{-1}$ were observed, which corresponds to the stretching vibrations of C=C bonds. There were also no significant spectral differences in the range of 1156 $cm^{-1}$ corresponding to the O=C-O-C bonds originating from succinic acid esters [3].
To assess the elasticity parameters, surface microgeometry maps and Young's modulus distributions were also generated using AFM. The results of the study are presented in Figs.4 and 5.

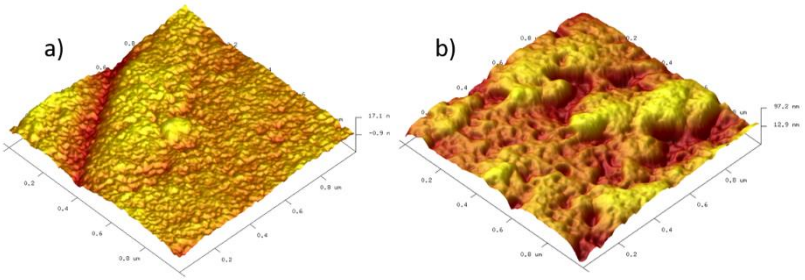



**Fig.4.** Surface microgeometry maps obtained using the AFM microscopy method: a) Lublin amber, b) Ukrainian amber.

The surface analysis conducted using atomic force microscopy (AFM) revealed significant differences in the microscopic image of Lublin and Ukrainian amber.
The research showed a higher value of Young's modulus for Ukrainian amber compared to Lublin amber. The value of Young's modulus determined for Lublin amber is 5236 MPa, while for Ukrainian amber 7207 MPa (Table 1).

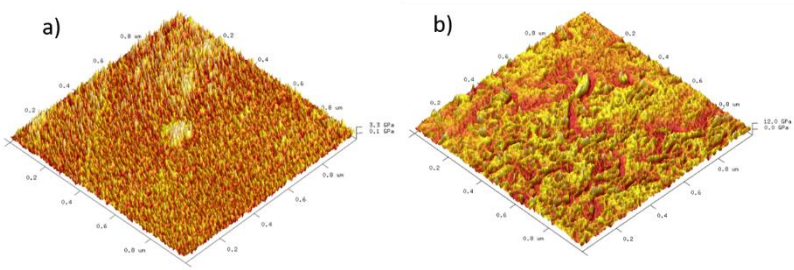



**Fig.5.** Young's modulus distribution maps obtained using the AFM microscopy method: a) Lublin amber, b) Ukrainian amber.

**Table 1.** The values of Young's modulus obtained using the AFM microscopy method for Lublin and Ukrainian amber.

| Sample name | Young's modulus [MPa] |
|---|---|
| Lublin amber | 5236 |
| Ukrainian amber | 7207 |

**Conclusions:** The longitudinal elasticity modulus, also known as the Young's modulus (E), is a physical parameter describing a material. This is the ratio of the normal stress (σ) to the linear strain (ε) of the material under given conditions. This parameter can provide valuable information for selecting appropriate tools for the mechanical processing of a given material. The more elastic the material, the greater stresses it can withstand and the ability to regain its original shapes. This is particularly important in the processing of gemstones and amber in the jewellery industry. The samples of Lublin and Ukrainian amber were subjected to examination for determination of the Young's modulus using atomic force microscopy (AFM) and Fourier-transform infrared spectroscopy (FTIR). The nanomechanical studies revealed a significantly higher value of the Young's modulus for Ukrainian amber, indicating its greater elasticity. However, the Fourier-transform infrared spectroscopy (FTIR) analyses did not show significant differences in the position or intensity of signals. Considering the fact that Lublin and Ukrainian amber is treated as equal-aged resins, the differences in the Young's modulus values of these materials are most likely conditioned by the physicochemistry of the place of deposition of these resins and the time and conditions of their stay on land.

**Acknowledgements:** The research was carried out using the apparatus maintained based on the project INFRASTARt.

**References:**

1. R. Kasiński, Złoża bursztynu północnej Lubelszczyzny: historia poznania, budowa geologiczna, perspektywy, in: Lubelski bursztyn, znaleziska, geologia, złoża i perspektywy. PWSZ Chełm i Stellarium, 2016.
2. R. Kasiński, Geologiczne warunki występowania i eksploatacji złóż bursztynu nad Zatoką Gdańską, in: Lubelski bursztyn, znaleziska, geologia, złoża i perspektywy. PWSZ Chełm i Stellarium, 2016.
3. A. Matuszewska, Bursztyn (sukcynit) i inne żywice kopalne subfosylne i współczesne. Wydawnictwo Uniwersytetu Śląskiego, 2010.

# CHEMICAL ANALYSIS OF COFFEE WITH THE ADDITION OF CINNAMON, GINGER AND CARDAMON

**I. PAŃCZUK-FIGURA[1], W. SOFIŃSKA-CHMIEL[2], U. MACIOŁEK[2]**, [1]Maria Curie-Sklodowska University, Faculty of Chemistry, Institute of Chemical Sciences, Department of Inorganic Chemistry, M. Curie-Sklodowska Sq. 2, 20-031 Lublin, Poland, [2]Maria Curie-Sklodowska University, Faculty of Chemistry, Institute of Chemical Sciences, Analytical Laboratory, M. Curie-Sklodowska Sq. 3, 20-031 Lublin, Poland.

**Abstract:** The aim of the research was the chemical analysis of coffee samples with the addition of cinnamon, ginger and cardamom. The contents of caffeine in the coffee samples and the contents of cinnamaldehyde in coffee with 20% of cinnamon, 6-gingerol in coffee with 20% of ginger and contents of terpinyl acetate and 1,8-cineol in coffee with 20% of cardamom were determined. FTIR spectroscopic studies were also presented. The aim of spectroscopic tests was to examine whether this method is an effective tool for qualitative confirmation of the presence of cinnamon, ginger and cardamom in the coffee samples.

**Introduction:** Arabic coffee (*Coffea arabica L.*) is a plant from the madder family, also called the coffee tree or coffee tree. Coffee berries were known in Ethiopia over 2,000 years ago. Initially, they were eaten with butter and salt. Coffee as a drink was probably discovered around the 14th - 18th century in Yemen. Coffee is such a popular drink nowadays that we cannot imagine a morning without a cup of coffee. Additives that enrich the taste and aroma of coffee are spices that have been known for generations. They can have a positive effect on the human body. Studies have shown that cinnamon and its bioactive compounds can affect brain functioning and behavioral characteristics [1]. Coffee and cardamom are considered by many to be an ideal combination. Cardamom is a strong antioxidant that fights free radicals that damage body cells. In combination with coffee, which stimulates metabolic processes thanks to caffeine, cardamom cardamom helps in weight loss [2]. Ginger root extract is also known for its warming and anti-inflammatory effects and is used in degenerative joint diseases. Creams and ointments with ginger extract are also used externally in treatment to reduce pain and stiffness. Scientific research on the effects of ginger in this area is relatively new, but proves that ginger may have strong antidiabetic properties. In 2015, a study was conducted which showed that participants taking two grams of powdered ginger a day for 12 weeks reduced their fasting blood sugar levels by 12% [3]. The level of glycated hemoglobin (which is an important indicator of sugar levels in the long term) also decreased by as much as 10% in these participants. Such effects are already sufficient to reduce many of the troublesome side effects of type 2 diabetes.

Quantitative chromatographic tests of coffee with addition of high-quality 20% of cinnamon and ginger and 12% of cardamom will allow to determine the content of active substances in the infusions and may in the future allow the composition of mixtures of innovative functional food.

**Experimental:** The HPLC tests were carried out for quantitative determination of coffeine, cinnamaldehyde and 6-gingerol contents. 30 mg of the tested material was weighed and transferred to a vessel with methanol. The extraction of the sample was aided by ultrasound. Calibration solutions were made for caffeine, cinnamaldehyde and 6-gingerol. The measurements were performed using a liquid chromatograph with a PDA detector (Shimadzu Nexera-i). For quantitative determination of terpinyl acetate and 1,8-cineole contents there were carried out the test using the GC method. 30 mg of the tested material was weighed and transferred to a vessel with methanol. The extraction of samples was aided by ultrasound. Calibration solutions were prepared for terpinyl acetate and 1,8-cineole. Quantitative analysis of terpinyl acetate and 1,8-cineole in extracts obtained from coffee samples submitted for research was carried out on a gas chromatograph with an FID detector (Shimadzu 2010). FTIR spectra were taken using the ATR technique with a diamond crystal directly from the surface of ground coffee samples. The tests were carried at room temperature in the spectral range of 4000-400 $cm^{-1}$ and with a resolution of 4 $cm^{-1}$. A Nicolet 8700A FTIR spectrometer equipped with a DTGS detector was used for the research. The obtained spectra were subjected to ATR correction, baseline correction and normalization using the Omnic SpectaTM software. The analysis of content of microelements was performed using an ED-XRF Epsilon 5 spectrometer from Panalytical. All measurements were performed using the Auto Quantify method without a standard using the Genie 2000 software, the measurement was performed twice.

**Results:** The results of HPLC and GC tests are presented in Table 1.

**Table 1.** HPLC and GC analyses results.

| Sample name | Determined substance | Concentration (mg/g)* |
|---|---|---|
| 180g of coffee + 20g of cinnamon | Caffeine | 6,26±0,19 |
| | Cinnamaldehyde | 1,96±0,07 |
| 180g of coffee + 20g of ginger | Caffeine | 6,27±0,18 |
| | 6-Gingerol | 0,34±0,01 |
| 180g of coffee + 12g cardamon | Caffeine | 6,71±0,21 |
| | Terpinyl acetate | 0,49±0,01 |
| | 1,8-Cineole | 0,27±0,01 |

As follows from the tests the caffeine content in the tested samples was in the range of 6.26 - 6.71 mg/g. FTIR spectra were performed for chemical characterization of coffee in the samples. The results are presented in Fig.1.

According to the literature data, the main ingredients of coffee are: caffeine (0.5-2.6%), chlorogenic acid (4-6%), caffeic and quinic acids (10%), polysaccharides (25-30%), proteins (13 %), fats and waxes (0.1-0.8%), water (10-13%) and minerals (4%). The tests proved the presence of bands characteristic of coffee ingredients. In the range of 3000–3500 $cm^{-1}$, the O-H groups occurring in water, acids and polysaccharides were found [4]. Moreover, in the wavenumber range of 3030–2850 $cm^{-1}$, the FTIR tests showed the presence of stretching vibrations characteristic of C-H bonds originating from aliphatic and aromatic carbons [5].

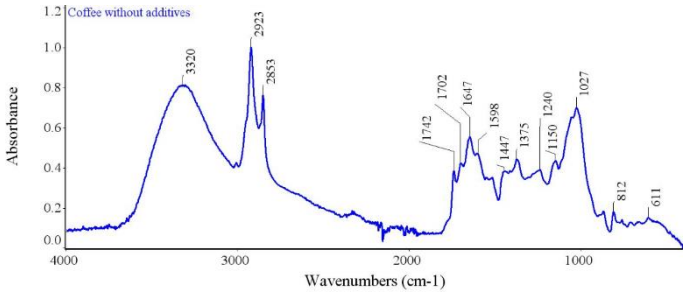



**Fig.1.** FTIR-ATR spectrum of the coffee without additives.

The research showed the presence of bands corresponding to the stretching vibrations of C=O bonds present in acids, proteins and fats in the range of 1800-1700 $cm^{-1}$. Moreover, spectroscopic studies revealed of bands in the range of 1680-1500 $cm^{-1}$ corresponding to the stretching vibrations of aromatic and aliphatic C=C bonds. These bonds occur in caffeine, fats and acids present in coffee. The spectral bands corresponding to deformation vibrations of N-H groups in the range of 1650-1500 $cm^{-1}$ and OH groups in the range of 1200-1450 $cm^{-1}$ were also observed in the FTIR spectra [4].
For qualitative determination of coffee additives there were carried out spectroscopic tests using the FTIR-ATR method. The research results are presented in Figs.2-4.

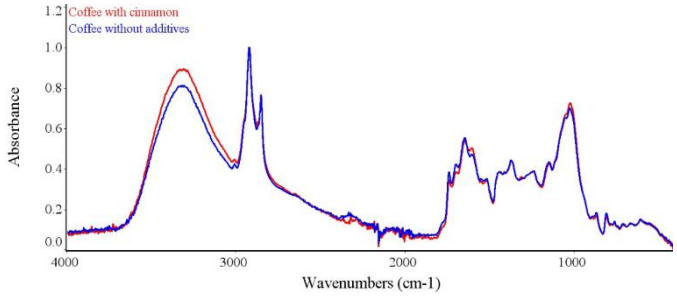



**Fig.2.** Comparison of the spectrum of coffee without additives and coffee with 20% of cinnamon.

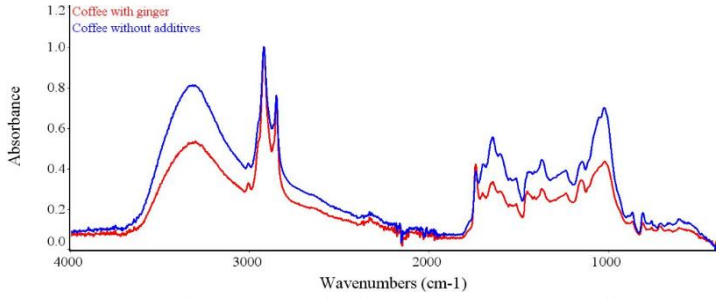



**Fig.3.** Comparison of the spectrum of coffee without additives and coffee with 20% of ginger.

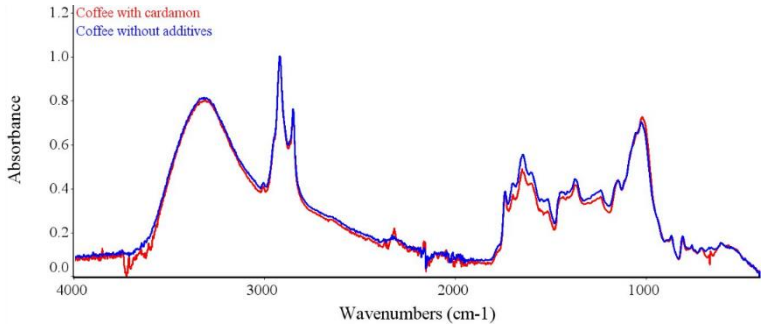



**Fig.4.** Comparison of the spectrum of coffee without additives and coffee with 20% of cardamom.

The research did not show any significant differences in the FTIR spectra of coffee without additives compared to coffee with 20% addition of cinnamon, ginger and cardamom. Comparison of the spectra showed that the positions of all bands in the spectra were unchanged. Only some differences in the peak intensities were observed. The greatest differences in band intensities were found in the spectrum of coffee with ginger. However, this should not be a diagnostic feature to confirm the presence of these components.

In order to determine the content of microelements, tests using XRF spectrometry were also carried out. The test results are presented in Table 2.

**Table 2**. WD-XRF analysis results.

| Elements | Concentration % | | | |
|---|---|---|---|---|
| | Coffee without additives | Coffee with cinnamon | Coffee with ginger | Coffee with cardamon |
| Mg | - | 0.262 | - | - |
| P | 0.236 | 0.193 | 0.244 | 0.159 |
| K | 4.616 | 3.946 | 4.677 | 3.779 |
| Ca | 0.621 | 0.899 | 0.624 | 0.568 |
| Mn | 0.015 | 0.030 | 0.017 | 0.027 |
| Fe | 0.026 | 0.050 | 0.026 | 0.027 |
| Cu | 0.032 | 0.022 | 0.034 | 0.025 |
| Zn | 0.005 | 0.008 | 0.005 | 0.008 |

**Conclusions:** The research techniques enabled determination of the caffeine content in the tested coffee samples. The caffeine content in the samples was in the range of 6.26 - 6.71 mg/g. According to the literature data, the caffeine content in the coffee beans available on the Polish market ranges from 3.2 to 29.5 mg/g [6]. Therefore the tested coffees can be classified as mild coffees with small caffeine content. Spectroscopic tests showed no significant differences in the FTIR-ATR spectra of coffee without additives and that with the addition of cinnamon, ginger and cardamom.

## References:

1. S. Nakhaee, A. Kooshki, A. Hormozi, A. Akbari, O. Mehrpour, K. Farrokhfall, Nutritional Neuroscience, (2023) 123.
2. C. Delgadillo-Puga, I. Torre-Villalvazo, Y.Y. Cariño-Cervantes, C. García-Luna, P. Soberanes-Chávez, P. de Gortari, L.G. Noriega, C.J. Bautista, L. Cisneros-Zevallos, International Journal of Molecular Sciences, 24 (2023) 3909.

3. N. Khandouzi. et al., Iranian Journal of Pharmaceutical Research, 14 (2015) 131.
4. A. P. Craig, A. S. Franca, L. S. Oliveira, Food Chemistry, 132 ( 2012) 1368.
5. M. Silverstein, F.X. Webster, D.J. Kiemle, Spektroskopowe metody identyfikacji związków organicznych, PWN Warszawa 2007.
6. M. Frankowski, A. Kowalski, A. Ociepa, J. Siepak, P. Niedzielski, Bromatologia i Chemia Toksykologiczna, 41 (2008) 21.

# FTIR SPECTROSCOPY AS A TOOL FOR ANALYSING CHANGES IN THE CELL WALL OF THE FUNGUS *CANDIDA ALBICANS* AFTER THE ACTION OF COMPOUNDS OF ANIMAL AND PLANT ORIGIN

**K. LEWTAK[1], W. SOFIŃSKA-CHMIEL[2], J. WYDRYCH[3], B. SIDORSKA[4], M. J. FIOŁKA[4]**, [1]Department of Cell Biology, Institute of Biological Sciences, Maria Curie-Skłodowska University, Lublin, Poland, [2]Analytical Laboratory, Institute of Chemical Sciences, Maria Curie-Skłodowska University, Lublin, Poland, [3]Department of Functional Anatomy and Cytobiology, Institute of Biological Sciences, Maria Curie-Skłodowska University, Lublin, Poland, [4]Department of Immunobiology, Institute of Biological Sciences, Maria Curie-Skłodowska University, Akademicka 19, 20-033 Lublin, Poland.

**Abstract:** The conducted research aimed to compare the effects of the antibiotic amphotericin B, the Venetin-1 complex from the coelomic fluid of earthworms *Dendrobaena veneta* and the *Sida hermaphrodita* seed extract on *Candida albicans* cells. For this purpose, fungal cells were incubated with the above preparations and then analysed using fluorescence microscopy and FTIR spectroscopy. The analyses showed that both the animal and plant preparations had a similar mechanism of influence on the cell wall of the analysed yeast. The antibiotic had a different effect and did not cause the exposure of β-glucans as was the case with the analysed preparations. The results of the FTIR analysis corresponded to observations using Congo red dye, which fluoresced red on the surface of the changed cell wall of *C. albicans*.

**Introduction:** *Candida albicans* is a fungus from the genus of yeasts associated with warm-blooded organisms. It is a saprophyte, but under certain conditions it can transform into a pathogenic form. *C. albicans* causes problems in both human and small animal therapy. Among invertebrates, earthworms are a known source of bioactive compounds. The body cavity fluid of earthworms exhibits a wide range of biological activities, such as antibacterial, proteolytic, hemolytic, antifungal, and anticancer properties. The polysaccharide-protein complex named Venetin-1 was obtained from the coelomic fluid of earthworms *Dendrobaena veneta*, which has anticancer action against A549 lung cancer [1, 2, 3] and colon cancer [4], shows antifungal action [5-8], as well as immunostimulating properties [9]. Toxicity of coelomic fluid to normal cells - epithelial cells [1, 4] and human skin fibroblasts was eliminated [5].
Plant species of the genus *Sida* are widely distributed due to their medicinal properties. *S. acuta*, *S. cordifolia*, *S. rhombifolia*, *S. cordata* and *S. galheirensis* are among the best known phytopharmacological raw materials. However, there has been no information about antimicrobial properties of *S. hermaphrodita* so far. The properties of the seed extract was compared with the protein-polysaccharide complex Venetin-1 extracted from the coelomic fluid of the earthworm *Dendrobaena veneta*.
Amphotericin B is one of the antibiotics most often used to treat systemic fungal infections, including candidiasis. This drug belongs to the class of polyene macrolides produced by the bacterium *Streptomyces nodosus*. It is characterized by its high

therapeutic efficacy, which has ensured its permanent place in the pharmaceutical market. The antibiotic amphotericin B can both bind to phospholipids through the lipophilic part of its molecule, forming a ribbon-like structure with two such molecules, or it can be incorporated into the membrane of liposomes made of phospholipids.
The aim of the study was to compare the effects of the preparation derived from earthworms and *Sida hermaphrodita* seeds with those of the antibiotic amphotericin B on the cell wall of the fungus *Candida albicans*, using microscopic methods and FTIR spectroscopy.

**Experimental:** After rinsing in water, adult earthworms were kept on moist lignin for 24 hours to cleanse the digestive tract. Coelomic fluid (CF) was obtained from individuals immersed in a small amount of 0.9% NaCl after applying a mild electric shock. Electrostimulation was performed with a current of 4.5 V for 1 min. The coelomic fluid was centrifuged (5000xg, 10 min) to separate the cells - coelomocytes. The supernatant was then filtered through 0.22 Millipore filters and incubated at 70°C for 10 minutes. The obtained fluid was transferred to a dialysis bag with a cut-off point of 12–14 kDa and dialyzed for 24 hours against water at 4°C. The obtained preparation (Venetin-1) was transferred to Eppendorf tubes, lyophilized and stored at -20°C. Protein concentration before the experiment was determined using the Bradford method.
The preparation of *Sida hermaphrodita* seed extract was carried out according to the following procedure. The seeds were surface sterilized in a 70% ethyl alcohol solution and rinsed in distilled water. Then, seeds were subjected to mechanical homogenization in Sörensen buffer (pH 6.0). Then the homogenate was frozen three times in liquid nitrogen and thawed in an ice bath. The obtained preparation - extract homogenate was centrifuged at 18,000 xg for 10 minutes and filtered through a microbiological filter with a pore diameter of 0.22 μm (Millipore). Next, the fluid was dialysed for 24 hours against water at 4°C (dialysis bag with MWCO of 12–14 kDa). The obtained preparation was lyophilized and stored at -20°C. Protein concentration before the experiment was determined using the Bradford method.
A clinical isolate of a wild strain of *Candida albicans* was used for microbiological analyses. Fungal cultivation was initially carried out in a liquid Sabouraud's medium at a temperature of 28°C, for 24 hours. After this time, 30 μl of *C. albicans* culture ($10^7$ CFU in the logarithmic growth phase) was taken and added to 150 μl of YPD-poor medium supplemented with streptomycin sulfate (Sigma) at a final concentration of 0.17 $mg \cdot mL^{-1}$ and amphotericin B (in 0,2% DMSO) or Venetin-1 complex (from coelomic fluid) or seed extract. The final concentrations of Venetin-1, the plant extract and the antibiotic used in the experiments were 100 $\mu g \cdot mL^{-1}$ for the above preparations and 0.5 $\mu g \cdot mL^{-1}$ for the antibiotic, respectively. Samples were incubated at 37°C for 48 hours in a shaking incubator.
Congo-red fluorochrome (Sigma-Aldrich) was used to visualize the β-1,4-glucan layer of the cell wall of the fungus *C. albicans* [8]. An aqueous solution of the dye (2%) was prepared and mixed with the suspension of the analysed fungal cells in a 1:1 ratio. The mixture was incubated for 10 minutes in complete darkness at room temperature. Then, 2 μl of the preparation was spotted on a glass slide and observed at excitation wavelength $\lambda = 440$ nm using a LSM 5 Pascal confocal laser scanning microscope (Carl Zeiss, Jena, Germany) with the magnification of 1000×.

In order to observe the changes occurring in the cell wall of *C. albicans* fungi, the FTIR spectra of the prepared samples were analysed: control, after treatment with amphotericin B at a concentration of 0.5 $\mu g \cdot mL^{-1}$, Venetin-1 and seed extract, both at a concentration of 100 $\mu g \cdot mL^{-1}$. The tests were carried out using the ATR technique directly from the sample surface at room temperature. Measurements were performed using a Thermo Nicolet 8700 FTIR spectrometer with an ATR Smart Orbit™ diamond attachment equipped with a DTGS detector (deuterated triglycine sulfate). The spectra were recorded in the mid-infrared range: 4000–650 $cm^{-1}$ with a spectral resolution of 4 $cm^{-1}$. The collected spectra were subjected to baseline correction and scaled normalization [8].

**Results:** After incubation of *C. albicans* fungus cells with the tested preparations and amphotericin B, a significant increase in the intensity of red fluorescence of *C. albicans* cells compared to the control culture cells and numerous division scars on the cell surface were observed (Fig.1). This suggests the exposure of deeper layers of the cell wall composed of β-glucans under the influence of both Venetin-1 and seed extract and the tested antifungal antibiotic. FTIR spectroscopic studies showed changes in signal intensities, both after the use of Venetin-1, seed extract and amphotericin B. FTIR spectroscopic analyses showed a similar effect of all analysed compounds on changes in the intensity of peaks, reflecting disturbances in the cell wall structure.
The cells of the control culture were oval and regular in shape. They were stained red, but did not show fluorescence (Fig.1A). After exposure to amphotericin B at a concentration of 0.5 $\mu g \cdot mL^{-1}$, individual cells visible in the field of view were characterized by small size and red fluorescence only in birth scar region (Fig.1B). *C. albicans* cells treated with both Venetin-1 fraction and seed extract both at the concentration of 100 $\mu g\ mL^{-1}$ were slightly enlarged in comparison to control cells and had a less regular shape. The fluorescence of the walls of these cells was irregular (Fig.1C-D). In the case of yeast cells treated with Venetin-1, fluorescence was particularly intense in places of numerous division scars and in places where cells were connected to each other (Fig.1C). In turn, the cells exposed to the extract showed intense fluorescence in their walls at the periphery (Fig.1D). More intense fluorescence may indicate a larger amount of β-glucans to which the Congo red dye has an affinity and/or the exposure of this layer of the yeast cell wall due to damage to the outer layer – mannans. As a consequence, the externalization of β-glucans may facilitate the immune system's recognition of these PAMPs (pathogen associated molecular patterns) and combat these pathogens more effectively. FTIR spectroscopic studies showed changes in signal intensities, both after the use of Venetin-1, seed extract and amphotericin B (Fig.2).

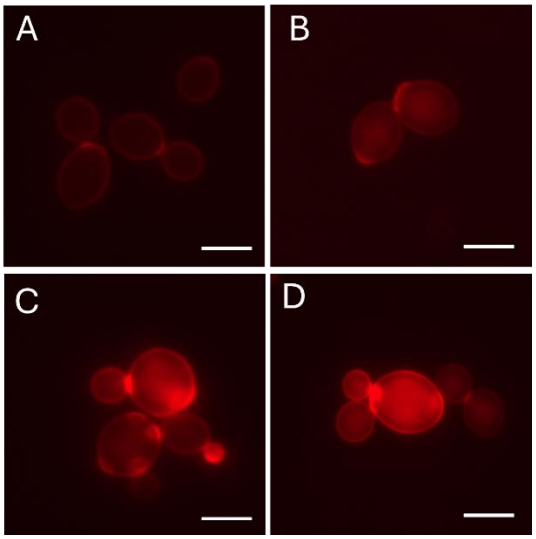



**Fig.1.** Images of *C. albicans* cells after staining with Congo red fluorochrome: a – control culture, B – *C. albicans* cells after incubation with amphotericin B at the concentration of 0.5 µg·mL$^{-1}$, C - after incubation with Venetin-1 at the concentration of 100 µg·mL$^{-1}$, D - after incubation with *S. hermaphrodita* seed extract at the concentration of 100 µg·mL$^{-1}$. In images C and D intense red glow of the cell wall was showed.

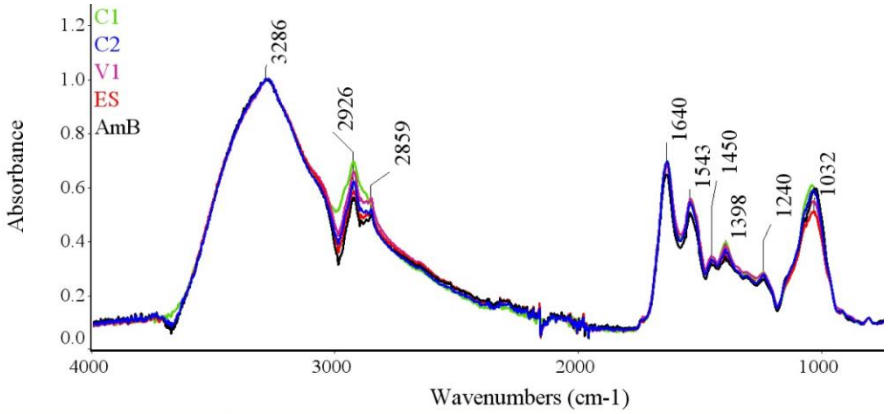



**Fig.2.** FTIR spectrum of the *C. albicans* control culture (C1), control culture with DMSO (C2), and after the treatment with Venetin-1 at 100 µg mL$^{-1}$ (V1), with seed extract at 100 µg·mL$^{-1}$ (ES), with amphotericin B at 0.5 µg·mL$^{-1}$ (AmB).

Two regions in the ranges of 3200–2800 cm$^{-1}$, and 1100–950 cm$^{-1}$ were analysed in the FTIR spectrum (Fig. 2). Signals originating from lipids were localised in the range of 3200–2800 cm$^{-1}$ and from polysaccharides at 1200–950 cm$^{-1}$. The tests showed a decrease in signals in the region of 3200-2800 cm$^{-1}$ both after the treatment of the *C. albicans* with the Venetin-1 (100 µg mL$^{-1}$), seed extract (100 µg mL$^{-1}$) and amphotericin B (0.5 µg mL$^{-1}$). However, the greatest differences were observed after antibiotic treatment.

A drop in signals at 900–1100 $cm^{-1}$ in the spectra of *C. albicans* cells after the treatment of Venetin-1 and seed extract was observed as well. In the case of the spectrum of amphotericin B treated yeast cells, no differences were noted in signal intensities in the described range in comparison to the controls (C1 and C2). Based on the literature data, selected signals were analysed with the assignment of characteristic chemical bonds [10]. The observed differences in signal intensities assigned to lipids (2926 $cm^{-1}$, 2859 $cm^{-1}$) may result from changes in the content of these components within the cell membrane. Differences in the intensities of signals corresponding to polysaccharides (1032 $cm^{-1}$), i.e. the lower intensity in the spectra of cells after treatment with the seed extract and Venetin-1 than in control is probably caused by reduction of mannans, which are polysaccharide components of the yeast cell wall. This corresponds to the images of cells obtained after staining with Congo red fluorochrome.

**Conclusions:** As a result of the research, a similar effect of Venetin-1 and seed extract on the cell wall of the fungus *C. albicans* was found. The obtained results indicate a different mechanism of action of the Venetin-1 fraction and the extract than that of the antibiotic amphotericin B. The FTIR analyses confirmed microscopic observations, indicating the exposure of β-glucans in the fungal cell wall caused by the influence of the tested plant and animal preparations. The obtained results indicate the validity of further research on the Venetin-1 complex and seed extract as potential antifungal drugs.

**Acknowledgements:** Presented research was supported by the Projects of the National Science Centre, Poland [2020/37/B/NZ7/00763; 2023/07/X/NZ3/00661].

**References:**

1. M.J. Fiołka, J. Rzymowska, S. Bilska, K. Lewtak, M. Dmoszyńska-Graniczka, K. Grzywnowicz, W. Kaźmierski, T. Urbanik-Sypniewska, Acta Pathologica et Microbiologica Scandinavica, 127 (2019) 435.
2. M. Rybicka, P. Czaplewska, J. Rzymowska, W. Sofińska-Chmiel, S. Wójcik-Mieszawska, K. Lewtak, K. Węgrzyn, P. Jurczak, A. Szpiech, J. Nowak, N. Musiał, M.J. Fiołka, Scientific Reports, 12 (2022) 1.
3. P. Czaplewska, A.E. Bogucka, K. Macur, M. Rybicka, M.J. Fiołka, Frontiers in Molecular Biosciences 10 (2023) 1.
4. A.M. Czerwonka, M.J. Fiołka, K. Jędrzejewska, E. Jankowska, A. Zając, W. Rzeski, Biomedicine & Pharmacotherapy, 126 (2020) 1.
5. M.J. Fiołka, P. Czaplewska, K. Macur, T. Buchwald, J. Kutkowska, R. Paduch, Z. Kaczyński, J. Wydrych, T. Urbanik-Sypniewska, PLoS ONE, 4 (2019) 1.
6. M.J. Fiołka, S. Mieszawska, P. Czaplewska, A. Szymańska, K. Stępnik, W. Sofińska-Chmiel, T. Buchwald, K. Lewtak, Scientific Reports, 10 (2020) 1.
7. M.J. Fiołka, P. Czaplewska, S. Wójcik-Mieszawska, A. Lewandowska, K. Lewtak, W. Sofińska-Chmiel, T. Buchwald, Scientific Reports, 11 (2021) 1.
8. S. Wójcik-Mieszawska, K. Lewtak, W. Sofińska-Chmiel, J. Wydrych, M.J. Fiołka, Scientific Reports, 13 (2023) 1.
9. Patent, Protein-sugar fraction isolated from the coelomic fluid of the earthworm *Dendrobaena veneta* for use in non-specific immunotherapy, P.429033, date of decision: May 25 (2021).
10. A. Dróżdż, D. Kubera, A. Sławińska-Brych, A. Matwijczuk, L. Ślusarczyk, G. Czernel, D. Karcz, A. Olender, A. Bogut, D. Pietrzak, W. Dąbrowski, A. Stepulak, A. Wójcik-Załuska, M. Gagoś, International Journal of Molecular Sciences, 24 (2023) 1.

# POTASSIUM POTENTIOMETRIC SENSORS FOR TESTING THE COMPOSITION OF PHARMACEUTICAL PREPARATIONS

**M. FIAŁEK[1], C. WARDAK[1], M. WARDAK[2]**, [1]Maria Curie-Sklodowska University, Faculty of Chemistry, Institute of Chemical Sciences, Department of Analytical Chemistry, M. Curie-Sklodowska Sq. 3, 20-031 Lublin, Poland, [2]Independent Public Health Care Center of the Ministry of Internal Affairs and Administration in Lublin, Sq. Grenadierów 3, 20-331 Lublin, Poland.

**Abstract:** Ion-selective electrodes are simple and cheap analytical tools that enable the determination of many ions in environmental, industrial, clinical, and pharmaceutical samples without the need for complicated sample preparation. This work presents a new ion-selective electrode with solid contact for the determination of potassium ions. Copper oxide nanoparticles (CuONPs) were used as an intermediate layer placed between the polymeric membrane and the substrate electrode. CuONPs are characterized by high surface-to-volume ratio and exhibit semiconducting properties. Due to presence of NPs layer the electroactive surface area is enlarged and electron transfer between ion sensitive membrane and inner electrode is enhanced. Thanks to this modification, a sensor with very good stability of indications was obtained, insensitive to changing measurement conditions, and showing good selectivity and sensitivity to potassium ions. The developed electrode was successfully used to determine the potassium content in pharmaceutical preparations.

**Introduction:** Potassium is a very important element necessary for the proper functioning of living organisms. This element is necessary to maintain proper electrolyte balance and the appropriate volume of body fluids, as well as for the proper burning of proteins and carbohydrates. It is also necessary in the process of oxygenating our brain and cells, and crucial for the proper functioning of muscles. According to WHO recommendations, adults should consume approximately 3500 mg of potassium per day, which could significantly improve the quality of life for many people and positively affect their health [1]. Potassium leaches from our bloodstream through urine and sweat. Therefore, it is extremely important to regularly consume products rich in potassium. This is especially important for physically active people and athletes, which is why dietary supplements containing potassium are recommended for them. There are many potassium preparations on the market that also contain other macro and microelements. Many of these dietary supplements are extended-release formulations. Determining the content of potassium ions is important not only in medicine, where blood and urine samples help assess patients‘ health condition, but also in pharmaceutical preparations to control both the content of this element and the its release rate. For this purpose, ion-selective electrodes are successfully used [2,3].

In recent years a new version of ISEs was introduced, which involved the removal of the internal electrolyte solution [4,5]. Thanks to this, these sensors called solid contact ion-selective electrodes (SCISEs) have become easier to handle, use and transport [6]. Moreover, miniaturization of ISEs has become possible. For this type of electrodes, it is very important to select the appropriate material that will act as an ion-electron

transducer, thus enabling the proper operation of the electrodes, by ensuring appropriate stability and reproducibility of the potential. There are many materials used in the role of a solid contact. The most popular materials include carbon based nanomaterials such as carbon nanotubes and nanofibers, conductive polymers, metal and metal oxide nanoparticles, and ionic liquids, among others [6-8].
In this paper the properties of a new potassium ion-selective electrode with copper oxide nanoparticles solid contact and its analytical application in pharmaceutical analysis is presented.

**Experimental:** The preparation of the electrode included two stages: applying an intermediate layer by dropping 10 µl of nanoparticles suspension (1 mg/ml) onto the previously cleaned surface of the substrate electrode and, after the nanoparticle layer had dried, applying an ion-selective membrane, also using the drop method. The composition of the membrane was as follows: 2 % w/w ionophore (valinomycin), 0.6 % ionic additive (potassium tetrakis(p-chlorophenyl) borate), 33 % polyvinyl chloride and 63.4 % plasticizer (dioctyl sebacate). Before measurements, the electrodes were conditioned in a $1\times10^{-3}$ M KCl solution. They were stored in the same solution between measurements. In order to compare and evaluate the effect of introducing nanoparticles, electrodes without an intermediate layer of CuONPs were prepared and tested in parallel. In this case, the same polymer membrane was applied directly to the electrode substrate. The properties of the electrodes were examined by conducting potentiometric measurements (two-electrode system: ion-selective electrode - Ag/AgCl reference electrode (Metrohm 6.0733.100) using the Lawson Labs multi-channel potentiometric data collection system and electrochemical impedance spectroscopy measurements (in a three-electrode system with an additional auxiliary electrode GCE using the µAutolab electrochemical analyzer). pH measurements were made using a glass electrode Orion 91-07 BN and an Elmetron CX-742 pH meter.
Samples of pharmaceutical preparations for potassium determination were prepared in the following way. Ten tablets of each preparation were weighed, ground in a bowl and then weighed out an amount equivalent to the weight of one tablet. The contents were placed in a beaker, poured with distilled water and placed in an ultrasonic bath for 15 minutes. Then the solution was filtered and quantitatively transferred to a 100 ml flask and diluted with water.

**Results:** The effect of introducing an additional intermediate layer of CuONPs into the electrode was evaluated by determining the analytical parameters of the electrodes, i.e. detection limit, measurement range, slope of the characteristic, pH range, selectivity, stability and reversibility of the potential, and electrical parameters, i.e. membrane resistance, electrical capacity and charge transfer resistance at the phase boundary. membrane internal electrode. These parameters are summarized in Table 1. The resistance of the electrodes to changes in measurement conditions, i.e. changes in gas content, changes in redox potential, and variable lighting intensity, was also checked.

**Table 1.** Selected analytical parameters of potassium ion-selectives: electrode 1 (unmodified simple coated disc electrode) and electrode 2 with an interlayer of CuONPs.

| Parameter | | Electrode 1 | Electrode 2 |
|---|---|---|---|
| Slope of characteristic mV/decade | | 55.2 | 57.5 |
| Limit of detection M | | $6.2\times10^{-6}$ | $1.2\times10^{-6}$ |
| Linear range M | | $1\times10^{-5}$-0.1 | $5\times10^{-6}$-0.1 |
| pH range, pH | | 4.0-11.0 | 4.0-11.0 |
| Potential drift, µV/min | | 93 | 8.2 |
| Potential reversibility SD (n=5), mV[a] | | 3.45 | 0.72 |
| Selectivity coefficient | $K^{pot}_{K/Na}$ | $1.6\times10^{-5}$ | $1.3\times10^{-5}$ |
| | $K^{pot}_{K/NH4}$ | $2.3\times10^{-4}$ | $2.4\times10^{-4}$ |
| | $K^{pot}_{K/Ca}$ | $1.6\times10^{-5}$ | $1.2\times10^{-5}$ |
| | $K^{pot}_{K/Mg}$ | $1.6\times10^{-5}$ | $8.3\times10^{-6}$ |
| Membrane resistance, MΩ | | 0.883 | 0.078 |
| Capacitance, µF | | $0.12\times10^{-3}$ | 0.11 |

[a] The reversibility of the potential is given as the standard deviation from the average value of the potential from five measurements in KCl solution with a concentration of $1\times10^{-4}$ M.

Analyzing the data in Table 1, it can undoubtedly be concluded that the introduction of an additional intermediate layer in the form of CuNPs improves the parameters of the potassium electrode, but to a varying degree. The greatest differences were observed in the stability and reversibility of the potential. The potential drift value for the electrode with the CuONPs layer is more than ten times lower than for the myomodified electrode. It was similar in the case of the reversibility of potential. A quantitative measure of this property of the electrode is the standard deviation from the average value of several potential measurements at a given concentration when the measurement is performed alternately in solutions of different concentrations. The table shows the SD value for a concentration of $1\times x10^{-4}$ M KCl. As it can be seen, the modified electrode shows much better potential reversibility (lower SD value) compared to the electrode without a layer of CuONPs. This improvement in the stability of the electrode readings is the result of the properties of the material of the intermediate layer. The introduced CuO nanoparticles exhibit mixed ion-electron conductivity. Additionally, as a nanomaterial, they have a very large surface area. Thanks to these features, the process of transferring charge between the membrane and the substrate electrode is much more efficient. This is confirmed by the values of electrical parameters, i.e. membrane resistance and electrical capacitance, which are much better for the modified electrode. It is worth noting that the CuONPs based electrode also has better sensitivity, a wider measurement range and a lower detection limit.

The selectivity of the electrodes remained unchanged. The values of selectivity coefficients and the pH range are very similar for both electrodes. This is understandable because the selectivity of the electrode is determined by the ionophore, which in this case is the same. The presence of a layer of nanoparticles that partially penetrate the polymer membrane does not significantly affect the ionic affinities of the membrane. It should be emphasized that the introduction of the CuONPs mediation layer did not make the sensors sensitive to changing measurement conditions. Changes in the electrode potential were recorded in $1\times10^{-3}$ M KCl saturated with oxygen and $CO_2$, respectively, and in the same solution but saturated with nitrogen. No changes in the electrode

potential were observed as a result of changes in gas concentration. Similar results were obtained by testing electrodes based on CuONPs in KCl solutions with different redox potential (containing Fe(II) and Fe(III) ions in different concentration ratio).
Good analytical parameters of the modified electrode, especially low detection limit, a wide measurement range, very good selectivity and good signal stability make the electrode a suitable tool for analyzing real samples.
Its analytical usefulness was confirmed when it was used to determine potassium in various pharmaceutical preparations in which potassium was present in the form of various compounds. The determinations were made using the standard addition method. The determination results were compared with those obtained by atomic absorption spectroscopy and with the manufacturer's data (Table 2). In all cases, good consistency of results was obtained.

**Table 2.** Results of potassium determination in pharmaceutical preparations using proposed K-SCISE and atomic absorption spectroscopy (AAS) as control method.

| Sample/potassium compound | Producer's data [mg/tablet] | Found by K-SCISE [mg/tablet ] | Relative error [%][a] | Found by AAS [mg/tablet ] |
|---|---|---|---|---|
| DOZ Product Potas/ potassium chloride | 157 | 159.3±3.2 (n=5) | 1.46 | 160.2 |
| Aspargin/ potassium hydrogen aspartate | 54 | 54.3±1.6 (n=5) | 0.55 | 55.0 |
| Potas+Magnez+$B_6$/potassium citrate | 250 | 246.1±3.7 (n=5) | 1.90 | 251.3 |

[a] The relative error was calculated with reference to the producer's data.

**Conclusions:** The results of the presented research confirm the usefulness of copper oxide nanoparticles in the construction of potassium ion-selective electrodes with solid contact. As a result of using this material in the form of an intermediate layer placed between the polymer membrane and the GC electrode, a sensor with low detection limit $1.2\times10^{-6}$ M, wide measuring range, slope of characteristic close to the theoretical value and good selectivity. The most important achievement of the introduction of CuONPs is the very good stability and repeatability of the sensor readings, which largely influences the accuracy and precision of the determination results. The developed electrode can be successfully applied to the analysis of real samples, as shown with the example of pharmaceutical preparations.

## References:

1. WHO. Guideline: Potassium intake for adults and children. Geneva, World Health Organization (WHO), 2012.
2. L. van de Velde, E. d'Angremont, W. Olthuis, Talanta, 160 (2016) 56.
3. J. Lenik, IEEE Sensors Journal, 17 (2017) 1215.
4. A. Cadogan, Z. Gao, A. Lewenstam, A. Ivaska, Analytical Chemistry, 64 (1992) 2496.
5. J. Bobacka, A. Ivaska, A. Lewenstam, Chemical Review, 108 (2008) 329.
6. C. Wardak, Electroanalysis, 24 (2014) 864.
7. C. Wardak, K. Pietrzak, K. Morawska, M. Grabarczyk, Sensors, 23 (2023) 5839.
8. C. Wardak, K. Morawska, K. Pietrzak, Materials, 16 (2023) 5779.

# THE INFLUENCE OF SURFACTIVE SUBSTANCES WITH DIFFERENT CHARGE ON THE VOLTAMPEROMETRIC SIGNAL OF GALLIUM

**M. FIAŁEK[1]**, **M. GRABARCZYK[1]**, **M. WARDAK[2]**, [1]Maria Curie-Sklodowska University, Faculty of Chemistry, Institute of Chemical Sciences, Department of Analytical Chemistry, M. Curie-Sklodowska Sq. 3, 20-031 Lublin, Poland, [2]Independent Public Health Care Center of the Ministry of Internal Affairs and Administration in Lublin, Sq. Grenadierów 3, 20-331 Lublin, Poland.

**Abstract: a** brief characterization and division of surfactants according to their chemical structure was made. The influence of three types of surfactants on the voltammetric signal of gallium was investigated. Triton X-100, sodium dodecyl sulfate (SDS) and cetyltrimethylammonium bromide (CTAB) were used as non-ionic, anionic and cationic surfactants, respectively. Based on the results obtained, it was found that all tested surfactants in the tested concentration range reduce the analytical signal of Ga(III). In order to minimize these interferences, the tested solution was pre-mixed with Amberlite XAD-7 resin with adsorption properties. It has been proven that owing to the use of this polymer sorbent, it is possible to analyze Ga(III) in water samples containing organic substances at a concentration of 0,5 - 2 mg $L^{-1}$.

**Introduction:** Due to the high sensitivity of voltammetric methods, the appearance of interference has a significant impact on the determination results. In the stripping voltammetry method, the main cause of disruption of the analytical signal are organic substances, which very often interfere and sometimes even preclude direct measurement as a result of adsorption of these substances on the working electrode surface. These substances are commonly present in real samples, especially in the form of surface-active compounds called surfactants. Surfactants belong to an important group of chemical compounds currently used on a large scale in industry and chemical laboratories. Therefore, the release of the above compounds into the environment is inevitable.

Each of us has direct contact with surface-active substances every day, for example using liquids with cleaning properties. Detergents remove lipophilic impurities (e.g. excess sebum) and hydrophilic impurities (water-soluble impurities, such as mineral salts found in our sweat) from the skin. These specific properties of surfactants result from their chemical structure. The surfactant molecule consists of two parts with opposite properties in relation to water: the hydrophilic part (owing to which the entire molecule is able to dissolve in water and other polar liquids) and the hydrophobic part (responsible for the good solubility of the entire surfactant molecule in oils).

Due to their chemical structure, surfactants can be divided into those that dissociate in water to form negative or positive ions or whose electric charge depends on the pH of the environment. This group of compounds are ionic surfactants. Surface-active compounds with polar groups that cannot dissociate are included in the class of non-ionic surfactants.

**Experimental:** In work [1] adsorptive stripping voltammetric (AdSV) method for Ga(III) determination at a multiwall carbon nanotube/spherical glassy carbon (MWCNT/SGC) electrode modified with a lead film was proposed. This AdSV procedure is based on the preconcentration of gallium in the form of a complex with cupferron on the working electrode surface at a potential value of -0.75 V for 30 s. After that, the analytical signal is obtained by changing the potential in the negative direction (from -0.7 to -1.2 V), which results in a reduction of the accumulated complex. This procedure has been successfully used to determine gallium in certified reference material and real water samples [1].

In course of the elaborated of the mentioned procedure, the influence of various surfactants on the voltammetric gallium signal was thoroughly examined. Triton X-100 was used as a non-ionic surfactant. It is the trade name for a polymer ether of polyethylene glycol (PEG) and p-tert-octylphenol. As a chemically neutral detergent, Triton X-100 is used in molecular biology and biochemistry. It acts as an enhancer in some reactions [2,3]. It is widely used in the production of textiles and fibers due to its excellent ability to wetting and removing grease and oil from hard surfaces [4]. Sodium dodecyl sulfate (SDS) was used as the anionic surfactant. This compound was selected due to its high solubility in water and because it is widely used as an ingredient of cosmetics, personal hygiene products and household chemicals [5-7]. An equally well-known commercial surfactant is cetyltrimethylammonium bromide (CTAB), which dissociates in water to produce positive ions. This cationic surfactant is widely used in household products such as fabric softeners and all types of hair products (conditioners, soaps, shampoos). This group of surfactants has antibacterial properties, therefore they are commonly used as disinfectants and antiseptics in disinfectant products. Due to their positive charge, cationic surfactants strongly adsorb on negatively charged surfaces of sludge, soil and sediments [8,9]. The widespread use as well as the sorption properties of cationic surfactants make these surfactants predominate in the environment.

Based on literature data showing that natural waters contain surfactants with a surfactant effect similar to the effect caused by 0,2 – 2,0 ppm Triton X-100 [10], the tests were carried out using the same concentrations of the tested surface-active compounds. The measurements were also carried out after introducing an additional step of mixing the tested samples with the Amberlite XAD-7 resin. It has been proven that mixing the solution with resin leads to the complete or at least partial removal of organic substances from environmental samples. It is possible owing to the sorption properties of Amberlite XAD-7 resin, on the surface of which both hydrophobic compounds from aqueous solutions and hydrophilic compounds from organic solvents can be sorbed. This polymer sorbent is widely used in various industries to purify water from organic pollutants (dyes, pesticides, detergents), purify enzymes, secrete antibiotics and separate other biologically active substances [11].

**Results:** Figures 1 and 2 present the results obtained during the examination of the influence of surfactants, such as Triton X-100 (a), SDS (b) and CTAB (c), on the voltammetric signal of gallium at a concentration of $1 \times 10^{-7}$ mol $L^{-1}$, without preliminary mixing the sample with resin and after applying pre-mixing the sample with Amberlite XAD-7 resin, respectively.

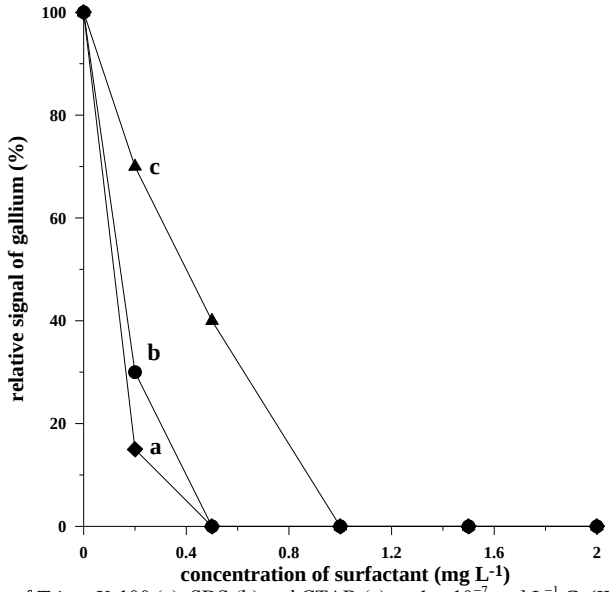



**Fig.1.** The influence of Triton X-100 (a), SDS (b) and CTAB (c) on $1 \times 10^{-7}$ mol $L^{-1}$ Ga(III) peak current. All measurement were carried out without the addition of Amberlite XAD-7 resin to the tested sample.

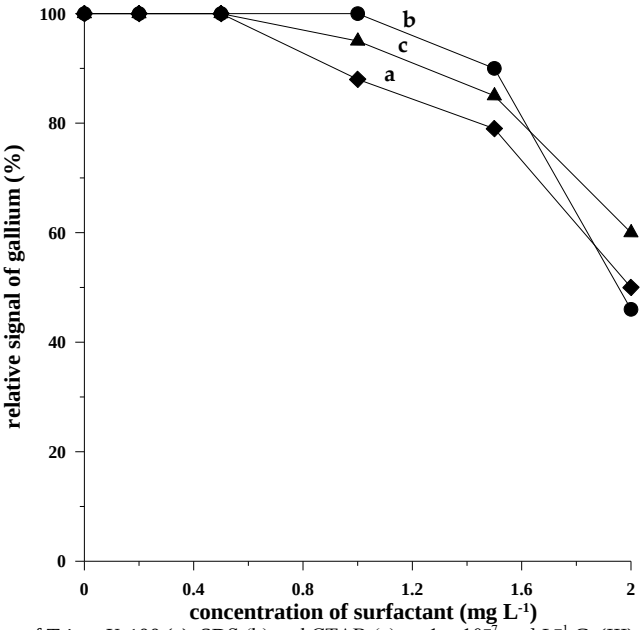



**Fig.2**. The influence of Triton X-100 (a), SDS (b) and CTAB (c) on $1 \times 10^{-7}$ mol $L^{-1}$ Ga(III) peak current upon addition of Amberlite XAD-7 resin to the tested sample.

As can be seen in Fig.1, without the use of preliminary mixing of the sample with the resin, all tested surfactants cause a significant reduction of the analytical signal of

gallium, making it impossible to determine this element at the concentration of each of the tested surfactants equal to 0.5 mg $L^{-1}$. However, as Fig.2 shows, the use of pre-mixing the sample with Amberlite XAD-7 resin significantly reduces these interferences. The influence of organic compounds is visible only at concentrations higher than 0.5 mg $L^{-1}$, but it is not as significant as without the use of the resin. An undisturbed gallium signal is obtained in the presence of 0.5 mg $L^{-1}$ Triton X-100 and CTAB as well as 1 mg $L^{-1}$ SDS. At higher concentrations of the above surfactants, it is also possible to determine gallium, but with a loss in the sensitivity of the determination. At the highest tested concentration of Triton X-100, SDS and CTAB (i.e. 2 mg $L^{-1}$), a reduction of the gallium signal to 50, 46 and 60%, respectively, is achieved.

**Conclusions:** To sum up, it can be stated that the procedure of pre-mixing samples with resin is an efficacious method of eliminating organic substances that allows direct analysis of natural environmental samples rich in organic compounds using stripping voltammetry.

## References:

1. M. Grabarczyk, M. Fialek, E. Wlazlowska, Materials, 17 (2024) 966.
2. W. Jason, J.B. Karen, M.R. Mark, Analytica Chimica Acta, 503 (2004) 241.
3. Z. Changqing, Z. Hong, L. Donghui, L. Shunhua, X. Jingou, Spectrochimica Acta Part A: Molecular and Biomolecular Spectroscopy, 60 (2004) 3173.
4. G. Haiyan, Chinese Journal of Practical Technology, 46 (1997) 24.
5. M.H. Li, Chemosphere, 70 (2008) 1796.
6. E. Montoneri, V. Boffa, P. Savarino, F. Tambone, F. Adani, L. Micheletti, C. Gianotti, R. Chiono, Waste Manage, 29 (2009) 383. 7. I. Lavilla, N. Cabaleiro, M. Costas, I. de la Calle, C. Bendicho, Talanta, 80 (2009) 109.
8. K. Agrawal, G. Agnihotri, K. Shrivas, G.L. Mundhara, K.S. Patel, P. Hoffmann, Microchimica Acta, 147 (2004) 273.
9. R. Patel, K.S. Patel, Talanta, 48 (1999) 923.
10. B. Cosovic, V. Vojvodic, Limnology and Oceanography, 27 (1982) 361.
11. Z. Floriańczyk, S. Penczuka, Chemia polimerów, Tom III, Oficyna Wydawnicza Politechniki Warszawskiej, Warszawa, 1998.

# RESEARCH ON THE "CAP-PAIR" EFFECT FOR Bi(III) IONS IN AQUEOUS-ORGANIC ENVIRONMENTS. EFFECT OF SELECTED IONIC SURFACTANTS ON THE ELECTRODE PROCESS

**A. PAWLAK, A. NOSAL-WIERCIŃSKA**, Maria Curie-Sklodowska University, Faculty of Chemistry, Institute of Chemical Sciences, Department of Analytical Chemistry and Instrumental Analysis, M. Curie-Sklodowska Sq. 3, 20-031 Lublin, Poland.

**Abstract:** Bi(III) ions electroreduction in the presence of surfactants at cyclically renewable liquid silver amalgam film electrode (R-AgLAFE) has been studied by voltammetric methods. The realized studies point that water-organic environment also influence the rate of Bi(III) electroreduction process.

**Introduction:** The Bi(III) ions electroreduction on both a mercury electrode and a thin film electrode of cyclic renewable liquid silver amalgam (R-AgLAFE) was an issue subjected to detailed research by Professor Wiercińska and her team [1]. In aqueous solutions, the multistage nature of the process was confirmed, and an attempt was also made to elucidate its mechanism [1]. Changes in the dynamics of electroreduction of depolarizer ions through the use of suitable organic substances, containing sulphur or nitrogen atoms in their structure, having free electron pairs capable of forming active complexes with depolarizer ions in the electrode layer, is a key issue, analysed in the context of studies of the kinetics of electrode reactions ('cap-pair' effect) [3]. The location of the reduction potential of the depolarizer in the region of the labile adsorption equilibrium of the organic substance also plays an important role. Nevertheless, the scientific literature lacks references to this effect in the context of Bi(III) ions in aqueous-organic systems, which is an important gap in the study of the kinetics of electrode reactions.

Methanol, which is a polar protic solvent that easily mixes with water in an unlimited ratio, is characterized by the presence of so-called 'acidic hydrogen atoms' that can easily release H+ ions and form hydrogen bonds. Due to these properties and easy availability, methanol is used in chemistry, biochemistry and various industrial sectors, both as a solvent and as a substrate for chemical reactions. Its use also includes the production of dyes, plastics, resins and synthetic fibers. One of the factors influencing the kinetic parameters of electrode reactions is the adsorption of substances on the electrode surface. As a result of this process, the electrical double layer is modified. Scientific studies are pointing to the adsorption of methanol on a mercury electrode [4] and this suggests the occurrence of a similar mechanism also on an electrode made of cyclic renewable liquid silver amalgam (R-AgLAFE).

The aim of the present study was to investigate the effects of selected ionic surfactants (sulfonic acid sodium salt (1OSASS; anionic surfactant) and hexadecyltrimethylammonium bromide (CTAB; cationic surfactant)) on the kinetics and mechanism of Bi(III) ions electroreduction in aqueous-organic electrolyte solutions in the aspect of the "cap - pair" effect).

**Experimental:** Voltammetric studies were performed using a potentiostat - µAutolab type III/ GpES galvanostat version 4.9 (EcoChemie B. V., Utrecht, the Netherlands) and a programmable M165D electrode stand (mtm anko, Krakow, Poland). A classical three-electrode system was used, in which the working electrode was made of a cyclic renewable film of liquid silver amalgam (R-AgLAFE).

The following reagents were used to prepare the base electrolytes (BE):$Bi(NO_3)_3{\cdot}5H_2O$ (Sigma-Aldrich), $NaClO_4$ (Fluka), $HClO_4$ (Sigma-Aldrich), methanol, redistilled water. Mixed water-organic BE solutions were prepared containing 0.5 $mol{\cdot}dm^{-3}$ $NaClO_4$, 0.5 $mol{\cdot}dm^{-3}$ $HClO_4$, water and methanol in different volume ratios. The BEs were labelled according to the scheme: **a** indicates solution of 1 $mol{\cdot}dm^{-3}$ $chlorates(VII)_{(aq)}$ where, chlorate(VII):methanol ratio = 4:0 (A - 0 % MeOH); **B** indicates solution of 1 $mol{\cdot}dm^{-3}$ chlorates(VII) where chlorate(VII):methanol ratio = 3:1 (B - $25\%_{(v/v)}$ MeOH); **C** indicates solution of 1 $mol{\cdot}dm^{-3}$ $chlorates(VII)_{(aq)}$ where chlorate(VII):methanol ratio = 2:2 (C - $50\%_{(v/v)}$ MeOH). Each BE solution contained Bi(III) depolarizer ions at a constant concentration of $1{\cdot}10^{-3}$ $mol{\cdot}dm^{-3}$. Samples containing surfactants were always prepared just before the measurements.

**Results:** Figures 1-3 indicate the correlations obtained from voltammetric measurements, which allow qualitative evaluation of the effect of methanol present in the base electrolyte on the rate of the electroreduction process. Both the presence and increase in the amount of methanol in the base electrolyte solution cause a decrease in the reversibility of Bi(III) ions electroreduction processes. This is evidenced by a decrease in the SWV peak currents (Fig.1), a decrease in the slope of the DC polarographic waveform (Fig.2) and an increase in the potential difference between the anodic and cathodic peak (ΔE) in the CV curves (Fig.3).

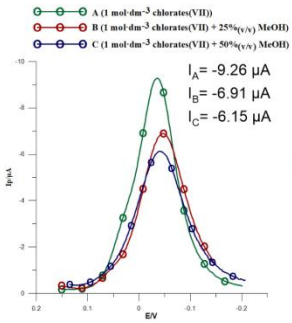



**Fig.1.** SWV peaks of Bi(III) ions electroreduction in 1 $mol{\cdot}dm^{-3}$ chlorates(VII) with increasing methanol concentration included in the legend.

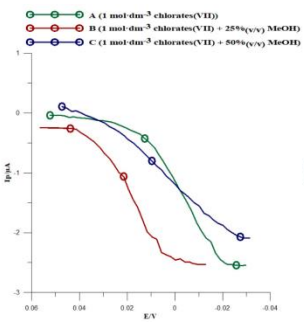



**Fig.2.** DC polarographic waves of Bi(III) ions electroreduction in aqueous-organic BE solutions.

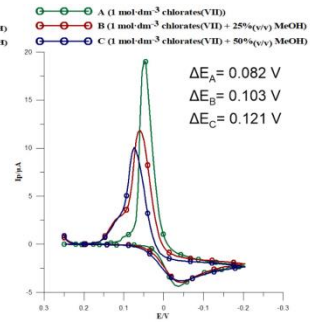



**Fig.3.** Voltammetric CV curves of Bi(III) ions electroreduction in aqueous-organic solutions of the BEs.

The addition of 1OSASS causes a decrease in the values of SWV peak currents (Fig.4) in all analysed BE solutions. As the concentration of CTAB in solutions increases, the values of SWV peak currents increase and the width of the peaks at mid-height decreases (Fig.4). The dynamics of Bi(III) ions electroreduction in mixed electrolyte solutions, due to the presence of CTAB and 1OSASS, is significantly changed. With increasing alcohol

content in EP solutions, peak currents decrease and the definition of peaks gets worse (Fig.5).

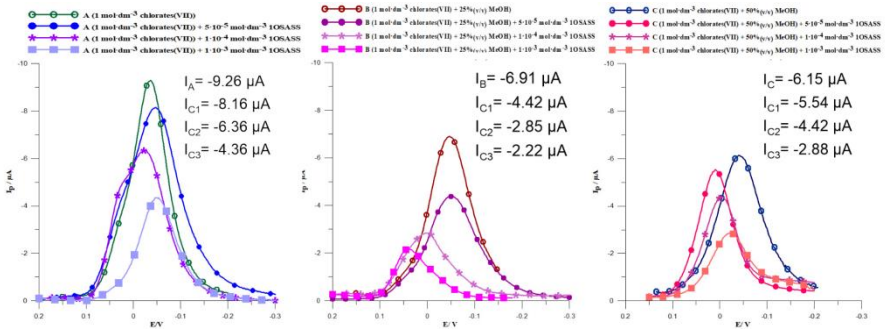



**Fig.4.** SWV peaks of Bi(III) ions electroreduction in solutions of the BEs in the presence of different concentrations 1OSASS (● 5· $10^{-5}$ mol· $dm^{-3}$; ✱ 1· $10^{-4}$ mol· $dm^{-3}$; ■ 1· $10^{-3}$ mol· $dm^{-3}$).

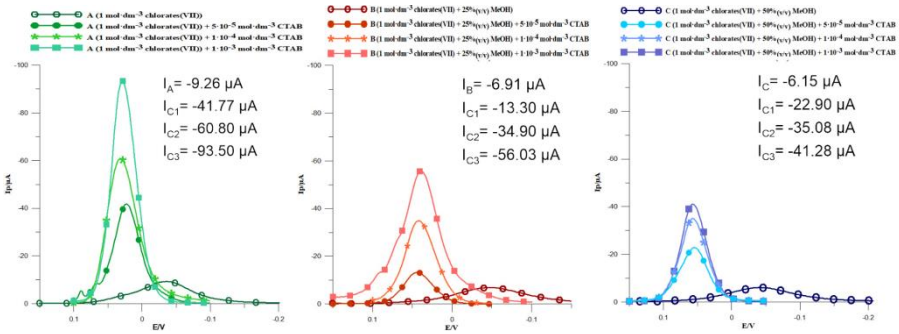



**Fig.5.** SWV peaks of Bi(III) ions electroreduction in solutions of the BEs in the presence of different concentrations CTAB (● 5· $10^{-5}$ mol· $dm^{-3}$; ✱ 1· $10^{-4}$ mol· $dm^{-3}$; ■ 1· $10^{-3}$ mol· $dm^{-3}$).

Previous studies have shown a sophisticated mechanism for the of Bi(III) ions electroreduction process on a mercury electrode [1] and suggest a chemical reaction of the formation of active complexes involved in electron transition process [2]. They suggest a similar multi-step electrode mechanism also in the studied systems. The literature confirms the adsorption of alcohol on the electrode [4], with the result that it blocks and possibly reduces the amount of Bi - CTAB active complexes in the adsorption layer. In the other way, 1OSASS, adsorbing strongly on the electrode, itself blocks access to it, which inhibits the process. The formed Bi -1OSASS active complexes have no chance to access the electrode surface, and the additional presence of methanol in the base electrolyte solution, strengthens this blockade. The determined kinetic parameters α and ks based on CV curves have quantitatively indicated the kinetics of Bi(III) ions electroreduction in the presence of surfactants and its changes due to the presence of methanol in the base electrolyte solutions (Table 1).

**Table 1.** Values of cathodic transition coefficients (α) and standard rate constants (ks) of Bi(III) ions electroreduction in aqueous-organic BE solutions and in the presence of CTAB and 1OSASS.

| $C_{CTAB}$ [mol·dm$^{-3}$] | α | $10^4 k_s$ [cm·s$^{-1}$] | | $C_{1OSASS}$ [mol·dm$^{-3}$] | α | $10^4 k_s$ [cm·s$^{-1}$] |
|---|---|---|---|---|---|---|
| Solution a (1 mol·dm$^{-3}$ chlorates(VII)) | | | | | | |
| 0 | 0.35 | 1.30 | | 0 | 0.35 | 1.30 |
| $5 \cdot 10^{-5}$ | 0.44 | 32.40 | | $5 \cdot 10^{-5}$ | 0.25 | 1.00 |
| $1 \cdot 10^{-4}$ | 0.57 | 54.41 | | $1 \cdot 10^{-4}$ | 0.23 | 0.95 |
| $1 \cdot 10^{-3}$ | 0.68 | 76.50 | | $1 \cdot 10^{-3}$ | 0.20 | 0.84 |
| Solution B (1 mol·dm$^{-3}$ chlorates(VII) + 25%(v/v) MeOH)) | | | | | | |
| 0 | 0.32 | 0.70 | | 0 | 0.32 | 0.70 |
| $5 \cdot 10^{-5}$ | 0.41 | 7.07 | | $5 \cdot 10^{-5}$ | 0.22 | 0.80 |
| $1 \cdot 10^{-4}$ | 0.55 | 34.70 | | $1 \cdot 10^{-4}$ | 0.20 | 0.40 |
| $1 \cdot 10^{-3}$ | 0.60 | 49.10 | | $1 \cdot 10^{-3}$ | 0.17 | 0.18 |
| Solution C (1 mol·dm$^{-3}$ chlorates(VII) + 50%(v/v) MeOH) | | | | | | |
| 0 | 0.30 | 0.46 | | 0 | 0.30 | 0.46 |
| $5 \cdot 10^{-5}$ | 0.38 | 4.06 | | $5 \cdot 10^{-5}$ | 0.20 | 0.38 |
| $1 \cdot 10^{-4}$ | 0.49 | 12.88 | | $1 \cdot 10^{-4}$ | 0.18 | 0.21 |
| $1 \cdot 10^{-3}$ | -* | -* | | $1 \cdot 10^{-3}$ | 0.16 | 0.12 |

*- The substance has not dissolved.

Increasing the concentration of CTAB causes an increase in both α and $k_s$ values, which indicates an increase in the rate of the electrode process (Table 1). In comparison, the opposite situation is observed in the presence of 1OSASS (Table 1). Both parameters are decreasing with an increase of the concentration of surfactants in the base electrolyte solutions, which evidently suggests changes in dynamics of the electrode process towards inhibition.

The presence of methanol changes the dynamics of the catalytic action of CTAB and 1OSASS inhibition on the electrode process.

**Conclusions:** The rate of Bi(III) ions electroreduction is affected by the presence of the surfactant and the type of base electrolyte. CTAB accelerates the Bi(III) ions electroreduction process in all the basic electrolyte solutions tested, while 1-OSASS inhibits this process. The presence of methanol changes the dynamics of the catalytic action of CTAB and 1OSASS inhibition on the electrode process, which we explain by changing the mechanism of the electrode process.

## References:

1. A. Nosal-Wiercińska, Electroanalysis, 26 (2014) 1013.
2. A. Nosal-Wiercińska, M. Martyna, M. Wiśniewska, Applied Nanoscience, 13 (2023) 4737.
3. K. Sykut, G. Dalmata, B. Nowicka, J. Saba, Journal of Electroanalytical Chemistry, 90 (1978) 299.
4. B. Marczewska, Przyspieszanie procesu elektroredukcji jonów Zn(II) na elektrodzie rtęciowej przez niektóre związki organiczne, w wybranych mieszanych rozpuszczalnikach wodno-organicznych, Lublin 1998.

# CONSTRUCTION AND PROPERTIES OF ION SELECTIVE ELECTRODES FOR CHLORHEXIDINE DETERMINATION

**J. LENIK, C. WARDAK**, Maria Curie-Sklodowska University, Faculty of Chemistry, Institute of Chemical Sciences, Department of Analytical Chemistry, M. Curie--Sklodowska Sq. 3, 20-031 Lublin, Poland.

**Abstract:** The aim of the research was to create the electrodes with a polymeric (PVC) membrane phase with chlorhexidine function to establish its analytical parameters and analytical application. The construction of the sensor was simple and low cost. The membranes were based on neutral ionophores with lipophilic salt potassium tetrakis(4-chlorophenyl) borate, dissolved in plasticizer, DOS (dioctyl sebacate) or NPOE (nitrophenyl octyl ether). The presented electrodes are characterized by a near Nernstian response slope of 22.5 – 30.4 mV decade$^{-1}$ over the linear range $1 \cdot 10^{-3}$ - $1 \cdot 10^{-5}$ mol L$^{-1}$ or $1 \cdot 10^{-3}$ - $1 \cdot 10^{-6}$ mol L$^{-1}$, the value of the correlation coefficient 0.0048 - 0.9972. The optimised electrode was successfully applied for determination of chlorhexidine digluconate in pure samples and in liquid mouthwash Corsodyl (Glaxo Smith) with relative error 0.76 - 5.81% and precision RSD 0.35 - 7.60 %.

**Introduction:** Chlorhexidine was first synthesised in England in 1950 by Imperial Chemical Industries (now AkzoNobel) and is considered to be one of the most widely used bactericidal and bacteriostatic agents. Chlorhexidine (CHXD), a biguanide derivative (1,1'-hexamethylene-bis-(5-p-chlorophenyl)biguanide), consists of two symmetrically placed 4-chlorophenols rings and two guanidine rings groups centrally connected by a hexamethylene chain (Fig.1).
The biochemical mechanism of destruction of microorganisms involves irreversible damage to their cytoplasmic membranes. The preparations are most often used in the form of salt, digluconate, hydrochloride, acetate, at a pH close to neutral. In an alkaline environment, a sparingly soluble alkaline form of chlorhexidine precipitates [1].

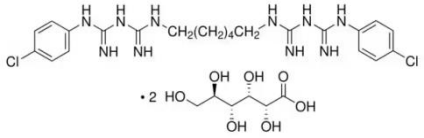



**Fig.1.** Bis(p-chlorophenyl) diguanidohexane digluconate.

Digluconate, acetate and hydrochloride are non-irritating to mucous membranes and skin and are used in preparations for hand disinfection, surgical field washing and disinfection of room equipment. In addition, chlorhexidine salts are used in wound disinfectants in mouthwashes, toothpastes, tablets, and nose and eye drops [2]. CHXD is widely used in dentistry. It is an antibacterial agent that reduces the levels of *S. mutans* in saliva and plaque, and has a stronger bactericidal effect on *E. faecalis* bacteria found in dentinal tubules than calcium hydroxide. In addition, chlorhexidine is used in dentistry

as a component of rinses at a concentration of 0.2%, and at a concentration of 1-2% in gels for rinsing dects and root canals [3].
A wide range of products requires quality control, pharmacodynamic analytical tests, and pharmacokinetic studies, which remain valid. This is supported by numerous scientific works, including a review article [4] that describes detailed methods for analyzing chlorhexidine, such as spectrometry, chromatography, colorimetric reactions, solid-phase extraction, and capillary electrophoresis. Among the methods available in the literature, ion selective electrodes are very popular. The fabrication and analytical costs of potentiometric sensors are significantly lower than many other analytical techniques. In addition, these sensors have many other advantages in pharmaceutical analysis, such as selectivity for a drug, good reproducibility, stability, adequate accuracy and precision of measurement. They are easy to prepare, simple to use and compatible with the sample to be analysed. The formation of an analytical signal in ion-selective electrodes is related to the transitions of an ion across the interface between two phases: the solution phase in which the electrode is immersed - the membrane phase in which the receptor is placed. The change in potential can be caused by ion exchange or by a complexation reaction with a suitable electroactive component called an ion exchanger or ionophore.
Based on literature data, it can be assumed that CHXD will form labile complexes with crown ethers [5]. In this new concept, solid contact, PVC membrane electrodes supporting two different macrocyclic compounds, dibenzo-18-crown-6 (DBC) and heptakis (2,3,6-tri-O-benzoyl)-$\beta$-cyclodextrin (HSBβCD) were tested. A study was also carried out for a so-called blank electrode containing no active substance. TEHP - tris(2-ethylhexyl) phosphate was used as a plasticiser for the polymeric membrane. This task were implemented in taking successive stages research:
1) optimization of qualitative composition of polymeric membranes consisting in preparation of membranes for selected components, i.e. ionophores, plasticizers, and then their appraisal on the basis of parameters determined from the response curves of the obtained ion-selective electrodes,
2) determination of basic analytical parameters (selectivity, reversibility) of the constructed ion-selective electrodes,
3) analytical application of the constructed optimal electrode – determination in pure chlorhexidine and pharmaceutical preparation.

**Experimental:** In this paper it was described the Ag/AgCl solid contact electrodes for CHXD determination. The construction of the sensor was simple and low cost and was published in the previous papers and chapters of the book [6,7]. The membrane mixture shall be composed the following ingredients: for electrode 1: 6 mg DBC, 4 mg KTpClBP (potassium tetrakis(4-chlorophenyl) borate), 130 mg DOS, 60 mg PVC, for electrode 2: 6 mg DBC, 4 mg KTpClBP, 130 mg NPOE, 60 mg PVC, for electrode 3: 6 mg HSBβCD, 4 mg KTpClBP, 130 mg DOS, 60 mg PVC, for electrode 4: 6 mg HSBβCD, 4 mg KTpClBP, 130 mg NPOE, 60 mg PVC, for electrode 5: 130 mg TEHP, 70 mg PVC Two sensors were prepared for each electrode. The membrane components were dissolved in THF and placed drop-by-drop three times on the plasticised layer. The fresh electrodes were stored in the air for at least three days. Then, before the first measurement, they were conditioned in $10^{-3}$ mol $L^{-1}$ of CHXD solution for 24 hours. The electrodes were stored in the air between measurements.

The measurements of EMF of the CHXD electrode – reference electrode (Orion 90-02) system were made at 22±1 °C using the Electrochemistry EMF Interface system (Lawson Labs. Inc., USA) and IBM PC computer. A Thermo Orion 81-72 glass electrode and a Multi-functional Computer device CX – 721 Elmetron (±0.1 mV) (Poland) was used for pH measurements.

**Results:** The obtained results of electrodes response and their properties are given in Table 1. As seen two selected sensors with DBC+NPOE, HSB$\beta$CD+DOS results near Nernstian sensitivity in the same, widest linear range ($1\cdot10^{-6}$ – $1\cdot10^{-3}$ mol $L^{-1}$) and the lower limit of detection 2 – $5\cdot10^{-7}$ mol $L^{-1}$. The calibration graphs of electrodes 1-5 have a good correlation coefficient of about 0.995-0.997. Lower sensitivities in the shorter linear range ($1\cdot10^{-5}$ – $1\cdot10^{-3}$ mol $L^{-1}$) were noticed for electrodes 1 , 4 and 5. The achieved parameter values are indicative of the influence of the plasticizer on the extraction properties of the polymer membrane.

**Table 1.** The basing analytical parameters for electrodes no. 1-5.

| Electrode no. | S±s, mV decade$^{-1}$ | $E^0$, mV | $R^2$ | n | Linear range (mol $L^{-1}$) | LD mol $L^{-1}$ |
|---|---|---|---|---|---|---|
| 1 | 22.5±5.8 | 279.6±74.6 | 0.9959±0.0048 | 5 | $1\cdot10^{-5}$– $1\cdot10^{-3}$ | $3\cdot10^{-6}$ |
| 2 | 26.7±3.7 | 96.7±77.0 | 0.9948±0.0026 | 5 | $1\cdot10^{-6}$– $1\cdot10^{-3}$ | $5\cdot10^{-7}$ |
| 3 | 30.4±2.9 | 214.7±40.6 | 0.9970±0.0026 | 6 | $1\cdot10^{-6}$– $1\cdot10^{-3}$ | $4\cdot10^{-7}$ |
| 4 | 11.0±3.2 | 477.6±58.9 | 0.9972±0.0027 | 5 | $1\cdot10^{-5}$– $1\cdot10^{-3}$ | $2\cdot10^{-6}$ |
| 5 | 25.0±3.6 | 398.6±45.9 | 0.9946±0.0028 | 3 | $1\cdot10^{-5}$– $1\cdot10^{-3}$ | $2\cdot10^{-6}$ |

The next study was to determine the selectivity coefficients for the best electrodes DBC+NPOE and electrode HSBβCD+DOS. The separate solution method (SSM) was used to determine potential values with constant concentration of the main ion and interfering $c_{CHXD} = c_j = 10^{-3}$ mol $L^{-1}$. The results for the chosen selectivity coefficients for the studied sensors are presented in Table 2.

**Table 2.** Selectivity coefficients of the selected electrodes.

| | $K^{pot}_{CHXD/Interf}$ | |
|---|---|---|
| | Electrode 2 | Electrode 3 |
| KCl | 8.36 | $1.19\cdot10^{-1}$ |
| NaCl | 2.33 | 1.08 |
| $CaCl_2$ | $1.46\cdot10^{-5}$ | $4.03\cdot10^{-5}$ |
| $MgCl_2$ | $4.84\cdot10^{-5}$ | $3.98\cdot10^{-5}$ |
| Citrate | $7.97\cdot10^{-6}$ | $3.4\cdot10^{-8}$ |
| Mannitol | $2.52\cdot10^{-5}$ | $1.04\cdot10^{-7}$ |
| Glucose | $9.39\cdot10^{-5}$ | $1.05\cdot10^{-7}$ |
| SDS | $6.42\cdot10^{-3}$ | $2.23\cdot10^{-6}$ |
| Glycerine | $1.79\cdot10^{-4}$ | $1.48\cdot10^{-4}$ |
| Glycol | $1.51\cdot10^{-4}$ | $2.64\cdot10^{-4}$ |
| Sucralose | $1.01\cdot10^{-4}$ | $4.37\cdot10^{-4}$ |
| Xylitol | $1.93\cdot10^{-3}$ | $1.47\cdot10^{-3}$ |

From the data presented in Table 2 it can be seen that for certain ionic molecules the K values are different. Very valuable and small values of the selectivity coefficients

towards $K^+$, $Mg^{2+}$, sodium citrate, mannitol, glucose, SDS for electrode no. 3, were obtained. It is not possible to clearly determine which sensor has the best selectivity. However, the K values obtained are favourable in both cases and the ions and molecules tested should not affect the determination result in real samples.
In order to evaluate the reversibility of the potential, the selected electrodes no 2,3, were repeatedly immersed in chlorhexidine digluconate solutions at three different concentrations ($10^{-3}$, $10^{-4}$, $10^{-5}$ mol $L^{-1}$). The results obtained for one-month-old electrodes are shown in Figure 1. The potential of electrode no. 3 amounted to 182±0.7 mV, 153±3.3 mV and 117±1.3 mV in adequate CHXD solutions with RSD within the range of 1,0 -1,8%.

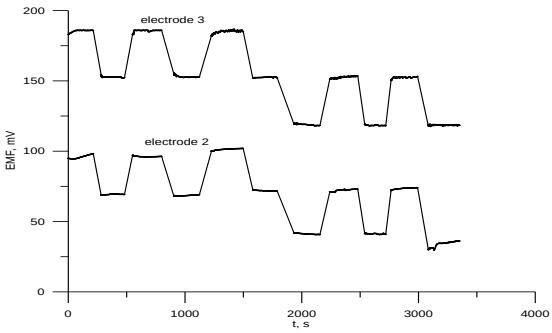



**Fig.1.** Potential reversibility of electrodes 2 and 3.

The selected electrode no 3. was used to determining chlorhexidine digluconate in pure samples and in pharmaceutical preparations. The obtained values from 3 replicate measurements for the determination of chlorhexidine in Corsodyl were 99,5 – 95%, (RSD 0,35%). The obtained results are characterized by the exactness precision and makes the electrode suitable for the pharmaceutical and other research laboratories.

**Conclusions:** The comparative study of the Ag/AgCl solid contact electrodes based on macrocyclic compounds have shown that electrodes containing in the membrane respectively heptakis (2,3,6-tri-O-benzoyl)-β-cyclodextrin, dibenzo-18-crown-6 have a similar potentiometric response. Significant differences were found in parameters such as selectivity and potential reversibility.

## References:

1. M. Pawłowski, Chemia Leków, PZWL, Warszawa, 2020.
2. A. Zejc, M. Gorczyca, Chemia leków. Warszawa, PZWL, 2004.
3. M. Łukomska - Szymańska, J. Sokołowski, B. Łapińska Journal of Stomatology, 70 (2017) 405.
4. A. Flávia, F. Másquio, A. C. Marcos, R. Hérida, Critical Reviews in Analytical Chemistry, 40 (2010) 89.
5. Y. M Ahmed, S. S. Badawy, F. Abdel-Haleem, Microchemical Journal, 177 (2022) 107276.
6. J. Lenik, C. Wardak, IEEE Sensors Journal, 13 (2013) 4638.
7. V. Kumar Thakur, M. Kumar, Thakur, Handbook of Polymers for Pharmaceutical Technologies Processing and Applications, Wiley Scrivener Publishing Beverly MA, USA, 2015.

# NITRATE ION-SELECTIVE ELECTRODES WITH NANOCOMPOSITE-MODIFIED ION-SENSITIVE MEMBRANE

**K. MORAWSKA[1], C. WARDAK[1], J. LENIK[1], M. WARDAK[2]**, [1]Maria Curie-Sklodowska University, Faculty of Chemistry, Institute of Chemical Sciences, Department of Analytical Chemistry, M. Curie-Sklodowska Sq. 3, 20-031 Lublin, Poland, [2]Independent Public Health Care Center of the Ministry of Internal Affairs and Administration in Lublin, Grenadierów St. 3, 20-331 Lublin, Poland.

**Abstract:** Because of the rapid development of technology and the increasing requirements for conducting analysis, the best possible measuring device is constantly being sought. In potentiometry, solid contact ion-selective electrodes are often used as indicator electrodes. Our team has developed a new type of solid contact ion-selective electrode (SCISE) in which the composition of the ion-sensitive membrane (ISM) has been modified. The polymeric ion-selective membrane consisting of polyvinyl chloride (PVC) as a membrane matrix, 2-nitrophenyl octyl ether (NPOE) as a plasticizer, complex of cobalt(II) nitrate and 4,7-diphenyl-1,10-phenanthroline ($Co(Bphen)_2(NO_3)_2(H_2O)_2$) as an ionophore, and trihexyltetradecylphosphonium chloride (THTDPCl) as an lipophilic ionic additive was further enriched with a nanocomposite consisting of copper(II) oxide nanoparticles and multi-walled carbon nanotubes (MWCNTs/CuONPs). To verify whether the additional implementation of conductive materials into the membrane composition improved the performance of the electrodes, a series of tests were carried out, including the determination of characteristic of the electrodes, linearity range, detection limit and slope, selectivity, as well as measurements of stability and potential reversibility.

**Introduction:** Nitrates are one of the most widespread compounds in the environment. Nitrogen compounds are formed spontaneously, e.g. as a result of the decomposition of organisms. Still, also their excessive growth has an anthropogenic basis and is mainly caused by human industrial activity, i.e. the transfer of nitrogen along with fertilizers from soils to water. This unfortunately has a negative impact on the environment, as evidenced, among other things, by excessive eutrophication of the water reservoirs. In addition, due to the release of nitrates into soils, it is crucial to monitor their concentration in both groundwater and surface water. Excessive concentrations of $NO_3^-$ ions negatively affect flora and fauna, including humans. Overexposure to these ions causes several health problems. The most common diseases associated with increased nitrate intake from water and food include methemoglobinemia, diabetes, or even cancer. The most vulnerable to the toxic effects of nitrates are the elderly and sickly, but also infants. It has been proven that heightened concentrations above the limit (according to the WHO it is 50 mg/L) increase the risk of birth defects and cancers [1-3]. Therefore, it is very crucial to determine the amount of nitrates in food and drinking water. For this purpose, spectroscopic and electrochemical techniques, i.e. voltammetry and potentiometry, are most often chosen.

Potentiometry is a method of measuring the electromotive force of a cell in a two-electrode system. One of the electrodes has a constant and independent potential from

the composition and concentration of the sample (this is the reference electrode), while the other electrode is the working (indicator) electrode, with a potential that depends on the composition and concentration of the sample [4]. Among working electrodes, the most popular electrodes are those with solid contact (SCISEs). They exhibit lower detection limits, and longer lifetimes, and are simpler to handle and store compared to classical liquid-contact ion-selective electrodes [5]. Unfortunately, the disadvantage of these electrodes is the problem of unstable and poorly reversible potential, the cause of which is the difficulty of transporting and transforming the charge into an electrical signal. To improve ion-to-electron conductivity, an intermediate layer is implemented in the electrode construction, or an additional component is introduced into the ion-sensitive membrane, which minimizes defects in electrodes with a solid contact [6]. Some of the more commonly chosen single-conductive materials, among others, are carbon nanomaterials, conductive polymers, metal nanoparticles, and metal oxides [7]. Recently, composite materials have become quite popular and highly effective in improving the analytical performance of SCISEs [8]. Our research team has used as mediation material a nanocomposite consisting of copper oxide nanoparticles and multi-walled carbon nanotubes, which was implemented into a polymer nitrate sensitive membrane.

**Experimental:** As a preliminary step, solid contact electrodes with glassy carbon substrates were pretreated. It involved mechanical polishing of the SCISEs on felt with wetted aluminum oxide. The electrodes were then rinsed with distilled water and then placed in an ultrasonic bath to remove any residual $Al_2O_3$. In the next step, the nanocomposite mixture was prepared - 2.5 mg each of multi-walled carbon nanotubes (MWCNTs) and copper oxide nanoparticles (CuONPs) were weighed, 0.5 ml of tetrahydrofuran (THF) was added, and the whole mixture was dispersed in the ultrasonic bath for 1 h. The mixture was left for 24 hours to evaporate the solvent. An active complex with the formula $Co(Bphen)_2(NO_3)_2(H_2O)_2$ was prepared by the reaction of an aqueous solution of cobalt(II) nitrate with 4,7-diphenyl-1,10-phenanthroline (Bphen) (the complex acted as an ionophore). The process was carried out in the same way as described in publication [9]. Subsequently, 0.3 g of membrane mixture was prepared with the following percentage composition of weight - 2% MWCNTs/CuONPs nanocomposite, 62% NPOE, 32% PVC, and 6% $Co(Bphen)_2(NO_3)_2(H_2O)_2$ (for unmodified electrodes, the weight % composition is 0% MWCNTs/CuONPs, 62% NPOE, 32% PVC, 6% $Co(Bphen)_2(NO_3)_2(H_2O)_2$). The weighted components were dissolved in 3 ml of THF to make a membrane cocktail, which was then spotted onto the surface of the glassy carbon electrode in three series of 50 µl. The electrodes were left to evaporate the THF for 24 hours in a tripod and then immersed in $1\times10^{-3}$ M $KNO_3$ solution for several days to condition them. As a result, two pairs of electrodes were obtained - a pair of unmodified electrodes (GCE/ISM) and a pair of electrodes with a nanocomposite-modified membrane (GCE/NC+ISM).

**Results:** The calibration curve in the concentration range of $1\times10^{-7}$-$1\times10^{-1}$ M was determined for the electrodes prepared as described above by adding appropriate additions of the standard solution. From the plotted response curves, the slope of the characteristic, the range of linearity and the detection limit were determined and presented in Table 1.

**Table 1.** Parameters determined on the basis of response curves of solid contact ion-selective electrodes.

| Parameter | GCE/ISM | GCE/NC+ISM |
|---|---|---|
| Slope [mV/decade] | 58.16 | 59.56 |
| Linearity range [M] | $1\times10^{-1}$-$5\times10^{-6}$ | $1\times10^{-1}$-$1\times10^{-6}$ |
| Detection limit [M] | $5.58\times10^{-6}$ | $9.89\times10^{-7}$ |

To test whether the mediating material introduced into the membrane performs its function and improves the ion-to-electron conductivity, a measurement of short-term potential stability was performed. The measurement was carried out for about 4 hours in $1\times10^{-1}$ M $KNO_3$ solution. The dependence on the electromotive force on time is graphically shown in Fig.1. From the resulting data, the potential drift was calculated (potential drift = $\Delta E/\Delta t$; where $\Delta E$ - a difference of initial and final potential, $\Delta t$ = a time difference), which defines at what extent the electrode shows potential stability. Respectively, for the electrode unmodified and modified with MWCNTs/CuONPs nanocomposite, it was 7.13 mV/h and 0.54 mV/h.

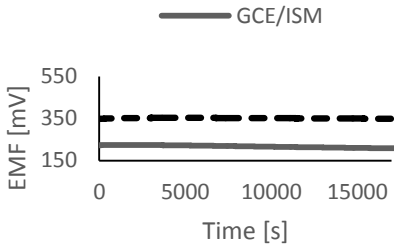



**Fig.1.** Short-term stability of the potential.

The parameter that determines whether modification of the membrane with the nanocomposite gave the desired results is, on par with the stability of the potential, the reversibility of the potential. To determine this parameter, alternating electromotive force measurements were carried out in solutions of $1\times10^{-4}$ M and $1\times10^{-3}$ M, in 5 series of 5 minutes each. Based on the results, the average values of the potential were determined along with the standard deviations for specific concentrations and included in Table 2.

**Table 2.** Mean potential values and standard deviations for nitrate SCISEs.

| Concentration of $KNO_3$ solution | GCE/ISM | GCE/NC+ISM |
|---|---|---|
| $1\times10^{-3}$ M | 485.12±1.29 | 421.65±0.31 |
| $1\times10^{-4}$ M | 532.87±1.69 | 475.87±0.82 |

In order to check whether the interfering ions in the test sample significantly affect the electrode potential and interfere with the measurement for the main ion, logarithmic selectivity coefficients were determined against four different interferents (Table 3).

Acetates ($CH_3COO^-$), carbonates ($CO_3^{2-}$), nitrite ($NO_2^-$) and chlorides ($Cl^-$) were selected as interfering anions.

**Table 3.** The values of the potentiometric selectivity coefficient of the tested $NO_3^-$-ISEs.

| Electrode | Potentiometric selectivity coefficient | | | |
|---|---|---|---|---|
| | $CH_3COO^-$ | $CO_3^{2-}$ | $NO_2^-$ | $Cl^-$ |
| GCE/ISM | -4.45 | -4.67 | -2.09 | -2.01 |
| GCE/NC+ISM | -5.78 | -4.96 | -3.19 | -2.49 |

**Conclusions:** This work aimed to improve the performance of nitrate ion-selective electrodes with a solid contact. For this purpose, a MWCNTs/CuONPs nanocomposite was used as a transducer media, which was introduced as one of the components of the ion-sensitive membrane. A series of tests were carried out, based on which a deeper analysis was performed. The values of the slope, detection limit, and linearity range were read from the characteristics of SCISEs. For both types of electrodes, these parameters were very similar, but those for the nanocomposite-modified electrode were the ones with better values - a slope closer to Nernst's value (59.16 mV/decade), a wider range of linearity and a lower detection limit. This confirms that the introduced conductive material fulfills its role. Furthermore, this is validated by the significantly better stability and potential reversibility values that were obtained. Those are two parameters by which we can most accurately evaluate the effectiveness of the introduced mediation material. A 13 times lower potential drift and relatively better reversibility as evidenced by lower standard deviation values were obtained for the GCE/NC+ISM electrode. To examine whether the modified membrane provides adequate selectivity for $NO_3^-$ ions against interfering ions, potentiometric selectivity coefficients were determined. The smaller values of this parameter for all interfering ions were obtained for the GCE/NC+ISM electrode, indicating that these interferents had little effect on the potential measured for the main ion. Accordingly, it was concluded that the implementation of a nanocomposite of multi-walled carbon nanotubes and copper(II) oxide nanoparticles into an ion-sensitive membrane contributed to the improvement of all tested parameters of nitrate SCISEs, which confirms that it performs very well in the role of transducer media.

## References:

1. M.H. Ward, R.R. Jones, J.D. Brender, T.M. De Kok, P.J. Weyer, B.T. Nolan, C.M. Villanueva, S.G. Van Breda, International Journal of Environmental Research and Public Health, 15 (2018) 1557.
2. S. Singh, A.G. Anil, V. Kumar, D. Kapoor, S. Subramanian, J. Singh, P.C. Ramamurthy, Chemosphere, 287 (2022) 131996.
3. M. Karwowska, A. Kononiuk, Antioxidants, 9 (2020) 241.
4. S.F. Oman, M.F. Camoes, K.J. Powell, R. Rajagopalan, P. Spitzer, Pure and Applied Chemistry, 79 (2007) 67.
5. J. Schwarz, K. Trommer, M. Mertig, American journal of Analytical Chemistry, 9 (2018) 591.
6. N.M. Ivanova, M.B. levin, K.N. Mikhelson, Russian Journal Bulletin, 61 (2013) 926.
7. C. Wardak, K. Morawska, K. Pietrzak, Materials, 16 (2023) 5779.
8. C. Wardak, K. Pietrzak, K. Morawska, M. Grabarczyk, Sensors, 23 (2023) 5839.
9. K. Pietrzak, C. Wardak, R. Łyszczek, Electroanalysis, 32 (2020) 724.

# APPLICATION OF COLD VAPOUR STRIPPING VOLTAMMETRY FOR DETERMINATION OF TOTAL MERCURY

**I. GĘCA, M. KOROLCZUK**, Maria Curie-Sklodowska University, Faculty of Chemistry, Institute of Chemical Sciences, Department of Analytical Chemistry, M. Curie-Sklodowska Sq. 3, 20-031 Lublin, Poland.

**Abstract:** a simple and sensitive procedure for mercury determination by cold vapour stripping voltammetry is described. Mercury ions present in the sample solution were reduced in a closed vessel to metallic mercury using $SnCl_2$. Then metallic mercury was transferred to a gas phase by using ultrasound irradiation. Accumulation of mercury was performed from the gas phase using a gold film electrode. An anodic stripping voltammogram was recorded from 0.1 mol $L^{-1}$ $HClO_4$ + $3\times10^{-3}$ mol $L^{-1}$ HCl solution. The calibration graph was linear from $1\times10^{-9}$ to $1\times10^{-8}$ mol $L^{-1}$ for the accumulation time of 300 s. The relative standard deviation of 4.3 % for $3\times10^{-9}$ mol $L^{-1}$ of Hg was obtained.

**Introduction:** The monitoring of mercury (Hg) in natural waters is a very important issue due to its high toxicity and a very high bioaccumulation factor in the food chain [1]. Concentration levels of mercury in the environment are very low so for its determination highly sensitive detection methods are needed. Traditionally, the cold vapour technique coupled with atomic absorption spectrometry, atomic fluorescence spectrometry or inductively coupled plasma-mass spectrometry are the most commonly used for determining mercury at trace-level concentrations. Anodic stripping voltammetry (ASV) is a widely used analytical technique that provides trace metal determination at low costs. A high sensitivity of ASV is a result of the 'built-in' preconcentration step, during which the target metals are preconcentrated on the surface of the working electrode. Among other heavy metals, mercury is one of the most frequently controlled pollutants by ASV. Various electrode materials have been proposed for the determination of mercury by stripping voltammetry. Gold and gold film electrodes are generally preferred since gold has a high affinity with mercury, which enhances the preconcentration effect by amalgam formation. Modified carbon electrodes have also been proposed for mercury quantification and its speciation. Accumulation of mercury at the working electrode has been usually carried out from a stirred sample solution. Some examples of mercury accumulation from the gas phase exploiting the cold vapour technique can be found in the literature [2-3]. In article [2] mercury from the vapour was accumulated at a gold rotating disk electrode and then the electrode was transferred to a suitable electrolyte and quantified by ASV. In paper [3] lower detection limits for Hg were reported following the accumulation of mercury from the gas phase. In this procedure, mercury vapour was directed to the electrode using a capillary while the gas containing mercury had to be dried using two drying tubes. The cold vapour technique was also used for the accumulation of mercury from a large volume sample and then for electrochemical determination [4] and for speciation of mercury [5].
Ultrasound–assisted vapour generation of mercury from liquid to a gas phase is known in the literature [6] and used for mercury determination and its speciation in water and

solid samples. In the mentioned work, mercury was determined using cold vapour atomic absorption spectrometry.
In the present work, a simple procedure for mercury quantification by ASV after its accumulation from the gas phase is presented. Thanks to using an uncomplicated, home-made arrangement the proposed procedure can be used under field conditions. Although reports on mercury determination by stripping voltammetry following accumulation from the gas phase can be found in the literature [2-3], in all reported procedures, the arrangement was unsuitable for measurements under field conditions. The preliminary experiments performed using a very simple arrangement, as shown in Fig. 1, prove that mercury can be determined with satisfactory precision, so optimization of the measuring conditions was performed.

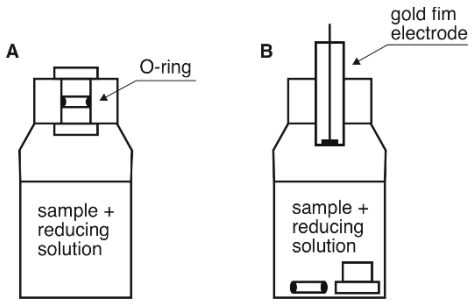



**Fig.1.** Schematic diagram of the sample preparation (A) and accumulation of mercury from the gas phase using a gold film electrode (B).

**Experimental:** The measurements were performed using μAutolab analyser made by Eco Chemie, the Netherlands. A classical three-electrode quartz cell of a volume of 10 mL was used. A glassy carbon electrode of diameter of 1 mm was polished daily using 0.3 μm alumina slurry on a Buehler polishing pad. Pt wire and Ag/AgCl were used as auxiliary and reference electrodes. The ultrasonic cleaner Sonic-3 was made by Polsonic, Poland.
The gold film was plated before each measurement at a glassy carbon electrode from a solution containing 0.025 mol $L^{-1}$ HCl + $2.5\times10^{-4}$ mol $L^{-1}$ $HAuCl_4$ + 4 g $L^{-1}$ urea. Gold was accumulated for 60 s at a potential of -0.6 V from a stirred solution. Then the electrode was washed with water and dried with a cold air stream. Such an electrode was used for mercury accumulation. After each measurement, the gold film was removed from a glassy carbon electrode by alternately electrode polarization at potentials of 0.9 V (1 s) and -0.6 V (1 s) from a solution containing 0.7 mol $L^{-1}$ HCl + 0.3 mol $L^{-1}$ $HNO_3$. Such a cycle was repeated thirty times. After this stage, an electrode was washed with water and transferred to the plating solution. The preparation of the new gold film electrode after each measurement lasted approximately 2 min. Although different procedures for a gold surface regeneration for mercury determinations by ASV can be found in the literature, the most reproducible results were obtained when a new gold film was plated before each measurement in the case of the presented research.
An aliquot of the analyzed sample was pipetted into the glass bottle and then 1.5 mL 2 mol $L^{-1}$ $H_2SO_4$ were added. If necessary, water was added to the volume of 15 mL. Next 1.5 mL of reducing solution was added and the bottle was closed as shown in Fig.1A.

The bottle with the sample was treated with ultrasounds for 1 min. During this time metallic mercury from the sample was transferred to a gas phase. Then the bottle was left for 2 min. At this stage microdroplets of the sample solution present in the gas phase went down to the solution. In such a way the vapour was partially dried before each measurement. The presence of the microdroplets of the sample solution in the gas phase led to poor reproducibility of the determination results because of blocking the surface of the electrode. Next, the gold film electrode was transferred to a gas phase by sticking it to the bottle with the sample solution as shown in Fig.1B and mercury was accumulated for 300 s without applying potential. Then the electrode with accumulated mercury was transferred to a voltammetric cell containing 0.1 mol $L^{-1}$ $HClO_4$ + 0.003 mol $L^{-1}$ HCl and a differential pulse voltammogram was recorded while the potential was scanned from +0.2 to +0.85 V (scan rate of 0.04 V $s^{-1}$). The amplitude and the potential step were 50 and 4 mV, respectively. The measurements were carried out at room temperature from undeaerated solutions. All solutions (reducing, plating and stripping solutions) were prepared daily before analysis. The total time of a single analysis with the accumulation time of 300 s was about 600 s.

**Results:** The results of optimization of a volume of the solution, time of ultrasounds irradiation and time of mercury accumulation are presented below.

In all measurements, the volume of the bottle was constant and equal to 33 mL. The volume of the solution used for measurements was changed from 5 to 25 mL. The measurements were carried out at standard conditions for the sample solution containing $3\times10^{-9}$ mol $L^{-1}$ Hg(II). The time of ultrasound irradiation and accumulation was 60 and 300 s, respectively. In these measurements, the volume of the reducing solution added to the sample was ten times smaller than the volume of the sample. For further measurements, the volume of the sample equal to 15 mL was chosen as an optimal value.

The time of ultrasound irradiation of the sample solution with the reducing solution was changed from 30 to 600 s. The measurements were carried out for the sample solution containing $3\times10^{-9}$ mol $L^{-1}$ Hg(II) and accumulation time equal to 300 s. For further measurements, an ultrasound irradiation time equal to 60 s was chosen.

The effect of the accumulation time of mercury from the gas phase was studied at standard conditions for a solution containing $3 \times 10^{-9}$ mol $L^{-1}$ Hg(II) from 30 to 600 s. It was observed that the mercury peak increased almost linearly with an increase of the accumulation time up to 300 s and then levels off. For further measurements, an accumulation time of 300 s was chosen.

The calibration plot for the accumulation time of 300 s was linear from $1\times10^{-9}$ to $1\times10^{-8}$ mol $L^{-1}$ and obeyed the equation $y = 0.43\ x + 0.01$, where y and x are the peak current (μA) and Hg(II) concentration (nmol $L^{-1}$), respectively. The correlation coefficient r was 0.998. The voltammograms obtained for various Hg(II) concentrations are presented in Fig.2. The relative standard deviation for Hg(II) determination at a concentration of $3\times10^{-9}$ mol $L^{-1}$ was 4.3 % (n=5). The detection limit was equal to $1.1\times10^{-10}$ mol $L^{-1}$ and was lower or comparable to values usually reported for determinations following direct accumulation from the sample solution. The blank value was caused by the presence of Hg(II) in reagents used for the preparation of the sample and from laboratory air. The blank value and detection limit can be decreased by using higher-quality reagents and performing the measurements in a cleaner room. Some papers in the literature report

lower detection limits than the presented one, but the determinations were carried out using blank subtraction [7] or very long preconcentration time [8].

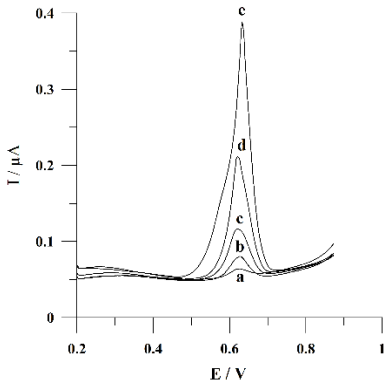



**Fig.2.** Differential pulse voltammograms obtained for various concentrations of Hg(II) following accumulation from the gas phase for 300 s. Concentration of Hg(II) ions: a) 0; b) $1\times10^{-9}$; c) $2\times10^{-9}$; d) $5\times10^{-9}$; e) $1\times10^{-8}$ mol $L^{-1}$.

The proposed procedure was applied for the mercury determination in certified reference material NASS-5. The material was not certified for mercury, however, the obtained result of 0.48 μg $L^{-1}$ with a standard deviation of 4.3 % (n=5) agrees well with the value of $0.53 \pm 0.07$ μg $L^{-1}$ reported in the article [9].

**Conclusions:** A simple procedure for mercury determination by cold vapour stripping voltammetry was proposed. Ultrasound irradiation of the sample is a simple and effective way to separate metallic mercury from liquid to a gas phase. Because of using a simple arrangement the procedure can be exploited under field conditions. The obtained detection limit is lower than most commonly reported ones following direct accumulation from a liquid sample. Interferences of the sample matrix are minimized because metallic mercury was transferred from the sample solution to the gas phase.

**References:**

1. K. Leopold, M. Foulkes, P.J Worsfold, Trends in Analytical Chemistry, 28 (2009) 426.
2. F. Scholz, L. Nitschke, G. Henrion, Analytica Chimica Acta, 199 (1987) 167.
3. M. Korolczuk, Microchemical Journal, 57 (1997) 81.
4. J. Chylkova, R. Selesovska, J. Machalikova, Central European Journal of Chemistry, 5 (2007) 479.
5. O. Abollino, A. Giacomino, M. Malandrino, S. Marro, E. Mentasti, Journal of Applied Electrochemistry, 39 (2009) 2209.
6. S. Gil, I. Lavilla, C. Bendicho, Analytical Chemistry, 78 (2006) 6260.
7. O. Abollino, A. Giacomino, M. Malandrino, G. Piscionieri, E. Mentasi, Electroanalysis, 20 (2008) 75.
8. Q. Wu, S. C. Apte, G. E. Batley, K. C. Bowles, Analytica Chimica Acta, 350 (1997) 129.
9. E. L. Seibert, V. L. Dressler, D. Pozebon, A. J. Curtius, Spectrochimica. Acta B, 56 (2001) 1963.

# DETERMINATION OF FOLIC ACID BY ADSORPTIVE STRIPPING VOLTAMMETRY USING A BISMUTH FILM-COATED GOLD MICROELECTRODE ARRAYS

**M. OCHAB, I. GĘCA**, Maria Curie-Sklodowska University, Faculty of Chemistry, Institute of Chemical Sciences, M. Curie-Sklodowska Sq. 3, 20-031 Lublin, Poland.

**Abstract:** Folic acid (FA) is one of the vitamins necessary for the proper functioning of the human body. Due to the limited possibility of synthesizing simple compounds from molecules, it should be provided through a properly balanced diet and supplementation. This communication presents a sensitive procedure for the determination of FA using bismuth film-coated gold microelectrode arrays as a working electrode by adsorptive stripping voltammetry. Under optimized conditions with an accumulation time of 60 s, a linear range of the calibration curve was obtained in the range from $1\times10^{-9}$ to $2\times10^{-8}$ mol $L^{-1}$ of FA. The procedure was used for determining folic acid in a pharmaceutical preparation.

**Introduction:** Folic acid is a compound essential for the normal growth and functioning of cells of the nervous and hematopoietic systems. It has an important role in tissues where intensive cell division occurs, for example, in the fetus's tissues and gastrointestinal epithelium. Since folic acid is not synthesized in the human body, it is necessary to take it in adequate amounts for the proper functioning of the body. In the case of its deficiency, it is necessary to balance the diet with products rich in natural folates and use an appropriate supplementation. It is especially recommended for women who are planning a pregnancy or are pregnant, and for people with megaloblastic anemia and diabetes. Folic acid participates in the synthesis of nucleic acids and is involved in the production of red blood cells, and is therefore essential for the proper growth of the unborn child [1]. Particularly important is the formation of the neural tube, from which the baby's brain and spinal cord are formed later. Defects in the neural tube lead to malformations of the child, such as brainlessness, cerebral hernia, spina bifida and many others. In Poland, neural tube defects are the most common cause of neonatal deaths [2,3]. For this reason, women of reproductive age and families burdened with neural tube defects should take 0.4 mg of folic acid daily in the form of pharmaceuticals in addition to dietary folate.

For the determination of folic acid, various analytical techniques are used, including spectrophotometry [4], chemiluminescence [5] or high-performance liquid chromatography [6]. Some of the mentioned techniques are nonspecific and time-consuming, and the measurement methods are associated with high costs, long analysis times, and the operation of the equipment required by qualified personnel. Electrochemical methods are an alternative to these methods. Folic acid is most often determined by adsorption stripping voltammetry (AdSV). Lead or bismuth film electrodes can be used for the voltammetric determination of FA [7,8]. Most often, glassy carbon is used as a substrate for generating a metal film but it is also possible to generate a metal film on the gold substrate. Gold, despite its disadvantage of price, is often used as an electrode material in voltammetry. This is due to its high passivity, wide anodic potential range (up to about 1.2 V) and high electrical conductivity. Gold is often

used in the form of solid microelectrodes, a gold film or as an additive to a composite material in the form of nanoparticles. In the case of a single disc-shaped gold microelectrode (less than 25 μm in diameter), the measured currents are on the order of nA, which requires very sensitive apparatus. The solution to this problem is to use an array of microelectrodes, where the array contains several or even several hundred microelectrodes connected in a common array (AuMEA). The measured current is the sum of the currents of the individual electrodes in the array.
The study aimed to develop a rapid and sensitive procedure for the determination of folic acid on bismuth film-coated gold microelectrode arrays (BiF/AuMEA).

**Experimental:** Measurements were carried out in a classical measuring cell (10 mL) in a three-electrode system using an Autolab PGSTAT 302N electrochemical analyzer. The reference electrode was the (Ag/AgCl) electrode while the counter electrode was a platinum wire. The working electrode was an electrode in the form of a gold microelectrode array, containing 796 single microelectrodes. The electrode was obtained by filling a quartz preform with melted gold under increased pressure. The active area of the electrode was estimated to be 0.076 $mm^2$. Preparation of the working electrode before measurements consisted of mechanically polishing it on 2500-grit sandpaper and rinsing it in an ultrasonic cleaner. A gold microelectrodes array coated with in situ generated bismuth film was used to determine folic acid by adsorptive stripping voltammetry. The measurements were carried out as follows: for 1 s the electrode was polarized with a potential of -2.0 V to activate the electrode. Then, for 60 s at a potential of -0.4 V, a bismuth film was simultaneously generated and folic acid was accumulated by adsorption. After a rest period of 10 s, the square wave adsorptive stripping voltammogram was recorded by changing the potential from -0.35 to -0.8 V. The frequency, amplitude and step potential were 200 Hz, 20 mV and 5 mV, respectively. All measurements were performed from an undeaerated solution.

**Results:** To optimize the analytical procedure, the effects of supporting electrolyte composition, bismuth film generation conditions, potential and accumulation time on the FA were investigated. Figure 1A shows the effect of acetate buffer concentration (pH 5.0) on the FA signal for an accumulation time of 60 s. Under optimized conditions, a linear range of the calibration curve from 1 to 20 nmol $L^{-1}$ was obtained for an accumulation time of 60 s. The value of the correlation coefficient $R^2$ was 0.9992. Fig. 1B shows the voltammograms recorded during the determination of the calibration curve of FA. The limit of detection of folic acid for an accumulation time of 60 s was 0.5 nmol $L^{-1}$.
The developed procedure was applied to the determination of folic acid in the pharmaceutical preparation "Kwas foliowy" made by DOZ PRODUCT, Poland. One tablet of the preparation contained a declared amount of 400 μg of folic acid. The sample was prepared by crushing the tablet in an agate mortar and then transferred to a volumetric flask with the addition of NaOH solution. The standard addition method was used to determine FA in the preparation. A FA content of 410 ± 14 μg per tablet was obtained, which is in accordance with the value declared by the manufacturer. Fig. 1C shows the voltammograms recorded during the determination of FA content in the pharmaceutical preparation.

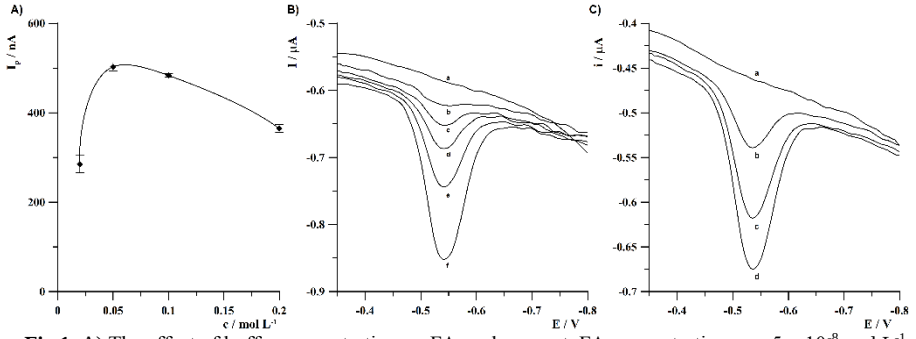



**Fig.1.** A) The effect of buffer concentration on FA peak current. FA concentration was $5 \times 10^{-8}$ mol $L^{-1}$. B) AdSV voltammograms obtained for increasing FA concentrations: a) blank; b) $1 \times 10^{-9}$; c) $2 \times 10^{-9}$; d) $5 \times 10^{-9}$; e) $1 \times 10^{-8}$; f) $2 \times 10^{-8}$ mol $L^{-1}$ of FA. C) AdSV voltammograms obtained during the determination of FA in a pharmaceutical preparation (Folic Acid 400 µg per tablet): a) sample; b) as (a) + $1 \times 10^{-8}$; c) as (a) + $2 \times 10^{-8}$; d) as (a) + $3 \times 10^{-8}$ mol $L^{-1}$ of FA. Deposition conditions: -0,4 V, 60 s; Bi(III) concentration: $2 \times 10^{-6}$ mol $L^{-1}$.

**Conclusions:** BiF/AuMEA can be used for rapid determination of nanomolar concentrations of folic acid by adsorptive stripping voltammetry. The detection limit of 0.5 nmol $L^{-1}$ for FA obtained on BiF/AuMEA is lower to the value obtained on BiFE/GCE (4.1 nmol $L^{-1}$ for an accumulation time of 30 s [7]) and comparable to PbFE/GCE. The advantage of BiF/AuMEA over PbFE is the lack of use of toxic lead ions for lead film formation.

## References:

1. A.J. Greenberg, J.S. Bell, Y. Guan, Y. Yan-hong, Reviews in Obstetrics & Gynecology, 4 (2011) 52.
2. Z.J Brzeziński, T. Mazurczak, Pediatria Polska, 69 (1994) 684.
3. M. Makowska-Donajska, L. Hirnle, Ginekologia i Perinatologia Praktyczna, 4 (2017) 166.
4. P. Nagaraja, R.A Vasantha, H.S Yathirajan, Analytical Biochemistry, 307 (2002 ) 316.
5. S.M Wabaidur, S.M Alam, S.H Lee, Z.A Alothman, G.E. Eldesoky, Spectrochimica Acta Part A: Molecular and Biomolecular Spectroscopy, 105 **(**2013) 412.
6. A. Mahato, S. Vyas, N.S. Chatterjee, Journal of Analytical Chemistry and Microbiology, 103 (2020) 73.
7. M. Korolczuk, K. Tyszczuk, Electroanalysis, 19 (2007) 1959.
8. M. Štěpánková, R. Šelešovská, L. Janíková, J. Chýlková, I. Švancara, Monatshefte für Chemie - Chemical Monthly, 148 (2017) 423.

# STATE-OF-ART ELECTRODE MATERIALS IN VOLTAMMETRY ULTRATRACE ANALYSIS OF ACYCLOVIR

**D. GORYLEWSKI, K. TYSZCZUK-ROTKO, K. STANIEC, A. KELLER**, Maria Curie-Skłodowska University, Faculty of Chemistry, Institute of Chemical Sciences, Department of Analytical Chemistry, M. Curie-Skłodowska Sq. 3, 20-031 Lublin, Poland.

**Abstract:** There are many different types of electrode materials available for purchase, which most often constitute the basis for further modifications. The most popular are glassy carbon electrodes and paste electrodes, which can be easily modified by carbonaceous materials, metal oxides nanoparticles, ionic liquids as well as different types of polymers. The voltammetric procedures developed on their basis are complex, require multi-stage preparation process and are characterized by average analytical parameters in acyclovir (ACY) analysis. Very interesting electrode material is screen-printed carbon (SPC), which can be easily electrochemically activated before voltammetric measurements. This work presents a summary of the literature data concerning the newest voltammetric procedures for the determination of ACY.

**Introduction:** The *Herpesviridae* family contains numerous viruses that can be found globally and infect a variety of organisms, including humans. These viruses are classified as a double-stranded DNA viruses and have a strong preference for their host. Two specific types: Herpes simplex virus type 1 (HSV-1) and type 2 (HSV-2), target the human body. Symptoms of infection vary depending on the type of virus and often manifesting as a painful red blisters on the lips or genital area. Herpes viruses can establish latent infections, becoming active during certain triggers and then entering a dormant phase. There is currently no vaccine available to prevent Herpes simplex infection, requiring the use of antiviral drug therapy to manage symptoms. Research indicates that a significant part of population is seropositive for HSV type 2, and connections have been made between HSV and Alzheimer's disease. Ongoing efforts are dedicated to developing treatments for alleviation of symptoms of HSV, with drugs like ganciclovir (GCV), penciclovir (PCV), and acyclovir (ACY) commonly used to treat infections [1].

Acyclovir (2-amino-9-[(2-hydroxyethoxy)methyl]-3.9-dihydro-6H-purin-6-one, ACY) which summary formula is shown in Fig.1 is a guanine analogue that is one of the most popular antiviral drug for descending HSV infection symptoms. This drug is valued for its high selectivity and high safety. ACY is metabolized in the human body by only 15–20%, and the rest is excreted in urine in an unchanged form becoming a pollutant that could potentially end up in the natural environment affecting living organisms [1].

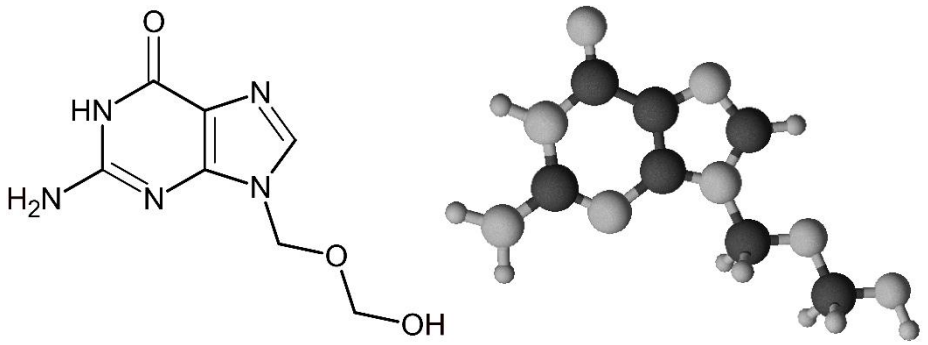



**Fig.1.** Structural formula of acyclovir.

Many methods for ACY determination utilize chromatography and spectroscopy has been presented in the literature [2-4]. However concentration of acyclovir in the environment and in sewage are very small as well as these methods do not allow for direct analysis of ACY and require complicated sample preparation steps. The potential solution to these problems comes from voltammetry - an electrochemical analytical technique that uses the relationship between the applied potential (U) and the current response (I) that accompanies electrode reaction. Voltammetric procedures are highly sensitive and repeatable, allowing to achieve quite low detection limits of the tested electroactive substances, including acyclovir [1, 5-9]. Most of the presented concepts of acyclovir determination are using complex modified sensors based on glassy carbon electrode (GCE) [6], carbon paste electrodes (CPE) [7, 8] and pencil graphite electrode (PGE) [5]. Performing measurements on unmodified sensor is associated with low sensitivity of the determinations. Therefore most of the presented sensors are chemically modified.

Very interesting electrode material is screen-printed carbon (SPC), which can be easily electrochemically activated before voltammetric measurements [1].

**Results:** A numerous of electrochemical procedures for the determination of acyclovir in samples with various matrices have been described in the literature, and are presented in Table 1 [1, 5-9]. Most of them are time-consuming and require a complicated process of sensor preparation before analysis. The presented chemically modified electrodes are characterized by quite wide ranges of calibration curve linearity, and the lowest detection limit value was obtained in the case of pencil graphite electrode modified by ruthenium nanoparticles and thiobarbituric acid (RuNPs/TBA/PGE) – $8.0 \times 10^{-10}$ mol $L^{-1}$. The purpose of modifying commercially available electrodes is to increase the sensitivity of the performed analyses. Usually, unmodified electrodes have significantly weaker parameters than their modified counterparts and cannot compete with complex sensors [9]. In the case of electrochemically activated screen-printed carbon electrode (aSPCE), the trend turned out to be different. This sensor is only electrochemically activated before the series of voltammetric measurements. This easy form of sensor preparation allowed to develop very sensitive voltammetric procedure for ACY determination, which outperforms modified and complicated sensors presented in the literature [5-8].

**Table 1.** Voltammetric ACY determination procedures.

| Sensor | Technique | Linear range [μmol $L^{-1}$] | LOD [μmol $L^{-1}$] | Ref. |
|---|---|---|---|---|
| aSPCE | DPAdSV | 0.5–50.0<br>50.0–1000.0 | 0.00012 | [1] |
| RuNPs/TBA/PGE | DPAdSV | 0.003–0.030<br>0.030–3.0 | 0.00080 | [5] |
| GC/CNT/ILC/RGO/$MnO_2$ | DPV | 0.01–30 | 0.00084 | [6] |
| ND@Dy2O3-IL/CPE | SWV | 0.097–116.6 | 0.029 | [7] |
| P-OAP/MWCNTs-ZnO NPs-CPE | DPV | 0.399–35.36 | 0.30 | [8] |
| FTO | SWV | 4.0–40.0 | 1.25 | [9] |

**Techniques**: DPAdSV – differential-pulse adsorptive stripping voltammetry; DPV – differential-pulse voltammetry; SWV – square-wave voltammetry.
**Sensors:** aSPCE—electrochemically activated screen-printed carbon electrode; RuNPs/TBA/PGE – pencil graphite electrode modified by ruthenium nanoparticles and thiobarbituric acid; GC/CNT/ILC/RGO/$MnO_2$ – glassy carbon electrode modified with layers of multi-walled carbon nanotubes (CNT), an ionic liquid crystal (ILC), graphene (RGO) and $MnO_2$; P-OAP/MWCNTs-ZnO NPs-CPE – poly (o-aminophenol)/multi-walled carbon nanotubes-ZnO nanoparticles-carbon paste electrode; P-OAP/MWCNTs-ZnO NPs-CPE – poly (o-aminophenol)/multi-walled carbon nanotubes-ZnO nanoparticles-carbon paste electrode; FTO – fluoride doped oxide electrode.

**Conclusions:** Voltammetric procedures described in the literature [1, 5-9] have been used to determine acyclovir in pharmaceuticals and body fluids samples. Most of them utilize complex sensors based on multi-stage preparation procedures. Glassy carbon electrodes and paste electrodes are usually used as a base for more complicated modifications by carbonaceous materials, metal oxides nanoparticles, ionic liquids as well as different types of polymers. However, elaboration of electrochemically activated screen-printed carbon electrode (aSPCE) showed that achieving good analytical performance does not have to involve a complicated preparation procedure of sensor.

## References:

1. K. Tyszczuk-Rotko, K. Staniec, D. Gorylewski, A. Keller, Sensors, 24 (2024) 1125.
2. M.M. Ayad, H.E. Abdellatef, M.M. El-Henawee, H.M. El-Sayed, Spectrochimica Acta Part A: Molecular and Biomolecular Spectroscopy, 66 (2007) 106.
3. L. Yu, B. Xiang, Microchemical Journal, 90 (2008) 63.
4. C. Shao, Journal of Analytical & Bioanalytical Techniques, 3 (2012) 139.
5. M. Lalei, K. Zarei, Microchemical Journal, 190 (2023) 108667.
6. N.F. Atta, A. Galal, Y.M. Ahmed, Journal of Electroanalytical Chemistry, 838 (2019) 107.
7. M. Ghadirinataj, S.K. Hassaninejad-Darzi, H. Emadi, Electrochimica Acta, 450 (2023) 142274.
8. G. Karim-Nezhad, A. Sarkary, Z. Khorablou, P.S. Dorraji, Iranian Journal of Pharmaceutical Research, 9 (2018) 52.
9. F. Martínez-Rojas, M.A. Del Valle, M. Isaacs, G. Ramírez, F. Armijo, Electroanalysis, 29 (2017) 2888.

# FAST, SIMPLE AND SENSITIVE VOLTAMMETRIC DETERMINATION OF CURCUMIN VIA VARIOUS SENSORS

**D. GORYLEWSKI, K. TYSZCZUK-ROTKO, A. KELLER, K. STANIEC**, Maria Curie-Skłodowska University, Faculty of Chemistry, Institute of Chemical Sciences, Department of Analytical Chemistry, M. Curie-Skłodowska Sq. 3, 20-031 Lublin, Poland.

**Abstract:** This paper describes very sensitive electrochemical sensors used for the voltammetric determination of curcumin (CCM) - yellow polyphenolic antioxidant compound, which exhibits keto-enol tautomerism and is derived from the root of the *Curcuma longa* (turmeric) plant. The developed procedures use screen-printed electrodes as well as are based on glassy carbon and paste electrodes. This sensors were often modified and thanks to this step it were possible to develop a new high sensitive procedures with a wide range of linearity of the calibration curves. These voltammetric procedures have been used to determine CCM in various food products.

**Introduction:** Curcumin (Curcumin ((E,E)-1,7-bis(4-Hydroxy-3-methoxyphenyl)-1,6-heptadiene-3,5-dione, CCM) is a yellow polyphenolic compound exhibits keto-enol tautomerism and is derived from the root of the *Curcuma longa* (turmeric) plant (**Fig. 1**). CCM has anti-tumoral, anti-amyloid, and anti-inflammatory properties and exhibits diverse biological activities as well as pharmacological effects, including its antioxidant properties, which involve curcumin's ability to prevent the production of free radicals in the bloodstream and tissues. CCM is used for treating conditions like malaria, diabetes, arthritis, skin diseases, and cardiovascular diseases, as well as those related to the nervous system like dementia, Alzheimer's, or multiple sclerosis. CCM is deemed safe with no toxic, teratogenic, or genotoxic effects. However, excessive doses exceeding 12 g per day can lead to health issues like diarrhea, nausea, and chronic abdominal pain [1-4]. Curcumin is used most often as a coloring agent in food industry as well as a spice.

Because of the increasing interest in the benefic qualities of CCM and the subsequent rise in the number of research about this compound, there is a demand for development of precise and reliable methods for detecting CCM. For this purpose many chromatographic and spectroscopic methods has been presented in the literature [5-7]. Also many CCM determination procedures utilize electrochemical methods has been described [2, 8-10]. Electrochemical methods are characterized by high sensitivity, repeatability and low consumption of sample and reagents. Voltammetry, which is one of the electrochemical techniques is determined by much higher sensitivity compared to the chromatographic methods, enabling to establish very low limits of detection (LOD) and quantification (LOQ) in direct analysis. This means that a complicated sample preparation step is usually not required, which may be limited to filtering the sample through a syringe filter with an appropriate pore diameter. Very good analytical parameters are usually associated with the use of an additional stage of accumulating the analyte onto the surface of the working electrode, before the stage of recording the analytical signal.

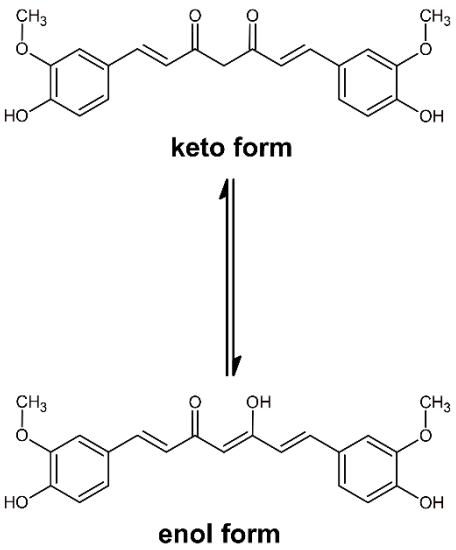



**Fig.1.** Tautomeric structure of curcumin.

One of the most popular working electrode used in voltammetry is glassy carbon electrode (GCE), which have many advantages such as: wide working potential window, chemical inertness, good electrical conductivity, low cost of purchase as well as high repeatability of measurements. Glassy carbon material is obtained by controlled, gradual heating of phenol-formaldehyde resin in an inert atmosphere. The carbonization process is carried out slowly in the temperature range of 300-1200 °C in order to eliminate oxygen, nitrogen and hydrogen. The result is a very hard material with high density, chemical resistance in corrosive conditions, low porosity and good electrical conductivity. Due to the low porosity of the surface, it is possible to repeatedly obtain almost the same surface each time the electrode is mechanically cleaned [11-13].

Another popular electrode material is diamond doped with acceptors such as boron, which is usually acquired by chemical vapor deposition and used for production of conventional sensors as well as screen printed electrodes. The material obtained in this way is characterized by: high resistivity, long lifetime, chemical stability and inertness as well as wide range of work potentials [8]. The inks utilized in screen-printed sensors preparation process include a use of an organic binder made up of a variety of resins and additives, which ultimately leads to a deceleration in the rate of electrochemical reactions. The electrodes are electrochemically activated to eliminate the organic components of the ink, leading to an enhancement in the roughness and active surface area of the working electrode. This process also enables functionalization, ultimately improving the performance of the utilized sensors. There is only one reference [8] in the literature showing the use of electrochemically activated screen-printed boron-doped diamond electrode (aSPBDDE) for the determination of CCM.

Carbon paste electrodes (CPE) are obtained in the most easiest way by mixing of carbon graphite powder and silicone oil in specific ratio in an agate mortar with a pestle to ensure uniformity. The resulting paste is next packed into a Teflon tube and connected to

a copper wire for electrical contact and dried. The electrode surface is smoothed with weighing paper and cleaned with distilled water and the sensor is ready for measurements. One of the variety of CPE used in CCM analysis is sodium dodecyl sulfate modified carbon nanocomposite paste electrode (SDS/nPE) [9].

**Results:** Table 1 shows the analytical parameters of the procedures developed on the basis of previously described sensors, as well as suitable examples of their practical applications has been presented. The developed sensors are characterized by quite good analytical parameters and have been successfully used in the analysis of CCM in food products. However, there is a significant improvement in the analytical parameters, especially in the limit of detection of procedure based on the aSPBDDE.

**Table 1.** Voltammetric CCM determination procedures.

| Sensor | Technique | Linear range [nmol $L^{-1}$] | LOD [nmol $L^{-1}$] | Application | Ref. |
|---|---|---|---|---|---|
| aSPBDDE | DPAdSV | 0.002 – 0.02,<br>0.02 – 0.2,<br>0.2 – 2.0,<br>2.0 – 20.0 | 0.0005 | herbal tea, shot | [8] |
| SDS/nPE | DPV | 200.0 – 1000.0<br>15000.0 – 45000.0 | 27.0 | food supplement | [9] |
| FCNTs/GCE | SWV | 2000.0 – 14000.0 | 60.0 | spice extract turmeric extract | [2] |
| GCE | CV | 9900 – 107000.0 | 410.0 | spice extract | [10] |

**Techniques**: DPAdSV – differential-pulse adsorptive stripping voltammetry; DPV – differential-pulse voltammetry; SWV – square wave voltammetry; CV – cyclic voltammetry.
**Sensors:** aSPBDDE - electrochemically activated screen-printed boron-doped diamond electrode; SDS/nPE - sodium dodecyl sulfate modified carbon nanocomposite paste electrode; FCNTs/GCE – glassy carbon electrode modified with functionalized carbon nanotubes; GCE – glassy carbon electrode.

**Conclusions:** Voltammetric procedures described in the literature [2, 8-10] have been used to determine curcumin in food samples. Most of them have average analytical parameters, including a high limit of detection. The developed procedure using aSPBDDE with conjunction with stripping analysis technique allowed to achieve the lowest LOD values and is characterized with great advantages e.g. immediate readiness for operation, short duration of one measurement and wide linear ranges of calibration curves.

## References:

1. A.H.M.T. Ahmed, H. Naskar, S. Banerjee, B. Ghatak, N. Das, B. Tudu, R. Bandyopadhyay, Sensors and Actuators A: Physical, 344 (2022) 113748.
2. S. Sahoo, A.K. Satpati, Journal of Analysis and Testing, 7 (2023) 136.
3. G. Tigari; J.G. Manjunatha, Monatshefte für Chemie, 151 (2020) 1681.
4. C. Raril, J.G. Manjunatha, G. Tigari, Instrumentation Science & Technology, 48 (2020) 561.
5. S. Noori, A.R. Kiasat, M. Kolahi, R. Mirzajani, S.M.S. Nejad, Journal of Saudi Chemical Society, 26 (2022) 101479.
6. Q. Qin Hu, L. Gao, S. Rao, Z. Yang, T. Li, X. Gong, Food Chemistry, 280 (2019) 195.
7. N. Altunay, A. Elik, R. Gürkan, Food Chemistry, 310 (2020) 125933.
8. J. Kozak, K. Tyszczuk-Rotko, A. Keller, M. Wójciak, I. Sowa, Materials, 16 (2023) 6826.
9. Ch. Raril, J.G. Manjunatha, G. Tigari, Instrumentation Science & Technology, 48 (2020) 561.
10. G.K. Ziyatdinova, A.M. Nizamova, H.C. Budnikov, Journal of Analytical Chemistry, 67 (2012) 591.

11. J. Wang, Stripping Analysis: Principles, Instrumentation, and Applications, VCH Publishers, Weinheim, (1985) 66.
12. N. Y. Stozhko, N. A. Malakhova, M. V. Fyodorov, K. Z. Brainina, Journal of Solid State Electrochemistry, 12 (2008) 1185.
13. U. Bengi, O. A. Sibel, Combinatorial Chemistry & High Throughput Screening, 10 (2007) 295.

# DETERMINATION OF SELECTED MICRONUTRIENTS IN DRIED PLANTS BY X-RAY FLUORESCENCE

**J. BARAN, A. DROZD, A. LASSAK, M. KONDRACKA, A. WATROS**, Łukasiewicz Research Network – New Chemical Synthesis Institute, Analytical Laboratory, Al. Tysiąclecia Państwa Polskiego 13A, 24-100 Puławy, Poland.

**Abstract:** In this study, we present a novel analytical method for the rapid determination of copper (Cu) and manganese (Mn) concentrations in plant material utilizing X-ray fluorescence (XRF) spectroscopy. The method was developed to address the growing need for efficient and reliable techniques in elemental analysis of biological samples. XRF offers advantages such as specificity, rapid analysis, non-destructive nature, and high sensitivity, making it an ideal candidate for elemental analysis in plant materials. The developed method demonstrated excellent performance, exhibiting high sensitivity and accuracy in quantifying Cu and Mn concentrations across a wide range of plant species and tissue types. Moreover, the rapid analysis capability of XRF allows for high-throughput screening of plant samples, facilitating efficient monitoring of nutrient levels and potential environmental stressors. Overall, the presented analytical method offers a reliable and efficient approach for the rapid determination of Cu and Mn in plant material, with implications for agricultural research, environmental monitoring, and plant nutrition management. Its applicability extends to diverse fields such as agronomy, plant physiology, environmental science, and food safety, where accurate assessment of elemental composition in plant tissues is paramount.

**Introduction:** Optimal elemental nutrition is essential for high quality crop yields. It improves their biological and technical value and increases their size. Plants require a number of elements that are categorized as macronutrients (N, P, K, S, Ca and Mg) and micronutrients (Cu, Zn, Fe, Mn, B, Cl, Mo and Ni). Micronutrients are just as essential for plant growth as macronutrients but are required in smaller amounts and can be easily toxic [1,2]. Therefore, monitoring from crop to product is very important. One of the fundamental challenges in analytical chemistry is to strive to determine ever lower concentrations of analytes while ensuring the quality of the results obtained. Copper and manganese are examples of micronutrients in plants that are required for proper balance and normal growth. At the cellular level, copper plays an essential role in chlorophyll synthesis, cell wall metabolism, oxidative stress responses, hormone signalling, transcription and many others. Cu is responsible for the intensity of flavour or colour in vegetables or flowers. This redox active element can exist as monovalent Cu (I) or divalent Cu (II). In its reduced form copper binds sulphur-containing compounds with a thiol or thioether group and acts as a cofactor of many oxidases (the best known oxidase is the mitochondrial cytochrome c oxidase). In its oxidised form, copper coordinates mainly with oxygen or imidazole nitrogen groups [1,3,4]. Manganese also plays an important role in plant growth and development. It plays an important role in photosynthesis. Mn can exist in four oxidation states (II, III, IV and VII) allowing sequential transfer of electrons from photosystem II. In an addition to photosynthesis manganese is involved in respiration, hormone signalling and pathogen defence. This

micronutrient is a cofactor for manganese superoxide dismutase (located in mitochondria and peroxisomes), decarboxylases or dehydrogenases [1,5].
The specific method for the analysing of micronutrients in plants is inductively coupled plasma optical emission spectroscopy (ICP-OES) or flame atomic absorption spectroscopy (FASS). These methods require sample preparation as solutions, for which the use of expensive, high purity reagents is necessary. One solution to this problem could be wavelength dispersive X-ray fluorescence spectrometry (WDXRF). It is known as a fast, quantitative and qualitative analytical method dedicated to the determination of macro- and microelements in a wide range of samples especially in mining, environmental, geological, biological and pharmaceutical industries. This technique allows multielement analysis in a short time and with high precision compared to other traditional analytical methods [6,7].

**Experimental:** For the validation experiments certified reference materials - *Tea Leaves* INCT-TL-1 (Cu, Mn), *Mixed Polish Herbs* INCT-MPH-2 (Cu, Mn), *Apple Leaves* SRM NIST 1515 (Mn) and *Spinach Leaves* SRM NIST 1570a (Mn) were used. CRMs with different levels of content of Cu and Mn were selected according to similarity to the analysed samples in terms of the matrix. Reference materials were analysed by WDXRF, ICP-OES and FAAS methods.
For the analysis Cu and Mn in plants by wavelength dispersive X-ray fluorescence spectrometer WDXRF (ARL PERFORM'X Thermo Scientific), Uniquant - standardless, program has been used. Uniquant allows unknown samples to be measured in less than 14 minutes. Sample preparation is usually minimal or not required [8]. Plant materials are prepared as pressed pellets in HERZOG HTP hydraulic press (90kN/10s). The pellets should be durable and have a flat surface.
In the ICP-OES method, the concentration of an element in a sample is determined by measuring the intensity of radiation emitted at a wavelength characteristic of the element. When solid samples are analysed, they must be properly prepared. Plant material was mineralized (with the addition of concentrated nitric acid) in the Mars microwave digestion system. After this process, the solution from the vessels was quantitatively transferred to volumetric flasks (50ml) and made up to the mark with demineralised water. The elements were analysed using calibration curves prepared from standard solutions by diluting a ready-made commercial multi-element solution (Merck).
Prepared solutions of certified reference materials were also analysed using the FAAS method which is based on the principle, that atoms (and ions) can absorb light at a specific, unique wavelength. When this specific wavelength of light is applied, the energy (light) is absorbed by the atom. The electrons in the atom move from the ground state to an excited state. The amount of light absorbed is measured and the concentration of the element in the sample can be calculated. For the determination of Cu and Mn standard curves were prepared using standard solutions (J. T. Baker) of these elements.
Finally, copper and manganese were analysed in selected real samples of dried plants using the WDXRF method.

**Results:** Four certified reference materials were measured by the Uniquant programme. It was found that, under the given conditions (Cu - line: Kα1; angle 2θ=65,5°; analytical crystal: LiF220; detector: FPC, collimator: 0,15 and for Mn - line: Kα1; angle 2θ=95,2°; analytical crystal: LiF220; detector: FPC, collimator: 0,15), the XRF method is only

sensitive to the element being analysed. The results obtained were compared with the values given in the certificates ($x_{ref}$). The recovery (R) was calculated. At the same time, the CRMs selected for the validation process were analysed by ICP-OES and FAAS techniques. Calibration curves were plotted (measurement conditions and elements characteristics of calibration curves are summarised in Table 1) to measure the copper and manganese content of the CRMs in both methods.

**Table 1.** Measuring conditions and elements of calibration curve characteristics (determination of Cu and Mn) for ICP-OES and FAAS methods.

| | |
|---|---|
| ICP-OES<br>Inductively Coupled Plasma Optical Emission Spectrometer VARIAN 720es with autosampler SPS3 | Working parameters: spray chamber: quartz Scott type, *nebuliser*: concentric glass, *torch*- one-piece quartz, *frequency generator*: 40,3 MHz, *power of plasma generator*: 1200W, *pump rate*: 15 rpm, *integration time*: 15s, Wavelength: Cu=327,395 nm, Mn=257,610 nm, Number of points: 7, Working range: Cu 0,001 – 0,500 mg/l, Mn 0,0006-0,500 mg/l, $R^2$>0,999 |
| FAAS<br>Flame Atomic Absorption Spectrometer Varian AA 240 | Working parameters: *burner height*: 8mm, *slit*: Cu 0,5 nm, Mn 1,0 nm, *background corrector*: NO, *air to acetylene gas flow*: Cu 13,5/2,0 l/min, Mn 13,63/2,45 l/min<br>Wavelength Cu 324,8 nm, Mn 279,5 nm Number of points: 6, Working range: Cu 1 – 5 µg/ml, Mn 1 – 5 µg/ml, $R^2$>0,999 |

The results obtained are then compared with the values given in the certificates ($x_{ref}$). The recovery was calculated. The results obtained by the three methods are summarised in Table 2. In the case of trace elements, an acceptable R [%] value is in the range of 85 - 115%.

**Table 2.** Results obtained and calculated recovery R in measurement of CRMs by WDXRF, ICP-OES and FAAS.

| Mn | | | | | Cu | | | | |
|---|---|---|---|---|---|---|---|---|---|
| CRM | method | $x_{śr}$ mg/kg | $X_{ref}$ mg/kg | R [%] | CRM | method | $x_{śr}$ mg/kg | $X_{ref}$ mg/kg | R [%] |
| *Tea Leaves* INCT-TL-1 | WDXRF | 1700 | 1570 | 108 | *Tea Leaves* INCT-TL-1 | WDXRF | 20 | 20 | 100 |
| | ICP-OES | 1490 | | 111 | | ICP-OES | 20 | | 100 |
| | FAAS | 1750 | | 111 | | FAAS | 22 | | 109 |
| *Mixed Polish Herbs* INCT-MPH-2 | WDXRF | 199 | 191 | 104 | | | | | |
| | ICP-OES | 188 | | 98 | | | | | |
| | FAAS | 207 | | 108 | | | | | |
| *Apple Leaves* SRM NIST 1515 | WDXRF | 53 | 54 | 98 | *Mixed Polish Herbs* INCT-MPH-2 | WDXRF | 8,7 | 7,8 | 112 |
| | ICP-OES | 50 | | 93 | | ICP-OES | 7,6 | | 97 |
| | FAAS | 49 | | 90 | | FAAS | 7,2 | | 92 |
| *Spinach Leaves* SRM NIST 1570a | WDXRF | 86 | 76 | 113 | | | | | |
| | ICP-OES | 75 | | 99 | | | | | |
| | FAAS | 83 | | 109 | | | | | |

In addition, statistical parameters (SD, RSD) were calculated based on the results obtained from the measurements of INCT-TL-1 *Tea Leaves* in three repetitions . These parameters were used to determine accuracy and repeatability precision of the WDXRF method. The precision ($\delta_{rel}$) was determined on the basis of the triple marking of a single

tablet. It is assumed that the $\delta_{rel}$ value should be within 5%. The LOD and LOQ were also determined. The calculated parameters are presented in Table 3.

**Table 3.** Calculated statistical parameters used in the validation process of the WDXRF method.

| | Cu | Mn | | Cu | Mn |
|---|---|---|---|---|---|
| SD [mg/kg] | 1 | 10 | LOD [mg/kg] | 2,4 | 1,5 |
| RSD | 0,05 | 0,006 | LOQ [mg/kg] | 7,2 | 4,5 |
| $\delta_{rel}$ [%] | 5 | 0,2 | | | |

The validated WDXRF method was used to determine the content of Cu and Mn in dried plant material - black tea, green tea, mint and chamomile. The obtained contents are shown in the graphs (Fig.1).

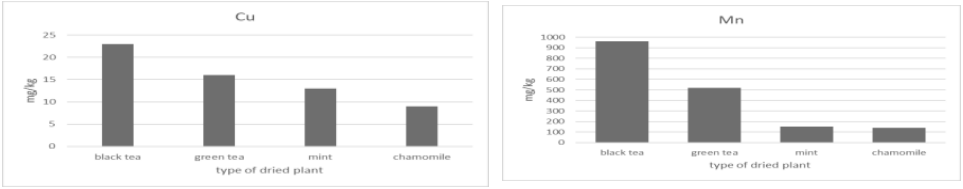



**Fig. 1.** Content of Cu and Mn in dried plant material (WDXRF method).

**Conclusions:** The use of X-ray fluorescence for the determination of Cu and Mn micronutrients will allows faster results using green chemistry principles. Future work could focus on extending the validation process. In addition, the method could be extended to include other micro- and macronutrients.

## References:

1. H. Kaur, H. Kaur, H. Kaur, S. Sirastava, Plant Growth Regulation, 100 (2023) 219.
2. M. Farooq, A.S. Khan, T. Shaheen, M. H. Almes, A. U. Malik, R. Anwar, R. Naveed-Ur-Rehman, S. Ali, M. Ul Hassan, Pakistan Journal of Botany, 55 (2023) 1305.
3. M.Y. Kohatsu, C.N. Lange, M.T. Pelegrino, J.C. Pieretti, G. Tortella, O. Rubilar, Journal Cleaner Production, 324 (2021) 129264.
4. H.-Y. Yuan, Q.-Q. Liu, J.-H. Fu, Y.-J. Wang, Y.-X. Zhang, Y.-M. Sun, Journal of Environmental Sciences, 124 (2023) 319.
5. I. de Oliveira, A. Chyscrgyris, T. C. Finimundy, M. Carocho, C. Santos-Buelga, R. C. Calhelha, N. Tzortzakis, L. Barros, S. A. Heleno, Food Chemistry, 438 (2024) 137976.
6. V. K. Singh, N. Sharma, V. K. Singh, X-Ray Spectrometry, 51 (2022) 304.
7. V. Ramirez, d. Lopez, V. Quintero-Hernandez, P. Lopez, G. Juarez, J. Martinez, J. A. Munive, A. Baez, International Journal of Environmental Science and Technology, 21 (2024) 4705.
8. www.thermofisher.com

# APPLICATION OF TG AND DCS ANALYSES TO EVALUATE THERMAL PROPERTIES OF POLYACRYLATE-BASED HYDROGELS

**A. DROZD[1], M. PALUCH[1], D. KOŁODYŃSKA[2]**, [1]Łukasiewicz Research Network - New Chemical Syntheses Institute, Tysiaclecia Panstwa Polskiego Ave., 24-100 Pulawy, Poland, [2]Maria Curie-Sklodowska University, Faculty of Chemistry, Institute of Chemical Sciences, Department of Inorganic Chemistry, M. Curie-Sklodowska Sq. 3, 20-031 Lublin, Poland.

**Abstract:** Polyacrylate-based hydrogels may be used as materials for the preparation of modern mineral fertilisers with controlled activity. TG and DSC experiments were carried out to verify the thermal stability and phase transitions, respectively. Hydrogels showed high thermal stability, with degradation at 190-570 °C. The glass transition temperature was approximately 110 °C.

**Introduction:** Hydrogels, also known as superabsorbents, are three-dimensional cross-linked polymers that are able to absorb and retain as much water as hundreds of times their dried mass [1]. Hydrophilic monomers with high water retention capacity, such as acrylic acid, acrylic esters, acrylamide, sodium acrylate, and other unsaturated monomers, are used in the synthesis of hydrogels. Hydrogels are extensively employed in many different fields, including food production, cosmetics, medicine, material development, and industrial separation procedures [1, 2]. They can also be used in horticulture and agriculture because they can enhance soil fertiliser retention, boost plant growth rates, and lower irrigation water consumption and plant mortality [3].
Thermal analysis of polymers involves different techniques: thermogravimetric analysis (TGA); differential thermal analysis (DTA); differential scanning calorimetry (DSC); and evolved gas analysis (EGA). The TGA and DSC are particularly notable among them. The combination of these methods can provide information about a material's oxidative and thermal stability, composition, and lifespan, as well as the impact of a reactive atmosphere, moisture and volatile content, and the kinetics of material decomposition [4-6].

**Experimental:** Thermogravimetric analysis was performed on a TA Instruments Q50 device. The tested sample, weighing approximately 5-10 mg, was placed on a platinum measuring pan and then in the apparatus's oven. It was heated at a constant rate of 10°C/min in the temperature range of 25-1000ºC, and the change in mass as a function of temperature was recorded. The obtained thermogravimetric data are presented as a curve of the percentage of mass loss as a function of temperature and as a curve of the first weight derivative as a function of temperature. The temperatures of the transformation beginning ($T_{onset}$) and the transformation end ($T_{endset}$), the temperature for a 5% mass loss ($T_{5\%}$), and the temperature of the maximum mass loss ($T_{max}$) were determined.
Differential scanning calorimetry measurements of hydrogels were investigated on a TA Instruments Q20 DSC device with a cooling system to -90°C in a nitrogen atmosphere.

The apparatus was calibrated using indium metal as a standard. Test samples weighing approximately 10 mg in an aluminum crucible were placed in the measurement cell. The sample was tested according to the following temperature program: cooling to 0°C and then heating to 500°C at a rate of 10°C/min. The result is presented as a curve of the dependence of heat flow per time unit on temperature.
The five commercial superabsorbents TerraHydrogel®Aqua (THA) (Terra, Poland), Zeba®Hydrogel (ZH) (Agrecol, Poland), Agro®Hydrogel (AH) (EverChem, Poland), Luquasorb 1161 (L1) (BASF, Germany), and Luquasorb 1280 (L2) (BASF, Germany) were selected for studies. They have slightly different matrices: AH-crosslinked acrylamide-polyacrylate, ZH-starch modified with substituted side chains of copolymers of polyacrylamide and acrylic acid, THA, L1, and L2-crosslinked polyacrylate.

**Results:** Thermogravimetric analysis (TGA) is most often used to determine the thermal stability of hydrogels, material composition, and degradation temperature. These parameters influence the optimization of the polymerization process. The use of the TGA method also allows for the impact assessment of additives on the thermal stability of the polymer material [4-8]. The main factors influencing the polymers thermostability are: the presence of low-molecular substances, cross-linking, the presence of aromatic rings and degradable functional groups. When polymers are heated to high temperatures, chemical bonds in the main and side chains are broken and low-molecular-weight gas products are released. Intramolecular cyclization and elimination reactions also often occur, and in the case of linear polymers, depolymerization, i.e., restoration of the monomer, may occur [9, 10].
Thermogravimetric analysis (TGA) of the polyacrylate-based hydrogels showed that in the whole range of heating temperatures (up to 1000ºC) four basic areas characterizing the change in sample mass can be distinguished. The first mass loss is related to the evaporation of water and, depending on the sample, ranges from approx. 5 to 10%, with the first stage starting from room temperature to approx. 230°C. Another weight loss is related to the slow, gradual decomposition of the polymer up to approximately 320°C [5]. In the temperature range of 230-500°C, the decomposition of side chains occurs, and in the range of 500-900°C, the complete decomposition of the main chain of the hydrogel occurs, i.e., organic substances burning up to approximately 60% of the sample mass [4, 5]. In the case of the ZH hydrogel based on starch modified with substituted side chains of polyacrylamide and acrylic acid copolymers, the starting temperature of the actual transformation associated with starch degradation is 230°C, while the end of the transformation occurs at 330°C [11, 12]. For AH and ZH hydrogels that contain polyacrylamide groups, the presence of sharp peaks at temperatures of approximately 220°C and 270°C was observed, which is related to the thermal decomposition of the amide group and side carboxyl groups of the polymer chain, respectively.
Figure 1 shows the TG and DTG curves of the tested hydrogels. The temperature of 5% mass loss is in the range of 45-129°C, which is related to the water content of 9-11% for THA and AH hydrogels, approximately 7% for ZH, and 1% for L1 and L2, respectively. Table 1 lists the temperatures characterizing thermal transformations obtained for individual hydrogels.

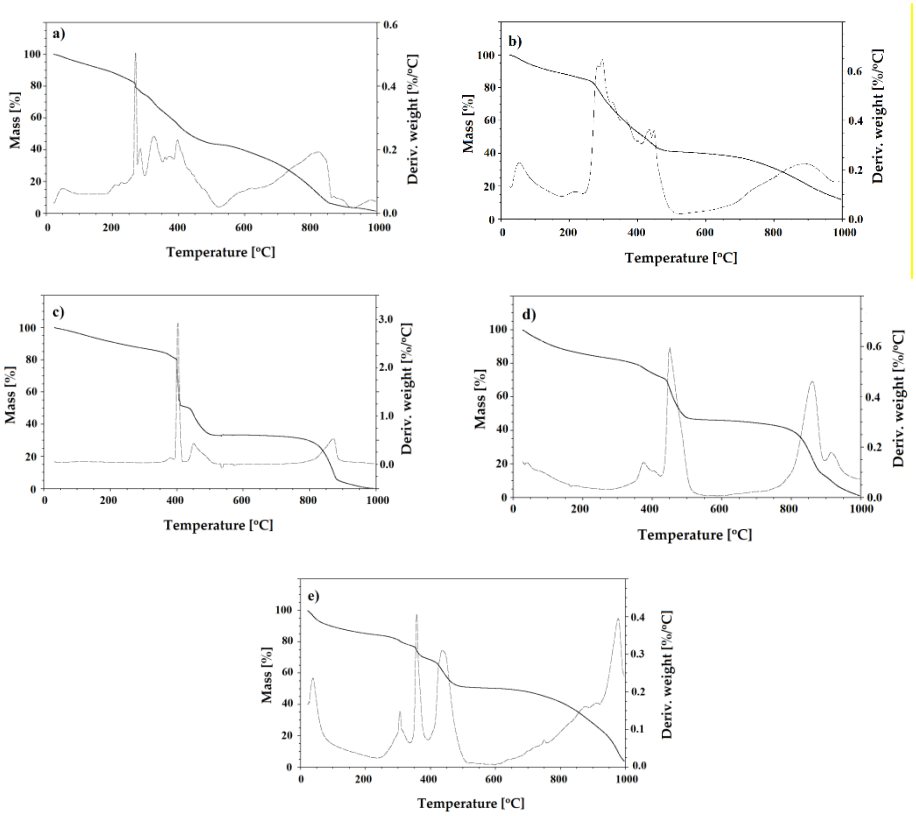


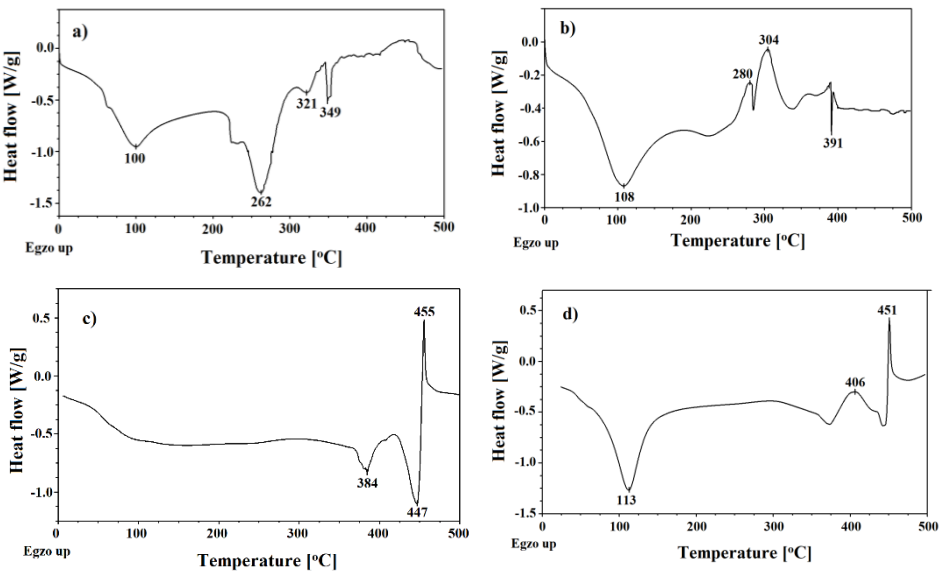

**Fig.1.** TG and DTG curves for hydrogels: a) AH, b) ZH, c) THA, d) L1, e) L2.

The use of the differential scanning calorimetry (DSC) method allows, among others, to determine typical thermal effects for polymer superabsorbents, such as glass transition temperatures, melting temperatures, onset of decomposition, phase transformations, oxidation, and crystallization.

At the beginning of the DSC curve showing energy transformations in hydrogel samples (except THA) in the temperature range of 100-114 °C, a small endothermic peak is visible related to the removal of physically adsorbed water [13]. In the case of the AH hydrogel (Fig.2), an endothermic peak is visible related to the melting of polyamide at a temperature of 262 °C [10]. The melting effect observed in the DSC curve appears to be a result of a decrease in the degree of crystallinity of the tested material due to the transition of the crystalline phase into the amorphous phase [9, 10]. Exothermic effects in the temperature range of 300-500 °C are related to the decomposition of organic substances [13].

**Table 1.** Summary of characteristic temperatures in the thermogravimetric analysis of the hydrogels.

| Hydrogel | Stage | $T_{onset}$ [ºC] | $T_{endset}$ [ºC] | $T_{max}$ [ºC] | $T_{5\%}$ [ºC] |
|---|---|---|---|---|---|
| AH | I | 20 | 230 | 227 | 98 |
| | II | 230 | 320 | 270 | |
| | III | 320 | 410 | 373 | |
| | IV | 410 | 900 | 822 | |
| ZH | I | 20 | 230 | 216 | 77 |
| | II | 230 | 330 | 296 | |
| | III | 330 | 465 | 447 | |
| | IV | 447 | 900 | 888 | |
| THA | I | 20 | 400 | 380 | 129 |
| | II | 400 | 440 | 403 | |
| | III | 442 | 500 | 451 | |
| | IV | 838 | 900 | 871 | |
| L1 | I | 20 | 360 | 66 | 66 |
| | II | 360 | 395 | 375 | |
| | III | 443 | 480 | 450 | |
| | IV | 823 | 900 | 860 | |
| L2 | I | 20 | 295 | 45 | 45 |
| | II | 295 | 420 | 357 | |
| | III | 420 | 470 | 435 | |
| | IV | 700 | 980 | 978 | |



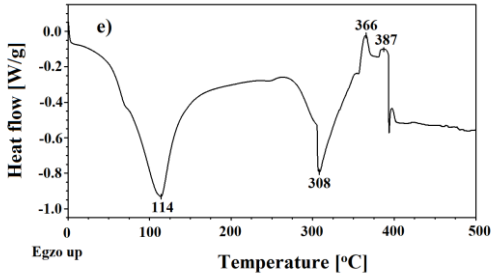



**Fig.2.** DSC curves of the hydrogels: a) AH, b) ZH, c) THA, d) L1, e) L2.

**Conclusions:** The thermal properties of hydrogels vary slightly depending on the polymer matrix. Based on the weight loss of the tested materials, it can be concluded that the starch-based ZH hydrogel is characterized by slightly lower thermal stability than other polyacrylic hydrogels. According to literature data, polymer cross-linking enhances the thermal properties of hydrogels and determines the transformation temperatures. However, the obtained results do not indicate significant differences in the thermal properties of AH, ZH, THA, L1 and L2 hydrogels.

## References:

1. E.M Ahmed, Hydogel: Journal of Advanced Research, 6 (2015) 105.
2. F. Ullah, M.B.H. Othman, Material Science Engineering C, 57 (2015) 414.
3. Y. Shen, H. Wang, W. Li, Z. Liu, Y. Liu, H. Wei, J. Li, International Journal of Biological Macromolecules, 164 (2020) 557.
4. X. Li, Q. Li, Y. Su, Q. Yue, B. Gao, Y. Su, Journal of the Taiwan Institute of Chemical Engineers, 55 (2015) 170.
5. K. Bialik-Wąs, B. Tyliszczak, E. Wilk, K. Pielichowski, Chemik, 67 (2013) 11.
6. A.G. Rusu, M. I. Popa, G. Lis, L. Vereştiuc, Thermochimica Acta, 613 (2015) 28.
7. B. Singh, V. Sharma, Carbohydrate Polymers, 157 (2017) 185.
8. J. Pagacz, A. Leszczyńska, M. Modesti, C. Boaretti, M. Roso, I. Malka, K. Pielichowski, Thermochimica Acta, 612 (2015) 40.
9. K. Pielichowski, Zastosowanie metod analizy termicznej w badaniu materiałów organicznych, Materiały Konferencyjne V Szkoły Analizy Termicznej, Zakopane 2008.
10. J.F. Rabek, Współczesna wiedza o polimerach, PWN, Warszawa, 2017.
11. M. Worzakowska, E.Torres-Garcia, Polymer Degradation and Stability, 139 (2017) 67.
12. X. Xiao, L. Yu, F. Xie, X. Bao, H. Liu, Z. Ji, L. Chen, Chemical Engineering Journal, 309 (2017) 607.
13. M. Szumera, Charakterystyka wybranych metod termicznych (cz. 2), LAB 1 (2018) 24.

# ABIOTIC AND BIOTIC DEGRADATION OF POLYETHYLENE – PHYSICOCHEMICAL PROPERTIES CHANGES

**J. KAPELEWSKA[1], U. KLEKOTKA[1], A. PIOTROWSKA-NICZYPORUK[2], U. CZYŻEWSKA[2], M. BARTOSZEWICZ[2], J. KARPIŃSKA[1]**, [1]University of Bialystok, Faculty of Chemistry, Ciolkowskiego 1K Street, 15-245 Bialystok, Poland; [2]University of Bialystok, Faculty of Biology, Ciolkowskiego 1J St., 15-245 Bialystok, Poland

**Abstract:** High-density polyethylene microplastic with a particle size of 125 μm was subjected to abiotic (UV-Vis radiation) and biotic (algae *Acutodesmus obliquus*, bacteria *Bacillus cereus 10987*, and fungi *Candida krusei*) degradation. Changes in physicochemical properties were observed using a scanning electron microscope (SEM), Fourier-transform IR spectra (FT-IR), and porosimetry.

**Introduction:** Since the 1950s, global plastic production has increased from 1.5 to over 400 million tonnes in 2022. The largest share in global production of these materials is polypropylene (PP, 19.3%), low and very low-density polyethylene (LDPE and LLDPE, 14.4%), polyvinyl chloride (PVC, 12.9%), high and medium-density polyethylene (HDPE and MDPE, 12.5%) [1]. For many years, the issue of the impact of mass production of plastics on the environment has been neglected, which has contributed to the accumulation of plastic waste in the ecosystem. Due to the size of plastic particles, we distinguish macroplastics (>25 mm), mesoplastics (25 - 5 mm), microplastics (5 mm - 1 μm) and nanoplastics (<1 μm) [2]. Plastic waste released into the environment undergoes aging, *i.e.*, weathering. Weathering of polymer waste may occur due to abiotic or/and biotic degradation. Abiotic degradation occurs under atmospheric (UV radiation) and physical (abrasion) factors. Biotic degradation (in other words, biodegradation, biological degradation or bio-oxidation) is the breakdown of plastics under the influence of enzymes produced by plants (algae) and microorganisms (bacteria, fungi or yeast) [3]. The degree of degradation depends on the properties of the polymer (molecular weight, chemical structure, specific surface area, degree of crystallinity or hydrophobicity). Degradation processes result in a reduction in particle size, fragmentation of the polymer chain due to the breaking of covalent bonds and a reduction in branching [4,5]. Changes in the physicochemical properties of degraded polymers can be observed using a scanning electron microscope, Fourier-transform IR spectra, thermogravimetry (TGA) and porosimetry [6].

**Experimental:** High-density polyethylene (HDPE) with a particle size of 125 μm in powder obtained from Sigma-Aldrich was selected to study changes in physicochemical properties after abiotic and biotic degradation.
Abiotic degradation of HDPE microplastics was performed by irradiation with simulated sunlight for 168 hours at an intensity of 1000 W/m$^2$ and a temperature of 44±2 °C. The tests were conducted in quartz glass vessels in an accelerated aging test chamber (SolarBox 3000e CO.FO.ME.GRA, Italy) equipped with a xenon lamp and a standard

solar filter with a 300-800 nm wavelength range. The microplastic mass was 2 g, and the volume of water was 200 ml. Throughout the aging tests, the sample was stirred, and the evaporated solution was topped up with milliQ water every day to the initial mark. After photoaging, the test samples were filtered through a glass fiber membrane with a pore diameter of 1.2 μm and then dried for 3 days at 25 °C.

Biotic degradation of HDPE was carried out under the influence of enzymes secreted by unicellular algae *Acutodesmus obliquus*, bacteria *Bacillus cereus 10987* and fungi *Candida krusei*. To carry out the biodegradation process of the tested MPs using algae, 25 mg of HDPE was weighed and placed in sterile conical flasks with added 45 mL of medium and 5 mL of algae (C=500 mg/L). The systems prepared in this way were grown for 5 days in controlled phytotron conditions, where the culture temperature was 22±1 °C and the relative humidity was 45±5%. Fluorescent lamps were used for illumination, and the illumination power was 50 $\mu M \cdot m^{-2} s^{-1}$ of photosynthetically active radiation (PAR). After completing the culture to separate the algae, the samples were centrifuged for 10 minutes at 4000 rpm. Then, the solution was quantitatively transferred to flat-bottomed 40 ml tubes. After a minimum of 24 hours, the embedded microplastics were filtered through 1.2 μm glass fiber filters and then allowed to dry for 48 hours at room temperature. The obtained filtrates were ready for further tests. We used Gram-positive bacteria *Bacillus cereus* (strains ATCC 10987) and fungi *Candida krusei* to analyse microplastic degradation by microorganisms. All strains are isolated from natural environments and available in the Department of Microbiology and Biotechnology, Faculty of Biology, Univerity of Bialystok). Inocula consisted of fresh cultures of individual microorganisms with an optical density of $O.D._{600}$=2.0. Bacteria were cultured in liquid LB medium (Luria-Bertani broth), while fungal cultures were carried out in YPD medium (Yeast extract-Peptone-Dextrose broth). The experiment was conducted in 250 ml of medium enriched with sterile HDPE (500 mg/L), independently for 7 day at 33 °C. A control experiment was also conducted without HDPE for each species, maintaining identical culturing conditions. Subsequently, microbial cultures were centrifuged to remove cells (10 minutes, 17000 x g), followed by filtration through 1.2 μm glass filters. The filters were rinsed with sterile distilled water. The collected microplastic was dried at room temperature for 48 hours and then subjected to further analysis.

The characteristics of virgin HDPE and after the abiotic and biotic degradation process were examined using a scanning electron microscope (SEM INSPEC S60 with FEI) at 15 kV. For measurement, a small amount of sample powder was placed on a carbon tape, and then a thin (5 nm) layer of Au was deposited to provide electron interaction. Fourier transform IR spectra were measured using a Thermo Scientific Nicolet 6700 infrared spectrometer operating in ATR reflectance mode. For measurement, a powder sample was placed on a diamond window. Porosity measurements were performed at -96 °C with nitrogen as the test gas in an ASAP 2020 porosimeter from Micromeritics. The samples were degassed at 2 mmHg at 100°C for 15 h before adsorption measurements.

**Results:** Figure 1 presents FTIR spectra of virgin and HDPE after abiotic and biotic degradation. Spectra show the presence of additional signals, regardless of typical for HDPE (2910-2847$cm^{-1}$, 1471 $cm^{-1}$ are assigned to symmetric and asymmetric bending of C–H bonds, bands at 730-717 $cm^{-1}$ confirms the presence of C–C bonds). In the spectra of HDPE after degradation, signals in the region between 1743-1527 $cm^{-1}$ occur,

suggesting the presence of C=O and C=C bands at the surface of HDPE [7]. In spectra of HDPE after degradation by algae, bacteria, and fungi, the band at 1060 $cm^{-1}$ can be seen, what confirms vibrations of polysaccharide rings related to the biofilm's presence [8]. Figure 2 depicts SEM images with magnifications 1000x and 5000x are depicted. A comparison of images of virgin and HDPE after abiotic and biotic degradation shows the presence of the biofilm on HDPE, but no significant signs of degradation at the micron-scale level can be seen.

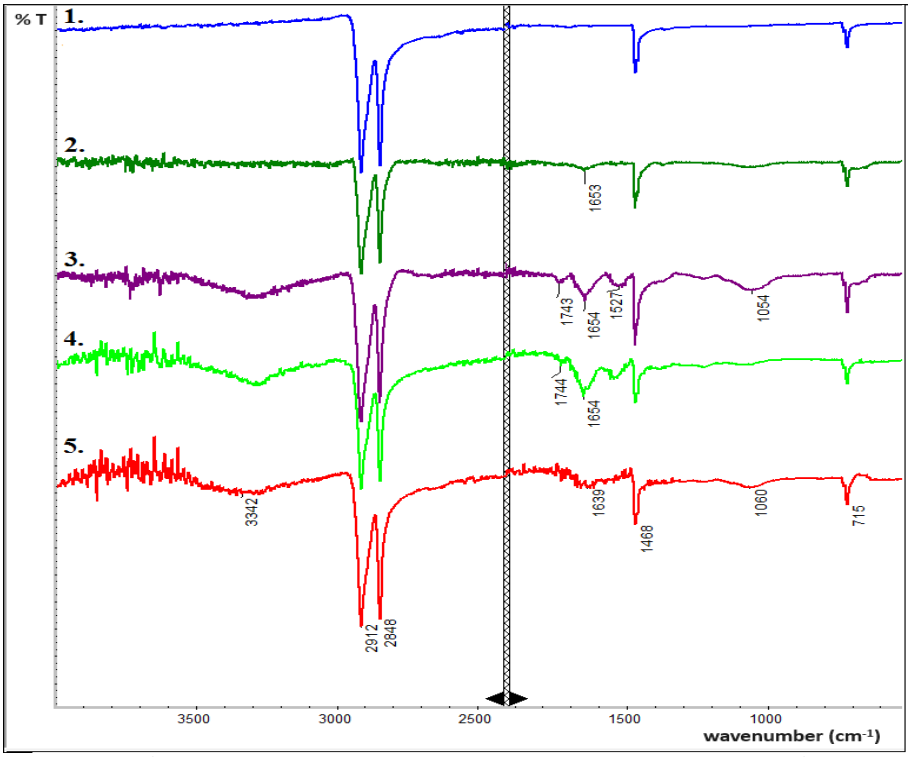



**Fig.1.** IR spectra of analyzed samples: (1) virgin HDPE, (2) HDPE under UV-Vis, (3) HDPE after cultivation of algae, (4) HDPE after cultivation of bacteria, and (5) HDPE after cultivation of fungi.

Characterization of surface properties of HDPE before and after degradation was also performed by nitrogen adsorption and by calculation of BET-specific surface area value. Here, BET values show a clear difference. Degradation of HDPE is observed in all tested processes. While UV-Vis degradated HDPE has a relatively small specific surface area compared to virgin HDPE, biotic degradation increases this parameter to 217-331 $m^2/g$. A similar effect is observed in total pore volume values. This information suggests that HDPE degradation occurs in every case, with a better effect on biotic than abiotic degradation.

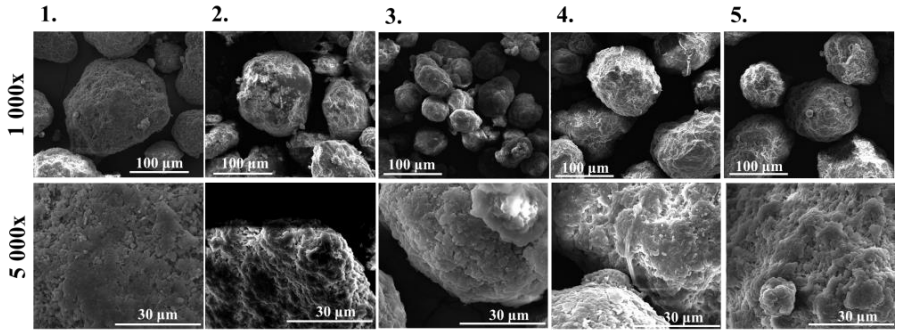



**Fig.2.** SEM images of analyzed samples: (1) virgin HDPE, (2) HDPE under UV-Vis, (3) HDPE after cultivation of algae, (4) HDPE after cultivation of bacteria, and (5) HDPE after cultivation of fungi.

**Conclusions:** This work studied the degradation of high-density polyethylene with a particle size of 125 µm under UV-Vis, algae (*Acutodesmus obliquus*), bacteria (*Bacillus cereus 10987*), and fungi (*Candida krusei*). Studies have shown that due to biodegradation, there were greater changes in the physicochemical properties of HDPE than due to abiotic degradation. Especially under the influence of bacteria and algae on HDPE particles, a significant difference was observed in the IR image compared to the image of virgin HDPE. The appearance of new functional groups containing oxygen and a double bond between carbon atoms was noted here. An increase in BET-specific surface area and total pore volume was also observed.

**Acknowledgements:** The work was partially financed by EU funds via the project with contract number POPW.01.03.00-20-034/09-00 and POPW.01.03.00-20-004/11-00.

**References:**

1. Plastics Europe. Plastics - the fast Facts 2023, 2023.
2. D.K.A. Barnes, F. Galgani, R.C. Thompson, M. Barlaz, Philosophical Transactions of the Royal Society B, 364 (2009)1985.
3. J.N. Hanun, F. Hassan, J.-J. Jiang Journal of Environmental Chemical Engineering, 9 (2021) 106290.
4. Arp HPH, Kühnel D., Rummel C., MacLeod M., Potthoff A., Reichelt S. Environmental Science & Technology, 55 (2021) 7246.
5. J. Kapelewska, U. Klekotka, E. Żadziłko, J. Karpińska, Science of The Total Environment, 789 (2021) 147979.
6. S. Mishra, S. Swain, M. Sahoo, S. Mishra, A.P. Das. Geomicrobiology Journal, 39 (2022) 259.
7. R.A. Meyers (ed.), Encyclopedia of Analytical Chemistry: Applications, Theory, and Instrumentation. Wiley, 2007.
8. G. Bhagwat, T.K.A. Tran, D. Lamb, A. Senathirajah, I. Grainge, W. O'Connor, Environmental Science & Technology, 55 (2021) 8877.

# SELECTED EMERGING ORGANIC POLLUTANTS OF THE AQUATIC ENVIRONMENT AND THE POSSIBILITIES OF THEIR REMOVAL FROM THE WATER

**M. I. BOLIŃSKA[1], J. PIEKUTIN[1], U. KOTOWSKA[2]**, [1]Bialystok University of Technology, Faculty of Civil Engineering and Environmental Sciences, Wiejska 45E Street, 15-351 Bialystok, Poland, [2]University of Bialystok, Faculty of Biology and Chemistry, K. Ciolkowskiego 1K St., 15-245 Bialystok, Poland.

**Abstract:** Today, with economic development, more and more pollutants are present in the water environment, among which are emerging pollutants (EPs). EPs are a very large group of compounds, among which are all substances that come from personal care products [1]. They include UV filters, repellents, antibacterial and antifungal agents, pharmaceuticals and endocrine disrupting chemicals (EDCs). In recent years, there has been an increase in EDCs concentration in aquatic environments attributed to the growing consumption of personal hygiene products. These compounds exhibit significant potential for harming aquatic organisms and, at higher concentrations, posing carcinogenic risks to humans [2, 3, 4]. Significantly, EDCs demonstrate resilience to conventional removal methods [5, 6], necessitating the exploration of new wastewater treatment technologies. Additionally, the study assesses the effectiveness of various water and wastewater treatment methods, checking practical insights for mitigation strategies.

**Introduction:** EDCs are chemical compounds that are not widely monitored or tested, though they often significantly affect the health of humans and other organisms [1-6]. Many are difficult to remove, and some show bioaccumulation capabilities [7]. They are special agents that interfere with the hormones in the human body [8] - they can act via serotonin, dopamine and norepinephrine receptors [1] and can control the production and breakdown of endogenous steroids [9, 10]. The list of EDCs continues to grow. Among them are compounds such as triclosan (TCS), benzophenones (BPs), diethylstilbestrol (DES), 4-octylphenol (4OP), estrone, estradiol, and many, many others. The European Chemicals Agency (ECHA) continuously monitors and updates the list of EDCs as part of classifying, assessing, and regulating chemical substances within the European Union [11]. Their efforts also include identifying new potential EDCs and evaluating their impact on human health and the environment. They have been associated with various diseases and health disorders, including hormonal system disorders such as thyroid dysfunction, insulin resistance, and fertility issues. They are also implicated in cancers such as breast, testicular, and prostate cancer, along with other hormone-related tumors [2,3,4]. Furthermore, EDC exposure has been linked to developmental disorders in children, neurological and behavioral issues, reproductive health problems [12]. Due to this, newer methods for their removal are constantly being sought and researched.

Many EPs and EDCs come from everyday use products like UV filters, repellents, pharmaceuticals, detergents etc. For instance: N, N-diethyl-m-toluamide (DEET) is one of the commonly used as an insect repellent sprayed on the surface of the skin [13]; BPs are compounds that have UV-absorbing properties, and they constitute a group of

32 varieties [14]; 4OP is used as non-ionic surfactants in production of detergents, fungicides, herbicides, pigments and other chemicals, as a representant of alkylphenol ethoxylates (APEOs) [15]; triclosan (TCS) is one of the antimicrobial agents, used as a disinfectant (e.g. in dental preparations) and in many daily hygiene products as mouthwashes, soaps, deodorants [16,17]; DES was widely used from the 1940s to the 1970s as gynaecological medicament for pregnant women [3], but nowadays it is still used in some countries – as a growth stimulant in animal feed and as a veterinary medicine [18].

Most EDCs are commonly present in aquatic environments (Table 1) by being washed off the body surface and migrating with wastewater to the aquatic environment (mainly sunscreens or skin pharmaceuticals like clotrimazole) [19] and by being excreted from organisms, entering wastewater (Table 2), and then they migrate from treated wastewater into receivers, i.e. surface waters (rivers).

**Table 1.** The concentrations of Personal Care Products (PCPs) in surface waters [7].

| Chemical substance | Type of PCP | Concentration range [ng/l] | Median concentration [ng/l] |
|---|---|---|---|
| Triclosan | Disinfectant | < 0.1-2300 | 48 |
| Methyl-triclosan | Disinfectant | 0.5-74 | - |
| Triclocarban | Disinfectant | 19-1425 | 95 |
| DEET | Repellent | 13-660 | 55 |
| 4-methylbenzylidene camphor (4MBC) | UV filter | 2.3-545 | 10.2 |
| 2-Hydroxy-4-methoxybenzophenone (BP3) | UV filter | 2.4-175 | 20.5 |
| Octocrylene (OC) | UV filter | 1.1-4450 | 1.9 |

**Table 2.** The concentrations of PCPs in crude sewage (µg/l) [7].

| Country | Nonylphenol | 2-Hydroxy-4-methoxybenzophenone (BP3) | Triclosan |
|---|---|---|---|
| Spain | 343 | 0.45 | 0.087 |
| Germany | 2.13 | 0.57 | 0.87 |
| Great Britain | 199 | 0.97 | 0.070 |
| Switzerland | 1.24 | 7.80 | 5.84 |
| USA | 0.34 | 10.40 | 16.60 |

In scientific studies, a variety of different methods for removing EDCs have been presented, often customized for specific substances. For example, other research has established that DEET can be broken down into various intermediates (transformation products) with the help of fungi – *Pseudomonas putida*. Also, degradation of DEET can be achieved through: enzymes (e.g. laccases, tyrosinases), nitrifying bacteria (e.g. *Nitrosomonas*) and nanoparticles [13], while other method for DEET removal is powdered activated carbon /ultrafiltration hybrid process (PAC/UF). PAC can adsorb particles and UF works like a barrier for PAC particles, which allowed the removal of DEET at 60% in conducted experiment [5]. BPs can be removed by the usage of

magnetic Fe-Cu bimetallic nanomaterials, while triclosan: in oxidation processes – 70% removal rate (UV, KMnO4, Fenton etc.), membrane filtration – 85 % removal rate, (nanofiltration (NF), reversed osmosis (RO), NF/RO), hybrid processes – 85 removal rate (e.g. PAC/UF) [20], microextraction by packed sorbent (MEPS) [21]. Studies conducted in Brazil based on MEPS, but in an automated form, utilizing a prototype autosampler. It performed flawlessly, allowing for increased work efficiency and extraction accuracy [22].

Other researches, focused on the removal of EDCs as a group of compounds, were conducted using MBR installations in wastewater treatment plants (WWTP). It was found that membranes, by increasing the contact time of wastewater with active sludge flocs, enhance the removal efficiency of EDCs by as much as 30% (depending on the specific substance). Similarly, studies on using RO for EDCs removal showed efficiencies above 92% after the first stage of RO, and over 99% after the second stage of RO [23].

Simpler methods, based on nanofiltration and ultrafiltration membranes modified with nanotubes, showed removal efficiency of selected EDCs at 90-95% and 70-92%, respectively [24]. In the case of hormones, also one of the EDCs, an effective and straightforward method for their removal is the application of activated carbon, which allows for the removal of estradiol by 46% and estrone by 64% (the process of adsorption). Tests conducted on NF and RO resulted in removal efficiencies reaching 90%, while oxidation increased to nearly 100% [25]. This means that employing a hybrid method would yield the best and fastest results and prove effective in treating the concentrate.

A somewhat different method studied, yet also based on microorganisms, was the utilization of a batch biofilter granular reactor (SBBGR) - characterized by a long retention time of the sediment and high biomass concentration. After four months of operation, the removal efficiencies ranged mainly between 67% and 87% [26], which is a less effective result compared to RO. Research was also conducted on the variation of MBR - Anaerobic MBR (AnMBR) with microalgae and light. After about 100 minutes, close to a 90% removal effect was achieved, while after 200 minutes, the removal of EDCs exceeded 99% [10].

**Conclusions:** This work shows the widespread and toxic nature of emerging pollutants - they pose a significant threat to the environment and human health. Their omnipresence, entering the water from various sources, requires urgent attention and focused interventions to safeguard water quality and mitigate the far-reaching impacts on ecosystems and well-being. Furthermore, escalating concentrations of these pollutants underscore the pressing need for continuous monitoring to mitigate associated risks. The effective removal of EDCs must be pursued cautiously to prevent further harm to the environment into which they are released. According to the presented analyses, the answer can be hybrid methods based on nanofiltration and reverse osmosis, supplemented with additional processes like oxidation, because of the promising results.

**Acknowledgements:** The research was carried out as part of the research work no. WZ/WB-IIŚ/2/2024 at the Bialystok University of Technology and was supported by the Polish National Centre of Science by grant 2019/03/X/ST10/01959.

## References:

1. V. Geissen, H. Mol, E. Klumpp, G. Umlauf, M. Nadal, M. van der Ploeg, S.E.A.T.M. van de Zee, C.J. Ritsema, International Soil and Water Conservation Research, 37 (2015) 57.
2. Ch.-L. Su, S.H. Lai, H.-Y. Yeh, Y.-T. Chang, International Biodeterioration & Biodegradation, 177 (2023) 105534.
3. R.M. Harris, R.H. Waring, Maturitas, 72 (2012) 108.
4. S. Humphry, D. Egbeare, International Journal of Surgery, 9 (2011) 547.
5. E. Rodriguez, M. Campinas, J.L. Acero, M.J. Rosa, Water, Air, and Soil Pollution, 227 (2016) 177.
6. M.S. Mitra, B.K. Philip, Encyclopedia of Toxicology (Third Edition), Academic Press, Oxford, 2014, 143.
7. A. Rosińska, Emerging pollutants pose a challenge for wastewater management (Polish title: Emerging pollutants wyzwaniem dla gospodarki wodno-ściekowej), Politechnika Częstochowska, Częstochowa, 2022.
8. O.T. Komesli, S. Bakırdere, C. Bayören, C.F. Gökçay, Environmental Monitoring and Assessment, 184 issue 8 (2012) 5215.
9. R.H. Waring, R.M. Harris, Maturitas, 68 (2011) 111.
10. M.R. Abargues, J.B. Giménez, J. Ferrer, A. Bouzas, A. Seco, Chemical Engineering Journal, 334 (2018) 313.
11. https://echa.europa.eu/hot-topics/endocrine-disruptors
12. M. Beszterda, R. Frański, Pediatric Endocrinology, Diabetes and metabolism, 24 (2018) 88.
13. R. Rani, D. Kumar, Environmental Monitoring and Assessment, 196 (2024) 238.
14. K. Sivakumar, A. Nalini, Journal of Molecular Liquids, 395 (2024) 123905.
15. N. Salgueiro-González, S. Castiglioni, E. Zuccato, I. Turnes-Carou, P. López-Mahía, S. Muniategui-Lorenzo, Analytica Chimica Acta, 1024 (2018) 39.
16. B.E. Taştan, G. Dönmez, Pesticide Biochemistry and Physiology, 118 (2015) 37.
17. M. Milanović, L. Đurić, N. Milošević, N. Milić, Environmental Science and Pollution Research, 30 (2023) 25119.
18. X. Ma, M. Chen, Sensors and Actuators B: Chemical, 2015 (2015) 445.
19. B. Karolewicz, M. Gajda, A. Owczarek, J. Pluta, A. Górniak, Tropical Journal of Pharmaceutical Research, 13 (2014) 1207.
20. E. Ozturk, Environmental Science and Pollution Research, 25 (2018) 30517,
21. I. González-Mariño, J.B. Quintana, I. Rodríguez, S. Schrader, M. Moeder, Analytica Chimica Acta, 684 (2011) 59.
22. M.D. Bocelli, D.A.V. Medina, F.M. Lanças, Á.J. dos Santos-Neto, Analytical and Bioanalytical Chemistry, 415 (2023) 6165.
23. M. Bodzek, Engineering and Protection of Environment, 16 (2013) 5.
24. E. Burdzik-Niemiec, M. Dudziak, Proceedings of ECOpole, 10 (2016) 607.
25. M. Włodarczyk-Makuła, LAB Laboratoria, Aparatura, Badania, 19 (2014) 20.
26. L. Balest, A. Lopez, G. Mascolo, C. Di Iaconi, Biochemical Engineering Journal, 41 (2008) 288.

# BIOSURFACTANTS AND THEIR APPLICATIONS IN SAMPLE PREPARATION TECHNIQUES

**M. HRYNIEWICKA**, University of Bialystok, Faculty of Chemistry, Department of Analytical and Inorganic Chemistry, Ciołkowskiego 1K, 15-245 Białystok, Poland.

**Abstract:** The work characterizes biosurfactants, their physicochemical properties, the possibilities of application in various types of industries and in sample preparation techniques. Moreover, the results of research of using bioemulsifiers for microextraction of selected phenolic acids and their metabolites from medicinal plants (including lemon balm, artichoke, rosemary and common thyme) are presented. The determination was performed using high-performance liquid chromatography coupled with electrospray ionization tandem mass spectrometry ESI(-)-LC-MS/MS.

**Introduction:** Biosurfactants are surface-active compounds produced by living microrganisms such as fungi, bacteria and algae. They are categorized on the basis of their chemical components. Generally, the hydrophilic part is an amino acid, mono-, di-, or polysaccharide, peptide, and the hydrophobic part consists of different lengths of fatty acid chains. Biosurfactants are also classified on the basis of their molecular mass. They are divided into low molecular mass compounds such as proteins, glycolipids (e.g. rhamnolipids, sophorolipids, trehalolipids), lipopeptides (e.g. surfactin, viscosin), and high molecular mass compounds such as polysaccharides, lipoproteins, and polymeric particles type. Low molecular mass compounds reduce surface tension, whereas high molecular mass compounds are mostly effective in formation of stable emulsions of oil-in water [1].

Biosurfactants are characterized by good emulsifying properties, therefore they effectively reduce interfacial tension and improve the solubility of substances in water. They are also characterized by low toxicity, effective biodegradability and thermal stability. Many biosurfactants also possess better surface activity compared to chemical surfactants. Therefore, biosurfactants are a good alternative to chemical surfactants in micelle-based extraction techniques [2]. The bioemulsifier market currently accounts for 5% of the entire surfactant production area. Despite the relatively high costs of producing natural surfactants, the global use of biosurfactants shows further increasing trends due to greater pro-ecological awareness of society. Natural bioemulsifiers are widely used in various industries such as agriculture, food production, pharmacy, horticulture and the cosmetics industry. In addition, natural surfactants due to their biodegradable properties are gaining recognition among ecological biotechnological solutions. The potential of such compounds can be used in nanotechnology, medicine, petrochemical, paper, dyeing and pollution control industries.

In recent years, scientific articles describing the use of biosurfactants for isolation analytes from environmental and biological samples were published. Mainly, mono or di-rhamnolipids produced by *Pseudomonas aeruginosa* were used for creation well defined aggregates. For example, biosorption-based dispersive liquid-liquid microextraction with extractant removal by magnetic nanoparticles based on the formation of microdroplet of rhamnolipid biosurfactant for isolation bisphenol a from

water samples was performed. In this technique, a colloidal mixture containing optimum amounts of rhamnolipid biosurfactant (as extraction solvent) and methanol (disperser solvent) was injected into aqueous samples. The sample was then vortexed and centrifuged to accelerate the separation of the colloidal phase from the bulk solution, which then, the colloidal phase (acceptor) was withdrawn using a micro-syringe and injected into the HPLC system for determination. The application of biosurfactant has eliminated the use of hazardous and toxic chlorinated solvents [3]. In another work, molecular imprinting solid-phase extraction (MI-SPE) combined with bio-dispersive liquid–liquid microextraction (Bio-DLLME), was established to extraction of the paracetamol from human urine samples. In this research, paracetamol was extracted into bioaggregates that composed of rhamnolipid biosurfactants as an extraction solvent. Rhamnolipid biosurfactants plays an important role in Bio-DLLME to create a stable cloudy state. Procedure based on biodegradable and nano size materials was faster and has the lower detection limit in comparison with conventional DLLME method [4].

In 2020, Abbasi et al. used rhamnolipid bioaggregates after dispersive solid phase extraction (DSPE) for enrichment of cardiovascular drugs (atorvastatin, valsartan, propranolol) from human urine samples. To formation a biodegradable emulsion which consisting of water compatible fine droplets, extracted phase (from the DSPE step) was spiked by rhamnolipid biosurfactants. The resulting emulsion from the dispersion of the rhamnolipid biosurfactants in the extracted phase provide a new phase with regions of diverse polarities that enhance its potential for solubilizing solutes through hydrophilic and hydrophobic interactions [5].

Other biosurfactants have also been applied in sample preparation techniques. Eco-friendly sophorolipids were used in reverse micelle extraction of antibiotics. Sophorolipids are commonly produced from non-pathogenic yeast *Candida bombicola* and consists of lactonic (non-ionic) form and acidic (anionic) form. The biosurfactant is produced from renewable sources and has the advantages of readily biodegradable and low toxicity. The properties of sophorolipids are reported to be comparable or even better than synthetic surfactants. Reverse micelle extraction of amoxicillin and erythromycin were completed within 200 s [6].

In another work, trehalose lipid biosurfactant was used as an extraction solvent in microextraction of organophosphorus pesticides (OPPs) in cabbage. This biosurfactant has attracted researchers in number of fields due to its capability to reduce interfacial tension and increase pseudo solubility of hydrophobic compounds. Different types of trehalose containing glycolipids are known to be produced by several microorganisms belonging to the mycolates group, such as *Mycobacterium, Rhodococcus, Arthrobacter, Nocardia* and *Gordonia*. The addition of this biosurfactant (40 mg) results in an increase in the extraction efficiency of OPPs in a short period of time (60 s) [7].

The literature review shows that natural surfactants have not been used so far to isolate phenolic acids and their metabolites from medicinal plants. Phenolic acids are bioactive food ingredients that mainly have antioxidant properties. Furthermore, phenolic acids are found ubiquitously and well documented for other health protective effects like antimicrobial, anticancer, anti-inflammatory, anti-mutagenis. These are secondary metabolites common in the plant world, which occur mainly in the form of glycosides and esters. Due to their structure, they are divided into two basic groups: hydroxycinnamic acids (e.g. caffeic, ferulic, p-coumaric and sinapic) and hydroxybenzoic acids (e.g. p-hydroxybenzoic, protocatechuic, vanillic, gallic, syringic).

They are present in all parts of plants: stems, leaves, flowers, roots, seeds and fruits. Their content may vary depending on the stage of plant development. A rich source of phenolic acids are primarily berries such as: rowan (103 mg/100g), chokeberry (96 mg/100g), blueberries (85 mg/100g) and blackberries (59 mg/100g). They also occur in all medicinal plants and are widely used in phytotherapy [8].

**Experimental:** Micellar microextraction (MME) of some phenolic acids (e.g caffeic acid, synapic acid) and their metabolites (e.g. syringin, sinapaldehyde) from infusion of medicinal plants was performed. The possibility of using various biosurfactants (rhamnolipids, trehalolipids, saponins, surfactin) was checked for the isolation of the tested compounds. The obtained extracts were analyzed using liquid chromatography coupled with tandem spectrometry mass (LC-MS/MS, Hitachi 8040, Japan, LabSolutions software) in multiple reaction monitoring mode (MRM) using electrospray ionization (ESI). Chromatographic measurements were recorded by monitoring characteristic negative ion fragmentation reactions precursor ions of the tested analytes with a selected ratio of their mass to charge (m/z).

**Results:** Several important variables were investigated and optimized comprehensively including type of biosurfactant and its concentration, extraction time, sample pH, shaking, heating and centrifugation time. In order to evaluate ionic strenght, the extraction recoveries were investigated at different concentration levels of inorganic salt (sodium chloride, calcium chloride, potassium bromide, sodium sulfate) within the range of (0-10%, w/v). The highest extraction efficiency was achieved using rhamnolipids as biosurfactants and calcium chloride as an electrolyte. The use of a miniaturized extraction method using natural bioemulsifiers as extraction solvents ensures effective separation of analytes from the tested herbal samples. Miniaturization of the developed isolation method allowed the use of extraction procedures using microliter volumes of biosurfactants. This action allows the enrichment of the tested analytes at the stage of preparing samples of medicinal plants. Moreover, natural biocomponents used in microextraction sample preparation techniques are characterized by low toxicity and susceptibility to biodegradation. Under the optimized microextraction and liquid chromatography with mass spectrometry conditions, the method demonstrated good linearity over the range of $4.65 \cdot 10^{-8}$ mol/L – $1.60 \cdot 10^{-5}$ mol/L (for synapic acid) with a coefficient of determination of $R^2 = 0.9966 \pm 0.0012$, low limit of detection ($1.53 \cdot 10^{-8}$ mol/L) and limit of quantification ($4.63 \cdot 10^{-8}$ mol/L). Calibration curves for the determination of phenolic acids using developed procedures and estimated parameters analytical methods (e.g. repeatability, reproducibility and detection and quantification limits) enable the detection of analytes at low concentration levels. The proposed method was successfully applied to six medicinal plants samples: lemon balm (*Melissa officinalis*), thyme (*Thymus vulgaris*), rosemary (*Salvia rosmarinus*), milk thistle (*Silybum marianum*), artichoke (*Cynara scolymus*) and common coltsfoot (*Tussilago farfara*). It was found that among the tested plants, the richest source of sinapic acid is lemon balm: 3.94 ± 0.25 mg/100g of product. There is a need to extend the developed procedure to include additional compounds from the polyphenol group.

**Conclusions:** Biosurfactants have several advantages over chemical surfactants such as environmental compatibility, biodegradability, and a large ratio of surface area to volume. So they are suitable to develop sample preparation techniques based on

environmental protection. The effectiveness of the use of natural surfactants as pro-ecological extractants for the isolation of selected phenolic acids and their metabolites from medicinal plants was confirmed. As a result of the experiment, it was determined that the best biosurfactants are rhamnolipids, which form well-formed micelles in the presence of calcium chloride used as an electrolyte. The ability of rhamnolipid biosurfactants to form a stable colloidal phase with regions of different polarities can lead to extraction analyte using Van der Waals interactions. The developed isolation and determination procedure (ESI-LC-MS/MS) is characterized by a wide range of linearity and a low detection limit. Replacing synthetic surfactants (e.g. sodium dodecylsulfate) with natural biocomponents is in line with current trends related to the use of biomolecules during the isolation of analytes.

**Acknowledgements:** The research was financed by the National Science Center as a result of the Miniatura 7 project no 2023/07/X/ST4/01282.

**References:**

1. T.R. Bjerk, P. Severino, S. Jain, C. Marques, A.M. Silva, T. Pashirova, E.B. Souto, Bioengineering, 8 (2021) 115.
2. J. Sharma, D. Sundar, P. Srivastava, Frontiers in Molecular Biosciences, 8 (2021) 727070.
3. N.E.A.M Subuhi, S.M. Saad, N.N.M. Zain, V. Lim, M. Miskam, S. Kamaruzam, Journal of Seperation Science, 43 (2020) 3294.
4. S. Abbasi, S.A. Haeri, S. Sajjadifar, Microchemical Journal, 146 (2019) 106.
5. S. Abbasi, S.A. Haeri, A. Naghipour, S. Sajjadifar, Microchemical Journal, 157 (2020) 104874.
6. S.C. Chuo, A. Ahmad, S.H. Mohd-Setapar, S.F. Mohamed, M. Rafatullah, Journal of Molecular Liquids, 276 (2019) 225.
7. F.W.M. Hassan, M. Raoov, S. Kamaruzaman, A.H. Mohamed, W.N.W. Ibrahim, N.S.M.Hanapi, N.N. M. Zain, N.Yahaya, D.D.Y. Chen, Journal of Food Composition and Analysis, 102 (2021) 104057.
8. N. Kumar, N. Goel, Biotechnology Reports, 24 (2019) e00370.

# EXPLORING THE VERSATILITY OF XEROGELS BASED ON AGAR AND GELATIN

**M. GOLISZEK, A. CHABROS, M. DREWNIAK, W. SOFIŃSKA-CHMIEL**, Maria Curie-Skłodowska University, Faculty of Chemistry, Institute of Chemical Science, Analytical Laboratory, M. Curie-Skłodowska Sq. 3, 20-031 Lublin, Poland.

**Abstract:** The main aim of our research was understanding the role played by the breaking/reforming of specific intermolecular H-bond interactions involving water molecules and the chemical groups present in the polymer network on their structures. By doing this, it is hoped that knowledge is gained regarding the structural features and stability of agar and gelatin based xerogels. Better understanding of structural and morphological properties will contribute to the improvement of their performance in various fields of application.

**Introduction:** Most of the biopolymer-based gels are biocompatible, environment-friendly, and safe to use in various applications**.**
Xerogels are defined as dried gels that retain, at least in part, their porous texture after drying. Nowadays, they are considered as new sustainable and eco-friendly materials with diverse potential applications. Xerogels based on agar and gelatin can be demonstrated as an example for this approach [1-3].
Numerous research articles considering the synthesis and utilization of hydrogels and corresponding xerogels in different fields have been published, and still restless labor is giving for the betterment of the product quality. The detailed investigation on xerogels considering current environmental issues will reach to its target of making the greener solution of sustainability [4-5].
Among the wide ranges of noncovalent bonds, hydrogen bonds are commonly found in natural systems, due to their bonding strength and low toxicity, and have been widely used to design functional hydrogels. Moreover, the hydrogen bonds in a hydrogel serve as sacrificial bonds and show an excellent toughening effect, by effectively dissipating external energy. Hydrogen bond-crosslinked hydrogels have attracted particular interest for polymeric biomaterials [6-7].
The research on biopolymeric xerogels is still in the initial stage, and further investigation is required for scaling up the application on an industrial scale [8].

**Experimental:** In this research work to obtain the xerogels the previously obtained gels were drying. Traditional drying was preceded by the use of solvent exchange. Water and glycerol were replaced by ethyl alcohol and acetone. Scheme of the xerogels preparation is presented in Fig.1. Surface morphologies of obtained xerogels were evaluated by scanning electron microscopy (SEM), Fourier-transform infrared (FTIR) analyses as well as X-Ray Diffraction (XRD). The SEM micrographs were taken using a FEI Phenom World scanning electron-ion microscope. FTIR spectra were obtained using the ATR technique with a diamond crystal using a Nicolet 8700A FTIR spectrometer. The tests were performed directly from the sample surface in the wavenumber range of 4000-400 $cm^{-1}$ and with a spectral resolution of 4 $cm^{-1}$. A DTGS detector was used for

the research. The obtained spectra were subjected to ATR correction, baseline correction, and normalization using Omnic SpectaTM software. XRD analyses were performed using the Empyrean X-ray diffractometer (Malvern PANalytical, Almelo, The Netherlands).

1. *PREPARATION OF HYDROGELS:*
   - 2AG – 2% agar in glycerol
   - 2AW – 2% agar in water
   - 5ZG – 5% gelatin in glycerol
   - 10ZW – 10% gelatin in water

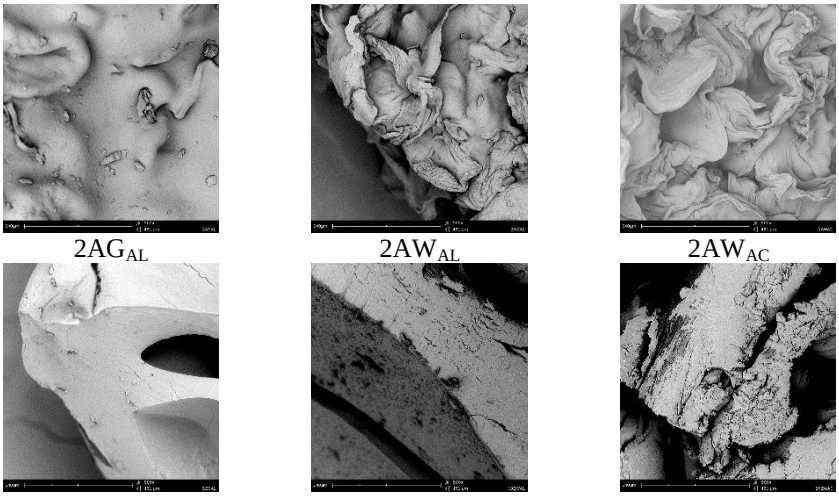
*2. SOLVENT EXCHANGE IN ETHANOL (AL) AND ACETONE (AC):*
   - 2AG – $2AG_{AL}$
   - 2AW – $2AW_{AL}$, $2AW_{AC}$
   - 5ZG – $5ZG_{AL}$
   - 10ZW – $10ZW_{AL}$, $10ZW_{AC}$

*3. TRADITIONAL DRYING:*
   - $2AG_{AL}$ - 78°C
   - $2AW_{AL}$, $2AW_{AC}$- 78°C and 56°C
   - $5ZG_{AL}$ - 78°C
   - $10ZW_{AL}$, $10ZW_{AC}$ - 78°C and 56°C

*4. ANALYSIS*
   - FTIR
   - SEM
   - XRD

**Fig.1.** Preparation of xerogels.

**Results:** Morphology of obtained xerogels based on agar and gelatin was examined using Scanning Electron Microscopy (SEM) and it is presented in Fig.2. FTIR spectroscopy was used to study hydrogen interactions. Fig.3 shows the FTIR spectra of xerogels in the region of hydroxyl groups. More information regarding the structure was provided by XRD studies. Changes in the structure of agar-based hydrogels compared to the starting component were observed. XRD diffractograms are presented in Fig.4.



$2AG_{AL}$ $2AW_{AL}$ $2AW_{AC}$

$5ZG_{AL}$ $10ZW_{AL}$ $10ZW_{AC}$



A) B)

**Fig.2.** SEM micrographs of the xerogels, agar (A) and gelatin (B).

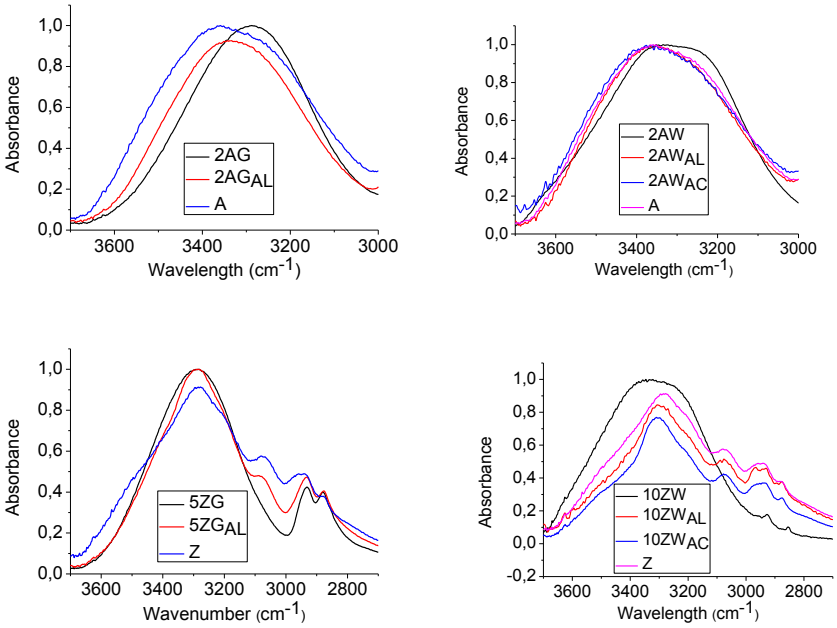



**Fig.3.** FTIR spectra of the xerogels in OH region.

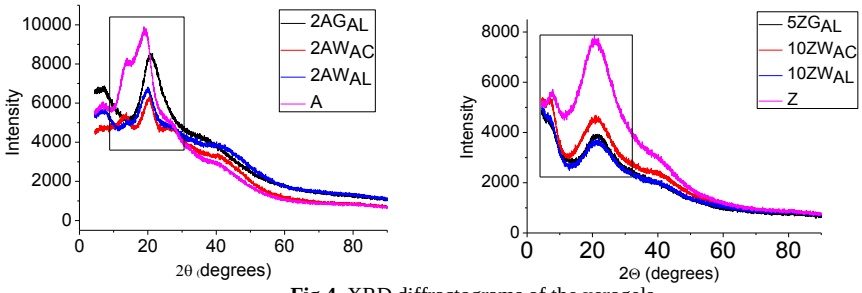



**Fig.4.** XRD diffractograms of the xerogels.

**Conclusions:** (1) The creation of additional network nodes containing triple helices of gelatin interacting with glycerol molecules may cause the evolution of rheological

properties, which is associated with an increase in the flexibility and strength of the gel formed by these complexes.
(2) Examination of glycerol complexes with polysaccharides (agar) and polypeptides (gelatin) shows that they exhibit similar rheological and structural effects due to the strong interactions between active groups in both components.
(3) The formation of glycerin-gelatin and glycerin-agar complexes can play the role of additional nodes in the network, thus strengthening (greater cross-linking) of the hardened supramolecular structure.

**Acknowledgements:** The research was carried out using the apparatus maintained based on the project INFRASTARt.

**Literature:**

1. G. Paladini, V. Venuti, V. Crupi, D. Majolino, A. Fiorati, C. Punta, Cellulose, 27 (2020) 8605.
2. R. Naohara, K. Narita, T. Ikeda-Fukazawa, Chemical Physics Letters, 670 (2017) 84.
3. H. P. S. Abdul Khalil, E. B. Yahya, H. A. Tajarudin, V. Balakrishnan, H. Nasution, Gels, 8 (2022) 334.
4. S. Yamasaki, W. Sakuma, H. Yasui, K. Daicho, T. Saito, S. Fujisawa, A. Isogai, K. Kanamori, Frontiers in Chemistry, 7 (2019) 316.
5. Y. Fukui, R. Inamura, K. Fujimoto, Polymer Journal, 53 (2021) 815.
6. H. Yu, Q. Xiao, G. Qi, F. Chen, B. Tu, S. Zhang, Y. Li, Y. Chen, H. Yu, P. Duan, Frontiers in Bioengineering and Biotechnology, 10 (2022) 855013.
7. L. Zhang, M. Liu, Y. Zhang, R. Pei, Biomacromolecules, 21(10) (2020) 3966.
8. G. Mummaleti, F. Kong, Journal of Agriculture and Food Research, 11 (2023) 100506.

# LIGNIN AS A SUSTAINABLE ADDITIVE FOR POLYMER PROTECTIVE MATERIALS

**M. GOLISZEK[1], K. SKRZYPIEC[1], B. PODKOŚCIELNA[2]**, [1]Maria Curie-Skłodowska University, Faculty of Chemistry, Institute of Chemical Science, Analytical Laboratory, M. Curie-Skłodowska Sq. 3, 20-031 Lublin, Poland, [2]Maria Curie-Skłodowska University, Faculty of Chemistry, Institute of Chemical Science, Department of Polymer Chemistry, M. Curie-Skłodowska Sq. 5, 20-031 Lublin, Poland.

**Abstract:** The study aimed to use technical kraft lignin as a functional additive for polymer protective materials and to replace part of the non-renewable product resources with bio-based ones. Lignin has a remarkable ability to act as a UV blocker due to the presence of UV chromosphere functional groups and therefore it has been widely used for the development of various UV-protective materials. The correlation between structural and morphological properties was revealed. Understanding the relationship between the structure, morphology and properties of the obtained polymer materials is a key aspect of their further functionalization.

**Introduction:** Recently, the concepts of green and sustainable chemistry have gained significant attention in the areas of research and development in both industry and academia, especially in developed industrial countries. Sustainable development is a crucial concept that recognizes our planet's limited resources, and therefore it is essential to reduce waste disposal and produce materials with the least energy consumption and from renewable resources. The development and implementation of green chemistry can contribute greatly to the sustainable development of our society. It can be achieved through developing novel scientific approaches to the relevant chemical processes and products, for example in the exploitation of renewable resources like biomasses [1-2].

Lignocellulosic biomass is an abundant and renewable resource from plants mainly composed of polysaccharides (cellulose and hemicelluloses) as well as an aromatic polymer (lignin). It has a high potential as an alternative to fossil resources to produce bio-sourced materials without compromising global food security [3].

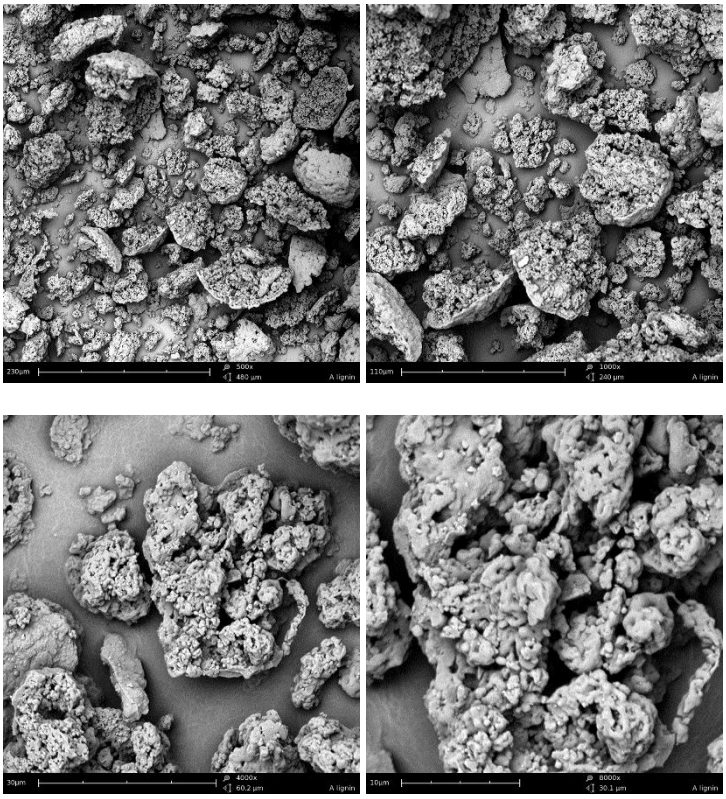
A promising candidate for the substitution of oil-derived polymer materials is lignin, the most abundant natural source of aromatics on our planet. It is a complex amorphous heteropolymer composed of phenylpropanoid building units: *p*-coumaryl, coniferyl, and sinapyl alcohol. Polyphenolic lignin reinforces plant cell walls and provides barrier properties against water, free radicals, microbes, and insects. The main chemical functional groups in lignin are the hydroxyl, methoxyl, carbonyl, and carboxylic groups. The proportion of these groups depends on the genetic origin and isolation processes applied. Lignin is a natural UV-blocking material; it exhibits excellent UV absorption ability owing to its aromatic structure. It is a by-product of the pulp and paper industry.

Lignin because of its unique structure and presence of various functional groups offers potential qualities for many applications, and yet it is underutilized as most of the lignin produced every year is burned as a low-value energy source. Its valorization is very

attractive from the sustainability point of view as well as from the perspective of transitioning toward a circular polymer economy [4-8].

**Experimental:**
All chemicals used were of analytical grade and were used as received without any further purification. Kraft lignin was obtained from Sigma-Aldrich. Diurethane polymer resin (URT-M) and reactive diluent (NVP), were purchased from Merck. The SEM micrographs were taken using a FEI Phenom World scanning electron-ion microscope. FTIR spectra were obtained using the ATR technique with a diamond crystal using a Nicolet 8700A FTIR spectrometer. The tests were performed directly from the sample surface in the wavenumber range of 4000-400 $cm^{-1}$ and with a spectral resolution of 4 $cm^{-1}$. A DTGS detector was used for the research. The obtained spectra were subjected to ATR correction, baseline correction, and normalization using Omnic SpectaTM software.

**Results:** The morphology of lignin as a key component of the obtained polymer protective materials was examined using Scanning Electron Microscopy (SEM). Lignin SEM micrographs are presented in Fig.1. It was shown that lignin particles are irregular in shape and agglomerate sizes. At high magnification of 8000 x and 15000x , it was observed that the surface of the agglomerates is a result of irregular granules attached.



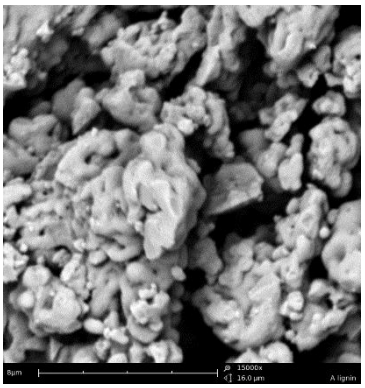


**Fig.1.** Lignin SEM micrographs (500x, 1000x, 4000x, 8000x and 15000x).

Fourier Transform Infrared Spectroscopy (FTIR) is a widely used technique in polymer science. It provides useful information about the chemical structure and functional groups present in the polymer which can help to understand its properties and behavior. FTIR spectra of the coatings are presented in Fig.2. Chemical structures of the coatings were investigated using ATR/FT-IT spectroscopy. The absorption bands coming from urethane NH- groups is observed between 3250-3500 $cm^{-1}$, and the bands visible in the range 2850–2960 $cm^{-1}$ are related to the $CH_2$ and carbonyl functional groups. The signal at 1717 $cm^{-1}$ is attributed to the ester groups from the urethane. The band at 1450 $cm^{-1}$ is ascribed to the bending vibration peaks of C–H in the acrylate network The C–O–C absorption band is observed at 1000–1250 $cm^{-1}$ and can be attributed to C–O ester and O–$CH_2$ groups of URT-M.

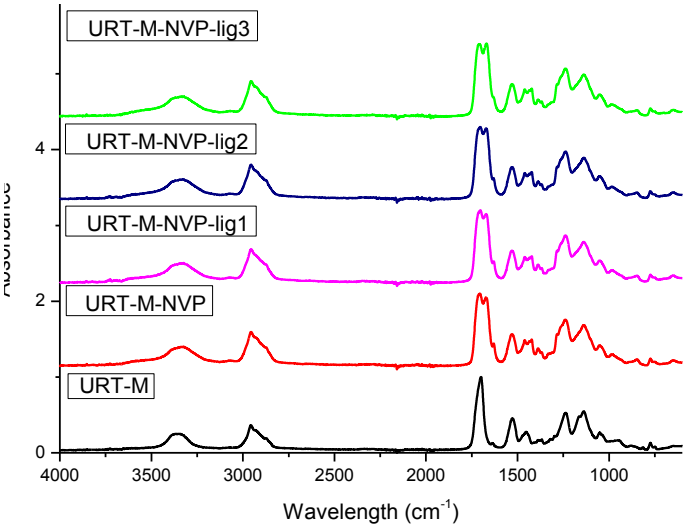



**Fig.2.** FTIR spectra of the polymers.

**Conclusions:** Polymer protective materials with lignin were synthesized by photopolymerization method. Lignin morphology was investigated using the SEM

technique. Their chemical structures and the presence of appropriate functional groups were confirmed using FTIR spectroscopy. The obtained results indicate the promising use of lignin as an environmentally friendly bio-additive for polymer protective materials and therefore contribute to its valorization.

**Acknowledgements:** The research was carried out using the apparatus maintained based on the project INFRASTARt.

**Literature:**

1. G. Jerald Maria Antony, S. Raja, S.T. Aruna, Chetan S. Jarali, Journal of the Mechanical Behavior of Biomedical Materials, 110 (2020) 103951.
2. B. Hararak, C. Winotapun, J. Inyai, P. Wannid, C. Prahsarn, Journal of Nanoparticle Research, 23 (2021) 193.
3. J. Azimvand, K. Didehban, S. Mirshokrai, BioResources, 13 (2018) 2887.
4. S. Beisl, A. Friedl, A. Miltner, International Journal of Molecular Sciences, 18 (2017) 2367.
5. A. Tagami, C. Gioia, M. Lauberts, T. Budnyak, R. Moriana, M.E. Lindström, O. Sevastyanova, Industrial Crops and Products, 129 (2019) 123.
6. J. Li, Q. Yan, X. Zhang, J. Zhang, Z. Cai, Polymers (Basel), 11 (2019) 623.
7. M.H. Tran, D.-P. Phana, E.Y. Lee, Green Chemistry, 23 (2021) 4633.
8. M. Goliszek, B. Podkościelna, N. Smyk, O.Sevastyanova, Pure and Applied Chemistry, 95 (2023) 475.

# SYNTHESIS AND CHARACTERISATION OF FIRE – RESISTANT POLY(URETHANE-METHACRYLATE) MATERIALS

**B. PODKOŚCIELNA[1], B. TARASIUK[1], K. MŁYNARCZYK[1], A. PUSZKA[1], K. DAWIDEK[2], A. GRYZIŃSKA[2]**, [1]Maria Curie-Sklodowska University, Faculty of Chemistry, Institute of Chemical Sciences, Department of Polymer Chemistry, Gliniana St. 33, 20-614 Lublin, Poland, [2]Elpar Cable Factory Sp. z o. o., Research and Development Department, Polna St. 40, 21-220 Parczew, Poland.

**Abstract:** This work aims to synthesize and study the properties of materials with enhanced flame retardancy. Poly(urethane-methacrylate) (UM) compositions consisting of oligo(urethane-methacrylate), diurethane dimethacrylate, *N*-vinyl-2-pyrrolidone, and flame retardant additives were obtained. The structure of the resulting composites was confirmed using ATR/FT-IR analysis. DSC studies were also carried out to determine the thermodynamic changes occurring in the samples as a result of temperature variations.

**Introduction:** One method of reducing the flammability of plastics is to modify them with special chemical additives - flame retardants. These compounds often contain atoms of elements such as chlorine, bromine, phosphorus, nitrogen, boron, or aluminium in their structure, which increase the fire resistance of the material. When different types of flame retardants are used together, e.g. chlorine compounds with antimony compounds or phosphorus compounds with nitrogen compounds, their effectiveness is enhanced through a synergistic effect. The working methods of flame retardant depend on its chemical structure. Flame retardants can act on the flame mechanism chemically and/or physically, in the vapour phase and/or in the solid phase. The chemical mechanism consists of deactivating the reactive radicals that sustain the burning process and producing a charred layer on the surface of the material. The physical mechanism, on the other hand, involves diluting the reaction mixture, absorbing the heat of the combustion reaction, and protecting the material from the access of oxygen and heat from the combustion zone. Several main factors can be distinguished that determine the use of a particular flame retardant. One aspect considered is the processing conditions of the material into which it is to be introduced. A fundamental reason for application is the effectiveness of the flame retardant. Halogen compounds and phosphorus compounds are recognized as the two most effective groups of flame retardants. However, more and more attention is now being paid to ensuring that the additives introduced into the material do not adversely affect the environment. This is the reason for the current trend away from halogen flame retardants, which is expected to lead to an increase in the use of halogen-free phosphorus compounds in the coming years [1].
This study presents the synthesis and characterization of compositions consisting of oligo(urethane-methacrylate), diurethane dimethacrylate, *N*-vinyl-2-pyrrolidone and flame retardant additives.

**Experimental:** Resin oligo(urethane-methacrylate) (OUM) was obtained by reacting an excess of 2,4- and 2,6-toluene diisocyante and poly(oxypropylene)diol with $M_\omega$=2000 g/mol and butane-1,4-diol in a 1:1 molar ratio. After the determination of the amount of unreacted NCO groups, the addition reaction was carried out with the calculated amount of 2-hydroxyethyl methacrylate and with 20% butyl acrylate as an active diluent [2].
Oligo(urethane-methacrylate) with $M_\omega$=850 g/mol is a dense liquid with a dynamic viscosity = 15500 mPa·s at 25 °C, a C=C double bond content of 2.315 mmol/g. Commercial diurethane dimethacrylate (DUDM) is a dense liquid with a refractive index of $n^{20}_D$ = 1.485, a density of 1.11 g/ml at 25 °C, an average mass $M_\omega$=470 g/mol, and a C=C double bond content of 4.255 mmol/g.
Figure 1 shows the formulas of the obtained resin oligo(urethane-methacrylate) and diurethane dimethacrylate resin.

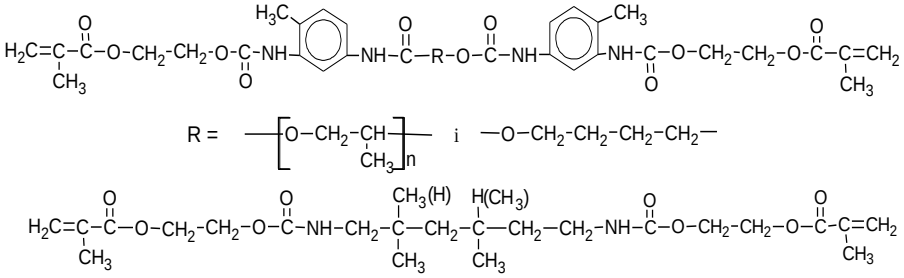


**Fig.1.** Fragment of chemical structures: resin oligo(urethane-methacrylate) [OUM] and diurethane methacrylate [DUDM].

The UM polymeric composition was obtained by mixing the components: resin oligo(urethane-methacrylate) (OUM), diurethane dimethacrylate (DUDM), *N*-vinyl-2-pyrrolidone (VP), polymerization photoinitiator 2,2-dimethoxy-2-phenylacetophenone (3% by weight) and a powdered flame retardant additive (FR), i.e. triallyl cyanurate (TAC), melamine and triallyl isocyanurate (1/1 weight) (Mel/TAiC), aluminium hydroxide/sodium metaborate (1/1 weight) or zinc oxide/boric acid (1/1 weight). The formulations and characteristics of the compositions obtained are shown in Table 1. Polymerization of the UM compositions was carried out by irradiating the samples with a UV lamp for 20 min.

**Table 1.** Composition and characteristics of the UM composition.

| Ex. nr. | OUM [g] | DUDM [g] | VP [g] | FR (*) | FR (*) [g] | Contents C=C [mmol/g] | Flexible segment [% weight] |
|---|---|---|---|---|---|---|---|
| 1 | 10.4 | 2.8 | 1.3 | - | - | 2.92 | 45.8 |
| 2 | 10.4 | 2.8 | 1.3 | TAC | 3.1 | 4.54 | 37.7 |
| 3 | 10.4 | 2.8 | 1.3 | Mel/TAiC | 3.9 | 3.56 | 36.0 |
| 4 | 10.4 | 2.8 | 1.3 | $Al(OH)_3/NaBO_2$ | 2.4 | 2.49 | 39.3 |
| 5 | 10.4 | 2.8 | 1.3 | $ZnO/H_3BO_3$ | 2.3 | 2.52 | 39.5 |

**Results:** ATR/FT-IR (attenuated reflectance technique) analysis was performed using a Bruker Tensor 27 FTIR spectroscope - Germany. Spectra were taken in the range 600-4000 $cm^{-1}$ in absorption mode. The resistance was 4 $cm^{-1}$ and 32 scans were taken for each sample spectrum. The spectra obtained are summarized in Fig.2.

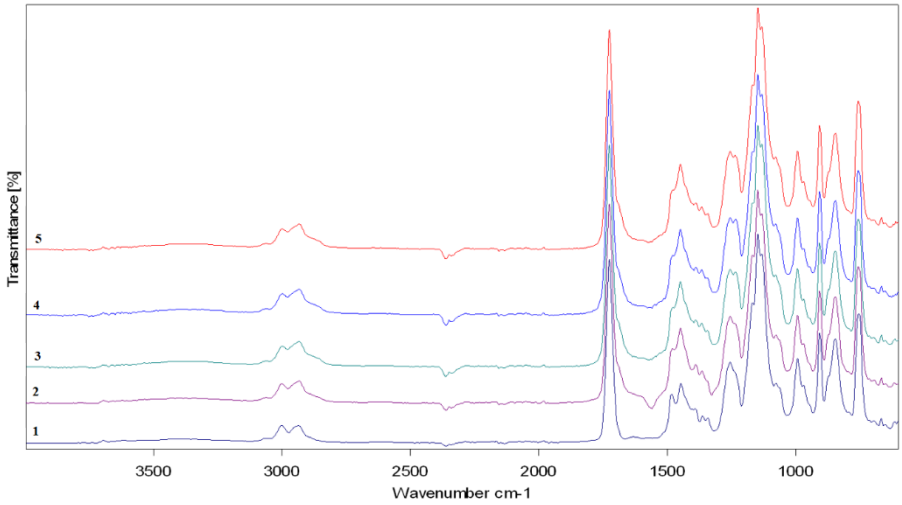



**Fig.2.** ATR/FT-IR spectra of the obtained varnish compositions.

Stretching vibrations from the -$CH_3$ aliphatic groups occur at wavelengths of approximately 2970 and 2870 $cm^{-1}$. C=O stretching vibrations are observed at wavelengths of 1710-1726 $cm^{-1}$. At approximately 1450 $cm^{-1}$, C=C stretching vibrations are visible. Bending vibrations of -$CH_3$- and -$CH_2$- are seen at a wavelength of approximately 1370 $cm^{-1}$. Stretching vibrations of C-N can be observed at a wavelength of approximately 1100 $cm^{-1}$.

Calorimetric scans were performed using differential scanning calorimetry (Netzsch DSC 204, Selb, Germany). The scans were performed at a heating rate of 10°C/min, with the first measurement performed at 25 °C – 200 °C (removal of moisture from samples) and the second measurement was performed from 0 °C to 550 °C in a nitrogen atmosphere (gas flow 30 $cm^3$/min). The sample mass was ~5-10 mg. An empty aluminium crucible was used as a reference. The data obtained from the experiments are shown in Fig.3 and summarized in Table 2.

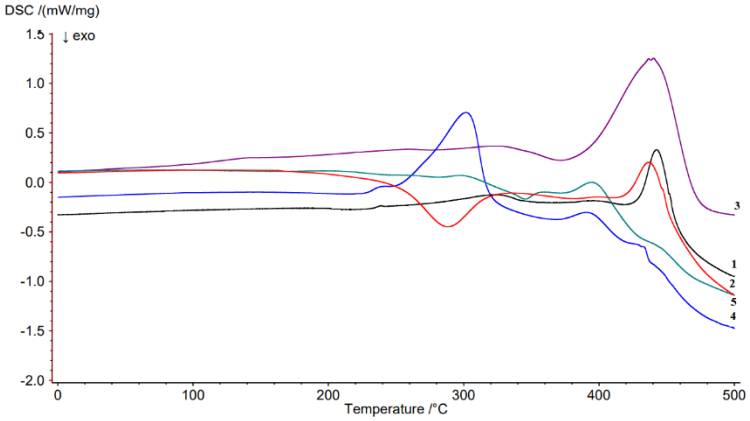



**Fig.3.** DSC spectra of compositions.

**Table 2.** DSC data of compositions.

| Composition | $T_1$ [°C] | $T_2$ [°C] |
|---|---|---|
| 1 | 442.6 | - |
| 2 | 288.3 | 436.7 |
| 3 | 440.2 | - |
| 4 | 301.6 | 390.5 |
| 5 | 394.4 | - |

The compositions exhibit good thermal resistance, as evidenced by the high degradation temperatures. For compositions 1, 3, and 5, one characteristic endothermic effect is observed in the temperature range of 394.4 - 442.6 °C.
This probably originates from the degradation of the composition components. For material 2, two effects are visible. The first, exothermic (288.3 °C), is due to the oxidation of the sample or the cross-linking of the composition. The second effect, endothermic (426.7 °C), is due to decomposition of the material. For composition 4, two endothermic effects are apparent (301.6 and 390.5 °C), which are responsible for the thermal decomposition of the material. Material 4 has the lowest decomposition temperature, while materials 3 and 1 have the highest [3].

**Conclusions:** UM compositions consisting of oligo(urethane-methacrylate), diurethane dimethacrylate, *N*-vinyl-2-pyrrolidone, and flame retardants: triallyl cyanurate, triallyl isocyanurate, melamine, aluminium hydroxide, sodium metaborate, zinc oxide, and boric acid were obtained. The structure of the materials obtained was confirmed using ATR/FT-IR techniques. The thermal resistance of the obtained coatings was determined. The highest resistance is characterized by a composition containing $Al(OH)_3/NaBO_2$ as a flame retardant, while the lowest thermal resistance has a composition without FR and containing Mel/TAiC.

**References:**

1. M. Gargol, T. Klepka, Ł. Klapiszewski, B. Podkościelna, Polymers, 13 (2021) 503.
2. B. Tarasiuk, Polish Journal of Chemical Technology, 5 (2003) 11.
3. K. Dziuba, K. Wnuczek, P. Wojtachnio, R. Sonnier, B. Podkościelna, Materials, 16 (2023) 1.

# PREPARATION AND STUDY OF PROPERTIES OF SOFT POLY(VINYL CHLORIDE) COMPOSITIONS WITH REDUCED FLAMMABILITY

**K. CIOSMAK[1], A. PUSZKA[1], A. GRYZIŃSKA[2], K. DAWIDEK[2], B. PODKOŚCIELNA[1]**, [1]Maria Curie-Sklodowska University, Faculty of Chemistry, Institute of Chemical Sciences, Department of Polymer Chemistry, Gliniana 33 St., 20-614 Lublin, Poland, [2]Elpar Cable Factory Sp. z o. o., Research and Development Department, Polna 40 St., 21-220 Parczew, Poland.

**Abstract:** In this work, the effects of triphenyl phosphate, pure aluminum hydroxide, and a commercial aluminum hydroxide-based flame retardant on selected properties of soft poly(vinyl chloride) compositions were investigated. The flammability, Shore hardness, and tensile properties of the obtained compounds have been tested. Based on the results obtained, it was found that the type and amount of flame retardant additive significantly influence the properties of the obtained compositions.

**Introduction:** Polymers are widely used materials of great economic and industrial importance and can be found in almost every material used in our daily lives [1]. Due to their particularly advantageous properties in the current world, such as good mechanical properties, durability, strength, renewability, resistance to a wide range of temperatures and atmospheric agents, biodegradability, recyclability, low production costs or the ease with which all of the above properties can be influenced by special additives, they are used in many different industries [2]. We can find them in building structures, packaging, thermal and electrical insulation, clothing, transport equipment, cosmetics, sanitary products or even medicines [2].

However, they have one major drawback, namely that they are quite flammable, which translates into risks for human and animal health, property damage, as well as environmental pollution due to the release of toxic gases and free radicals during the decomposition process. To prevent this, special flame retardants are added to plastics. This additive transforms them into low-flammability materials, thus extending their range of applications [1]. These flame retardants are mainly used in plastics from four areas: electronics, construction, equipment, and transport [3]. Their action is to impede the ignition of the material, retard the spread of fire, reduce the amount of smoke produced, and have a self-extinguishing effect. The addition of such a substance to plastic is not always inert and usually affects the mechanical and physical properties of the material to some extent. An important aspect of introducing flame retardants is to determine this effect in the final product and to select the type and content of flame retardant so that it protects the material as much as possible while having a minimal effect on its properties [1].

This study aimed to determine the effect of selected flame retardants (flame retardants) on the flammability and mechanical properties of poly(vinyl chloride) (PVC) plasticizers. The study aimed to compare the behaviour of flame retardant compositions during exposure to a flame, depending on the flame retardant used and its content in the

plastic. The second objective was to understand how different types of compositional modifications of the resulting materials affect their strength and hardness properties.

**Experimental:** Three types of soft PVC compositions with variable content (5, 10, 15, 20 and 30 wt.%) of flame retardant were obtained for the tests. The flame retardants used were triphenyl phosphate (TPP, Sigma Aldrich), aluminum hydroxide (ATH, Riedel-de Haën), and a commercial flame retardant based on aluminum hydroxide (FR WS, 421 West System). The base mixture of each composition was obtained by mixing PVC (®VINNOLIT E 68 SA, Westlake Vinnolit GmbH & Co. KG), epoxidized soybean oil (ERGOPLAST ES, Boryszew ERG), bis(2-ethylhexyl phthalate (ERGOPLAST FDO, Boryszew ERG), zinc stearate (ERGOTERM SZ, Boryszew ERG) and calcium stearate (ERGOTERM RC, Boryszew ERG). Appropriate masses of flame retardants were added to each of the mixtures of ingredients prepared in this way. To obtain hardened plasticizers, the mass was poured between two thin, rectangular glass panes and then heated in the dryer at 135°C for 20 minutes. After the heated molds were removed from the dryer and cooled to ambient temperature, the plasticizers were carefully pulled out from between the glass sheets. They were then cut into oblong rectangular strips measuring approximately 8 cm × 1 cm × 0.2 cm each (Fig.1).




**Fig.1.**Visual appearance of plasticizer molds and plasticizer shapes with 30 wt.% of flame retardant.

The obtained compositions were tested for flammability (by the PN-EN 60695-11-10:2014-02 standard), as well as hardness (following the International Standard EN ISO. 868:2003) and tensile strength (under the International Standard ISO 527- 2:2012).

**Results:** At the stage of heating the PVC composition, differences between the addition of individual flame retardants could be noticed. The general trend for all samples was an increase in structural heterogeneity (i.e. presence of air bubbles) with increasing flame retardant content in the composition (Fig.1). The blank was relatively uniform and had few air bubbles in its structure. Materials made of TPP had the most heterogeneous structure, while plastics with the addition of ATH had the most compact structure.
The flammability test confirmed that each flame retardant added to the plastic did its job to a greater or lesser extent, and its effect on flammability depended on the amount of flame retardant used. In all cases, while the samples were burning, black smoke rose, which is typical for PVC burning, and after the flame was extinguished, the smoke was bright (Fig.2).




**Fig.2.** The course of an exemplary process of burning a sample.

Among the compounds used, TPP had the best flame retardant properties, and its effectiveness increased with increasing amounts in the tested material. The optimal content of TPP in the material seems to be 15 wt.% due to the unchanged results of the length that was burned at higher contents and a minimally shorter burning time after extinguishing the fire source (Table 1). During combustion, the material with the addition of TPP was carbonized (Fig.3). TPP also turned out to be the most effective flame retardant among those tested, taking into account both parameters.

**Table 1.** The flammability, hardness and tensile test data of obtained compositions.

| Type of flame retardant | Amount of flame retardant [wt%] | The length of the material that was burned | | Self-extinguishing time [s] | Hardness [Sh A] | Elongation at break [%] | Tensile strenght [MPa] |
|---|---|---|---|---|---|---|---|
| | | [cm] | [%] | | | | |
| TPP | 5 | 1.3 | 16 | 3 | 65.6 | 134 | 1,75 |
| | 10 | 0.8 | 10 | 8 | 62.0 | 142 | 1.64 |
| | 15 | 0.5 | 6 | 3.5 | 57.8 | 152 | 1.64 |
| | 20 | 0.5 | 6 | 2.7 | 58.6 | 175 | 1.80 |
| | 30 | 0.5 | 6 | 2.5 | 47.2 | 163 | 1.09 |
| ATH | 5 | 1.8 | 23 | - | 67.8 | 131 | 1.67 |
| | 10 | 1.4 | 18 | 58 | 67.6 | 131 | 1.97 |
| | 15 | 0.8 | 10 | 19 | 68.6 | 128 | 1.84 |
| | 20 | 1.5 | 19 | 11 | 68.6 | 126 | 1.65 |
| | 30 | 0.2 | 3 | 18 | 68.4 | 127 | 1.68 |
| FR WS | 5 | 1.3 | 16 | - | 68.8 | 226 | 3.66 |
| | 10 | 1.6 | 20 | 30 | 68.2 | 226 | 3.48 |
| | 15 | 0.7 | 9 | 16 | 68.6 | 188 | 3.12 |
| | 20 | 1.0 | 13 | 7 | 68.6 | 181 | 2.94 |
| | 30 | 0.9 | 11 | 11 | 70.0 | 171 | 2.84 |
| 0% | | 2.3 | 29 | - | 68.6 | 100 | 1.58 |

In the case of ATH, the tendency is also relatively preserved: the higher the flame retardant content, the lower the losses and the shorter the burning time. It turned out to be the weakest additive among those tested, taking into account the relatively long burning time and the greatest losses of the burned substance at low concentrations. During burning, the sample showed a greater tendency to melt than to char. Taking into account FR WS, in terms of the section that was burned, the content of 15 wt.% was the best, while the sample with the content of 20 wt.% had the shortest burning time. The results for this compound are more scattered, but the tendency of decreasing flammability with increasing flame retardant content is still maintained.

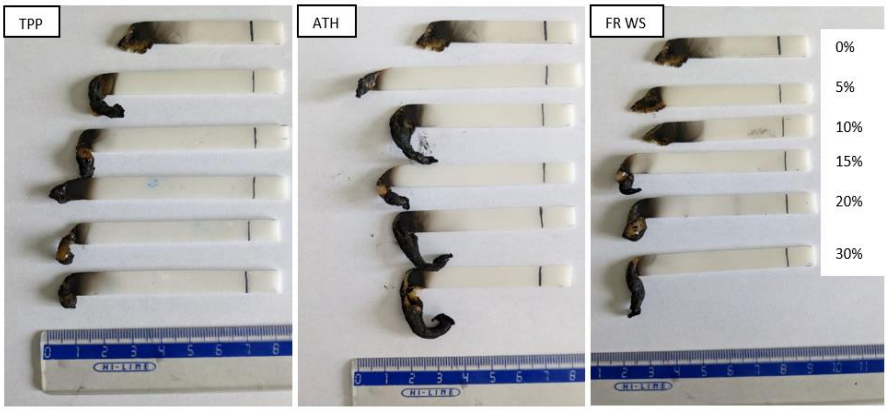



**Fig.3.** The appearance of fittings in all series after flammability tests.

The hardness test showed (Table 1) that the hardness of the composition is most influenced by the addition of TPP. Already with the addition of 5 wt.%, this value drops by 3 degrees and the decrease in value continues with each subsequent addition. At 30 wt.% it is less by about 20Sh. The addition of ATH affects this mechanical property to a minimal extent at low contents and practically does not affect it at higher values. FR WS is the only one that contributes to the increase in this value. Following the trend, the greater the mass addition, the harder the material becomes. However, this is a difference of 1.4Sh in the entire tested range. All flame retardants increased the strength and elongation of the tested material. When TPP is added, as its content increases, the elongation increases, but its tensile strength decreases. The exception is the sample with 20 wt.% TPP, which is characterized by the greatest elongation and the highest strength. The addition of ATH also had a positive effect on both values, but no significant relationship was observed between the mass content of ATH and the size of the effect. The addition of FR WS to the material had the greatest impact on both properties. The lower the share of FR WS in the product, the higher the elongation value and the higher the tensile strength.

**Conclusions:** Analysis of the flammability of the PVC compositions obtained showed a simple relationship that, regardless of the type of flame retardant, as its weight content in the composition increases, the rate of combustion and the burning time of the plastic after removal of the fire source decreases. The study also shows that TPP has the best flame-retardant properties of those tested. Considering the burning time of the sample after removal from the flame, TPP also showed the most favourable time, followed by FR WS and ATH.

## References:

1. H. Namazi, Bioimpacts, 7 (2017) 73.
2. E.W. Madyaratri, M.R. Ridho, M.A. Aristri, M.A.R. Lubis, A.H. Iswanto, D.S. Nawawi, P. Antov, L. Kristak, A. Majlingová, W. Fatriasari, Polymers, 14 (2022) 362.
3. Web page: https://www.chemicalsafetyfacts.org/flame-retardants/, access 21.03.2024.

# THE INFLUENCE OF SCREW ROTATION SPEED OF EXTRUDER TO GELATION PROCESS OF POLY(VINYL CHLORIDE)

**K. DAWIDEK**, **A. GRYZIŃSKA**, Elpar Cable Factory Sp. z o. o., Research and Development Department, Polna St. 40, 21-220 Parczew, Poland.

**Abstract:** The degree of gelation is an important parameter in poly(vinyl chloride) (PVC) processing. Its value for a given mixture is influenced by processing parameters such as temperature, pressure and shearing forces. The study examined the influence of changes in the rotational speed of the extruder screw on the change in the value of the gelation degree of the PVC mixture used for cable coatings. PVC granules available on the market were used in the experiment.

**Introduction:** The cable insulation and sheathing industry utilizes various types of plastics based on their intended usage. Among the critical factors influencing material selection are the physical and electrical properties. These properties vary depending on the chemical composition of the plastic mixture. Poly(vinyl chloride) (PVC) has been a primary material for cable wire coating for several decades [1]. PVC is a widely used polymer due to its affordability and versatility. In its pure form, PVC is a rigid polymer at room temperature with limited thermal stability. However, its properties can be easily adjusted by incorporating suitable additives. These additives include antioxidants, stabilizers, plasticizers, antistatic agents, flame retardants, and fillers etc. [2,3].
The physical properties of PVC used in the insulation and sheathing industry significantly impact product quality and pricing. Key properties include: hardness Shore (A), specific gravity (gm/cm³), elongation at break (%), tensile strength (MPa), volume resistivity (Ohm cm), (important for materials intended for the cable insulating layer). By understanding the proportions of compounds in the PVC mixture, manufacturers can tailor products to meet specific demands [1].
*Plastic extrusion proces:* Extrusion is a crucial and perhaps the oldest process for shaping thermoplastic polymers. To ensure quality during extrusion manufacturing, it's essential to identify, control, and monitor various parameters. These include equipment condition, working conditions, temperatures, pressures, die quality, composition of the processed material, and cooling methods (Fig.1) [4-6].

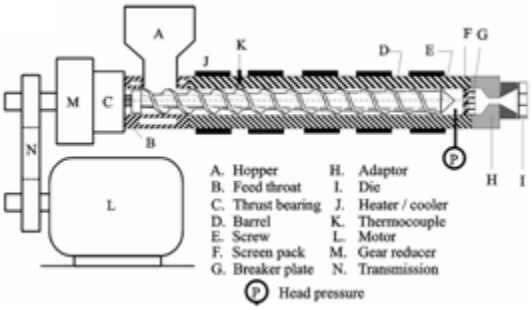



**Fig.1.** Components of a typical extruder [7].

Plastic extrusion is a high-volume manufacturing technique where raw plastic is melted and shaped into a continuous profile. The process begins by feeding plastic material (such as pellets, granules, flakes, or powders) from a hopper into the extruder's barrel. Mechanical energy from turning screws and heaters along the barrel gradually melts the material. The resulting molten polymer is then forced through a die, shaping it into a form that solidifies during cooling [4-6].

*Gelation proces:* In various scientific papers, it has been noted that during processing, PVC undergoes a gelation process that transforms its primary morphological structure into a secondary one. This transformation includes the crystalline phase present within PVC grains [8].

The degree of gelation is defined as the ratio of small, secondary crystallites (with melting points below Tp) to large primary crystallites (with melting points above Tp). The content of crystallites is determined by analyzing the enthalpies of fusion using techniques like Differential Scanning Calorimetry (DSC). These small crystallites, with melting points around Tp, manifest as a melting gap in DSC curves due to various recrystallization processes [9].

Gelation process occurs under the influence of the simultaneous action of heat, shearing forces and pressure. The action only of shearing forces causes the grain to crumble, while exclusive heating causes changes in their outer layer [10]. By the analysis of the effects related to PVC gelation, where the most often discussed value is the degree of gelation, the impact of shearing conditions is generally not include. The most discussed is the influence of temperaturę [9].

In this study, the gelation of PVC in the extrusion process was investigated depending on the rotational speed of the screw of a single-screw extruder, under established thermal conditions.

**Experimental:** To carry out the experimental test, coating formulation of PVC was used, with a density of 1.4 g/cm$^3$, a melt flow rate (175 °C, 15kg) MFR = 22.66 g/10min, hardness 88ShA, tensile strength 12.5MPa and relative elongation at break min. 150%. Conditions of experimental research: a classic three-zone screw with a diameter of D = 100 mm and a length to diameter ratio L/D = 25 was used. The tests were performed in the classic gravity feeding mode, i.e. without material dosing, in a wide range of rotational speeds (N = 5–80 rpm), with constant processing temperature conditions, tj. temperature of the extruded material 172±1$^o$C.

After stabilizing the extruder parameters and proper plasticization of the extruded material, samples of the extruded material were taken at various screw rotational speed settings for 36 s. Samples were taken from the material flashes after cooling in room conditions for further tests.

Additionally, rheological measurements of the PVC compound were conducted using a specially designed apparatus – Plastometer Mflow Zwick**.** The experimental conditions for MFR measurements were as presented in Table 1.

**Table 1.** Experimental conditions for MFR measurements.

| | |
|---|---|
| Barrel temperature | 175±2 $^o$C |
| Piston load | 15 kg |
| Piston diameter | 9.55 mm |
| Capillary die length | 8 mm |
| Capillary die diameter | 2.095 mm |
| Material heating time | 10 min |

The thermal transitions associated with the melting of primary and secondary crystallites were determined using differential scanning calorimetry (DSC). The experiments were conducted with a Netzsch 204 F1 Phoenix apparatus, operating at a heating rate of 10 °C/min, spanning a temperature range from 0 to 300 °C in an argon atmosphere. The average sample weight was 10.0 ± 2 mg.
The gelation degree (G) was calculated by two method. The first one included the DSC analysis and the second one by calculated indirectly from the MFR test result.
The gelation degree ($G_{DSC}$) by DSC analysis was calculated based on the melting enthalpies (in J/g) of primary (ΔHA) and secondary (ΔHB) crystallites, following the formula:

$$G_{DSC} = \frac{\Delta HA}{\Delta HA + \Delta HB} \cdot 100\%$$

The gelation degree ($G_{MFR}$) by MFR method was calculated according to the formula [6]:

$$G_{MFR} = \frac{MFR_{min} - MFR_X}{MFR_{min} - MFR_{max}} \cdot 100\%$$

where: $MFR_X$ – MFR of the tested material, $MFR_{max}$ – MFR material with the highest degree of gelation, $MFR_{min}$ – MFR plastic with the lowest degree of gelation.

Full characterization of processed PVC requires the use of various research methods. In practice, the most frequently used are: DSC analysis and rheological tests [6].

**Results:** As a result of the research, the following results were obtained. Table 2 presents numerical data of MFR and gelation degrees values, while Figs. 1-3 shows graphical dependences of MFR and gelation degrees on the screw rotation speed.

**Table 2.** Results of the tests.

| N | MFR | $G_{MFR}$ | $G_{DSC}$ |
|---|---|---|---|
| [rpm] | [g/10min] | [%] | [%] |
| 5 | 20.93 | 0.00 | 49.15 |
| 10 | 21.37 | 2.92 | 51.58 |
| 20 | 21.78 | 5.64 | 56.96 |
| 40 | 25.76 | 32.05 | 65.85 |
| 60 | 30.32 | 62.31 | 75.93 |
| 80 | 36.00 | 100.00 | 94.57 |

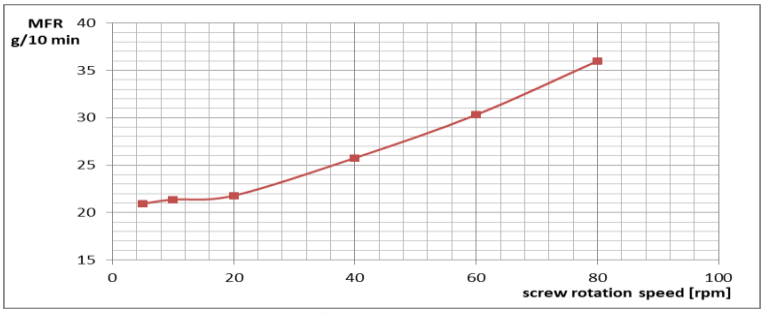



**Fig.2.** Dependence of MFR on the screw rotation speed.

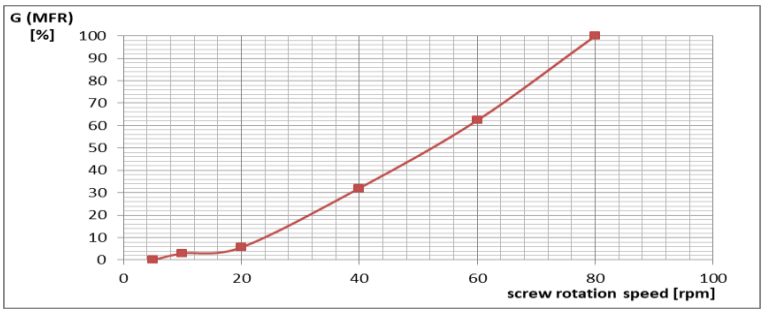



**Fig.3.** Dependence of gelation degree (from MFR) on the screw rotation speed.

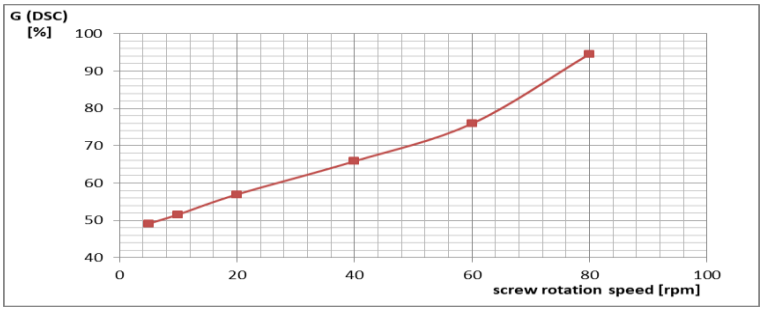



**Fig.4.** Dependence of gelation degree (from DSC) on the screw rotation speed.

**Conclusions:** The research has shown that increasing the screw rotational speed increases the degree of gelation of the processed material. Differences in values between the degree of gelation obtained using the DSC analyzer and using the MFR measurement may result from different research approaches. In the case of $G_{DSC}$, the result may be influenced by the amount of filler and the presence of a plasticizer.

## References:

1. A.H. Esmail, Scholars International Journal of Chemistry and Material Science, 3 (2020) 24.
2. A. Marcilla, S. Garcia, J.C. Garcia-Quesada, Polymer Testing, 27 (2008) 221.
3. S. Altarazi, R. Hemeimat, M. Wakileh, R. Qsous, A. Khreisat, International Scholarly and Scientific Research & Innovation, 7 (2013) 397.
4. K. Wilczyński, praca zbiorowa, Przetwórstwo tworzyw polimerowych, Oficyna Wydawnicza Politechniki Warszawskiej, Warszawa, 2018.
5. P. M. Patil, D.B. Sadaphale, International Journal of Latest Technology in Engineering, Management & Applied Science, 8 (2018) 13.
6. K. Piszczek, Żelowanie Suspensyjnego, Nieplastyfikowanego Poli(Chlorku Winylu), Wydawnictwa Uczelniane UTP, Bydgoszcz, Poland, 2009.
7. Chan I. Chung, Extrusion of Polymers Theory and Practice, Hanser, Munich, 2019.
8. K. Piszczek, J. Tomaszewska, T. Sterzyński, Polimery, 55 (2010) 106.
9. Z. K. Alobad, H. S. Alreheem, International Journal of Civil Engineering and Technology, 9 (2018) 2036.
10. S. Zajchowski, K. Piszczek, J. Tomaszewska, Polimery, 46 (2001) 232.

# STUDIES ON THERMAL AND MECHANICAL BEHAVIOR OF NEW BIPHENYL - DERIVATIVE THERMOPLASTIC POLYURETHANES

**M. ROGULSKA, M. MACIEJEWSKA**, Maria Curie-Skłodowska University, Faculty of Chemistry, Institute of Chemical Sciences, Department of Polymer Chemistry, Gliniana St. 33, 20-614 Lublin, Poland.

**Abstract:** In this study, new thermoplastic sulfur-containing polyurethanes were synthesized via a one-step melt polyaddition from biphenyl-derivative diol with two methylene groups in the aliphatic chain, i.e. 2,2'-[[1,1'-biphenyl]-4,4'-diylbis(methylenesulfanediyl)]diethanol as nonconventional chain extender, 1,1'-methanediylbis(4-isocyanatobenzene) and polyether soft segment formed from poly(oxytetramethylene) diol with the molar mass of 1000 g/mol. The polyurethanes, with hard-segment-contents ranged from 30 to 60 mass %, were studied in order to describe their thermal and mechanical properties by means of differential scanning calorimetry, thermogravimetry (TG) and TG coupled with FTIR spectroscopy, as well as Shore hardness and tensile tests.

**Introduction:** The present paper is a continuation of the studies on the synthesis, structure and properties of the new thermoplastic polyurethanes (TPUs) prepared from various α,ω-aliphatic-aromatic diols containing sulfide linkages used as nonconventional chain extenders, commercial diisocyanates as well as commercial polymer diol soft segments. According to the literature, the presence of sulfur atoms can improve some of their properties, such as adhesion to metals, chemical, radiative and microbial resistance or refractive index [1-3]. Herein, the synthesis and characterization of the new TPUs with hard segments built from 1,1'-methylenebis(4-isocyanatobenzene) (MDI) and 2,2'-[[1,1'-biphenyl]-4,4'-diylbis(methylenesulfanediyl)]diethanol (BMS-E diol), and polyether soft segments formed from poly(oxytetramethylene) diol (PTMO) with the molar mass of 1000 g/mol are reported.

**Experimental:** The BMS-E diol (m.p.=153–154 °C) was synthesized by the reaction of ([1,1'-biphenyl]-4,4'-diyl)dimethanethiol with 2-chloroethanol in a water-ethanolic sodium hydroxide solution and crystallized from toluene. MDI (98 %) from Sigma-Aldrich was used without further purification, while PTMO (Sigma-Aldrich) prior to the use was heated at 90 °C *in vacuo* for 10 h.
Reduced viscosities ($\eta_{red}$s) of 0.5 % TPU solution in 1,1,2,2-tetrachloroethane were measured in an Ubbelohde viscometer at 25 °C. ATR-FTIR spectra were performed using a Perkin-Elmer 1725X spectrometer. Samples were prepared as films. Thermogravimetric (TG) measurements were done on a Netzsch STA 449 F1 Jupiter thermal analyzer in synthetic air (flow = 20 $cm^3$/min) from 30 °C to 700 °C at the heating rate of 10 °C/min. The composition of gases evolved during the decomposition process was analyzed by a Bruker Tensor 27 FTIR spectrometer coupled on-line to a Netzsch STA instrument by the teflon transfer line heated to 200 °C. The FTIR spectra were recorded in the spectral range of 600–4000 $cm^{-1}$ with a 4 $cm^{-1}$ resolution and 16

repetitions. Differential scanning calorimetry (DSC) was carried out on a Netzsch DSC 204 instrument at a heating and cooling rate of 10 °C/min in the range of -100–200 °C. Glass-transition temperatures ($T_g$s) for the samples were defined as the inflection point on the curves of the heat-capacity changes, and the melting temperatures ($T_m$s) as endothermic peak maxima. Hardness was determined using the Shore method on a 7206/H04 hardness tester from Zwick at a temperature of 23 °C. The values were read after 15 s of measurement. Tensile testing was performed on a Zwick/Roell Z010 tensile-testing machine at the speed of 100 mm/min at 23 °C; tensile test pieces of 1 mm thick and 6 mm wide (for the section measured) were cut from the pressed sheet.

TPUs were obtained according to scheme shown in Fig.1. by a one-step melt polyaddition method at $I_{NCO}$=1. The process was carried out in a nitrogen atmosphere at a temperature of 140-150 °C for 2.5 hours.

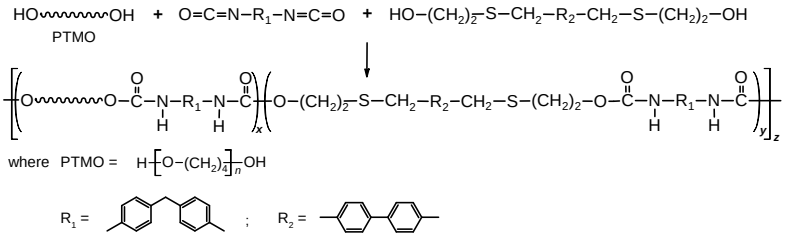



**Fig.1.** Schematic representation of the synthesis route of TPUs.

**Results:** The TPUs were slightly yellow elastomers with relatively low molar masses, as indicated by the $\eta_{red}$ values (Table 1). Their chemical structures were verified by ATR-FTIR spectroscopy.

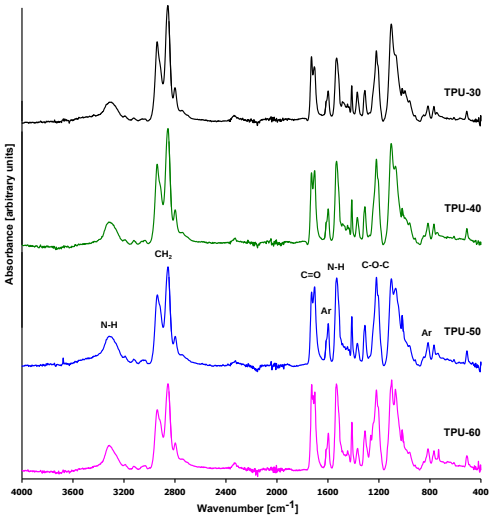



**Fig.2.** ATR-FTIR spectra of TPUs.

The major ATR-FTIR absorption bands (Fig.2) were as follows: 3315–3310 $cm^{-1}$ (N-H stretching), 1729–1703 $cm^{-1}$ (C=O stretching) and 1533-1531 $cm^{-1}$ (N-H bending) of the urethane group; 1104-1100 $cm^{-1}$ (C-O stretching of the ether group); 2940–2938 $cm^{-1}$

and 2856–2854 $cm^{-1}$ (asymmetric and symmetric C-H stretching of the methylene group); 1598–1597 $cm^{-1}$ (C-C stretching of the benzene ring); 815–814 $cm^{-1}$ (C-H bending of *p*-disubstituted benzene ring).

As can be seen from the above presented data, all the spectra exhibited the absorption bands of the urethane, ether and methylene groups and the benzene ring, but they did not show a band at ~2270–2260 $cm^{-1}$, which indicates that all isocyanate groups were converted to urethane ones.

The results obtained using DSC method (Table 1) revealed that the TPUs had amorphous (TPU-30 and TPU-40) or partially ordered structures within hard segments (TPU-50 and TPU-60). The definite $T_g$ values determined for them increased as the hard-segment content increased, from -37 °C to -19 °C (first heating scans) or to -1 °C (second heating scans). The comparison of the $T_g$ of the pure PTMO soft segment (-77 °C) and those of the synthesized TPUs shows that the new polymers possessed a relatively low degree of microphase separation.

**Table 1.** Designations, $\eta_{red}$ values, DSC and TG-DTG data obtained for TPUs.

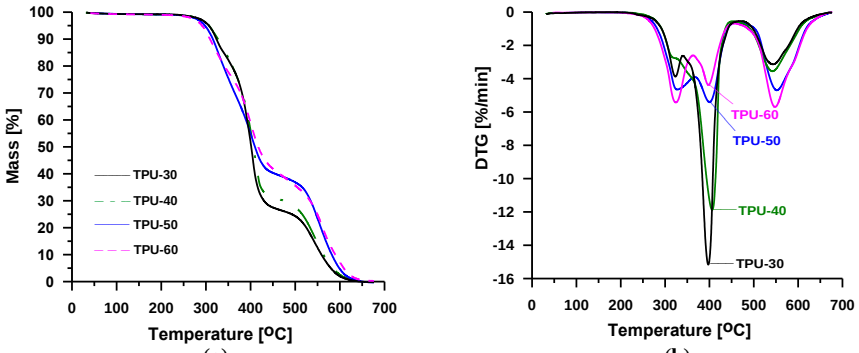
| TPU | Hard-segment content [mass %] | $\eta_{red}$ [dL/g] | $T_5$[a] [°C] | $T_{10}$[a] [°C] | $T_{50}$[a] [°C] | $T_{max}$[b] [°C] | $T_g$[c] [°C] | $T_g$[d] [°C] | $T_m$[c] [°C] | $\Delta H_m$[c] [J/g] |
|---|---|---|---|---|---|---|---|---|---|---|
| TPU-30 | 30 | 0.51 | 306 | 323 | 401 | 323, 397, 543 | -37 | -37 | | |
| TPU-40 | 40 | 0.41 | 305 | 322 | 405 | 324, 406, 542 | -25 | -25 | | |
| TPU-50 | 50 | 0.45 | 297 | 315 | 408 | 327, 400, 552 | -19 | -2 | 212 | 8.6 |
| TPU-60 | 60 | 0.15 | 293 | 310 | 420 | 324, 398, 548 | -19 | -1 | 220 | 20.7 |

[a] the temperature of 5, 10 and 50% mass loss from the TG curve, respectively; [b] the temperature of the maximum rate of mass loss from the differential TG (DTG) curve; [c,d] first and second heating scan, respectively.

As is clear from the TG study of the TPUs (Table 1, Fig.3) they all were characterized by a quite good thermal stability, though dependent on the content of hard segments. The $T_5$s and $T_{10}$s were contained in the range of 293-306 °C and 310-323 °C, respectively. These temperature indicators decreased as the amount of hard segments grew. From this study it also follows that the TPUs decomposed in three stages. The first stage, with a maximum at 323-327 °C, was mainly connected with the decomposition of hard segments and the second one, with a maximum at 397-406 °C, was related to the decomposition of the PTMO soft segments. In turn, the third stage indicates the occurrence of oxidative processes of products formed in previous stages.

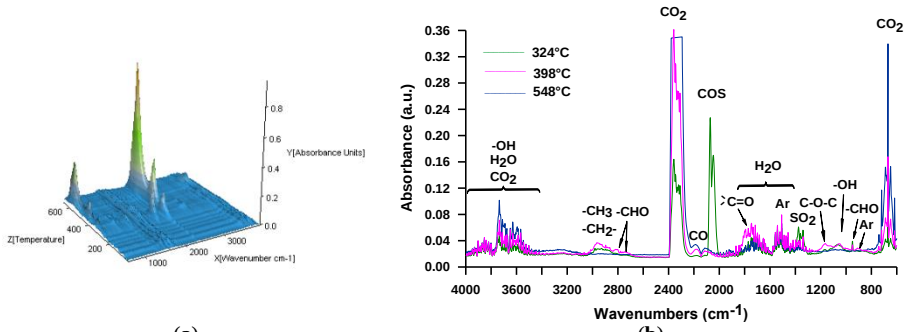
The TPUs decomposition was associated with the evolution of the following volatile products (Fig.4): carbon dioxide, carbon monoxide, carbonyl sulfide, sulfur dioxide, aliphatic aldehydes, alcohols and ethers as well as aromatic compounds. The analysis of volatile products confirms that the decomposition of sulfide bonds occurred in the first stage (release of carbonyl sulfide and sulfide oxide), and the decomposition of ether bonds took place in the second stage.

Tests of the mechanical properties (Table 2) showed that TPU-40 and TPU-50 had good tensile strength. Moreover, it was found that as the content of hard segments in TPU increased, elongation at break decreased, while the modulus of elasticity and Shore a hardness increased.




(**a**) (**b**)

**Fig.3.** TG (**a**) and DTG (**b**) curves of TPUs.




(**a**) (**b**)

**Fig.4.** FTIR spectra of volatile products evolved during thermal decomposition of TPU-60: (**a**) 3D and (**b**) extracted at the maxima of decomposition.

**Table 2.** Hardness and tensile properties of TPUs.

| TPU | Shore A/D hardness [°Sh] | Modulus of elasticity [MPa] | Tensile strength [MPa] | Elongation at break [%] |
|---|---|---|---|---|
| TPU-30 | 34/– | 0.4 | 7.3 | 750 |
| TPU-40 | 65/21 | 9.3 | 25.1 | 700 |
| TPU-50 | 73/28 | 18.9 | 31.3 | 475 |
| TPU-60 | 76/26 | 25.0 | 7.2 | 175 |

**Conclusions:** The new thermoplastic poly(ether-urethane)s, with hard-segments content of 30-60 mass %, were amorphous or partially ordered elastomers with low molar masses. They were characterized by relatively good thermooxidative stability, and some of them also had good tensile strength.

## References:

1. A. Kultys, Sulfur-containing polymers. In: Encyclopedia of polymers science and technology, Wiley, New Jersey, 2003.
2. A. Puszka, A. Kultys, Polymers for Advanced Technologies, 28 (2017) 1937.
3. M. Rogulska, A. Kultys, E. Olszewska, Journal of Thermal Analysis and Calorimetry, 114 (2013) 903.

# UV-VIS SPECTROSCOPY IN THE STUDY OF SOLUTE-SOLVENT HYDROGEN BONDING OF DONOR AND ACCEPTOR TYPES

**E. KRYSTKOWIAK**, Adam Mickiewicz University in Poznań, Faculty of Chemistry, Uniwersytetu Poznańskiego 8, 61-614 Poznań, Poland.

**Abstract:** The work includes spectral (absorption and emission) studies for a solution of 2-amino-7-nitrofluorene (ANF) in 1-chloro-n-butane with the addition of solvents forming hydrogen bonds of different types. The research were performed with solvents forming hydrogen bonds of the acceptor type (type C): dimethyl sulfoxide (DMSO) and ethyl acetate (EA), and also with solvents forming hydrogen bonds of the donor type (types a and B): 2,2,2-trifluoroethanol (TFE) and perfluoro-tert-butanol (PFTB). The spectra of ANF-solvent complexes formed by hydrogen bonds with a stoichiometry of 1:1 were determined. The position of the bands in both the absorption and fluorescence spectra was found to be characteristic of ANF-solvent complexes formed by a given type of hydrogen bonds.

**Introduction:** Spectral solvatochromic studies are widely conducted. They often concern chemical compounds with complex structures. Molecules of these compounds contain numerous heteroatoms (e.g. N, O, S) or functional groups with a protic hydrogen atom (e.g. –OH, $–NH_2$, –NHR). Therefore, they can form hydrogen bonds with protic and aprotic solvent molecules. Since electronic excitation of molecules containing donor and acceptor groups in their structure leads to a significant change in electron density, the solute-solvent hydrogen bond energy also changes. The measured absorption and fluorescence spectra are strongly influenced by both the polarity of the solvent and its ability to form hydrogen bonds. Therefore, it is very important to properly select solvents with specific properties depending on the purpose of the study [1, 2].

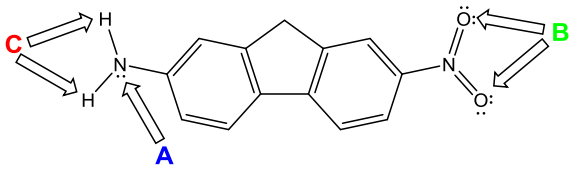



**Fig.1.** 2-amino-7-nitrofluorene (ANF) molecule structure with hydrogen bonds of A, B and C type formation sites.

2-amino-7-nitrofluorene (ANF) is an aromatic compound composed of three rings. To the outermost aromatic rings are attached functional groups: amine $–NH_2$ and nitro $–NO_2$. Having such groups in the structure of the molecule ANF shows donor-acceptor properties. It can form complexes with protic solvent molecules through hydrogen bonds of two types, a and B, and with aprotic solvent molecules through C-type hydrogen bonds (Fig.1). ANF is often used as a probe for solvatochromic studies [3, 4]. The long-wavelength band in the absorption spectra of ANF-solvent complexes formed by A-type

hydrogen bond is shifted hypsochromically and by B and C type hydrogen bonds batochromically compared to $S_0 \rightarrow S_1$ band in the ANF absorption spectrum [5-7].
The aim of the study was to determine spectral emission properties of the ANF-solvent complexes of different type. To be sure, the effect of one type of solute-solvent hydrogen bonding is being studied, solvents characterized by the ability to form hydrogen bonds only of the donor type (A and B) or only of the acceptor type (C) were used.

**Experimental:** 2-amino-7-nitrofluorene (ANF) (Aldrich, 99%) and the solvents: dimethylsulfoxide (DMSO) (Sigma-Aldrich, ≥99,9%), ethyl acetate (EA) (POCH, ≥99.5%), 2,2,2-trifluoroethanol (TFE) (Merck ,≥99,7%) and perfluoro-tert-butanol (PFTB) (Aldrich, 99%) were used as recived. 1-chloro-n-butane (POCH, 99,8%) was dried with molecular sieves (A3).
The absorption spectra were measured on a spectrophotometer Jasco V-650. The emission spectra were recorded on a Jobin Yvon-Spex Fluorolog 3-22 spectrofluorimeter and corrected for the sensitivity of the detection system. The fluorescence spectra obtained in the form of intensity per wavelength interval, were multiplied by a factor $\lambda^2$ to convert to the wavenumber scale [8]. Fluorescence quantum yields were measured by a relative method using quinine sulfate in 0.05 M $H_2SO_4$ ($\phi_F$ = 0.52) as a standard [9]. All measurements were taken at room temperature for solutions of ANF in 1-chloro-n-butane with concentration, $c \approx 5 \times 10^{-5}$ mol·dm$^{-3}$.

**Results:** Absorption and emission spectral studies were conducted for solutions of ANF in 1-chloro-n-butane (solvent interacting with ANF only nonspecifically) without and with the addition of various concentrations of hydrogen bond-forming solvents. On the basis of the results of the absorption studies [6, 7], the amount of added solvent was limited so that ANF-solvent complexes with 1:1 stoichiometry were formed. As for the absorption spectra [5-7], the measured fluorescence spectra of ANF in 1-chloro-n-butane with the addition of hydrogen bond-forming solvents are the summed fluorescence spectra of ANF and emitting ANF-solvent complexes. Appropriate selection of the excitation wavelength ($\lambda_{exc}$) from the range in which only one of the species, i.e. ANF or one type of ANF-solvent complexes, absorbs, and at least the contribution of one of the species to the absorption is considerably greater than the others, can allow observation of the fluorescence of selected species.
For solutions of ANF in 1-chloro-n-butane with the addition of solvents forming hydrogen bonds of the donor type (A and B) the fluorescence spectra were measured at $\lambda_{exc}$=388 nm, corresponding to the maximum of the absorption band of ANF in 1-chloro-n-butane, shorter excitation wavelengths of 310 and 320 nm, where the contribution of the absorbance of ANF-solvent complexes of type a dominates, and longer excitation wavelengths of 500 and 520 nm, where the contribution of the absorbance of ANF-solvent complexes of type B is possibly the largest. Regardless of the excitation wavelength, the maximum of the fluorescence band shifts to longer wavelengths with an increase in the concentration of added solvent and the fluorescence intensity decreases. No shape changes are observed on the short-wavelength side of fluorescence band. For solutions of ANF in 1-chloro-n-butane with the addition of solvents that form acceptor type (C) hydrogen bonds, fluorescence spectra were measured at $\lambda_{exc}$=388 nm (ANF absorption maximum) and at 480 and 500 nm where the absorbance contribution of C-

type ANF-solvent complexes is possibly highest. As the concentration of added solvent increases, the fluorescence spectra shift batochromically.

**Table 1.** Absorption and emission spectral characteristic of ANF and ANF-solvent (1:1) complexes formed by A, B and C types hydrogen bonds in 1-chloro-n-butane.

| Species | $\lambda_A^{max}$ [nm] | $\nu_A^{max}$ [$cm^{-1}$] | $\lambda_F^{max}$ [nm] | $\nu_F^{max}$ [$cm^{-1}$] | $\Delta\nu_{A\text{-}F}^{max}$ [$cm^{-1}$] |
|---|---|---|---|---|---|
| ANF | 388 | 25770 | 545 | 18350 | 7420 |
| ANF-PFTB (A) | 348 | 28730 | - | - | - |
| ANF-PFTB (B) | 447 | 22370 | 615 | 16260 | 6110 |
| ANF-TFE (A) | 345 | 28980 | - | - | - |
| ANF-TFE (B) | 442 | 22620 | 608 | 16450 | 6170 |
| ANF-DMSO (C) | 423 | 23640 | 595 | 16810 | 6830 |
| ANF-EA (C) | 420 | 23810 | 599 | 16690 | 7120 |

These results show that ANF-solvent complexes of type B or C emit in the longer wavelength range than ANF, while no fluorescence of ANF-solvent complexes of type a is observed. Using the method of subtracting the proportion of ANF fluorescence in the experimental spectra, similar to the absorption spectra [5], the fluorescence spectra of ANF-solvent complexes of type B and C of stoichiometry 1:1 were determined. The shift of the band maximum to longer wavelengths compared to the fluorescence spectrum of ANF in 1-chloro-n-butane is due to an increase in the energy of B-type and C-type hydrogen bonds in the $S_1$ excited state. The weakening of the A-type hydrogen bonds in the $S_1$ state must be so great that the ANF-solvent complexes decay very rapidly and no fluorescence is observed (Fig. 2). The values of absorption ($\lambda_A^{max}$, $\nu_A^{max}$) and fluorescence ($\lambda_F^{max}$, $\nu_F^{max}$) bands maxima positions together with Stoke's shiftt values ($\Delta\nu_{A\text{-}F}^{max}$) for ANF-solvent complexes (1:1) compared to ANF are presented in the Table 1.

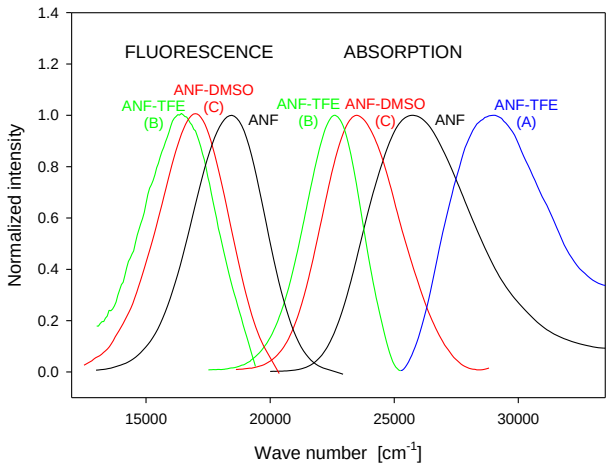



**Fig.2.** Comparison of the absorption and fluorescence spectra of ANF and ANF-solvent complexes (1:1) formed by A-, B- and C-type hydrogen bonds in 1-chloro-n-butane.

To make sure that there are no emitting impurities in the solutions of ANF in 1-chloro-n-butane with and without hydrogen bond-forming solvents and the observed fluorescence comes only from excited ANF molecules and ANF-solvent complexes, measurements of emission excitation spectra were performed.

**Conclusions:** The obtained results show that the position of the band maximum in the fluorescence spectra of ANF-solvent complexes (1:1) is characteristic for complexes formed by a given type of hydrogen bonds, just like in the absorption spectra [5-7]. The maximum of the fluorescence band of ANF-solvent complexes formed by a B-type bond is shifted to longer wavelength and are characterized by smaller Stoke's shift values than ANF-solvent complexes formed by a C-type bond. The spectra for the B- and C-type ANF-solvent complexes are shifted batochromically and the Stoke's shift values for them are smaller than those for ANF in 1-chloro-n-butane. The position of the fluorescence band of the ANF-solvent complexes of type a was not determined, since the emission of this type of complexes was not observed for the studied systems [10].

**Acknowledgements:** I am grateful to Weronika Różańska, M.Sc., for carrying out the absorption and fluorescence spectra measurements and compiling the results.

**References:**

1. K.-L. Han, G.-J. Zhao (ed.), Hydrogen Bonding and Transfer in the Excited State, Wiley, Chippenham 2011.
2. E. Krystkowiak, Effect of Solute–Solvent Hydrogen-Bonding on Spectral and Photophysical Properties of Aromatic Probes, in: Hydrogen-Bonding Research in Photochemistry, Photobiology, and Optoelectronic Materials, World Scientific, New Jersey 2019.
3. V. Karunakaran, M. Pfaffe, I. Ioffe, T. Senyushkina, S. A. Kovalenko, R. Mahrwald, V. Fartzdinov, H. Sklenar, N. P. Ernsting, The Journal of Physical Chemistry A, 112 (2008) 4294.
4. V. Karunakaran, T. Senyushkina, G. Saroja, J. Liebscher, N. P. Ernsting, The Journal of Physical Chemistry A, 111 (2007) 10944.
5. E. Krystkowiak, N. Tarczyńska, A. Maciejewski, Właściwości absorpcyjne kompleksów tworzonych przez związki o właściwościach donorowo-akceptorowych z rozpuszczalnikami protycznymi, in: Nauka i przemysł – metody spektroskopowe w praktyce, nowe wyzwania i możliwości, Wydawnictwo Uniwersytetu Marii Curie-Skłodowskiej, Lublin 2020.
6. E. Krystkowiak, B. Pinkiewicz, T. Łuczak, A. Maciejewski, Badania absorpcyjne wiązan wodorwych w kompleksach tworzonych przez związki typu donorowo-akceptorowego, in: Nauka i przemysł – metody spektroskopowe w praktyce, nowe wyzwania i możliwości, Wydawnictwo Uniwersytetu Marii Curie-Skłodowskiej, Lublin 2022.
7. E. Krystkowiak, E. Refermat, A. K. Przybył, Właściwości absorpcyjne kompleksów 2-amino-7-nitrofluorenu z rozpuszczalnikami aprotycznymi, in: Nauka i przemysł – metody spektroskopowe w praktyce, nowe wyzwania i możliwości, Wydawnictwo Uniwersytetu Marii Curie-Skłodowskiej, Lublin 2023.
8. J.R. Lakowicz, Principles of Fluorescence Spectroscopy, Third ed., Springer 2006.
9. K. Suzuki, A. Kobayashi, S. Kaneko, K. Takehira, T. Yoshihara, H. Ishida, Y. Shiina, S. Oishi, S. Tobita, Physical Chemistry Chemical Physics, 11 (2009) 9850.
10. W. Różańska, Master thesis, Poznań 2023.

# ECONOMICAL ASPECTS OF FOOD BY-PRODUCTS VALORIZATION BY SUPERCRITICAL FLUID EXTRACTION

**B. PAWLAK[1], K. TYŚKIEWICZ[1], M. GRUBA[1], A. WZIĄTEK[1], M. KONKOL[1], G. FLORKOWSKI[1], Z. FEKNER[1], V. MONTES JIMÉNEZ[2], J. VERSPREET[3]**, [1]Supercritical Extraction Research Group, Łukasiewicz Research Network – New Chemical Syntheses Institute, Tysiąclecia Państwa Polskiego Ave. 13A, 24-110 Puławy, Poland, [2]Department of Organic and Inorganic Chemistry, University of Extremadura, Badajoz, Spain, [3]Flemish Institute for Technological Research (VITO), Boeretang 200, 2400 Mol, Belgium.

**Abstract:** Olive pomace is a by-product generated during the process of olive oil extraction. It consists of the leftover pulp, skin, seeds, and other solid remnants of olives after the first pressing. This residue still contains a significant amount of oil, typically around 13 wt% as was analyzed in this study. The residual oil in olive pomace can be extracted using solvents such as hexane. This oil, known as pomace oil, is lower in quality compared to virgin or extra virgin olive oil but can still be used for cooking, especially in industrial applications or blended with other oils.

**Introduction:** The aim of the ROBOCOOP project is to implement regional closed-loop bio-business models for the valorization of waste streams from the agri-food processing of olives, grapes and stone fruit. The waste stream of the olive sector includes pomace, consisting of skins (<1%), pulp (80%), pits (17%) and grains (2%), a liquid residue consisting largely of oil and protein by-products, and also unused biomass from olive tree pruning (28%).

The aim of olive pomace extraction is to recover valuable resources from the by-products generated during the olive oil extraction process. Olive pomace consists of olive pits, pulp, skin, and some residual oil. Instead of disposing of this waste, which can be environmentally problematic, olive pomace extraction aims to extract any remaining oil and other useful substances from the pomace. This process not only reduces waste but also maximizes the utilization of resources in the olive oil production chain, making it more economically and environmentally sustainable. The extracted oil can be used for various purposes such as biofuel production, animal feed, or even further refining for consumption. Additionally, other components extracted from olive pomace, such as antioxidants or dietary fiber, can find applications in various industries including food, pharmaceuticals, and cosmetics. Thus, the aim of olive pomace extraction is to turn what would otherwise be waste into valuable products, contributing to both economic efficiency and environmental stewardship in the olive oil industry.

Calculating the total cost of manufacturing (COM) provides a comprehensive understanding of all expenses incurred in the production process of goods or services. This calculation encompasses not only direct costs directly associated with production, such as raw materials and labor, but also indirect costs like overhead, utilities, equipment depreciation, and any other expenses related to manufacturing operations.

**Experimental:** Supercritical fluid extraction (SFE) of olive pomace (TROIL Vegas Atlas, Spain) was performed in a laboratory scale (1 L extractor, Micronisation unit,

Sitech, Effretikon, Switzerland) as well as quarter-technical scale (40 L extractor, ELAB, Puławy, Poland) installation.
The cost of manufacturing between two installations was compared based on equation and Polish data. For the sake of this study, the COM was calculated as EUR/kg of extract:

$$COM\ [EUR/kg] = 0.304\ FCI + 2.73\ COL + 1.23\ (CUT + CWT + CRM)$$

where: FCI [EUR/kg] – the fixed capital investment, COL [EUR/kg] – the operational labor cost, CUT [EUR/kg] – the utility cost, CWT [EUR/kg] – the waste treatment cost, and CRM [EUR/kg] – the raw material cost [1–3].

**Results:** Supercritical fluid extraction of olive pomace resulted in extraction efficiency at the level of 13.12–13.22 wt%. Similar results were obtained for the extraction of olive pomace in a laboratory scale and quarter technical scale installations. The feed, extract and residues are presented in Fig. 1. The scale-up from 1 L to 40 L extractor resulted in decreasing the $CO_2$ consumption from 100 to 50 kg of $CO_2$, which has significant influence on the total cost of manufacturing, especially if the production scale is being considered. On the basis of results listed in Table 1, the COM may be decreased by almost 4 times when the extraction scale is increased 40 times (from 1 L do 40 L extractor).




**Fig.1.** Feed, extract and residues of olive pomace used for supercritical fluid extraction.

**Table 1.** Total cost of manufacturing for olive pomace on a laboratory and quarter-technical scale installation.

| Experiment | Temperature [°C] | Pressure [bar] | $CO_2$ consumption [$kgCO_2/kg$] | Extraction yield [wt%] | COM [EUR/kg] |
|---|---|---|---|---|---|
| Lab scale | 60 | 300 | 100 | 13.22 ± 0.56 | 408.98 |
| Quarter-technical scale | 60 | 300 | 50 | 13.12 ± 0.32 | 110.47 |

**Conclusions:** Supercritical fluid extraction is a process used to extract valuable compounds from various materials, including food by-products, using supercritical fluids as the extracting solvent. A supercritical fluid is a substance that is above its critical temperature and pressure, where it exhibits properties of both a liquid and a gas. Carbon dioxide ($CO_2$) is the most commonly used supercritical fluid for extraction in the food industry due to its low toxicity, non-flammability, and relatively low critical temperature and pressure. The extracted compounds can undergo further processing, such as

purification or concentration, to obtain the desired product. The remaining $CO_2$ can be recycled in the system, making the process environmentally friendly and cost-effective.

**Acknowledgements:** The research was financed by the European Commission as a part of the Circular Bio-based Europe Joint Undertaking project, entitled: circulaR bioecOnomy Business mOdels owned by agroCOOPeratives (project no. 101112407, project acronym: ROBOCOOP-EU).

**References:**

1. R. Turton, R.C. Bailie, W.B. Whiting, J.A. Shaeiwitz, Analysis, Synthesis and Design of Chemical Processes, 2nd ed., Prentice Hall, New Jersey 2018, United States.
2. P.T.V. Rosa, M.A.A. Meireles, Journal of Food Engineering, 67 (2005) 235.
3. S. Milovanović, I. Lukić, M. Stamenić, P. Kamiński, G. Florkowski, K. Tyśkiewicz, M. Konkol, The Journal of Supercritical Fluids, 188 (2022) 105676.

# SPECTROSCOPIC CHARACTERIZATION OF COBALT(II) COMPLEXES WITH 4,4'-STILBENEDICARBOXYLIC ACID AND N-DONOR LIGANDS

**M. GROSZEK, R. ŁYSZCZEK, A. OSTASZ**, Maria Curie-Sklodowska University, Faculty of Chemistry, Institute of Chemical Sciences, Department of General and Coordination Chemistry and Crystallography, M. Curie-Sklodowska Sq. 2, 20-031 Lublin, Poland.

**Abstract:** Spectroscopic characterization of heteroleptic coordination polymers with Co(II) and Cu(II) ions was carried out, in which the main organic ligand was 4,4'-stilbenedicarboxylic acid ($H_2SDC$), while: 1,10-phenanthroline, 4,4'-bipyridine and piperazine were used as N-donor ligands. The described metal complexes were synthesized using the solvothermal or sonochemical method in the environment of N,N-dimethylformamide or a mixture of N,N-dimethylformamide, dimethylsulfoxide and ethylene glycol. The confirmation of the deprotonation process of both COOH groups of $H_2SDC$ acid and the occurrence of coordination of metal ions through both the O- and N-donor ligands was based on the analysis of FTR spectra of complexes in the solid phase, which were recorded using the ATR method. The chemical composition and the thermal properties of the obtained metal complexes were determined using the TG-DTG-DSC method in the air atmosphere.

**Introduction:** Heteroleptic coordination polymers are metal complexes that consist of metal centers and two or more different organic ligands. The main purpose of using two ligands with different chemical properties is to strengthen the properties of a well-known coordination polymer or to give it completely new properties while maintaining the defined structure [1,2]. Infrared spectroscopy utilizing Fourier transform infrared spectroscopy (FTIR) is a widely used research method, particularly in the assessment of functional groups present in chemical substances. It is a rapid technique enabling precise determination of molecular characteristics in a short period of time. Coordination polymers, due to their unique structure and properties, find applications across various fields of science and technology. They are utilized as catalysts in chemical reactions, influencing the rate and efficiency of these processes [3,4]. Additionally, coordination polymers are being investigated for their potential use in optical technology, particularly as materials for optical applications such as optical fibers or optical sensors. In the field of magnetic materials, coordination polymers containing transition metal ions exhibit intriguing magnetic properties, making them encouraging materials for magnetic applications such as magnetization or data storage [5,6]. Furthermore, research into the utilization of coordination polymers as drugs is increasingly promising due to their ability to control drug release [7]. They also hold potential applications in electronics, where they can be employed in technologies related to solar cells, organic light-emitting diodes (OLEDs), and optical memories [8].

The aim of the work was the synthesis and infrared spectroscopic characterization of new metal complexes of cobalt(II) and copper(II) ions with 4,4'-stilbenedicarboxylic acid ($H_2SDC$) as a bridge ligand and selected N-donor ligands in the N,N-

dimethylformamide or a mixture of N,N-dimethylformamide, dimethylsulfoxide and ethylene glycol environment. Infrared spectroscopic studies of the obtained solid phases were performed using the total internal reflection technique. Additionally, thermal analysis (TG-DTG-DSC) of the attained metal complexes were performed.

**Experimental:** Heteroleptic metal complex were synthesized by the solvothermal method, which used 4,4'-stilbenedicarboxylic acid ($C_{16}H_{12}O_4$, $H_2SDC$), cobalt(II) nitrate $Co(NO_3)_2 \cdot 6H_2O$ and an N-donor ligand - 1,10-phenanthroline or 4,4'-bipyridine (molar ratio 2:1:1). Both cobalt(II) nitrate(V) and N-donor organic ligands were dissolved in 10 mL of DMF, and $H_2SDC$ acid in 20 mL of DMF. The solutions of the metal center precursor and organic ligands - 1,10-phenanthroline and 4,4'-stilbenedicarboxylic acid - prepared in this way were at one moment transferred to a Teflon vessel, then placed in a steel autoclave, tightly closed, and transferred to a laboratory dryer. The synthesis of metal complex with 4,4'-bipyridine was performed in an analogous manner. The temperature program was set to isothermal heating at 100 °C for 72 hours.
The synthesis of a coordination polymer based on copper(II) ions with 4,4'-stilbenedicarboxylic acid and piperazine (molar ratio 2:1:1) was performed using a sonochemical method. Copper(II) acetate dihydrate was dissolved in 20 mL of DMSO, 4,4'-stilbenedicarboxylic acid in a DMF/DMSO mixture (in a 1:2 volume ratio), and piperazine in 20 mL of ethylene glycol. The solutions prepared in this way were subjected to sonochemical activation in an ultrasonic bath at a temperature of 40°C for 15 minutes. The solutions were then combined and reactivated under the same conditions.
The resulting precipitates were filtered and left to dry at room temperature. The ATR-FTIR spectra of the ligands and the obtained compounds were registered in the range 4000-600 $cm^{-1}$ by using a Nicolet 6700 (Thermo Scientific) spectrophotometer equipped with a universal ATR Smart iTR diamond attachment. Thermal analyses (thermogravimetric-TG and differential scanning calorimetry-DSC) were carried out in a flowing air atmosphere using the SETSYS 16/18 analyser (Setaram).

**Results:** New cobalt(II) and copper(II) complexes with mixed ligands - 4,4'-stilbenedicarboxylic acid ($H_2SDC$) and 1,10-phenanthroline, 4,4'-bipyridine or piperazine were obtained using the solvothermal or sonochemical method from a DMF solution or a mixture of N,N-dimethylformamide, dimethylsulfoxide and ethylene glycol. Based on the thermogravimetric tests and infrared spectroscopic analysis, the following complex formulas were established: Co(SDC)(phen)(DMF), Co(SDC)(4,4'-bpy)(DMF) and Cu(SDC)(PIP) (where: SDC = $C_{16}H_{10}O_4^{2-}$; phen = $C_{12}H_8N_2$; 4,4'-bpy = $C_{10}H_8N_2$; PIP = $C_4H_{10}N_2$).
The ATR-FTIR spectrum of 4,4'-stilbenedicarboxylic acid shows bands characteristic of COOH groups: OH, C=O and COH. In the range of 2820-2540 $cm^{-1}$ there is a wide band originating from stretching vibrations ν(OH) and ν(CH). However, at the wavenumber of 1670 $cm^{-1}$, a very intense band due to stretching vibrations ν(C=O) is observed. The bands from stretching vibrations $\nu(C_{Ar}\text{-}C_{Ar})$, bending $\beta(C_{Ar}\text{-}C_{Ar})$ and deformation vibrations $\gamma(C_{Ar}\text{-}C_{Ar})$ are located in the ranges of 1605-1518 $cm^{-1}$, at 1422 $cm^{-1}$ and at 697 $cm^{-1}$. Bands associated with the vibrations of COH groups occur at wavenumbers 1320 $cm^{-1}$ and 1290 $cm^{-1}$. Bands from bending vibrations in plane $\beta(C_{Ar}\text{-}H)$ are observed in the infrared spectrum in the range of 1221-963 $cm^{-1}$. The β(OH) deformation vibration

is visible at 946 $cm^{-1}$. A series of sharp and intense bands in the range of 920-740 $cm^{-1}$ are assigned to out-of-plane deformation vibrations $\gamma(C_{Ar}\text{-}H)$.

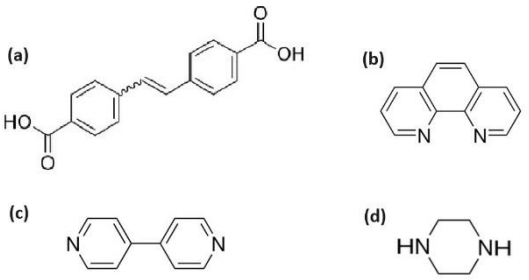



**Fig.1.** Molecules of free organic ligands used in the synthesis of coordination polymers: (a) 4,4'-stilbenedicarboxylic acid, (b) 1,10-phenanthroline, (c) 4,4'-bipyridine and (d) piperazine.

The comparison the FTIR spectra of the free organic ligands with the FTIR spectra of the obtained metal complexes allow to confirm coordination of metal centers simultaneously through O- and N-donor ligands. In the FTIR spectra of the prepared coordination polymers (Fig.2 and Fig.3), no characteristic bands of COOH groups from $H_2SDC$ acid are observed, which confirms the deprotonation of both carboxylic groups and coordination bonds formation among metal(II) centers and carboxylate oxygen atoms. The $\nu_{as}(COO)$ vibration bands are present at 1557 $cm^{-1}$, 1540 $cm^{-1}$ and 1544 $cm^{-1}$, while the $\nu_{sym}(COO)$ vibration bands are visible at 1385 $cm^{-1}$, 1413 $cm^{-1}$ and 1386 $cm^{-1}$ for the Co(SDC)(phen)(DMF), Co(SDC)(4,4'-bpy)(DMF) and Cu(SDC)(PIP), respectively. The $\nu(C=O)$ vibration coming from the solvent used (DMF) is visible in the spectra of the Co(SDC)(phen)(DMF) and Co(SDC)(4,4'-bpy)(DMF) coordination polymers (Fig.2) at wavenumbers: 1669 $cm^{-1}$ and 1679 $cm^{-1}$, respectively. In the FTIR spectrum of the complex with 1,10-phenanthroline (Fig.2a), in the fingerprint region there are a bands (out-of-plane deformation vibrations $\gamma(C_{Ar}\text{-}H)$) visible at the wavenumber of 851 $cm^{-1}$ and 725 $cm^{-1}$, which were qualified as the band originating from the 1,10-phenanthroline. In turn, in the FTIR spectrum of the Co(SDC)(4,4'-bpy)(DMF) complex, the $\gamma(CH)$ and $\gamma(C_{Ar}\text{-}C_{Ar})$ bands coming from the N-donor ligand used are located at wavenumbers 814 $cm^{-1}$ and 731 $cm^{-1}$, respectively, while the bands characteristic of piperazine (Fig.2) are visible at wavenumbers: 946 $cm^{-1}$ – $\beta(C\text{-}N)$; 882 $cm^{-1}$ – $\beta(C\text{-}N)$ and 761 $cm^{-1}$ - out-of-plane deformation vibrations $\gamma(C_{Ar}\text{-}H)$.

Thermal analysis (TG-DTG-DSC) in an air atmosphere showed that thermal decomposition of Co(SDC)(phen)(DMF) and Co(SDC)(4,4'-bpy)(DMF) consists of two stages, the first of them is related to the release of DMF solvent molecules and is located on the TG curve in the temperature range of 60-240 °C, while the second stage is associated with the decomposition of the desolvated forms of complexes and combustion of the organic ligands in the temperature range of 340-510 °C. The total mass loss recorded for Co(SDC)(phen)(DMF) and Co(SDC)(4,4'-bpy)(DMF) is 87% and 85%, respectively. The Cu(SDC)(PIP) is stable up to 220 °C, then there is a visible thermal decomposition on the TG curve in the range of 230-530 °C, which is associated with the degradation and combustion of an organic ligands. The total mass loss was 81%.

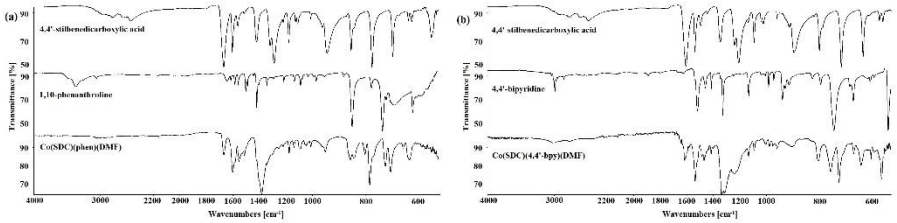



**Fig.2.** FTIR spectra of metal complexes obtained by solvothermal method with $H_2SDC$ acid, (a) cobalt(II) ions and 1,10-phenanthroline; (b) cobalt(II) ions and 4,4'-bipyridine.

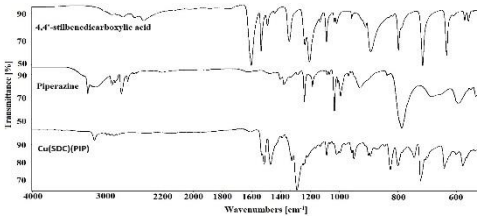



**Fig.3.** FTIR spectra of metal complex obtained by sonochemical method with $H_2SDC$ acid, copper(II) ions and piperazine.

**Conclusions:** New heteroleptic coordination polymers of cobalt(II) and copper(II) ions with 4,4'-stilbenedicarboxylic acid and selected N-donor ligands were synthesized using solvothermal and sonochemical methods. Analysis of the infrared spectra of the metal complexes in the solid state confirms presence of both O- and N-donor ligands in their structures. Further efforts will be undertaken for the obtaining of such complexes in the single-crystals forms for structural investigations.

**References:**

[1] M.B Taj, M.D.F Alkahtani, U. Ali, A. Raheel, W. Alelwani, A.M. Alnajeebi, N.A Babteen, S. Noor, H. Alshater, Molecules, 25 (2020) 4252.
[2] M. Baskin, N. Fridman, M. Kosa, G. Maayan, Dalton Transactions, 46 (2017) 15330.
[3] R. Sanchis-Gual, M. Coronado-Puchau, T. Mallah, E. Coronado, Coordination Chemistry Reviews, 480 (2023) 215025.
[4] J. Hou, L. Si, Z. Shi, C. Miao, Y. Zhao, X. Ji, Q. Hou, S. Ai, Chemosphere, 311 (2023) 136903.
[5] C. Xu, R. Luo, C. Fan, C. Xie, X. Zhang, D.Zhang, Y. Fan, Optical Materials, 136 (2023) 113459.
[6] W. Cao, F. Zhao, L. Tian, Journal of Molecular Structure, 1285 (2023) 135489.
[7] E. S. Pena, L. M. Lifshits, M. Eckshtain-Levi, E. M. Bachelder, K. M. Ainslie, WIREs Nanomedicine and Nanobiotechnology, 15 (2023) 4.
[8] Y. Wu, C. Yang, J. Liu, M. Zhang, W. Liu, W. Li, C. Wu, G. Cheng, Q. Yang, G. Wei, C. Che, Chemical Science, 12 (2021) 10165.

# SUPERCRITICAL CARBON DIOXIDE EXTRACTS FROM CLOVE BUDS WITH ANTIFUNGAL PROPERTIES

**K. TYŚKIEWICZ[1], M. GRUBA[1], M. KONDRACKA[2], R. TYŚKIEWICZ[2], A. WZIĄTEK[1], M. KONKOL[1], R. WIEJAK[1], R. KOWALSKI[1], A. BIAŁEK[3],**
[1]Supercritical Extraction Research Group, Łukasiewicz Research Network – New Chemical Syntheses Institute, Tysiąclecia Państwa Polskiego Ave. 13A, 24-110 Puławy, Poland, [2]Analytical Laboratory, Łukasiewicz Research Network – New Chemical Syntheses Institute, Tysiąclecia Państwa Polskiego Ave. 13A, 24-110 Puławy, Poland, [3]Hortulanus Agrochemical Solutions, Sygietyńskiego St. 25, 96-316 Stare Budy, Poland.

**Abstract:** Supercritical $CO_2$ extracts from various plant materials (seeds, herbs, leaves, etc.) contain bioactive compounds, which have antifungal properties. These extracts can be formulated into growth-promoting solutions or sprays that stimulate root development, enhance nutrient absorption, and promote overall plant vigor. On the example of $scCO_2$ extracts from clove buds, the antifungal properties were studied against *Fusarium culmorum*, which is one of the most serious plant diseases. The research resulted in 100% *F. culmorum* growth inhibition by all studied extracts from clove buds with different content of eugenol as a dominant compound.

**Introduction:** Diseases caused by pests and microorganisms expose crops to damage both during growth and after harvest. These factors could result in a significant reduction in annual global food production levels, which, depending on the source, could decline by as much as 25–50%. One third of these losses are caused by fungal diseases. Over 10,000 species of fungi have been classified as a potential cause of plant mycosis. Therefore, preparations supporting plant metabolism and effective and environmentally safe plant protection products against phytopathogenic fungi are sought.

**Hop cones** (*Humulus lupulus*) can be used as an agent to protect the plant against phytopathogens due to the presence of a wide range of compounds from the polyphenol group. Hop is a perennial plant that, due to its valuable properties, is mainly used in the brewing industry. These properties are attributed to alpha- and beta-acids (responsible for bitterness), essential oils and polyphenols, which constitute 24.1 and 5% by weight, respectively. Phenolic compounds present in hops have been tested for their anticancer, antioxidant and anti-inflammatory properties [1–2].

Cloves (*Syzygium aromaticum*) contain significant amounts of essential oil, main representative of which is eugenol. Other compounds responsible for the characteristic smell of the plant are alpha- and beta-humulene, methyl salicylate and beta-pinene. Clove is one of the main plant sources of phenolic compounds (flavonoids, hydroxybenzoic acid and hydroxycinnamic acid). Aromatic clove has antibacterial potential, which is used in cosmetic products to fight pathogens [3].

Bladderwrack (*Fucus vesiculosus*) contains, among others, microelements, macroelements and metallic elements. It also contains nutritional compounds such as carbohydrates (including fiber), proteins, amino acids, fats, vitamins (vitamin C, B vitamins and fat-soluble vitamins A, D, E and K), carotenoid pigments and phenolic compounds (phlorotannins). Algae extracts obtained by supercritical fluid extraction do

not pose any negative risk to human health, or the environment. Instead, they are a mixture of various active substances, mainly phenolic compounds such as flavonoids and coumarins. Preparations based on various macerates and extracts of plant-like protozoa (algae) and *Cyanobacteria* have a broad spectrum of activity against various classes of plant phytopathogens, and also inhibit the germination of conidia and the vegetative growth of hyphae and the degradation of hyphae using lytic enzymes [4–5].

**Experimental:** Clove buds (milled) were subjected to supercritical fluid extraction (SFE) with carbon dioxide in a supercritical state. The studies were carried out with the use of laboratory scale installation equipped with 1L extractor.
For quantitative analyzes of eugenol, the UPC$^2$ (Waters) chromatographic method was used equipped with HSS C18SB column (3.0 x 1000 mm; 1.8µm) at the temperature of 40 °C and an ABPR pressure of 1500 psi. Quantitative determinations were made based on a calibration curve. The calibration curves obtained from 6 solutions prepared by diluting the working solution showed satisfactory linearity with high values of the correlation coefficient ($R^2$). Quantitative analysis was carried out using carbon dioxide with the addition of methanol in the ratio of 97.7:2.3.
The research on antifungal activity of crude extracts on *Fusarium culmorum* was conducted. Fungal strains were obtained from the fungi collection of the Plant Diseases Clinic and Bank of Pathogens of the Institute of Plant Protection – NRI in Poznań, Poland. Bioassays were carried out using the following protocol. The crude $scCO_2$ extracts (1 mL) were transferred separately to 20 mL of dissolved PDA medium, cooled to 45 °C, and mixed thoroughly. The mixture was then transferred to a Petri dish (90 mm diameter) and allowed to solidify. Agar discs (9.0 mm diameter) overgrown with *Fusarium mycelium* were taken from the initial cultures (grown on PDA medium for 7 days at 28 °C) and transferred to the center of the prepared medium (PDA + extract). Additionally, a negative control (PDA + fungus) was included. All plates were then incubated at 28 °C for 5 days. The effect of extracts was determined by measuring the diameter of the colonies and expressed as the inhibition percentage of mycelial growth compared to the negative control.

**Results:** The results obtained for clove buds $scCO_2$ extracts revealed 100% of *Fusarium culmorum* growth inhibition. The extracts E1–E15 (Fig.1) were performed in different extraction conditions (temperature range of 40–50 °C; pressure range of 100–200 bar; $CO_2$ consumption range of 25–75 $kgCO_2/kg$). As a result of the experiments performed, extraction efficiencies ranging from 19.83–26.61% were obtained. Even though, different parameters were chosen for the SFE, the extracts did not vary in antifungal properties.

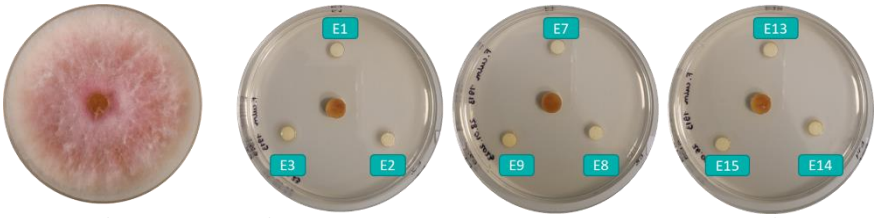



**Fig.1.** Antifungal properties of cloves $scCO_2$ extract on *Fusarium culmorum* (examples of extracts in regard to control (on the left)) .

The highest content of eugenol (73.10 wt%) was analyzed in extract obtained in Exp. No. 13, while the lowest content of eugenol (51.60 wt%) was analyzed in Exp. No. 9 (Table 1). Different content of eugenol did not influence the antifungal properties on *F. culmorum*. All studied extracts were characterized by the same percentage of *F. culmorum* inhibition.

**Table 1.** The content of eugenol (wt%) in studied $scCO_2$ extracts against *F. culmorum.*

| Experiment No. | Eugenol content, wt% |
|---|---|
| E1 | 57.00 |
| E2 | 55.80 |
| E3 | 55.50 |
| E4 | 54.60 |
| E5 | 51.80 |
| E6 | 57.70 |
| E7 | 57.50 |
| E8 | 56.00 |
| E9 | 51.60 |
| E10 | 55.30 |
| E11 | 57.00 |
| E12 | 57.70 |
| E13 | 73.10 |
| E14 | 56.10 |
| E15 | 60.20 |

**Conclusions:** Solvents ensuring the extraction of active substances that inhibit the growth and development of phytopathogens are being sought. The disadvantage of most solvents is the selective extraction of compounds from biological material, inhibition of the physiological properties of active substances and side effects. As it turns out, the best solutions are offered by modern methods of supercritical extraction using carbon dioxide - SFE (supercritical fluid extraction), which guarantee the extraction of biologically active compounds without losing their properties and positive impact on the environment, plants and animals. The supercritical fluid extraction (SFE) technique allows for the extraction of various groups of compounds, including polyphenols, lipids (fatty acids, triacylglycerols), micro- and macroelements, vitamins, plant growth hormones and other compounds. As was studied within our project, clove buds $scCO_2$ extracts with high antifungal properties may be further studies in terms of additives for biostimulants and/or plant protection products.

**Acknowledgements:** The research was financed by Polish National Center for Research and Development as a part of the project entitled Natural products as a basis for ecological, sustainable preparations (project acronym: EUREKA/2021/114/NatBioPrep/2022).

**References:**

1. R.S. Inumaro, R.F.A. Casalvara, R.C.G. Corrêa, L. Barros, C. Pereira, R.M. Calhelha, S.A. Heleno, T.C. Pimentel, J.E. Gonçalves, L.Cardozo-Filho, Journal of $CO_2$ Utilization, 72 (2023) 102498.
2. A. Formato, M. Gallo, D. Ianniello, D. Montesano, D. Naviglio, The Journal of Supercritical Fluids, 84 (2013) 113.

3. F. Yazdani, M. Mafi, F. Farhadi, K. Tabar-Heidar, Aghapoor, M. Kioumars, D. Farshid, R. Hossein, Zeitschrift für Naturforschung B, 60 (2005) 1197.
4. K. Tyśkiewicz, R. Tyśkiewicz, M. Konkol, E. Rój, J. Jaroszuk-Ściseł, K. Skalicka-Woźniak, Molecules, 28 (2019) 3518.
5. I. Michalak, K. Tyśkiewicz, M. Konkol, E. Rój, K. Chojnacka, in book: Biostimulants for sustainable crop production, 2020.

# CHALCOPHILE ELEMENTS COMPOSITION OF NORTH-EAST KAZAKHSTAN SALT LAKES' MUD

**A. SABITOVA[1], K. AKIMZHANOVA[1], B. MUSSABAYEVA[2]**, [1]Shakarim University, Faculty of Engineering and Technology, Department of Chemical Technology and Ecology, Glinka, 20A, 071412, Semey, Kazakhstan, [2]Astana International University, Higher School of Natural Sciences; Kabanbai Batyr Ave., 8, 010000, Astana, Kazakhstan.

**Abstract:** The article presents the results of a study of the composition of chalcophile elements of the natural mud of Moiyldy, Tuzkala, Arasan, Shoshkaly, the eastern coast of Lake Alakol salt lakes of the North-Eastern region of Kazakhstan. All samples are characterized by a high content of bismuth compared to its content in the Earth's Crust, which indicates the need for monitoring of the composition and studying the possible effects of using these native muds.

**Introduction:** Chalcophile elements, due to their low affinity for oxygen and high affinity for sulfur in the form of poorly soluble sulfides, exhibit toxicity in small concentrations and are very dangerous for the environment due to their high ability to form organometallic compounds. Mud can be informative medium in tracking changes in the flows of elements in the biosphere over time under different climatic, geochemical and environmental conditions, that characterize both the lake and its surrounding ecosystem [1]. Long-term monitoring studies of the physicochemical composition and ecological state of natural peloids were carried out by the groups of the following scientists: Muradov et al. (Russia) [2], Pavlovska et al. (Latvia) [3] and Bergamaschi et al. (Italy) [4]. Three factors influence the formation of the chemical composition and genesis of silt mud: the salt composition of the brine of a reservoir, soil, and organic matter of plant and animal origin. At the same time, the degree of accumulation of mud is greatly influenced by the morphological features of water bodies, water salinity, the geological structure of the shores and the landscape features associated with it [5,6]. The purpose of this study was to give a characterization of composition of chalcophile elements of the natural mud of the lakes of the North-Eastern region of Kazakhstan. The objects of study and their codes were the following peloids: 1-AlBP - the black peloid from the eastern coast of Lake Alakol (46° 03′ 36″N 82° 02′ 12″ E); 2-ArBP - the black peloid of Lake Arasan, located in the Zharma district of Kalbatau village (49°15′51″ N 81°44′28″ E); 3-ShBP - the black and 4-ShWP – the white peloid of Lake Shoshkaly, located in the northwestern part of the Beskaragay district (51°16'57.9"N 78°41'58.7"E); 5-TKBP – the black peloid of Lake Tuzkala, located in the Lebyazhinsky district (51°52′11″ N 77°28′29″ E); 6-MBP - the black peloid of Lake Moiyldy in the Pavlodar region (52°23'48" N 77°04'03" E). The interpretation of the results will make it possible to determine the possible therapeutic effects of mud that are now actively used by tourists without medical supervision.

**Experimental:** Samples were taken to a depth of up to 20 cm in one layer using the point method: the area was divided into 4 equal parts and samples were taken from the

center of each square, weighing at least 200 g each according to Government Standard (GOST) 17.1.5.01-80. Approximately the distance between each sample was 4-5 m. The 4-ShWP was sampled from a depth of 20-40 cm. The GPS location at the time of sampling was determined using the Google Maps mobile phone application. Sampling was carried out in the autumn period (September 2022). The averaged samples were stored in clean polyethylene containers with tightly closed lids at 40 °C in a dark place. To determine the gross concentrations of chalcophile elements a quadrupole mass spectrometer with inductively coupled plasma ICP-MS Agilent 7500cx manufactured by Agilent Technologies (USA) was used. According to the calibration schedule, the analysis result was provided by the instrument software.

**Results:** The obtained data were compared with the accepted content in the continental crust (CC) according to Taylor and Vinogradov [7,8]. The content of arsenic (1.5–8.0), silver (2.3–4.3), antimony (2.4–7.0), cadmium (4.3–6.3), and bismuth (41–126) increased in all studied samples (Table 1).

**Table 1.** Total concentration of chalcophile elements in the mud samples [mg/kg].

| Elements | 1- AlBP | 2-ArBP | 3-ShBP | 4-ShWP | 5-TKBP | 6-MBP |
|---|---|---|---|---|---|---|
| Ag | 0.3211±0.005 | 0.2298±0.003 | 0.1724±0.002 | 0.3135±0.004 | 0.2188±0.003 | 0.2054±0.003 |
| Bi | 1.0760±0.015 | 0.4607±0.008 | 1.0740±0.015 | 0.7878±0.010 | 0.5744±0.008 | 0.3521±0.005 |
| Cd | 0.876±0.012 | 0.6431±0.010 | 0.747±0.012 | 0.939±0.015 | 0.880±0.013 | 0.658±0.010 |
| Sb | 0.648±0.010 | 1.407±0.020 | 0.795±0.012 | 0.801±0.011 | 0.739±0.011 | 0.471±0.009 |
| Tl | 0.1630±0.002 | 0.1544±0.002 | 0.1142±0.002 | 0.1142±0.002 | 0.0811±0.001 | 0.1242±0.001 |
| As | 4.40±0.06 | 14.38±0.16 | 2.78±0.03 | 3.47±0.04 | 3.75±0.05 | 2.89±0.03 |
| Pb | 18.27±0.24 | 16.38±0.23 | 39.82±0.52 | 26.46±0.41 | 26.6±0.36 | 14.14±0.21 |
| Cu | 16.3±0.1 | 27.1±0.4 | 47.1±0.6 | 25.1±0.4 | 26.2±0.4 | 18.8±0.2 |
| Zn | 27.9±0.4 | 40.6±0.5 | 50.4±0.7 | 39.1±0.5 | 34.92±0.4 | 25.7±0.3 |

Sample 2 has the highest content of arsenic and antimony. This may correlate with the high content of iron in this sample, since these metals have a high affinity for iron-bearing minerals [9,10]. Since sample 2 differs in its textural features, including a fine clay fraction, this can also confirm its high adsorption properties [11]. Sample 4 is characterized by cadmium maximum concentration. All samples are distinguished by a high content of bismuth, especially samples 1 and 3. Samples 3-5 in their composition show an excess of lead concentration by 1.9-2.8 times with a maximum value for sample 3. High content of bismuth can be explained by the fact that the content of bismuth in sulfide minerals varies by several orders of magnitude and tends to be concentrated to a greater extent together with galena. Especially these results correlate in the case of sample 3 with the highest content of lead and bismuth in comparison with other samples. Elements that are in increased concentrations in the studied samples compared to the values in CC are included in the group of chalcophile metals according to Goldschmidt and have a specific affinity for sulfur. Most of the elements that exceed the concentrations in the studied samples can potentially exhibit limited mobility in a neutral and slightly alkaline environment with a low content of organic matter and, despite toxicity, may not adversely affect the quality of natural mud. However, other factors, such as temperature, the ratio of cations to anions, ionic strength, microbial metabolites,

etc., can significantly change the mobility of elements [11]. The analysis of the elemental composition showed that there is no stable dependence of the concentration of elements on the geographical location. Comparison with research data from other regions of Kazakhstan is not possible due to their absence.

**Conclusions:** The analysis of the gross content of chalcophile elements in the mud showed an increased content to varying degrees in all samples of arsenic, silver, antimony, cadmium, bismuth in comparison with their weight clarkes. Most of these metals may have limited mobility in slightly alkaline media. However, most other factors can affect the mobility of ions, which indicates the need for constant monitoring and careful application of these muds in the absence of medical control. Its rich mineral composition enables scientific substantiation of the conditions for its complex use in balneology, and also promotes new extensive research to explore all the potential benefits and risks.

**References:**

1. V. Dauvalter, Geochemistry International, 44 (2006) 205.
2. S.V. Muradov, A.I. Khomenko, S.V. Rogatykh, IOP Conference Series: Earth and Environmental Science, 249 (2019) e12039.
3. I. Pavlovska, A. Klavina, A. Auce, I. Vanadzins, A. Silova, L. Komarovska, B. Silamikele, L. Dobkevica, L. Paegle, Scientific Reports, 10 (2020) 21527 .
4. B. Bergamaschi, L. Marzola, M. Radice, S. Manfredini, E. Baldini, C.B. Vicentini, E. Marrocchino, S. Molesini, P. Ziosi, C. Vaccaro, S. Vertuani, Life, 10 (2020) 78.
5. A. Baricz, E.A. Levei, M. Şenilă, S.C. Pînzaru, M. Aluaş, A. Vulpoi, C. Filip, C. Tripon, D. Dădârlat, D.M. Buda, F.V. Dulf, A. Pintea, A. Cristea, V. Muntean, Z.G. Keresztes, M. Alexe, H. Leonard Banciu, Scientific Reports, 11 (2021) 18633.
6. M. Suárez, P. González, R. Domínguez, A. Bravo, C. Melián, M. Pérez, I. Herrera, D. Blanco, R. Hernández, J.R. Fagundo, The Journal of Alternative and Complementary Medicine, 17 (2011) 155.
7. S. R. Taylor, Geochimica et Cosmochimica Acta, 28 (1964) 1273.
8. A.P. Vinogradov, Geokhimiya, 7 (1962) 555.
9. Ç. Karakaya, M.N. Karakaya, Turkish Journal of Earth Sciences, 27 (2018) 191.
10. Y. Ai, G. Liu, H. Wang, C. Wu, W. Liu, Z. Lin, Surfaces and Interfaces, 20 (2020) 100584.
11. T. Sherene, Biological Forum - an International Journal, 2 (2010) 112.

# THE EFFECT OF THE COMPOSITION OF ELECTROLYTES ON THE ANODE-FREE LITHIUM-ION BATTERIES

**A. SABITOVA, A. ABDRAKHMANOVA**, Shakarim University, Faculty of Engineering and Technology, Department of Chemical Technology and Ecology, Glinka, 20A, 071412, Semey, Kazakhstan.

**Abstract:** Anode-free lithium-ion batteries accumulate 60% more energy per unit volume than conventional lithium-ion cells. However, these elements, as a rule, quickly lose capacity and have a short cycle life, and their practical implementation is hindered by significant problems, such as the growth of lithium dendrites and low Coulomb cycling efficiency. The development of electrolytic systems with optimal structure and composition contributes to the development of lithium power supplies, including their electrochemical characteristics. In lithium-ion batteries, the electrolyte acts as a medium for the transfer of lithium ions between electrodes during charge-discharge processes. For this reason, this component is necessary for the operation of these devices. It is necessary to take into account that electrolytic systems include components in the form of additives, solvents and salts. Electrolyte solutions based on a combination of fluorinated and traditional carbonate solvents were studied in anode-free lithium-ion cells using copper foil as the anode and $Li_{1.05}Ni_{0.33}Mn_{0.33}Co_{0.33}O_2$ as the cathode. Excellent performance characteristics were achieved by replacing traditional alkyl carbonate solvents in electrolyte solutions with a mixture with fluorinated co-solvents. The use of fluoroethylene carbonate has significantly improved the cyclic behavior of elements charged up to 4.5 V. The improvement achieved is due to the formation of stable and protective surface films on cathode particles due to unique surface reactions that are possible due to the nature of fluorinated solvent molecules. Surface films formed on lithium cathodes of transition metal oxide isolate the active mass, which has a high reactivity with respect to electrophilic alkyl carbonates, from ongoing side reactions with solution particles.

**Introduction:** Anode-free lithium–ion batteries are a type of lithium-ion rechargeable batteries that are used in many devices, including mobile phones, tablets, laptops and electric cars. They got their name because of the absence of a negative electrode (anode), which means that the electrodes in the battery consist only of a positive electrode (cathode) and an electrolyte. This type of battery usually provides a higher energy density and a longer service life than other types of batteries. They also have fast charging speeds and additional safety due to the absence of lithium on the anode, which can cause a fire. Anode-free lithium metal cells provide 60% higher energy density than lithium-ion cells. As an example, consider an anode-free and lithium-ion cell. Both cells use the same $Li[Ni_{0.5}Mn_{0.3}Co_{0.2}]O_2$ cathode (NMC532), but instead of a graphite anode, an element without an anode accumulates a charge in the form of lithium metal with a galvanic coating. In anode—free cells, zero excess lithium is used - 100% lithium comes from the positive electrode (cathode) [1,2]. Many lithium-metal cells reported in the literature are actually less energy intensive than lithium-ion cells due to the significant amount of excess lithium used [3]. Moreover, the use of lithium foil with

a thickness of more than 60 microns makes lithium metal cells less energy-intensive than lithium-ion cells. Moreover, avoiding the use of lithium foil will reduce costs and increase compatibility with the existing cell production infrastructure [4]. With zero excess lithium, non-anode cells often lose capacity quickly. A common occurrence is a service life of less than 20 cycles, reducing up to 80% of the initial performance [5]. The failure of the element may be associated with the loss of lithium as a result of side reactions of the lithium electrolyte, leading to the formation of an interfacial layer of solid electrolyte (Solid Electrolyte Interface - SEI) and electrically isolated lithium [6]. Both mechanisms lead to the formation of "dead" lithium and are aggravated by morphology with a large surface area, which tends to form in conventional electrolytes [7]. Electrolyte optimization [8] and the application of mechanical pressure [9] are among the strategies used to increase service life because they contribute to the dense morphology of lithium. In addition to the service life, the safety of electrochemical cells remains an urgent problem. The safety problems of lithium metal cells have been studied since the 1980s. Safety is often discussed in the literature, but rarely tested in real-world conditions. In some works, the use of "non-flammable" electrolytes is mentioned, since electrolyte-impregnated separators do not ignite when exposed to flame.

**Experimental:** The positive electrode was prepared on the basis of lithium, nickel, manganese, cobalt oxide: $Li_{1.05}Ni_{0.33}Mn_{0.33}Co_{0.33}O_2$ (NMC111). A copper foil pretreated in plasma was used as a negative electrode in order to remove molecular traces of various kinds of contaminants in the Diener Atto low-pressure plasma unit. To remove moisture residues, the cut-out negative electrodes were kept in a BINDER VD-23 drying vacuum cabinet for two hours at 120 °C and a pressure of about 1 mbar, then transported to a glove box for cell assembly without any air exposure. The separator was used – Celgard 2300. The assembly of button-type cells from ready-made electrodes with a form factor of 2032 was carried out in a SPEKS GB02M glove box in an argon atmosphere with a humidity level of less than 0.1 millionths and an oxygen concentration of less than 1.0 millionths. Push-button batteries were formed by a hydraulic press MTI-MSK-110. Electrochemical studies of samples of the 2032 format were carried out by the method of galvanostatic charge-discharge cycling on an eight-channel analyzer of MTI BST8–MA power supplies in the voltage range of 3 - 4.5 V. This device is designed for testing portable batteries, as well as studying the resource of electrode materials. The voltage was recalculated relative to $Li^+/Li$ based on the charge/discharge curves of negative electrodes obtained in cells with lithium metal at the same current densities. The specific capacity was normalized by the mass of the active material.

**Results:** Studies show (Fig.1) that an element with an electrolyte of 1 M LiDFOB in FEC:DME at a volume of 3:7 remains stable and has a discharge capacity of ≈ 200 mAh/g, while a sample with an electrolyte of the same salt in a mixture of PC:DME solvents has a capacity of 170 mAh/g. Coulomb efficiency is one of the most important characteristics of anode-free lithium batteries, indicating the relative volume of lithium stored at the anode after a full charge-discharge cycle. The Coulomb efficiency of the studied samples is = 96% for samples with 1M LiDFOB electrolyte in FEC:DME and 92% for 1 M LiDFOB composition in PC:DME.
The improvement achieved is explained by the formation of stable and protective surface films on the cathode particles due to the unique surface reactions that are possible due to

the nature of fluorinated solvent molecules. Surface films formed on lithium cathodes of transition metal oxide isolate the active mass, which has a high reactivity with respect to electrophilic alkyl carbonates, from ongoing harmful reactions with solution particles. The exceptional electrochemical stability of these electrolyte solutions makes them suitable for other anode free lithium-ion cells.

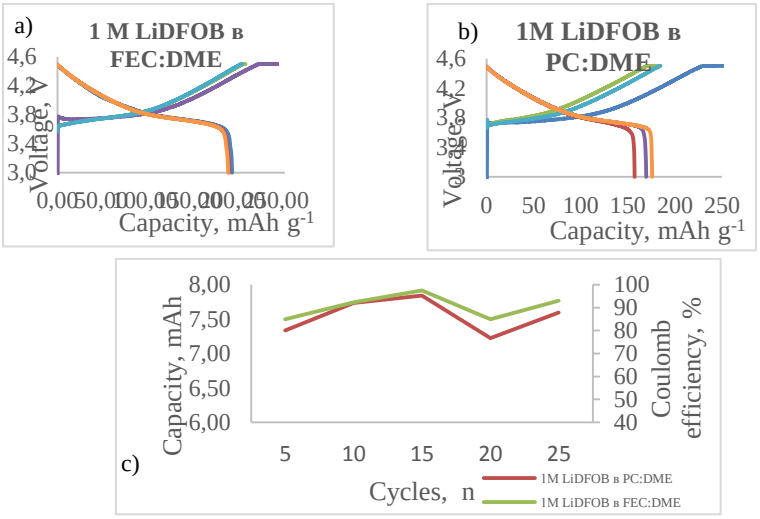



**Fig.1.** Charge-discharge curves of the first three cycles without anode lithium cells with electrolytes: a) 1 M LiDFOB in FEC:DME in volume 3:7; b) 1 M LiDFOB in PC:DME in volume 3:7; c) the dependence of Coulomb efficiency on the number of cycles.

**Conclusion:** The key advantage of using this electrolyte is the reversibility of the lithium coating application/removal process (96% cyclicity of Coulomb efficiency). The work also proves that the Coulomb efficiency of anode-free batteries can be improved through the use of a slow charging/fast discharging protocol, which leads to an exceptionally high Coulomb efficiency of more than 99.8%. The lithium produced directly (during charging) is largely stabilized by minimizing reactions between the lithium-coated and concentrated electrolyte.

**Reference:**

1. B. J. Neudecke, N. J. Dudney, J.B. Bates, Journal of Electrochemical Society, 47 (2000) 517.
2. J. Qian, B.D. Adams, J. Zheng, W. Xu, W.A. Henderson, J. Wang, M.E. Bowden, S. Xu, J. Hu, J.G. Zhang, Advanced Functional Materials, 26 (2016) 7094.
3. J. Liu, Z. Bao, Y. Cui, Nature Energy, 4 (2019) 180.
4. R. Schmuch, R. Wagner, G. Hörpel, T. Placke, M. Winter, Nature Energy, 3 (2018) 267.
5. L.H. Abrha, T.A. Zegeye, T.T. Hagos, H. Sutiono, B.J. Hwang, Electrochimica Acta, 325 (2019) 134825.
6. C. Fang, J. Li, M. Zhang, Y. Zhang, F. Yang, J.Z. Lee, M.-H. Lee, J. Alvarado, M.A. Schroeder, Y. Yang, B. Lu, N. Williams, M. Ceja, L.Yang, M. Cai, J. Gu, K. Xu, X. Wang, Y.S. Meng, Nature, 572 (2019) 511.
7. K.N. Wood, E. Kazyak, A.F. Chadwick, K.H. Chen, J.G. Zhang, K. Thornton, N.P. Dasgupta, ACS Central Science, 2 (2016) 790.
8. R. Rodriguez, R.A. Edison, R.M. Stephens, H.H. Sun, A. Heller, C.B. Mullins, Journal of Materials Chemistry A, 8 (2020) 3999.
9. X. Yin, W. Tang, I.D. Jung, K.C. Phua, G.W. Zheng, Nano Energy, 50 (2018) 659.

# POLYHALITE: WHAT KIND OF FERTILIZER IS IT?

**A. MYKA[1], R. ŁYSZCZEK[2], A. BIŃCZAK[1]**, [1]Łukasiewicz Research Network – New Chemical Syntheses Institute, Fertilizers Research Group, Tysiąclecia Państwa Polskiego Ave. 13A, 24-110 Puławy, Poland, [2]Maria Curie-Sklodowska University, Faculty of Chemistry, Institute of Chemical Sciences, Department of General and Coordination Chemistry and Crystallography, M. Curie-Sklodowska Sq. 3, 20-031 Lublin, Poland.

**Abstract:** This paper presents the results of a study on polyhalite - a natural fertilizer currently mined in the UK only. Recent press reports have confirmed the existence of rich deposits of this fertilizer in Poland, with plans to exploit them in the future. The study of polyhalite focused on its chemical composition, the presence of impurities and its thermal behaviour when heated. The obtained results confirmed high content of nutrients (K, Ca, Mg, S) and very low concentration of heavy metals. Polysulphate is a mineral with high potential as one of the components of NPK fertilizers.

**Introduction:** Fertilization is an integral part of crop yield improvement. Polyhalite (polysulphate, $K_2MgCa_2(SO_4)_4 \cdot 2H_2O$) is a natural multi-nutrient fertilizer and a source of potassium, calcium, magnesium and sulphur [1]. Naturally occurring polysulphate may also contain elements such as Fe, Zn, Ni, Cu, and Mn [2]. Polyhalite has a lower environmental impact than other fertilizers and releases nutrients more slowly than conventional fertilizers, which can help to increase the efficiency of fertilizer use [3]. Today, polyhalite is mined in only one place in the world, the Boulby Mine, located under the North Sea off the coast of North Yorkshire, UK, by Israel Chemical Limited (ICL) [4]. ICL currently sells around 500 kt/y as polysulphate and it is sold in three grades (polysulphate standard, polysulphate mini granular and polysulphate granular). The products available on the market are shown in Fig.1.




**Fig.1.** The products of polyhalite avaible on the market.

Recent press reports have confirmed the existence of rich polyhalite resources beneath the Puck district in Poland. It is estimated that these resources could support production of 2.5 million tonnes per year for a period of approximately 25 years [5]. In 2019, Regulation (EU) 2019/1009 of the European Parliament and of the Council of 5 June 2019, laying down rules

for making EU fertilizer products available on the market, amending Regulations (EC) No 1069/2009 and (EC) No 1107/2009 entered into force and repealed Regulation (EC) No 2003/2003 [6]. Regulation (EU) 2019/1009 is applicable from 16 July 2022 and has created opportunities for the development of innovative fertilizers that are efficient for agriculture and environmentally friendly. The main objectives of the Regulation are a more resource-efficient use of nutrients, in line with the idea of a circular economy, and a sustainable and greener version of agriculture within the Common Agricultural Policy. It also regulates the marketing of all products with fertilizer value that meet the quality requirements laid down in the Regulation. It is well known that the development of fertilizer production technology is a multi-stage process. The potential raw material must be subjected to an evaluation of its physicochemical properties. It is necessary to determine the main nutrients, the content of which can be declared in fertilizers, as well as the content of heavy metals, which are limited according to the European Fertilizers legislation [7]. Fulfillment of the above criteria is a prerequisite for further research. The use of polyhalite as a component for NPK fertilizers is a very interesting research topic a nd is in line with the new regulations. The aim of the study was to accurately characterize the physico-chemical properties of polyhalite, which are essential to assess the possibilities and limitations of using the fertilizer as a component of NPK fertilizers.

**Experimental:** A sample of polyhalite, previously ground in a laboratory mill, was used for the study. The contents of the individual components were determined by standard methods in accordance with fertilizer regulations. The heavy metal concentration (As, Cd, Pb, Cu, Cr, Ni) was determined by a laboratory test procedure using inductively coupled plasma optical emission spectroscopy (ICP-OES) with a Varian 720-ES emission spectrometer and by atomic absorption spectrometry (AAS) with amalgamation technique with a DMA-80 EVO mercury analyser (Hg). The crystalline phase was identified by X-ray powder diffraction (XRPD). Measurements were performed on a PANanalytical Empyrean powder diffractometer operating in Bragg-Brentano geometry. Thermal properties were determined using techniques such as termogravimetry (TG) and differential scanning calorimetry (DSC). Measurements were carried out using a STA 449 F3 thermal analyser (Netzsch) in a dynamic synthetic air atmosphere.

**Results:** The physical properties, chemical composition and heavy metal concentrations of polyhalite are shown in Table 1 and Table 2. As can be seen in Table 1, in addition to the primary fertilizer macronutrient potassium, polyhalite contains secondary macronutrients such as calcium, magnesium and sulphur.

**Table 1.** Physical properties and chemical composition of polyhalite.

| | Chemical composition, (mass / %) |
|---|---|
| $K_2O$ | 13.90 |
| CaO | 17.00 |
| MgO | 6.00 |
| $SO_3$ | 48.00 |
| $Cl^-$ | 3.33 |
| Moisture | 0.07 |
| pH | 6.80 |

Chlorides are also present in the sample at 3.33%. Table 2 shows the concentration limits of heavy metals in inorganic fertilizers according to the European fertilization legislation. The concentrations of metals such as As, Cd, Pb, Hg, Cu, Ni in the analysed sample were much lower than the acceptable limits. The chromium(VI) content was not determined due to the very low concentration of total chromium.

**Table 2.** Limits of heavy metals content in inorganic fertilizers according to the European fertilization law and their concentration in polyhalite.

| Element | As | Cd | Pb | Hg | Cu | Cr(VI) | Ni |
|---|---|---|---|---|---|---|---|
| $mg \cdot kg^{-1}$ | | | | | | | |
| Limit | 40 | 3 | 120 | 1 | 600 | 2 | 100 |
| Polysulphate | < 3.0 | < 0.5 | < 4.0 | < 0.003 | < 1.0 | < 1.0* | < 1.0 |

*total chromium

The powder diffractogram of a polyhalite sample is shown in Fig.2. From the analysis of the diffractogram it can be concluded that the dominant crystalline phase is the one of polyhalite based on ICDD database card 00-021-0982. The polyhalite phase has characteristic reflections for angles 2Θ: 28.04°; 30.66°; 30.92°, 14.75°. A phase corresponding to calcium sulphate and sodium chloride is also visible in the sample, identified from ICSD database cards 01-080-6360 (2Θ: 25.42°; 31.36°; 55.73°) and 01-080-3939 (2Θ: 31.69°; 45.43°; 56.45°), respectively.

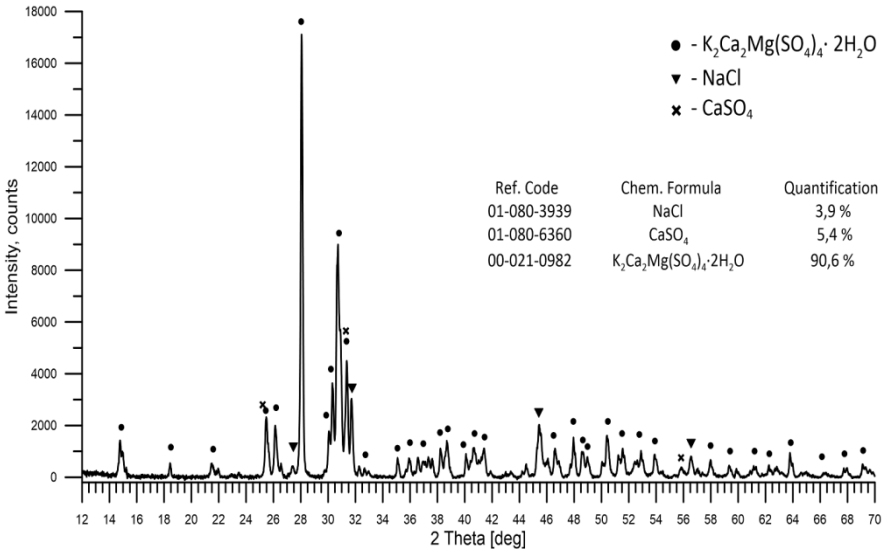



**Fig.2.** XRPD diffractogram of polyhalite.

TG/DSC curves of the thermal decomposition of polyhalite are shown in Fig.3.

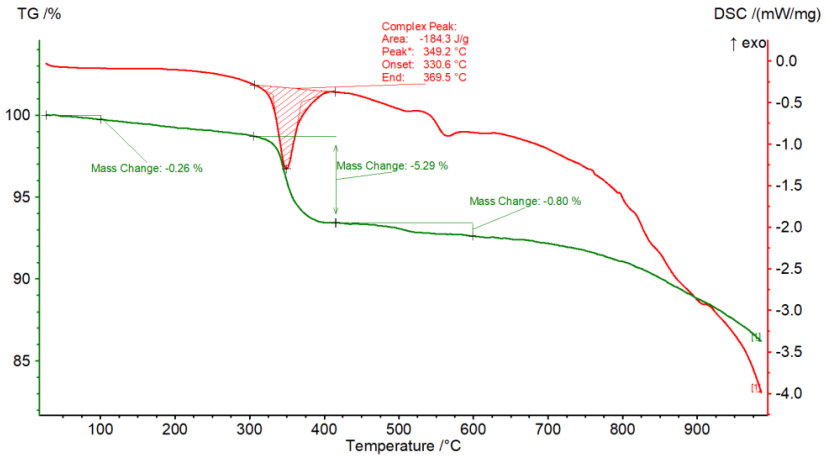



**Fig.3.** TG/DSC curves of decomposition of polyhalite.

The sample has been heated to 1000 °C. The first stage of very low mass loss (up to about 300 °C) is caused by the presence of moisture and a small amount of impurities. From about 330 °C to 370 °C an endothermic DSC peak is visible, corresponding to a mass loss of 5.29%. This is the effect of dehydration of polyhalite [8]. The lower mass loss than for pure polyhalite (5.98%) is probably due to the presence of impurities (mainly sodium chloride and calcium sulphate). A small loss of mass (0.80%) and associated endothermic effect occurs at a temperature of about 550 °C. At temperature above 700 °C, there is a marked decrease in mass loss due to sample decomposition.

**Conclusions:** Polyhalite is a valuable agricultural fertilizer, characterized by easy solubility and rapid uptake by plants, which can contribute to the development of sustainable agriculture. The presence of deposits of this raw material in Poland creates opportunities for its use not only as a straight fertilizer, but also as a component in multi-component fertilizers. Due to the current prices of fertilizer raw materials, it is a valuable source of potassium, as well as calcium, magnesium and sulphur. It also has a very low content of heavy metals and impurities. The current fertilizer regulation (EU) 2019/1009 allows the use of a wide range of products from different sources to produce inorganic, organic and organic-mineral fertilizers.

## References:

1. U. Yermiyahua , I. Ziporia, I. Faingolda, L. Yusopova, N. Fausta, A. Bar-Talb, Israel Journal of Plant Sciences, 64 (2017) 145.
2. B. Marcel, C.L. Yuncong, L. Guodong, H. Zhenli, R. Mylavarapu, S Zhang, Agricultural Research & Technology Open Access Journal, 6 (2017) 555690.
3. R. Bhatt; P. Singh, O.M. Ali, A.A.H Abdel Latef, A.M. Laing, A. Hossain, Sustainability, 13 (2021) 10689.
4. https://www.saltworkconsultants.com/downloads/39%20Polyhalite.pdf/downloaded 04.04.24.
5. https://gmina.puck.pl/zloza-polihalitu-szansa-na-rozwoj-i-prace/downloaded 3.04.2024
6. Regulation (EU) 2019/1009 of the European Parliament and of the Council of 5 June 2019 laying down rules on the making available on the market of EU fertilizing products and amending Regulations (EC) No 1069/2009 and (EC) No 1107/2009 and repealing Regulation (EC) No 2003/2003.
7. A. Myka, R. Łyszczek, A. Zdunek, P. Rusek, Journal of Thermal Analysis and Calorimetry, 147 (2022) 9923.
8. H. Xu, X. Guo, J. Bai, Physics and Chemistry of Minerals, 44 (2017) 125.

# TECHNOLOGY FOR PRODUCING CONTROLLED-RELEASE MINERAL FERTILIZERS (CRFs) USING BIODEGRADABLE MATERIALS IN THE COATING PROCESS

**Ł. RUSEK**, Łukasiewicz Research Network - New Chemical Syntheses Institute, Tysiąclecia Państwa Polskiego Ave. 13A, 24-110 Puławy, Poland.

**Abstract:** The study addresses innovative approaches to plant fertilization in the context of environmental protection and growing global food needs. In view of population growth projections, the authors suggest the use of 'smart fertilizers' with delayed or controlled release of ingredients, based on biodegradable coatings. Experimental studies conducted by spraying in a granulation drum showed differences in nutrient release depending on the type of fertilizer and coating. Controlled-release fertilizers based on vegetable oil appear to be promising, but further research is needed, especially in the context of coating layer optimization and coating weight ratio.

**Introduction:** Fertilizer consumption declined the most in 2022, mainly due to the high prices of raw materials needed for fertilizer production. Natural gas prices, which account for up to 90% of variable costs in the fertilizer production process, have played a significant role [1]. Annual mineral fertilizer consumption is expected to decline by 4.6% over the next 10 years [2]. In the European Union, the decline in consumption is mainly due to restrictions imposed on the use of fertilizers in Western member countries [3]. These are mainly the effects of the European Union's ambitious green goals, such as the European Green Deal, which are challenging the fertilizer sector. To optimize the use of nutrients by plants and at the same time reduce the negative environmental impact of fertilization, innovative solutions such as smart fertilizers can be used [3-4]. Fertilizers with slowed or controlled release of nutrients (SRF/CRF) may be the answer to these challenges. Although they are currently available on the market, their main problem is that non-biodegradable coatings accumulate in the soil and cause permanent soil contamination. Therefore, it is important to continue to develop innovative solutions that will allow the efficient use of fertilizers while minimizing negative environmental effects [5-6].

**Experimental:** The coating process was carried out in batches at ambient temperature. A total of 6 trials were performed where 3 variants of envelopes were used for two fertilizers. The difference in the envelopes was the change of the catalyst content in the oil:

- Envelope 1 - no catalyst in the oil
- Envelope 2 - 0.5 wt. % catalyst in oil
- Envelope 3 - 1% wt. of catalyst in oil

All coating tests were carried out in an analogous manner. After filling the drum with fertilizer, coating additives were introduced, starting with linseed oil and then, after proper mixing where the drum speed was 28 rpm (about 2 min), bulk material in the form of lignite dust was added (2 min). The addition of coal was intended to increase the ability of the granular material to accept more oil. To harden the applied layer, the fertilizer was poured into cuvettes and subjected to a drying process at 80°C. The

residence time of the fertilizers in the chamber dryer was 45-60 minutes, depending on the observation of the surface. Covers with the addition of a catalyst cured in up to 20 min less time, compared to covers without a catalyst. All the samples produced were coated with a total of 7 layers. The first layer consisted solely of oil, representing 1 wt.% of the NPK fertilizer. Layers 2-6 were covered with oil and lignite, applied in amounts of 1 wt. % each to the fertilizer. Layer 7 was oil alone (1% by weight of fertilizer). The first layer of oil was intended to prepare the surface of the granules by closing the pores. The last layer was to further seal the envelope. The fertilizers, due to their porous surface and irregular shape, contained 10-14 wt. % of the areola. The obtained coated fertilizers were subjected to macronutrient release tests after 24 h and after 28 days.

**Results:** Figures 1-3 show the kinetics of macronutrient release from the encapsulated fertilizers, which were produced on the basis of Polifoska Start and Polifoska 6 fertilizer.

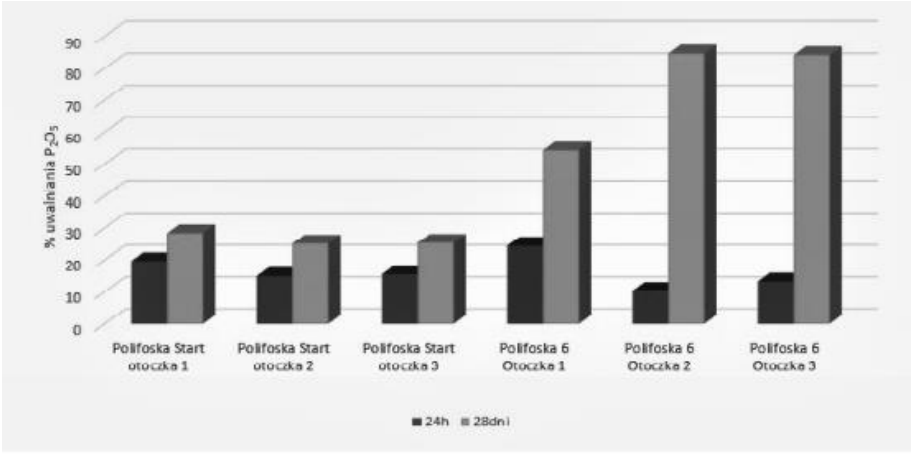



**Fig. 1.** $P_2O_5$ release rate from coated fertilizers after 24 hours and 28 days.

For all samples tested, the level of nitrogen release at close to 40% during the first day was too high for the standard [7]. The other macro-components of the fertilizer, potassium and phosphorus, were released at levels not exceeding 15% during the first day. Of all the fertilizers analyzed, none exceeded 75% of the released components after 28 days. Analysis of the results indicates that nutrient release efficiency was closely related to the characteristics of the envelope and the type of fertilizers. Particularly promising, given the results obtained and observations in the application and especially curing process, where the addition of a catalyst in the case of otoles 2 and 3 for both Polyphoska Start and Polyphoska 6 accelerated the curing process by about 20 minutes compared to otoles in which no catalyst was applied. Higher contents of individual components (N, P, K) in the fertilizers also affect the level of their release.

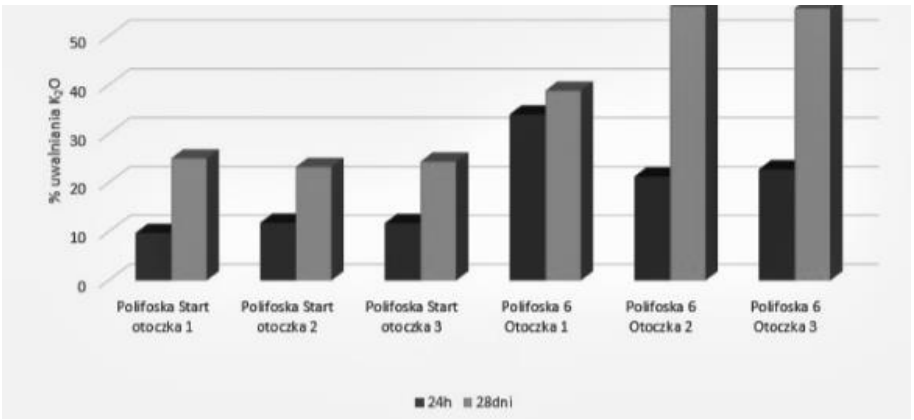



**Fig. 2.** $K_2O$ release rate from coated fertilizers after 24 hours and 28 days.

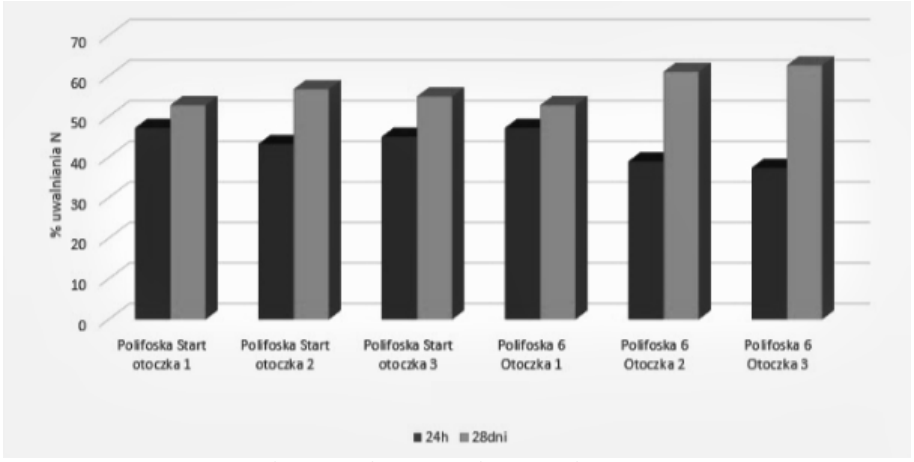



**Fig. 3.** The rate of N release from coated fertilizers after 24 hours and 28 days.

Polyphoska Start with twice the nitrogen content compared to Polyphoska 6 released more nitrogen per day, between 5% and 10%. On the other hand, in the case of phosphorus and potassium content, which are almost twice as much in Polifoska 6, the level of release of these components was also higher for the fertilizer with a higher content of these components.

**Conclusions:** Based on the results obtained, coatings based on linseed oil with the addition of a catalyst can be used to produce slow-acting coated fertilizers. The effectiveness of this type of coatings depends largely on the type of fertilizer contained in them. The number of layers in the systems used is too large (7 layers) and efforts should be made to reduce their number and mass fraction of coatings. The materials used to produce the coating are of natural origin and there is no information in the literature on their toxicity. Due to the lack of standards to carry out this type of analysis, the assessment of their toxicity and biodegradability will be carried out at a later stage. It seems that different types of fertilizers (Polifoska Start and Polifoska 6) and different

coatings (1, 2, 3) have a significant impact on the level of nutrient release into the soil. It is also worth remembering that the effectiveness of this type of fertilizers also depends on other factors, such as soil type, weather conditions and application methods. Therefore, further research will be needed to better understand the processes occurring in the system: fertilizer - coating - soil – plant.

**References:**

1. L. Cross, A. Gruère, Medium-Term Fertilizer Outlook 2022–2026, Rapor IFA Annual Conference, 30.05–01.06.2022, Wienna 2022.
2. https://www.fertilizerseurope.com/wp-content/uploads/2022/09/. Industry-Facts-and-Figures-2022.pdf, access 2023.
3. https://www.fertilizerseurope.com/AnnualOverview/images/FER-AR22%20web.pdf, access 2023.
4. E. Gorlach, T. Mazur, Chemia rolna. Podstawy żywienia i zasady nawożenia roślin, Wydawnictwo Naukowe PWN, Warszawa 2001.
5. R. Czuba, Nawożenie mineralne roślin uprawnych, Wyd. Z.Ch. „Police", Police 1996.
6. A. Akelah, Materials Science and Engineering C, 4 (1996) 83.
7. PN-EN 13266/2003, Nawozy wolnodziałające. Oznaczenie uwalniania składników odżywczych. Metoda dla nawozów otoczkowanych.

# IMPROVING THE EFFICIENCY OF PALLADIUM(II) CEMENTATION FROM DILUTE SOLUTIONS BY USING SILVER-COPPER ALLOY POWDERS

**T. MICHAŁEK, M. WOJNICKI**, AGH University of Krakow, Faculty of Non-Ferrous Metals, Mickiewicza Ave. 30, 30-059 Krakow, Poland.

**Abstract:** This study investigates the efficacy of utilizing silver-copper alloy powders as substitutes for zinc in the cementation of palladium(II) from dilute solutions. Thermodynamic analyses reveal the behavior of pure zinc, copper and silver in a chloride system containing palladium. Microstructural analysis of the synthesized alloy powder demonstrates its potential for optimizing the cementation process.

**Introduction:** Palladium, a member of the platinum group metals (PGMs), is highly esteemed for its paramount role in environmental conservation efforts, such as catalytic converters, crucial components in the automotive sector for reducing harmful emissions [1]. Its diverse range of applications spans from electronics [2] to pharmaceuticals [3] and even jewelry [4]. Palladium is considered a critical raw material, which emphasizes the importance of improving its recycling technologies [5]. Currently, to treat solutions containing a minuscule concentration of palladium(II), cementation by zinc powder is usually employed [6]. However, this method may result in a significant percentage of palladium(II) remaining in the solution, even when a stoichiometric excess of zinc is added [7]. The low effectiveness of cementation by zinc may be contributed to hydrogen evolution, which takes place during the process, resulting in its dissolution. Moreover, gaseous hydrogen bubbles may adhere to the zinc surface, further reducing the effectiveness of cementation [8]. In this work we analyze the possibility of substituting zinc with more noble metals (copper and silver), to increase the amount of palladium recovered.

**Experimental:** Calculations of Gibbs free energy changes in the function of temperature for the reactions taking place during palladium cementation, as well as Pourbaix diagram of Pd-Cl-$H_2O$ system were made using the HSC software (version 5.11). SEM images of synthesized Ag-Cu alloy powder were taken using JEOL-6000 instrument (JEOL, Tokyo, Japan) equipped with an energy dispersive X-ray spectrometer (EDS).

**Results:** The first thing to consider is a chemical composition of low-concentrated waste palladium(II) solutions from industry. A typical waste solution would usually contain chloride or cyanide anions (from the leaching process) and a low concentration of palladium(II) in the form of complexes. In this work we will focus on Pd-Cl-$H_2O$ system from an electrochemical and thermodynamical standpoint. Using HSC software, it is easy to simulate such a system and create a Pourbaix diagram (Fig.1).

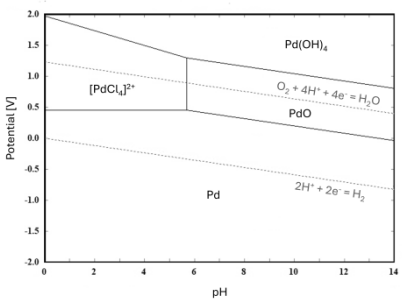



**Fig.1.** Pourbaix diagram for Pd-Cl-$H_2O$ system. Temperature = 25 °C, Pd concentration = 0.1 mM, Cl concentration = 1 M.

As shown in Fig.1, if the pH of the solution is highly acidic, then the dominant palladium species should be the $[PdCl_4]^{2-}$ complex. This conclusion aligns with previous work, in which the share of palladium complexes was calculated using Boily equilibrium constants [9]. With knowledge of the dominant complex in the system, it is possible to calculate Gibbs free energy changes and determine which reactions are thermodynamically favored. The results of these calculations are shown in Fig.2a-b.

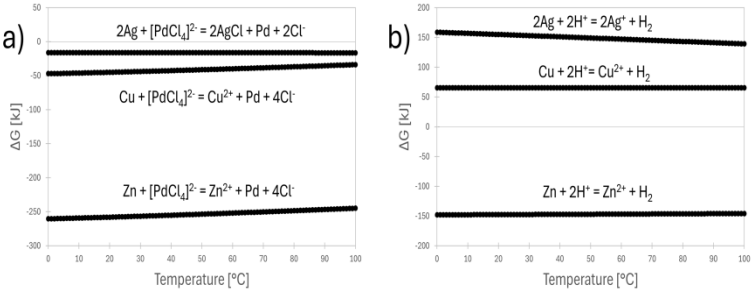



**Fig.2.** Gibbs free energy changes for: (a) $[PdCl_4]^{2-}$ cementation reactions by Zn, Cu and Ag; (b) hydrogen evolution reactions by Zn, Cu and Ag.

The results depicted in Fig.2a correlate well with the difference in standard potentials between palladium and other metals, which is the primary factor in cementation reactions. Cementation by silver is the least thermodynamically favored as the difference in standard potentials is very low. Another issue is the precipitation of AgCl in chloride media, as it may reduce the effective surface area of silver powder during the cementation. Since the potential difference between palladium and zinc is the highest, this reaction is the most thermodynamically favored. Metals with negative values of standard potential (such as zinc) indeed generate a high potential difference with palladium; however, as their potential is also lower than that of the standard hydrogen electrode, using them results in hydrogen evolution during cementation. This effect results in Zn dissolution, reducing the effectiveness of the process.

The results from Fig.2b suggest that hydrogen evolution will occur in the system with zinc, while it will not occur in the systems with copper and silver. This indicates that copper may be the effective in the cementation of Pd(II), as its usage will not result in

either hydrogen evolution or the precipitation of chloride salt (since $CuCl_2$ is highly soluble in aqueous media).
Another important aspect of thermodynamic analysis in the cementation process is to calculate the equilibrium concentrations of Pd(II) for various metals, as illustrated in equation:

$$E^0_{Pd} + \frac{RT}{nF} \cdot \ln C_{eqPd} = E^0_{Me} + \frac{RT}{nF} \cdot \ln(C_{0Pd} - C_{eqPd})$$

where: $E^0$ is the standard electrode potential, $R$ is the gas constant, $T$ is the temperature of the system, n represents the number of moles of electrons transferred in the redox reaction, $F$ is the Faraday's constant, $C_{eq}$ is the equilibrium concentration, and $C_0$ is the initial concentration. *Me* refers to metal used for palladium$^{2+}$ cementation.

Using the above equation, the following results were obtained and are depicted in Table 1.

**Table 1.** Equilibrium concentrations of Pd(II) for the cementation process with different metals. Temperature = 25 °C, initial Pd(II) concentration = 1 mM.

| Metal | Standard electrode potential [V] | Pd(II) equilibrium concentration [mM] |
|---|---|---|
| Zinc | −0.76 | $8.85\times10^{-59}$ |
| Copper | +0.34 | $2.17\times10^{-21}$ |
| Silver | +0.80 | $6.96\times10^{-6}$ |

Once again, while theoretically zinc is the most optimal metal for palladium(II) cementation among those analyzed, in practice, it often experiences low process efficiency. To further enhance the effectiveness of copper in palladium cementation, several approaches may be employed. Kinetics, and therefore the efficiency of the cementation process, will be greatly influenced by the surface area of contact between the solid and liquid phases. This implies that using powders with highly developed surface areas would be advantageous. Another approach would involve utilizing contact electrification, which generates a potential change when two different conductors are in contact [10]. To ensure the constant contact of copper and silver, an alloy powder of those metals may be utilized, preferably with a highly developed surface for the reason stated above. As the change in potential of metals in contact is dependent on the contact surface, alloys with different compositions would exhibit different potential differences; thus, there should theoretically exist an optimal composition for palladium cementation. We managed to synthesize an alloy powder of copper and silver, obtained SEM images show that its surface is highly developed (Fig.3a-b), while EDS analysis confirms that it is indeed an alloy, with relatively stable composition of copper and silver (Fig.3c-d).

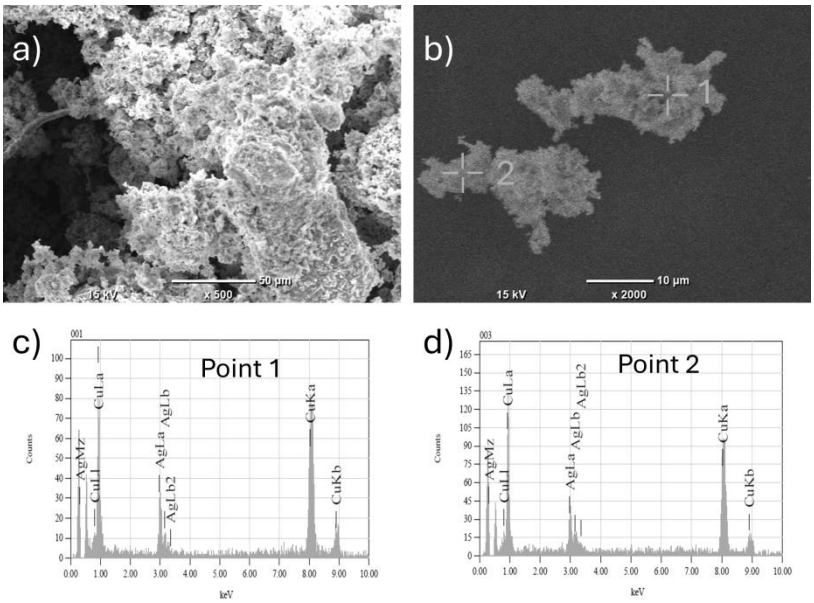



**Fig.3.** (a-b) SEM images of Ag-Cu alloy powder; (c-d) EDS analysis of Ag-Cu alloy powder.

The next stage will be the synthesis of powders with varying compositions, and experimentally testing their efficiency in palladium cementation process.

**Conclusions:** An alloy powder of copper and silver may prove to be an effective substrate for palladium recovery, as it does not result in hydrogen evolution during the process, unlike zinc. In such an alloy, silver would be more stable compared to pure silver, thereby lessening the interference caused by AgCl precipitation during the process. Further experiments are needed to determine the optimal composition of copper and silver in an alloy for palladium cementation.

**Acknowledgements:** This work was financed by AGH Initiative for Excellence-Research University, grant no. 6824/2023 (Tomasz Michałek).

**References:**

1. B. Xu, Y.F. Chen, Y.J. Zhou, B.S. Zhang, G.Q. Liu, Q. Li, Y.B. Yang, Metals, 12 (2022) 533.
2. A.E. Hughes, N. Haque, S.A. Northey, S. Giddey, Resources, 10 (2021) 93.
3. S. Bi, N. Ahmad, Materials Today: Proceedings, 62 (2022) 3172.
4. C. Corti, Platinum Metals Review, 53 (2009) 21.
5. T. Michalek, V. Hessel, M. Wojnicki, Materials, 17 (2023) 45.
6. V.N. Nguyen, S.J. Song, M.S. Lee, Metals, 11 (2021) 1320.
7. C.N. Mpinga, S.M. Bradshaw, G. Akdogan, C.A. Snyders, J.J. Eksteen, Hydrometallurgy, 142 (2014) 36.
8. J. Chen, Y. Lei, C. Zhu, C. Sun, Q. Xu, H. Cheng, X. Zou, X. Lu, Hydrometallurgy, 210 (2022) 105847.
9. A. Podborska, M. Wojnicki, Journal of Molecular Structure, 1128 (2017) 117.
10. P. Peljo, J.A. Manzanares, H.H. Girault, Langmuir, 32 (2016) 5765.

# TESTING THE SPECTRAL CHARACTERISTICS OF REFLECTIVE MATERIALS USING A MULTI-ANGLE ATTACHMENT

**M. SKRZETUSZEWSKI[1,2], Ł. LITWINIUK[1], M. ZAJKOWSKI[2], S. GÓRNIK[1], K. HOVOROVA[1]**, [1]Central Office of Measures, Electricity and Radiation Department, Elektoralna 2 St., 00-139 Warsaw, Poland, [2]Bialystok University of Technology, Faculty of Electrical Engineering**,** Wiejska 45D St., 15-351 Bialystok, Poland**.**

**Abstract:** This paper presents a measuring setup which has been used to determine multi-angled characterization of the spectral reflectance standards. The main problem considered in this publication is the study of a new methodology for calibration process based on measurements of the directional reflection coefficient at any measurement angle and the study of the effect of various elements of the UMA accessory on measurement uncertainty.

**Introduction:** One of the tasks of the Central Office of Measures (GUM) is to transfer units of measurement to interested entities. In the Electricity and Radiation Department, the Colour Standard Group performs tests related to, among others: the issues of reflectance colorimetry. Our laboratory performs measurements of such types of reflective surfaces as: ceramic samples, teflon samples, mirror samples, chromatic samples, achromatic samples, gray scale samples. During reflected light measurements, it is therefore important to determine the measurement geometry that includes the angles of incidence and angles of reflection (angles at which the detector is located).
In our laboratory, we have devices enabling measurements in the following geometries: 0°:45°, 45°:0°, d:0°, d:8°, 0°:d, 8°:d [1,2].
In order to expand the possibilities of studying spectral characteristics of different reflecting surfaces, as well as to be able to establish a primary realisation of a unit of colour, it is necessary to extend the range of measurement geometries. Recently our Lab has acquired a new measuring instrument – CARY spectrophotometer with a multi-angle adapter Cary Universal Measurement Accessory (UMA), that allow measurements in any measurement geometries. The results of preliminary measurements with UMA are presented below [3].

**Experimental:** Multi-angle characteristics tests for reflected light were carried out with the multi-angle accessory UMA which scheme is shown in Fig.1 [3].
In the article it is described the research on mirror samples and teflon sample: N1 mirror (5 x 5) cm, N2 mirror (4 x 4) cm, the Spectralon diffuse reflectance standard (5 cm in diameter) made of sintered Polytetrafluoroethylene (PTFE sample).
To support the measurement accuracy which depends on the reflective characteristics of the material, the UMA provides different sample beam detector apertures (from 1° to 5°). During the tests were used detector apertures $1^{o}$ and $3^{o}$ [3].

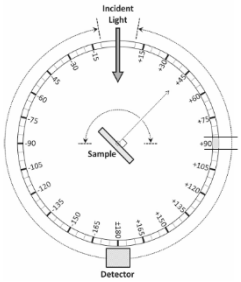



**Fig.1.** Schematic of the UMA attachment measurement system.

A new measurement methodology is being developed to verify the accuracy of the accessory. Based on the rule that a mirror reflects light at the same angle as angle of incident light, it is possible to test the precision of detector angles and locations for samples available.

**Results:** In order to verify the correctness of the settings of UMA the measurements with mirrors have been carried out. The sample was set at an angle of $45^{o}$, the detector readings were recorded at angles from $88^{o}$ to $92^{o}$ with a resolution of $0{,}2^{o}$. Fig.2 shows the measurement results of mirror N1 with a $1^{o}$ and $3^{o}$ detector aperture, which in case of $1^{o}$ detector aperture hardly meet the theoretical assumptions for mirroring angles.

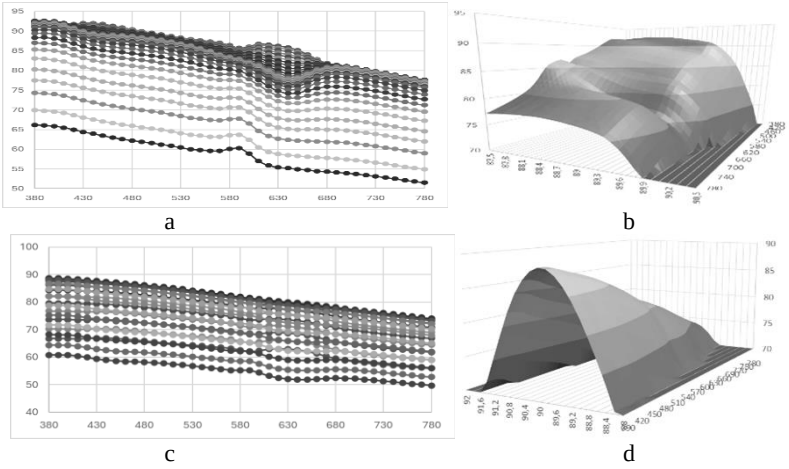



**Fig.2.** Spectral reflection characteristics of a mirror N1:
sample beam detector aperture 1° - a) spectral reflectance characteristics, b) 3D spectral reflectance characteristic; sample beam detector aperture 3° - c) spectral reflectance characteristics, d) 3D spectral reflectance characteristic.

Instead of the expected flat characteristics of the spectral reflectance, results containing unusual curvatures were obtained, which is most visible in Fig.2a for the wavelength range from 580 nm to 680 nm. Fig.2b shows the 3D spectral characteristics of the dependence on the detector angle and the obtained level of the light signal reflected from the sample. In order to find similarity or difference in the shape of the spectral reflectance

characteristics measurements with other parameters with theoretically greater uncertainty have been carried out. Therefore, a $3^o$ sample beam detector aperture was used during subsequent measurements. The obtained results are presented in Fig.2c and Fig.2d.
In this case, the change of the aperture influenced the shape of the spectral characteristics by smoothing their curvatures (Fig.2c), and also makes it easier to find the angle for which, the maximum of the reflected signal was obtained (expected as for $90^o$ (Fig.2d).
To investigate possible reasons for the obtained measurement results, the mirror surface plane was investigated. The check was carried out in the Length Department at the GUM using the MetroPro program. The obtained three-dimensional surface characterization is presented in Fig.3.

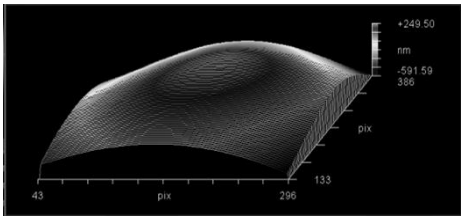



**Fig.3.** Characteristics of the mirror N1 surface profile.

This way it was confirmed that the presented shape of the mirror surface might cause the unexpected curvatures in the spectral characteristics (when using a detector aperture 1°) shown in Fig.2a.
Next, in order to check the influence of the unevenness of the mirror surface on the shape of the spectral characteristics, another mirror N2 was measured. Fig.4 presents the obtained measurement results of mirror N2 using a detector aperture 1° and 3°, which, similarly to mirror N1, do not fully correspond to the theoretical assumptions.

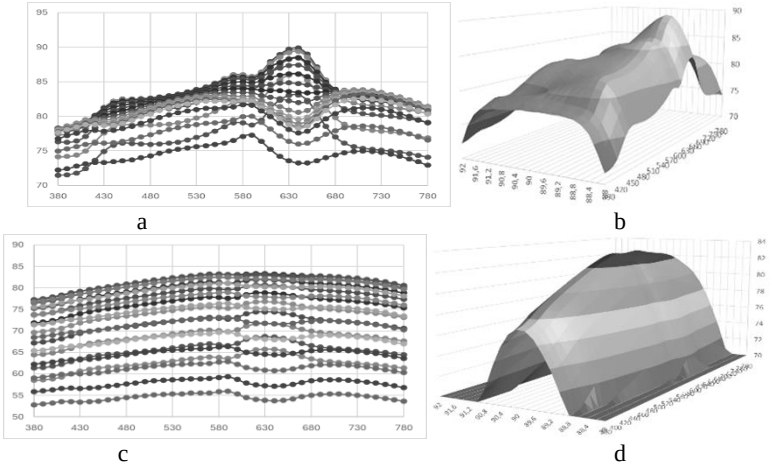
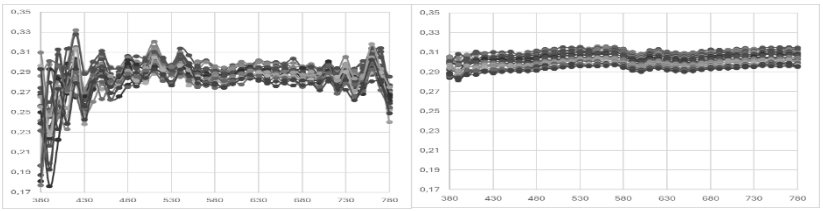



**Fig.4.** Spectral reflection characteristics of a mirror N2:
sample beam detector aperture 1° - a) spectral reflectance characteristics, b) 3D spectral reflectance characteristic; sample beam detector aperture 3° - c) spectral reflectance characteristics, d) 3D spectral reflectance characteristic.

As in the case of mirror N1, here also the curvatures of the spectral reflectance (Fig.4a) and distortions in the 3D characteristics are visible (Fig.4b).
To confirm the assumptions related to the influence of the shape of the material surface on the spectral characteristics, based on previous experiments with the mirror, measurements were made on another reflective material - PTFE sample (matt, almost perfect Lambertian diffuser). The obtained results are presented in Fig.5.



a b

**Fig.5.** Spectral reflectance characteristics of Spectralon diffuse reflectance standard PTFE a) sample beam detector aperture 1°, b) sample beam detector aperture 3°.

In line with theoretical expectations, we obtained flat spectral characteristics both when using a $1^{o}$ aperture (Fig.5a) and a $3^{o}$ aperture (Fig.5b).

**Conclusions:** Measurements made at a 1° aperture allowed for obtaining additional information regarding surface imperfections of the tested mirrors. By changing the aperture to 3°, the theoretical considerations were confirmed and it allowed us to find the angle with maximum signal for the light reflected from the mirror, which, as expected, was 90°. This relationship verified the precision an repeatability of the device settings (detector, sample table). For the PTFE sample, the reflected radiation is constant.

**References:**

1. Commission Internationale de l'Eclairage, Technical report. Colorimetry, CIE 130 (2004).
2. S. Górnik, A. Zydorowicz, Metrologia i Probiernictwo, 3 (2015) 14.
3. Instrument manual of Agilent Cary Universal Measurement Accessory (UMA), (2013).

# MIGRATION OF RADIOACTIVE ISOTOPES IN SOILS AT RARE EARTH AND THORIUM ORE PROCESSING SITES

**Z. IDRISHEVA[1], I. OSTOLSKA[2], E. SANDYBAEV[3], E. SKWAREK[2], G. DAUMOVA[1], M. WIŚNIEWSKA[2]**, [1]D. Serikbayev East Kazakhstan Technical University, Ust-Kamenogorsk 070001, Kazakhstan, [2]Maria Curie-Sklodowska University, Faculty of Chemistry, Institute of Chemical Sciences, Department of Radiochemistry and Environmental Chemistry, M. Curie-Sklodowska Sq. 3, 20-031 Lublin, Poland, [3]ECOSERVICE-S LLP, Ust-Kamenogorsk 070000, Kazakhstan.

**Abstract:** Mining, and in particular the processing industry, is the driving force behind many economic sectors. Unfortunately, many technological processes can also be a source of contamination, posing a serious ecological threat not only to surrounding ecosystems but also to human habitats. The extraction and processing of rare earth elements involves the separation of the minerals that are associated with the ores. These materials often contain naturally occurring radioactive materials. Therefore, their storage may be a source of secondary contamination and post-production areas should be subject to continuous radiological monitoring.

**Introduction:** Technologically Enhanced Naturally Occurring Radioactive Material (TENORM) is defined as naturally occurring radioactive materials that have been concentrated or exposed to the accessible environment as a result of human activities such as manufacturing, mineral extraction, or water processing. In such a case the radiological, physical, and chemical properties of the radioactive material have been concentrated or further altered by having been processed, or beneficiated, or disturbed in a way that increases the potential for human and/or environmental exposures [1].
Radioactive elements are present in many soils and rock formations, and consequently in the water that comes into contact with them. Extraction and processing of these resources may expose or concentrate NORM (Naturally Occurring Radioactive Material), causing them to be classified as TENORM [2].
Rare earth elements (REE), being a source of lanthanides (atomic numbers 57-71) as well as yttrium (Z=39) and scandium (Z=21), are processed primarily from ores and minerals that also naturally contain uranium and thorium [3]. Processing rare earth minerals involves the separation and removal of uranium and thorium, which results in TENORM wastes. The importance and vulnerability to supply chain disruptions has led to the designation of all the rare earth elements as "critical minerals" by the United States Geological Survey.

**Experimental:** Field surveys were carried out over a total area of at least 1500 $m^2$ using an SRP 68-01 portable geological radiometer and a DKS-96 radiometer-dosimeter (DOZA). Fixed point measurements were made by placing the radiometer sleeve tip on the ground collecting the data over 5-10 sec. The geographic information system MapInfo Professional was used to plot gamma exposure dose values on a topographic base of the area (Fig.1). Gamma exposure doses were measured in boreholes up to 1 m deep along the borehole wall using an SRP-88 radiometer in layers ranging from 0 to

100 cm. Gross alpha/ beta particle activity is a measure of the total amount of radioactivity in a sample attributable to the radioactive decay of alpha or beta-emitting radionuclides. The isotopes contributing to the considered sum parameter, are in particular K-40, the uranium or thorium series nuclides e.g. U-238, U-235, Th-232 as well as Ra-226 and Po-210.

Samples were taken from previously drilled boreholes (Fig. 1), layer by layer along the length of the hole, every 20 cm from the surface. Soil samples were prepared as follows. A 120-130 cm deep pit was excavated along the borehole. Samples were taken sequentially at intervals of 0-20 cm, 20-40 cm, 40-60 cm, 60-80 cm and 80-100 cm along the trench wall in a 20 x 20 cm grid. The material was cleaned (roots, insects, stones, glass, etc. were removed) and sieved through a 5mm mesh. Selected samples were dried in an oven at a temperature not exceeding 105°C. Soil samples were ground in a laboratory planetary mill to a particle size of less than 71 μm. A 5.0 g sample was then taken and transferred to a porcelain vessel. The sample was calcined in a muffle furnace at 350°C for 1 hour to minimise the interfering effects of Rn-222 and its decay products on the measurement result. After calcination, the sample was cooled to room temperature and homogenised, then 1.0 g was transferred to a measurement cell previously cleaned with ethanol. To obtain a homogeneous, evenly distributed sample, a few drops of ethanol were added to the cuvette. The sample was dried under an infrared lamp. At least three test specimens were taken from each sample. The samples were sequentially placed in a calibrated low-level UMF-2000 radiometer (DOZA) with silicon detector, which recorded the count rate of alpha and beta particles. Each sample was measured 3 times between 2000 and 5000 s (depending on its activity). The relative method was used to calculate the total specific activity of the alpha or beta emitting radionuclides considering the background radiation.

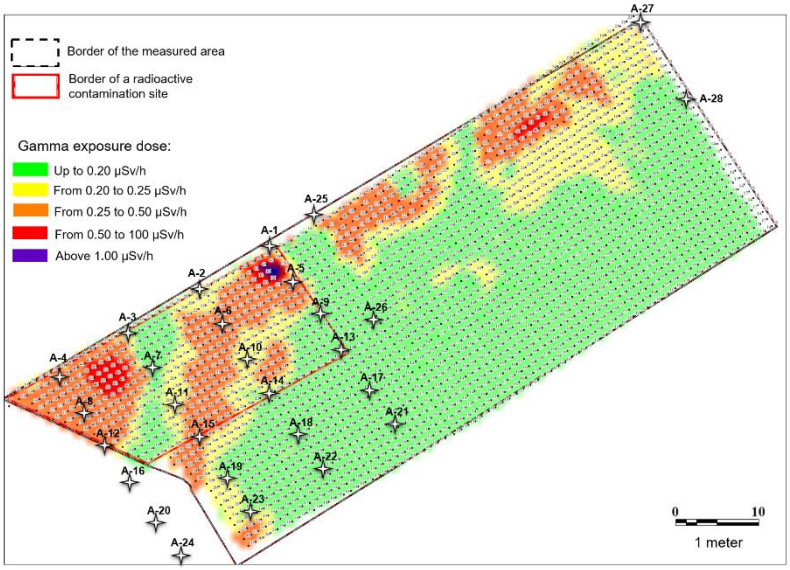



**Fig.1.** Gamma exposure dose measurements in the contaminated area.

Coordinates of the corner points of the radioactive contamination site: 49° 57' 32,68836" N, 82° 35' 31,96824" E; 49° 57' 32,46552" N, 82° 35' 32,81208" E; 49° 57' 33,29028" N, 82° 35' 33,58824" E; 49° 57' 32,89896" N, 82° 35' 34,02492" E;

**Results:** The results of the gamma exposure dose measurements are given in Table 1. As can be seen, surface gamma doses are well above 140 nSv/h, which is the natural background radiation characteristic of the area. The absorbed dose increases significantly with depth. This suggests that radionuclides brought to the surface by the rare earth minerals processing activities may migrate deep into the soil and accumulate in deeper soil layers. Comparing the obtained results with the dose received by the inhabitants of Lublin city (measured about 1.5 m above the ground), it is clear that the site was contaminated with radioactive substances.

**Table 1.** Gamma radiation exposure doses recorded for a given borehole.

| Borehole number | Exposure dose rate (EDR) of gamma radiation [nSv/h] in a borehole at a depth [cm] | | | | |
|---|---|---|---|---|---|
| Depth [cm] | 0 | 20 | 40 | 80 | 100 |
| A-1 | 320 | 1056 | 1760 | 1620 | 1540 |
| A-5 | 304 | 512 | 600 | 1356 | 1320 |
| A-8 | 314 | 661 | 900 | 1121 | 1087 |
| A-21 | 260 | 478 | 582 | 1106 | 1136 |
| A-27 | 255 | 270 | 370 | 360 | 300 |
| Gamma ray exposure dose in Lublin city: 104 nSv/h (Station PL0002 Lublin, 21.03.2024 at 5 a.m.); measurement at 1.5m above ground level [4]. | | | | | |

Changes in total alpha and beta emitter content in soil samples from boreholes A1 – A28 are shown in Figs. 2, 3. It should be noted that monazite (a phosphate mineral containing thorium) is an important source of a number of rare earth metals. As a result, its processing residues are included in the TENORM group. As can be seen, alpha emitters exhibit higher activity than beta radioisotopes at all analyzed depths. This is due to the presence of numerous alpha emitters in the Th-232 radioactive series (Th-232, Th-228, Ra-224, gaseous Rn-220, Po-210 and Po-212, and Bi-212). Beta-minus particle emitters include primarily naturally occurring K-40, Ra-226, Pb-212, Pb-210, Ac-228. Moreover, the spatial distribution and concentration of the radionuclides are likely to depend on the storage site. It should be emphasised that radionuclides have accumulated in deeper soil layers.

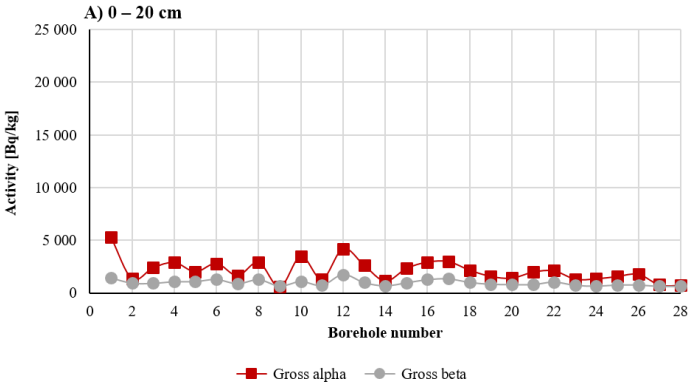



**Fig.2.** Gross alpha and beta emitters in samples taken from boreholes at depth of 0-20 cm.

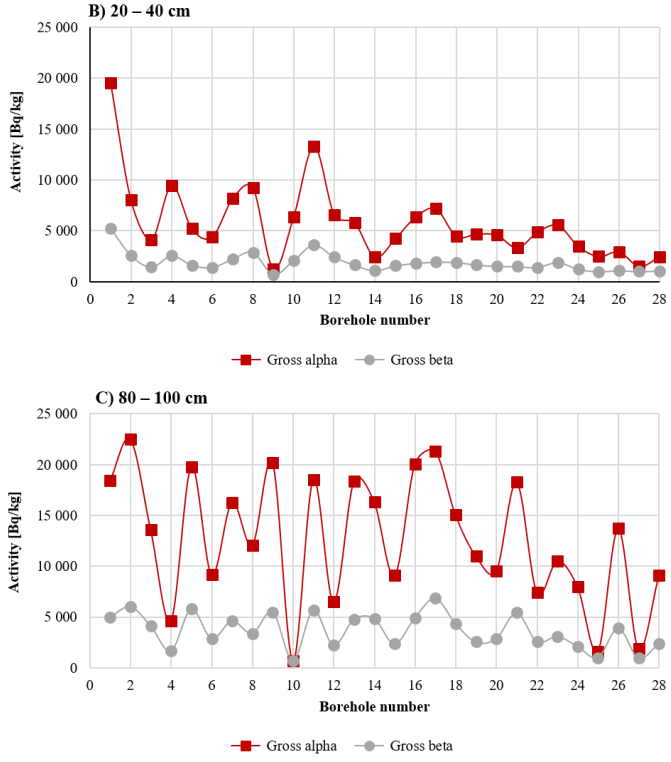



**Fig.3.** Gross alpha and beta emitters in samples at depths of: B) 20-40 cm, C) 80-100 cm.

Radionuclides could enter groundwater supplies through migration deep into the soil. In addition, at depths of more than 40 cm, the root systems of perennial plants and trees are found. Hence, there is high risk of incorporating these radionuclides into the food chain, posing a significant threat to animals living in the area. Although contamination is relatively low at the surface (and in the near-surface soil layer), the potential for

secondary contamination of further areas through soil erosion and leaching of radionuclides by precipitation should be taken into account.

**Conclusions:** Investigations made at the thorium ore and REE processing plant clearly indicate that the area has undoubtedly been contaminated by radioactive substances. The distribution of alpha or beta emitters in the soil profile shows that they accumulate above 40 cm. As the roots of perennial plants are located at this depth, there is a significant risk of entering the food chain. The presence of radioactive substances also poses a threat to animals living in the deeper soil layers. Analysis of the data indicates that a significant part of the site can be considered as high-level waste (areas with total alpha-emitter activity > 10 000 Bq/kg).

**References:**

1. F. Bou-Rabee, A.Z. Al-Zamel, R.A. Al-Fares, H. Bem, Nukleonika, 54 (2009) 3.
2. I. Bahari, N. Mohsen, P. Abdullah, Journal of Environmental Radioactivity, 95 (2007) 161.
3. V. Balaram, Geoscience Frontiers, 10 (2019) 1285.
4. National Atomic Energy Agency, https://monitoring.paa.gov.pl/maps-portal/ (accessed on 21.03.2024).

# INNOVATIVE METHODS FOR THE EXTRACTION OF BIOACTIVE COMPOUNDS FROM PLANT SOURCES

**A. SKRZYPEK[1], B. PAW[2], J. MATYSIAK[1]**, [1]University of Life Science in Lublin, Department of Chemistry, Akademicka St. 15, 20-950 Lublin, Poland, [2]Medical University of Lublin, Department of Medicinal Chemistry, Jaczewskiego St. 4, 20-090 Lublin, Poland.

**Abstract:** Plants represent valuable sources of chemical compounds with potential bioactive properties. These substances fulfill essential metabolic functions in plants, such as defense against pathogens and growth regulation. Upon isolation, they are utilized as dietary supplement ingredients and find application in the prevention of various disorders and the treatment of chronic diseases. They exhibit advantages over chemical preparations as they are readily absorbed by the body, mostly devoid of side effects, do not accumulate in the organism, and their harmful effects are limited. Isolated bioactive substances exert beneficial effects on the human body through various pharmacological properties, including antioxidative, anti-inflammatory, anticancer, antibacterial, and antiviral activities. Among them are polyphenolic compounds, glycosides, saponins, pectins, alkaloids, mucilages, terpenes, mineral components and vitamins, enzymes, and pigments. However, it is important to note that some of them may have undesirable effects. Nevertheless, bioactive compounds from plants are of immense significance from both health and therapeutic perspectives. Consequently, research in this direction holds substantial importance for the development of new medical therapies and the promotion of a healthy lifestyle. This review presents selected methods for the extraction of bioactive compounds, enabling their isolation in an economical, efficient, and environmentally friendly manner.

**Introduction:** Plants have been utilized by humanity for centuries as a source of diverse bioactive compounds possessing potential pharmacological, health-promoting and cosmetic properties. With the advancement of isolation and analysis methods, it has become increasingly feasible to extract and characterize these substances with greater precision. Extraction is the most popular method for isolating bioactive compounds from plant materials. The traditional solvent extraction method utilizes various chemical substances to extract compounds from plants. However, due to increasing environmental pollution and legal constraints, there is a growing interest in "green" extraction methods, such as supercritical carbon dioxide ($CO_2$) extraction, ultrasound-assisted extraction, microwave-assisted extraction, and cold extraction [1-3].

Supercritical $CO_2$ extraction: extraction with a fluid in a supercritical state is currently one of the most rapidly evolving extraction techniques, as evidenced by a significant number of publications on this topic [4-6]. Supercritical fluids used as extractants in the SFE technique, with supercritical carbon dioxide (SC-$CO_2$) being the most commonly used. Carbon dioxide is considered safe for use in the food industry, has low surface tension and viscosity, but its diffusivity is two to three times greater than that of other solvents. It is worth noting that the efficiency of extraction may also be influenced by specific matrix characteristics, such as moisture content. The supercritical state of

a solvent is achieved by heating it above its critical temperature ($T_c$) and pressurizing it above its critical pressure ($p_c$). Supercritical fluids exhibit viscosity similar to gases, liquid-like density, and high diffusivity. The properties of a fluid in a supercritical state can be easily altered by changes in pressure and temperature. For $CO_2$, the critical temperature is 31.1 °C, and the critical pressure is 73.8 bar. Upon transitioning the solvent into a supercritical state, the extraction rate increases, and the separation step is shortened compared to traditional methods. This method is particularly useful for extracting substances with low molecular weight, such as essential oils and certain alkaloids [4-7].

Advantages of supercritical $CO_2$ extraction include: (a) selectivity: specific compounds can be extracted from plant materials while preserving their structure and biological activity, by appropriately adjusting extraction parameters; (b) safety: carbon dioxide is non-flammable, non-toxic, and easily removable, making this method safe for both the environment and the health of workers; (c) eco-friendliness: SFE utilizes $CO_2$, a natural component of the atmosphere, thereby reducing chemical emissions into the environment compared to traditional solvents;

(d) higher quality extracts: low extraction temperatures enable the preservation of high-quality and bioactive compounds, which may degrade under high temperatures;

(e) absence of solvent residues: after the extraction process, $CO_2$ readily condenses and evaporates, leaving behind solvent-free extracts.

The main disadvantages of SFE are its high cost and somewhat complex system configuration, requiring significant investment and appropriately trained personnel for preparation and monitoring compared to conventional methods [8].

Supercritical carbon dioxide extraction finds applications in various fields such as the pharmaceutical, cosmetic, food industries, and dietary supplement production. Numerous examples in the literature demonstrate its utility in isolating bioactive substances from herbs, including medicinal compounds from aloe vera, peppermint, lavender, ginger, and ginkgo biloba [9-12]. The method offers significantly higher efficiency (up to 95%) compared to traditional solvent-based organic extraction methods and yields extracts of high purity. Additionally, research has shown its effectiveness in extracting essential oils from herbs while preserving their natural olfactory profile and chemical composition, as well as in obtaining natural dyes and flavors from plants [13-15].

Ultrasound-Assisted Extraction (UAE) involves the utilization of ultrasonic waves to stimulate the extraction process. The main mechanism of this method is acoustic cavitation. Collapsing cavitation bubbles and sound waves can induce phenomena such as fragmentation, local erosion, pore formation, shear force, increased absorption, and swelling index in the plant cell matrix. Cavitation bubbles generate shock waves, and accelerated collisions between particles lead to rapid fragmentation of the cell structure. This results in the solubilization of bioactive components in the solvent due to particle size reduction, increased surface area, and high mass transfer rates in the solid matrix boundary layer. Ultrasound causes localized damage to plant tissues. This method is characterized by shorter extraction times and the ability to use smaller amounts of solvents compared to traditional methods [16].

Ultrasound technique was applied to extract essential oils from peppermint leaves (*Mentha piperita*). The results showed that UAE enables faster and more efficient extraction of essential oils compared to traditional steam distillation [17]. Additionally, the ultrasound method allowed for higher extraction yields at lower temperatures,

preserving a greater amount of active components in the essential oils. With good efficiency and in a short time, polyphenols were isolated from goji and acai berries using ultrasonic techniques [18]. In studies by Li [19], this technique was applied to extract alkaloids from *Sophora flavescens* roots and flavonoids from *Calendula officinalis* flowers [20]. UAE allows for the effective extraction of these valuable compounds, characterized by strong antioxidant and anti-inflammatory properties. Additionally, the ultrasound method accelerated the extraction process, which is beneficial in terms of production efficiency and economy. UAE has been used for the extraction of terpenoids from tea tree leaves (*Melaleuca alternifolia*), lignans from flax seeds (*Linum usitatissimum*), phenolic acids from Chinese chestnut fruits (*Aesculus chinensis*), polysaccharides from reishi mushrooms (*Ganoderma lucidum*), and iridoid glycosides from *Lysimachia christinae*. These extracts demonstrate immunomodulatory and anticancer potential, as well as anti-inflammatory and analgesic properties [21-23].

Microwave Assisted Extraction (MAE) is a process that utilizes the absorption of microwave energy by chemical substances to extract extract from raw material. The material along with the solvent is placed in a vessel generating microwave radiation, where the temperature reaches approximately 190 °C. The energy affects the movement of ions and dipoles in the electromagnetic field, leading to heat generation, thereby increasing the efficiency of the process. The selection of the solvent is based on its non-zero dipole moment. After the process, product separation and vessel cooling are necessary. The efficiency of this extraction method is high considering the short process time; however, the high temperature, which may lead to product degradation, the use of organic substances, and the need to separate the product from extraction residues, demonstrate the drawbacks of microwave-assisted extraction. The extraction process using MAE occurs in several stages. Initially, the plant material is crushed or ground to increase the contact surface area with the extractant and facilitate microwave penetration. Then, the sample is placed in a closed microwave chamber. Under the influence of this radiation, there is a rapid increase in temperature inside the sample, leading to the extraction of bioactive compounds. After extraction, the extract is separated from the remaining plant components through filtration or decantation [24-26]. Microwave extraction finds wide application in various fields, including the pharmaceutical, cosmetic, and food industries, due to its speed, efficiency, and the possibility of controlled adjustment of extraction parameters. Using MAE, polyphenols and catechins have been extracted from green tea leaves (*Camellia sinensis*) [27]. Additionally, articles are available on the isolation of essential oils from peppermint leaves (*Mentha piperita*), phenolic acids from acai berries (*Euterpe oleracea*), which exhibit antioxidant and anticancer potential, as well as alkaloids from ginseng roots (*Panax ginseng*) with anti-inflammatory, anticancer, and antimicrobial properties. This technique successfully serves for the extraction of essential oils from rosemary leaves (*Rosmarinus officinalis*), carotenoids from carrots (*Daucus carota*), anthocyanidins from berries (*Rubus*) [28-31].

Cold Press Extraction is a technique that involves using low temperatures to extract compounds from plant materials. This extraction method allows for the preservation of most of the nutritional and bioactive components that may degrade due to high temperatures. This method is particularly popular for extracting plant oils. The extraction temperature is maintained at a low level (below 50°C) to preserve the quality and full spectrum of nutrients and bioactive compounds. The process takes place without the use

of high pressure, chemical solvents, or other auxiliary substances, making it an exceptionally environmentally friendly method. The technique involves several key steps. Initially, seeds, fruits, leaves, or roots are carefully prepared through crushing, grinding, or comminution. The aim of this step is to increase the contact surface area with the extract and facilitate the release of bioactive compounds. The prepared raw material is then placed in a press, where under low temperature, the oil or extract is squeezed out, which is then separated from the remaining plant components through filtration, decantation, and other separation techniques. In some cases, especially in the food and pharmaceutical industries, extracts undergo additional purification steps to remove unwanted impurities. They are then stored under appropriate conditions to preserve their quality and shelf life. The advantages of cold press extraction include the preservation of nutrients, lack of auxiliary substances, maintenance of good sensory properties, and ecological benefits. As a result, Cold Press Extraction is gaining popularity among consumers looking for natural and high-quality products [32, 33]. The development of technologies related to cold press extraction continues, leading to increasingly efficient and precise extraction methods that can be used in various industries. This technique is used, among others, in the production of flaxseed oil (*Linum usitatissimum*), as it allows for the preservation of the richness of omega-3 fatty acids, vitamins, and other components that are susceptible to degradation at high temperatures. Cold-pressed flaxseed oil is considered exceptionally valuable due to its health-promoting properties. This technique is also used in the production of essential oils, coconut oil, and vegetable and fruit juices, ensuring that products retain valuable nutrients, enzymes, and the natural taste and aroma important to consumers. It is worth noting that although Cold Press Extraction is not used for the isolation of individual bioactive compounds, products obtained using this method can be rich in diverse nutrients and bioactive components, which provide health benefits [34, 35].

Enzyme Assisted Extraction (EAE) is a technique based on the use of specific hydrolytic enzymes (peptidases, proteinases, glycosidases) capable of breaking down high molecular weight compounds located in the plant cell wall, including glycoproteins and polysaccharides. The presence of these compounds hinders the penetration of the solvent into the plant cells and thus the extraction of bioactive compounds. Therefore, the addition of appropriate hydrolytic enzymes in the EAE method results in the weakening of the cell wall structure, consequently facilitating the release of intracellular active substances into the solvent. EAE extraction is usually conducted in the same manner as conventional methods, with the difference being the addition of the enzyme to the extractant. In addition to the enzyme specific to the plant species and substance, it is also necessary to select the appropriate temperature, pH, and reaction time. EAE is a more selective and efficient technique, generating fewer impurities and being less time-consuming compared to classical extraction methods. Furthermore, the EAE technique is characterized by lower energy consumption compared to ultrasound and microwave-assisted extraction. The main drawback of this method is the difficulty in selecting appropriate extraction conditions. However, due to its numerous advantages, EAE is becoming increasingly popular in the extraction of bioactive substances from plants, including polysaccharides, polyphenols, and other antioxidants [36-39].

**Conclusions:** These modern extraction methods provide efficient and environmentally friendly ways of extracting bioactive compounds from plant materials, contributing to

the further development of the pharmaceutical, cosmetic, and dietary supplement industries. In Poland, there are long-standing traditions of producing bioactive compounds from plants and herbs. On an industrial scale, solvent extraction and steam distillation are mainly used for isolation. However, these methods have disadvantages such as low efficiency, presence of toxic solvent residues in the extract, and formation of undesired compounds under prolonged exposure to high temperatures. Therefore, there is a need to search for alternative and innovative extraction methods. One of the simplest ways to intensify extraction was to use organic solvents and their mixtures instead of water. Assisting with ultrasonic and microwave waves improves the efficiency of the process compared to traditional extraction techniques. Additionally, energy consumption is lower than in "hot" extraction, and the concentration of substances in the extract increases, with new bioactive components appearing. This demonstrates the high usefulness of applying innovative techniques in extraction processes.

**References:**

1. R. Martins, A. Barbosa, B. Advinha, R. Pontes, J. Nunes, Processes, 11 (2023) 2255.
2. C. Picot-Allain, M.F. Mahomoodally, G. Ak, G. Zengin, Current Opinion in Food Science, 40 (2021) 144.
3. I. Majid, S. Khan, A. Aladel, A.H. Dar, M. Adnan, M.I. Khan, A. Mahgoub Awadelkareem, S.A. Ashraf, S.A. CyTA-Journal of Food, 21 (2023) 101.
4. M. Herrero, M. Castro-Puyana, J.A. Mendiola, E. Ibañez, Trends in Analytical Chemistry, 43 (2013) 67.
5. M. Herrero, A.P. Sánchez-Camargo, A. Cifuentes, E. Ibáñez, Trends in Analytical Chemistry, 71 (2015) 26.
6. A.T. Quitain, T. KaI, M. Sasaki, M. Goto, Journal of Agricultural and Food Chemistry, 61 (2013) 5792.
7. P. Stepnowski, E. Synak, B. Szafranek, Z. Kaczyński, Separation Techniques, University of Gdańsk Publishing, Gdańsk, 2010.
8. W. Szczepaniak, Instrumental Methods in Chemical Analysis, PWN Scientific Publishing, Warsaw, 2010.
9. J. Hu, Z. Guo, M. Glasius, K. Kristensen, L. Xiao, X. Xu, Journal of Chromatography A, 1218 (2011) 5765.
10. C. Liu, Y. Cui, F. Pi, Y. Cheng, Y. Guo, H. Qian, Molecules, 24 (2019) 1554.
11. M. Ivanović, M. Islamčević Razboršek, M. Kolar, Plants, 9 (2020) 1428.
12. L. Ge, S.P. Li, G. Lisak, Journal Of Pharmaceutical And Biomedical Analysis, 2 (2020) 179.
13. O. Wrona, K. Rafińska, C. Możeńska, B. Buszewski, Journal of AOAC International, 100 (2017) 1624.
14. A.A. Marzlan, B.J. Muhialdin, N.H. Zainal Abedin, N.K. Mohammed, M.M.T. Abadl, B.H. Mohd Roby, A.S. Meor Hussin, Industrial Crops and Products, 154 (2020) 112581.
15. T. Abou Elmaaty, K. Sayed-Ahmed, M. Magdi, Scientific Reports, 13 (2023) 1.
16. M. Ashokkumar, Ultrasonics Sonochemistry, 25 (2015) 17.
17. J. Dai, V. Orsat, G.S.V. Raghavan, V. Yaylayan, Journal of Food Engineering, 96 (2010) 540.
18. M. Hanula, J. Wyrwisz, M. Moczkowska, O.K. Horbańczuk, E. Pogorzelska-Nowicka, A. Wierzbicka, Applied Sciences, 10 (2020) 8325.
19. J.C. Li, Z.J. Zhang, D. Liu, M.Y. Jiang, R.T. Li, H.M. Li, Natural Product Research, 36 (2022) 1781.
20. X. Song, C. Liu, Y. Zhang, X. Xiao, G. Han, K. Sun, Y. Li, Ultrasonics Sonochemistry, 94 (2023) 106344.
21. M. Saifullah, R. McCullum, A. McCluskey, Q. Vuong, Heliyon, 6 (2020) 3666.
22. E. Bouloumpasi, A. Skendi, S. Christaki, C.G. Biliaderis, M. Irakli, Industrial Crops and Products, 207 (2024) 117770.
23. J. Suomi, H. Sirén, K. Hartonen, M.L. Riekkola, Journal of Chromatography A, 868 (2000) 73.
24. M.A. Farajzadeh, M. Ghorbani, M. Yousefi, M. Palma, Trends in Food Science and Technology, 110 (2021) 70.
25. F. Chemat, M. Abert-Vian, F. Visinoni, Microwave hydrodiffusion for isolation of natural products, European Patent, 2008, 749.
26. Z. Li, H. Wang, J.Y. Wan, C. Wang, Critical Reviews in Food Science and Nutrition, 60 (2020) 119.
27. M.F. Barroso, A. Alcázar, I. Hermosín-Gutiérrez, Royal Society of Chemistry, 24 (2021) 191.
28. L. Bandici, A.C. Teusdea, V.D. Soproni, F.I. Hathazi, M.N. Arion, C.O. Molnar, S.I. Vicas, Materials, 15 (2022) 7789.
29. S. Youn-Yuen, K. Ming. Microchemical Journal, 74 (2003) 131.
30. A. Elik, D. Koçak, F. Göğüş, LWT-Food Science and Technology, 123 (2020) 109100.
31. E. Espada-Bellido, M. Ferreiro-González, C. Carrera, M. Palma, J.A. Álvarez, F. Barbero, G. Ayuso, Journal of Agronomy, 9 (2019) 745.

32. W.S. Pawar, S. Sugreev, P. Gangakhedkar, Indian Food Industry Mag, 4 (2023) 63.
33. A. Kabutey, D. Herák, C. Mizera, Foods, 12 (2023) 3636.
34. N. Rombaut, R. Savoire, B. Thomasset, J. Castello, Industrial Crops and Products, 63 (2015) 26.
35. E. Ramesh, A.A. Alshatwi, Food and Chemical Toxicology, 51 (2013) 97.
36. J. Azmir, I.S.M. Zaidul, M.M. Rahman, K.M. Sharif, A. Mohamed, F. Sahena, M.H.A. Jahurul, K. Ghafoor, N.A.N. Norulaini, A.K.M. Omar, Journal of Food Engineering, 117 (2013) 426.
37. T. Wang, R. Jónsdóttir, H.G. Kristinsson, G.O. Hreggvidsson, J.O. Jónsson, G. Thorkelsson, G. Ólafsdóttir, Food Science and Technology, 43 (2021) 451.
38. Li S., Zhang H., Han D., Row K.H., Korean Journal of Chemical Engineering, 29 (2012) 650.
39. K. Rafińska, O. Wrona, A. Krakowska-Sieprawska, J. Walczak-Skierska, A. Kiełbasa, Z. Rafiński, P. Pomastowski, M. Kolankowski, B. Buszewski, Industrial Crops and Products, 187 (2022) 115424.

# STATISTICAL ANALYSIS OF FLUORESCENCE SPECTRA IN APPLICATION TO VEGETABLE OIL IDENTIFICATION

**P. MUSZYŃSKI, J. MATYSIAK**, University of Life Sciences in Lublin, Faculty of Food Sciences and Biotechnology, Department of Chemistry, 15 Akademicka St. 20-950 Lublin, Poland.

**Abstract:** The paper presents an example of the use of statistical methods to interpret the results of measurements obtained using the fluorescence technique. Visually, fragments of the spectrum that were characterized by the greatest variability were selected. The wavelengths that most differentiated the tested samples were selected as characteristic distinguishing features of the tested oils. The highlighted parts of the spectra were then statistically analyzed to find differences in the spectral data that allowed the test samples to be distinguished. Chemometric methods of learning with and without supervision were used to process the data.

**Introduction:** Fluorescence in combination with statistical methods is used, among other things, to control the quality and authenticity of food products. Vegetable oil studies use excitation and emission spectra, total fluorescence spectra and synchronous fluorescence spectra. Synchronous spectra are obtained by conducting fluorescence measurements while maintaining a certain difference between simultaneously varying excitation and emission wavelengths ($\Delta\lambda$). Compared to emission spectra and excitation spectra, synchronous spectra have greater sensitivity and selectivity. Typically, synchronous spectra are recorded at a fixed value of $\Delta\lambda$, chosen empirically. The components of vegetable oils with absorption and emission properties are tocopherols, chlorophylls and phenolic compounds. Measurement of fluorescence provides information about certain characteristics of the tested oil samples, which can be analyzed by chemometric (exploratory and discriminatory) methods. Of the pre-selected variables for building a chemometric model, the most optimal for its predictive or classification ability is used. The dependent variable in the models is usually the addition of an inferior oil and the independent variables the entire range or part of the fluorescence spectrum [1-5].

**Experimental:** The test material was commercially available edible oils: extra virgin olive oil (OEV) and refined rapeseed oil (ORR). 1% (V/V) solutions of the tested vegetable oils in n-hexane and model oil mixtures were prepared in proportions (% of ORR oil added):

10% - mixture OEV90+ORR10
20% - mixture OEV80+ORR20
30% - mixture OEV70+ORR30
40% - mixture OEV60+ORR40
50% - mixture OEV50+ORR50.

Measurements were carried out in a quartz cuvette (1 cm) using a Cary Eclipse spectrophotometer (Varian). Emission and synchronous spectra were recorded for each of the tested solutions in the wavelength range 270-700 nm, with a constant wavelength

difference (Δλ) between excitation and emission equal to 10, 30 and 60 nm (measure 3 times). The spectra of pure oils were compared with those of extra virgin olive oil with the addition of refined rapeseed oil. The fluorescence intensity at the wavelengths most differentiating the spectra of the tested samples was read for each (Δλ).

**Results:** The spectra shown in Figs.1 and 2 are characteristic of oil samples and their mixtures. The differences are due to the specific chemical composition of the samples studied. Three bands are evident in the OEV spectrum obtained at Δλ = 10 (Fig.1): the first with a maximum at 303 nm (originating from compounds in the tocopherol group); the second occurring in the 340-480 nm wavelength range (attributed to compounds that have not been identified) and the third with a max at λ = 666 nm (associated with the presence of chlorophylls and their degradation products, such as pheophytins [5]). As Δλ increases, the short-wave and long-wave bands shift toward shorter wavelengths, while the band in the wavelength range (340-480 nm) disappears. The short-wave band at Δλ = 30 and 60 nm is broadened. It is also observed that the intensity of this band increases when Δλ = 30 and 60 compared to the intensity for Δλ = 10. On the other hand, the long-wave band with increasing Δλ shows significantly lower intensity and at high Δλ values (60) splits into two weak bands.

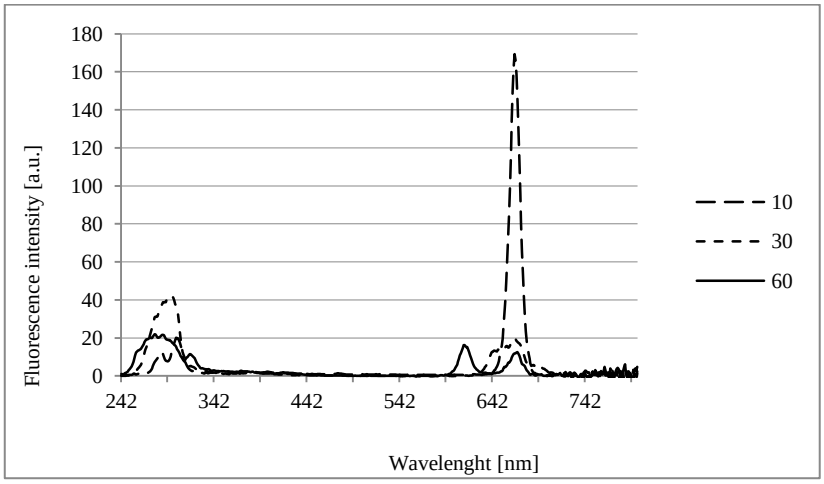



**Fig.1.** Synchronic fluorescence spectra of extra virgin olive oil (OEV) for different values of the parameter Δλ.

Figure 2 shows a comparison of the synchronous fluorescence spectra of OEV and ORR at Δλ = 10 nm. The ORR spectrum shows a band with a maximum at λ = 303 nm. Compared to the OEV spectrum, there is no band with a maximum at λ = 666 nm in the ORR spectrum. This band comes from chlorophyll pigments, the content of which in the oil depends, among other things, on its type and how it is obtained. During the production of refined oils, chlorophylls are removed and therefore no chlorophyll band was noted in the spectrum of the ORR studied.

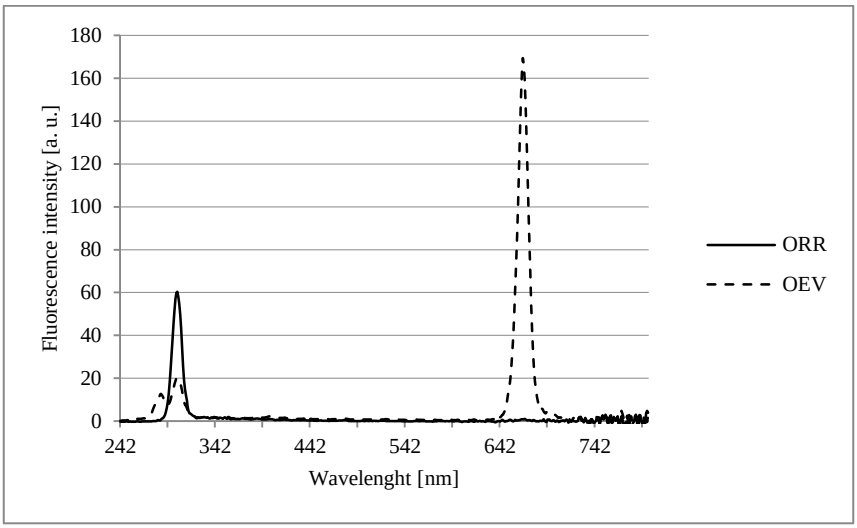



**Fig.2.** Synchronic fluorescence spectra for extra virgin olive oil (OEV) and refined rapeseed oil (ORR) at $\Delta\lambda$ = 10 nm.

The comparison presented here makes it possible to point out the most characteristic differences: the non-uniform intensity of the short-wave band for ORR and OEV, and the presence of a long-wave band in the case of OEV.
In further analysis, the wavelengths for which differences in fluorescence intensity were greatest were: 295, 303, 387 and 666 nm.

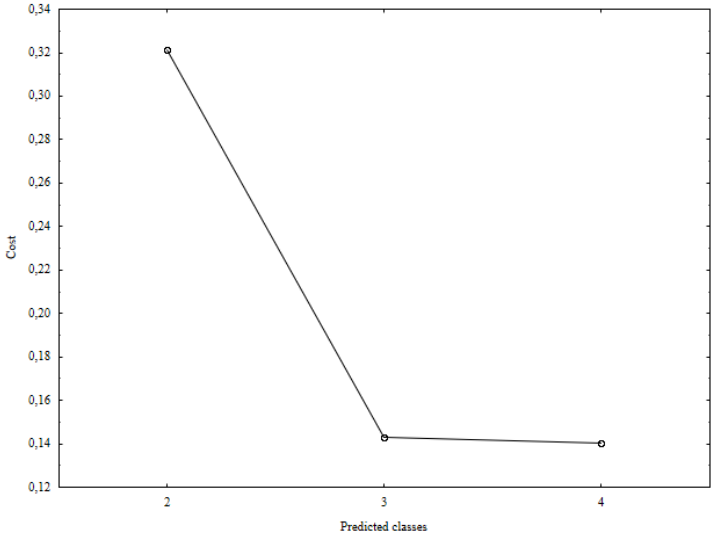



**Fig.3.** Cost sequence (Cluster analysis, k-means method).

**Table 1.** Averages of variables in classes obtained by the k-means method.

| Class | Fluorescence intensity at the following wavelengths | | | | Number of samples N | Percent [%] |
|---|---|---|---|---|---|---|
| | 295 [nm] | 303 [nm] | 387 [nm] | 666 [nm] | | |
| 1 | 51.3 | 140.8 | 23.7 | 2.8 | 11 | 40.7 |
| 2 | 55.5 | 103.0 | 35.7 | 231.1 | 5 | 18.5 |
| 3 | 24.8 | 52.8 | 23.5 | 322.1 | 11 | 40.7 |

At the outset of the statistical analysis, the number of clusters was estimated using the k-means method. Euclidean distance was chosen as the measure of distance between the studied objects. The division of the studied samples was performed using a v-fold cross-check. Analyzing the cost sequence graph (Fig.3), it can be seen that increasing the number of clusters from two to three increases the precision of partitioning. In contrast, increasing the number of clusters to four does not improve the quality of partitioning. Therefore, a structure consisting of three clusters with the following counts was considered the best: cluster 1 (count 11), cluster 2 (count 5), cluster 3 (count 11) (Table 1). Table 1 contains the average values of the variables on the basis of which characterization of each cluster can be carried out. Cluster 1 includes oils with the highest fluorescence intensity at 303 nm and at the same time showing the lowest fluorescence intensity at 666 nm. Oils belonging to clusters 1 and 2 are similar in fluorescence intensity at 295 nm. In contrast, they differ in fluorescence intensity at the other wavelengths. Cluster 3 includes oils with the highest fluorescence intensity at 666 nm. In contrast, the fluorescence intensity at 295, 303 and 397 nm is lower for this group compared to clusters 1 and 2. The analysis of p-values in the analysis of variance table (Table 2) shows that all variables were statistically significant ($p < 0.05$) in the classification process. The variables 666 and 303 differentiated the clusters to the greatest extent (the largest F-statistic values).

**Table 2.** Analysis of variance (ANOVA).

| Wavelenght [nm] | Between groups SS | df | Within the groups SS | df | F statistics | p-value |
|---|---|---|---|---|---|---|
| 295 | 5102.104 | 2 | 271.577 | 24 | 225.443 | 0.000 |
| 303 | 42754.801 | 2 | 1103.875 | 24 | 464.779 | 0.000 |
| 387 | 598.858 | 2 | 88.605 | 24 | 81.105 | 0.000 |
| 666 | 580212.762 | 2 | 4947.401 | 24 | 1407.315 | 0.000 |

From the data in Tables 3 and 4, it can be seen that not all variables met the assumptions of using analysis of variance (lack of normality of distribution of variable 387 in the OEV group; lack of homogeneity of variance for all variables). To verify the ANOVA results, an analysis of variance was performed using the Kruskal-Wallis rank method (Table 5). The results obtained by the rank method confirm the conclusions of the ANOVA analysis.

**Table 3.** Shapiro-Wilk test results (normality of distribution).

| Wavelenght [nm] | Typ of oil | Number of samples N | W statistics | p-value |
|---|---|---|---|---|
| 295 | OEV | 11 | 0.967 | 0.856 |
| 303 | OEV | 11 | 0.913 | 0.265 |
| 387 | OEV | 11 | 0.809 | 0.013 |
| 666 | OEV | 11 | 0.926 | 0.372 |
| 295 | ORR | 11 | 0.891 | 0.144 |
| 303 | ORR | 11 | 0.917 | 0.297 |
| 387 | ORR | 11 | 0.953 | 0.688 |
| 666 | ORR | 11 | 0.954 | 0.690 |
| 295 | mixture | 5 | 0.943 | 0.688 |
| 303 | mixture | 5 | 0.908 | 0.455 |
| 387 | mixture | 5 | 0.828 | 0.134 |
| 666 | mixture | 5 | 0.933 | 0.616 |

**Table 4.** Results of the homogeneity of variance test.

| Wavelenght [nm] | SS effect (Sum of square) | df effect (Degree of freedom) | MS effect (Mean square) | SS error | df error | MS error | F statistics | p-value |
|---|---|---|---|---|---|---|---|---|
| 295 | 29.129 | 2 | 14.565 | 89.929 | 24 | 3.747 | 3.887 | 0.034 |
| 303 | 307.390 | 2 | 153.695 | 307.416 | 24 | 12.809 | 11.999 | 0.000 |
| 387 | 13.710 | 2 | 6.855 | 43.619 | 24 | 1.817 | 3.772 | 0.038 |
| 666 | 2342.696 | 2 | 1171.348 | 1708.943 | 24 | 71.206 | 16.450 | 0.000 |

**Table 5.** Kruskal-Wallis test results.

| Wavelenght [nm] | Class | Number of samples N | Sum of ranks | Mean of ranks |
|---|---|---|---|---|
| Independent (grouping) variable: Resultant classification Kruskal-Wallis test: H (2, N = 27) = 19.705 p = 0.000 | | | | |
| 295 | 1 | 11 | 201.000 | 18.273 |
| | 2 | 5 | 111.000 | 22.200 |
| | 3 | 11 | 66.000 | 6.000 |
| Independent (grouping) variable: Resultant classification Kruskal-Wallis test: H (2, N = 27) = 22.356 p = 0.000 | | | | |
| 303 | 1 | 11 | 242.000 | 22.000 |
| | 2 | 5 | 70.000 | 14.000 |
| | 3 | 11 | 66.000 | 6.000 |
| Independent (grouping) variable: Resultant classification Kruskal-Wallis test: H (2, N = 27) = 11.911 p = 0.026 | | | | |
| 387 | 1 | 11 | 120.500 | 10.955 |
| | 2 | 5 | 125.000 | 25.000 |
| | 3 | 11 | 132.500 | 12.045 |
| Independent (grouping) variable: Resultant classification Kruskal-Wallis test: H (2, N = 27) = 22.349 p = 0.000 | | | | |
| 666 | 1 | 11 | 66.000 | 6.000 |
| | 2 | 5 | 70.000 | 14.000 |
| | 3 | 11 | 242.000 | 22.000 |

In a further stage of the analysis, a model of classification trees was built, taking into account the variables 295, 303, 387 and 666. In the setting, a priori probabilities proportional to the size of the classes were chosen and misclassification costs were equal for each class. The results of the analysis including all variables are shown in Fig. 4 and Tab. 6. The resulting tree contains divisions based on the variable 303 and 666. The generated rule is as follows: if the fluorescence intensity at 303 nm is less <= 70.75 then the test sample is an OEV sample. On the other hand, if the fluorescence intensity at 303 nm is greater > 70.75 and at the same time at 666 nm is less <= 91.7 then the test sample is ORR oil. If both criteria of this rule are not met then the sample is a mixture of these oils. The classification tree model 100% accurately predicts the cases belonging to the groups of oils and mixtures (Table 6).

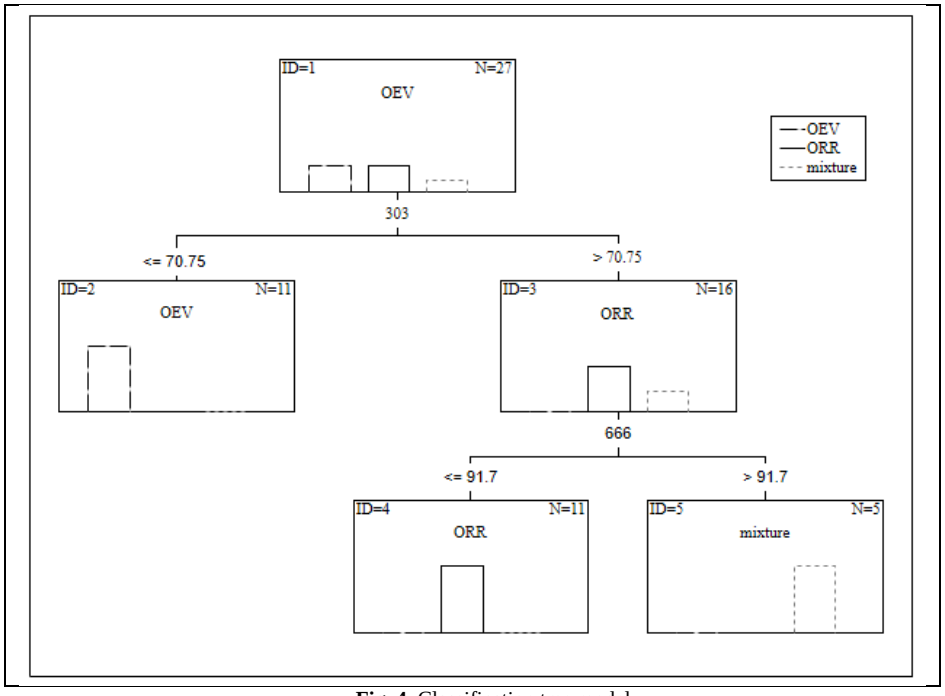



**Fig. 4.** Classification tree model.

**Table 6.** Classification matrix.

| | Observed OEV | Observed ORR | Observed mixture |
|---|---|---|---|
| Predicted OEV | 11 | | |
| Predicted ORR | | 11 | |
| Predicted mixture | | | 5 |

A classification model was also built using discriminant analysis. The grouping variable in the analysis was oil type and the independent variables were fluorescence intensities at wavelengths: 295, 303, 387 and 666 nm. The analysis resulted in two discriminant functions (elements) (Table 7). The low values of the Lambda Wilks test statistic and the p-value indicate that both functions are statistically significant. The first function explains > 90% of the intergroup variance and therefore has the largest contribution to discriminating groups (Table 8). Of the four variables, only three (295, 303 and 666) made a statistically significant contribution to distinguishing between the oil groups studied ($p < 0.05$) (Table 9). The classification model created using discriminant analysis correctly classified 100% of the cases (Table 10).

**Table 7.** Chi-kwadrat test results (Linear discriminant analysis).

| Elements removed | Eigenvalue | Canonical R | Lambda Wilksa | chi-kwadrat | df | p-value |
|---|---|---|---|---|---|---|
| 0 | 166.243 | 0.997 | 0.000 | 185.611 | 6 | 0.000 |
| 1 | 18.117 | 0.973 | 0.052 | 67.863 | 2 | 0,000 |

**Table 8.** Raw coefficients for canonical variables.

| Variable | Element 1 | Element 2 |
|---|---|---|
| 295 | 0.159 | -0.219 |
| 387 | -0.060 | -0.444 |
| 666 | -0.071 | -0.016 |
| Constant | 7.385 | 23.307 |
| Eigenvalue | 166.243 | 18.117 |
| Cumulative proportion | 0.902 | 1.000 |

**Table 9.** Linear discriminant analysis results.

| N = 27 | Lambda Wilksa | Partial Wilks' | F removal (2, 22) | p-value | Tolerance | 1-Tolerance |
|---|---|---|---|---|---|---|
| 295 | 0.001 | 0.298 | 25.937 | 0.000 | 0.880 | 0.120 |
| 387 | 0.001 | 0.363 | 19.287 | 0.000 | 0.904 | 0.096 |
| 666 | 0.008 | 0.041 | 254.572 | 0.000 | 0.890 | 0.110 |

**Table 10.** Classification matrix (Linear discriminant analysis).

| Class | Percent Correct | OEV p = 0.407 | ORR p = 0.407 | mixture p = 0.185 |
|---|---|---|---|---|
| OEV | 100 | 11 | 0 | 0 |
| ORR | 100 | 0 | 11 | 0 |
| mixture | 100 | 0 | 0 | 5 |
| Total | 100 | 11 | 11 | 5 |

**Conclusions:** Classification models created with selected independent variables did not differ in classification quality. These models correctly classified 100% of the tested samples.

## References:

1. K.I. Poulli, G.A. Mousdis, C.A. Georgiou, Food Chemistry, 105 (2007) 369.
2. A. Dankowska, M. Małecka, European Journal of Lipid Science and Technology, 111 (2009) 1233.
3. A. Dankowska, M. Małecka, W. Kowalewski, Żywność. Nauka.Technologia. Jakość, 2/87 (2013) 106.
4. A. Dankowska, M. Małecka, W. Kowalewski, Grasasy aceites, 64/4 (2013) 425.
5. E. Sikorska, Metody fluorescencyjne w badaniach żywności. Wyd. Akademii Ekonomicznej w Poznaniu, 2008.

# SYNTHESIS AND STUDY OF SELECTED PROPERTIES OF THE HYDROXYAPATITE/$TiO_2$ COMPOSITE

**E. SKWAREK[1], K. MISIOŁEK[1], P. SKWAREK[2],** [1]Maria Curie-Sklodowska University, Faculty of Chemistry, Institute of Chemical Sciences, Department of Radiochemistry and Environmental Chemistry, M. Curie-Sklodowska Sq. 3, 20-031 Lublin, Poland, [2]Medical University of Karol Marcinkowski, Faculty of Medicine, Bukowska 70 St., 60-812 Poznań, Poland.

**Abstract:** A composite of hydroxyapatite and anatase was obtained. The crystallographic structure was determined by X-ray diffraction. Then the particle sizes were tested. From the results obtained, it was found that the composite has a larger particle size than pure anatase. In the last stage of the research, the dependence of the zeta potential on pH and the $pH_{IEP}$ value were measured.

**Introduction:** Hydroxyapatite (HAP) nanocomposite with titanium(IV) oxide can be used as an electrochemical sensor in the quantitative determination of specific biomarkers para-aminohippuric acid (PAH) and uric acid (UA). One of the best-known sources of many biomarkers is human urine, which can become a quick, non-invasive, inexpensive and effective diagnostic tool for various human diseases. Para-aminohippuric acid (PAH), a derivative of urinary hippuric acid, is used as a biomarker in the diagnosis of renal disorders. PAH tests determine the ability of the kidneys to combine benzoic acid with PAH by determining whether the PAH is excreted in urine or blood serum [1]. After ingestion, benzoic acid is biotransformed to hippuric acid and is excreted in urine [2]. Moreover, hippuric acid synthesis takes place in the liver and is removed by the kidneys [3]. The average amount of PAH in healthy people is approximately 1.24–1.83 mM in urine; in disease states, the amount of PAH either increases or decreases, depending on the functioning of the organ [4]. So, kidney function and liver disease can be diagnosed by measuring the amount of PHA excreted in urine after saturation with benzoic acid. Moreover, PHA is also a frequently used biomarker in biological monitoring of occupational exposure to toluene [5]. Conventional methods such as high-performance liquid chromatography [6], mass spectroscopy [7], UV-Vis spectroscopy [8] and capillary electrophoresis [9] have been used to detect PHA. Guan et al. 2005 [10] described the determination of uric acid and para-aminopuric acid in human saliva and urine by capillary electrophoresis with electrochemical detection in a buffer with pH 9.2. An equally important biomarker in human urine is uric acid (UA), which is one of the end products of purine metabolism. It indicates several diseases such as hyperuricemia, gout, leukemia, pneumonia and Lesch-Nyhan syndrome. UA concentration varies depending on individual health status and during hypouricemia or hyperuricemia [11]. The typical range of UA in plasma or blood serum is 100-400, and in urine 1.4-4.1 mM [13]. Z.Wang et al. [12] reported a stabilized multi-wall carbon nanotube sensor with gold clusters for uric acid detection with the lowest detection limit of 40 nM in the moderate detectable range of 0.1-300 mM. Therefore, both PAH and UA were detected by the electrochemical method, which has several advantages such as immediate response, high sensitivity, selectivity, and

repeatability. Moreover, the selection of an appropriate electrode material increases the electrocatalytic activity and performance of the sensor, as demonstrated in the case of uric acid [14].

**Experimental:** To synthesize hydroxyapatite and its composite with anatase, the following reagents were used: calcium hydroxide $Ca(OH)_2$ from Aldrich, hydrated calcium hydrogen phosphate $CaHPO_4 \cdot 2H_2O$ from Fluka, 80% acetic acid from POCh Gliwice, titanium oxide - anatase (from Sigma Aldrich). The synthesis was carried out using the wet method. The pH value and reaction temperature were selected so that the resulting hydroxyapatite had appropriate dispersity and grain size. After obtaining the composite, it was washed with redistilled water and then centrifuged to remove impurities from the obtained syntheses. Washing was carried out until a constant value of water conductivity over the adsorbents was obtained. The precipitate was then dried. XRD diffraction studies were carried out using an Empyrean X-ray diffractometer by PANalytical, manufactured in 2012. This diffractometer enables phase analyzes and structural tests of powder samples in standard measurement geometries. Particle size and zeta potential measurements were performed using the Zetasizer Nano-ZS90 device from Malvern, and the calculations were performed using appropriate software devices. During ζ-potential measurements, the following solution was used: 0.001 mol/dm$^3$ $NaNO_3$ solution.

**Results:** The identified reflections on powder diffractograms reveal two phases: anatase and hydroxyapatite. The powder diffractogram of the $TiO_2$/HAP and HAP samples showed an intense and sharp peak at approximately 30°, indicating the preferential stacking of hexagonal prismatic hydroxyapatite nanocrystals. Additionally, peaks from anatase and hydroxyapatite could overlap at a given temperature, causing an increase in peak intensity. The presented powder diffraction patterns showed slightly wider diffraction lines, which indicated very small crystallites with appropriate order. Based on the phase composition content, a phase ratio of 1:1 was achieved in the $TiO_2$/HAP sample. The composite sample is proof that HAP covers $TiO_2$ evenly during the synthesis process, so the phases were evenly distributed. Hydroxyapatite itself has small crystallite size values, indicating nanoparticles. Microstructural parameters showed that the synthesis procedure led to crystal growth, partial ordering and lack of uniformly distributed volume of the initial phases. The presence of hydroxyapatite in the synthesis results in the formation of less crystalline forms, which has a positive significance for some applications of these biomaterials. The values of the grain diameters of the tested substances, i.e.: $TiO_2$ (anatase) 79 nm, composite of hydroxyapatite with $TiO_2$ (anatase) 236 nm. The obtained results show that we mainly have agglomerates that can be crushed using, for example, ball milling. The resulting composites have a larger grain size than their starting component anatase. These data (Figs.1-3) indicate that aggregation occurs when hydroxyapatite is deposited on titanium oxide samples.

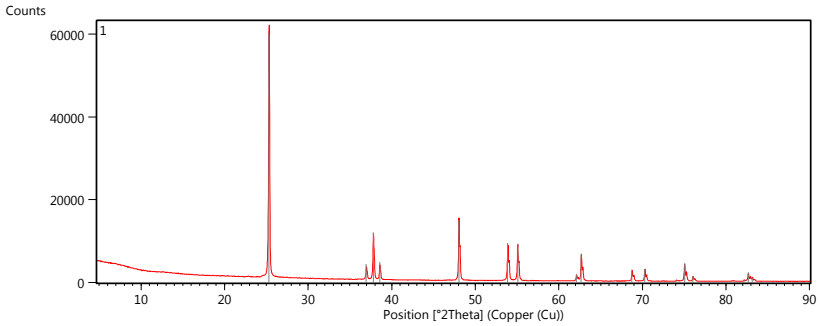



**Fig.1.** Difractogram $TiO_2$ –anataz.

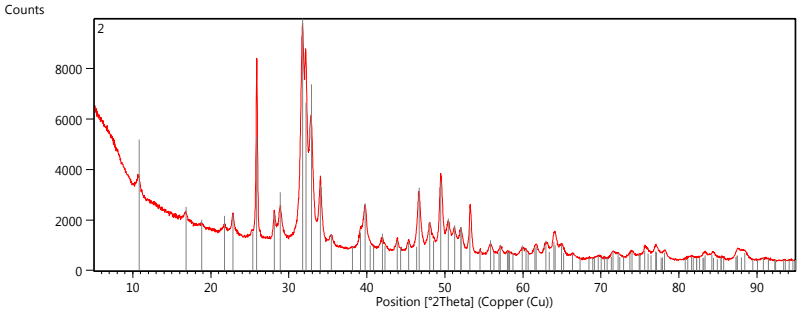



**Fig.2.** Difractogram HAP.

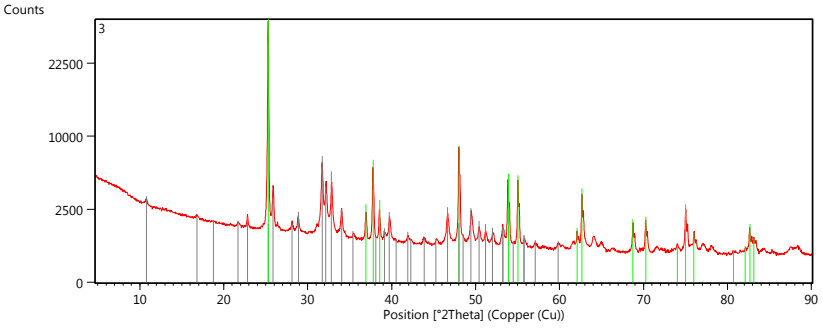



**Fig.3.** Composite diffractogram: HAP/ ($TiO_2$ – anataz).

One of the basic experimental parameters describing the solid/solution phase boundaries is the zeta potential, most often calculated from the electrophoretic mobility. The concentration of potential-forming ions ($H^+$) at which the zeta potential is zero is called the isoelectric point ($pH_{IEP}$). It assumes that the potential of the diffusion layer is equal to the zeta potential, at the $pH_{IEP}$ point the surface concentration of positively charged groups is equal to the concentration of surface negatively charged groups. The magnitude of the zeta potential describes the mutual interactions of electrons at the phase

boundary in dispersive systems. Knowing the value of the zeta potential, you can determine the causes of flocculation and aggregation of particles in a given colloidal system, thanks to which you can, for example, improve the stability of a given colloidal system, which can then be used for applications, e.g. in cosmetics. Based on the results, we can conclude that the obtained composite and titanium oxide have $pH_{IEP}$ values less than 2. This may be due to the pH of the synthesis environment and acidic impurities of the reagents used for individual reactions, as well as impurities that were not thoroughly washed from the obtained composites. Specific ion adsorption may also occur at the tested phase boundaries. In the case of a basic electrolyte, such a situation may occur for porous systems characterized by surface energetic heterogeneity. The tested samples belong to porous systems, so there is a possibility that for these adsorbent/electrolyte interfaces, double layers from individual pore walls may overlap, the pores may be 'clogged' during electrophoresis and the properties of this part of the solid surface will not be revealed in this phenomenon. Due to the fact that a significant part of the charge can be compensated inside the pores of the particle, and only the part that comes from the groups ionized on the sample surface is responsible for the electrophoretic mobility. Dependences of the zeta potential on pH for anatase and its composite with hydroxyapatite in Table 1.

**Table 1.** Dependence of zeta potential on pH.

| Anataz | | | | | |
|---|---|---|---|---|---|
| pH | 2 | 5 | 7 | 9 | 11 |
| ζ [mV] | -25 | -30 | -35 | -30 | -33 |
| Anataz/HAP | | | | | |
| ζ [mV] | -12 | -40 | -45 | -40 | -35 |

During the experiment, the influence of the type of adsorbent on the stability of the dispersion of the composite of titanium oxides and hydroxyapatite was noticed. It was noticed that at pH values <3 the dispersion sedimented quickly. In the further pH range, it is stable, the composite of hydroxyapatite and anatase was more stable. In the case of composites, it can be noticed that with increasing pH, the zeta potential drops to pH = 7 and then increases slightly, but the system remains colloidally stable.

**Conclusions:** A composite was synthesized using the thermal method: hydroxyapatite with anatase. The crystallographic structure was determined by X-ray diffraction, and after comparison with the database, it was found that fine-crystalline forms of adsorbents were formed. The particle sizes of each sample were then examined. The obtained results show that the composites are much larger in size than the oxide varieties themselves, which results from the formation of agglomerates. In the last stage of the research, the dependence of the zeta potential on pH and the $pH_{IEP}$ value were measured, which was less than 2 for all tested systems. At pH values <3 for the tested solid/electrolyte interface, the dispersion quickly undergoes the sedimentation process. In the further pH range, it is stable, the composite of hydroxyapatite and anatase was more stable than that of hydroxyapatite and rutile.

## References:

1. V. Jokanovič, D. Izvonar, M.D. Dramićanin, B. Jokanovič, V. Živginović, D. Marković, B. Dačic Journal of Materials Science: Materials in Medicine, 17 (2006) 539.

2. H.J. Lees, J.R. Swann, I.D. Wilson, J.K. Nicholson, E. Holmes, Journal of Proteome Research, 12 (2013) 1527.
3. S. Baba, K. Akira, H. Suzuki, M. Imachi, Biological and Pharmaceutical Bulletin, 18 (1995) 643.
4. T.B. Vree, Y.A. Hekster, P.G. Anderson, Annals of Pharmacotherapy, 26 (1992) 1421.
5. K. Oginawati, A.A.H. Anka, S.H. Susetyo, S.A. Febriana, I. Tanziha, C.R. S. Prakoeswa, Heliyon, 7 (2021) 8.
6. P.Y. Han, P.N. Shaw, C.M.J. Kirkpatrick, Journal of Chromatography B, 877 (2009) 3215.
7. D. Farthing, D.A. Sica, I. Fakhry, T. Larus, S. Ghosh, C. Farthing, M. Vranian, T. Gehr, Journal of Chromatography B, 826 (2005) 267.
8. M. Kiguchi, J.I. Sudo, The Journal of Toxicological Sciences, 12 (1987) 301.
9. Y. Guan, T. Wu, J. Ye, Journal of Chromatography B, 821 (2005) 229.
10. C.E. Ekpenyong, N. Daniel, PharmaNutrition, 3 (2) (2015) 29.
11. A. Goçenoglu Sarıkaya, B. Osman, T. Cam, A. Denizli, Sensors Actuators B, 251 (2017) 314.
12. Z. Wang, H. Guo, R. Gui, H. Jin, J. Xia, F. Zhang, Sensors and Actuators B: Chemical 255 (2018) 2069.
13. S. Tajik, Y. Orooji, F. Karimi, Z. Ghazanfari, H. Beitollahi, M. Shokouhimehr, R. S. Varma, H.W. Jang, Measurement: Food, 15 (2021) 4617.
14. Y. Orooji, P.N. Asrami, H. Beitollahi, S. Tajik, M. Alizadeh, S. Salmanpour, M. Baghayeri, J. Rouhi, A.L. Sanati, F. Karimi, Measurement: Food, 15 (2021) 4098.

# CHARACTERIZATION OF SELECTED PROPERTIES OF HYDROXYAPATITE-CHITOSAN COMPOSITES

**E. SKWAREK[1], O. GONCHARUK[2], L. NOSACH[2], P. SKWAREK[3],** [1]Maria Curie-Sklodowska University, Faculty of Chemistry, Institute of Chemical Sciences, Department of Radiochemistry and Environmental Chemistry, M. Curie-Sklodowska Sq. 3, 20-031 Lublin, Poland, [2]Chuiko Institute of Surface Chemistry, NAS of Ukraine, Department of Amorphous and Structurally Ordered Oxides, Gen. Naumov St. 17, 03164 Kyiv, Ukraine, [3]Medical University of Karol Marcinkowski, Faculty of Medicine, Bukowska St. 70, 60-812 Poznań.

**Abstract:** Porous hydroxyapatite (HAP) composite frameworks, HAP/chitosan and HAP/chitosan/alginate, were synthesized by in situ coprecipitation method. Characterization tests were performed using the methods: SEM microscopy, nitrogen adsorption and desorption ASAP method. A very large reduction in the specific surface area compared to pure HAP and an increase in the average pore radius for the tested samples were found due to the presence of chitosan and alginate on the surface. SEM images also confirm the coverage of the specific surface with copolymers. However, the pore diameter increases as the amount of composite ingredients increases.

**Introduction:** Hydroxyapatite is of great importance as a filler for chromatographic columns, an ion exchanger, and a drug carrier. Ceramic materials using hydroxyapatite are considered one of the main materials in bone surgery due to their high degree of biocompatibility and the ability to create chemical bonds with living tissues [1]. The porous material is gradually replaced by the developing bone, thanks to which the regeneration process is similar to that following the implantation of autogenous cancellous bone. At the same time, the implant is eliminated and the bone tissue is mineralized. Hydroxyapatite in bone surgery can be obtained as: a porous material, a component of a composite material, a layer on various types of substrates. A very important property of hydroxyapatite is its surface porosity, which must be greater than 55% in medical applications. Thanks to the presence of open pores in the material, it is possible to create a natural bond by growing bone and connective tissue into the porous layer. This creates a permanent connection at the implant-bone interface. The mechanical compressive and tensile strength depends exponentially on the total number of pores. Once the total porosity is exceeded, the mechanical strength is drastically reduced. Chitosan is being investigated as a useful biomaterial with various applications in tissue engineering due to its low cost, high availability, antimicrobial activity, and biocompatibility. Contrary to the common belief that it is a biocompatible tissue material, chitosan is weak and unstable and unable to maintain its shape during transplantation due to swelling. Research on combining chitosan with other polymers is common, aiming to improve its mechanical and biological properties in a wide range. Alginic acid, as a biocompatible, hydrophilic and biodegradable compound under normal physiological conditions, has been widely used as a gel in bone tissue engineering [2-4]. However, many biopolymers are brittle and do not demonstrate unquestionable biocompatibility, and their mechanical properties do not allow them to be used in

conditions requiring weight. In order to increase bioactivity and mechanical properties, some composites of polymers and bioactive ceramics have been prepared for use in bone tissue engineering. These composites meet the requirements to be used as elements of the skeletal system, teeth or cells of organisms. Among them, polymer and HAP composites attract much attention because such composites may have osteoconductive properties due to the presence of HAP, whose composition and chemical structure are similar to those of the mineral phase of bones and hard tissues. For this reason, HAP-polymer composite frameworks are of interest in the biomedical field, and the preparation of HAP-containing polymer composite frameworks has been reported several times so far. In this study, we undertook the creation of HAP/chitosan and HAP/chitosan/sodium alginate composite frameworks using the in situ co-precipitation method.

**Experimental:** Chitosan (viscosity >200 cP - one percent solution in one percent acetic acid solution in the Brookefield method) from Sigma-Aldrich (St. Louis, USA) is deactylated at the level of 85%. Sodium alginate (viscosity 200-400 cP for a one percent solution at 20$^{o}$C) from Sigma-Aldrich. HAP/chitosan and HAP/chitosan/alginate composite frameworks were synthesized by in situ coprecipitation. An aqueous chitosan solution was prepared by dissolving 3.84 g of chitosan powder in 64 mL of monomolar acetic acid. To prepare the alginate solution, 3.84 g of sodium alginate powder was dissolved in 96 ml of one-molar sodium hydroxide. To obtain HAP, HAP/chitosan, HAP/chitosan/sodium alginate, composite frameworks, $H_3PO_4$ and $Ca(OH)_2$ were successively added to the aqueous chitosan solution. The ratio of chitosan to $H_3PO_4$ and alginate to $Ca(OH)_2$ was adjusted to the final weight ratio of HAP, chitosan and sodium alginate at 10/90 and 30/70. The resulting suspension was continuously stirred in a flask for 1 h. The obtained composites were kept in a freezer at -15 $^{o}$C until freezing. The samples were then freeze-dried for 24 hours at a temperature of -80 $^{o}$C. After a 24-hour immersion in distilled water, the substance was washed three times and then dried. Samples of hydroxyapatite (HAP) and its composites, HAP/chitosan, HAP/chitosan/sodium alginate, were used in the tests. They were obtained using the wet method at the Department of Radiochemistry and Colloid Chemistry. Characterization tests were performed using the following methods: SEM microscopy, nitrogen adsorption and desorption ASAP method.

**Results:** A standard method of low-temperature nitrogen adsorption-desorption was used to determine the parameters of the porous structure of hydroxyapatite. The measurements were carried out using an automatic adsorption analyzer type ASAP 2405 (Accelerated Surface Area and Porosimetry) from Micromeritics Instruments, Co. Measurements of nitrogen adsorption and desorption isotherms were carried out after degassing the samples under reduced pressure (Table 1).
Table 1 shows selected structural parameters of hydroxyapatite and composites: hydroxyapatite/chitosan; hydroxyapatite/chitosan/sodium alginate. We see that the specific surface area of the composites is substantially smaller than that of pure hydroxyapatite and the average pore radius increases due to the complete coverage of the surface with chitosan. Such a large pore size of the composites, approximately 30.41-51.09 nm, constitutes a structure conducive to their use as a biomaterial for cell attachment and the growth of new bone tissue in living organisms.

**Table 1.** Selected structural parameters of hydroxyapatite, hydroxyapatite/chitosan, hydroxyapatite/chitosan/sodium alginate.

| Parameters | HAP | HAP/ chitosan | HAP /chitosan/ sodium alginate |
|---|---|---|---|
| BET surface area [$m^2/g$] | 105 | 8 | 3 |
| Surface area from the Langmuir isotherm [$m^2/g$] | 134 | 12 | 5 |
| BJH adsorption cumulative volume of pores between 1.7 and 300 nm diameter [$cm^3/g$] | 0.54 | 0.008 | 0.004 |
| BJH desorption cumulative volume of pores between 1.7 and 300 nm diameter [$cm^3/g$] | 0.53 | 0.008 | 0.004 |
| Average pore radius from the BET method [nm] | 17.72 | 41.35 | 51.09 |
| Average pore radius from adsorption - BJH method [nm] | 18.08 | 37.39 | 42.27 |
| Average pore radius from desorption – BJH method [nm] | 17.46 | 21.15 | 27.89 |

Figures 1 and 2 show SEM images: HAP/chitosan, HAP/chitosan/sodium alginate. In all cases, a very high degree of coverage of hydroxyapatite with chitosan or sodium alginate can be seen. The pore diameter increased with the increase in the types and amounts of copolymers on the surface.

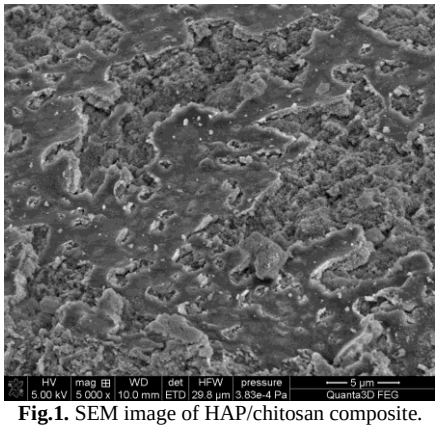



**Fig.1.** SEM image of HAP/chitosan composite.

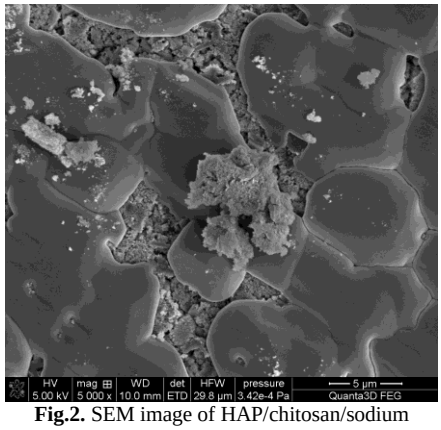



**Fig.2.** SEM image of HAP/chitosan/sodium alginate composite.

The pore structure of the composite frameworks was similar to the chitosan? alginate copolymer complex, and the morphology of the uniform microstructures remained unchanged by the presence of HAP. Despite this, the pore diameter of the composites was larger compared to pure HAP, up to approximately 30%. Ultimately, it is assumed that the pore structure of the composite collapsed in places and seemed to agglomerate.

**Conclusions:** HAP/chitosan, and HAP/chitosan/sodium alginate porous composite frameworks were successfully synthesized by in situ coprecipitation method. Thanks to this, it was proven that composites of hydroxyapatite with sodium alginate and chitosan change the surface structure, due to which they may have application properties in medicine. The research results presented in this work can be summarized as follows: the sample surfaces were characterized by nitrogen adsorption and desorption, a very significant reduction in specific surface area and an increase in the average pore radius for the tested samples were found due to the presence of chitosan and alginate on the surface. Additionally, scanning electron microscopy (SEM) images further confirm the coverage of the specific surface with copolymers.

**Acknowledgements:** This work was supported by the International Visegrad Fund (ID 52300028).

**References:**

1. V. Jokanovič, D. Izvonar, M.D. Dramićanin, B. Jokanovič, V. Živginović, D. Marković, B. Dačic, Journals of Materials Science Materials in Medicine, 17 (2006) 539.
2. Y. Sun, G. Guo, Ceramics International, 32 (2006) 951.
3. X. Yao, S.Tan, D. Jiang, Journals of Materials Science Materials in Medicine, 16 (2005) 161.
4. K. Skartsila, N. Spanos, Journal of Colloid and Interface Science, 308 (2007) 405.

# IODINE CONTRAST AGENTS - FATE AND OCCURRENCE IN THE ENVIRONMENT

**K. WRZESIŃSKA, J. CZERWIŃSKI**, Lublin University of Technology, Faculty of Environmental Engineering, 40B Nadbystrzycka St., 20-618 Lublin, Poland.

**Abstract:** Numerous studies have shown that surface waters contain a plethora of substances used in the diagnosis and treatment of patients. Hospitalized patients urinate along with contrast agents in the hospital. The highest concentrations have been observed on weekdays, when most scheduled tests are performed. An effect on the change in concentration was noted depending on the season. This is due to the reduced temperature of the water, and thus the biodegradation process is hindered.

**Introduction:** The use of iodine in contrast agents is due to its low toxicity and strong absorption of X-rays. All currently used iodine contrast agents are chemical modifications of the 2,4,6-triiodate benzene ring. Benzoic acid is obtained by introducing an acid group at position 1 of the benzene ring, which allows the formation of salts or amides that affect solubility in water. 2,4,6- triiodobenzoic acid is obtained by introducing iodine atoms at positions 2, 4 and 6. Triiodobenzoic acid is less toxic and less lipophilic, due to the introduction of side chains [1,2].

Pharmaceutical products enter the environment primarily from wastewater treatment plants, but also from the use of sewage sludge and from animal feces. Most pharmaceutical compounds are only partially converted by the body, so they are excreted as a mixture of drugs and metabolites into sewage systems. Although wastewater treatment plants can remove pharmaceutical compounds during the treatment process, the effectiveness of such treatment varies depending on the operation of the treatment system and also on the treatment plant itself. The biodegradability of iodine-based contrast agents is estimated to be around 20%. Laboratory treatment of wastewater was carried out, where the test model substance was iopromide. Iopromide undergoes degradation, which results in the iopromide amine is formed. Further degradation of the iopromide metabolite occurred slowly, completely after 23 weeks. It has been demonstrated that the free amine is sensitive to photolysis. It was shown that initially a short-lived intermediate product is formed – the iodide, and in the end photolysis results in a completely deiodinated product [3]. It is difficult to predict what happens in the natural environment, but if the same thing happens as it does in laboratory conditions, the free amine from wastewater, in the upper layers of water undergoes photodegradation to 5-amino-N,N'-bis(2,3-dihydroxypropyl) Nmethylisophthalamide, while in deeper layers by bacterial degradation, namely by cleavage of the side chains, so that they more rapidly subsequently undergo photolysis than the original compound, iopromide. a comparative evaluation results obtained in the laboratory and in the natural environment is difficult for a variety of reasons: by differences in consumption at a given site, unevenly wastewater treatment process, and varying degrees of dilution of surface and groundwater surface and groundwater. Wastewater treatment plants create a barrier against the release of potentially harmful substances into the aquatic environment [4]. As a result of insufficient degradation degradation, chemical compounds can enter

waterways. Another pathway of getting potentially harmful substances into the soil is the use of sewage sludge as fertilizer or for land reclamation. Pharmaceuticals can be eliminated by slow filtration on sand filters, ozonation, techniques based on advanced oxidation and electrochemical oxidation, adsorption on granular activated carbon, and membrane techniques, particularly nanofiltration and reverse osmosis. One of the advanced methods to remove micropollutants from wastewater and water is the process of deep oxidation. The method tapo relies on the generation of reactive radicals, which have the property of oxidizing virtually any organic compound to carbon dioxide, water and inorganic compounds. To obtain the radicals, hydrogen peroxide, ozone, UV radiation, catalyst additives and combinations thereof are used [5]. Many wastewater treatment plants are dominated by traditional wastewater treatment methods due to financial considerations, technological limitations and lack of regulation. It has been shown that in a wastewater treatment plant contrasting agents are not removed in large quantities by conventional treatment methods [6,7].

**Conclusions:** Evaluation of the ecotoxicity of triiodine contrast agents must include its transformation products. Further research on this topic is needed. Regulating permissible concentrations in treated wastewater and surface water may be helpful. Monitoring concentrations in water would allow assessment of the efficiency of photolysis and bacterial biodegradation, so that when the efficiency decreases, we can react in time by applying additional wastewater treatment methods. In addition, the reduction in the amount of contrast agents entering the wastewater can be reduced by optimizing the amounts administered to patients.

**References:**

1. T.A. Ternes, M. Bonerz, N. Herrmann, D. Loffler, E. Keller, B. Bagó Lacida, A. C. Alder, Journal of Chromatography A, 1067 (2005)213.
2. S. Pérez, D. Barceló, Analytical and Bioanalytical Chemistry, 387 (2007) 123.
4. T.A. Ternes, A. Joss, H. Siegrist, Environmental Science & Technology, 38 (2004) 392A.
5. A. Bogdanowicz, J. Wąsowski, Gaz, Woda i Technika Sanitarna, 2 (2018) 63.
6. B. Czech, Adsorbenty i Katalizatory Wybrane Technologie a Środowisko, 433 (2012).
7. K. Wontorska, J. Wąsowski, Gaz, Woda i Technika Sanitarna, 1 ( 2018) 30.

# PHARMACOLOGY AND APPLICATIONS OF IODINE CONTRAST AGENTS

**K. WRZESIŃSKA**, **J. CZERWIŃSKI**, Lublin University of Technology, Faculty of Environmental Engineering, 40B Nadbystrzycka St., 20-618 Lublin, Poland.

**Abstract:** Contrast agents used during magnetic resonance imaging and computed tomography are injected intravenously, and during angigraphy they are injected intra-arterially. Conventional contrast agents contain iodine and, based on their physical and chemical properties, are divided into ionic and non-ionic agents with different viscosities and osmolality.

**Introduction:** Diagnostic imaging is one of the most dynamically developing branches of modern medicine. This is particularly true of computed tomography, which has undergone very many degrees of technological development since its invention in 1972. The number of annual computed tomography examinations performed is approximately 2.2 million in Poland, 63 million in Japan, and 85 million in the United States, which makes several hundred million examinations per year worldwide, and at the same time the number of installed computed tomography machines and the number of examinations performed are increasing every year. The most commonly used contrast agents are iodine-based preparations, which have the ability to suppress rengen radiation [1].

Iodine contrast agents (Fig.1) are concentrated organic solutions of iodine salts administered intravenously, intra-arterially or, less commonly, into body cavities. Their structure is based on the structure of a benzene ring linked to iodine molecules and with side chains at positions 1, 3 and 5 of the carbon ring.

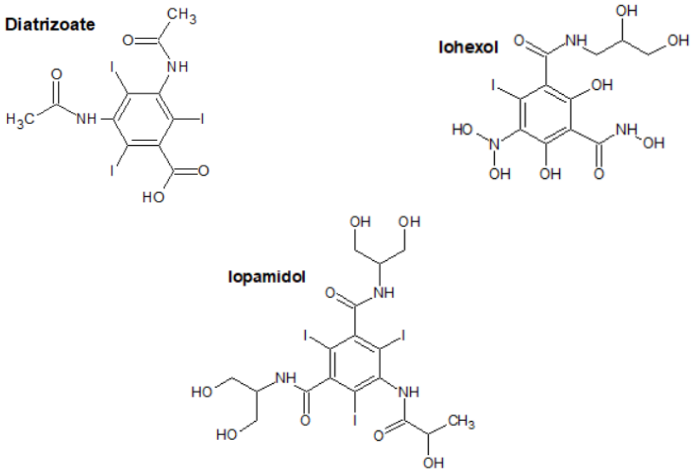



**Fig.1.** Chemical structures of the most commonly used ICM.

These compounds differ in osmolality, viscosity and iodine content [2]. Based on their structure and physicochemical properties, ICMs are divided into four groups: 1) ionic

monomers with high osmolality, on the order of 2000 mOsm/kg $H_2O$, toxicity associated with their dissociation and binding to serum calcium cations; 2) non-ionic monomers with low osmolality; 3) ionic dimers with low osmolality; 4) non-ionic dimers with intermediate osmolality (isotonic with plasma 300 mOsm/kg $H_2O$). All of the above-mentioned types of preparations can cause hypersensitivity reactions, but the different groups of compounds differ in the incidence and severity of the symptoms they cause. Ionic monomers with high osmolality are considered to be the most common to cause hypersensitivity reactions and the least safe, while their opposite in both respects are non-ionic compounds with low osmolality [3]. Table 1 shows selected physical and chemical properties of the most commonly used ICM.

**Table 1.** Physical and chemical properties of selected iodine contrast agents [4].

| Properties | Diatrizoate | Iohexol | Iopamidol |
|---|---|---|---|
| Molecular formula | $C_{11}H_9I_3N_2O_4$ | $C_{19}H_{26}I_3N_3O_9$ | $C_{17}H_{22}I_3N_3O_8$ |
| Molecular weight, g/mol | 613.916 | 821.142 | 777.089 |
| Charge | Ionic | Non-ionic | Non-ionic |
| Solubility, mg/mL | 0.107 | 0.796 | 0.117 |
| Melting point, °C | 261–262 | 174–180 | 300 |
| Osmolality | High | Low | Low |

Contrast agents are used in radiological studies to primarily visualize tissues. In addition, in classical X-ray angiography, it is possible to observe the lumen of the vessels and thus assess the vascularization of pathological lesions. In urography, these measures are used to check organ function, for example, by observing the process of excretion by the kidneys. It is also possible to map the appearance of the walls of anatomical structures, which is very desirable for the diagnosis of diseases, and is also used in assessing the tightness of anastomoses after any surgical procedures [5]. There are also cases when contrast agents are used to visualize foreign bodies lodged in the esophagus, for example. There are two types of contrast agents used in medicine - negative and positive. Negative agents include gases such as carbon dioxide, molecular oxygen. They reduce the absorption of X-rays, which makes the examined image darker. Positive contrast agents, on the other hand, are barium sulfate and iodine-based contrast agents. Iodine-based contrast agents are water-soluble, while barium sulfate is insoluble. Their role is to increase the absorption of radiation and to brighten the anatomical structures under examination. Technological developments in computed tomography have made it possible to expand the range of indications for the examination and significantly increase its clinical use both in the diagnosis of patients with complaints and practical symptoms of all organs and areas of the body, but also in screening, evaluation of advanced malignancies, diagnosis of postoperative complications and monitoring of radiation therapy and chemotherapy [6].

**Conclusions:** Contrast agents significantly increase the diagnostic value of the procedures performed, making it possible to assess whether given anatomical structures remain free of pathological features. In the human body, contrast agents maintain metabolic stability. In their unchanged, original form, excreted in the urine and feces of patients, they end up in the sewage network and then in the sewage treatment plant.

Therefore, it is important to look at what happens to the liters of contrast agents used daily, and what effects we may be exposed to in the future.

**References:**

1. K. Brockow, Quantitative imaging in medicine and surgery, 10 (2020) 537.
2. S. J. Park, D.Y. Kang, K.H. Sohn, S.H. Yoon, W. Lee, Y.H. Cho, H.R Kang, Radiology, 288 (2018) 710.
3. E. Lim, J.H Jang, D. Yoon, Y.G Min, H.H Kim, International Medical Journal of Experimental and Clinical Research, 26 (2020) 921303.
4. National Institutes of Health, https://pubchem.ncbi.nlm.nih.gov [Accessed: 28-March-2024].
5. P. Giri, C. Pal, American Journal of Drug Discovery, 1 (2014) 10.
6. S. Khan, M. Naushad, M. Govarthanan, J. Iqbal, S.M. Alfadul, Environmental Research, 207 (2022) 112609.

# STUDY OF THE RELEASE OF CHLOROPHYLLS OF THE *LAMIACEAE* FAMILY BY THE SPECTROPHOTOMETRIC METHOD

**A. KUSTOVSKA[1], V. PAIENTKO[2], O. PINCHUK[1], Y. BUYAN[1], A. BRYAZUN[1], E. SKWAREK[3]**, [1]Dragomanov Ukrainian State University, Faculty of Natural Sciences, Department of Biology, 03164 Kyiv, Ukraine, [2]Chuiko Institute of Surface Chemistry, NAS of Ukraine, Department of Amorphous and Structurally Ordered Oxides, Gen. Naumov St. 17, 03164 Kyiv, Ukraine, [3]Maria Curie-Sklodowska University, Faculty of Chemistry, Institute of Chemical Sciences, Department of Radiochemistry and Environmental Chemistry, M. Curie-Sklodowska Sq. 3, 20-031 Lublin, Poland.

**Abstract:** The study is devoted to the analysis of chlorophyll content in plants of the *Lamiaceae* family, which includes many medicinal plants. Since there is a relationship between the intensity of the colour of the solution under study and the content of the substance in the solution, which is expressed by the Lambert-Beer law, the use of spectrophotometry allows us to accurately determine the quantitative indicators of chlorophyll content in plants. The results of this study may shed more light on the biochemical characteristics of the *Lamiaceae* family and its potential use in the pharmaceutical and cosmetic industries

**Introduction:** Phytotherapy has come a long way from occultism and primitive empirical observations and guesses of primitive man to the disclosure of certain secrets of the action of the constituent parts of individual plants. Doctors' ignorance of botany, herbal medicine, and their hostile attitude to the use of plants in medical practice have caused much damage to medical science and health care. Medicinal plants have gained great popularity in the 21st century and are attracting increasing attention from scientists in a variety of fields, from cosmetology to cooking. Plant pigments may have health benefits.

The physiological role of chlorophylls in plants is due to their participation in the absorption and transformation of energy, which is used in the synthesis of specific substances that are necessary for plant growth and development [1]. When eating green plants, humans consume a lot of chlorophyll. Its physiological effects on the human body are less well understood than those of carotenoids. However, clinical studies have shown [7- 9] that chlorophyll in the human body promotes the formation of hemoglobin and can be used in medicine as a valuable therapeutic agent that accelerates hematopoiesis and stabilizes the circulatory system. In order to control the absorption of these valuable compounds from food or medicines and dietary supplements or to nourish the skin or hair with cosmetics a combination of yellow clay and selected plants of the *Lamiaceae* family can be offered as a complex system as nutrient carriers. Yellow clay is an effective sorbent, so it is promising for use in cosmetics [3]. Also, one of the important characteristics of yellow clay as a component of cosmetic compositions is its ability to exhibit antibacterial effects against gram-positive and gram-negative bacteria *Staphylococcus aureus*, *Klebsiella pneumoniae*, and *Pseudomonas aeruginosa* [5].

Clay minerals are widely used in cosmetics and are included in toothpastes, masks and shampoos because they have the ability to catalyse biochemical reactions, including: in contact with the skin, which contributes to the normalization of metabolic processes responsible for cell growth and tissue regeneration. The structure of natural aluminosilicates gives them properties such as dispersion, adsorption capacity, gelation and the possibility of being used as an abrasive material, which creates a wide range of applications in cosmetics. Particularly noteworthy is their use as functional fillers in cosmetic products and carriers of biologically active substances, including vitamins. The release kinetics of SBCs are controlled by the chemical nature of the surface and the porous structure of the carrier. By changing the surface properties and porosity by using aluminosilicate matrices with different structures as carriers, it is possible to control the release of biologically active substances, extending the period of their effective use. In addition to the fact that these carriers enable the transport of biologically active substances, they are biocompatible and bioavailable and do not cause allergic reactions. Natural minerals contain various trace elements that also influence the properties of biologically active substances, forming complex compounds with them. Currently, clays are widely used in the pharmaceutical and cosmetic industries. In the first case, they are used both as auxiliary substances in the production of oral, sublingual, transdermal and other medicinal forms, and as active ingredients in antidiarrheal and anti-inflammatory agents. The pharmacological effect of clays results mainly from their enveloping and absorbing properties. In the second case, clay minerals are part of pastes, masks, shampoos, because they have the ability to catalyse biochemical reactions, including those in contact with the skin, which contributes to the normalization of metabolic processes responsible for cell growth and tissue regeneration.The factors that determine the advantages of using clays as cosmetic products are: colour, pH, viscosity, mineralogical purity, presence of metal ions, electrolyte compatibility, cation exchange capacity and associative minerals.

Immobilization is a set of techniques that lead to partial or complete limitation of movement by binding molecules, substances or biological materials to a carrier. Composites are excellent materials for using this phenomenon in practice. Creating new forms of delivering biologically active substances is an important and urgent problem of modern pharmacology and cosmetology. The use of carriers for biologically active substances allows to obtain dosage forms with improved solubility in biological fluids, controlled entry time into the body, high stability during storage, etc. Clays, natural micro/nanostructured materials can be used as inorganic ingredients. This makes it possible to obtain nanostructured composites based on clay with specific additives, and allows to control such practically important features as morphological, structural, textural, mechanical, abrasive, thermal and other complex materials. Clay can be easily mixed with other micro- or nanostructured materials, including silicas, diatomite's, hydroxyapatite, metal powders, bioactive (e.g. natural) materials used in medical and cosmetic applications, etc. By changing the composition and structure of such composite materials, we can influence the necessary load-bearing capacity and regulate the kinetics of the release of active substances. It should be noted that bound water and hydrogen bonds at the interfacial surfaces of nanostructured solids play an important role that strongly influences the properties of composites and natural bioactive materials. Some synergistic effects on the properties of nanostructured hybrid composites can be expected due to component interference and changes in morphological and other

properties during composite preparation and processing. Virtually all of these effects concern surface layers and interfacial phenomena in nanostructured materials.
The aim of our study was to investigate the release of chlorophylls from the composite mixtures of yellow clay and raw materials of *Lamiaceae* species with the spectrophometric method and the physicochemical properties of composite mixtures of yellow clay and raw materials of plants of the *Lamiaceae* family.

**Experimental:** White and yellow clay from "Mel-OK", Kyiv, Ukraine were used for experiments (Fig.1).



**Fig.1.** White clay and yellow clay.

The component of the crystalline phase of yellow clay is kaolinite and α-quartz, it is a composite consisting of $Al_4(OH)_8Si_4O_{10}$, $SiO_2$, muscovite, illite. Its average hydrodynamic radius is 1.75 mm. The component of the crystalline phase of china clay is kaolinite, it is a composite consisting of $Al_4(OH)_8Si_4O_{10}$, muscovite and illite. Its average hydrodynamic radius is 1.15 mm.
In order to mix all powders thoroughly, but without strong mechanical stress, they were processed in a Chemland knife mill (250W) for 3 min at room temperature (Fig.2).

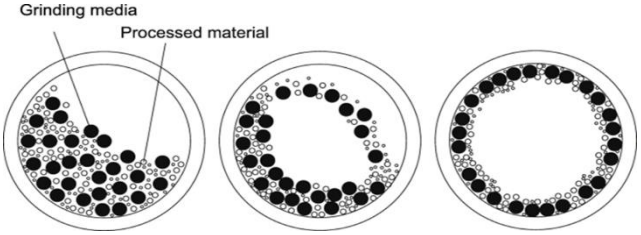



**Fig.2.** Scheme of mechanochemical activation.

A selection and analysis of literature related to the topic of this study was carried out. The study was carried out using the spectrophotometric method, which is based on measuring the absorption of light at a certain wavelength (monochromatic radiation), which corresponds to the maximum absorption for the substance under study. The optical density was determined at λ=649 nm and λ=665 nm for chlorophyll using a spectrophotometer SF-46 (LOMO, Russia) in cuvettes with a layer thickness of 1 cm. For comparison, a solution containing 96% ethyl alcohol was used.

**Results:** In general, the highest concentration of released chlorophyll (A+B) was observed for the systems based on *Ocimum basilicum L.* (15.79) and *Thymus vulgaris L.* (14.92), the lowest for the systems based on *Lavandula angustifolia Mill* (2.55) and *Ocimum basilicum L.* (2.77). The concentration of extracted compounds was calculated according to Equations [6]:

$$C_a=13.70\cdot A665-5.76\cdot A649$$

$$C_b=25.80\cdot A649-7.60\cdot A665$$

$$C_{tot}=6.10\cdot A665+20.04\cdot A649$$

where: A649 is the absorbance measured at 649 nm, A665 the absorbance measured at 665 nm, $C_a$ is the concentration of chlorophyll a (mg/g), $C_b$ is the concentration of chlorophyll B (mg/g), $C_{tot}$ is the total chlorophyll concentration (sum of chlorophylls a and B) (mg/g) [6].

The kinetic release may be related to the following factors: the structure of the pigment molecules being released, temperature, pH, or light availability. Another important issue is the choice of the type and proportion of composite phases. Each composite formulation can provide different results in the kinetic release of chlorophylls due to the different structure and stability of the resulting systems (Tables 1 and 2).

**Table 1.** Results of the study of chlorophyll release in *Lamiaceae* raw materials/yellow clay.

| Yellow clay/Plant name | λ 665 nm | λ 649nm | $C_a$ | $C_b$ | $C_{tot}$ |
|---|---|---|---|---|---|
| Lavandula angustifolia Mill | 0.129 | 0.088 | 1.26 | 1.29 | 2.55 |
| Melissa officinalis L. | 0.507 | 0.520 | 3.95 | 9.56 | 13.51 |
| Mentha piperita L. | 0.527 | 0.226 | 5.91 | 1.82 | 7.73 |
| Ocimum basilicum L. | 0.139 | 0.096 | 1.35 | 1.42 | 2.77 |
| Ocimum purpura L. | 0.770 | 0.554 | 7.35 | 8.44 | 15.79 |
| Origanum vulgare L. | 0.225 | 0.407 | 0.73 | 8.79 | 9.52 |
| Salvia officinalis L. | 0.621 | 0.491 | 5.67 | 7.94 | 13.61 |
| Thymus vulgaris L. | 0.674 | 0.540 | 6.12 | 8.80 | 14.92 |

**Table 2.** Results of the study of chlorophyll release in *Lamiaceae* raw materials/white clay.

| Yellow clay/Plant name | λ 665 nm | λ 649 nm | $C_a$ | $C_b$ | $C_{tot}$ |
|---|---|---|---|---|---|
| Lavandula angustifolia Mill | 0.062 | 0.037 | 0.63 | 0.48 | 1.11 |
| Melissa officinalis L. | 0.091 | 0.048 | 0.97 | 0.54 | 1.51 |
| Mentha piperita L. | 0.39 | 0.171 | 4.35 | 1.44 | 5.8 |
| Ocimum basilicum L. | 0.111 | 0.053 | 1.21 | 0.52 | 1.73 |
| Ocimum purpura L. | 0.257 | 0.132 | 2.76 | 1.45 | 4.21 |
| Origanum vulgare L. | 0.108 | 0.058 | 1.14 | 0.67 | 1.82 |
| Salvia officinalis L. | 0.215 | 0.097 | 2.38 | 0.86 | 3.25 |
| Thymus vulgaris L. | 0.026 | 0.016 | 0.26 | 0.21 | 0.47 |

**Conclusions:** The kinetics of chlorophyll release (chlorophylls a and B and their sum) from white clay/plant and yellow clay/plant composites of different composition was studied and the data on chlorophyll concentration were presented. Different release of compounds may be associated with different composition and degree of dispersion of the composite components. The latest approaches in phytotherapy and biochemistry, particularly, the creation of composite nano-mixtures from plant materials, open many interesting opportunities in the search for effective therapeutic and care products and

means, so the obtained composites require a more detailed study and are promising for use in cosmetology.

## References:

1. G.B. Brudacher, H.A. Weiser, International Journal for Vitamin and Nutrition Research, 21 (1985) 5.
2. P. Matthiele, G. Stefan, H. Thomas, Annual Review of Plant Physiology and Plant Molecular Biology, 50 (1999) 1.
3. DSTU 2472:2006. Perfume and cosmetic products. Terms and definitions. [In force since 2007-07-01]. K.: Gosstandart of Ukraine, 2008.
4. Medicinal and Aromatic Plants: Prospects and Challenges for Agripreneures: https://justagriculture.in/files/newsletter/2023/february/31.Medicinal%20and%20Aromatic%20Plants%20%20Prospects%20and%20Challenges%20for%20Agripreneures.pdf
5. I. Protsak, V.V. Paientko, O.I. Oranska, Yu.I. Gornikov, P.A. Prokhnenko, S.A. Alekseev, L.M. Babenko, N.A. Liedienov, A.V. Pashchenko, G.G. Levchenko, V.M. Gun'ko, Colloids and Surfaces A: Physicochemical and Engineering Aspects, 586 (2020) 124238.
6. J.F.G.M. Wintermans, A. De Mots, Biochimica et Biophysica Acta, 109 (1965) 18.
7. M. Chwiej Studia i opracowanie metody oraz zalozen technologiczno-projectowych do wydobycia likopenu z odpadow pomidorowych – Warszawa 1983.
8. R. Josse, Food Engineering, 12 (1987) 44.
9. H. Klaui, O. Isler, Chemie in unserer Zeit, 15 (1981) 1.

# THE INFLUENCE OF THE BIODEGRADATION PROCESS ON THE ANTIOXIDANT PROPERTIES OF POLYPHENOLS

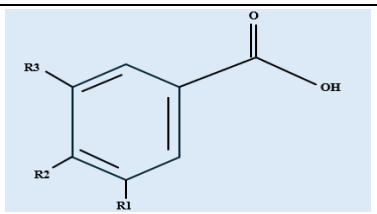
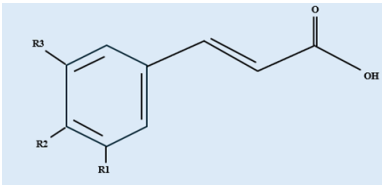
**R. CHOIŃSKA[1], A. DĄBROWSKA[1], R. ŚWISŁOCKA[2], W. LEWANDOWSKI[2],**
[1]Institute of Agricultural and Food Biotechnology-State Research Institute, Rakowiecka Sq. 36, 02-532 Warsaw, Poland; [2]Bialystok University of Technology, Faculty of Civil Engineering and Environmental Sciences, Department of Chemistry, Biology and Biotechnology Wiejska Sq. 45E, 15-351 Bialystok, Poland.

**Abstract:** Biodegradation of bioactive compounds acting as antioxidants via microorganisms is a natural process and leads to the formation of new compounds with different antioxidant capacities (AC) than their precursor. In the case of polyphenols, belonging to the group of antioxidants commonly found in plant-based foods, their biodegradation results primarily from the defense mechanisms of microorganisms. Most polyphenols have antimicrobial properties, therefore to detoxify them, microorganisms activate available enzymes, especially from the group of esterases, reductases and decarboxylases resulting in the formation of less harmful derivatives. As research shows, the observed changes in total antioxidant capacity depend on the compound's structure, the type of microorganisms and their metabolic activity and exogenous factors. Among microorganisms involved in the biodegradation of polyphenols, the most commonly studied are bacteria and yeast species. This review summarizes recent findings on the impact of microbial-mediated degradation of polyphenols on their antioxidant capacity.

**Introduction:** Polyphenols are compounds commonly found in foods of plant origin, such as Brassicaceae, berries, wine, coffee, cereals, and tea. These compounds not only affect the appearance and taste but also increase the antioxidant properties of food [1]. Food polyphenols are known for their strong free radical scavenging effects, thus contributing to reducing the risk of developing chronic diseases such as diabetes, and cardiovascular and neurodegenerative diseases [2]. However, the original composition of polyphenols, their structure, and properties often change under the influence of biological factors and/or the processing of natural raw materials. For example, the biodegradation process, which is a natural process driven by microorganisms such as bacteria or yeasts, leads to the formation of new compounds with different properties than their precursor. The metabolic activity of microorganisms imparts the structural changes of the polyphenols and the formation of simpler metabolites with lower molecular weight, higher bioavailability and often completely different antioxidant properties. In the case of polyphenols, their biodegradation results primarily from the defense mechanisms of microorganisms. To survive in a matrix containing polyphenols, microorganisms use enzymes to detoxify polyphenols, transforming them into less harmful compounds.
The article will review reports on the impact of the biodegradation process on changes in the structure and antioxidant activity of one of the main groups of polyphenols, *i.e.* phenolic acids. The proposed routes of the decomposition of phenolic acids in plant matrices and the influence of environmental factors on the formed derivatives will be presented.

Phenolic acids belong to the group of polyphenols of natural origin that are responsible for the sour and bitter taste of products. Phenolic acids are divided into derivatives of benzoic acid (e.g. protocatechuic acid, hydroxybenzoic acid, gallic acid) and cinnamic acid (e.g. caffeic acid, ferulic acid, coumaric acid, sinapic acid). Hydroxybenzoic acids occur less frequently in nature than hydroxycinnamic acids and can be found in conjugated forms such as glucosides [3].

**Table 1.** Phenolic compounds.

| Class of phenolic compound | Basic chemical structure | Examples |
|---|---|---|
| Hydroxybenzoic acids |  | p-hydroxybenzoic acid ($R_1$,$R_3$-H; $R_2$-OH)<br>protocatechuic acid ($R_1$,$R_2$ - OH;$R_3$-H)<br>gallic acid ($R_1$,$R_2$, $R_3$ - OH)<br>vanilic acid ($R_1$-$OCH_3$; $R_2$-OH; $R_3$-H) |
| Hydroxycinnamic acids |  | p-coumaric acid ($R_1$,$R_3$- H; $R_2$-OH)<br>ferulic acid ($R_1$-$OCH_3$; $R_2$-OH; $R_3$-H)<br>caffeic acid ($R_1$, $R_2$-OH; $R_3$-OH) |

The research shows that the following enzymes are involved in the biodegradation of polyphenols: esterase, decarboxylase, and reductase. The type of enzymes involved depends on the structure of the polyphenols and the type of microorganisms. For example, the biodegradation of hydroxycinnamic acids by lactic acid bacteria (LAB) involves esterase, decarboxylase, and reductase. However, hydroxybenzoic acids are degraded by the action of esterase (tannase) or decarboxylase [4]. The schematic route of the biodegradation process of hydroxycinnamic acids is shown in Fig.1

In the plant matrix, hydroxycinnamic acids occur mainly in the glycosylated (esterified) form, covalently bound to the plant cell wall, and in the soluble form in the cytoplasm. The breakdown of ester bonds, catalyzed by cinnamoyl ester hydrolases (cinnamoyl esterase) between polymers, leads to the release of free phenolic acids, which may be subsequently degraded by phenolic acid decarboxylases (PAD) [5-6]. As a result of the activity of decarboxylases, hydroxycinnamic acids are decarboxylated into corresponding vinyl derivatives, which in turn may be reduced to ethyl derivatives by reductases. In the case of reductase activity, hydroxycinnamic acids may be directly reduced to their phenyl propanoic derivatives [7]. Filannino et al. [8] studied the metabolism of the most common hydroxycinnamic acids in MRS medium, i.e. ferulic acid, caffeic acid, and p-coumaric acid, by bacterial strains, and hypothesized that bacteria use these acids

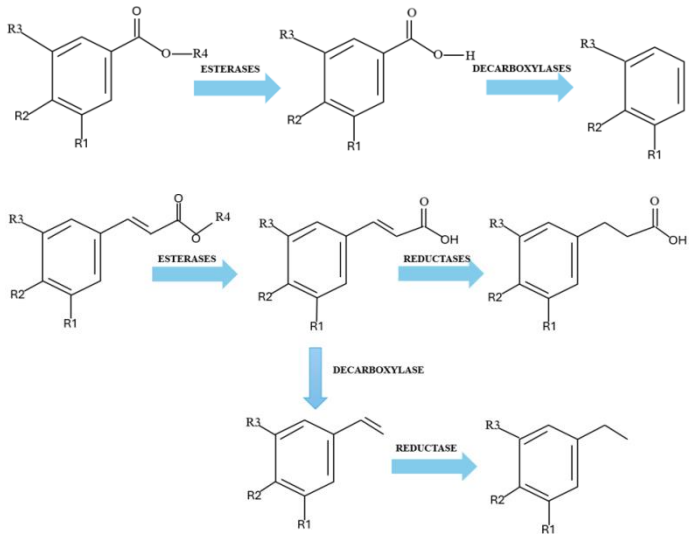



**Fig.1** Schematic route of biodegradation process of hydroxybenzoic and hydroxycinnamic acids acc. to [4].

as external electron acceptors to regenerate the reduced NADH cofactor. Moreover, chromatographic data showed that, depending on the bacterial strain, caffeic acid was reduced to dihydrocaffeic acid or decarboxylated by a phenolic acid decarboxylase enzyme to vinylcatechol and, in some cases, further reduced to ethylcatechol. Ferulic acid was reduced mainly to dihydroferulic acid, while the final products of p-coumaric acid degradation were phloretic acid, p-vinylphenol, and ethylphenol. Among the resulting derivatives, p-vinylphenol is a recognized food additive as a flavoring agent; ethylphenol is considered one of the most important flavoring agents in fermented soy sauce, while dihydrocaffeic acid has a higher AC than caffeic acid. The protective role of dihydrocaffeic acid against oxidative stress in human-derived EA.hy926 endothelial cells by scavenging intracellular reactive oxygen species was reported by Huang et al. [9] and Wang et al. [10]. The formation of vinylphenol derivatives, may or may not be desirable, depending on the food product and consumer acceptance. For example, in wines, 4-vinylphenol is considered off-flavor, while 4-vinylguaiacol, a reduction product of 4-vinylphenol, is an important component of the flavor profile of artisan bread [11]. The microorganism-mediated degradation of polyphenols in a complex plant matrix depends on various endogenous and exogenous factors, such as pH, temperature, and competitive microorganisms, and may differ from in vitro conditions [4]. Recently De Montijo-Prieto et al. [6] studied the influence of bacterial metabolism on the phenolic profile of avocado leaves and observed a strain-specific-dependent degradation modes. The metabolic activity of four of the five tested bacterial strains led to an increase in the total phenolic content. All bacterial strains increased the content of dihydro-p-coumaric acid, while the content of chlorogenic acid, an ester of caffeic and quinic acid, was significantly reduced. In the case of studied *L. plantarum*, CECT 748T its metabolic activity led to a significant decrease in the concentration of p-coumaroylglycolic acid (p-coumaric acid ester) and also p-coumaric acid, suggesting initial hydrolysis of the ester by cinnamoyl esterase and subsequent decarboxylase activity. Ripari et al. [12] analyzing the

transformation of polyphenols in wheat sourdough, observed bacterial degradation of free ferulic acid to vinylguaiacol, ethylguaiacol, and dihydroferulic acid. However, no conversion was found in the case of other phenolic acids, including coumaric, sinapic, and vanillic acids.

Among yeast species, the conversion of ferulic acid has been widely studied in *Saccharomyces cerevisiae* strains. Boudaoud et al. [13] showed that the tested strain of *S. cerevisiae*, which expresses two genes: phenylacrylic acid decarboxylase and ferulic acid decarboxylase (PAD1 and FDC1, respectively), acting synergistically to decarboxylate hydroxycinnamic acids, assimilates ferulic acid and converts it into 4-vinylguaiacol. They also proved that the tested *S. cerevisiae* strains that assimilated all ferulic acid yielded the same amount of 4-vinylguaiacol compared to those that did not assimilate all ferulic acid, suggesting that decarboxylation is the limiting step in ferulic acid metabolism.

On the other hand, Liang et al. [14] studied the conversion of ferulic acid by strains of *S. cerevisiae* and *Aspergillus oryzae*. The test results showed that free ferulic acid was converted to vanillin and vanillic acid in *S. cerevisiae* and *A. oryzae* samples, respectively. The presence of cinnamic acid and ferulic acid was also confirmed for both microorganisms. 4-vinylguaiacol was not detected in any of the tested samples. As the authors explain, the reason may be the alternative metabolic pathway of 4-vinylguaiacol, in which 4-vinylguaiacol can be converted directly into vanillin and vanillic acid through oxidation. This assumption may be confirmed by the presence of vanillin and vanillic acid in the tested samples.

Most studies on AC of plant extracts and their changes under the influence of various processes correlate its value with the total phenol content (TPC). This is because in most cases both an increase in TPC and AC is observed and therefore it has been suggested that phenolic compounds are the main contributors to AC. However, it should be noted that the AC of plant extracts is determined not only by polyphenols (phenolic acids, flavonoids) but also by non-polar bioactive compounds, e.g. vitamin E. In the study performed by Kaprasob et al. [15] on the effect of bacterial metabolic activity on the polyphenol content in cashew apple juice, no significant changes in the total phenol content were observed, although, a significant decrease in AC of the juice was noted. Analysis of the reported data from various studies indicates that a relatively reliable in vitro assessment of AC of phenolic compounds of plant origin can be obtained by combining commonly used radical scavenging tests: DPPH, ABTS, and FRAP. The differences in the chemical structure of the precursor and its reduced derivatives were used by Miyagusuku-Cruzado et al. [11] to develop a simple and rapid approach using UV-Vis spectroscopy to monitor the ability of bacteria to decarboxylate hydroxycinnamic acids. Based on the hypsochromic shifts $\lambda_{max}$ from 285–300 nm for hydroxycinnamic acids to 260 nm for 4-vinylphenols, the researchers selected only three of the 22 tested bacterial strains that were able to decarboxylate all the tested acids, i.e.: p-coumaric, caffeic and ferulic acids to the corresponding 4-vinyl derivatives.

**Conclusions:** Polyphenol biodegradation is a phenomenon underlying biochemical processes occurring in nature. The observed changes in the structure of the compounds resulting from the metabolic activity of microorganisms are specific to a given plant matrix and unique characteristics of the microorganism. Knowledge of possible structural transformations under the influence of available enzymes may help control the

biodegradation process through the appropriate selection of microorganisms to obtain derivatives with desired bioaccessibility and antioxidant capacity.

**Acknowledgements:** This work was financially supported by National Science Centre, Poland, under the research project number 2018/31/B/NZ7/03083.

**References:**

1. L.A. de la Rosa, J.O. Moreno-Escamilla, J. Rodrigo-García, E. Alvarez-Parrilla, Postharvest Physiology and Biochemistry of Fruits and Vegetables, Elsevier, 2019.
2. A. Zeb, A. Hussain, Heliyon, 2020.
3. A. Bento-Silva, V.M. Koistinen, P. Mena, M.R. Bronze, K. Hanhineva, S. Sahlstrøm, V. Kitrytė, S. Moco, A.M. Aura, European Journal of Nutrition, 59 (2020) 1275.
4. G. Gaur, M.G. Gänzle, Current Research in Food Science, 6 (2023) 100448.
5. B.A. Acosta-Estrada, J.A. Gutiérrez-Uribe, S.O. Serna-Saldívar, Food Chemistry, 152 (2014) 46.
6. S. De Montijo-Prieto, M. Razola-Díaz, F. Barbieri, G. Tabanelli, F. Gardini, M. Jiménez-Valera, A. Ruiz-Bravo, V. Verardo, A.M. Gómez-Caravaca, Antioxidants, 12 (2023) 298.
7. H. Rodríguez, J.A. Curiel, J.M. Landete, B. de las Rivas, F.L. de Felipe, C. Gómez-Cordovés, C., J.M. Mancheno, R. Muñoz, International Journal of Food Microbiology, 132 (2009) 79.
8. P. Filannino, M. Gobbetti, M. De Angelis, R. Di Cagno, Applied and Environmental Microbiology 80 (2014) 7574.
9. J. Huang, T. de Paulis, J.M. May, The Journal of Nutritional Biochemistry, 15 (2004) 722.
10. S. Wang, B. Sarriá, R. Mateos, L. Goya, L. Bravo-Clemente, International Journal of Food Sciences and Nutrition, 70(3) (2019) 267.
11. G. Miyagusuku-Cruzado, I. García-Cano, D. Rocha-Mendoza, R. Jim´enez-Flores, M.M. Giusti, Molecules 25 (2020) 3142.
12. V. Ripari, Y. Bai, M.G. Gänzle, Food Microbiology, 77 (2019) 43.
13. S. Boudaoud, C. Aouf, H. Devillers, D. Sicard, D. Segond, Food Microbiology, 98 (2021) 103790.
14. Z. Liang, Y. Huang, P. Zhang, Z. Fang , Food Bioscience, 56 (2023) 103147.
15. R. Kaprasob, O. Kerdchoechuen, N. Laohakunjit, D. Sarkar, K. Shetty, Process Biochemistry, 59 (2017) 141.

# THEORETICAL STRUCTURAL STUDIES OF PICOLINIC ACID-DERIVED HERBICIDES

**N. KOWALCZYK, G. ŚWIDERSKI**, Białystok University of Technology, Faculty of Civil Engineering and Environmental Sciences, Institute of Environmental Engineering, Department of Chemistry, Biology and Biotechnology, Wiejska 45E, 15-351 Białystok, Poland.

**Abstract:** Pyridinecarboxylic acid herbicides mimic action of auxin – natural plant hormone. They are widely used for broadleaf weed control. Some of residual herbicide may end up in soil, which thanks to their structure may result in reactions with soil occurring molecules. This paper presents results of theoretical reactivity investigation of pyridinecarboxylic acid herbicides in comparison with picolinic acid. Calculations of theoretical parameters were carried out through Gaussian 09 software.

**Introduction:** Pyridinecarboxylic acid herbicides are group of compounds derived from picolinic acid that are used for weed control in crops [1], most widely used against broadleaf weeds [2]. According to Herbicide Resistance Action Committee (HRAC), there are five compounds in pyridinecarboxylic acid derivatives family - florpyrauxifen, aminopyralid, clopyralid, picloram and halauxifen. Their structures are shown in Fig.1.

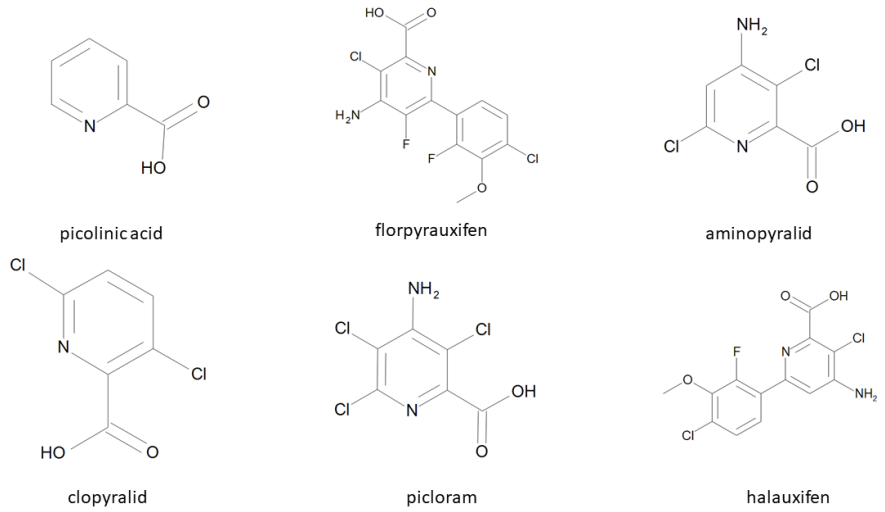



**Fig.1.** Structures of picolinic acid and its herbicide derivatives.

HRAC classifies pyridinecarboxylic acid herbicides as synthetic auxins [3], which means that they mimic natural plant hormones – auxins (indole-3-acetic acid (IAA)) [2]. IAA in low concentrations stimulates plant growth, cell division and general development, but its high concentrations are lethal [4]. Synthetic auxin herbicides imitate that effect causing deregulation of growth manifested by tissue swelling and stem curling, stomatal closure and

tissue decay [5]. Behind acetolactate synthase inhibitors and glyphosate, synthetic auxins are third most commonly used group of herbicides [2], [6].
As stated by EUROSTAT, in 2022 sales of pyridinecarboxylic acid herbicides in Poland was 129 561 kg. It was the highest value among European countries (according to available data) [7]. This means that potentially a lot of residual herbicides end up in soil where they can interact with variety of molecules, ions and compounds [8]. Structure of pyridinecarboxylic acid herbicides – presence of pyridine ring and carboxyl group – makes them susceptible to forming complexes [9]. Therefore, the study of their reactivity is essential to determine their potential fate in the environment. To determine and compare reactivity of picolinic acid and its herbicide derivatives, calculations of theoretical reactivity parameters were carried out.

**Experimental:** Calculations of theoretical parameters of picolinic acid and its herbicide derivatives were carried out using Gaussian 09 software through 3-611 G++ (d, p) basis set with B3LYP DFT method.

**Results:** Results of carried out calculations are presented in Table 1 and obtained shapes of HOMO and LUMO are shown in Fig.2.

**Table 1.** Calculated theoretical parameters of picolinic acid and its herbicide derivatives

| Parameter | Picolinic acid | Clopyralid | Aminopyralid | Picloram | Halauxifen | Florpyrauxifen |
|---|---|---|---|---|---|---|
| Total energy [eV] | -11818.6667 | -36903.6658 | -38410.6992 | -50917.2025 | -50517.3222 | -53021.9833 |
| Dipole moment [D] | 2.6586 | 2.3299 | 4.4075 | 3.3496 | 3.1644 | 3.7743 |
| $E_{HOMO}$ [eV] | -9.9937 | -7.8663 | -7.7961 | -7.7327 | -7.9956 | -8.0247 |
| $E_{LUMO}$ [eV] | -5.7200 | -5.4786 | -5.0876 | -4.8498 | -5.0411 | -4.8909 |
| $\Delta E = E_{LUMO} - E_{HOMO}$ [eV] | 4.2737 | 2.3877 | 2.7086 | 2.8830 | 2.9545 | 3.1339 |
| Ionization potential $I = -E_{HOMO}$ | 9.9937 | 7.8663 | 7.7961 | 7.7327 | 7.9956 | 8.0247 |
| Electron affinity $A = -E_{LUMO}$ | 5.7200 | 5.4786 | 5.0876 | 4.8498 | 5.0411 | 4.8909 |
| Electronegativity $\chi = \frac{I + A}{2}$ | 7.8568 | 6.6725 | 6.4419 | 6.2912 | 6.5183 | 6.4578 |
| Chemical potential $\mu = -\frac{I + A}{2}$ | -7.8568 | -6.6725 | -6.4419 | -6.2912 | -6.5183 | -6.4578 |
| Chemical hardness $\eta = \frac{I-A}{2}$ | 2,1369 | 1.1939 | 1.3543 | 1.4415 | 1.4773 | 1.5669 |
| Chemical softness $S = \frac{1}{2\eta}$ | 0.2340 | 0.4188 | 0.3692 | 0.3469 | 0.3385 | 0.3191 |
| Electrophilicity index $\omega = \frac{\mu^2}{2\eta}$ | 14.4440 | 18.6460 | 15.3209 | 13.7288 | 14.3808 | 13.3072 |

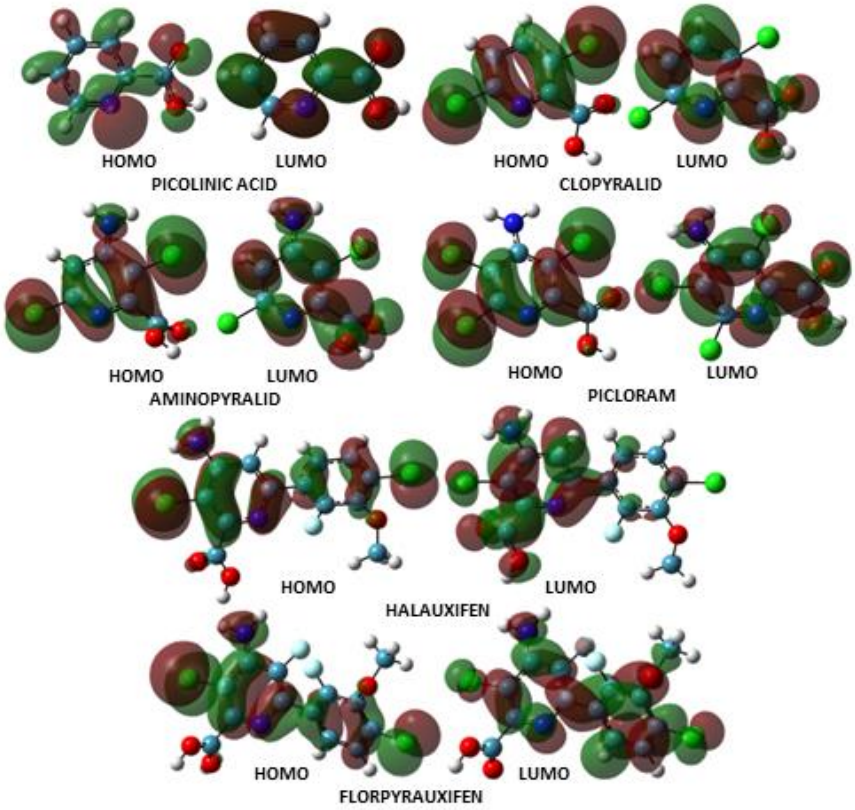



**Fig.2.** Shapes of HOMO and LUMO of picolinic acid and its herbicide derivatives.

The lower values of total energies of the herbicides compared to picolinic acid indicate their greater stability [10]. It can also be concluded that stability increases with increasing complexity of the molecule. The dipole moment resulting from uneven distribution of charges on the individual atoms present in a molecule can be an indicator of molecular reactivity - the strength of the intermolecular interactions increases with an increase in the dipole moment [11] suggesting that the most active herbicide from picolinic acid derivatives is aminopyralid. Energies of HOMO (Highest Occupied Molecular Orbital) and LUMO (Lowest Unoccupied Molecular orbital) are important indicators of bioactivity [12]. The lower the value of $E_{LUMO}$ the greater the molecule's ability to accept electrons and the higher the $E_{HOMO}$ the greater the ability to donate electrons [11,12]. Among the studied compound the highest value $E_{HOMO}$ was shown by picloram while the lowest value of $E_{LUMO}$ was shown by picolinic acid, but overall there was no great difference between investigated herbicides and picolinic acid was the most divergent. Negative values of mentioned energies also indicate stability of studied molecules [13]. Another parameter of stability is energy gap between HOMO and LUMO ($\Delta E$). $\Delta E$ is directly related to chemical softness (S) and hardness ($\eta$), with soft molecules having smaller values of $\Delta E$ and hard molecules having larger values of $\Delta E$. Soft molecules acquire less energy for excitation and therefore are generally less stable

and more chemically reactive than harder ones [11,13]. Out of the investigated compounds picolinic acid is the hardest and clopyralid is the softest. The electrophilicity index also informs about stability in energy [13]. Shalini et al. suggest that it can be used as a descriptor for predicting toxicological properties of molecules, with the higher value indicating greater toxicity [14]. According to that clopyralid would be the most toxic pyridinecarboxylic acid herbicide.

**Conclusions:** Theoretical parameters for picolinic acid, clopyralid, aminopyralid, picloram, halauxifen and florpyrauxifen were calculated. Obtained values indicate that clopyralid, aminopyralid and picloram are more reactive than florpyrauxifen and halauxifen which is likely caused by the fact that two pyridine rings provide more stability to the structure therefore decreasing reactivity of the molecule. Out of the investigated herbicides clopyralid seems to show highest reactivity which might result from it having the least complex structure. The results obtained provide a basis for further experimental studies on the reactivity of herbicides from the picolinic acid derivative group.

**Acknowledgements:** The research was carried out as part of research work WZ/WB-IIS/2/2023 at the Department of Chemistry,Biology and Biotechnology of the Białystok University of Technology and financed from the 2024 subsidy provided by Minister of Science and Higher Education.

**References:**

1. T. Feng, Q. Liu, Z.-Y. Xu, H.-T. Li, W. Wei, R.-C. Shi, L. Zhang, Y.-M. Cao, S.-Z. Liu, Molecules, 28 (2023) 1431.
2. R. Busi, D. E. Goggin, I. M. Heap, M. J. Horak, M. Jugulam, R. A. Masters, R. M. Napier, D. S. Riar, N. M. Satchivi, J. Torra, P. Westra, T. R. Wright, Pest Management Science, 74 (2018) 2265.
3. R. Beffa, H. Menne, H. Köcher, Modern Crop Protection Compounds, (2019) 5.
4. C.-L. Do-Thanh, J. J. Vargas, J. W. Thomas, G. R. Armel, M. D. Best, Journal of Agricultural and Food Chemistry, 64 (2016) 3533.
5. K. Grossmann, Pest Management Science, 66 (2010) 113.
6. J. Prusinska, V. Uzunova, P. Schmitzer, M. Weimer, J. Bell, R. M. Napier, Pest Management Science, 79 (2023) 1305.
7. Pesticide Sales Source of Data: EUROSTAT. Available online: https://ec.europa.eu/eurostat/databrowser/view/aei_fm_salpest09__custom_9508612/default/table?lang=en [access: 30.01.2024]
8. P. P. Choudhury, Herbicide Residue Research in India, Springer, 2019.
9. S. Pal, Pyridine, InechOpen, 2018.
10. R. Alzahrani, I. Althagafi, A. Alsoliemy, K. S. Abou-Melha, A. F. Alrefaei, G. A. M. Mersal, N. El-Metwaly, Journal of Molecular Structure, 1243 (2021) 130855.
11. W. Boufas, N. Dupont, M. Berredjem, K. Berrezag, I. Becheker, H. Berredjem, N.-E. Aouf, Journal of Molecular Structure, 1074 (2014) 180.
12. J.-X. Mu, Z.-W. Zhai, M.-Y. Yang, Z.-H. Sun, H.-K. Wu, X.-H. Liu, Crystals, 6 (2015) 4.
13. S. K. Patel, R. N. Patel, A. K. Patel, N. Patel, D. Choquesillo-Lazarte, Journal of Molecular Structure, 1257 (2022) 132545.
14. A. Shalini, H. Tandon, T. Chakraborty, Journal of Bioequivalence & Bioavailability, 9 (2017) 518.

# METAL COMPLEXES WITH HYDROXYPICOLINIC ACID - SPECTROSCOPIC STUDIES AND THERMAL ANALYSIS

**N. KOWALCZYK, G. TYNIECKA, E. GOŁĘBIEWSKA, G. ŚWIDERSKI**, Białystok University of Technology, Faculty of Civil Engineering and Environmental Sciences, Institute of Environmental Engineering, Department of Chemistry, Biology and Biotechnology, Wiejska 45E, 15-351 Białystok, Poland.

**Abstract:** Metal complexes have been known and studied as a therapeutics for centuries. Among other applications, they can be used in cancer treatment, as a neuroprotectants and antioxidants. 3-hydroxypicolinic acid (3-HPA) is a molecule with relatively simple structure that can acts as a versatile ligand. Complexes of 3-HPA with Cu (II), Co (II) and Mn (II) were synthesised, and then studied using FTIR, thermal and elemental analysis. Calculations of structures and reactivity parameters of studied compound were calculated.

**Introduction:** Metal complexes, especially those containing transition metals, possess potential to undergo a redox reaction and therefore are connected to proper functioning of biological processes and normal wellbeing [1]. Ability to lose electrons easily makes metal atoms soluble in biological fluids and allows variety of interactions with biomolecules such as DNA or proteins [2]. Discovery of anticancer activity of cisplatin was without a doubt a huge breakthrough in research on metal compounds and their therapeutic properties. Some examples of metals with potential application in drugs are among others gold, cobalt, copper and manganese [3,4]. Cu complexes have anticancer effect and can acts as a neuroprotective agent [5], Co compounds are known for their antimicrobial, antiviral and antitumor activity [6,7] and complexes with Mn show potential as antioxidants [4].
Derivatives of picolinic acid are relevant components of bioactive molecules. 3-hydroxypicolinic acid (3-HPA) is a key building unit of several bacterial secondary metabolites [8] and thanks to its relatively simple structure (Fig.1), can acts as a versatile ligand [9]. Therefore 3-HPA is commonly used to synthesize complex compounds with first-row transition metal centres. There are studies that suggest that metal complexes of 3-HPA possess variety of useful physiological properties such as acting as a insulin mimetic [10].

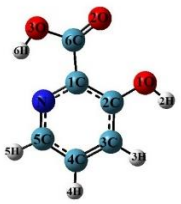


**Fig.1.** Theoretical structure of 3-hydroxypicolinic acid.

**Experimental:** Complex compounds of 3-HPA with copper(II), cobalt(II) and manganese (II) were prepared in a molar ratio of 2:1. FTIR spectroscopic spectra of 3-

HPA and the resulting complexes were recorded using a transmission method with a KBr matrix. Elemental and thermal analysis of the obtained acid complexes was also carried out. Theoretical optimalization and calculations of the structure of 3-HPA and its complexes were performed in the Gaussian software. Calculations were carried out using the DFT method, B3LYP functionals and the 6-311++G(d,p) orbital basis.

**Results:** Table 1 shows the wavenumbers and intensities of selected bands present in the infrared spectra recorded for hydroxypicolinic acid and its complexes with manganese, cobalt and copper. The presence of bands associated with the vibration of the carboxylate anion (VCOO- stretching bands) was observed in the spectra of the complexes. An increase in the values of the wave numbers of the bands associated with the vibration of the aromatic system in the ligand after the complex formation was observed. Transition metals increase the stabilization of the aromatic system in the ligand.

**Table 1.** Results of FTIR spectroscopy of hydroxypicolinic acid and their complexes with manganese, cobalt and copper.

| Hydroxypicolinic acid | hydroxypicolinate | | | Assingments |
|---|---|---|---|---|
| | manganese | cobalt | copper | |
| 3436 M | 3423 VS | 3422 VS | 3447 S | $\upsilon(OH)_{ar}$ |
| 3115 M | | | 3091 M | $\upsilon(CH)_{ar}$ |
| 2921 M | 2922 W | 2923 W | 2920 M | $\upsilon_{as}(CH_2)$ |
| 2857 M | | | 2852 M | $\upsilon_{sym}(CH_2)$ |
| 1678 M | | | | $\upsilon(C=O)$ |
| | 1656 S | 1627 S | 1647 VS | $\upsilon_{as}(COO^-)$ |
| 1610 S | | 1603 S | 1610 S | $\upsilon(C-N)$ |
| 1525 VS | | 1533 W | 1538 M | $\upsilon(CC)_{ar}$ |
| 1467 S | 1482 M | 1480 M | 1470 VS | $\upsilon(CC)_{ar}$ |
| | 1452 VS | 1453 VW | 1455 VS | $\upsilon(CC)_{ar}$ |
| | | 1408 M | 1403 S | $\upsilon(CC)_{ar}$ |
| 1385 S | 1397 S | | 1387 S | $\delta(O–H)$ |
| | 1341 S | 1343 M | 1328 VS | $\upsilon_s(CO_2)$ |
| 1195 M | | | | $\beta(CH)$ |
| 1146 M | 1140 W | 1142 W | 1152 S | $\beta(CH)$ |
| 948 M | | | | $\beta(OH)$ |
| 863 M | 891 W | 894 W | 898 S | $\gamma(CH)$ |
| 669 M | 698 M | 688 M | 695 VS | $\Phi(CC)$ |
| 548 W | 559 W | 567 W | 576 M | $\gamma(CH)$ |
| 449 W | 459 W | 459 VW | 452 M | $\gamma(CH)$ |

Table 2 shows results of elemental analysis of synthesized complexes. Results of thermal analysis are shown in Fig.2 and Table 2. The 3d-transition metal complexing 3-HPA binds to the ligand in a ratio of 1:2. The cobalt(II) and manganese(II) complexes contain 1.5 molecules of water, while the copper(II) complex was anhydrous. The loss of water occurs at temperatures between about 100 $^{o}$C and 170 $^{o}$C. Thermal degradation of complexes occurs in several stages, intermediate products can be metal carbonates and the final products are metal oxides. The cobalt complex has the highest thermal stability,

with decomposition starting at 305 $^{o}$C, while the manganese(II) complex is the least thermally stable, with decomposition starting at 250 $^{o}$C.

**Table 2.** Results of elemental analysis of 3-HPA complexes with Co(II), Cu(II) and Mn(II).

| Compex | Content C [%] | | Content H [%] | |
|---|---|---|---|---|
| | Calc. | Exp. | Calc. | Exp. |
| $Co(C_6H_4NO_3)_2 \cdot 1.5H_2O$ | 40,69 | 40,11 | 2,015 | 2,29 |
| $Cu(C_6H_4NO_3)_2$ | 42,42 | 41,15 | 2,37 | 2,67 |
| $Mn(C_6H_4NO_3)_2 \cdot 1.5H_2O$ | 41,64 | 40,98 | 2,04 | 2,14 |

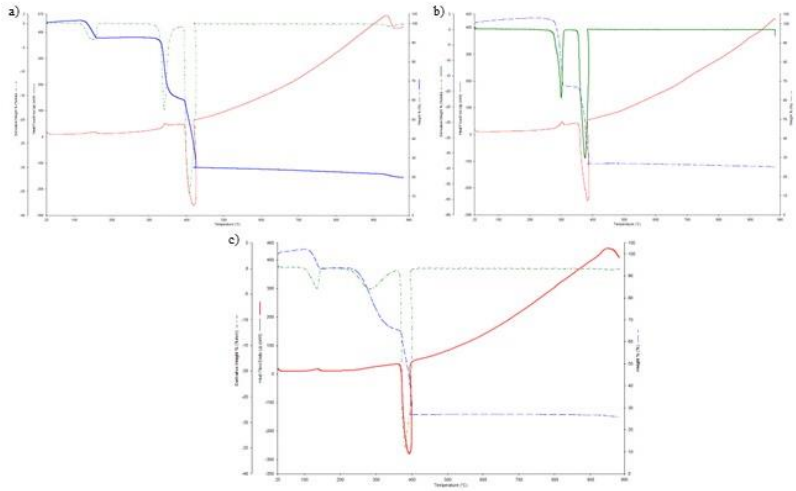



**Fig.2.** TG (blue), DTG (green) and DSC (red) thermal decomposition curves of 3-HPA complexes with a) Co(II), b) Cu(II) and c) Mn(II).

**Table 3.** Results of thermal analysis of 3-HPA complexes with Co(II), Cu(II) and Mn(II).

| Complex | Stage | TG $T_{range}$ [$^{o}$C] | DTG $T_{max.\ peaks}$ [$^{o}$C] | Mass loss [%] | | Process | Final residue |
|---|---|---|---|---|---|---|---|
| | | | | Calc. | Exp. | | |
| $Co(C_6H_4NO_3)_2 \cdot 1.5H_2O$ | I | 105-170 | 148.7 | 7.4 | 7.6 | D | $Co_3O_4$ |
| | II | 305-430 | 342.9 | 77.8 | 78.3 | TD | |
| $Cu(C_6H_4NO_3)_2$ | I | 290-306 | 300.1 | - | 33.7 | TD | CuO |
| | II | 355-391 | 406.5 | 76,5 | 74.9 | TD | |
| $Mn(C_6H_4NO_3)_2 \cdot 1.5H_2O$ | I | 105-150 | 134.6 | 7.5 | 6.8 | D | $Mn_2O_3$ |
| | II | 250-368 | 284.4 | - | 35.2 | TD | |
| | III | 370-405 | 381.3 | 77.9 | 76.2 | TD | |

where D – Dehydratation; TD – Thermal degradation

Results of theoretical calculations are shown in Table 4. Decrease in energy gap between HOMO and LUMO orbitals of complexes comparing to 3-HPA indicate their higher reactivity. Out of the tested compound 3-HPA is the hardest – most stable, and Cu(3-HPA)$_2$ is the softest – most reactive [11,12]. According to Shalini et al. electrophilicity index can inform about potential toxicity of a molecule which would mean that Cu(II) and Mn(II) complexes can potentially be more toxic [13].

**Table 4.** Calculated theoretical parameters of 3-HPA and its complexes with Co(II), Cu(II) and Mn(II).

| Parameter | 3-HPA | $Co(3\text{-}HPA)_2$ | $Cu(3\text{-}HPA)_2$ | $Mn(3\text{-}HPA)_2$ |
|---|---|---|---|---|
| $E_{HOMO}$ [eV] | -9.2856 | -7.6872 | -5.6417 | -7.0720 |
| $E_{LUMO}$ [eV] | -5.6796 | -5.6875 | -5.3269 | -6.5849 |
| $\Delta E = E_{LUMO} - E_{HOMO}$ [eV] | 3.6061 | 1.9998 | 0.3148 | 0.4871 |
| Ionization potential, $I = -E_{HOMO}$ | 9.2856 | 7.6872 | 5.6417 | 7.0720 |
| Electron affinity, $A = -E_{LUMO}$ | 5.6796 | 5.6875 | 5.3269 | 6.5849 |
| Electronegativity, $\chi = \frac{I+A}{2}$ | 7.4826 | 6.6873 | 5.4843 | 6.8284 |
| Chemical potential, $\mu = -\frac{I+A}{2}$ | -7.4826 | -6.6873 | -5.4843 | -6.8284 |
| Chemical hardness, $\eta = \frac{I-A}{2}$ | 1.8030 | 0.9999 | 0.1574 | 0.2435 |
| Chemical softness, $S = \frac{1}{2\eta}$ | 0.2773 | 0.5001 | 3.1766 | 2.0534 |
| Electrophilicity index, $\omega = \frac{\mu^2}{2\eta}$ | 15.5267 | 22.3622 | 95.5449 | 95.7434 |

**Conclusions:** Studies showed that cobalt(II), copper(II) and manganese(II) complexes with 3-hydroxypicolinic acid are formed by the binding of a metal ion to a ligand via the oxygen atom of the carboxyl group and the nitrogen atom of the aromatic ring. Metal ions have stabilizing influence on the ligand. Elemental and thermal analysis show that Mn(II) and Co(II) complexes are hydrated while Cu(II) complex is anhydrous. The most thermically stable out of tested compounds was Co(II) complex (decomposition at 305 $^{o}$C). Calculations of HOMO and LUMO indicated that Cu(II) complex exhibits the highest reactivity.

**Acknowledgements:** The research was carried out as part of research work WZ/WB-IIS/2/2023 at the Department of Chemistry, Biology and Biotechnology of the Białystok University of Technology and financed from the 2024 subsidy provided by Ministry of Science and Higher Education.

**References:**

1. U. Ndagi, N. Mhlongo, M. Soliman, Drug Design, Development and Therapy, 11 (2017) 599.
2. M. Claudel, J. V. Schwarte, K. M. Fromm, Chemistry, 2 (2020) 849.
3. J. do Couto Almeida, I. M. Marzano, M. Pivatto, N. P. Lopes, A. M. Da Costa Ferreira, F.R. Pavan, I.C. Silva, E. C. Pereira-Maia, G. Von Poelhsitz, W. Guerra, Inorganica Chimica Acta, 446 (2016) 87.
4. P. Failli, D. Bani, A. Bencini, M. Cantore, L. Di Cesare Mannelli, C. Ghelardini, C. Giorgi, M. Innocenti, F. Rugi, A. Spepi, R. Udisti, B. Valtancoli§ Journal of Medicinal Chemistry, 52 (2009) 7273.
5. C. Duncan, A. R. White, Metallomics, 4 (2012) 127.
6. E. L. Chang, C. Simmers, D. A. Knight, Pharmaceuticals, 3 (2010) 1711.
7. C. R. Munteanu, K. Suntharalingam, Dalton Transactions, 44 (2015) 13796.
8. X. Yun, Q. Zhang, M. Lv, H. Deng, Z. Deng, Y. Yu, Organic & Biomolecular Chemistry, 17 (2019) 454.
9. P. I. Girginova, F. A. Almeida Paz, H. I. S. Nogueira, N. J. O. Silva, V. S. Amaral, J. Klinowski, T. Trindade, Polyhedron, 24 (2005) 563.
10. B.-M. Kukovec, P. D.Vaz, M. J. Calhorda, Z. Popović, Polyhedron, 39 (2012) 66.
11. W. Boufas, N. Dupont, M. Berredjem, K. Berrezag, I. Becheker, H. Berredjem, N.-E. Aouf, Journal of Molecular Structure, 1074 (2014) 180.
12. S. K. Patel, R. N. Patel, A. K. Patel, N. Patel, D. Choquesillo-Lazarte, Journal of Molecular Structure, 1257 (2022) 132545.
13. A. Shalini, H. Tandon, T. Chakraborty, Journal of Bioequivalence & Bioavailability, 9 (2017) 518.

# PHYSICOCHEMICAL AND BIOLOGICAL PROPERTIES OF METHOXYBENZOIC ACIDS AND THEIR COMPLEXES WITH Cr(III) AND Fe(III)

**R. ŚWISŁOCKA, A.I. ZINIEWICZ**, Bialystok University of Technology, Faculty of Civil Engineering and Environmental Sciences, Department of Chemistry, Biology and Biotechnology Wiejska Sq. 45E, 15-351 Bialystok, Poland.

**Abstract:** The synthesis of iron(III) and chromium(III) ions with methoxybenzoic acids was carried out. Infrared spectroscopy (FT-IR) was used to characterise the resulting complex compounds. The toxicity of the compounds was determined using the MTT assay.

**Introduction:** 3,4-Dimethoxybenzoic acid (veratric acid) occurs naturally in various species of false hellebore (*Veratrum*), including *Veratrum sabadilla*, as well as in the seeds of the officinal sabadilla (*Schoenocaulon officinale*) [1]. This acid has been detected but not quantified in cilantro and olives. Therefore, it may serve as a potential biomarker for the consumption of these products [2]. 3,4,5-Trimethoxybenzoic acid is a natural product found in *Verbesina myriocephala* and *Engelhardia roxburghiana* [3]. Several scientists have undertaken the investigation of the properties of 3,4-dimethoxybenzoic acid and 3,4,5-trimethoxybenzoic acid (Fig.1) and their complexes with metals (copper and cobalt) [4]. For complexes of both acids with transition metals, it has been reported that metal complexes exhibit increased biological activity compared to free ligands [4]. As part of the study, the toxicity of chromium and iron complexes with acids: 2,3-dimethoxybenzoic and 3,4,5-trimethoxybenzoic was investigated. These acids differ in the number of methoxy groups substituted on the aromatic ring of benzoic acid (Fig.1).

a/ b/

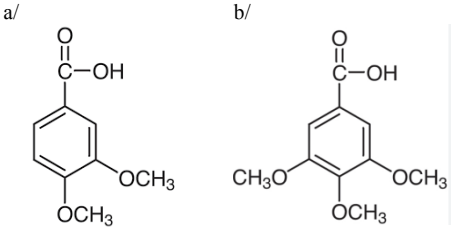



**Fig.1.** Formulas of 3,4-dimethoxybenzoic and 3,4,5-trimethoxybenzoic acids.

**Experimental:** The synthesis of methoxybenzoic acid complexes was performed using iron(III) and chromium(III) chlorides. A balance of the acid was dissolved in an appropriate amount of NaOH solution of 0.1 mol/dm$^3$, in a molar ratio of 1:1. The mixture was placed in an ultrasonic bath for better dissolution of the acid in sodium hydroxide. To the sodium salt solution prepared in this way, a stoichiometric amount of transition metal chloride solutions was added, in a ratio of 3:1. The samples were left for several days, then the precipitates were drained off and allowed to dry. The resulting methoxybenzoate complexes were subjected to spectroscopic analysis. FT-IR spectra of the KBr lozenge in the range of 4000 - 400 cm$^{-1}$ and a resolution of 4 cm$^{-1}$ were recorded

using an Alpha Transmission spectrophotometer from Bruker. Bioassays were performed on cell cultures of gram-negative *Escherichia coli* and gram-positive *Staphylococcus aureus* bacteria. The strains were cultured overnight in Mueller Hinton II broth at 37 °C. The following day, the cultures were diluted in fresh MH II broth to obtain a concentration of $10^8$ CFU/ml (CFU - colony forming units). Solutions of the complexes were prepared as follows: Aliquots of complexes dried on filters were dissolved in 2 $cm^3$ of DMSO solution, yielding solutions of 40 mM concentration. A series of dilutions of the solutions were made during the test, taking 0.5 $cm^3$ from each well to the next. Solutions of pure 3,4-dimethoxybenzoic acid and 3,4,5-dimethoxybenzoic acid were made, as well as solutions of the acid-transition metal complexes tested. The range of molar concentrations of the solutions obtained are: 40 mM, 20 mM, 10 mM, 5 mM, 2.5 mM, 1.25 mM, 0.625 mM and control. Each sample was made in 2 wells. Equal volumes (90 µl) of the solutions were then introduced into the wells of GloMax microplates containing Escherichia coli and Staphylococcus aureus colonies. 10 µl of MTT solution (5 mg/ml in PBS) was added to each well and incubated in the dark for 2 hours. After this time, 100 µl of DMSO solution was added to each well to dissolve the purple formazan crystals. The plates were placed on a Mini-Shaker: Multi Bio 3D matrix and shaken for approximately 15 minutes. The liquid was then removed from the wells of the plates and absorbance was measured at 570 nm on a GloMax-Multi Microplate Multimode Reader.

**Results:** FTIR spectra of the investigated acids and complexes with selected metals have been recorded (Fig.2). The wavenumber values of the bands are summarized in Table 1. In the spectra of methoxybenzoic acids, a characteristic band is observed at 1677 $cm^{-1}$ (for 3,4-dimethoxybenzoic acid) and 1686 $cm^{-1}$ (for 3,4,5-trimethoxybenzoic acid), originating from the stretching vibrations of the carboxyl group [5]. In the spectra of the complexes, this band disappears, while two bands appear in the ranges of 1601-1564 $cm^{-1}$ and 1402-1392 $cm^{-1}$, which can be attributed to asymmetric and symmetric stretching vibrations of the -COO- groups, respectively. Bands assigned to asymmetric and symmetric stretching vibrations of $-CH_3$ groups are observed in the spectra of acids and complexes, respectively, in the ranges of 3088-2935 $cm^{-1}$ and 3004-2838 $cm^{-1}$. Characteristic broad absorption bands originating from stretching vibrations of -OH are observed in the spectra in the wavenumber range of 3424-3452 $cm^{-1}$. The broadness of the bands is caused by interference from hydrogen bonding interactions, which are a common feature for all molecules bonded by hydrogen bonds with a hydroxyl group [6]. Stretching vibrations ν(OH) and stretching vibrations of aryl -CH groups overlap. Deformation vibrations in the plane of C-H bonds are observed in the range of 1100-1400 $cm^{-1}$. Additionally, in the spectra of complexes, bands associated with stretching of M(metal)-O bonds are visible at wavenumbers in the range of 633-593 $cm^{-1}$. Changes (shifts of bands) originating from vibrations of the aromatic system have also been observed. Most of these bands in the spectra of complexes shift towards higher wavenumbers compared to the corresponding bands in the acid spectrum, indicating stabilization of the ligand's π-electron system [7].

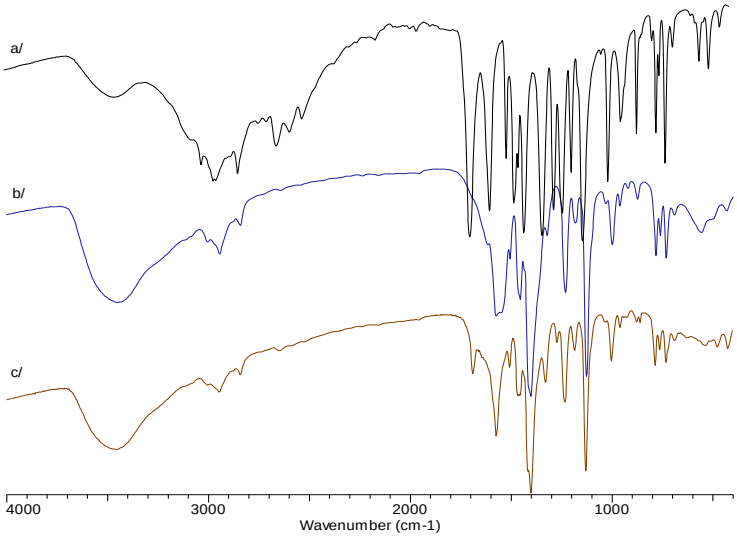



**Fig.2.** FT-IR spectra of 3,4,5-trimethoxybenzoic acid (a) and chromium(III) 3,4,5-trimethoxybenzoate (b) and iron(III) 3,4,5-trimethoxybenzoate (c).

**Table 1.** Wave number values [$cm^{-1}$] and intensities of selected bands in FT-IR spectra of methoxybenzoic acid complexes with chromium(III) and iron(III).

| 3,4-dimethoxy-benzoic acid | 3,4-dimethoxybenzoate | | 3,4,5-trimethoxy-benzoic acid | 3,4,5-trimethoxy-benzoate | | Assignment |
|---|---|---|---|---|---|---|
| | Cr(III) | Fe(III) | | Cr(III) | Fe(III) | |
| 3442 | 3423 | 3452 | 3453 | 3449 | 3442 | ν(OH) |
| 3088 | 3086 | 2935 | 3020 | 2942 | 2942 | $\nu_{as}(CH_3)$ |
| 3004 | 2840 | 2841 | - | 2840 | 2838 | $\nu_{s}(CH_3)$ |
| 1677 | - | - | 1686 | - | - | ν(CO) |
| 1599 | - | 1601 | 1588 | 1615 | 1640 | ν(CC) |
| - | 1601 | 1564 | - | 1574 | 1569 | $\nu_{as}(COO)$ |
| 1599 | 1518 | 1517 | 1588 | 1506 | 1504 | ν(CC) |
| 1469 | 1421 | 1419 | 1467 | 1455 | 1453 | $\beta(CH_3)$ |
| - | 1395 | 1392 | - | 1402 | 1398 | $\nu_{s}(COO^{-})$ |
| 1272 | 1271 | 1273 | 1271 | 1322 | 1326 | ν(CC) |
| 1187 | 1186 | 1184 | 1183 | 1183 | 1183 | $\nu(O\text{-}CH_3)$ |
| 1110 | 1125 | 1123 | 1126 | 1127 | 1127 | $\beta(CH_3)$ |
| 931 | 935 | 935 | 933 | 962 | 959 | ν(CH) |
| | 871 | 779 | | 874 | 783 | $\beta_{s}(COO)$ |
| 762 | - | - | 762 | - | - | β(CO) |
| - | 633 | 636 | - | 693 | 687 | ν(OM) |

In Table 2, the wavenumber values of bands present in the spectra of salts/complexes originating from stretching vibrations of the carboxyl group are listed. This served as the basis for determining the coordination type of the respective compound. The reference was the difference and position of bands originating from asymmetric and symmetric vibrations of the carboxyl group in the spectra of sodium 3,4-dimethoxybenzoate and sodium 3,4,5-trimethoxybenzoate. In the case of complexes of 3,4-dimethoxybenzoic

acid, a bidentate chelating coordination takes place, while complexes of 3,4,5-trimethoxybenzoic acid are characterized by a bidentate bridging coordination [8].

**Table 2.** Spectroscopic data of the 3,4-dimethoxybenzoates Fe(III), Cr(III) and Na(I) and the 3,4,5 trimethoxybenzoates Fe(III), Cr(III) and Na(I) ($cm^{-1}$).

| Compound | ν/$cm^{-1}$ | | |
|---|---|---|---|
| | $\nu_{as}(COO^-)$ | $\nu_s(COO^-)$ | $\Delta\nu(COO^-)$ |
| sodium 3,4-dimethoxybenzoate | 1559 | 1375 | 184 |
| iron(III) 3,4-dimethoxybenzoate | 1564 | 1392 | 172 |
| chromium(III) 3,4-dimethoxybenzoate | 1576 | 1353 | 223 |
| sodium 3,4,5-trimethoxybenzoate | 1579 | 1380 | 199 |
| iron(III) 3,4,5-trimethoxybenzoate | 1569 | 1398 | 171 |
| chromium(III) 3,4,5-trimethoxybenzoate | 1574 | 1402 | 172 |

*Biological studies*: The biological properties of complexes of 3,4-dimethoxybenzoic acid and 3,4,5-trimethoxybenzoic acid were examined using the MTT cytotoxicity assay (Figs.3-4). The MTT test is a colorimetric assay used to assess the metabolic activity of cells [9]. NAD(P)H-dependent cellular oxidoreductase enzymes can, under certain conditions, reflect the number of viable cells present. These enzymes are capable of reducing the tetrazolium dye MTT (3-(4,5-dimethylthiazol-2-yl)-2,5-diphenyltetrazolium bromide) to its insoluble formazan, which has a purple color [10]. Subsequently, a solubilizing solution (sodium dodecyl sulfate in diluted hydrochloric acid) was added to dissolve the insoluble purple formazan into a colored solution. The absorbance of this colored solution can be quantified by measuring at a specific wavelength (typically between 500 and 600 nm). The degree of light absorption depends on the concentration of formazan accumulated inside and on the surface of the cell. The higher the concentration of formazan, the deeper the purple color, and consequently, the higher the absorbance [11].

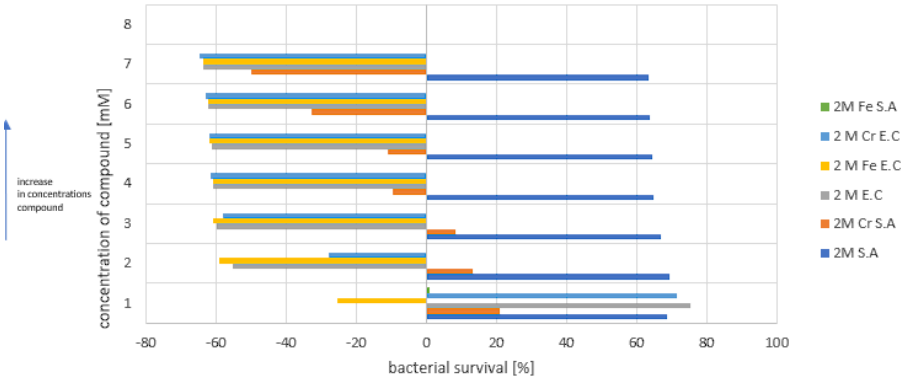



**Fig.3.** Graph of the dependence of the relative survival of bacteria from the species: *Staphylococcus aureus* (S.A) and *E.coli* (E.C) on the concentration of 3,4-dimethoxybenzoic acid (2M) and complexes in chromium(III) (2M Cr) and iron(III) (2M Fe).

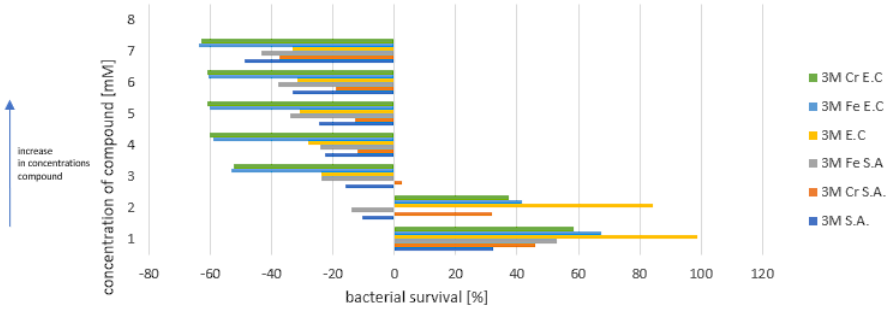



**Fig.4.** Graph of the dependence of the relative survival of bacteria from the species: Staphylococcus aureus (S.A) and E.coli (E.C) on the concentration of 3,4,5-trimethoxybenzoic acid (2M) and complexes in chromium(III) (3M Cr) and iron(III) (3M Fe).

The MTT test showed that chromium(III) 3,4,5-trimethoxybenzoate was the most toxic compound to *Staphylococcus aureus* cultures, while chromium(III) 3,4-dimethoxybenzoate was the most toxic to *Escherichia coli* bacteria. Ferric 3,4-dimethoxybenzoate showed the least toxicity to *Staphylococcus aureus*, while *Escherichia coli* bacteria were killed to the least extent after administration of 3,4,5-trimethoxybenzoic acid. When 3,4,5-trimethoxybenzoic acid was administered, it was more toxic to *Staphylococcus aureus* bacteria, while 3,4-dimethoxybenzoic acid killed or inhibited cellular metabolism to a greater extent in *Escherichia coli* bacteria. In the case of complexes of both acids, the 3,4,5-trimethoxybenzoic acid complexes were more toxic. Higher mortality compared to the control sample was observed for most complexes.

**Conclusions:** The experiments conducted and described in the study aimed to investigate the physicochemical and biological properties of 3,4-dimethoxybenzoic acid and 3,4,5-trimethoxybenzoic acid, as well as their complexes with iron(III) and chromium(III). Analysis of the FT-IR spectra of acids and complexes confirmed the occurrence of complexation reactions. It was determined that in the complexes of 3,4-dimethoxybenzoic acid, there is a bidentate chelating coordination type, while in the complexes of 3,4,5-trimethoxybenzoic acid, a bidentate bridging coordination type is present. The results of the MTT assay demonstrated increasing mortality of bacterial cultures with increasing concentrations of all tested compounds. The MTT assay revealed that the most toxic compound towards Staphylococcus aureus bacterial culture is chromium(III) 3,4,5-trimethoxybenzoate, whereas towards Escherichia coli bacteria, it is chromium(III) 3,4-dimethoxybenzoate. This study confirmed that both acids and their complexes with chromium and iron are cytotoxic, which may inhibit the metabolic activity of cells, leading to apoptosis.

**Acknowledgements:** This work financially supported by National Science Centre, Poland, under the research project number 2020/39/B/NZ9/01894.

**References:**

1. M.R. Dobbs, Clinical Neurotoxicology: Syndromes, Substances, Environments, Elsevier, 2009.
2. S.W. Shin, E. Jung, S. Kim, K.E. Lee, J.K. Youm, D. Park, Molecules, 18 (2013) 5405.

3. National Center for Biotechnology Information. PubChem Compound Summary for CID 8357, 3,4,5-Trimethoxybenzoic, 2023.
4. W. Ferenc, A. Walków-Dziewulska, J. Sarzynski, Journal of the Serbian Chemical Society, 70 (2005) 1075.
5. K. Burger, Coordination Chemistry: Experimental Methods, Butterworth, London 1973.
6. L.J. Bellamy, The Infrared Spectra of Complex Molecules, Springer, 2013.
7. G.B. Tolstorozhev, M.V. Belǫkov, I.V. Skornyakov, O.K. Bazyl, Journal of Applied Spectroscopy, 81 (2014) 109.
8. V. Bhatt, Chapter 3 - Isomerism in Coordination Complexes, Elsevier, 2016.
9. J.C. Stockert, R.W. Horobin, L.L. Colombo, A. Blázquez-Castro, Acta Histochemica, 120 (2018) 159.
10. G. Mahshid, T. Turnbull, S. Sebastian, I. Kempson, International Journal of Molecular Sciences, 22 (2021) 12827.
11. T.L. Riss, R.A. Moravec, A.L. Niles, S. Duellman, H.A. Benink, T.J. Worzella, L Minor, Assay Guidance Manual, Eli Lilly & Company and the National Center for Advancing Translational Sciences, Bethesda, 2023.

# APPLICATION OF FLAVONOID POTENTIAL FOR METAL COMPLEXING IN FOOD TECHNOLOGY AND NUTRITION

**A. GOLONKO[1,2], A. SZKLARUK[1], R. ŚWISŁOCKA[2,3], W. LEWANDOWSKI[2,3],**
[1]Clinical Research Centre, Medical University of Bialystok, M. Sklodowska 24 St., 15-950 Bialystok, Poland, [2]Professor Wacław Dąbrowski Institute of Agricultural and Food Biotechnology, Rakowiecka 36 St., 02-532 Warsaw, [3]Bialystok University of Technology, Faculty of Civil Engineering and Environmental Sciences, Department of Chemistry, Biology and Biotechnology, Wiejska 54E St., 15-351 Bialystok.

**Abstract:** Flavonoids, known for their antioxidative, anti-inflammatory, and anticancer properties, are being explored for innovative applications in food technology, particularly in food preservation and packaging. Recent studies highlight the potential of flavonoid/metal ion complexes to serve as antioxidant agents, capable of scavenging free radicals and enhancing the nutritional and sensory qualities of foods. The synthesis of biofunctional metal-phenolic films from dietary flavonoids like quercetin and myricetin has shown promising results in creating antimicrobial and antioxidative packaging films, demonstrating significant radical scavenging activity. These advances suggest the utility of flavonoids in enhancing food safety and quality, underscoring their role in developing sustainable food systems.

**Introduction:** Flavonoids represent a diverse and widespread class of naturally occurring polyphenolic compounds, primarily known for their significant presence in the plant kingdom. Structurally, these compounds are characterized by their 15-carbon skeleton, consisting of two phenyl rings and a heterocyclic ring, which collectively contribute to a wide range of biological activities. In food technology and nutrition, flavonoids have garnered attention due to their multifaceted roles, including their potential as natural antioxidants, their contribution to the sensory properties of foods, and their health-promoting effects [1]. The interest in flavonoids within the realm of food science and nutrition primarily stems from their antioxidant properties, which are crucial in combating oxidative stress in the human body. This oxidative stress is a contributing factor to various chronic diseases such as cardiovascular diseases, cancers, and neurodegenerative disorders. By scavenging free radicals and chelating metal ions, flavonoids help mitigate the damage caused by oxidative stress, underscoring their therapeutic potential [2]. Beyond their health benefits, flavonoids also play a pivotal role in the sensory characteristics of foods. They are responsible for a range of flavors, colors, and aromas in fruits, vegetables, and beverages such as tea, wine, and cocoa. These sensory properties not only enhance the appeal of food products but also contribute to food preservation by inhibiting microbial growth and oxidative spoilage [3]. In recent years, the interaction of flavonoids with metal ions has opened new avenues for research, particularly in enhancing the bioavailability and functionality of these compounds in food systems. The formation of flavonoid-metal complexes can alter their solubility, stability, and antioxidant capacity, which has implications for their use as functional food ingredients and in the development of novel food packaging and preservation technologies [4]. The ongoing research into

flavonoids underscores their importance in food technology and nutrition, highlighting their role not just as bioactive compounds that contribute to health, but also as key ingredients that can improve the quality and safety of food products. As our understanding of flavonoids continues to evolve, so too will their applications in creating healthier, more sustainable food systems [5].

**Discussion:** Flavonoids, as bioactive polyphenolic phytochemicals, have demonstrated a wide array of health benefits, including antioxidative, anti-inflammatory, and anticancer properties. Their ability to interact with metal ions enhances these properties, potentially leading to novel applications in food preservation, enhancement of nutritional value, and even in the development of new therapeutic strategies [2]. The bioavailability and biological activities of flavonoids in humans are influenced by their chemical structure. Over 5,000 flavonoid compounds have been identified, contributing to a wide range of functions in plants and, when consumed, offering health benefits to humans. These benefits are primarily attributed to their antioxidative properties, which can be significantly impacted by the interaction with metal ions [6]. Flavonoids are synthesized in all parts of plants and contribute to color, fragrance, and taste, affecting food quality parameters such as astringency, bitterness, sourness, sweetness, aroma, and color formation. The content and composition of flavonoids in food can vary widely, depending on the source and how the food is processed. Recent studies have explored the interaction between flavonoids and metal ions like iron(III), highlighting the potential of flavonoid/metal ion complexes to serve as antioxidant agents capable of scavenging free radicals. This interaction not only underscores the health-promoting aspects of flavonoids when included in the diet but also suggests their utility in creating biofunctional materials, such as cytoprotective and anti-inflammatory coatings for medical implants [4].

*Strategy to iron overload therapy:* Metal overload in the body, often resulting from excessive exposure to metals such as iron, copper, and lead, can lead to toxicity and various health issues. This condition can cause oxidative stress, organ damage, and increased risk of chronic diseases. Traditional treatments for metal overload include chelation therapy, which uses synthetic agents to bind metals and facilitate their excretion. However, these synthetic chelators often have side effects and may not be suitable for long-term use. Flavonoids can bind excess metal ions, reducing their bioavailability and mitigating the formation of harmful free radicals through Fenton reactions, which are chemical reactions producing oxidative stress. By chelating metal ions, flavonoids prevent these ions from participating in reactions that generate reactive oxygen species (ROS), thereby protecting cellular components from oxidative damage [7,8]. Additionally, flavonoids antioxidant properties further bolster cellular defense mechanisms against oxidative stress, enhancing the body's natural detoxification processes [8]. Buerkli et al. developed a natural polyphenol supplement, incorporating black tea powder, cocoa powder, and grape juice extract for its strong iron-chelating properties in vitro, aiming to reduce non-heme iron absorption in hereditary hemochromatosis patients. This multi-center, placebo-controlled trial demonstrated that the supplement significantly decreased dietary iron absorption by about 40%, suggesting a potential to lower body iron accumulation and reduce phlebotomy frequency in these patients. (clinicaltrials.gov under NCT03990181). One of main flavonoids in that mixture -quercetin's structure, specifically its catechol moiety in the B ring and multiple

free hydroxyl groups, facilitates its ability to chelate iron, forming complexes where iron is stabilized and becomes less prone to participate in pro-oxidant reactions [9].

*Complexing pro-oxidative metal ions in meat products:* Haemoproteins can accelerate peroxyl radical formation, impacting meat's oxidative stability. Variable valence metals like iron and copper catalyze lipid peroxidation, initiating and propagating oxidative damage in meat. Direct and indirect initiation mechanisms, including Fenton-type reactions and the interaction with haem and non-haem iron, lead to lipid peroxidation. Transition metals can initiate lipid peroxidation through various mechanisms presented in Table 1. Flavonoids can inhibit the catalytic activity of metals such as iron and copper, which are pivotal in the initiation and propagation of lipid peroxidation due to their variable valence and capability to participate in redox reactions as presented in Table 1.

**Table 1.** Mechanisms of meat preservation by flavonoids through chelation of metal ions.

| Mechanism | Description | Example | Ref. |
|---|---|---|---|
| PUFA radical formation | Flavonoids chelate Fe(III) or Cu(II), preventing PUFA radical formation by inhibiting electron transfer or $H^+$ evolution catalyzed by metals. | Inhibition of lipoxygenase reactions. | [10] |
| Superoxide anion ($O_2^{-}\cdot$) generation | By chelating transition metals, flavonoids reduce the formation of $O_2^{-}\cdot$ and subsequent ROS by interfering with metal-mediated reactions. | - | [10] |
| Oxygen activation via phospholipid flavin | Flavonoids prevent the oxidation of flavin cofactors by chelating metals, blocking the indirect oxygen activation and ROS generation. | - | [10] |
| Metal interaction with $O_2$ and peroxides | Chelation by flavonoids prevents metals from facilitating oxene transfer and forming reactive oxocations (e.g., $Fe^{5+} = O_2^{-}$). | Prevents cytochrome P450 from interacting with $O_2$ . | [10] |
| Fenton-type reaction prevention | Flavonoids chelate Fe(III), inhibiting hydroxyl radical formation via Fenton reactions, a direct initiation path of lipid peroxidation. | - | [11] |
| Hypervalent iron complex inhibition | The chelation of Fe(III) by flavonoids prevents the formation of hypervalent iron complexes that can initiate ROS generation. | Inhibits active hem proteins and porphyrin compound formation. | [12] |
| Iron-catalyzed degradation disruption | By chelating Fe(II/III), flavonoids disrupt the degradation of hydroperoxides to peroxyl radicals ($LOO\cdot$) and $H^+$ abstraction from unsaturated fatty acids. | Prevents the chain reaction in lipid peroxidation. | [12] |

Flavonoids, such as epigallocatechin gallate (EGCG) from green tea extract, rosmarinic acid from rosemary, and curcumin from turmeric extract, have been incorporated into various packaging materials to enhance the oxidative stability and extend the shelf life of meat products [10]. Studies have demonstrated the effectiveness of these flavonoid-enriched coatings and glazes in inhibiting lipid peroxidation, thereby preserving the quality and freshness of meat, fish, and poultry during storage [12].

*Foodborn pathogenes:* Flavonoid-metal nanoparticles, such as silver nanoparticles coated with hesperidin and pectin (HP-AgNPs), and those functionalized with kaempferol (KH-AgNPs), have shown promising antibacterial activities against foodborne pathogens like *Escherichia coli*. These nanoparticles exhibit enhanced antimicrobial properties by causing oxidative stress and damaging the cell walls of bacteria, which leads to their death. Gold nanoparticles coated with flavonoids, specifically chrysin, kaempferol, and quercetin, have shown promising antibacterial

properties against specific Gram-negative bacteria strains such as *E. coli*, *P. aeruginosa*, and *P. vulgaris*, with varying minimum inhibitory concentrations (MICs) indicating their potential efficacy in food safety applications [13]. Certain flavonoids complexed with copper and magnesium ions have emerged as noteworthy candidates due to their potent antibacterial properties against specific pathogens. The $Cu^{2+}$ complexes with flavonoids such as baicalin and naringin stand out for their enhanced antimicrobial activity. Baicalin, when complexed with $Cu^{2+}$, exhibits increased effectiveness against several bacterial strains, with Minimum Inhibitory Concentration (MIC) values in the range of $10^{-4}$ to $10^{-3}$ mol/L, surpassing the activity of the free ligand and showing greater potency than when complexed with $Al^{3+}$. Naringin, another flavonoid, forms a $Cu^{2+}$ complex that also shows moderate but significant increased antimicrobial activity compared to the flavonoid alone [14]. On the other hand, $Mg^{2+}$ complexes with flavonoids such as morin have been highlighted for their remarkable antibacterial properties. Specifically, $Mg^{2+}$ complexes with morin demonstrate significant activity against Micrococcus flavus and *Staphylococcus aureus*. This activity is notable because it opens the door to using such complexes in food preservation, where the safety of the metal ion is a critical consideration [14].

*Food colouring:* The importance of color in defining consumer expectations about food's organoleptic properties highlights the food industry's ongoing effort to enhance product appeal through color addition or improvement. Despite the rigorous safety assessments of coloring agents in the European Union, concerns over intolerance, allergies, or hyperactivity linked to their consumption have fueled a shift towards natural additives over artificial ones. The search for natural color alternatives has focused on chlorophylls, carotenoids, betalains, and notably flavonoids, with flavonols and anthocyanins emerging as prominent natural pigments providing a spectrum of colors from cream and yellow to red, blue, and black. Anthocyanins, already approved for use in the food sector (E163), exhibit pH-dependent color changes, offering stability and intense coloring, especially from sources like methylated grape anthocyanins. The exploration of flavonoids for natural food coloring predominantly centers on anthocyanins, investigating their stability enhancements through copigmentation, which involves noncovalent interactions with copigments or metal ions, leading to intensified color and stability. Their color variability with pH changes and interactions with metal ions enhances their applicability in food technology, providing stability and intensity modifications crucial for food aesthetics [14]. Flavonoids, sourced from plants like *Reseda luteola*, *Maclura tinctoria*, and *Genista tinctoria*, have been historically utilized as natural pigments due to their vibrant colors, derived from chromophores such as luteolin and apigenin. The addition of metal salts, flavonoid extracts induces a bathochromic shift in their absorption spectra, enhancing color intensity and stability, a method anciently applied in the creation of durable and vivid dyes. These flavonoid-metal complexes exhibit enhanced stability and adherence when used as mordants on fibers, where metal ions like $Al^{3+}$, $Fe^{3+}$, and $Cu^{2+}$ form bonds with fiber proteins, ensuring the pigment's resistance to degradation.

*Innovation in food packaging:* In the realm of food technology, particularly in the development of food packaging materials, the integration of flavonoid-metal complexes presents an innovative approach that harnesses both the antimicrobial and antioxidant properties of flavonoids. A notable example is synthesis of biofunctional metal-phenolic films from dietary flavonoids like quercetin, myricetin, luteolin, and fisetin. These films,

as reported by Bertleff-Zieschang et al. (2017), not only exhibit radical scavenging activity but also have the potential for applications within the pharmaceutical and food industries due to their ability to form thin, surface-bound films with particularly benefits in food packaging, contributing to the extension of food shelf life and improvement of food safety by protecting against oxidative damage and microbial contamination [4]. Furthermore, the general synthetic procedure for creating bioflavonoid-metal complexes, as outlined in research focused on the synthesis and characterization of such complexes, underscores the versatility and potential of these compounds in food technology. The use of flavonoids like dihydromyricetin (DHM) in combination with various metal ions (Zn, Cu, Fe) to form complexes highlights a methodological foundation for producing materials with enhanced biological, especially antioxidant activity [15].

**Conclusions:** The exploration of flavonoid-metal complexes in food technology opens new pathways for enhancing food preservation, packaging, and overall nutritional value. As research progresses, the focus will likely shift towards optimizing these complexes for broader application in food systems, including scalability and regulatory approval for safe use. Further investigations into the bioavailability and interaction mechanisms of these complexes within food matrices will enhance their practical application, promising a future where flavonoid-metal complexes play a central role in advancing food safety, quality, and health benefits.

**References:**

1. S. Ruiz- Cruz, S. Chaparro- Hernández, K.L. Hernández- Ruiz, L.A. Cira- Chávez, M.I. Estrada-Alvarado, L.E. GassosOrtega, J. de J. Ornelas- Paz, M.A.L. Mata, S. Ruiz- Cruz, S. Chaparro- Hernández, Flavonoids - From Biosynthesis to Human Health, IntechOpen, 2017.
2. M. Li, M. Qian, Q. Jiang, B. Tan, Y. Yin, X. Han, Antioxidants, 12 (2023) 527.
3. S.H. Hassanpour, A. Doroudi, Avicenna Journal of Phytomedicine, 13 (2023) 354.
4. N. Bertleff-Zieschang, M. Arifur Rahim, Y. Ju, J.A. Braunger, T. Suma, Y. Dai, S. Pan, F. Cavalieri, F. Caruso, Chemical Communications, 53 (2017) 1068.
5. N. Terahara, Natural Product Communications, 10 (2015) 1934578X1501000334.
6. E. Masson, Available online: https://www.em-consulte.com/article/1474138/antioxidant-properties-of-flavonoid-metal-complexe (accessed on 27 March 2024).
7. X. Wang, Y. Li, L. Han, J. Li, C. Liu, C. Sun, Frontiers in Cell and Developmental Biology, 9 (2021).
8. N.B. Rathod, N. Elabed, S. Punia, F. Ozogul, S.-K. Kim, J.M. Rocha, Plants, 12 (2023) 1217.
9. A. Scarano, B. Laddomada, F. Blando, S. De Santis, G. Verna, M. Chieppa, A. Santino, Antioxidants (Basel), 12 (2023) 630.
10. S.O. Yaman, A. Ayhanci, In Accenting Lipid Peroxidation, IntechOpen, 2021.
11. Z. Cheng, Y. Li, Chemical Reviews, 107 (2007) 748.
12. D.L. Gilbert, In Reactive Oxygen Species in Biological Systems: An Interdisciplinary Approach, Springer US, Boston, MA, 2002.
13. S. Sysak, B. Czarczynska-Goslinska, P. Szyk, T. Koczorowski, D.T. Mlynarczyk, W. Szczolko, R. Lesyk, T. Goslinski, Nanomaterials, 13 (2023) 1531.
14. M.M. Kasprzak, A. Erxleben, J. Ochocki, RSC Advances, 5 (2015) 45853.
15. Y. Yao, M. Zhang, L. He, Y. Wang, S. Chen, Frontiers in Chemistry, 8 (2020).

# AMYLASE INHIBITORY ACTIVITIES OF MATCHA TEA AQUEOUS EXTRACT

**M. SAMSONOWICZ, A. ANTONIUK, A. DOWBYSZ**, Bialystok University of Technology, Faculty of Civil Engineering and Environmental Sciences, Institute of Environmental Engineering, Department of Chemistry, Biology and Biotechnology, Wiejska 45E St., 15-351 Bialystok, Poland.

**Abstract:** Inhibition of α-amylase has a beneficial effect on the improvement of postprandial hyperglycemia. One of the ways to support the treatment of diabetes is the use of plant preparations. In this study, the inhibitory effect of Matcha tea extracts (depending on their country of origin: China or Japan) on α-amylase was explored by enzyme kinetics and spectroscopy approaches. For determination of the type of inhibition, the Lineweaver-Burk plot was depicted. The α-amylase inhibition assay was performed using the 3,5-dinitrosalicylic acid (DNS) method. Both aqueous extracts from Matcha from China and Japan were found to have inhibitory efficiency against α-amylase in mixed−type manners. The percentage inhibition at an extract concentration of 80 $mg_{d.w}$/ml was 41.77 and 47.69 % for Matcha from China and Japan, respectively.

**Introduction:** In recent years, there has been a significant increase in the incidence of diabetes. Diabetes prevention and treatment is an important public health problem. Chronic hyperglycemia caused by uncontrolled diabetes leads to serious damage to the heart, blood vessels and kidneys. Long-term excessive consumption of starchy foods is one of the causes of hyperglycemia [1]. Starch is catalytically digested by pancreatic α-amylase in the small intestine, producing reducing sugars such as maltose, maltotriose and dextrin, followed by being hydrolyzed to glucose by α-glucosidase. For this reason, both enzymes are considered crucial in the starch digestion process [2].

One of the effective ways to delay the increase in blood glucose levels (especially after a meal - postprandial hyperglycemia) is to reduce the rate of starch hydrolysis by inhibiting certain digestive enzymes by some drugs, which unfortunately also cause side effects (abdominal pain, nausea, vomiting, or diarrhea) [3]. Therefore, there is a constant increase in interest in plant extracts as a potential alternative to drugs, because some of them have been shown to have inhibitory effects on α-amylase and α-glucosidase [4].

Tea is one of the most widely consumed beverages in the world. It is valued primarily for its characteristic aroma and taste, as well as its health-promoting properties [5]. Tea is made from the leaf of *Camellia sinensis*, and its types depend on processing or harvested leaf development (black – fermented, green – non-fermented, and oolong – semi-fermented). Matcha is a powdered green tea made from tencha leaves that is grown, processed, and prepared differently than other teas. Traditionally, the bushes are covered with bamboo mats about 20-30 days before harvesting to protect the leaves from too strong direct sunlight [6]. In such conditions, the plant produces higher amounts of bioactive compounds, including polyphenols, amino acids, chlorophyll and theanine [5,7]. The aim of the study is to determine the α-amylase inhibitory activities of Matcha tea aqueous extracts from China and Japan and the type of inhibition caused by the presence of the extracts.

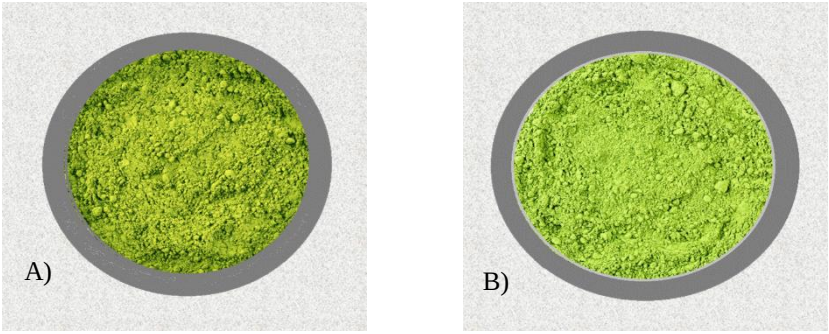



**Fig.1.** Powdered Matcha from A) China, B) Japan.

**Experimental:** Preparation of extracts: The research material consisted of two powdered Matcha green teas from China and Japan, commercially available on the market. In order to obtain the tested extracts, the simple extraction method was used. The extract was prepared by adding 150 mL of deionized water at 80 ℃ to 2 g of Matcha powder and then shaking at the same temperature for 30 min with the use of the shaking incubator (KS 3000 ic control IKA). The samples were then centrifuged at 3000 rpm for 10 minutes using a laboratory centrifuge (MPW-251, MPW Med. Instruments). The obtained extracts were transferred to a round-bottomed flask and concentrated in a vacuum evaporator at 40 °C to a volume of 25 ml. The test samples contained 80 mg of raw material in 1 mL. The process of extraction was made in triplicate for each tea.

GC/MS analysis: Gas chromatography to mass spectrometry (Agilent GC/MS Triple Quad 7000C) was used for the determination of phenolic compounds in Matcha tea extracts. The HP-5MS capillary column (polydimethylsiloxane with 5% phenyl groups) with dimensions of 30 m x 0.25 mm and film thickness of 0.25 µm was used. 1 mL of the concentrated aqueous extract was extracted three times for 15 minutes with ethyl acetate, using 2 mL of the solvent for each extraction. The obtained extracts were combined, dried by adding anhydrous sodium sulfate, and then evaporated to dryness at 35 $^{o}$C. The dry residue after extraction was derivatized by adding 220 µL of anhydrous pyridine and 80 µL of bis-trimethylsilane-trifluoroacetamide, and then the mixture was heated at 80 $^{o}$C for 60 minutes. The identification was done on the basis of retention time and chromatograms of standard substances from the NIST mass spectra database.

α-amylase inhibition assay: The α-amylase inhibitory ability of the tested extracts was assessed using the 3,5-dinitrosalicylic acid (DNS) test described in [8] with some modifications. The test is based on measuring the absorbance of the sample under the influence of the action α-amylase enzyme releasing maltose from starch. Maltose is a reducing sugar and can be detected using DNS, which is converted into 3-amino-5-nitrosalicylic acid, orange in color, which strongly absorbs light in the wavelength range from 450 to 540 nm. The intensity of the color depends on the amount of reducing sugars released during the action of the enzymes [8]. The stronger the enzyme inhibition ability of the tested extract, the lower the absorbance of the sample after adding DNS.

The 400 µL of water extract was incubated with 500 µL of an α-amylase (from *Aspergillus oryzae*, Sigma-Aldrich) solution (enzyme solution (2 units/mL) and 500 µL of phosphate buffer (PB) solution (0.02 M; pH = 6.9) for 10 min at ambient temperature.

Then 500 µL of 1% starch solution was added and incubated at the same temperature for 5 min. 1.5 ml of DNS was further added to stop the reaction and after that, the reaction mixture was incubated in a water bath at 100 °C for 10 min. Then it was cooled and topped up with water to 10 ml. Absorbance was measured at 530 nm in the spectrophotometer (NANOCOLOR VIS, Macherey-Nagel). The inhibition percentage of α-amylase was assessed by the following formula: Inhibition (%) = [(Ac−As)/Ac] x 100%, where: Ac - absorbance of the control sample, As - absorbance of the analyzed sample. Microsoft Excel 2013 was used to perform statistical analysis. All determinations were performed in at least three repetitions. The results were expressed as the mean value ± SD (standard deviation). The Michaelis-Menten kinetic model: $v = \frac{V_{max}\ [S]}{K_m + [S]}$ was used to evaluate the effect of Matcha tea on starch hydrolysis catalyzed by α-amylase (where $V_{max}$ is the maximal velocity, $[S]$ is the substrate concentration, and $K_m$ is the Michaelis-Menten constant). Whereas the Lineweaver – Burk plot was used for determining the type of α-amylase inhibition.

**Results:** The results of testing the inhibitory activity of Matcha tea extracts are presented in Table 1. The obtained results indicate that the extracts (in the analyzed concentrations) inhibit α-amylase by 41.77 and 47.69%, for Matcha from China and Japan, respectively. The results for other green teas indicate that the degree of α-amylase inhibition depended on the concentration and origin of the enzyme, the concentration and type of substrate, and the reaction conditions (pH, T, reaction time).

**Table 1.** Kinetic parameters of α-amylase in the presence and absence of inhibitor and percentage of inhibition.

| Plant material (origin) | Inhibition* [%] | $K_M$ [mg/mL] no inhibitor | $K_M$ [mg/mL] with inhibitor | $V_{max}$ [µmol/min] no inhibitor | $V_{max}$ [µmol/min] with inhibitor | Type of inhibition |
|---|---|---|---|---|---|---|
| Matcha (China) | 41.77±6.35 | 0.238±0.015 | 0.354±0.023 | 0.578±0.034 | 0.582±0.042 | competitive |
| Matcha (Japan) | 47.69±2.35 | 0.238±0.015 | 0.347±0.041 | 0.578±0.034 | 0.602±0.024 | competitive |

*At 80 mg/mL

The chromatographic analysis showed that both teas contain large amounts of catechins: gallocatechin (GC), epigallocatechin (EGC), epicatechin (EC), epicatechin gallate (ECG), and epigallocatechin gallate (EGCG). Many studies show that the presence of catechins in green teas, including Matcha, influences the inhibitory activity of extracts towards amylase (Fig.1). It is suggested, that this is due to hydrogen bonds formed between the hydroxyl groups of catechins and the catalytic residues of the binding site and the formation of a conjugated π system, which stabilizes the interaction with the active site of the enzyme [9].

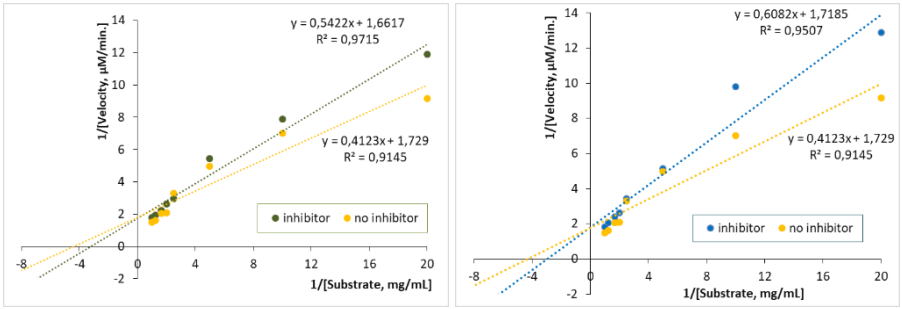



**Fig.2.** α-Amylase inhibition kinetics study using Lineweaver–Burk plots a) Matcha extract from Japan, b) Matcha extract from China.

The Lineweaver-Burk plots were used to determine the type of α-amylase inhibition by Matcha extracts and to determine the kinetic parameters shown in Figure 2. The $K_m$ and $V_{max}$ values for the reaction catalyzed by α-amylase in the presence and absence of the inhibitor are summarized in Table 1. It was found that for reactions in the presence of extracts, the $K_m$ values are significantly higher, while the $V_{max}$ values are similar (increased slightly). The results indicate competitive inhibition of α-amylase by Matcha extracts. According to the literature, some components of the extracts may act as competitive (EGCG) [11], non-competitive (EC, catechin gallate, catechin) [12], or mixed inhibitors (EGC) [11].

**Conclusions:** In the presented work, a spectroscopic method was used to analyze the possibility of using Matcha extracts to inhibit the activity of α-amylase, which is an important enzyme in hyperglycemia. The research demonstrated that aqueous extracts from Matcha tea from China and Japan did not differ significantly due to the inhibition of α-amylase activity. Both extracts (in the analyzed concentrations) showed inhibitory effects. The determined kinetic parameters indicate a competitive type of inhibition caused by the presence of Matcha extracts. The chromatographic analysis showed the presence of a number of compounds in the extracts, especially from the catechin group, with the potential to inhibit α-amylase activity. This suggests the use of Matcha extract as a natural inhibitor for glycemic control.

**Acknowledgements:** The research was carried out as part of work W/WB-IIŚ/2/2023 at the Department of Chemistry, Biology and Biotechnology of the Białystok University of Technology and financed from the subsidy 2024 provided by the Minister of Science and Higher Education.

**References:**

1. E. Studzińska-Sroka, I. Czapska-Pietrzak, W. Bylka, Acta Poloniae Pharmaceutica - Drug Research, 76 (2019) 1037.
2. L. Suna, M. ing Miaob, Critical Reviews in Food Science and Nutrition, 60 (2020) 541.
3. M. Yilmazer-Musa, A. M. Griffith, A. J. Michels, E. Schneider, B. Frei, Journal of Agricultural and Food Chemistry, 60 (2012) 8924.
4. M. Miao, B. Jiang, H. Jiang, T. Zhang, X. Li, Food Chemistry, 186 (2015) 20.

5. K. Jakubczyk, J. Kochman, A. Kwiatkowska, J. Kałduńska, K. Dec, D. Kawczuga, K. Janda, Foods. 9 (2020) 483.
6. S. Farooq, A. Sehgal, Current Research in Nutrition and Food Science Journal, 6 (2018) 35.
7. E. Nishitani, Y.M. Sagesaka, Journal of Food Composition and Analysis, 17 (2004) 675.
8. P. Bernfeld, Amylase α and β. Methods in Enzymology, 1 (1955) 149.
9. J. Xiao, X. Ni, G. Kai, X. Chen, Critical Reviews in Food Science and Nutrition, 53 (2013) 497.
10. R.Z. Cer, U. Mudunuri, R. Stephens, F.J. Lebeda, Nucleic Acids Research, 37 (2009) 441.
11. L. Sun, F.J. Warren, G. Netzel, M.J. Gidley, Journal of Functional Foods, 26 (2016) 144.
12. Y. Hara, M. Honda, Agricultural and Biological Chemistry, 54 (1990) 1939.

# FUNCTIONALIZATION OF ZEOLITE WITH CELLULOSE ETHERS OF DIFFERENT IONIC NATURE

**U. MACIOŁEK[1], J. MATUSIAK[2], E. GRZĄDKA[1], W. FRANUS[2]**, [1]Maria Curie-Sklodowska University, Institute of Chemical Sciences, Faculty of Chemistry, M. Curie-Sklodowska Sq. 3, 20-031 Lublin, Poland, [2]Lublin University of Technology, Department of Construction Materials Engineering and Geoengineering, Faculty of Civil Engineering and Architecture, Nadbystrzycka 40, 20-618 Lublin, Poland.

**Abstract:** New hybrid materials containing zeolite and different polymers (anionic carboxymethyl cellulose and cationic cellulose) were obtained. The alterations in the surface composition and chemical bonding within the materials (zeolite/cationic or anionic polymer) were assessed *via* Fourier-Transform Infrared Spectroscopy (FT-IR) and powder X-ray diffraction (XRD), while some additional insights into textural properties, surface morphology, and composition were analyzed using SEM and BET, respectively.

**Introduction:** Zeolites are microporous crystalline aluminosilicates with a three-dimensional framework structure consisting of $AlO_4$ and $SiO_4$ tetrahedra linked by shared oxygen atoms (T-O-T bridges). Their structures contain interconnected channels and cavities (typically 2.5-10 Å) with exchangeable cations and $H_2O$ molecules [1-6]. Cellulose ethers are water-soluble derivatives of cellulose that are widely applied in different branches of industry, for example in construction materials production, food and pharmaceutics. Among them, anionic carboxymethylcellulose and cationic cellulose can be mentioned. Developing composite or hybrid materials of zeolites and polymers is an important step towards obtaining new materials with enhanced properties and applications, which can contribute to the advancement of industrial technologies, environmental protection, and sustainable development. Considering this combination of two components, that are widely recognized as safe for the mankind and environment, is the first step for sustainable materials.

**Experimental:** All the chemicals were of analytical grade and were used without further purification. Cationic cellulose (CC) was purchased from DOW. Sodium carboxymethyl cellulose (CMC) was purchased from Sigma-Aldrich. Zeolite was obtained following the general procedure by Panek et al. [7]. The hybrid materials were obtained by adsorptive modification of Na-X zeolite with the high concentration of CC or CMC (2000 ppm). To separate the solid and liquid phases the samples were centrifuged. White powders obtained in such a way were dried (24 h, 70˚C) and ground in the mortar. Scanning electron microscopy (SEM, Quanta 3D FEG, FEI) was used to analyze the morphology of the sample. The applied voltage was 5 kV. The obtained hybrid materials were characterized using low temperature adsorption/desorption of nitrogen (ASAP 2420, Micrometrics). The samples were degassed under vacuum at 80°C for 24 hours. Powder diffraction data were collected at room temperature employing an Empyrean diffractometer equipped with a PIXcel3D detector (PANalytical, Netherlands), utilizing monochromated Co-Kα radiation (λ = 1.54184 Å). The infrared spectra in the

transmission mode using KBr pressed discs were acquired using a Nicolet 8700 FT-IR/NXR (Thermo Scientific) in the range of 4000–400 $cm^{-1}$. 64 scans were averaged for each spectrum. The baseline corrections were applied.

**Results:** Figure 1 presents the SEM micrographs of the studied hybrid materials and micrograph of native zeolite particles. As indicated by the presented micrographs, the surface of zeolite was coated with polymers as a result of their adsorption.

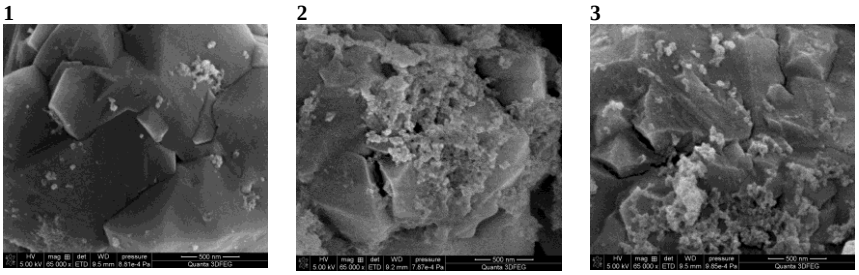



**Fig.1.** Scanning electron microscope micrographs depict: **1** zeolite, **2** zeolite/cationic polymer hybrid material, **3** zeolite/anionic polymer hybrid material. Magnification: 65000x.

The XRD pattern analyses for both the native zeolite and the hybrid material samples are depicted in Fig.2. The results illustrated in Fig.2 demonstrate that all the materials are highly crystalline solids, along with the clearly resolved reflections. These observations validate the existence of well-ordered zeolite structures. No notable alterations were detected in the characteristic reflections of the matrices following the polymer modification. This observation suggests that these materials maintain their initial structure and crystalline arrangement.

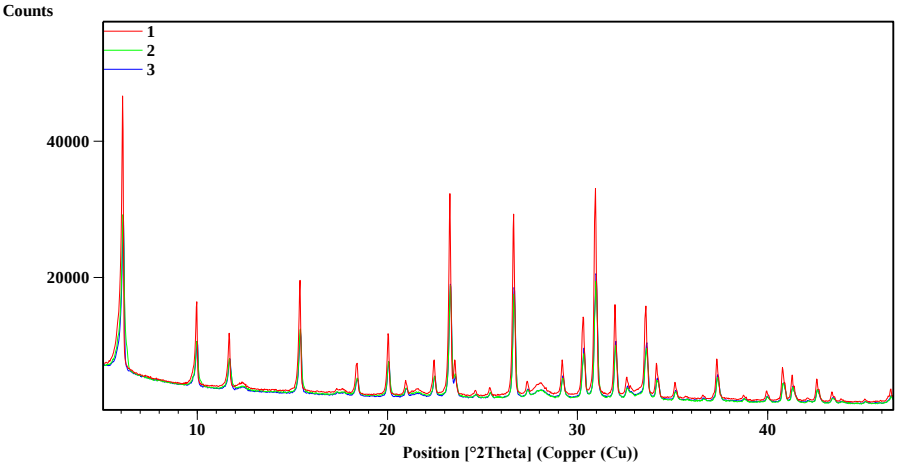



**Fig.2.** XRD patterns of the: **1** zeolite, **2** zeolite/cationic polymer and **3** zeolite/anionic polymer hybrid materials.

The FT-IR spectra of pure zeolite as well as hybrid materials, are shown in Fig.3. Comparing the FT-IR spectra of zeolite **1** and hybrid materials **2**, **3** can indicate that the modified zeolites maintain the spectral profile of the native zeolite. The FT-IR spectra of the hybrid materials exhibit new absorption bands in the range of 3000 – 2800 $cm^{-1}$ (C-H stretching vibrational modes in the D-glucose units and alkyl -$CH_2$ groups of the cellulose derivatives) and 1500 – 1200 $cm^{-1}$ (bending modes as well as the ether C-O-C stretch and the scissoring of the $N^+$-$CH_3$ moiety) [8]. The spectral data confirm the adsorption of anionic carboxymethyl cellulose and cationic cellulose, suggesting their predominant adsorption on the outer surface of zeolite.

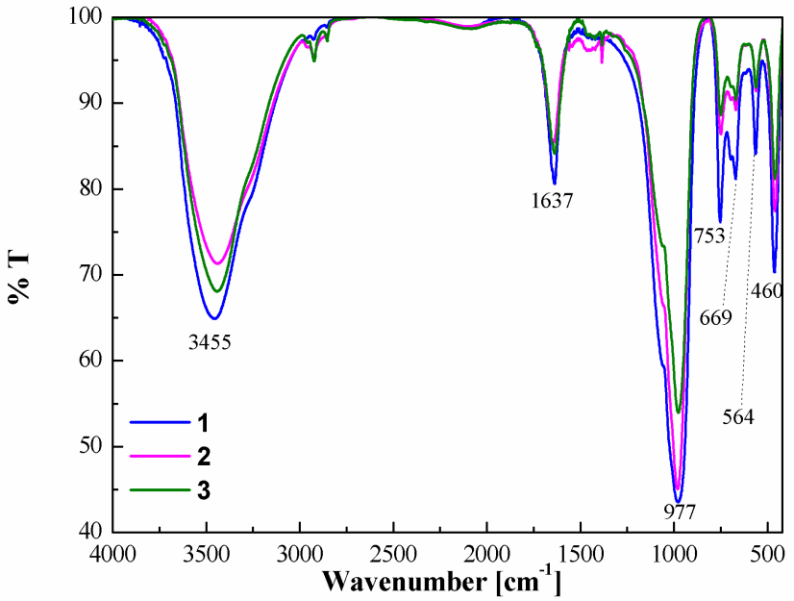



**Fig.3.** Comparison of the **1** zeolite FT-IR spectra with the **2** zeolite/cationic polymer and **3** zeolite/anionic polymer hybrid materials.

Table 1 shows that both the starting material and the hybrid ones are characterized by a highly microporous structure, with the percentage of micropores in the total surface area ($S_{BET}$) about 90.4% for **1** and 91.5% for **2** and **3** materials. The percentage of micropores in the total volume is 72.7% for **1**, 80.0% for **2**, and 80.9% for **3**. The analysis of these data indicates that the polysaccharides adsorption occurs primarily on the outer surface of the matrix. The data in Table 1 reveal that in the **2** hybrid material, the initial micropore surface area and volume remain unoccupied and unfilled, whereas in the **3** sample, a slight increase in these parameters as well as the total surface area ($S_{BET}$) can be observed. This may be attributed to the intrinsic porosity of microcrystalline carboxymethyl cellulose adsorbed on the external zeolite surface. This is an evidence that the micropores in the zeolite are not involved in the sorption of the polymers. Therefore, the adsorption of cationic cellulose and carboxymethyl cellulose was limited to the external surface area of the zeolite. The presented data indicate that the size of the polysaccharide macromolecules was large enough, to prevent them from penetrating the zeolite framework.

**Table 1.** The surface properties of the **1** zeolite and the **2, 3** hybrid materials determined from the nitrogen adsorption-desorption isotherms at -196 °C. SD lower than 4%.

| Sample | $S_{BET}$ [$m^2/g$] | t-Plot micropore area [$m^2/g$] | t-Plot external surface area [$m^2/g$] | Mesopore Diameter, dp= $4Vp/S_{BET}$ [nm] | Mesopore Diameter, dp, BJH(Ads) [nm] | Mesopores Diameter, dp, BJH (Des) [nm] | Vp, volume of pore/micropore*, [$cm^3/g$] |
|---|---|---|---|---|---|---|---|
| **1** | 447.5 | 404.4 | 43.0 | 1.93 | 7.54 | 6.92 | 0.22/0.16* |
| **2** | 442.3 | 404.8 | 37.5 | 1.84 | 6.85 | 6.04 | 0.20/0.16* |
| **3** | 462.5 | 423.2 | 39.2 | 1.85 | 7.11 | 5.97 | 0.21/0.17* |

The analysis of the FT-IR spectra (Fig.3) shows that the interactions between the zeolite and the anionic and cationic polymers occur in the studied system, leading to formation of polymer-zeolite materials. The electrostatic interactions between the anionic polymer and the negatively charged zeolite surface hinder the formation of the polymer-zeolite materials due to the charge repulsion effect. As a result, the adsorption of this polymer onto the mineral matrix occurs primarily through a weak hydrogen bonding and hydrophobic interactions.

In contrast, cationic cellulose can be readily adsorbed onto the negatively charged surface of zeolite. The electrostatic attraction occurs between the polymer and zeolite surface groups. It can be also assumed that the adsorption process is electrostatic in nature. Furthermore, the FT-IR spectra indicate different sorption mechanisms of these two polymers on the zeolite surface, depending on their character (Fig.3). A characteristic feature of the **3** spectrum is a marked decrease in the intensity of the absorption bands at 977 $cm^{-1}$ and in the 800 – 400 $cm^{-1}$ region, which are associated with the valence and deformation vibrations of the T-O-T bridges (Fig. 3). A progressive reduction in the water content was also observed in the **3** and **2** spectra (indicated by a relative decrease in the intensity of the -OH group at ~3340 and ~1644 $cm^{-1}$) (Fig.3).

**Conclusions:** In this study, two zeolite composite/hybrid materials with cellulose derivatives of different ionic nature were examined. The FT-IR method demonstrated that both anionic and cationic polymers adsorb onto the surface of zeolite, although through entirely different mechanisms. The development of such materials was further confirmed by the results of SEM and BET measurements.

## References:

1. M. Tatič, B. Držaj, Studies in Surface Science and Catalysis, Elsevier, Netherlands, 1985.
2. D.W. Breck, Zeolite Molecular Sieves: Structure, Chemistry and Uses, Wiley, New York, 1974.
3. F. Akhtar, L. Andersson, S. Ogunwumi, N.Hedin, L. Bergström, Journal of the European Ceramic Society, 34 (2014) 1643.
4. R. M. Barrer, Studies in Surface Science and Catalysis, Elsevier, Netherlands, 1988.
5. M. Anbia, F. Bandarchian, Journal of Applied Chemical Research, 9 (2015) 71.
6. N. Öztürk, S. Bahçeli, Journal of Science and Technology, 13 (2020) 1042.
7. R. Panek, J. Madej, L. Bandura, G. Słowik, Materials, 14 (2021) 1413.
8. M. Zaman, H. Xiao, F. Chibante, Y. Ni, Carbohydrate Polymers, 89 (2012) 163.

# SYNTHESIS, SPECTRAL CHARACTERIZATION, AND FLUORESCENT PROPERTIES IN THE SOLID STATE AND SOLUTION OF DYSPROSIUM(III) IONS COMPLEX WITH NALIDIXIC ACID

**M. KOSIŃSKA-PEZDA[1], U. MACIOŁEK[2], A. NOWICKA[2], M. DREWNIAK[2],**
[1]Rzeszow University of Technology, Faculty of Chemistry, Department of Inorganic and Analytical Chemistry, Powstańców Warszawy Ave. 6, 35-959 Rzeszów, Poland, [2]Maria Curie-Sklodowska University, Institute of Chemical Sciences, Faculty of Chemistry, Analytical Laboratory, M. Curie-Sklodowska Sq. 3, 20-031 Lublin, Poland.

**Abstract:** A new solid dysprosium complex with nalidixic acid (HNal) was synthesized and characterized using various techniques, including elemental analysis, XRF, complexometric titration, gravimetric analysis, molar conductivity, solubility measurements, powder X-Ray diffraction, UV-Vis spectroscopy, and infrared (FT-IR) spectroscopy. Additionally, its luminescent properties were investigated both in the solid state and solutions.

**Introduction:** Lanthanides attract much attention mostly due to their luminescent properties which make them useful for wide applications in light emitting diodes (OLEDs), liquid crystal, fluoroimmunoassays, biophysics, laser technology, optical telecommunication systems, and as MRI contrast agents in medical diagnosis and therapy, biomarkers for immunoassays, photodynamic therapy (PDT), bioimaging and multimodal imaging agents [1]. However, the application of lanthanide-based luminescence has two serious drawbacks. Firstly, free Ln(III) has small extinction coefficients due to the f–f electron transitions which are forbidden and result in insignificant luminescence intensity. Secondly, non-radiative O–H oscillators, such as water deactivate their excited states efficiently [1]. Therefore, it is necessary to sensitize the lanthanide ions with chelating organic chromophores [1]. Nalidixic acid is a compound suitable for the starting material in the synthesis of complexes with lanthanide ions characterized by proper fluorescence. Due to the presence of functional groups (–COOH, C=O), it can act as a monodentate, bidentate or even tridentate ligand. Furthermore, it can coordinate metal ions creating systems similar to those that form diketones with Ln(III) ions and which are one of the most effective luminescence sensitizers for lanthanides [2].

**Experimental:** The solid-state complex was obtained at $c_{Dy}$:$c_{NaNal}$ = 1:3 (where: $c_{Dy}$, $c_{NaNal}$ – the molar concentrations of dysprosium ion and sodium nalidixate, respectively). 100 ml of the aqueous solution of dysprosium chloride (0.01 mol $dm^{-3}$) was heated to 40 °C. Then 300 ml of the heated solution of sodium nalidixate (0.01 mol $dm^{-3}$) heated at 40 °C was added while stirring continuously. The reaction mixture was stirred for 1 hour at 40 °C. After 24 hours, the obtained precipitate was centrifuged, washed with distilled water several times up to the elimination of chloride ions (qualitative test with the $AgNO_3$ solution) and air-dried at room temperature. The metal content was determined using the ED XRF method with an Epsilon 5 instrument (PANalytical, The Netherlands).

Carbon, nitrogen, and hydrogen were determined by the microanalytical procedures with the EuroEA3000 Elemental Analyser (EuroVector). To determine the hydration water content, the gravimetric method was employed. The XRPD patterns of nalidixic acid and the studied compound were recorded using the Empyrean diffractometer (PANalytical, The Netherlands). UV–Vis spectra of nalidixic acid and the obtained complex were recorded using the V-670 UV–VIS-NIR dual beam spectrophotometer (Jasco, Japan). Infrared spectra were obtained by means of the Nicolet 8700 FTIR/NXR 9650 with the Smart Orbit™ diamond ATR attachment. Fluorescence spectra were obtained at room temperature applying the Hitachi F-2700 fluorescence spectrophotometer. Solubility at 20 °C was studied by means of the saturation solubility technique and spectrophotometry. Molar conductance was measured at room temperature using the SevenCompact Duo S213-meter with the InLab 731-ISM conductivity sensor (Mettler Toledo).

**Results:** The complex was obtained as hydrate and the experimental data are in good agreement with those calculated based on the molecular formula proposed as $[Dy(Nal)_3]\cdot 5.5H_2O$ (where: Nal = $C_{12}H_{11}N_2O_3$) (Table 1).

**Table 1.** Results of XRF, elemental and gravimetric analyses, molecular conductance and solubility of $[Dy(Nal)_3]\cdot 5.5H_2O$.

| Content/% found (calculated) | | Solubility | | | |
|---|---|---|---|---|---|
| Tb | 17.20 (17.01) | in methanol | | in water | |
| C | 45.46 (45.26) | mg $cm^{-3}$ | mol $dm^{-3}$ | μg $cm^{-3}$ | mol $dm^{-3}$ |
| H | 5.14 (4.64) | 63.3 | $6.6\cdot10^{-2}$ | 40 | $4.6\cdot10^{-5}$ |
| N | 9.09 (8.80) | Molar conductance/ $\Omega^{-1}cm^2mol^{-1}$ | | | |
| $H_2O$ | 10.48 (10.37) | 3 | | | |

The quantified solubility data revealed that the dysprosium complex exhibits high solubility in methanol, but only slight solubility in water. Morover, the complex demonstrates significantly enhanced solubility in methanol compared to free nalidixic acid (1.05 mg $cm^{-3}$). Conversely, its solubility in water is notably improved compared to free nalidixic acid (20 μg $cm^{-1}$).

Additionally, the comparison of X-ray diffraction patterns between the free ligand and the synthesized product (Fig.1) indicates clearly substantial differences, confirming the effective synthesis of a new phase distinct from nalidixic acid.

The UV–Vis spectra of nalidixic acid (Fig.2) show two characteristic absorption bands: one between 280 and 370 nm (designated as band I) and another between 240 and 280 nm (designated as band II). Band I originates from an $n \rightarrow \pi^*$ electronic transition, while intense absorption band II is attributed to the $\pi \rightarrow \pi^*$ transition of the aromatic ring [3]. The UV-Vis spectra of the complex exhibit also two prominent absorption bands, resembling closely those of nalidixic acid. Regardless of the solvent, band II exhibits a minimal shift compared to the spectra of nalidixic acid. However, it is noteworthy that the longest wavelength maximum exhibits a slight red shift in the electronic spectra of the Dy(III) complex compared to the free ligand ones. This alteration suggests the involvement of both the carboxylate group and the ketone group of the organic ligand in the complexation process with Ln(III) ions.

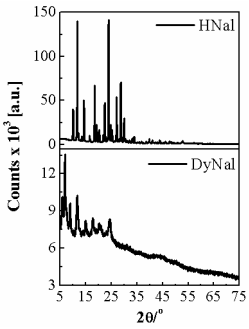



**Fig.1.** XRPD patterns of HNal and DyNal.

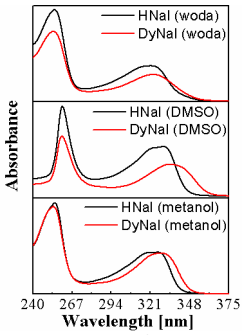



**Fig.2.** UV–VIS spectra of HNal and DyNal.

The most significant bands in the infrared spectra of nalidixic acid and the Dy(III) complex, along with their respective assignments are summarized in Table 2.

**Table 2.** The most characteristic bands (in $cm^{-1}$) in the infrared spectra of HNal, NaNal, and DyNal.

| Compound | Asignments | | | | | | | | |
|---|---|---|---|---|---|---|---|---|---|
| | $\nu_{O-H}$ ($H_2O$) | $\nu_{O-H}$ (-COOH) | $\nu_{C=O}$ (-COOH) | $\nu_{C=O}$ | $\nu_{as(COO^-)}$ | $\nu_{s(COO^-)}$ | $\Delta\nu = \nu_{as(COO^-)} - \nu_{s(COO^-)}$ | $\pi_{O-H}$ (-COOH) | $\nu_{(M-O)}$ |
| HNal | - | 2800–2200 | 1708 | 1647 | - | - | - | 971 | - |
| NaNal | 3700–3100 | - | - | 1668 | 1574 | 1386 | 188 | - | |
| DyNal | 3700–3100 | - | - | 1641 | 1567 | 1390 | 177 | - | 560, 433 |

In comparison with the spectrum of nalidixic acid, a new band of significant intensity appears in the spectrum of the obtained complex in the range of 3700–3100 $cm^{-1}$. This band is characteristic of the OH stretching vibrations in water molecules.

Instead of the stretching vibration band of the carbonyl group in the carboxyl group, the spectra of NaNal and DyNal exhibit two new, intense bands originating from the asymmetric and symmetric stretching vibrations of the $COO^-$ group. The data presented in Table 2 show that the Δν value for the tested complex is lower than that for NaNal. Based on the commonly used spectroscopic criteria, it can be inferred that in the obtained compound, the ligands coordinate the Dy(III) ions through a bidentate bridging carboxylate group [4]. The position of the band corresponding to the stretching vibrations of the carbonyl group of the pyridone moiety of the ligand also changed; in the spectrum of the complex, it is shifted towards lower wavenumbers. This shift confirms the participation of this group in the coordination of metal ions [5]. The overall changes in the FT-IR spectrum suggest that the nalidixate ions in the obtained lanthanide complexes behave like the chelato-bridging mode ligands, binding to the metal ions through the pyridine oxygen and one of the carboxylate oxygens, while the second carboxylate oxygen forms a bridge with another Ln(III) ion. Additionally, the coordination of lanthanide ions by two functional groups of the ligand is confirmed by the appearance of two new bands of medium intensity in the low-frequency range.

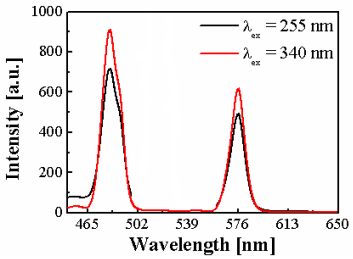



**Fig.3.** Emission spectra of solid DyNal.

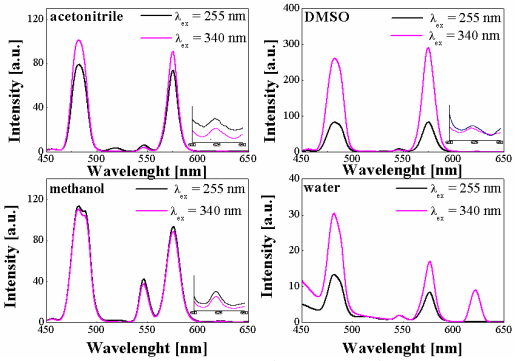



**Fig.4.** Emission spectra of solutions of DyNal.

For the solid dysprosium complex, the emission spectrum (Fig.3) shows two distinct emission peaks at the excitation 255 nm or 340 nm located at 481 and 576 nm, corresponding to the characteristic blue and yellow emission transitions $^4F_{9/2} \rightarrow {}^6H_J$ (J = 15/2, 13/2) of Dy(III) ion, respectively [6]. The fluorescence properties of DyNal in solution (Fig.4) depend largely on the both solvent and the excitation wavelength. It could be seen that in the solution not only the strongest emission peaks at 482 and 575 nm are present, but also other emission peaks occur apart from those observed in the spectrum registered in the solid state. The fluorescence intensities of DyNal at the most effective excitation wavelength decreased in the following order: DMSO > $CH_3OH$ > $CH_3CN$ > $H_2O$.

**Conclusions:** As a result of the synthesis, there was obtained a compound with the composition $[Dy(C_{12}H_{11}N_2O_3)_3]\cdot 5.5H_2O$. Spectroscopic methods confirmed the participation of both the carboxylate group of the nalidixic acid anion and the carbonyl group of the pyridone moiety in the coordination of Dy(III) ions. Emission spectra of the complex in both solid-state and solutions confirmed the presence of emission bands characteristic of dysprosium(III) ions, indicating the fluorescent properties of the newly obtained complex with potential applications.

**Acknowledgements:** The research was carried out using the apparatus maintained based on the project INFRASTARt.

**References:**

1. Z.A. Taha, A.M. Ajlouni, K.A. Al-Hassan, A.K. Hijazi, A.B. Faiq, Spectrochimica Acta a Molecular and Biomolecular Spectroscopy, 81 (2011) 317.
2. H.-F. Li, G.-M. Li, P. Chen, W.-B. Sun, P.-F. Yan, Spectrochimica Acta a Molecular and Biomolecular Spectroscopy, 97 (2012) 197.
3. U. Neugebauer, A. Szeghalmi, M. Schmitt, W. Kiefer, J. Popp, U. Holzgrabe, Spectrochimica Acta a Molecular and Biomolecular Spectroscopy, 61 (2005) 1505.
3. F. Arjmand, I. Yousuf, T. ben Hadda, L. Toupet, European Journal of Medicinal Chemistry, 81 (2014) 76.
4. K. Nakamoto, Infrared and Raman Spectra of Inorganic and Coordination Compounds, 4th ed., John Wiley & Sons, 1986.
5. M. Bashir, I. Yousuf, C.P. Prasad, Spectrochimica Acta a Molecular and Biomolecular Spectroscopy, 271 (2022) 120910.

# OPTIMIZATION OF TOTAL COST OF MANUFACTURING OF CLOVE BUDS $scCO_2$ EXTRACTS

**K. TYŚKIEWICZ[1], M. GRUBA[1], M. KONDRACKA[2], A. WZIĄTEK[1], M. KONKOL[1], R. WIEJAK[1], R. KOWALSKI[1], A. BIAŁEK[3]**, [1]Supercritical Extraction Research Group, Łukasiewicz Research Network – New Chemical Syntheses Institute, Tysiąclecia Państwa Polskiego Ave, 13A, 24-110 Puławy, Poland, [2]Analytical Laboratory, Łukasiewicz Research Network – New Chemical Syntheses Institute, Tysiąclecia Państwa Polskiego Ave. 13A, 24-110 Puławy, Poland, [3]Hortulanus Agrochemical Solutions, Sygietyńskiego St. 25, 96-316 Stare Budy, Poland.

**Abstract:** Cost optimization in manufacturing often goes hand in hand with sustainability initiatives. By reducing waste, energy consumption, and environmental impact, companies can contribute to a more sustainable future while also realizing cost savings. Clove buds are a promising candidate for production-scale supercritical fluid extraction (SFE) due to several factors. For instance, clove buds contain various bioactive compounds, with eugenol being the most abundant. Eugenol possesses numerous health benefits, including antioxidant, anti-inflammatory, antimicrobial, and analgesic properties. These compounds make clove buds valuable for extraction in industries such as pharmaceuticals, food, and cosmetics. The cost of manufacturing optimization resulted in obtaining extraction costs in the range of 10.33–19.77 EUR/kg of extract. The lowest COM was obtained for Exp. No. 4.

**Introduction:** Clove buds are the dried flower buds of the *Syzygium aromaticum* tree, which is native to Indonesia and other parts of Southeast Asia. These aromatic buds are widely used as a spice in cooking and have a long history of medicinal and culinary applications. Clove buds are small, dark brown, nail-shaped structures with a bulbous head, typically measuring about 1 centimeter (0.4 inches) in length. They have a strong, pungent aroma and a warm, sweet, and slightly bitter taste. This distinctive flavor is due to the presence of eugenol, a compound that also contributes to clove's medicinal properties. Medicinally, clove buds have been used for centuries in traditional medicine to alleviate toothaches and oral discomfort due to their natural analgesic and antibacterial properties. They are also believed to aid digestion, relieve respiratory issues, and have antioxidant properties [1–2]. Supercritical fluid extraction (SFE) is a modern extraction technique used to obtain bioactive compounds from natural sources like clove buds. In this process, a supercritical fluid, typically carbon dioxide ($CO_2$), is used as the solvent. When $CO_2$ is pressurized and heated beyond its critical point (73.8 bar, 31.1 °C), it becomes a supercritical fluid with properties between those of a gas and a liquid. This supercritical $CO_2$ can effectively extract desired compounds from the clove buds while leaving behind no residual solvent [3–4]. One of the crucial aspects regarding production of extracts is total cost of manufacturing which optimized may influence the significantly the business model. By optimizing manufacturing costs, companies can mitigate financial risks associated with fluctuations in raw material prices, labor costs, or other factors affecting production expenses. Efficient manufacturing processes can result in higher-quality products delivered to customers at competitive prices. This leads to

increased customer satisfaction and loyalty, driving repeat business and positive word-of-mouth referrals [5].

**Experimental:** Supercritical fluid extraction of clove buds was performed in the range of temperature of 40-50 °C, pressure of 100-200 bar and $CO_2$ consumption of 25-75 kg $CO_2$/kg of feed. Laboratory scale (1 L extractor) installation was used for all experiments. Box-Behnken methodology was utilized for the optimization of the extraction process. As a criterion, total cost of manufacturing (COM) was chosen.

**Results:** According to literature data, extraction of cloves with supercritical carbon dioxide at the tested pressures (110, 164, 190 bar) and temperatures (52, 70, 80, 143 °C) gave an efficiency of 12-13 wt. % based on the dry weight of the raw material, and at the optimal conditions, the extract contained 86.7% and 13.3% of eugenol and eugenyl acetate, respectively. The eugenol content was higher than in extracts obtained by steam distillation (SD) and microwave-assisted extraction (MAE). The results showed that eugenol is the main compound, and its extracts accounted for 86.70, 81.47, and 79.08% for SFE, MAE, and SD, respectively. The extraction recoveries from dry floral material were 12-13, 14.2, and 17% for SFE, MAE, and SD, respectively. The results showed that SFE is an effective and selective method for the recovery of eugenol and eugenyl acetate [6]. In other studies, clove essential oil was isolated by extraction with supercritical $CO_2$ at a pressure of 90 bar and a temperature of 50 °C [7]. In the tests carried out as part of this project, the highest efficiency (26.61 wt. %) was obtained by extraction at a temperature of 45 °C, a pressure of 200 bar and a $CO_2$ consumption of 75 kg $CO_2$/kg.
Response Surface Methodology (RSM) is a statistical and mathematical technique used for modeling and analyzing the relationship between multiple variables and a response of interest. On the basis of RSM analysis, temperature ($X_1$), pressure ($X_2$), $CO_2$ consumption ($X_3$) as well as temperature x pressure ($X_1X_2$) and pressure x pressure ($X_2^2$) were factors influencing total cost of manufacturing of cloves sc$CO_2$ extracts. The lowest COM was obtained for Exp. No. 4 (10.33 EUR/kg), while the highest for Exp. No. 5 (19.77 EUR/kg). The highest COM in Exp. No. 5 did not correspond to the highest extraction yield. For the highest extraction yield (26.61 wt. %), the COM resulted in 16.23 EUR/kg (Fig.1, Table 1).

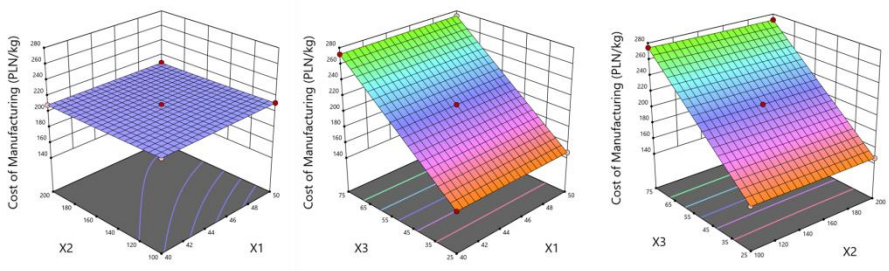



**Fig.1.** Influence of extraction temperature ($X_1$), pressure ($X_2$) and $CO_2$ consumption ($X_3$) on total cost of manufacturing.

**Table 1.** Total cost of manufacturing (COM) for clove buds $scCO_2$ extracts – predicted values for half-technical scale (40 L) installation.

| Experiment | Temperature [° C] | Pressure [bar] | $CO_2$ consumption [$kgCO_2/kg$] | Extraction yield [wt. %] | COM [EUR/kg] |
|---|---|---|---|---|---|
| 1 | 45 | 200 | 75 | 26.61 | 16.23 |
| 2 | 50 | 100 | 50 | 23.33 | 14.42 |
| 3 | 45 | 100 | 25 | 19.83 | 11.83 |
| 4 | 45 | 200 | 25 | 22.54 | 10.33 |
| 5 | 45 | 100 | 75 | 22.03 | 19.77 |
| 6 | 40 | 150 | 25 | 20.82 | 11.18 |
| 7 | 45 | 150 | 50 | 22.44 | 14.83 |
| 8 | 40 | 100 | 50 | 22.00 | 15.13 |
| 9 | 50 | 150 | 75 | 26.26 | 16.50 |
| 10 | 45 | 150 | 50 | 25.16 | 13.23 |
| 11 | 40 | 150 | 75 | 25.17 | 17.15 |
| 12 | 40 | 200 | 50 | 24.87 | 13.35 |
| 13 | 50 | 150 | 25 | 21.88 | 10.67 |
| 14 | 50 | 200 | 50 | 24.93 | 13.35 |
| 15 | 45 | 150 | 50 | 23.35 | 14.25 |

There are several clove oil preparations on the market that vary especially in price. For instance, cloves oil 15 mL MEDI-FLOWERY®, cloves oil 10 mL EcoSpa® and clove oil 15 mL dōTERRA Clove® costs 400 EUR/1L, 420 EUR/1L and 2200 EUR/1L, respectively.

**Conclusions:** Supercritical fluid extraction (SFE) may be a cost-effective method for cloves extract production. The cost of manufacturing for clove buds $scCO_2$ extracts is much lower as compared with commercially available products. The COM may be even lower when production scale installations is to be used for extraction of this raw material.

**Acknowledgements:** The research was financed by Polish National Center for Research and Development as a part of the project entitled *Natural products as a basis for ecological, sustainable preparations* (project acronym: EUREKA/2021/114/NatBioPrep/2022).

**References:**

1. D.F. Cortés-Rojas, C.R. Fernandes de Souza, W. Pereira Oliveira, Asian Pacific Journal of Tropical Biomedicine, 4 (2014) 90.
2. D.B. Hassine, S.K. El Euch, R. Rahmani, N. Ghazouani, R. Kane, M. Abderrabba, J. Bouajila, BioMed Research International, 81 (2021) 736.
3. S. Milovanović, A. Grzegorczyk, Ł. Świątek, A. Grzęda, A. Dębczak, K. Tyśkiewicz, M. Konkol, Food and Bioprocess Technology, 16 (2023) 1806.
4. S. Milovanović, A. Grzegorczyk, Ł. Świątek, A. Dębczak, K. Dastan Asserzhanov, M. Konkol, Sustainable Chemistry and Pharmacy, 29 (2022) 100796.
5. U. Sievers, Chemical Engineering and Processing: Process Intensification, 37 (1998) 451.
6. F. Yazdani, M. Mafi, F. Farhadi, K. Tabar-Heidar, K. Aghapoor, F. Mohenzadeh, H.R. Darabi, Zeitschrift für Naturforschung B, 60 (2014) 1197.
7. E. Reverchon, C. Marrone, Chemical Engineering Science, 52 (1997) 3421.

# SPECTROSCOPIC AND MICROSCOPIC STUDIES OF UV FILTERS IN SELECTED HAIR COSMETICS

**M. JÓZWICKI[1], K. SKRZYPIEC[2], W. JÓZWICKA[1], P. JANUSZ[2], A. KICZOR[1], P. MERGO[1], W. SOFIŃSKA-CHMIEL[2]**, [1]Maria Curie-Sklodowska University, Faculty of Chemistry, Institute of Chemical Sciences, Laboratory of Optical Fibers Technology, M. Curie-Sklodowska Sq. 3, 20-031 Lublin, Poland, [2]Maria Curie-Sklodowska University, Faculty of Chemistry, Institute of Chemical Sciences, Analitycal Laboratory, M. Curie-Sklodowska Sq. 3, 20-031 Lublin, Poland.

**Abstract:** The aim of the research was the physicochemical characterization of hair preparations with UV protection. FTIR-ATR spectroscopic tests and spectrophotometric tests were performed. The spectral range of protection of the preparations and their duration of action were examined. Microscopic examinations of the hair structure before and after use of preparations were also performed.

**Introduction:** Ultraviolet radiation is one of the most important environmental factors affecting the appearance and condition of the skin and hair [1]. In order to reduce the danger associated with the negative effects of sunlight, the use of UV filters has become common. They have the ability to reflect or absorb sunlight, preventing them from penetrating into the deep layers of the skin and hair. Due to their mechanism of action, physical and chemical filters are distinguished. Physical filters are pigments (e.g. titanium, zinc and iron oxide) that reflect or scatter sunlight after application. The mechanism of action of chemical filters is to absorb UV radiation (e.g. esters of alkylaminoaromatic acids, derivatives of benzophenone, camphor and coumarin). Chemical filters are classified depending on the wavelength of the absorbed material UV radiation into: UVB, UVA and broadband filters (UVA + UVB). The UVB filters absorb radiation in the range of approx. 290-320 nm, UVA filters in the range of approx. 320-400 nm and broadband filters in the range of 290 - 400 nm [2].

**Experimental:** Three hair preparations with UV protection, commercially available in drugstores, were selected for the study. Spectrophotometric tests were carried out using a U5600PC spectrophotometer at a wavelength of 350-1050 nm. The preparations were placed on defatted laboratory slides in an acetone-chloroform-dichloromethane mixture for 30 minutes. The slides were wiped and washed with acetone. After applying a thin layer of the preparation, the slides were placed on a heating spot and covered tightly with aluminum foil so that the temperature in the created climatic chamber was 30 ºC. Spectrophotometric measurements were performed every 15, 60, 120, 180, 240 minutes. FTIR spectra of the tested cosmetic preparations were performed using the Nicolet 8700A FTIR spectrometer from Thermo Scientific. The Smart Orbit ATR attachment with a diamond crystal was used. The tests were carried out in the wave number range of 4000-400 $cm^{-1}$ and with a spectral resolution of 4 $cm^{-1}$ directly from the surface of the dried preparations. A DTGS detector was used for the research. The obtained spectra were

subjected to ATR correction, baseline correction and normalization using the Omnic SpectaTM software. Microscopic examinations were performed using a Nikon MA 200 microscope with 408 nm laser.

**Results:** The FTIR-ATR spectra of the tested preparations with a UV filter are presented in Figs.1-3.

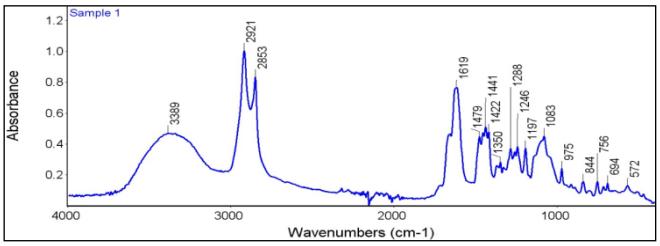



**Fig.1.** FTIR-ATR of sample 1.

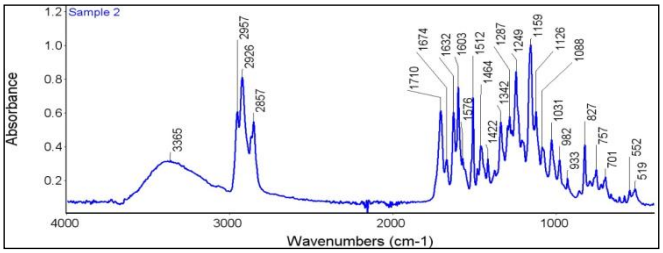



**Fig.2.** FTIR-ATR of sample 2.

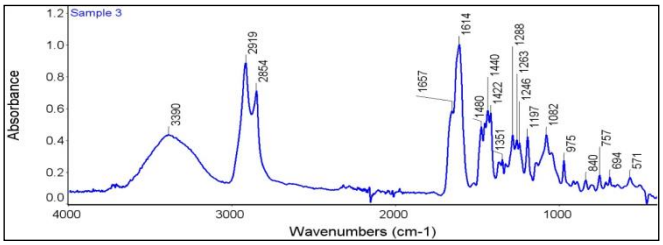



**Fig.3.** FTIR-ATR of sample 3.

The main goal of the FTIR-ATR study was the physicochemical characterization of preparations with a UV filter. The tests carried out showed the presence of bands responsible for UV protection. The FTIR spectra of the tested preparations reveal the presence of bands characteristic of stretching vibrations of OH groups in the range of 3500-3000 $cm^{-1}$ and the presence of bands corresponding to C-H stretching vibrations in the range of 2850-3000 $cm^{-1}$. The FTIR-ATR spectra showed also the
presence of C=O stretching vibrations originating from acids and esters in the range of 1600-1870 $cm^{-1}$. These compounds are characteristic of chemical UV filters. Peaks characteristic of C-O bonds in the range of 1050-1430 $cm^{-1}$ were found in the FTIR-ATR spectra. The presence of bands characteristic of Si-O-C, $CH_2$=CH-Si and Si-O-Si bonds was found [3]. In order to observe the effectiveness of the tested preparations as

protection of hair against UV radiation, tests were carried out using a U5600PC spectrophotometer at a wavelength of 320-800 nm. The research aimed to determine the range of radiation in which the tested preparations protect hair as well as the time of their action. The test results are presented in Fig.4.

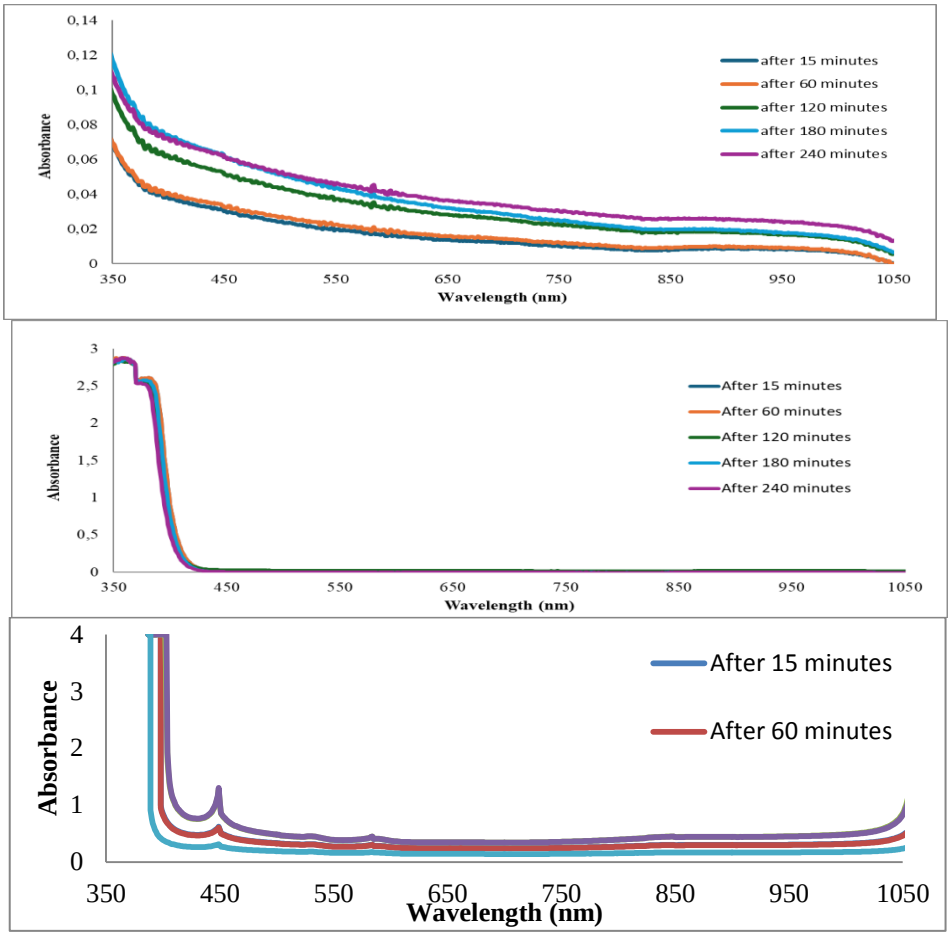



**Fig.4.** Results of spectrophotometric tests of preparation 1, 2, 3 looking from above carried out after: 15, 60, 120, 180 and 240 minutes of preparation application.

The tests showed the maximum absorbance for the preparation. The absorbance value was 0.12. For preparation 2, the maximum absorbance value was 2.87, and for preparation 3 it was above 4 (above the operating range of the device). The protection of preparation 1 depends on the time of application to the hair. The maximum protection was achieved after 180 minutes. This preparation absorbs radiation in the range of 350-1050 nm. The spectrophotometric tests of preparation 2 showed the maximum protection against UV radiation after 15 minutes. The spectral range of the preparation was 350-420 nm. In the case of preparation 3, the operating range was 350-1050 nm, while the maximum protection was obtained in the range of 350-500 nm. The maximum protection

against UV radiation was achieved 180 minutes after applying the preparation. After this time, the effectiveness of the preparation decreases. In order to characterize physicochemical features of the tested preparations, microscopic photos were also taken in the light of a laser with a wavelength of 408 nm. The test results are presented in Fig.5.

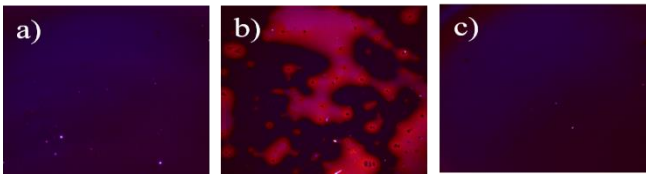



**Fig.5.** Microscopic photos of the tested preparations in the light of a 408 nm laser: a) preparation 1, b) preparation 2, c) preparation 3.

The research using optical mixcopy was also carried out. Microscopic photos of the hair were taken before and after using the preparations. The test results are presented in Figs.6-7.

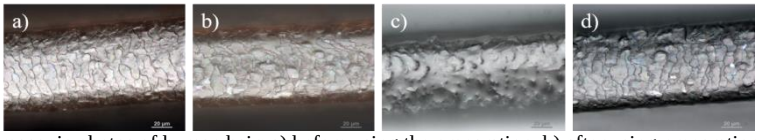



**Fig.6.** Microscopic photos of human hair: a) before using the preparation, b) after using preparation 1, c) after using preparation 2, c) after using preparation 3.

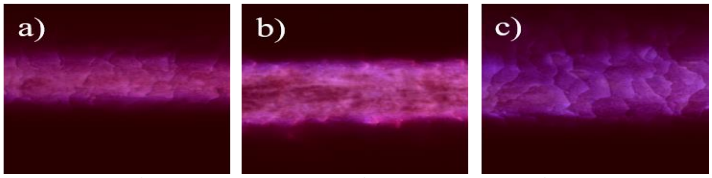



**Fig.7.** Microscopic photos of human hair in the light of a 408 nm laser: a) after using preparation 1, b) after using preparation 2, c) after using preparation 3.

**Conclusions:** The research enabled determination of the UV protection range of the tested preparations as well as the duration of their effective protection. As follows as from the tests all of the tested preparations can be classified as UVA filters. Unfortunately, the operating range of the spectrophotometer did not make it possible to determine whether the tested filters were broadband. The research proved that the protection of preparation 1 is most effective 240 minutes after applying it for the hair. In the case of preparation 2, the effectiveness of the preparation does not change in the period from 15-240 minutes. In the case of preparation 3, maximum protection was obtained 180 minutes after application. After this time, the radiation absorption decreased.

**Acknowledgements:** The research was carried out using the apparatus maintained based on the project INFRASTARt.

## References:

1. B. Stanisz, Kosmetologia, 65 (2009) 363.
2. H. Bojarowicz, N. Bartnikowska, Problemy Higieny i Epidemiologii, 95 (2014) 596.
3. M. Silverstein, F.X. Webster, D.J. Kiemle, Spektroskopowe metody identyfikacji związków organicznych, PWN, Warszawa, 2007.

# DETERMINATION OF ANTIOXIDANTS IN EDIBLE OILS USING A FLOW SYSTEM WITH CHEMILUMINESCENCE DETECTION

**E. NALEWAJKO-SIELIWONIUK[1], I. WYSOCKA[2], A. KALINOWSKA[1]**, University of Bialystok, Faculty of Chemistry, Department of Analytical and Inorganic Chemistry, K. Ciołkowskiego 1K, 15-245 Białystok, Poland, [2] University of Bialystok, Doctoral School of Exact and Natural Sciences, Ciołkowskiego 1K, 15-245 Białystok, Poland.

**Abstract:** Edible oils are an important component of the human diet. Their composition includes essential fatty acids (EFAs), such as omega-3 and omega-6, numerous lipid compounds, and vitamins. Oils also contain antioxidant compounds that ensure the neutralisation of free radicals. A new chemiluminescence (CL) method based on a direct-injection detector (DID) integrated with the multi-pumping flow system (MPFS) to chemiluminescence determination of the total content of hydrophilic and lipophilic antioxidants present in edible oil is presented. The proposed DID-CL-MPFS method is based on the chemiluminescence of luminol oxidized by $K_3[Fe(CN)_6]$. Under the optimized experimental conditions, the chemiluminescence intensities are proportional to the concentration of gallic acid (a representative of hydrophilic antioxidants) and α-tocopherol (a representative of lipophilic antioxidants). The DID-CL-MPFS method offers several advantages, including a low detection limit, high precision, and high sample throughput. The proposed method has been successfully applied to determine the total content of hydrophilic and lipophilic antioxidants (expressed as gallic acid/ α-tocopherol equivalent) in various oil samples.

**Introduction:** Free radicals are very unstable and reactive species with unpaired electron in an atomic orbital. The best-known free radicals are reactive oxygen species, such as superoxide anion radical ($O2^{\cdot-}$), hydrogen peroxide radical ($HO_2^{\cdot}$), hydroxyl radical ($^{\cdot}OH$), alkoxy radical ($RO^{\cdot}$), superoxide radical ($ROO^{\cdot}$), and reactive nitrogen species, such as nitrogen monoxide ($NO^{\cdot}$) and nitrogen dioxide ($NO_2^{\cdot}$) [1]. Their appearance in the human body may be caused by factors like, e.g. improper diet, long-term stress, UV light, or environmental pollution. Due to a lack of electron, free radicals readily interact with biological cells, causing DNA damage and oxidation of proteins and lipids which changes their structure and function. The activity of free radicals contributes to oxidative stress when an imbalance between free radicals and antioxidant concentration exists. Oxidative stress may lead to the development of civilization diseases such as Alzheimer's disease, Parkinson's disease, atherosclerosis, diabetes, and various cancers [2]. Antioxidants are tremendously essential compounds, and even at their low concentration, they protect our bodies against the adverse effects of oxidative stress. Fresh vegetables, fruits, nuts, and edible oils are good sources of antioxidants in our diet. The main groups of those compounds are phenolic compounds, carotenoids, tocochromanols, vitamins, and betalains. Phenolic compounds are secondary metabolites of plants that have one or more phenol rings and single or multiple hydroxyl groups (-OH) bound together. The most known polyphenols are, among others, gallic acid,

caffeic acid, *p*-coumaric acid, kaempferol, quercetin, or catechin. The best sources of phenolic compounds are, e.g. apples, berries, green tea, or broccoli [3]. Carotenoids, such as α- and β-carotene, are precursors of vitamin A, essential for developing the sense of sight. The diet should be rich in these substances, which are present in, e.g. carrots, citrus fruits, or tomatoes. Tocochromanols are a group of lipophilic compounds, which include tocopherols and tocotrienols. α-tocopherol is the main form of vitamin E. It has the most significant biological importance among other tocopherols, making it a great free radicals scavenger. Food's primary sources of tocochromanols are oilseeds, edible oils, and nuts [4]. Vitamin C is the best-known antioxidant in food. Ascorbic acid – the primary form of vitamin C, has a significant role in the proper functioning of the human body. It participates in various biochemical processes, such as synthesizing collagen and hormones. High levels of vitamin C can be found in rosehips, blackcurrants, peppers, and parsley [5]. Betalains are red pigments in vegetables like beetroot, Swiss chard, and ulluco. Unfortunately, these compounds are in low concentration in plant sources since 0,5 g of betanin, the main betalain of beetroot, may be obtained from 1 kg of this vegetable. Nevertheless, betalains have high antioxidant and radical-scavenging abilities [6]. Therefore, a balanced diet is essential to provide the human body with the necessary antioxidants. Edible oils should be the essential components of the human diet. They are produced from various sources, such as fruit or oilseeds. The most well-known and widespread oils are rapeseed, sunflower, olive, coconut, and palm oil [7]. Their consumption provides the body with energy and nutrients such as essential fatty acids (EFAs), triglycerides, phospholipids, phytosterols, and vitamins. Those compounds support the proper functioning of the organism, prevent cardiovascular disease, and are responsible for maintaining good cholesterol levels [8]. Oils are also rich sources of lipophilic antioxidants such as vitamin E (tocochromanols) and vitamin a (carotenoids), but also hydrophilic antioxidants like plant phenolic compounds (phenolic acids, flavonoids, lignans, and stilbenes) [9]. Different methods are used to determine antioxidant compounds and their antioxidant activity in oil samples. Most of them are stationary methods based on fluorescence, chemiluminescence, or spectrophotometric detection. Among spectrophotometric methods those based on $DPPH^{\cdot}$ (2,2-diphenyl-1-picrylhydrazyl radical), $ABTS^{\cdot+}$ (2,2'-azobis(3-ethylbenzothiazoline-6-sulfonate radical), FRAP (ferric ion reducing antioxidant parameter), or CUPRAC/CRA (cupric reducing antioxidant capacity/copper reduction assay) are the most frequently used [10]. The fluorescence method requires luminophores and involves measuring the intensity of the emitted radiation after excitation of the reaction product at the appropriate wavelength [11]. The chemiluminescence detection of antioxidants is based on the quenching effect of these compounds on the emission of light generated by luminophores (e.g. luminol, lucigenin) during their oxidation process [12]. Compared to stationary methods, flow methods are characterized by shorter analysis time, lower consumption of reagents, mechanization of measurements, and better precision. Therefore, they are a good alternative to batch methods for the determination of antioxidant compounds in food samples.

**Experimental:** The determination of the total content of hydrophilic and lipophilic antioxidants present in oil extracts was carried out based on the chemiluminescent reaction of oxidation of luminol by potassium hexacyanoferrate(III) in an alkaline medium. In the study, potassium hexacyanoferrate(II) was also used because its addition

to the luminol solution reduced the baseline noises. Antioxidants in the oil samples inhibited the chemiluminescence of luminol proportional to their concentration, which was the basis for developing a flow-based method for their determination. The measurements were conducted in the DID-CL-MPFS manifold presented in Fig.1.

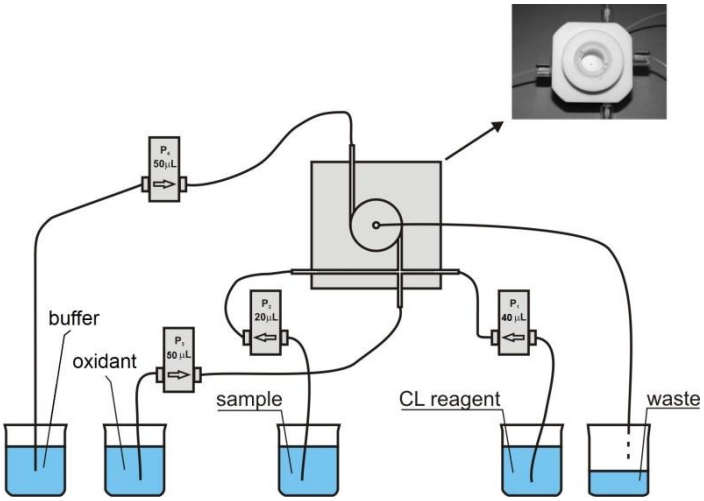



**Fig.1.** Schematic diagram of the DID-CL-MPFS system for the determination of the total content of hydrophilic and hydrophobic antioxidants. $P_1$, $P_2$, $P_3$, and $P_4$ are the solenoid micro-pumps.

The multi-pumping flow system consisted of four solenoid micro-pumps ($P_1$–$P_4$) (Cole-Parmer, USA) of a nominal volume of 20, 40, and 50 μL, PTFE tubing (0.8 mm i.d.) and the direct-injection chemiluminescence detector. All solutions were injected simultaneously into the cone-shaped reaction-detection chamber (with a total volume of 280 μL) using solenoid micro-pumps.

**Results:** The first stage of developing the DID-CL-MPFS method was choosing the optimal measurement conditions. Several parameters were optimized, i.e., concentration of reagents (luminol, NaOH, $K_3[Fe(CN)_6]$, $K_4[Fe(CN)_6]$), the selection of the organic solvent in which the samples were prepared, the volume of injected reagents, the volume of buffer necessary for washing the reaction and detection chamber between subsequent sample injections, the time after which the washing of the chamber was started and the voltage of the photomultiplier tube. For the optimization studies, gallic acid and α-tocopherol were used because they are present in oil samples and are known for their potent antioxidant properties. The developed method was successfully applied to determine the total content of hydrophilic and lipophilic antioxidants in various edible oils. The results were expressed as milligrams of gallic acid/α-tocopherol equivalent per milliliter of a sample.

**Conclusions:** A novel and environmentally friendly DID-CL-MPFS method for the determination of the total content of hydrophilic and lipophilic antioxidants in edible oils was developed. The DID-CL-MPFS method fulfils the criteria of green analytical

chemistry. Its main advantages are low cost, small weight, and size of the flow system, as well as low consumption of reagents and energy.

## References:

1. F. Collin, Int. Journal of Molecular Science, 20 (2019) 2407.
2. V. Lobo, A. Patil, A. Phatak, N. Chandra, Pharmacognosy Reviews, 4 (2010) 118.
3. A. Rana, M. Samtiya, T. Dhewa, V. Mishra, R.E. Aluko, Journal of Food Biochemistry, 46 (2022) e14264.
4. Z.E. Sikorski, H. Staroszczyk, Chemia Żywności 2. Biologiczne właściwości składników żywności. Wyd. Naukowe PWN, Warszawa, 2017.
5. K. Janda, M. Kasprzak, J. Wolska, Pomeranian Journal of Life Sciences, 61 (2018) 419.
6. T. Sawicki, M. Surma, H. Zieliński, W. Wiczkowski, Journal of Separation Science, 39 (2016) 2986.
7. Ś. Ziemlański, M. Nogala-Kałucka, J. Gawęcki, A. Siger, Żywienie człowieka. Podstawy nauki o żywieniu. Wyd. PWN, Warszawa, 2022.
8. H.D. Belitz, W. Grosch, P. Schieberle, Food Chemistry, 4th ed., Springer-Verlag Berlin Heidelberg, Berlin, Heidelberg, 2009.
9. W. Grajek, Przeciwutleniacze w żywności. Aspekty zdrowotne, technologiczne, molekularne i analityczne. Wyd. Naukowo-Techniczne, Warszawa, 2007.
10. A. Wilczyńska, Bromatologia i Chemia Toksykologiczna, XLII (2009) 870.
11. A. Nikokavoura, D. Christodouleas, E. Yannakopoulou, K. Papadopoulos, A. C. Calokerinos, Talanta, 84 (2011) 874.
12. J. Koss-Mikołajczyk, M. Baranowska, J. Namieśnik, A. Bartoszek, Postępy Higieny i Medycyny Doświadczalnej, 71 (2017) 1.

# GREEN LEACHING AGENTS FOR SUSTAINABLE COPPER RECOVERY FROM E-WASTE

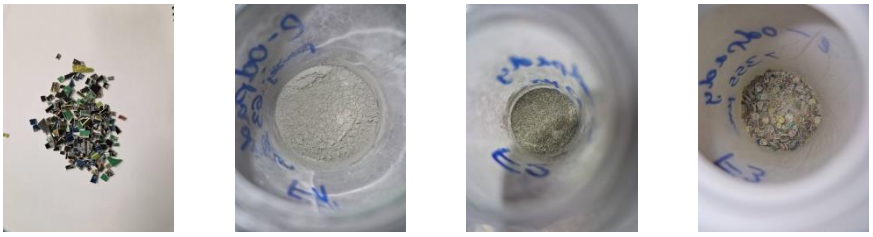
**P. KLUCZYŃSKI, M. EMMONS-BURZYŃSKA, E. JĘDRZEJCZAK, M. WYSOKOWSKI, M. REGEL-ROSOCKA**, Poznan University of Technology, Faculty of Chemical Technology, Institute of Chemical Technology and Engineering, Berdychowo St. 4, 60-965 Poznań, Poland.

**Abstract:** Two green leaching agents, deep eutectic solvents (DESs), such as mixtures of lactic acid (Lac) – as a hydrogen bond donor (HBD) – and choline chloride (ChCl) or urea (Ur), acting as hydrogen bond acceptors (HBA) were studied for recovering copper from e-waste (PCB). For comparison, also 3.1 M lactic acid (Lac) was used as a leaching agent. Part of the leaching experiments was conducted with the addition of an oxidizer (30% $H_2O_2$). It was found that the amount of the added 30% $H_2O_2$ had a positive effect on the amount of the Cu(II) leached. The most noticeable change in the leaching results occurred in the systems with DESs, while in the experiments with lactic acid, the positive effect of $H_2O_2$ was not as pronounced.

**Introduction:** The current environmental situation requires innovative technological solutions in the spirit of sustainable development, due to issues such as the depletion of primary raw materials, pollution and the huge amount of solid waste. For this reason, the recycling of resources and the creation of circular economies and technologies are strongly emphasized [1]. Electronic waste (e-waste) is a significant global problem that poses a threat to human health and ecosystems [2]. Globally, over 50 million metric tons of e-waste are generated annually, with a predicted exponential increase to 74.7 Mt by 2030. The management of e-waste is necessary not only due to its negative environmental impact but also because it contains many elements of high economic value [3]. E-waste comprises various materials, including plastics, metals, and glass, some of which can be systematically recovered, making it a valuable source of raw materials [4]. It is worth noting that the concentration of valuable metals in e-waste, such as copper, silver or gold, is much higher than in their respective primary resources, i.e. metal ores [5]. In recent years, hydrometallurgical methods have been increasingly used to separate metals from e-waste [6,7]. Although a wide range of leaching agents have been used, including organic acids such as oxalic and citric [8,9], and inorganic acids like $H_2SO_4$ with $H_2O_2$ [10], the search for new, effective, selective, and environmentally friendly metal ion leaching agents continues. A relatively recent development in the field of metal ion recovery is the use of deep eutectic solvents (DESs) as leaching agents. These solvents are considered a sustainable alternative to noxious or highly corrosive leaching solutions and respond to the demands of green chemistry [11]. DES is formed by combining its components in the right proportions without the need for complex reactions, unit operations, or procedures. In addition, the wide range of different compounds that can act as hydrogen bond donors and acceptors (HBA and HBD) allows DES properties as solvents to be tailored and modified, not only reducing solvent toxicity but also lowering production costs. Recent studies have confirmed the effectiveness of DESs in separating, recycling, and recovering strategically important

metals [12,13]. The purpose of this study is to investigate the impact of leaching conditions, such as the type of HBA used and oxidant addition, on the efficiency and selectivity of metal leaching from various fractions of the e-waste under investigation.

**Experimental:** The e-waste material used in this work, i.e. printed circuit boards (PCBs) coming from various discarded desktop computers, was provided by IOK waste management in Belgium. The ground material was divided into three fractions depending on the size of the particles ($\phi$): fraction I $\phi < 63$ µm, fraction II 63 µm $< \phi >$ 355 µm, fraction III $\phi > 355$ µm (Fig.1).



(a) (b) (c) (d)

**Fig.1.** The e-waste material (PCBs) applied for the studies: a) cut before grinding b) fraction I $\phi < 63$ µm c) fraction II 63 µm $< \phi <$ 355 µm d) fraction III $\phi > 355$ µm.

Two deep eutectic solvents (DES) containing lactic acid (Lac) as a HBD and choline chloride (ChCl) or urea (Ur) acting as HBA, and 3.1 M lactic acid (Lac) were used as leaching agents (Fig.2). To overcome problems with mass transport resulting from high viscosity of the DESs synthesized, they were diluted with deionized water (1:2 DES:water). A 30% hydrogen peroxide solution (Avantor, Gliwice, Poland) was used as an oxidant in the leaching solution.

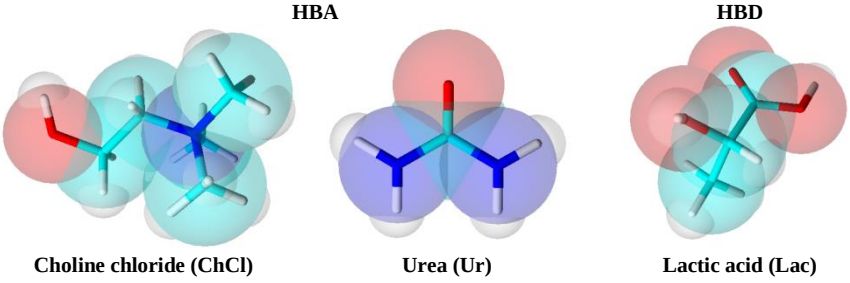
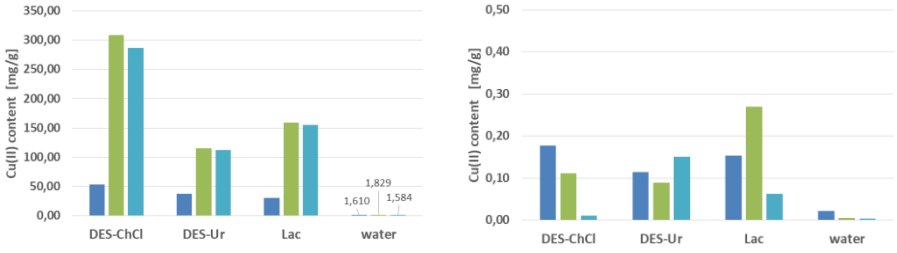



**Fig.2.** Molecular structures of the HBA and HBD used in forming the DES mixtures.

Leaching was carried out in a reactor of 50 $cm^3$. Portions of 0.5 g of the ground material from a specific fraction (I, II or III, printed circuit boards from PC motherboards, PCBs) were placed in the reactor. The solid to liquid ratio (S/L) used was 1/20 $g/cm^3$. 5 $cm^3$ of a DES solution with a v/v ratio of 1:2 or 3.1 M acid (Lac) and 5 $cm^3$ of deionized water or in some cases mixtures of the deionized water and $H_2O_2$ were used as leaching agents. All experiments were carried out at 23 ± 2 °C for 3 h using a magnetic stirrer (WIGO ES 24). The leachates were separated from the leached material using a centrifuge (5804,

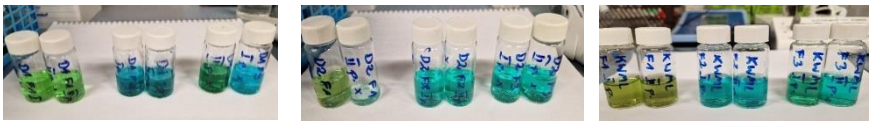
Eppendorf, Germany) and appropriately diluted with 1.5% $HNO_3$ solution to determine concentrations of Cu(II) ions. A 0.3 g of the powdered PCBs was mineralized in 25 $cm^3$ of aqua regia (ambient temperature, 72 h). Atomic absorption spectroscopy (ContrAA300, Analytik Jena, Germany) was applied to determine the concentrations of Cu(II)in the aqueous solutions at the wavelengths of 324.8 nm.

**Results:** Based on the results, it was discovered that the inclusion of an oxidant has a substantial impact on the quantity of copper that is leached from individual fractions of PCBs. The presence of $H_2O_2$ enabled the leaching of several hundred times more copper than without an oxidant (Fig.3a). When leaching was conducted without the addition of hydrogen peroxide, the highest amount of copper (0.270 mg/g) was retrieved from fraction II using Lac (Fig.3b). Overall, the type of HBA did not have an effect on copper leaching without the addition of $H_2O_2$. However, when $H_2O_2$ was added, DES-ChCl demonstrated greater efficiency compared to Lac and DES-Ur. The amount of Cu leached in $H_2O_2$-added systems decreased in the following order: DES-ChCl (308.7 mg Cu(II)/g e-waste) > Lac (158 mg Cu(II)/g e-waste) > DES-Ur (115 mg Cu(II)/g e-waste).




(a) (b)

**Fig.3.** Leaching of Cu from specific fractions of the ground PCBs ( ) I, ( ) II, ( ) III for different leaching agents used in the presence (a) $H_2O_2$ or (b) its absence.



(a) (b) (c)

**Fig.4.** Changes in colors of solutions after using different leaching agents with $H_2O_2$ (a) DES-ChCl (b) DES-Ur (c) Lac.

The colorful solutions, shown in Fig.4, confirm that Cu(II) was leached efficiently, and $CuCl_4^{2-}$ chlorocomplexes or hydrated $CuCl_2 \cdot 2H_2O$ were formed.

**Conclusions:** In a non-oxidizing environment, DES containing choline chloride or urea as the hydrogen bond acceptor (HBA) and lactic acid as the hydrogen bond donor (HBD) are less effective leaching agents than a solution of lactic acid. However, in the presence of hydrogen peroxide, all systems are more effective in leaching copper. This suggests that the oxidant plays a primary role in the leaching of metals from PCBs. The study found that the amount of 30% $H_2O_2$ added had a positive effect on the amount of Cu(II) leached. Systems with 5 $cm^3$ of $H_2O_2$ added performed better than those with 1 $cm^3$

added. However, controlling the reaction becomes more difficult due to the large amount of gas released after more oxidant is added. The most significant change in leaching results occurred in systems with DES. In the lactic acid experiments, the positive effect of $H_2O_2$ was not as pronounced. The type of HBA in the DES does not have a significant effect on the leaching process. However, it appears that the presence of choline chloride in the leach mixture results in a higher copper content (in most cases) compared to the presence of urea. Furthermore, the highest amount of copper is leached from fraction II ($63\ \mu m < \phi < 355\ \mu m$), slightly less from fraction III and significantly less from fraction I with the smallest particle size. This is because fractions II and III contain the most copper from PCBs.

**Acknowledgements:** This work was supported by the Ministry of Science and Higher Education, Poland, grants No. 0912/SBAD/2410 and 0912/SBAD/2307.

**References:**

1. S. Geisendorf, F. Pietrulla, Thunderbird International Business Review, 60 (2018) 771.
2. O.A. Ogunseitan, J.M. Schoenung, J.D.M. Saphores, A.A. Shapiro, Science, 326 (2009) 670.
3. N.E. Petridis, K. Petridis, E. Stiakakis, Resources, Conservation and Recycling, 158 (2020) 104742.
4. M. Kaya, Waste Manage, 57(2016) 64.
5. A.K Awasthi, F. Cucchiella, F.I.D'Adamo, J. Li, P. Rosa, S. Terzi, G. Wei, X. Zeng, Science of the Total Environment, 613–614 (2018) 46.
6. G. Chauhan, P.R. Jadhaob, K.K. Pantb, K.D.P Nigamb, Journal of Environmental Chemical Engineering, 6 (2018) 1288.
7. J. Jui, L. Zhang, Journal of Hazardous Materials, 158 (2008) 228.
8. A. Janani, G.P. Arulraj, International Journal of Engineering and Advanced Technology, 8(2S2) (2019) 329.
9. M. Kolenčík, M. Urík, S. Čerňanský, M. Molnárová, P. Matúš, Fresenius Environmental Bulletin, 22 (2013) 3673.
10. A. Behnamfard, M.M. Salarirad, F. Veglio, Waste Manage, 33 (2013) 2354.
11. C. Florindo, F. Lima, B. D. Ribeiro, I.M. Marrucho, Green and Sustainable Chemistry, 18(2019) 31.
12. Z. Yuan, H. Liu, W.F Yong, Q. She, J. Esteban, Green Chemistry, 24 (2022) 1895.
13. M. Emmons-Burzyńska, M. Wysokowski, M. Regel-Rosocka, Nauka i przemysł - metody spektroskopowe w praktyce, nowe wyzwania i możliwości, red. Z. Hubicki, Wydawnictwo Uniwersytetu Marii Curie-Skłodowskiej, Lublin, Polska, 2023.

# BIOORGANIC PRECIPITATION OF PLATINUM GROUP METAL NANOPARTICLES

**W. STACHOWICZ[1], M. RZELEWSKA-PIEKUT[1], W. SMUŁEK[2], M. REGEL-ROSOCKA[1]**, [1]Poznan University of Technology, Faculty of Chemical Technology, Institute of Chemical Technology and Engineering, Department of Chemical Technology, Berdychowo St. 4, 60-965 Poznan, Poland, [2]Poznan University of Technology, Faculty of Chemical Technology, Institute of Chemical Technology and Engineering, Department of Organic Chemistry, Berdychowo St. 4, 60-965 Poznan, Poland.

**Abstract:** This paper presents preliminary results on the precipitation of platinum group metal nanoparticles (PGM-NPs) using saponins from *Soapnut*, *Soapwort* and *Quillaja bark* as bioorganic reducing and stabilizing agents. The results have shown that saponins are efficient reducing agents for all studied PGMs (Pt(IV), Pd(II), Rh(III)), especially when the pH of the precursor solution is controlled and maintained at the value of 7. Also the addition of a weak reducing agent, i.e. ascorbic acid (AA), increases the precipitation efficiency. At pH 7, with the addition of AA, the precipitation efficiency with *Soapwort* saponin decreases in the following order: Pd (94.2%) > Pt (90.4%) > Rh (82.6%).

**Introduction:** Platinum group metals (PGMs), such as platinum, palladium, rhodium, iridium, ruthenium, and osmium, are essential in various industrial applications due to their unique catalytic, electrical, and physical properties [1]. However, conventional methods for extracting and purifying PGMs from primary and secondary resources often involve complex chemical processes, such as pyrometallurgy. These processes are energy-intensive, environmentally hazardous, and economically unsustainable. Therefore, it is important to investigate eco-friendly alternatives for the retrieval and recycling of PGMs [2]. For instance, our team proposed a hydrometallurgical process for treating Pt-Pd-Rh spent automotive converters (SACs), which involves leaching, extraction, and stripping. This process produces a PGM-containing leachate that is subsequently purified and used to enrich the stripping solution [3]. Nanoparticles (NPs) were formed from PGM-rich solutions using reducers such as $NaBH_4$ or ascorbic acid (AA) [4,5]. As a consequence, in the search for environmentally friendly systems for NP formation, a biomimetic approach for the reduction of PGMs to NPs has been inspired by reagents of natural origin, such as natural surfactants saponins or glucose, catechols, and represents a sustainable and renewable resource-based strategy, in line with the future-oriented technologies of bioinspired systems (Fig.1). So-called "green nanotechnology" provides techniques for converting biological systems into safe and cost-effective methods for the synthesis of nanomaterials [6]. Successful attempts have been made in forming catalytically active NPs of noble metals using reactants of natural origin, extracted from plants, or produced by bacteria or fungi [7]. An eco-friendly synthesis of Pt-NPs was achieved using an extract of algae *Caulerpa sertularioides*. The biosynthesized Pt-NPs exhibited excellent antioxidant activity. Additionally, toxicity studies using *Artemia nauplii* demonstrated strong biological activity and low toxicity of

the biosynthesized Pt-NPs [7]. *Fusarium oxysporum* fungus extract successfully reduced Pt-NPs of average size 25 nm, demonstrating efficient photocatalytic degradation of methyl orange in wastewater [8].

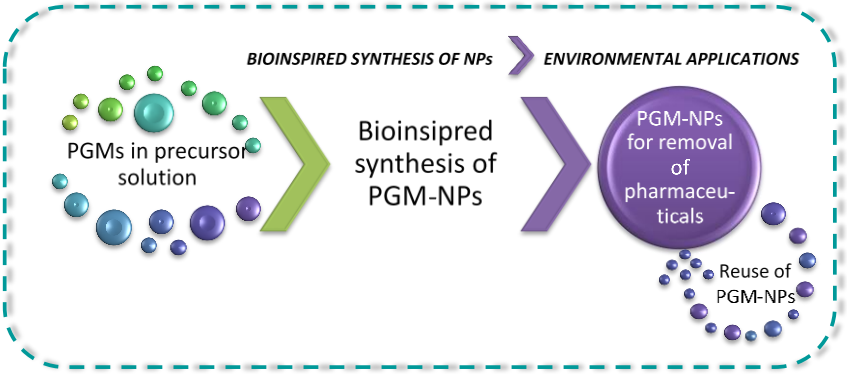



**Fig.1.** Scheme of bioinspired synthesis of PGM-NPs with potential application for pharmaceutical removal from water.

The aim of the presented studies is to screen saponins of natural origin (bioorganics) as reducing and stabilizing agents for precipitation of PGM-NPs.

**Experimental:** One-component model precursor solutions (Pt(IV), Pd(II), or Rh(III)) were prepared by dissolving the required amounts of $PtCl_4$ (96%), $PdCl_2$ (99.9%), or $RhCl_3$ (99.9%) in 0.1 M HCl (Sigma Aldrich, Germany). Saponins from *Soapnut*, *Soapwort* and *Quillaja bark* were used as bioorganic reducing agents and also as stabilizing agents in this study. The precipitation was carried out with pH control (~pH 7, with $Na_2CO_3$ (Chempur, Poland)) or without pH control (~pH 1.3). The concentration of Pt(IV) or Pd(II) in the precursor solution was measured 1 h or 24 h after precipitation. In some cases, ascorbic acid (AA, Chempur, Poland) was added as a weak reducing agent. The concentration of metal ions in the solution before and after precipitation were measured using atomic absorption spectrometry (AAS, ContrAA 300, Analytik Jena, Germany) at the following wavelengths: 266.0, 244.8, and 343.5 nm for Pt(IV), Pd(II), and Rh(III), respectively.

**Results:** The precipitation of nanoparticles of Pt(IV), Pd(II) and Rh(III) (PGM-NPs) has been carried out using saponins obtained from three different biomaterials: *Soapnut*, *Soapwort* and *Quillaja bark*. Generally, these preliminary studies are aimed at exploring different bio-inspired systems for NP conversion under diverse conditions, to be able to adjust particle size and, lastly, to characterize NP catalytic properties. The results presented in this paper include a study of the influence of pH control and the addition of ascorbic acid (as a weak reducing agent) on the precipitation efficiency of PGM NPs.

*Pt-NP precipitation*

Table 1 shows the precipitation efficiency of Pt-NPs using saponins from three different biomaterials as reducing agents.

**Table 1.** Precipitation efficiency of Pt-NPs.

| Saponins | Precipitation efficiency of Pt-NPs [%] | | | | | |
|---|---|---|---|---|---|---|
| | with pH control | | without pH control | | with pH control and AA | |
| | After 1 h | After 24 h | After 1 h | After 24 h | After 1 h | After 24 h |
| *Soapnut* | 87.0 | 92.5 | 55.3 | 65.6 | 89.9 | 93.5 |
| *Soapwort* | 86.4 | 82.3 | 48.8 | 39.6 | 90.4 | 86.7 |
| *Quillaja bark* | 86.6 | 89.1 | 61.7 | 68.2 | 88.5 | 93.9 |

Regardless of the biomaterials used, the Pt precipitation efficiency without pH control and AA addition did not exceed 70%. Nevertheless, it means that the saponins used have reducing properties towards Pt(IV) even when used alone, and the efficiency of their performance can be enhanced by pH control and addition of a weak reducing agent. Moreover, no time dependence was observed, as the Pt-NP precipitation after 1 or 24 h differed slightly (for *Soapnut* and *Soapwort*), within 5% of the error.

*Pd-NP precipitation*

The precipitation efficiency of Pd-NPs using saponins derived from three different biomaterials as reducing agents is shown in Table 2.

**Table 2.** Precipitation efficiency of Pd-NPs.

| Saponins | Precipitation efficiency of Pd-NPs [%] | | | | | |
|---|---|---|---|---|---|---|
| | with pH control | | without pH control | | with pH control and AA | |
| | After 1 h | After 24 h | After 1 h | After 24 h | After 1 h | After 24 h |
| *Soapnut* | 54.9 | 88.8 | 58.6 | 51.7 | 85.9 | 90.7 |
| *Soapwort* | 54.4 | 86.5 | 59.1 | 54.1 | 94.2 | 95.3 |
| *Quillaja bark* | 55.4 | 94.3 | 61.8 | 63.4 | 92.3 | 94.4 |

In the case of Pd, similar to Pt-NP precipitation, the highest precipitation efficiency (85-95%) was also achieved with pH control and AA addition. Both with and without pH control, the Pd precipitation efficiency after 1 h was 55-60%, regardless of the saponin used. However, in the pH-controlled samples, the Pd-precipitation efficiency after 24 h was ~90%. In samples without pH control, the Pd-NP precipitation efficiency after 24 h did not change compared to the efficiency after 1 h.

*Rh-NP precipitation*

The efficiency of Rh-NP precipitation using saponins from three different biomaterials as reducing agents is shown in Table 3.

**Table 3.** Precipitation efficiency of Rh-NPs.

| Saponins | Precipitation efficiency of Rh-NPs [%] | | | | | |
|---|---|---|---|---|---|---|
| | with pH control | | without pH control | | with pH control and AA | |
| | After 1 h | After 24 h | After 1 h | After 24 h | After 1 h | After 24 h |
| *Soapnut* | 83.2 | 82.8 | 69.5 | 69.2 | 83.5 | 83.8 |
| *Soapwort* | 83.1 | 82.6 | 71.6 | 70.5 | 82.6 | 83.5 |
| *Quillaja bark* | 78.9 | 71.8 | 67.4 | 60.7 | 76.3 | 72.7 |

For Rh samples with pH control for *Soapnut* and *Soapwort*, regardless of the presence of AA, the Rh-NP precipitation efficiency was approximately 83% after 1 and 24 hours. The efficiency of Rh-NP precipitation without pH control was approximately 10% lower than the precipitation efficiency with pH control. Additionally, there was no significant difference in the Rh precipitation efficiency after 1 and 24 hours in almost all cases.

**Conclusions:** Overall, bioorganic precipitation of PGMs represents a promising frontier in materials science, biotechnology, and environmental engineering. Saponins from bioorganic materials: *Soapnut, Soapwort* and *Quillaja bark* have the ability to reduce PGM ions. In particular, *Soapwort* saponins seem to be the most efficient in reducing Pt(IV), Pd(II) and Rh(III) from precursor solutions. The addition of ascorbic acid and pH control (~7) has a positive effect on the precipitation of PGM NPs, the highest precipitation efficiency for all PGMs studied was achieved in these systems. The results obtained in this study provide a background for the selection of the best precipitation systems and for further characterization of the morphology of the obtained NPs and investigation of their catalytic properties.

**Acknowledgements:** This research was financed by the Ministry of Science, Poland (grant No. 0912/SBAD/2410).

**References:**

1. A.E. Hughes, N. Haque, S.A. Northey, S. Giddey, Resources, 10 (2021) 93.
2. M. Rzelewska, M. Regel-Rosocka, Physical Sciences Reviews, 3 (2018) 20180021.
3. Z. Wiecka, M. Rzelewska-Piekut, M. Regel-Rosocka, Separation and Purification Technology, 280 (2022) 119933.
4. Z. Wolanczyk, W. Stachowicz, M. Rzelewska-Piekut, J. Zembrzuska, M. Regel-Rosocka, International Journal of Molecular Sciences, 25 (2024) 3147.
5. Z. Wiecka, I. Cota, B. Tylkowski, M. Regel‑Rosocka, Environmental Science and Pollution Research, 30 (2023) 90168.
6. M. Gholami-Shabani, F. Sotoodehnejadnematalahi, M. Shams-Ghahfarokhi, A. Eslamifar, M. Razzaghi-Abyaneh, Journal of Cluster Science, 34 (2023) 501.
7. S. Palanisamy, R. Anjali, S. Jeneeta, S. Mohandoss, D. Keerthana, I.S. Shin, S.G. You, N.M. Prabhu, Bioprocess and Biosystems Engineering, 46 (2023) 105.
8. K. Gupta, T.S. Chundawat, Materials Research Express, 6 (2019) 1050d6.

# THE EFFECT OF DIETARY FLAVONOIDS ON PROTEINS IN ALZHEIMER DISEASE

**H. NIKOLAICHUK, E. FORNAL**, Medical University of Lublin, Faculty of Biomedicine, Department of Bioanalytics, Jaczewskiego 8b, 20-090 Lublin, Poland.

**Abstract:** Dementia is a complex and growing challenge for the health of the global population. Dementia causes memory and cognitive impairment, leading to adverse consequences for individuals, families, and the economy. Numerous studies have indicated that a healthy lifestyle and a nutritional diet rich in vegetables, fruits, legumes, and herbs are associated with a lower risk of developing dementia. Naturally occurring dietary flavonoids have been identified as potential candidates for dementia therapy and protection, due to their highly diverse range of bioactive properties. In this review, we discuss general considerations, requirements, pitfalls, and future perspectives on the influence of dietary flavonoids on proteins involved in AD (Alzheimer disease).

**Introduction:** More than 55 million people worldwide are currently affected by dementia, and this figure is expected to increase to 152 million by 2050 [1]. The disease is estimated to affect approximately 6% of the population aged > 65 years, with its occurrence growing exponentially with age, reaching 40-70% for those aged > 95 years [2]. Dementia is a neurodegenerative disorder that causes memory and cognitive impairments, leading to negative consequences for individuals, families, and the economy. For example, in 2019, the global cost of dementia was estimated at 1.3 trillion US dollars [3]. The term 'pre-dementia syndromes' encompasses all conditions with age-related cognitive function decline, including a mild stage of cognitive impairment based on a normality model and pathological conditions predictive of early stage dementia.
AD accounts for approximately 50-60% of cases and is the most prevalent form of dementia. AD is a complex, multifactorial, slowly progressing disease that commonly starts with episodic memory impairments and appears to be unique to humans. Cognitive abilities typically diminish with age, and AD may be diagnosed when a patient exhibits a significant loss of memory and at least one additional cognitive function that negatively affects social or occupational functioning, which presents complex and unpredictable problems in multiple domains. In the advanced stages of AD, common symptoms such as confusion and gait disturbances become more pronounced and patients require increased assistance in activities of daily living. The age of onset, the rate of progression and the development of pathology are highly variable among patients. AD is characterized by three primary features: (i) extracellular accumulation of amyloid-beta (Aβ) plaques, (ii) intracellular neurofibrillary tangles (NFT) consisting of hyperphosphorylated tau and (iii) continuous cognitive decline. Both Aβ and NFT contribute to the worsening of cognitive function. Specifically, Aβ peptides form plaques that damage neuronal connections, while NFT destabilizes microtubule proteins and disrupt sneuronal communication. There are two main causes of AD: genetic (approximately 70%) and environmental (approximately 30%). There are two genetic forms of AD: familial AD (accounting for 90% of cases), which develops later in life (after 65 years) and is associated with a family history of the disease, and sporadic AD,

which accounts for the remaining 10% of cases, for example, in individuals with a genetic variant of the apolipoprotein gene, APOE-4. Despite the efforts of researchers over the past few decades, no definitive cure or pharmaceutical intervention is currently available for treating or preventing dementia. Six FDA-approved drugs are used to treat mild-to-moderate AD (donepezil, tacrine, galantamine, and rivastigmine as cholinesterase inhibitors; memantine as *N*-methyl-D-aspartate receptor; and aducanumab as monoclonal IgG1 antibody). All pharmaceuticals offer limited relief from disease symptoms. Although our understanding of risk factors and dementia diagnosis has improved, a considerable knowledge gap remains [1-3].

Many environmental and genetic factors contribute to the onset of AD, including physical activity, diet, and associated metabolic illnesses. A meta-analysis evaluated the population-attributable risk of AD caused by seven modifiable risk factors: diabetes, midlife hypertension, midlife obesity, physical inactivity, depression, smoking, and low educational attainment. The analysis revealed that, when combined, these factors were responsible for 50% of all AD cases, highlighting the significant influence of lifestyle factors on AD pathogenesis. Supporting people improve their quality of life is possible by preventing, delaying, or intervening in cognitive decline. Oxidative stress and inflammation are the factors that contribute to AD. Oxidative stress, inflammation, and aging are interconnected and affect each other through various mechanisms, including post-translational modifications. Increased oxidative stress causes a pro-inflammatory response that is linked to aging, a phenomenon known as 'inflammageing' [4-6].

Certain dietary patterns and lifestyles have been linked to a reduced incidence of AD. Research indicates that maintaining a healthy diet can affect several risk factors for cognitive decline, such as inflammation and oxidative stress, and following the Mediterranean diet (MeDi) and Mediterranean-DASH diet interventions for neurodegenerative delay (MIND) appears to be beneficial. The MeDi and MIND dietary patterns are characterized by high consumption of vegetables, fruits, nuts, legumes, cereals and fish, low intake of meat and dairy products, and moderate alcohol consumption. Observational studies have indicated that both the MeDi and MIND diets are associated with a lower risk of oxidative stress, inflammation, and dementia than a Western-style diet that typically includes more red meat, saturated fats, and sugar [5-10].

Recent studies suggested that dietary supplementation studies have shown that a high intake of flavonoid-rich plants or food extracts influences cognition and learning in humans and animal models of diseases. Notably, some phytochemicals can attenuate blood-brain barrier inflammation and exert neuroprotective effects. The relationship between dietary flavonoids and Aβ and tau pathologies remains unclear, but it is known that flavonoid-rich foods can increase BDNF levels in brain regions responsible for learning and memory [11]. Naturally occurring dietary flavonoids exhibit anti-amyloidogenic, antioxidative, and anti-inflammatory properties. For example, luteolin, myricetin, quercetin, kaempferol, apigenin, orobol, and genistein, dietary flavonoids found in food, exhibit a variety of biological activities, including the ability to modulate the aggregation of metal-bound beta-amyloid, inhibition of acetylcholinesterase, radical scavenging free radicals, antioxidant and anti-inflammation activities, and potential learning and memory enhancement ability and promotion. Recent epidemiological studies have suggested that a higher intake of total flavonoid constituents is associated with a slower decline rate in global cognition and multiple cognition domains. Several mechanisms have been proposed for the ability of flavonoids to prevent the onset or slow the progression of the disease. Several mechanisms involve interactions with crucial

signaling pathways in the brain, such as phosphatidylinositol 3-kinase/Akt and mitogen-activated protein kinase pathways. These pathways regulate the expression of prosurvival transcription factors and genes. Other processes involve disruption of amyloid-β aggregation and alterations in amyloid precursor protein processing. This occurs through the inhibition of β-secretase and/or activation of α-secretase as well as the inhibition of cyclin-dependent kinase-5 and glycogen synthase kinase-3β activation, preventing abnormal tau phosphorylation. Despite extensive research on flavonoids, none of the compounds under investigation has been successfully registered as drugs. They are often classified as invalid/improbable metabolic panaceas (IMPs), lacking drug-like characteristics, such as specific interactions with definable receptors, or as pan-assay interference compounds (PAINs) that can interact with numerous targets in *in vitro* assays [12]. Additionally, *in vitro* and *in vivo* studies have demonstrated that the antioxidant capacity alone is not responsible for the ability of flavonoids to prevent or reverse cognitive decline [13-18].

**Conclusions:** Flavonoids, commonly found in natural foods, are a popular choice for treating AD due to their effectiveness in cell cultures and animal models. They have demonstrated beneficial properties to combat the general mechanisms of AD. However, further research is needed to understand the specific mechanisms by which flavonoids exert their potential neuroprotective effects. This information is crucial before flavonoid-based dietary applications can be used to reduce the risk of AD. Further research on the mechanisms underlying flavonoid-protein interactions in AD may lead to the development of novel neuroprotective strategies for neurodegenerative diseases, thereby providing a promising goal for future research.

**Acknowledgments:** This work was supported by National Center Science grant no 2023/07/X/NZ9/01446.

**References:**

1. G. Livingston, J. Huntley, A. Sommerlad, The Lancet, 396 (2020) 10248.
2. D.Q. Beversdorf, H.W. Crosby, J.I. Shenker, Missouri Medicine, 120 (2023) 1.
3. F.I. Baptista, A.G. Henriques, A.M.S. Silva, J. Wiltfang, E. Da Cruz, O.A.B. Silva, ACS Chemical Neuroscience, 5 (2014) 2.
4. R.F. Townsend, J.V. Woodside, F. Prinelli, R.F. O'Neill, C.T. McEvoy, Frontiers in Nutrition, 9 (2022) 806006.
5. G. Nam, M. Hong, J. Lee, Chemical Science, 11 (2020) 37.
6. B.J. Baranowski, D.M. Marko, R.K. Fenech, A.J.T. Yang, R.E.K. Macpherson, Applied Physiology, Nutrition and Metabolism, 45 (2020) 10.
7. V. Solfrizzi, V. Frisardi, D. Seripa, Current Alzheimer Research, 8 (2011) 5.
8. M.C. Morris, Y. Wang, L.L. Barnes, D.A. Bennett, B. Dawson-Hughes, S.L. Booth, Neurology, 90 (2018) 3.
9. M. Martucci, R. Ostan, F. Biondi, Nutrition Reviews, 75 (2017) 6.
10. R.B. De Andrade Teles, T.C. Diniz, T.C. Costa Pinto, Oxidative Medicine and Cellular Longevity, 2018 (2018) 7043213.
11. M.O. Welcome, PharmaNutrition, 11 (2020) 100177.
12. D.S. Seigler, J.B. Friesen, J. Bisson, Frontiers in Nutrition, 8 (2021) 762753.
13. K.R. Gildawie, R.L. Galli, B. Shukitt-Hale, A.N. Carey, Current Nutrition Reports, 7 (2018) 2.
14. G. Nam, M. Hong, J. Lee, Chemical Science, 11 (2020) 37.
15. T.M. Holland, P. Agarwal, Y. Wang, Neurology, 94 (2020) 16.
16. C. Yuan, E. Fondell, A. Bhushan, Neurology, 92 (2019) 1.
17. Y. Kimura, D. Yoshida, T. Ohara, BMC Geriatrics, 22 (2022) 1.
18. T.S. Yeh, C. Yuan, A. Ascherio, B.A. Rosner, W.C. Willett, D. Blacker, Neurology, 97 (2021) 10.

# THE EFFECT OF DIETARY FLAVONOIDS ON POST-TRANSLATIONAL MODIFICATION OF PROTEINS IN THE CONTEXT OF DEGENERATIVE DISEASES

**H. NIKOLAICHUK, E. FORNAL**, Medical University of Lublin, Faculty of Biomedicine, Department of Bioanalytics, Jaczewskiego 8b, 20-090 Lublin, Poland.

**Abstract:** Recently, post-translational modifications (PTMs) have also been linked to the development and progression of neurodegenerative diseases such as Alzheimer's and Parkinson's disease. In this review, we discuss the growing evidence linking PTMs to the trinity of oxidative stress, inflammation, and aging, thus influencing multiple hallmarks of aging. Despite the extensive efforts made to define the molecular mechanisms underlying neurodegeneration, many aspects of these pathologies remain unclear.

**Introduction:** Over the last century, drastic changes in lifestyles and dietary habits have led to the emergence of various chronic non-communicable diseases such as cancer, cardiovascular disease, diabetes, inflammation, and neurodegenerative disorders. Several studies have shown that many diseases and ailments can be prevented and controlled by a balanced, adequate, diverse, and nutrient-rich plant-based diet [1-4].

In recent years, increasing attention has been drawn to the importance of post-translational modifications (PTMs) in the development and progression of these diseases. PTMs can be enzyme-catalyzed or spontaneous chemical reactions that involve attachment, removal, exchange, or rearrangement of a functional group of the proteome and metabolome; PTMs are generally divided into two categories: enzymatic and non-enzymatic. Enzymatically catalyzed PTMs are tightly regulated, specific to their substrates, and largely reversible. In contrast, non-enzymatic post-translational modifications (nPTMs) are spontaneous and not very regulated chemical reactions between electrophilic metabolites (endogenously or exogenously derived) and nucleophilic amino side chains of proteins and lipids (or protein *N*-termini) that lead to chemical group addition reactions [5]. Enzymatic and non-enzymatic PTMs has been found in molecular aging and dysfunction [6], chronic kidney disease [7], cardiovascular disease [8,9], diabetes [10] and cancer [11]. Most recently nPTMs have been linked to the development and progression of neurodegeneration such as Alzheimer's (AD) and Parkinson's (PD) diseases, *e.g.*, oxidation of amino side of lysine, arginine, proline, histidine, tyrosine and cysteine; nitration of amino acids in tyrosine which caused degradation of α-synuclein; glycation of lysine and arginine in proteins and lipids which caused advanced glycation end-product (AGE) [12] as well as carbonylation of cysteine, lysine and histidine [13]. Enzymatic PTMs have been linked to the phosphorylation of tau in AD, acetylation of α-synuclein in PD, and the phosphorylation of huntingtin in Huntington's disease (HD)[14]. Another recent study provided detailed insight into the growing evidence that PTMs link the trinity of oxidative stress, inflammation and aging, thereby influencing multiple hallmarks of aging [15].

Neurodegenerative diseases are multifactorial incapacitating disorders of the nervous system, affecting approximately 30 million individuals worldwide. The origins of neurodegenerative diseases such as AD, PD, HD, and amyotrophic lateral sclerosis are

protein misfolding and dysfunctional trafficking. Additionally, the onset of neurodegenerative diseases is associated with oxidative stress, mitochondrial dysfunction, and/or environmental variables that are closely associated with aging. Throughout the years of intense research that these factors significantly contribute to the etiology of common neurodegenerative diseases. Despite the extensive efforts made to define the molecular mechanisms underlying neurodegeneration, many aspects of these pathologies remain unclear. The most common neurological condition is AD; it is a significant burden that is expected to triple in frequency worldwide by 2050. Due to the irreversible loss of neurons and their functional networks in the brain, AD is characterized by clinical symptoms, such as cognitive decline, memory loss, language difficulties, and trouble performing daily tasks. Patients in the early stages of the illness have trouble recalling their recent discussions, names, or events. Poor communication, disorientation, confusion, behavioral changes, trouble speaking and swallowing, and lack of motor coordination are characteristics of the later phases. Since AD was first defined at the turn of the 20$^{th}$ century, its definition has evolved and now takes into account both biological and clinical traits. The cost of AD treatment is increasing worldwide. Despite significant efforts, the development of clinical treatment options for has consistently failed. In order to address the unmet medical requirements of AD, reliable disease pathways, biomarkers, and drug targets must be sought. This is because the palliative treatments available today are temporary. A further concern raised by the difficulties in drug discovery is the strategies used in contemporary conventional diagnosis, drug design, and knowledge of illness pathways, biomarkers, and targets. In this setting, PTMs control protein trafficking, function, and degradation, and their thorough research is crucial to discovering new biomarkers and drug targets. Proteins pertinent to a disease can have abnormal PTMs that set off pathological processes and cause the disease to progress.

PD is the second most common neurological condition after AD. It has increased significantly over the past 20 years, making it one of the neurological disorders with the fastest worldwide growth rates. Diagnosis is based primarily on clinical evaluation, but early diagnosis, prognostic indicators, and disease-modifying therapies are still lacking. Evidence is mounting that there may be a prodromal stage (5-15 years before motor signs show) that could allow for an earlier diagnosis using biomarkers and a window of therapy. PET/SPECT imaging could identify preclinical dopamine dysfunction in high-risk individuals

Phytochemicals, plant-derived entities, can interact favorably with the human body and hence produce beneficial effects in terms of health promotion and therefore play a significant role in the prevention and treatment of diseases and ailments. Currently, medicinal plants such as *Rhodiola rosea* L., *Clitoria ternatea* L., and *Humulus lupulus* L. are renowned. For example, salidroside, a bioactive polyphenolic compound inherent in *Rhodiola rosea* L., with various pharmacological effects such as antioxidant, anti-inflammation, anti-cancer neuroprotective including AD and PD, anti-stroke, anti-depressive and anxiolytic, reduction of oxidative stress, additionally improve learning and memory performance [16-21]; rosavin, also known from as a phenylpropanoid glycoside constituent from *Rhodiola rosea* L., displayed a wide range of activities such as antioxidant, anti-inflammation, anti-diabetic, attenuation oxidative stress, and amelioration neurodegenerative diseases [22-24]; taraxerol, from *Clitoria ternatea* L. and *Hypericum perforatum* L., an oleanane-type pentacyclic triterpene, is considered an

antioxidant, anti-diabetic, anti-inflammatory, anti-cancer and neuroprotective agent [25,26]; xanthohumol from *Humulus lupulus* L., prenilated flavonoid was found to be an antioxidant, anti-inflammatory, antiproliferative, chemopreventive, anti-neoplatic, anti-cancer, and neuroprotective agent [27,28]; quercetin and kaempferol, which are widely distributed in edible plants, as a flavonoids significantly contributed to human health and showed antioxidant, anti-inflammatory and neuroprotective activities [29-31]. There are numerous *in vitro*, *in vivo*, and clinical studies on the abovementioned compounds. However, the exact molecular mechanisms underlying their health-promoting effects are still unclear or poorly described. Therefore, a significant study the role of these compounds in human health is needed.

Rosavin, salidroside, taraxerol, xanthohumol, quercetin, and kaempferol are potentially soft electrophiles that may be involved in non-enzymatic post-translational modifications (nPTM) of regulatory proteins, lipoproteins, and peptides. As a result, this leads to the elimination of inflammation and the reduction of cellular oxidative stress. Many nPTMs have been proposed only as indicators of various cellular stresses or as biomarkers of aging, diabetes, cancer, neurodegenerative diseases, *etc*. However, nPTMs are central to understanding fundamental problems in biology and play essential roles in cellular metabolism, human health, and aging. Therefore, reliable detection and qualification of these emerging modified biomarkers are becoming increasingly important for accurate risk stratification and the development of prevention and intervention strategies [5,15,32,33].

**Conclusions:** Drastic changes in lifestyles and dietary habits have led to the emergence of various chronic non-communicable diseases such as cancer, cardiovascular disease, diabetes, inflammation, and neurodegenerative disorders. A balanced, adequate, diverse and nutrient-rich plant-based diet can prevent and control many of these diseases. Recently, post-translational modifications (PTMs) have been linked to the development and progression of these diseases. PTMs can be enzyme-catalyzed or spontaneous chemical reactions that involve the attachment, removal, exchange, or rearrangement of a functional group of the proteome and metabolome. Future research needs to elucidate the effect of specific dietary composition on proteins and improve the overall quality of life of the human population.

**Acknowledgements:** This work was supported by the National Center Science grant no. 2023/07/X/NZ9/01446.

**References:**

1. G. Sogari, T. Pucci, V. Caputo, E.J. Van Loo, Food Quality and Preference, 104 (2023) 123.
2. N. Afshar, A.M. Hodge, N. Shivappa, J.R. Hébert, Cancer Epidemiology, 82 (2023) 752.
3. J. Lee, D.-G. Jo, D. Park, H.Y. Chung, M.P. Mattson, Pharmacological Review, 66 (2014) 815.
4. L. Dai, L. Schurgers, P.G. Shiels, P. Stenvinkel, Clinical Science, 135 (2021) 369.
5. E.Q. Jennings, K.S. Fritz, J.J. Galligan, Molecular Aspects of Medicine, 86 (2022) 1075.
6. L. Gorisse, C. Pietrement, V. Vuiblet, C.E.H. Schmelzer, Proceedings of the National Academy of Sciences of the USA, 113 (2016) 125.
7. J. Laget, F. Duranton, À.Argilés, N. Gayrard, Molecular Aspects of Medicine, 86 (2022) 369.
8. M. Lehrke, J. Moellmann, F. Kahles, N. Marx, Molecular Aspects of Medicine, 86 (2022) 869.
9. Z. Wu, V. Jankowski, J. Jankowski, Molecular Aspects of Medicine, 86 (2022) 569.
10. A. Fountas, L.N. Diamantopoulos, A. Tsatsoulis, Trends in Endocrinology and Metabolism, 26 (2015) 636.
11. S. Pan, R. Chen, Molecular Aspects of Medicine, 86 (2022) 1236.

12. S. Schmidt, D.M. Vogt Weisenhorn, W. Wurst, Molecular Aspects of Medicine, 86 (2022) 101096.
13. R. Harmel, D. Fiedler, Nature Chemical Biology, 14 (2018) 2369.
14. J. Hermann, L. Schurgers, V. Jankowski, Molecular Aspects of Medicine, 86 (2022) 569.
15. T. Ebert, N. Tran, L. Schurgers, P. Stenvinkel, P.G. Shiels, Molecular Aspects of Medicine, 86 (2022) 86.
16. M. Jin, C. Wang, Y. Xu, Z. Zhang, et.al., Biomedicine and Pharmacotherapy, 156 (2022) 639.
17. J. Gao, R. Zhou, X. You, F. Luo, et.al., Metabolic Brain Disease, 31 (2016) 771.
18. G. Zhao, A. Shi, Z. Fan, Y. Du, Oncology Reports, 33 (2015) 2553.
19. S. Guan, H. Feng, B. Song, W. Guo, International Immunopharmacology, 11 (2011) 2194.
20. K.C. Wen, C.S. Chang, Y.C. Chien, H.W. Wang, International Journal of Molecular Sciences, 14 (2013) 23420.
21. Z. Zhong, J. Han, J. Zhang, Q. Xiao, Drug Design, Development and Therapy, 12 (2018) 1479.
22. R. Albadawy, A.H. Hasanin, S.H.A. Agwa, S. Hamady, International Journal of Molecular Science, 23 (2022) 17.
23. W. Zhou, K. Chen, Q. Lu, Y. Luo, Chemistry and Biodiversity 17 (2020) 8569.
24. A. Elameen, V.M. Kosman, M. Thomsen, O.N. Pozharitskaya, Molecules, 25 (2020).
25. A.A. Mus, L.P.W. Goh, H. Marbawi, J.A. Gansau, Biomedicines, 10 (2022) 4.
26. T.E. Berté, A.P. Dalmagro, P.L. Zimath, A.E. Gonçalves, Steroids, 132 (2018) 5.
27. T.L. Yen, C.K. Hsu, W.J. Lu, C.Y. Hsieh, Journal of Agricultural and Food Chemistry, 60 (2012) 1937.
28. M. Liu, P. Hansen, G. Wang, L. Qiu, J. Dong, Molecules, 20 (2015) 754.
29. W.M. Dabeek, M.V. Marra, Nutrients, 11 (2019) 2288.
30. J. Silva dos Santos, J.P. Gonçalves Cirino, P. de Oliveira Carvalho, M.M. Ortega, Frontiers in Pharmacology, 11 (2021) 1023.
31. A. Anand David, R. Arulmoli, S. Parasuraman, Pharmacognosy Reviews, 10 (2016) 84.
32. M. Tang, S. Kalim, Molecular Aspects of Medicine, 86 (2022) 785.
33. M.A. Keller, G. Piedrafita, M. Ralser, Current Opinion in Biotechnology, 34 (2015) 153.

# COACERVATE AS A FORM OF HAND WASH COSMETIC

**T. WASILEWSKI[1], A. KRZYSZOWSKA[2], Z. HORDYJEWICZ-BARAN[2],** [1]University of Radom, Faculty of Applied Chemistry, Department of Industrial Chemistry, Chrobrego 27, 26-600 Radom, Poland, [2]Łukasiewicz Research Network - Institute of Heavy Organic Synthesis "Blachownia", Energetykow 9, 47-225 Kedzierzyn-Kozle, Poland.

**Abstract:** The study presents the results of research focused on developing a model hand washing preparation in the form of a coacervate. A composition of surfactants consisting of Sodium Laureth Sulfate (SLES) and Disodium Cocoyl Glutamate (DSCG) was utilized in the research. The study analyzed the impact of sodium chloride concentration on the dynamics of the coacervation process. The obtained coacervates were characterized in terms of their fundamental physicochemical and performance properties.

**Introduction:** Hand washing products constitute one of the most popular groups of cosmetics. Along with changing consumer preferences regarding the requirements for cosmetic products, formulations based on raw materials derived from renewable sources and with the least possible negative impact on the environment are increasingly required. Preliminary research conducted to date indicates that coacervates can be used as functional forms of cosmetic cleaning agents that are in line with current market trends [1-3].

Coacervate products are an aqueous dispersion consisting of lamellar droplets made up of surfactant molecules, formed through the separation of a surfactant-rich phase. The coacervation process, which leads to the creation of this surfactant-rich phase, can be initiated by introducing an appropriate concentration of an electrolyte, such as sodium chloride, which is preferred for this purpose [4-5]. An increase in the concentration of sodium chloride, results in the initiation of the coacervation process caused by changes in the structure of the micelles present in solution and the interactions occurring between the micelles [1,2].

In response to increasing electrolyte concentration, the initially small spherical micelles present in the solution grow into larger spherical aggregates. These then transform into cylindrical micelles, marked by a significant increase in the system's viscosity. Adding further quantities of sodium chloride causes the micelles to evolve into flat bilayer structures known as lamellae, leading to a noticeable decrease in viscosity. Continued addition of electrolyte prompts further changes in the shapes of structures formed in the solution. The lamellae reorganize into aggregates resembling liposomes, termed lamellar droplets, which consist of two or more bilayers. A high electrolyte concentration reduces the repulsion between individual aggregates, encouraging their fusion and agglomeration. This aggregation of droplets ultimately results in phase separation, i.e., the coacervation process [1-5]. The resulting coacervate is characterized by a very high concentration of surfactants, with minimal amounts of solvent and salts, while the remainder is an aqueous sodium chloride solution containing negligible surfactant quantities.

In this study, the impact of the quantity of added salt, specifically sodium chloride, on the physicochemical and performance properties of the resulting model hand washing liquids in the form of coacervates was investigated.

**Experimental:** For viscosity measurements, a Brookfield RVDV2T rheometer was utilized. All measurements were conducted at 22 °C with a rotation speed of 10 rpm. The result was recorded 3 seconds after the viscometer was activated. The final result was calculated as the arithmetic mean of three measurements.
To a 250 ml beaker, 3 g of model fat soiling was added and evenly spread across the bottom of the beaker. The beaker was then placed in the refrigerator for 1 hour. After this period, the beaker was brought to room temperature. A 0.4% coacervate solution heated to 40 °C was poured into the beaker containing the fat and stirred using a mechanical stirrer for 5 minutes at 300 rpm. Following this procedure, the solution was drained from the beaker, which was then rinsed with 5 ml of distilled water. The beaker was dried to a constant weight at 105 °C, and the residue was weighed. The final result was determined as the arithmetic mean of three independent measurements.
100 ml of a 1% (w/w) aqueous solution of the test coacervate was placed in a 250 ml cylinder. The foam was then generated (whipping time: 60 seconds; number of complete cycles: 60) using a perforated disc attached to a metal rod. The foaming ability was quantified as the volume of foam measured 10 seconds after its formation. The final result was determined as the arithmetic mean of three independent measurements.

**Results:** *Coacervate preparation:* The composition of the initial formulation for coacervate production is presented in Table 1.

**Table 1.** Composition of the formulation for producing a hand wash cosmetic in coacervate form.

| Ingredient name (INCI) | Concentration, % (w/w) | | | |
|---|---|---|---|---|
| Sodium Laureth Sulfate | 6 | | | |
| Sodium Cocoyl Glutamate | 2 | | | |
| Cocamidopropyl Betaine | 0.5 | | | |
| Coco-Glucoside | 1.5 | | | |
| Sodium Citrate | 0.5 | | | |
| Propanediol | 1 | | | |
| Sodium Benzoate, Potassium Sorbate | 0.45 | | | |
| Citric Acid | 0.3 | | | |
| Aqua | to 100 | | | |
| Sample (coacervate) | | | | |
| Concentration of NaCl added to initial formulation, % (w/w) | | | | |
| - | | C_NaCl_23.5 | C_NaCl_24.5 | C_NaCl_25.5 |
| Sodium Chloride | - | 23.5 | 24.5 | 25.5 |

100 grams of the initial composition were placed in a 200 ml beaker. Sodium chloride was subsequently added to the beaker in increments of 0.5 grams. After each addition, the preparation was thoroughly stirred until the salt dissolved. If there was no clear separation into two phases, another portion of sodium chloride was added. The amount of sodium chloride that induced separation into two distinct phases in less than 5 minutes

was considered the final result. The coacervation process is illustrated schematically in Fig.1. The lower section of Table 1 displays the percentage concentrations of sodium chloride added to the initial formulation to generate the tested coacervates.

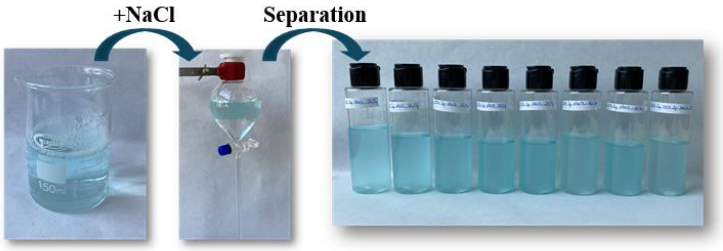



**Fig.1.** Scheme of the process for producing a hand wash cosmetic in coacervate form.

The results of the performed studies are shown in Figs.2-5.

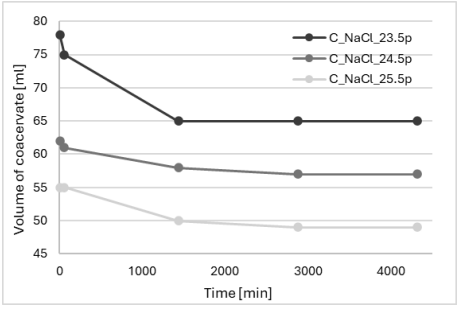



**Fig.2.** The dynamics of the coacervation process.

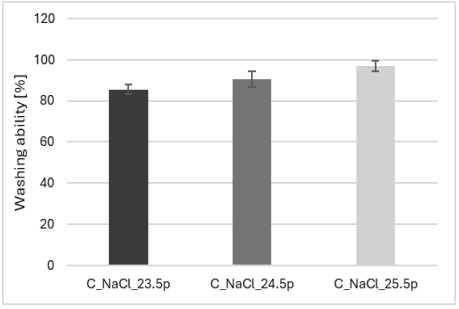



**Fig.3.** Detergency capacity of model hand wash cosmetic in coacervate form.

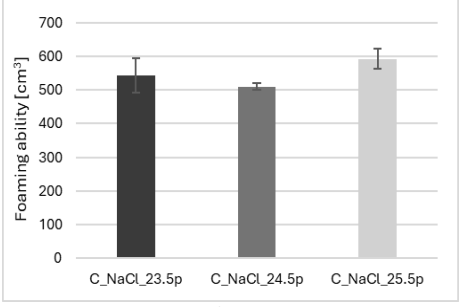



**Fig.4.** Foaming ability of model hand wash cosmetic in coacervate form.

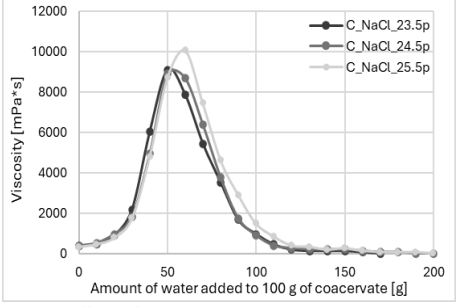



**Fig.5.** Effect of water amount addedt to coacervates on their dynamic viscosity.

All the studied coacervates demonstrated stability 24 hours after the initiation of the coacervation process (Fig.2). Assessment of detergency capacity (Fig.3) revealed that all the model coacervate formulations exhibited excellent detergency capacity, ranging from 86% to 97%. The detergency capacity increased with the concentration of salt added to

the initial formulation, suggesting a higher content of active substances in the coacervate formulations studied at elevated electrolyte concentrations.
The foaming ability was observed to be highest for the formulation with the highest concentration of added salt (Fig.4).
The addition of water to the coacervates (Fig.5) led to a notable increase in dynamic viscosity until reaching a maximum value, specific to the formulation. Further additions of water resulted in a decrease in the coacervate's viscosity. The electrolyte concentration affected both the maximum viscosity value and the amount of water at which this value occurred. The highest $\eta_{max}$ value was observed in the coacervate with the highest concentration of added salt.
However, the volume of the coacervates obtained was lowest for the formulation with the highest concentration of added salt (Fig.2). The obtained results indicate that the volume of the resulting coacervate phase may not be directly related to the lowest surfactant content, but rather to the increased degree of agglomeration of the lamellar droplets and the enhanced packing of particles in the solution.

**Conclusions:** The model handwashing liquids obtained in the form of coacervates exhibit variable parameters depending on the concentration of sodium chloride used in the coacervation process. The amount of sodium chloride added to 100 g of the initial composition influences both the process dynamics and the properties of the resulting coacervates. The increase in viscosity upon addition of water to the coacervates presents an intriguing correlation, allowing for the development of cosmetic concentrates or concentrated hand-washing products. Implementing this technology for producing a concentrated form of handwashing liquids represents a promising response to evolving market trends concerning environmental responsibility and aligns with sustainable development initiatives.

**References:**

1. T. Wasilewski, T. Bujak, Industrial and Engineering Chemistry Research, 53 (2014) 13356.
2. A. Seweryn, T. Wasilewski, T. Bujak, Industrial & Engineering Chemistry Research, 55 (2016) 1134.
3. T. Wasilewski, Journal of Surfactants and Detergents, 13 (2010) 513.
4. T. Wasilewski, SOFW Journal, 8 (2009) 37.
5. T. Bujak, T. Wasilewski, Z. Nizioł-Łukaszewska, Pure and Applied Chemistry, 91 (2019) 1521.

# LASER ABLATION REMOTE IONISATION MASS SPECTROMETRY IMAGING FOR DETECTION OF BIOMARKERS AND METABOLITES

**Z. KRUPA[1], J. NIZIOŁ[2], T. RUMAN[2]**, [1]Doctoral School of Engineering and Technical Sciences at the Rzeszów University of Technology, Rzeszów, Poland, [2]Rzeszów University of Technology, Faculty of Chemistry, Rzeszów, Poland.

**Abstract:** In the following paper, mass spectrometry imaging employing a system for laser ablation remote atmospheric pressure chemical ionization in negative mode for analysis of normal and cancerous bladder tissue was conducted. The results indicate six potential biomarkers for bladder cancer. Acquired ion images provide conclusive differentiation, proving laser ablation with remote ionization to be a suitable method for the analysis of spatial distribution of compounds in human tissues.

**Introduction:** Mass spectrometry imaging (MSI) is an important analytical tool for visualization and analysis of spatial distribution of compounds in biological samples, such as plant or animal tissues. Current methods for MSI, most commonly employed in MS research are MALDI-MS and SALDI-MS, including being used in research conducted in order to identify cancer biomarkers [1]. Both methods, however, require previous matrix or surface-assistant agent application, leading to additional signals on the spectrum, which is particularly an issue with organic matrices used in MALDI-MS. Those techniques, moreover, are conducted in a vacuum, which can lead to object deformation. Methods for ionization under ambient conditions in MSI are also developed, most known being desorption electrospray ionization (DESI), but also other laser ablation-based techniques such as LAESI, LARESI, and others [2]. The approach employed in research presented in this paper utilizes a mid-IR laser, similarly to other methods of laser ablation-preceded ionization, in order to achieve an adequate depth of sampling, greater than possible for UV laser in accordance with biological tissues [3]. The ionization method – atmospheric pressure chemical ionization, as well as negative-mode analysis, was employed due to previous research, not presented here, proving favorable to ESI ionization in terms of identifiable signal number and their intensities for the constructed setup.

**Experimental:** Bladder cancerous and normal tissue samples were collected from diagnosed patients at John Paul II Hospital in Kolbuszowa (Poland) [4]. The samples were not treated in any way before analysis other than freezing on Peltier cooler module in -18 °C. The laser ablation system consisted of Nd/YAG-pumped, OPO laser, an airtight chamber pressurized with nitrogen flow, aspheric lens, mounted on Z-axis stage, motorized XY-stage, Peltier cooling plate, and a 50 x 50 mm sample stage, similarly to a previously presented system [3]. During laser ablation, the sample is moved by the XY-stage controlled by designated software, while the laser focal point is fixed in space. The laser ablation plumes are entrained into the nitrogen gas flow and transported to the atmospheric pressure chemical ionization (APCI) source of Bruker Impact II QTOF mass spectrometer through a PTFE tube mounted to the ablation module and MS

sampling cone in the APCI source. The analysis was conducted in negative-mode ionization. Imaging was performed with resolution of 400 μm, laser shot duration of 1000 ms, delay between pixels of 1200 ms and between each new line of 3000 ms. The analysis of the results, as well as ion image generation was conducted in a dedicated software designated for the ablation system.

**Results:** The imaging of bladder cancer and control tissue allowed for identification of 49 metabolites in total, with six of them found in significantly higher intensities in the region of BC tissue, as seen in Fig.1. The identification has been based on previous LC-MS analysis of bladder cancer and the Ideom database. To obtain the LC-MS dataset, sectioned tissue underwent extracion to polar and low-polar fractions, subsequently analyzed on a C18 and HILIC column, as described in our previous publication [4]. Based on signal intensities, the results suggest significantly lower concentrations of amino acids in cancerous tissue in comparison to the normal tissue. The MSI analysis shows higher intensities of hippuric acid, ribitol, diphenylamine, 2-aminoacetophenone, urea, and creatinine in the region corresponding to cancerous tissue.

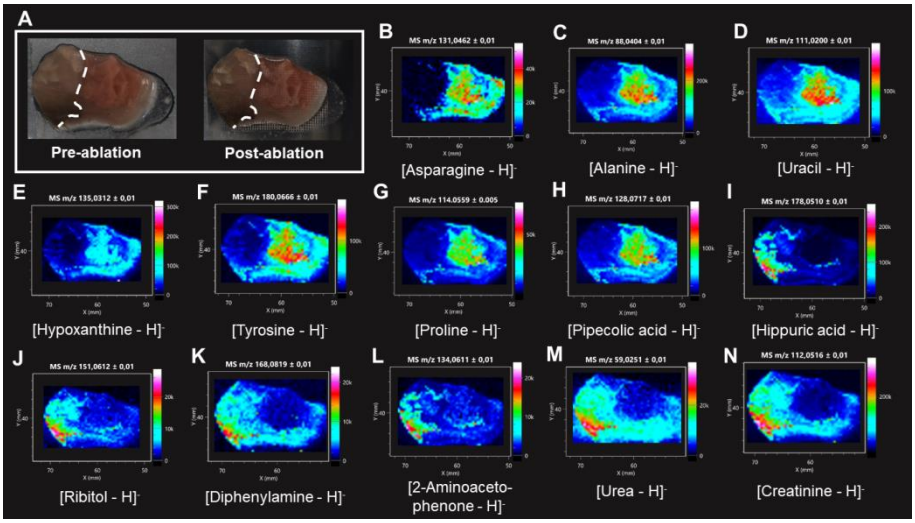



**Fig.1.** Image of analyzed tissues (A): bladder cancer tissue on the left of the white dotted line, normal tissue on the right, and ion images corresponding to chosen differentiating metabolites prevalent in noncancerous (B-H) and cancerous (I-N) tissue.

Hippuric acid (Fig.1I) is metabolized from phenylalanine in a pathway that has been reported to be altered in cancerous tissues of a bladder, and fluctuations of its occurrence have been linked to immunity disturbances and systemic inflammatory response, as well as hypertension. Similarly, creatine, of which creatinine (Fig.1N) is a breakdown product, as well as ribitol (Fig.1J) have been determined to be a differentiating compound between cancerous tissue and control bladder sample [5]. Aminoacetophenone (Fig.1L) has been associated with bladder cancer, its higher concentrations in cancerous tissue potentially resulting from disturbed metabolism of tryptophan [6].

**Conclusions:** Laser ablation remote ionization mass spectrometry imaging analysis provides a way to obtain ion images of varying suitable resolutions of various animal tissue metabolites, including potential cancer biomarkers, illustrating clear differentiation between normal and cancerous tissue regions. The important advantage of the method is the minimal need for sample preparation. The compounds prevalent exclusively in the cancerous part of analyzed bladder tissue are hippuric acid, ribitol, diphenylamine, 2-aminoacetophenone, urea, and creatinine.

**Acknowledgements:** The research was supported by National Science Centre (Poland) research project Sonata Bis number 2022/46/E/ST4/00016.

**References:**

1. A. Arendowski, Metabolites, 14 (2024) 173.
2. C.J. Perez, A.K. Bagga, S.S. Prova, M.Y. Taemeh, D.R. Ifa Rapid Commun Mass Spectrometry, 33 (2019) 27.
3. J. Nizioł, J. Sunner. I. Beech, K. Ossoliński, A. Ossolińska, T. Ossoliński, A. Płaza, T. Ruman, Analytical Chemistry, 92 (2020) 4251.
4. J. Nizioł, K. Ossoliński, A. Płaza-Altamer, A. Kołodziej, A. Ossolińska, T. Ossoliński, Z. Krupa, T. Ruman, Journal of Pharmaceutical and Biomedical Analysis, 240 (2024) 115966.
5. G. Petrella, G. Ciufolini, R. Vago, D.O. Cicero, Metabolites, 31 (2021) 756.
6. H. Kaseda, T. Noguchi, R. Kido, The Journal of Biochemistry, 74 (1973) 127.

# BIOPROSPECTING OF MICROBIAL ENZYMES FOR INDUSTIAL APPLICATION

**L. SENEROVIC**, **M. ATANASKOVIC, A. DJOKIC, N. STANKOVIC, L. DJOKIC, I. MORIC**, Institute of Molecular Genetics and Genetic Engineering, University of Belgrade, Vojvode Stepe 444a, 11042 Belgrade, Serbia.

**Abstract:** Biofilms have a major impact on human and animal health, pose a problem for food safety and contaminate drinking water supplies. They are one of the main causes of tolerance to antibiotics or disinfectants and thus represent a persistent bacterial reservoir for the spread of infections or contamination of food. A promising strategy to combat biofilms is to combine antimicrobial agents with enzymes that inhibit the formation of biofilms or are able to disintegrate components of the biofilm matrix, thus facilitating the penetration of antimicrobial agents and increasing their efficacy. New anti-biofilm enzymes in a unique proprietary collection of non-pathogenic environmental bacteria is searched. The enzymes candidates are heterologously expressed, purified and thoroughly analysed for their biological activity and stability. This approach has proven successful in the bioprospecting of enzymes that combat biofilms of pathogenic bacteria and can be used in the food and feed industry or as therapeutics.

**Introduction:** In recent decades, the exploration of microbial enzymes for industrial applications has increased significantly, driven by the growing demand for sustainable and environmentally friendly solutions in various sectors. This practise, known as bioprospecting, involves the systematic search, identification and utilisation of enzymes produced by microorganisms from different habitats. Microbial enzymes offer distinct advantages over chemical counterparts, including higher specificity, efficiency and environmental compatibility, making them invaluable tools for numerous industrial processes spanning food and beverages, pharmaceuticals, textiles, biofuels and bioremediation. These enzymes catalyse biochemical reactions under mild conditions, reducing energy consumption and minimising waste, which contributes to sustainable production processes. In addition, the great microbial diversity in nature offers an extensive repertoire of enzymes with unique properties and functions that provide a rich source for bioprospecting efforts. Our research focuses on a particularly pressing challenge in healthcare and other sectors: biofilms. Biofilms are complex communities of microorganisms enclosed in a self-produced extracellular matrix composed of extracellular DNA, polysaccharides and proteins [1]. They pose a major challenge due to their role in persistent infections and contamination of medical equipment, industrial facilities and food processing plants. It is estimated that biofilms are responsible for 60-80% of human infections, posing an enormous challenge to healthcare professionals. Furthermore, bacterial cells in biofilms can be up to 1000 times less sensitive to antibacterial agents than their free-living forms [2], rendering conventional treatment/cleaning strategies ineffective. In an effort to combat biofilms, the focus has been on anti-biofilm microbial enzymes. The new enzymes are searched in our unique microbial collection which has been collected over a period of 30 years and includes more than 1000 isolates from a variety of geographically unexplored regions (mountains,

caves, thermal springs, glacial and soda lakes). The collection also includes samples from archaeological excavations, bacterial isolates associated with ethnomedicinal and endemic plants, and strains associated with other species unique to the region (e.g. indigenous bat, goat and bee species, as well as freshwater fish and sponges). Thus, our collection is a remarkable natural source of diverse enzyme classes with a wide range of activities, specificities and structural stability. In particular, the searching for enzymes that either 1) interfere with cellular signalling pathways regulating biofilm formation (quorum quenching enzymes), or 2) degrade structural components of the biofilm matrix (DNase, glycoside hydrolase and protease) was performed. These enzymes have the potential to prevent biofilm formation, inhibit biofilm maturation or eliminate mature biofilms, offering new strategies for the treatment of biofilm-related problems such as chronic infections or food contamination. By elucidating the mechanisms of action of these anti-biofilm enzymes and exploring their potential applications in healthcare and other industries, our research aims to contribute to the development of innovative approaches for combating persistent infections and promoting public health and safety.

**Experimental:** It was applied bioactivity-guided screening of environmental bacterial collection using two approaches: 1) selective bacterial propagation on minimal media with AHLs as a sole carbon source (to identify lactonase and acylase) and 2) substrate-based screening on solid media supplemented with cellulose, alginate, xylan, starch, DNA or skimmed milk as a protein source to identify glycoside hydrolase, DNase and protease activity. Genes of interest were cloned and expressed in *Escherichia coli* and the enzymes were purified using metal affinity chromatography. The AHL hydrolytic activity of purified YtnP was tested using AHL specific biosensor strains [3]. Anti-biofilm activity was assessed using static biofilm assay in 96-well polystyrene plates. Biofilm biomass was stained with crystal violet (0.1%, v/v) and optical density was measured at 570 nm. Fluorescenly labeled bacteria were observed under a fluorescent microscope (10× magnification).

**Results:** *Pseudomonas aeruginosa* is an opportunistic pathogen that often causes chronic infections through biofilm formation on patients tissue or medical devices. According to the World Health Organisation, it is a critical pathogen for which new treatment methods need to be developed. Since biofilm formation in *P. aeruginosa* is controlled by quorum sensing (QS), hydrolysis of QS signalling molecules (quorum quenching-QQ) using lactonases has shown promise as a therapeutic approach against this bacterium, but also against other Gram-negative pathogens that use similar QS systems [3,4].
*Cryseobacterium aquaticum* SRL1 was isolated from a freshwater sponge using minimal medium supplemented with N-hexanoyl-L-homoserine lactone (C6-AHL). as a sole carbon source. Purified YtnP degraded C4-AHL and C12-AHL in dose-dependent manner and showed QQ activity inhibiting two different QS systems in *P. aeruginosa*, namely Las and Rhl. YtnP inhibited *P. aeruginosa* biofilm formation in a dose-dependent manner, and 50% inhibition was reached at an enzyme concentration of 100 μg $mL^{-1}$ (Fig.1A). YtnP dose-dependently decomposed 24-hour-old biofilm in *P. aeruginosa* (Fig.1B).

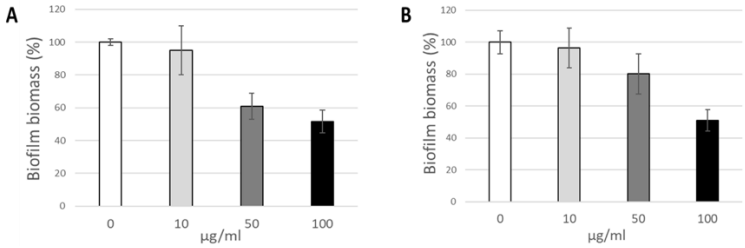



**Fig.1.** Anti-biofilm activity of recombinant YtnP lactonase. Values are presented as mean ± SD.

The food industry has constantly been challenged by the biofilm formation of foodborne pathogens. Once established, biofilm becomes the reservoir for recurrent food contamination. The most common foodborne pathogen is *Salmonella Enteritidis* that usually causes inflammatory gastroenteritis with relatively mild symptoms, but sometimes it can lead to fatal complications such as systemic infections with bacteremia. The biofilm formation of this pathogen in a non-host environment is mostly facilitated by cellulose as the dominant structural component of the biofilm matrix. Cellulose is a polysaccharide composed of β-D-glucosyl residues that are readily hydrolysed by β-glucosidase enzymes.

Bacterial collection from bream fish gills was searched for anti-biofilm enzymes to be utilized in the food industry. *Microbacterium* sp. BG28 showed strong cellulolytic activity originated from β-glucosidase B [5]. BglB-BG28 efficiently inhibited formation of biofilms in *Esherichia coli* and several serotypes of *S. enterica* (Fig.2) containing cellulose as the structural component of the biofilm matrix. Weak biofilm inhibition was observed in *P. aeruginosa*, while no effect on *Staphylococcus aureus* biofilm was detected. BglB-BG28 effectively inhibited *S.* Enteritidis biofilms on glass, plastic and metal surfaces. Pre-treatment with BglB-BG28 increased the biofilm removal efficiency of commonly used disinfectant Oxicide®S.

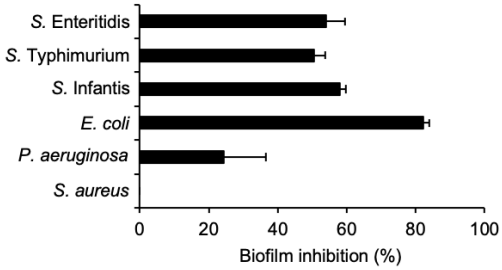



**Fig.2.** Anti-biofilm activity of BglB-BG28 (200 µg $mL^{-1}$). Values are presented as mean ± SD.

**Conclusions:** By harnessing the biochemical diversity of nature, bioprospecting promises to develop novel enzymes with customised properties that meet the evolving needs of modern industry while promoting sustainability and environmental protection. The YtnP lactonase and β-glucosidase B presented here showed strong anti-biofilm

activity and are suitable for biofilm prevention or treatment in both the healthcare and food industries.

**Acknowledgements:** This study has been funded by the Ministry of Education, Science and Technological Development, Serbia (grant number 451-03-66/2024-03/200042 and EUREKA Project 17236).

**References:**

1. H-C. Flemming, J. Wingender, Nature Reviews Microbiology, 8 (2010) 623.
2. J. L. Balcázar, J. Subirats, C. M. Borrego, Frontiers in Microbiology, 6 (2015) 1216.
3. K. Papenfort, B. L. Bassler, Nature Reviews Microbiology, 14 (2016) 576.
4. L. Djokic, N. Stankovic, I. Galic Moric, N. Radakovic, S. Šegan, A. Pavic, L. Senerovic, Frontiers in Microbiology, 13 (2022) 906312.
5. M. Atanaskovic, I. Moric, M.B. Rokic, A. Djokic, J. Pantovic, D. Despotović, L. Senerovic, Food Bioscience, 123 (2024) 103543.

# $CO_2$ HYDROGENATION IN THE PRESENCE OF ALUMINA AND SILICA SUPPORTED NICKEL CATALYSTS

**K. KARPIŃSKA-WLIZŁO, W. GAC, W. ZAWADZKI, G. SŁOWIK**, Maria Curie-Sklodowska University, Faculty of Chemistry, Institute of Chemical Sciences, Department of Chemical Technology, M. Curie-Sklodowska Sq. 3, 20-031 Lublin, Poland

**Abstract:** The catalytic methanation process can make a positive contribution to the fight against climate change caused by excessive carbon dioxide emissions. It is therefore reasonable to search for highly active and selective to methane or higher hydrocarbons catalytic systems. For this purpose, two catalytic systems with 10 wt. % nickel on two different supports - alumina and silica - were obtained by a modified wet impregnation method. The multiple role of support was evidenced, including the way of formation of metallic nickel crystallites, their surface properties and the course of elementary surface catalytic reactions. Both catalysts showed high $CO_2$ conversion, approaching 80-90% with over 95% selectivity to methane in the range of 350-400 °C. In-situ FTIR spectroscopic studies pointed out that higher activity of alumina supported catalysts, despite similar Ni crystallite size, can be ascribed to the facilitation of $CO_2$ activation via formation of the intermediate bicarbonate and carbonate species and their more effective successive hydrogenation to methane.

**Introduction:** The moment of the Industrial Revolution is undeniably a turning point in human history. With the invention of the first steam engines, the process of technological, economic and even social and cultural change took off exponentially. In the 18$^{th}$ century, however, no one could have foreseen the long-term consequences of using fossil fuels that we face today. The concentration of carbon dioxide in the atmosphere is reaching alarming levels - in March 2024, according to the Global Monitoring Laboratory (GML) of the National Oceanic and Atmospheric Administration (NOAA), it was 426.35 ppm, and is steadily rising year after year. The level to aim for to avoid further critical climate change is a minimum of 350 ppm. Not surprisingly, extensive measures are being taken to both reduce $CO_2$ emissions and manage it.

$CO_2$ is an attractive raw material that cannot only be captured and stored, but also converted into valuable chemicals. This involves the catalytic reaction of carbon dioxide with green hydrogen to obtain methane or higher hydrocarbons, which can be used both as a form of stored fuel and as a substrate for complex chemical syntheses, boosting a sustainable economy.

Although catalysts with different types of support have been extensively studied, including those based on alumina, ceria, zirconia or silica, there is still a lack of complete knowledge of the effect of the support on their catalytic properties and reaction mechanism. The present work aims to determine the influence of alumina and silica supports on the properties of the active phase, the activity and selectivity of highly dispersed nickel catalysts, and the course of elementary surface steps in the $CO_2$ hydrogenation reaction.

**Experimental:** Catalytic systems with 10 wt.% nickel content were obtained by a modified wet impregnation method [1-3]. Two types of commercially available supports were used: $\gamma$-$Al_2O_3$ (Alfa Aesar) and $SiO_2$ (Merck, Kieselgel 40, 35-70 mesh). The catalyst were calcined at 400 °C. The obtained materials were investigated by the low-temperature nitrogen adsorption-desorption method to determine the specific surface area and porosity (ASAP 2405N analyser, Micromeritics Instr. Corp.). Nickel content was determined by the X-ray fluorescence method. Reducibility of catalysts was studied by the temperature-programmed reduction (Micromeritics AutoChemII 2920). The nature of surface nickel sites was determined by the volumetric hydrogen chemisorption method (ASAP 2020C, Micromeritics Instr. Corp.) and temperature-programmed hydrogen desorption (Micromeritics AutoChemII 2920). The properties of catalysts after reduction were investigated by the X-ray diffraction (Empyrean, PANalytical diffractometer) and transmission electron microscopy (Titan G2 60-300 kV microscope, FEI Company) [1-3]. The course of $CO_2$ methanation reaction was determined by in-situ DRIFTS studies using FT-IR spectrometer (Nicolet 6700, Thermo Scientific) and Praying Mantis High-temperature Reaction Chamber (Harrick) [2]. $CO_2$ hydrogenation activity and selectivity studies were carried out by the application of Microactivity Effi system (PID Eng & Tech) coupled to a Bruker gas chromatographs [1-3].

**Results:** The main physicochemical properties of the Ni-$Al_2O_3$ and Ni-$SiO_2$ catalysts are summarized in Table 1. Although the catalysts show different porous properties and significantly differ in the specific surface area they contain nickel crystallites of similar size. However, the different way in which nickel crystallites are formed, as well as the different electron-acceptor properties of silica and alumina supports, result in the appearance of specific differences in the surface properties of the metallic nickel crystallites (Table 1).

**Table 1.** Properties of the catalysts.

| Catalyst | Ni content (wt. %) | Specific surface area ($m^2g^{-1}$) | Average pore diameter (nm) | Ni crystallite size (nm) | Active surface area ($m^2g^{-1}$) |
|---|---|---|---|---|---|
| Ni-$Al_2O_3$ | 10.65 | 234.8 | 10.2 | 10.1 | 8.4 |
| Ni-$SiO_2$ | 8.92 | 561.1 | 3.40 | 8.3 | 8.7 |

The adsorption and then decomposition of nickel precursors, diffusion and growth of NiO particles at the calcination stage, as well as formation of metal crystallites during reduction stage is influenced both by the porous properties of supports and the nature of metal-support interactions. The results of the temperature-programmed reduction (TPR) studies presented in Fig.1a underline a complex nature of nickel oxide phase in the catalysts. The TPR curves reveal the presence of small amounts of "free" NiO species and oxide phases more strongly interacted with support, including surface and bulk aluminates or silicates, respectively. The contribution of the more difficult-reducible phases is higher in alumina supported catalysts.

Catalysts despite similar active phase content also differ in the proportion of centers with different adsorption properties. Hydrogen temperature-programmed desorption curves

shown in Fig.1b evidence the larger contribution of weaker hydrogen adsorption sites in the silica supported catalyst.

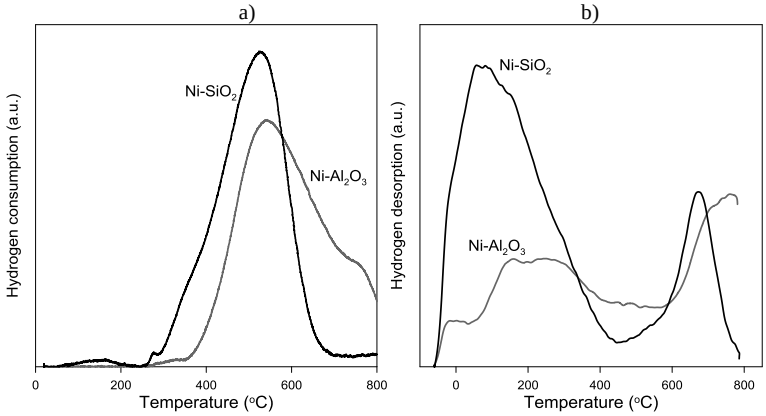



**Fig.1.** a) Temperature-programmed reduction of catalysts; b) Hydrogen temperature-programmed desorption curves.

The in-situ DRIFTS studies have identified differences in the $CO_2$ hydrogenation reaction occurred on the surface of Ni-$Al_2O_3$ and Ni-$SiO_2$ catalysts. The presence of absorption bands in the range 2200-1750 $cm^{-1}$ on the DRIFTS spectra shown in Fig.2 implies that $CO_2$ undergoes dissociative adsorption in the initial stages of the reaction with the formation of linearly and bridge-coordinated carbonyl groups. Small variations in their position and intensity suggest different surface properties of the nickel crystallites.

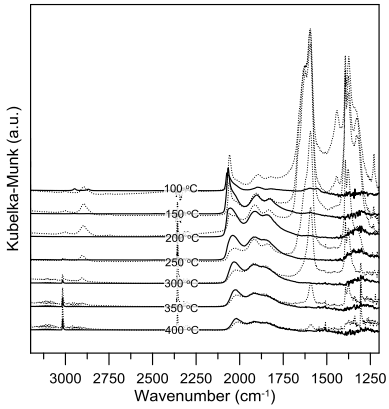



**Fig.2.** In-situ DRIFTS spectra recorded in the $CO_2$ methanation reaction carried out at selected temperatures in the presence of nickel catalysts supported with alumina (dashed lines) and silica (solid lines).

In turn, the presence of strong absorption bands only on the spectra of Ni-$Al_2O_3$ catalyst in the range 3000-2700 and 1750-1200 $cm^{-1}$ reveals the formation of differently coordinated surface carbonates and bicarbonates and their transformation to formates at relatively low temperatures (100-150 $^oC$). The observed effects underline important role of acid-base properties of supports on the course of hydrogenation reaction. A single

characteristic band of methane is visible at ca. 3020 $cm^{-1}$ on the spectra recorded at higher temperatures (above 250 °C, Fig.3). This proves both the high activity and selectivity of these systems.

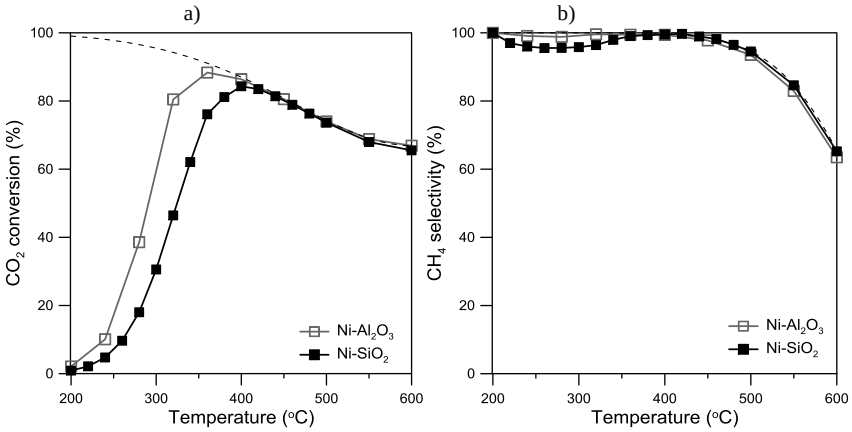



**Fig.3.** $CO_2$ conversion (a) and selectivity to methane (b) in the $CO_2$ hydrogenation reaction carried out in the presence of alumina and silica supported catalysts.

The onset of $CO_2$ hydrogenation occurs at about 200 °C. The alumina-supported nickel catalyst achieves higher $CO_2$ conversion at a lower temperature with a maximum of about 90% at ca. 360 °C. Ni-$SiO_2$ catalyst is also active, but $CO_2$ conversion at the same temperature is only about 75%. The selectivity of catalysts to methane is more than 95% in the temperature range of 200-400 °C. According to the thermodynamic limit, as the reaction temperature increases, the selectivity to methane decreases while it successively increases to carbon monoxide

**Conclusions:** Both obtained catalysts - Ni-$Al_2O_3$ as well as Ni-$SiO_2$ - show high activity and selectivity to methane in $CO_2$ hydrogenation process at low temperatures. The studies discussed above clearly indicate that the support influences the way of formation of nickel crystallites as well as can differentiate the nature of the catalyst's surface centers, which in turn determines its activity in the $CO_2$ hydrogenation process. The presented catalytic systems have large application potential in $CO_2$ methanation reaction due to their low manufacturing cost and high activity. Further studies are warranted to improve their catalytic performance at low temperatures, e.g. by introducing promoters that can modify the properties of nickel crystallites by alloying them with noble or non-noble metals, such as Fe, or by adding alkaline or rare earth metal oxides to induce appropriate changes in the acid-base or redox properties of the supports.

**References:**

1. W. Gac, W. Zawadzki, M. Rotko, M. Greluk, G. Słowik, G. Kolb, Catalysis Today, 357 (2020) 468.
2. W. Gac, W. Zawadzki, M. Greluk, G. Słowik, M. Rotko, M. Kuśmierz, Catalysts, 12 (2022) 13.
3. W. Gac, W. Zawadzki, M. Kuśmierz, G. Słowik, W. Grudziński, Applied Surface Science, 631 (2023) 157542.

# NEAR INFRARED REFLECTANCE SPECTROMETRY (NIRS) METHOD IN NATIONAL AND INTERNATIONAL FEED COMPARATIVE STUDIES

**S. WALCZYŃSKI, W. KOROL**, National Research Institute of Animal Production in Kraków, National Laboratory for Feedingstuffs, Chmielna St. 2, 20-079 Lublin, Poland.

**Abstract:** Results of national and international comparative studies on the content of basic feed constituent performed by the Near Infrared Reflectance Spectrometry (NIRS) method were presented. The obtained data made it possible to compare the results predicted by the NIR apparatus with those obtained in the leading European laboratories and used by leading feed manufacturers in the country. This was the optimal way to confirm their reliability and monitor their validity in daily laboratory practice in the field of feed. It made it possible to calculate the method bias depending on the type feed being scsnned according to the standard [1]. The matrices obtained from the comparative tests were a valuable reference material for supervising the correct operation of the NIR apparatus. Participation in the study created conditions for the inclusion of the NIRS method in the scope of accredited National Laboratory for Feedinstuffs methods.

**Introduction:** Near-infrared spectrometry NIRS is used to predict the content of organic compounds, e.g. in plant and animal materials and their mixtures. The method uses interactions occuring in a sample irridiated with an electromagnetic wave beam ranging from 770 nm to 2500 nm. During the absorption of infrared radiation, the particles of the test materials generate vibrations of the individual bonds in a manner similar to a diatomic oscillator. The excitation of vibrations of chemical bonds is correlated with energy absorption. The test apparatus allows to determine the content of compound containing characteristic functional groups, such as CH-, OH-, NH. The sent wave beam, when reflected from the sample, is received by the detector of the NIR apparatus providing important infrormation about the chemical compound in the test material. The calibration software of the spectrometer enables the identification of characteristic functional groups and their quantitative evaluation [2,3].

In the field of feed testing, the NIRS method allows to predict such parameters as moisture, crude protein, crude ash, crude fat, crude fiber, NDF fiber, starch, amino acids and others. Depending on the calibrations developed and validated, this technique can be used to estimate the energy value of the compound feed, its homogeneity and even to confirm the adulteration of the feed product [4].

Obtaining reliable results with an NIR apparatus requires its continuous monitoring and confirming compliance with the assumptions of the standard [5]. An appropriate way to obtain objective evidence in this respect is to involve a laboratory using the NIRS apparatus in the comparative studies of feedingstuffs. It is then possible to check the correct operation of your calibrations and compare your results with those of other study participants. The data obtained in this way form the basis for calculating the method bias depending on the tested matrix. The calculated corrections shall be applied to the corrections of the results in daily laboratory practice.

The aim of the paper was to compare the results of scanning samples of typical feed materials and feed mixture obtained from European countries (PT NIRS – Agroscope, AGES) and Poland (PT NIRS – Multi-year Task A15) carried out with NIRS devices of different manufactures.

**Experimental:** Comparative samples were scanned using the FOSS InfraXact 7500 NIR spectrometer operating in the spectral range from 570 nm to 1848 nm. The apparatus was equipped with FOSS calibration software for materials and feed mixtures in the range of such parameters as moisture, crude ash, crude protein, crude fat, crude fibre, starch, metabolic energy, amino acids.
Between 2018 and 2024, the National Laboratory for Feedingstuffs in Lublin participated in 6 rounds of proficiency tests organised by a consortium consisting of the International Analysis Group (IAG), the Austrian Agency for Health and Food Safety (AGES) and the Swiss Centre od Excellence for Agricultural Research (Agroscope). More than 20 laboratories belonging to European research organisations participated in each study. Thirty-nine samples were evaluated with 3 to 6 parameters each. These were samples of feed mixtures for poultry, cattle and pigs, as well as maize, wheat, barley, rapeseed and soybeans. The reference values were the mean values of the data reported by the laboratories participating in the PT after the removal of the outliers. The study organizer also included in the reports submitted the results of analyses obtained by reference methods with analytical tolerances obtained by the VDLUFA (Association of German Agricultural Analytic and Research Institutes) [6].
Subsequent comparative studies were organised by the National Laboratory for Feedingstuffs in Lublin, as one of the tasks of the multiannual programme in the years 2016-2020 and 2021-2025. During this period, 5 inter-laboratory comparisons were organised for national feed manufacturers with NIR equipment. The number of participants ranged from 12 to 15. The test materials were samples of compounf feed for poultry, piglets and feed materials: wheat, maize, soybean meal [2]. Comparisons were carried out in accordance with the requirements of PN-EN ISO/IEC 17043:2010 [5]. The reference values, as in the international studies, were the mean values of the data reported by the laboratories participating in the ILC after removal of the outliers.
Based on the obtained data from interlaboratory comparisons, the NIR bias for the InfraXact 7500 apparatus and mean square error of the RMSEP prediction and the expanded uncertainty of the results with coefficient of expanding k=2, were calculated according to each parameter of the test material.

**Results:** The results of the European inter-laboratory comparisons were evaluated. An exemplary individual final repost og the IAG NIRS Ring Trial 2023 is presented in the Table 1 below. The data received from the organizer, including z-scores and standard deviations for the proficiency test $\sigma_{PT}$, as well as differences between the assigned values and the results obtained in the InfraXact 7500 enabled the calculation of the method bias for individual parameters and matrices, the mean square errors of the RMSEP prediction and uncertainty of the results. Table 2 summarizes selected data regarding the testing of the poultry mixture. In the studies, almost 100% of NLF achieved results were satisfactory. The results that appeared ‘doubtful‘ after taking into account the uncertainty of the method were given a status of ‘satisfactory‘, with z-score below 2.

**Table 1.** Individual final report of the IAG NIRS Ring Trial 2023 [6].

IAG NIRS Ring Trial 2023

Laboratory report

laboratory number: A02
Institution: National Research Institute of Animal Production, National Laboratory for Feedingstuffs

| Sample | Measurand | mean.labor | sd.labor | Mean | Reproducibility s.d. | Z | Recovery rate % | Outlier |
|---|---|---|---|---|---|---|---|---|
| 1. Ruminant feed (compound feed) | moisture | 11.01 | 0.05 | | | | | |
| 1. Ruminant feed (compound feed) | XA | 4.18 | 0.02 | 3.45 | 1.27 | 0.58 | 121.3 | |
| 1. Ruminant feed (compound feed) | XF | 4.30 | 0.04 | 4.05 | 0.60 | 0.41 | 106.1 | |
| 1. Ruminant feed (compound feed) | XL | 2.71 | 0.03 | 3.07 | 0.35 | -1.04 | 88.1 | |
| 1. Ruminant feed (compound feed) | XP | 10.80 | 0.26 | 11.23 | 1.25 | -0.34 | 96.2 | |
| 1. Ruminant feed (compound feed) | XS | 60.70 | 0.08 | 61.24 | 2.62 | -0.21 | 99.1 | |
| 2. Pig feed (compound feed) | moisture | 9.11 | 0.03 | | | | | |
| 2. Pig feed (compound feed) | XA | 6.43 | 0.06 | 5.79 | 1.44 | 0.44 | 111.0 | |
| 2. Pig feed (compound feed) | XF | 4.85 | 0.10 | 4.87 | 1.04 | -0.02 | 99.6 | |
| 2. Pig feed (compound feed) | XL | 6.52 | 0.11 | 6.69 | 0.55 | -0.32 | 97.4 | |
| 2. Pig feed (compound feed) | XP | 19.60 | 0.34 | 20.58 | 1.10 | -0.89 | 95.2 | |
| 2. Pig feed (compound feed) | XS | 42.20 | 0.26 | 40.84 | 3.60 | 0.38 | 103.3 | |
| 3. Poultry feed (compound feed) | moisture | 9.45 | 0.02 | | | | | |
| 3. Poultry feed (compound feed) | XA | 7.45 | 0.02 | 12.93 | 4.09 | -1.34 | 57.7 | |
| 3. Poultry feed (compound feed) | XF | 4.26 | 0.08 | 4.54 | 0.63 | -0.45 | 93.8 | |
| 3. Poultry feed (compound feed) | XL | 7.03 | 0.04 | 6.22 | 0.59 | 1.37 | 113.0 | |
| 3. Poultry feed (compound feed) | XP | 25.02 | 0.30 | 23.62 | 1.38 | 1.02 | 106.0 | |
| 3. Poultry feed (compound feed) | XS | 37.38 | 0.25 | 34.79 | 2.60 | 1.00 | 107.4 | |
| 4. Corn/Maize (whole kernels) | moisture | 10.96 | 0.02 | | | | | |
| 4. Corn/Maize (whole kernels) | XF | 2.32 | 0.06 | 2.36 | 0.74 | -0.06 | 98.1 | |
| 4. Corn/Maize (whole kernels) | XL | 3.39 | 0.10 | 3.62 | 0.51 | -0.46 | 93.5 | |
| 4. Corn/Maize (whole kernels) | XP | 7.58 | 0.15 | 7.51 | 0.73 | 0.10 | 101.0 | |
| 4. Corn/Maize (whole kernels) | XS | 63.70 | 0.00 | 75.94 | 5.85 | -2.09 | 83.9 | E |
| 5. Wheat | moisture | 11.32 | 0.01 | | | | | |
| 5. Wheat | XA | 1.81 | 0.01 | 1.79 | 0.22 | 0.08 | 101.0 | |
| 5. Wheat | XF | 1.91 | 0.04 | 2.60 | 0.44 | -1.56 | 73.6 | |
| 5. Wheat | XL | 1.01 | 0.03 | 1.80 | 0.57 | -1.40 | 55.8 | |
| 5. Wheat | XP | 13.78 | 0.10 | 13.23 | 0.72 | 0.75 | 104.1 | |
| 5. Wheat | XS | 66.25 | 0.06 | 66.80 | 1.81 | -0.30 | 99.2 | |
| 6. Barley | moisture | 10.86 | 0.01 | | | | | |
| 6. Barley | XA | 1.94 | 0.01 | 2.28 | 0.39 | -0.87 | 85.2 | |
| 6. Barley | XF | 3.99 | 0.21 | 5.21 | 0.82 | -1.49 | 76.5 | |
| 6. Barley | XL | 1.58 | 0.06 | 2.13 | 0.48 | -1.14 | 74.4 | |
| 6. Barley | XP | 11.40 | 0.08 | 11.53 | 0.62 | -0.21 | 98.9 | |
| 6. Barley | XS | 65.62 | 0.34 | 61.13 | 2.21 | 2.03 | 107.4 | E |
| 7. Soybean cake | moisture | 8.82 | 0.02 | | | | | |
| 7. Soybean cake | XL | 1.51 | 0.04 | 1.97 | 0.64 | -0.72 | 76.5 | |
| 7. Soybean cake | XP | 54.90 | 0.08 | 56.83 | 1.52 | -1.27 | 96.6 | |

Mean labor.- assigned value; Mean- NLF result; z-score, a coefficient between -2.0 and 2. Indicates satisfactory results; XA- crude ash, XF-crude fiber, XL-crude fat, XP-crude protein, XS-starch

The available calibrations equipped with the NIRS analyser have proven their effectiveness in predicting the results of samples of test materials in interlaboratory comparisons. It has been found that this technique can be applied to typical feed materials such as cereal grains including maize, soybean meal and standard compound feed for farm animals.

The bias value of the NIRS method in international and national studies was compared. Depending on the matrix, these value did not differ significantly. In the IAG NIRS Ring trial the bias for poultry feed and parameters – moisture, crude protein, crude fat, crude fibre were: -0.41; -0.49; -0.38; -0.32, respectively. For national studies, the method bias for these parameters were: -0.08; -0.25; -0.48; -0.39, respectively.

**Table 2.** Results of prediction of selected basic nutrients using the NIRS method in the comparative studies IAG NIRS Ring trial in the years 2018-2023 – poultry feed.

| Year | Parameter | AV | NLF result | z-score NIRS | Bias | RMSEP | Uncertainty* |
|---|---|---|---|---|---|---|---|
| 2018 | Crude protein, % m/m | 22.20 | 22.67 | 0.52 | -0.49 | 1.02 | 2.04 |
| 2019 | | 19.89 | 21.02 | 1.90 | | | |
| 2021 | | 22.12 | 22.75 | 0.45 | | | |
| 2022 | | 24.10 | 22.92 | -0.59 | | | |
| 2023 | | 23.62 | 25.02 | 1.02 | | | |
| 2018 | Crude fat, % m/m | 3.83 | 4.04 | 0.59 | -0.38 | 0.48 | 0.96 |
| 2019 | | 5.55 | 5.22 | -0.54 | | | |
| 2021 | | 6.64 | 7.28 | 1.55 | | | |
| 2022 | | 5.71 | 5.90 | 0.37 | | | |
| 2023 | | 6.22 | 7.03 | 1.37 | | | |

AV-assigned value; RMSEP – mean square error of prediction,* Expended uncertainty with coefficient of expanding k=2

**Conclusions:** Comparative studies of feedingstuffs provide valuable information on the reliability of results predicted by NIRS. They also allow the calibrations used to be verified to reveal outliers in typical feed matrices appearing on the market. They were also the basis for activities aimed at including the NIRS method according to PN-ISO 12099:2017 in the scope of accreditation of NLF methods and acceptance of this scope by the Polish Accreditation Centre.

## References:

1. PN-ISO 12099:2017. Animal feeding stuffs, cereals and milled cereal products – Guidelines for application of near infrared spectrometry.
2. Interlaboratory comparisons reports 2016-2023, Multi-year Task A15, National Research Institute of Animal Production, National Laboratory for Feedingstuffs, Lublin, Poland.
3. D.A.Burns, E.W. Ciurczak, Handbook of near-infrared analysis, Third edition, CRC Press. USA, Chapter 7, 2008.
4. S.J. Noel, H. Johs, H. Jorgensen, K.E.B. Knudsen, The use of near-infrared spectroscopy (NIRS) to determine the energy value of individual feedstuffs and mixed siets for pigs, Animal Feed Science and Technology, 2021, https://doi.org/10.1016/j.anifeedsci.2021.115156.
5. PN-EN ISO/IEC 17043:2010. Conformity assessment. General requirements for proficiency testing.
6. Reports of NIRS Ringtest 2018-2023. International Analytical Group, Wien, Austria.
7. S. Samadi, A. Wajizach, A. Munawar, Near infrared spectroscopy (NIRS) data analysis for a rapid and simultaneous prediction of feed nutrive parameters, Data in brief 29 (2020), Elsevier.

# ENCAPSULATION OF GREEN TEA LEAVES EXTRACT BY SPRAY DRYING

**A. ŽUGIĆ[1], J. MUDRIĆ[1], N. KRGOVIĆ[1], M. TASIĆ KOSTOV[2], V. M. TADIĆ[1],**
[1]Institute for Medicinal Plants Research "Dr. Josif Pančić", 11000 Belgrade, Serbia,
[2]University of Niš, Faculty of Medicine, Department of Pharmacy, 18000 Niš, Serbia.

**Introduction:** In recent years, leaves of green tea (*Theae folium* (*Camellia sinensis*, Theaceae)) have been abundantly investigated due to their high content of polyphenolic, especially catechins including epigallocatechin-3-gallate (EGCG), epigallocatechin (EGC), epicatechin-3-gallate (ECG) and epicatechin (EC), shown to possess many health-promoting effects, such as hypoglycemic (anti-diabetic), anticarcinogenic, anti-inflammatory, antimicrobial and antioxidant activities [1]. The stability of bioactive compounds of green tea leaves, otherwise sensitive to environmental factors (such as light, heat, moisture, pH, and oxygen), may be preserved by their encapsulation within a coating material, i.e. their conversion from liquid to dry form, which additionally may enable their controlled release and prolong shelf life. Spray drying (SD) using encapsulating agents such as natural biopolymers from the group of polysaccharides and/or proteins has been widely used for the stated purpose, enabling the production of powders suitable for further usage in the pharmaceutical or food industry [2]. In this study, SD was used for drying green tea leaves extract, with or without the addition of pectin in various concentrations, which was used as an encapsulating agent.

**Experimental:** *Preparation of extract***:** The extract was obtained by percolation of green tea leaves with 50% (*v/v*) ethanol, (D:E = 1:5), in which the alcohol was evaporated to less than 5%, after which a dry residue of 7% (*m/m*) was determined.
*Spray Drying Process:* Samples without the addition of pectin (sample A) or with the addition of pectin in ratio of 1:2, 1:1 and 2:1 relative to dry residue (samples B, C and D, respectively) were dried using spray dryer (Labtex ESDTi, Labtex, Hudders eld, UK) with a needle diameter of 0.5 mm, the inlet temperature of 130±1°C, outlet temperature of 65±10°C, pressure of 2.2. bars, pump speed of 4, and airflow of 11. *Technological and Physicochemical Properties of the Microencapsulates:* In the obtained extracts the yield was calculated considering the initial mass of the liquid extract, i.e. the content of dry residue in the extract, the concentration of pectin, and the mass of the obtained dry extract. Flowability was determined based on bulk and tapped density, according to Ph Eur 10.0. The encapsulation efficiency of the marker compounds (EGCG, EGC, ECG, and EC) was determined using an appropriate HPLC method that allowed their quantification in the liquid extract and the resulting powders (spray-dried extracts). Scanning electron microscopy (SEM) was used for visualization of the size and surface morphology of the particles in the dried extracts, while the dissolution of EGCG, EGC, ECG, and EC from the dried extracts was determined in 0.1 M hydrochloric acid (pH = 1.2) at 37 °C.

**Results:** The powder yield was in the range of 53.50 to 60.63% and was the highest in samples a and C (without pectin and with pectin in ratio 1:1 relative to dry residue,

respectively). The addition of pectin led to a consequent improvement in the flowability of the dried extracts up to a ratio of pectin and dry residue of 1:1 (sample C). A further increase in the proportion of pectin in sample D did not lead to a comparative improvement in flowability. Similarly, in the SEM micrographs of sample a (without added pectin), the presence of particles of uniform size, irregular spherical shape with a wrinkled surface may be detected. With an increase in the proportion of pectin in samples B and C, the appearance of a fraction of spherical particles may be seen, which can be related to the presence of the encapsulating agent. In sample B, the regular spheres are similar in size to the particles of the wrinkled surface, and in sample C, the regular spheres were slightly larger compared to the ones in sample A. In sample D, where pectin content is twice as high compared to the dry residue, the presence of large spherical particles compared to small particles with a wrinkled surface is evident. Encapsulation efficiency was highest in sample C, with the exception of EGC and EC, where the highest encapsulation efficiency was detected in sample B. When it comes to the dissolution of marker compounds, the addition of pectin slowed down the dissolution rate of all tested compounds, and this effect was the most pronounced in sample C (in which the ratio of dry residue and pectin was 1:1), while the further increase of pectin content did not lead to a comparative increase in the dissolution rate of the tested compounds.

**Conclusions:** Results of the current study singled out the sample in which green tea leaves extract was dried with pectin and in which pectin to dry residue ratio was 1:1 due to the best yield, encapsulation efficiency, and flowability. Also, the slowest release of bioactive compounds was detected in this dry extract, which will be the basis for our further research.

**Acknowledgments:** Financial support for this work from the Ministry of Education, Science and Technological Development of the Republic of Serbia (Project No. E! 17236 (NATBIOPREP, Eureka Programme) and Grant number 451-03-66/2024-03/200003 are gratefully acknowledged.

**References:**

1. W.C. Reygaert, BioMed Research International, 2018 (2018) 9105261.
2. K.L. Baltrusch, M.D. Torres, H. Domínguez, N. Florez-Fernandez, International Journal of Biological Macromolecules, 203 (2022) 417.

# ANTIIFLAMMATORY ACTIVITY OF *PINUS* SP. ISOLATES

**A. ŽUGIĆ[1], S. MIRKOVIĆ[2], M. TOMOVIĆ[3], M. ANĐIĆ[3], A. PETROVIĆ[3], I. NEŠIĆ[4], V.M. TADIĆ[1]**, [1]Institute for Medicinal Plants Research "Dr. Josif Pančić", 11000 Belgrade, Serbia, [2]PHI Hospital "Sveti Vračevi", Bijeljina, Bosnia and Herzegovina, [3]Faculty of Medical Sciences, University of Kragujevac, Department of Pharmacy, 34000 Kragujevac, Serbia, [4]University of Niš, Faculty of Medicine, Department of Pharmacy, 18000 Niš, Serbia.

**Introduction:** Although topical preparations made from various *Pinus* species have ethnotherapeutic use in the treatment of various skin diseases (eczema, acne, alopecia, psoriasis, fungal diseases) and wound healing, the literature to confirm their potential for use in topical products are scarce. Therefore, in an attempt to develop a product based on natural ingredients for potential local treatment of inflammatory skin conditions, *in vivo* antiinflammatory activity of isolates of *Pinus* sp. green cones (essential oil, EO and the extract, E) prior to and after incorporation into liposomes was evaluated.

**Experimental:** EO was isolated from the crushed plant material by steam distillation using a Clevenger apparatus, while E was obtained *via* Soxhlet apparatus using 70% (v/v) ethanol. Four liposomal dispersions were prepared using purified water and Phosal 40 IP (Lipoid, Germany): blank dispersion (sample L), dispersion with encapsulated EO (sample L-EO), blank dispersion with the addition of E in the outer phase (sample L-E) and with encapsulated EO (sample LEO-E). Zetasizer Lab Blue Label was used for liposome size and zeta potential evaluation, while measurements of pH and electrical conductivity were performed using pH-meter HI 9321 and conductometer CDM 230, respectively. In order to check the preliminary physico-chemical stability of the prepared samples, measurements of pH, electrical conductivity, liposome size, and zeta potential were re-evaluated after 30 and 90 days of room temperature storage. The potential anti-inflammatory effects of the examined EO, E, and liposomal dispersions were evaluated *in vivo* using the carrageenan-induced rat paw edema test. Paw edema was induced in a left hind paw of each rat by intraplantar injection of 500 μl of 1% carrageenan (1). All rats were randomly divided into the following groups, depending of applied formulations: L, L-EO, L-E, LEO-E, EOP (water with E and EO), E (water with E), PE (water with E and Polysorbate 20), P (water with Polysorbate 20), HC (hydrocortisone as a standard), CTRL (control, untreated group). Examined formulations were administered topically, 60 min before the carrageenan injection, in an amount of 0.3 g and gently rubbed 50 times with the index finger. To quantify the anti-inflammatory effect, the thickness of the left paw tissue of rats was measured at specific time intervals: immediately before inducing inflammation (moment 0), and 1, 2, 3, and 4 hours after inflammation (moments 1, 2, 3, and 4). The tissue thickness was measured in the middle of the rat paw using a digital caliper and the percentage of inhibition of paw edema was calculated according to the formula.

**Results:** The droplet size of the prepared liposomes was in the range of 197.4 to 250 nm. The average droplet size in the sample L was 217.0. The addition of EO led to a decrease in droplet size, while the addition of E had an inverse effect. In all samples, the

polydispersity index, as a measure of droplet size distribution uniformity was lower than 0.2 indicating that the liposomes were relatively monodisperse. The zeta potential of tested liposomes ranged from – 36.63 to -41.16 mV, suggesting good kinetic stability. pH from 4.0 to 5.01 in all tested samples indicated their applicability in skin products. The addition of EO led to the decrease of conductivity compared to the sample L, while the addition of E led to its increase. Repeated measurements of tested physicochemical characteristics of the investigated liposomes did not change applicability, suggesting satisfactory preliminary stability.

The administration of LEO, LEOE, and LE led to significant inhibition of paw edema compared to the control group. The most significant reduction in edema was observed after the third and fourth hour. Hydrocortisone as a standard anti-inflammatory drug showed the most pronounced degree of inhibition compared to the control group. However, in the fourth hour, the LE and LEOE exhibited a similar effect as this standard drug with a percentage inhibition ranging from approximately 69% to 87%. Considering that LEO, LEOE, and LE exhibited the most prominent effects during the later phase of carrageenan-induced inflammation, we may hypothesize that these formulations affect the release of arachidonate metabolites, possibly by modulating the activity of cyclooxygenase 1 and 2 (2).

**Conclusions:** In the present study, liposomes with EO and E isolated from green cones of *Pinus* sp. revealed satisfactory physico-chemical characteristics/stability, and anti-inflammatory activity suggesting their prospective usage in the preparation of the products based on natural ingredients for potential local treatment of inflammatory skin conditions.

**Acknowledgements:** This study was supported by the Ministry of Science, Technological Development and Innovation of the Republic of Serbia, (grant number 451-03-66/2024-03/200003. and NATBIOPREP Eureka E117236).

**References:**

1. N. Nedeljković, M. Nikolić, P. Čanović, M. Zarić, R. Živković Zarić, J. Bošković, M. Vesović, J. Bradić, M. Anđić, A. Kočović, M. Nikolić, V. Jakovljević, Z. Vujić, V. Dobričić, Pharmaceutics, 16 (2023), doi: 10.3390/pharmaceutics16010001.

2. T Mićović, JS Katanić Stanković, R Bauer, X Nöst, Z Marković, D Milenković, V Jakovljević, M Tomović, J Bradić, D Stešević, D Stojanović, Z Maksimović. Journal of Ethnopharmacology, 293 (2022) 115201.

# PERCOLATION VS ULTRASOUND ASSISTED EXTRACTION: IMPACT ON CHEMICAL COMPOSITION AND PHARMACOLOGICAL ACTIVITIES OF *Vaccinium myrtillus* FRUIT EXTRACTS

**N. KRGOVIĆ[1], J. MUDRIĆ[1], M. MARTINOVIĆ[2], A. ŽUGIĆ[1], V. M. TADIĆ[1],**
[1]Institute for Medicinal Plants Research "Dr. Josif Pančić", 11000 Belgrade, Serbia,
[2]University of Niš, Faculty of Medicine, Department of Pharmacy, 18000 Niš, Serbia.

**Introduction:** Fruits, particularly berries, are one of the most important sources of phenolic compounds. Apart from diet, fruits are used for the production of herbal preparations intended for use in phytotherapy. At the industrial scale, percolation is the most widespread conventional extraction method for the recovery of phenolics from plant material, while ultrasound-assisted extraction, an unconventional extraction method, is considered a highly efficient alternative [1]. According to numerous reports, anthocyanins, the main phenolic constituents of wild bilberry (*Vaccinium myrtillus* L., Ericaceae), are connected with anti-inflammatory, antioxidant, vasoprotective, as well as hypoglycemic and hypolipidemic effects [2]. In this context, our study aimed to compare the phenolics profile, *in vitro* antioxidant and hypoglycemic activities of dry hydroethanolic extracts prepared from fresh berries (*Myrtilli fructus*) by percolation (P) and ultrasound-assisted extraction (UAE).

**Experimental:** *Plant material and preparation of extracts:* The ripe fruits of wild bilberry were collected from a locality in Montenegro (Bijelo Polje) in August 2021. Before the analysis, the fruits were stored at –4 °C in the freezer. Percolation and ultrasound-assisted extraction were employed for the preparation of extracts from fresh berries (1:10, w/v) with 50% ethanol. The extraction was performed at room temperature, which lasted for 24 h in the case of percolation, and 2 h for the UAE.
*Chemical analysis:* To determine total phenolics, the Folin–Ciocalteu (FC) spectrophotometric method was applied [3], while total anthocyanins were estimated by following the procedure with 0.1% hydrochloric acid in methanol, described in 10$^{th}$ European Pharmacopoeia [4]. The HPLC method was used for the identification and quantification of active principles in the bilberry extracts. Analysis was performed on Agilent 1200 HPLC system equipped with a photodiode-array (PDA) detector and Lichrospher 100RP 18e column (250 × 4.6 mm; 5.0 µm particle size). The mobile phase consisted of 0.1 M phosphoric acid solution (phase A) and pure acetonitrile (phase B). Total run time was 60 min, flow rate 0.8 mL/min, injection volume 4 µL, and column temperature 25 $^{o}$C; the PDA detector was set at 520 nm. For flavonoids and phenolcarboxylic acids analysis, different chromatographic conditions were applied, and the total run time was 70 min, flow rate 1.0 mL/min, injection volume 10 µL and column temperature 25 $^{o}$C; PDA detector was set at 260, 280, and 325 nm.
*In vitro pharmacological activities:* The antioxidant capacity of extracts was assessed by the DPPH, FRAP and ABTS [5] assays. The hypoglycemic potential was evaluated by the ability of extracts to inhibit α-amylase [6] and α-glucosidase [7], using potato

starch/3,5-dinitrosalicylic acid and p-nitrophenyl-α-D-glucopyranoside methods, respectively.

**Results:** Colorimetrically assays revealed higher total phenolic (39.67 vs 45.94 mg GAE/g) and total anthocyanins content (26.46 vs 31.00 mg CGE/g) in UAE extract. Regarding HPLC analysis, the same chemical profile was observed in both extracts, with little differences in the determined active principles amount. The main identified and quantified secondary metabolites included anthocyanins (delphinidin-3-O-glucoside: 3.08 vs 4.53 and cyanidin-3-O-glucoside: 3.77 vs 4.48, being the most abundant), phenolic acids (gallic acid: 0.30 vs 0.27; protocatechuic acid: 0.81 vs 0.78; chlorogenic acid: 2.02 vs 2.02 mg/g) and flavonols (hyperoside: 0.91 vs 0.77; quercetin: 0.09 vs 0.10 mg/g). All applied antioxidant assays, DPPH ($IC_{50}$: 149.16 vs 141.06 μg/ml), ABTS ($IC_{50}$: 26.64 vs 23.85 μg/ml), and FRAP (0.81 vs 1.09 mmol $Fe^{2+}$/g), showed the similar antioxidant capacity of investigated extracts. By testing the ability of extracts to inhibit carbohydrate-digesting enzymes, it was noticed almost equal for α-amylase ($IC_{50}$: 900 vs 770 μg/ml) and stronger inhibitory potential of the UAE for α-glucosidase ($IC_{50}$: 74.86 vs 35.85 μg/ml).

**Conclusions:** Considering the chemical composition and pharmacological properties of bilberry extracts, a similar trend was remarked for the UAE and P extraction methods.

**Acknowledgments:** Financial support for this work from the Ministry of Education, Science and Technological Development of the Republic of Serbia (Project No. E! 17236 (NATBIOPREP, Eureka Programme) and Grant number 451-03-66/2024-03/200003 are gratefully acknowledged.

**References:**

1. A.R. Abubakar, M. Haque, Journal of Pharmacy and Bioallied Sciences, 12 (2020) 1.
2. J. Liu, H. Zhou, L. Song, Z. Yang, M. Qiu, J. Wang, S. Shi, Molecules, 26 (2021) 3807.
3. Y.S. Velioglu, G. Mazza, L. Gao, B.D. Oomah, Journal of Agricultural and Food Chemistry, 46 (1998) 4113.
4. Council of Europe Platform on Ethics, Transparency and Integrity in Education. European Directorate for the Quality of Medicines and Health Care of the Council of Europe; European Medicines Agency: Strasbourg, France, 2019.
5. A. Zugic, S. Djordjevic, I. Arsic, G. Markovic, J. Zivkovic, S. Jovanovic, V. Tadic, Industrial Crops &Products, 52 (2014) 519.
6. O.A. Idris, O.A. Wintola, A.J. Afolayan, Asian Pacific Journal of Tropical Biomedicine, 7 (2017) 1071.
7. D. Ahmed, Q.M. Mughal, S. Younas, M. Ikram, Pakistan Journal of Pharmaceutical Sciences, 26 (2013) 553.
8. A.W. Indrianingsih, S. Tachibana, K. Itoh, Procedia Environmental Sciences, 28 (2015) 639.

# SYNTHESIS OF ALGINATE HYDROGELS DOPED WITH IRON MICROPARTICLES: RHEOLOGICAL AND SPECTROSCOPIC CHARACTERIZATION

**O. KAPUSTA, M. KACZMARCZYK, M. BARCZAK**, Maria Curie-Sklodowska University, Faculty of Chemistry, Institute of Chemical Sciences, M. Curie-Sklodowska Sq. 3, 20-031 Lublin, Poland.

**Abstract:** In this study, the possibility of dispersing of amine-functionalized iron microparticles in a alginate hydrogel framework was tested and the impact of such modification on the magnetorheological properties (that is, the change in rheological/mechanical properties under the action of an external magnetic field) of the obtained hydrogels was assessed.

**Introduction:** Magnetic hydrogels have been attracted significant interest due to their wide range of potential applications, including magnetic resonance imaging (MRI) contrast agents, hyperthermia therapy agents, drug delivery and release systems, tissue engineering, cancer therapy [1]. Among different hydrogels formulations, alginate-based hydrogels are considered as one of the preferred ones, due to low cost and excellent biocompatibility [2]. To fabricate 'smart' materials, alginate hydrogels can be doped with magnetically susceptible particles able to actuate upon action of the external magnetic field to provide additional features: stimuli-responsive action or tailorable rheological properties. This makes such ferrogels potentially useful in various fields, including: biomedicine [3,4], environmental protection [5] or nanotechnology [6].

**Experimental:** Following a published procedure [7], 1% alginate hydrogels (ALHs) were synthesized with magnetic iron microparticles (IMPs). Calcium carbonate was added to vials containing sodium alginate solution. The mixture was shaken until a cloudy solution formed, indicating complete dispersion. D-glucono-1,5-lactone was then added and dissolved. After allowing the solution to set for gelation, a portion was used as a control (ALG-0). The remaining solution was divided: one part was mixed with a lower amount of IMPs (ALG-1), and the other with a higher amount (ALG-2). Both mixtures were vortexed and sonicated before being cast into molds. Rheological shear strain tests of the obtained hydrogels were determined at 25 $^{o}$C using the MCR 301 magneto rheometer (Anton Paar) using a plate-plate geometry of 20 mm of diameter according methodology described by us previously [6]. The ATR-FTIR spectra were measured using the FTIR 6200 spectrophotometer (Jasco) in the range of 4000–400 $cm^{-1}$, with the resolution 4 $cm^{-1}$, via averaging 32 scans. After that, the spectra were analyzed using Spectra Manager v2.0 software. We followed our reported procedure [7].

**Results:** Storage modulus (G') and loss modulus (G") characterize the elastic and viscous properties of the material, respectively. More exactly, G` quantifies the energy which is stored in the sample and which will be released after mechanical stress, while the G" - the loss of energy which is transferred through friction into heat. The values of

G' and G" were constant in the shear strain up to ~10% shown in Fig.1, indicating the elastic structure of the hydrogel within the shear strain range of 0.01-10%.

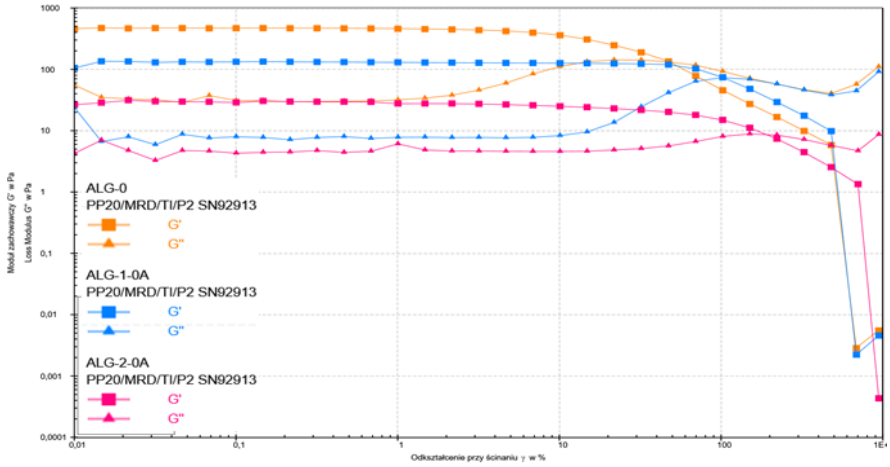



**Fig.1.** G' and G" moduli as a function of shear strain for reference 1% alginate hydrogels.

This wide region resembling a plateau is called the linear viscoelastic region (LVR). In Fig.1, the intersection point of the curves of both moduli for the reference alginate hydrogel was observed at an oscillatory strain of about 110% (noted for measurements without the application of a magnetic field). With the increase in the addition of iron microparticles, the value of the strain at the intersection point also decreased - a drastic decrease was observed at an oscillatory strain of 9% when a magnetic field of 2A was applied. Figure 2 shows that alginate hydrogel samples doped with a small amount of IMPs (0.0053 g) with a magnetic field applied in the range of 0A-2A did not show significant differences.

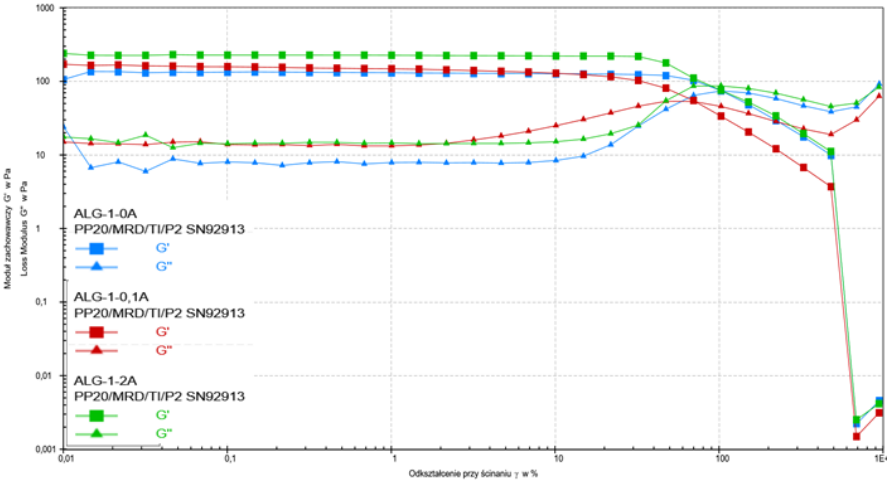



**Fig.2.** G' and G" moduli as a function of shear strain for 1% alginate hydrogels with the lower content of IMPs in the presence of a magnetic field: 0A; 0,1A; 2A.

However, Fig.3 shows that increasing the value of the applied magnetic field (2A) for samples with the highest amount of IMPs showed higher values of G' and G", significantly different from samples with non (0A) or low (0.1A) magnetic field applied. Nevertheless, there are clear dependencies resulting from the presence of IMPs and differences resulting from the imposition of a magnetic field, which are expected to provide possible control of the mechanical properties of these hydrogels.

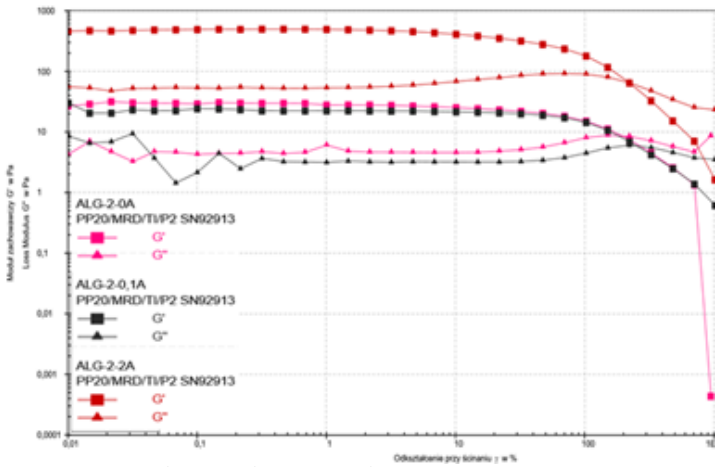



**Fig. 3.** G' and G" moduli as a function of shear strain for 1% alginate hydrogels with the higher content of IMPS in the presence of a magnetic field: 0A; 0,1A; 2A.

The obtained magnetic alginate hydrogels were spectroscopically characterized using ATR FTIR technique; the results are shown in Fig.4.

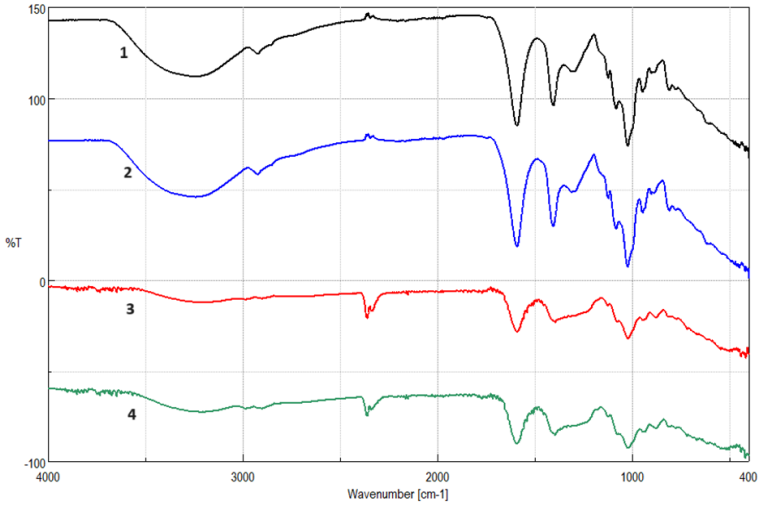



**Fig.4.** FT-IR spectra: 1 - pure sodium alginate powder; 2 – dried 1% ALG hydrogel; 3 – dried alginate hydrogel with the lower content of IMPs (0.0053 g); 4 – dried alginate hydrogel with the higher content of IMPs (0.0268 g).

Characteristic bands are observed in the collected ATR FTIR spectra: (i) bands in the region of ~2940-2880 $cm^{-1}$ due to the stretching vibrations of C-H groups, (ii) bands due to the asymmetric (1590 $cm^{-1}$) and symmetric (1405 $cm^{-1}$) stretching vibrations of the COO- group, (iii) a band due to the C-O vibrations of the alginate backbone, located at ~1290 $cm^{-1}$. Apart that, there are bands at 945 $cm^{-1}$, 885 $cm^{-1}$, and 812 $cm^{-1}$ are specific for mannuronic acid and guluronic acid, which are the building blocks of alginate [8]. It is worth noting that this group of bands is quite important, as it can be used to estimate the relative amounts of mannuronic acid and guluronic acid contained in a particular alginate.

**Conclusions:** The obtained alginate hydrogels showed various mechanical properties depended on the content of the added IMPs. Storage and loss moduli (G' and G") for IMPs-free hydrogels were noticeably higher than for IMPs doped ones when magnetic field was not applied. However upon a high magnetic field, hydrogels with higher content of IMPs exhibited the highest G' and G" values. Therefore, it was demonstrated, that amine-functionalized iron microparticles dispersed in a alginate hydrogel framework can affect the properties of the resulting ferrogels. Moreover, these properties can be remotely affected upon the action of external magnetic field.

**Acknowledgements:** This research was funded by the Polish National Science Centre, grant number 2021/41/B/ST5/03490, titled Hierarchically cross-linked hydrogels: theoretical and experimental design for biomedical applications.

**References:**

1. S.R.S. Veloso, P.M.T. Ferreira, J.A. Martins, P.J.G. Coutinho, E.M.S. Castanheira, Pharmaceutics, 10 (2018) 1.
2. S.L. Tomić, M.M. Babić Radić, J.S. Vuković, V.V. Filipović, J. Nikodinovic-Runic, M. Vukomanović, Marine Drugs, 21 (2023) 1.
3. O. Kapusta, A. Jarosz, K. Stadnik, D.A. Giannakoudakis, B. Barczyński, M. Barczak, International Journal of Molecular Sciences, 24 (2023) 2191.
4. A. Jarosz, O. Kapusta, D. Gugała-Fekner, M. Barczak, Materials, 16 (2023) 6042.
5. Y.A. Bustos-Terrones, Polymers, 16 (2024) 788.
6. M.A. Lee, X. Jin, S. Muthupalani, N.A. Bakh, X. Gong, M.S. Strano, Nanobiotechnology, 21 (2023) 1.
7. M. Barczak, P. Borowski, C. Gila-Vilchez, M. Alaminos, F. González-Caballero, 8. M.T. López-López, Carbohydrate Polymers, 247 (2020) 116747.
9. M.Z.I. Mollah, M.R.I. Faruque, D.A. Bradley, M.U. Khandaker, Saphwan Al Assaf, Radiation Physics and Chemistry 202 (2023) 110500.

# AMMONIA EQUILIBRIUM IN AQUEOUS SOLUTION: EFFECT OF pH, SALINITY AND TEMPERATURE

**A. JAKÓBIK-KOLON, J. BOK-BADURA, B. SAGAN-SZENDZIELORZ**, Silesian University of Technology, Faculty of Chemistry, Department of Inorganic, Analytical Chemistry and Electrochemistry, B. Krzywoustego 6, 44 -100 Gliwice, Poland

**Abstract:** An experimental method has been developed for determining the contribution of un-ionized ammonia to the total concentration of ammonia nitrogen as a function of temperature and pH of the system using an ion-selective electrode for ammonium ion. Using the method the percentage of un-ionized ammonia in total ammonia nitrogen as a function of pH was determined for real flue gas desulfurization (FGD) wastewater at temperature 35 °C, which is extremely important to optimize membrane method for ammonium nitrogen removal. Comparison of experimental results with these calculated using available calculator based on empirical equations showed good agreement between the results, especially in the applicability range of used calculator (pH < 10).

**Introduction:** Wastewater from wet FGD processes represents a critical environmental concern in industries reliant on fossil fuels, particularly coal-fired power plants. As a byproduct of the FGD system designed to mitigate sulfur dioxide emissions, this wastewater presents unique challenges due to its composition, which typically contains high levels of suspended solids, heavy metals, and alkaline substances. Managing this wastewater effectively is essential to prevent environmental contamination and ensure compliance with regulatory standards. Ammonium nitrogen is one of this wastewater parameter, which has to be monitored and kept below permitted limit. The presence of ammonia in FGD wastewater poses an environmental challenge due to its potential toxicity to aquatic organisms. Its presence also promotes water eutrophication and can cause water quality deterioration. To address the presence of ammonia in FGD wastewater, treatment technologies such as biological nitrification-denitrification, chemical oxidation, ion exchange, thermal stripping and membrane processes are employed. Membrane processes offer promising solutions for the removal of ammonia from wastewater generated by FGD systems. In this method, un-ionized ammonia (gas) is transferred through a hydrophobic membrane to the receiving solution (inorganic acid solutions), where it reacts to form an ammonium salt [1,2]. Thus, the efficiency of ammonium nitrogen removal will be determined by the degree of conversion of ammonium nitrogen to un-ionized ammonia. Un-ionized ammonia ($NH_3$) exists in equilibrium in an aqueous solution with the ammonium ion ($NH_4^+$) and the hydroxide ion ($OH^-$):

$$NH_3 + H_2O = NH_4^+ + OH^-$$

As hydroxide ions are added to the system (resulting in an increase in the pH of the system), the equilibrium of the above reaction shifts to the left, thereby increasing the proportion of un-ionized ammonia and decreasing the proportion of ammonium ion. Therefore pH > 11 or even 12 is recommended to ensure high efficiency of ammonium nitrogen removal by membrane method. However such high pH value poses a number of

precipitates in the case of FGD wastewater due to high magnesium and calcium ions concentration. Thus, the development of a method to study the equilibrium of un-ionized ammonia - ammonium ion as a function of temperature and pH of the system is extremely important to optimize between the amount of precipitate formed and the efficiency of the membrane method of ammonium nitrogen removal. The equilibrium constant for above reaction is a function of temperature and the pH of the solution. Thus, if the equilibrium constant is known for a specific temperature and the pH of the solution is also known, the fraction of un-ionized ammonia can be calculated. Subsequently, if the total concentration of ammonium nitrogen is known from laboratory analysis, the concentration of un-ionized ammonia can be calculated. The literature contains theoretical calculations of the concentration of un-ionized ammonia in fresh water based on data (empirical equations for determining the equilibrium constant under specific conditions) presented by various authors [3,4]. These data are not supported by experimental data, and the applicability range of the derived empirical equations is also limited, typically to pH < 10. It should also be noted that the concentration of un-ionized ammonia depends on the ionic strength of the solution. With an increase in the ionic strength of the solution, there is a slight decrease in the contribution of un-ionized ammonia in the total concentration of ammonium nitrogen. One study presents a method for determining the contribution of un-ionized ammonia in saline waters based on theoretical calculations for specific conditions of the system: pH, temperature, and salinity. The applicability range of the determined empirical equation specified by the authors is 0-35 o/oo for salinity, 0-50 °C for temperature, and pH 6-10 [4].
In this work, an experimental method has been developed for determining the contribution of un-ionized ammonia to the total concentration of ammonia nitrogen as a function of temperature and pH of the system using an ion-selective electrode for ammonium ion. The ion-selective electrode method is the only method that allows the determination of the concentration of one of the individuals next to the other, i.e. the ammonium ion being in equilibrium with un-ionized ammonia, at a given temperature and pH and salinity of the solution, without changing this equilibrium. Other methods, such as the Kjeldahl method or spectrophotometric methods, either remove or bind one of the species, shifting the equilibrium of the reaction, and additionally do not allow for the measurement of this equilibrium at a given temperature (Kjeldahl method).

**Experimental:** The investigation utilized multifunctional measuring instruments from Mettler Toledo: a SevenDirect SD50 ion meter equipped with an ion-selective electrode for ammonium ion (ISE $NH_4^+$) and a reference electrode (INLAB REFERENCE), as well as a FiveGo pH meter equipped with a pH electrode (LE438 3in1). Measurements were conducted in a practically sealed vessel (with only a 2 mm diameter hole for the dosing of solutions to adjust pH) thermostated on a water bath placed on a magnetic stirrer with heating function (IKA C-MAG HS 7 control). The standard curve for ammonium ions was prepared using the matrix of the investigated FGD wastewater samples of low N-$NH_4$ content at a temperature of 35 °C. To determine the contribution of un-ionized ammonia in total ammonium nitrogen as a function of pH at 35 °C (temperature of FGD wastewater stream at real conditions), a wastewater sample (50 ml) of N-$NH_4$ concentration about 150 mg/l was placed in the measurement vessel, and then the pH value was lowered to pH < 7 (ammonia is completely ionized under these conditions) to determine the concentration of total ammonium nitrogen (as $NH_4$).

Subsequently, the pH value was increased in the range of 8.0-12.0 by dosing a concentrated NaOH solution (the dosed solution volume was negligible compared to the sample volume – collectively less than 0.2%), while simultaneously measuring the concentration of ammonium ion. Then, the concentration of un-ionized ammonia ($NH_3$) was calculated from the difference between the concentration of total ammonium nitrogen (as $NH_4$) and the concentration of ammonium ion, followed by its proportion (in mol/mol %) in total ammonium nitrogen as a function of pH at 35 °C. For pH values > 11, due to exceeding the measurement range of the ion-selective electrode and the presence of a significant amount of precipitate disturbing the electrode's operation, the presented results were determined by extrapolation utilizing the relationship established by Matlab software using experimental data. Salinity measurements were made using Elmetron's CC-105 laboratory salt meter in an open thermostated vessel (35 °C), placing an wastewater sample (50 ml) in it and varying the pH value in the range of 8.0-12.0 by dosing a concentrated NaOH solution (the volume of the dosed solution was negligible in relation to the volume of the sample - collectively less than 0.2%). The results indicated that there was no significant change in the salinity of the solution during the course of the experiment to determine the contribution of un-ionized ammonia to total ammonium nitrogen as a function of pH.

**Results:** The percentage of un-ionized ammonia in total ammonia nitrogen as a function of pH determined for real FGD wastewater at temperature 35 °C is shown in Figure 1 as 'exp' series. The contribution of un-ionized ammonia is increasing with pH increase, achieving above 70% in pH = 9.5 and almost 90% and 94% in pH = 10 and pH = 10.5, respectively. This illustrate that change in pH of the solution by 0.5 may significantly increase the efficiency of ammonium removal by membrane method. Increasing in the pH of the wastewater solution increases the amount of precipitates coming from magnesium and calcium ions, which are difficult to separate and consume NaOH, which is economically undesired. Therefore studies on optimization between the amount of precipitate formed and the efficiency of the membrane method of ammonium nitrogen removal have to be further performed. Obtained results were compared with results obtained by calculation of concentration of un-ionized ammonia at various pH, temperature and salinity using calculator, which was developed in Florida Department of Environmental Protection Chemistry Laboratory Methods Manual and based on empirical equations for determining the equilibrium constant under specific conditions (pH, temperature, salinity) [5]. The applicability range of the determined empirical equation specified by the authors is salinity: 0-35 g/l, temperature: 0-50 °C and pH 6-10. The results of calculation as the percentage of un-ionized ammonia in total ammonia nitrogen vs. pH at various temperature (15-35 °C) and salinity (0 and 35 g/l) are presented in Figure 1. The calculated values are in good agreement with experimental ones for the same conditions (salinity 35 g/l, temperature 35 °C) especially in pH < 10. Above this pH value the experimental results are slightly lower than calculated ones. It may be due to additional wastewater components, which may influence the ammonia-ammonium ion equilibrium. On the other hand the applicability range of used calculator is pH 6-10, thus the calculations for pH > 10 may be subject to some error. Calculated values proved that increase in salinity of solution as well as decrease in temperature decreases the percentage of un-ionized ammonia in total ammonia nitrogen. Lowering the temperature from 35 to 15 °C in pH = 10, the contribution of un-ionized ammonia in

total ammonium nitrogen diminishes by 20 percentage points (from 90 to 70%). This shows the importance of temperature as parameter in ammonium removal by membrane method.

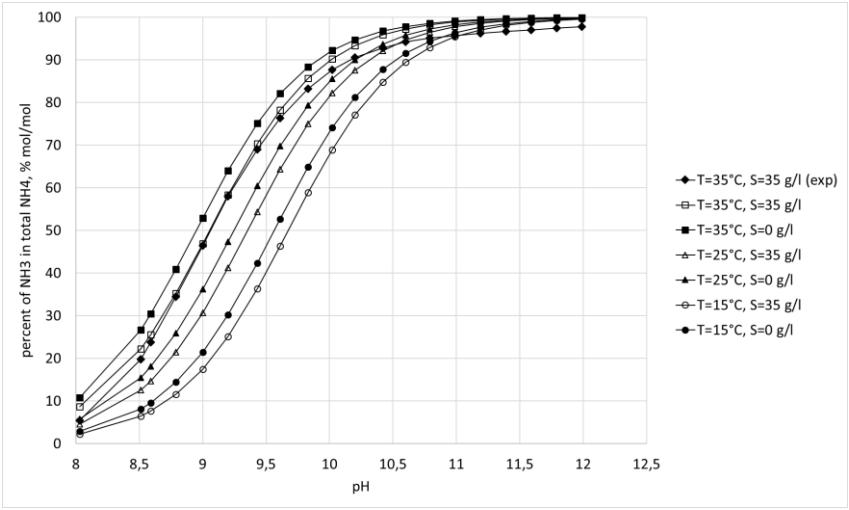



**Fig.1.** The percentage of un-ionized ammonia in total ammonia nitrogen as a function of pH calculated for various temperature and salinity using calculator [5] and determined at temperature 35°C for real FGD wastewater of salinity about 35 g/l (exp).

**Conclusions:** An experimental method utilizing an ion-selective electrode for ammonium ion is suitable for determining the contribution of un-ionized ammonia to the total concentration of ammonia nitrogen in saline solutions as a function of temperature and pH of the system. Obtained results may be applied to optimize membrane method for ammonium nitrogen removal. Experimental results are in good agreement with these calculated using available calculator based on empirical equations, especially in the applicability range of used calculator (pH < 10).

**Acknowledgements:** This research was funded by the Polish Ministry of Science and Higher Education, grant number BK-04/010/BK_24/1080.

**References:**

1. I.M. Sheikh, M. Reig, X. Vecino, J. Lopez, M. Rezakazemi, C.A. Valderrama, J.L. Cortina, Separation and Purification Technology, 283 (2022) 120212.
2. P.A. Aligwea, K.K. Sirkara, C.J. Canlasb, Separation and Purification Technology, 224 (2019) 580.
3. K. Emerson , R.C. Russo , R.E. Lund , R.V. Thurston, Journal of the Fisheries Research Board of Canada, 32 (1975) 2379.
4. Thurston, Aqueous Ammonia Equilibrium Calculations. Technical Report No. 74-1, Fisheries Bioassay Laboratory, Montana State University, Bozeman, MT., July 1977 revision.
5. Unionized Ammonia Calculator v1.2;. 2, after original by Dr. Landon Ross. 3, Florida Department of Environmental Protection (6-Unionized-Ammonia-Calculator.xlsx).

# OPTYMALIZATION THE METHODOLOGY OF $^{210}$Po DETERMINATION IN TOBACCO PRODUCTS

**S. WÓJCIK, K. SZARŁOWICZ**, AGH University of Krakow, Faculty of Energy and Fuels, Department of Nuclear Energy and Radiochemistry, A. Mickiewicza Ave. 30, 30-059 Krakow, Poland.

**Abstract:** Optimizing chemical procedures is important to obtain the best possible results from the available products. This also applies to the optimization of the $^{210}$Po determination procedure in products from the tobacco industry. Each step must be carefully analyzed and the procedure must be properly adapted to the analyzed products in terms of radionuclide determination. Various tobacco products with different characteristics are subject to labelling.
The aim of this study was to optymalize some steps in the radiochemical procedure for $^{210}$Po determined in tobacco cartidges. The process consists of the following stages: weighting, digestion, concentration, deposition and measurement. In particular, experimental activities included the selection of the amount of material and mixture for decomposition, as well as the conditions of microwave decomposition and the conditions of deposition of polonium on silver disc. On the basis of optimisation studies, an appropriate procedure with the highest radiochemical efficiency was selected.

**Introduction:** Polonium is an element from the group of radioactive metals, discovered in 1898, there are three most important radioisotopes: $^{208}$Po, $^{209}$Po and $^{210}$Po, which is highly radioactive and toxic. These radioisotopes emit mainly alpha radiation. The half-life of $^{210}$Po is 138 days. Alpha radiation can be stopped by a thin sheet of paper or skin. However, when it enters the body through food consumption, inhalation, or skin wounds, it wreaks great havoc. It gradually destroys internal organs, leading to many diseases and failures [1,2]. $^{210}$Po comes from the decay of $^{238}$U and is commonly found in nature. It occurs in soil, sediments, sand, water, and the atmosphere. As a result of many radioactive decays, this radionuclide circulates in the environment; for example, the main source of its emission into the atmosphere is $^{222}$Rn from the ground. Its occurrence is also related to industry and human activity. These are so-called anthropogenic sources. An important issue related to the presence of $^{210}$Po is TENORM (Technologically Enhanced Naturally Occurring Radioactive Material), a reintroduced, concentrated radioisotope [3,4]. All of these paths also occur in the tobacco industry. Tobacco, as a plant itself, has a structure that facilitates the penetration of elements into its interior. An extensive root system allows compounds to be absorbed from the soil and water, and the large, spreading leaves have a fuzz that facilitates the adhesion of compounds, including radionuclides. Radionuclides can enter the plant through various routes. As a result of decay, $^{210}$Po can be deposited in the plant, especially on large, fuzzy leaves. This is a consequence of the decay that occurs around and in the atmosphere, and precipitation also contributes to the occurrence of radionuclides and deposition on the plant, as well as absorption into the soil and uptake by the roots. In terms of tobacco cultivation, radionuclides including $^{210}$Po is released mainly through the use of fertilizers. It is also important what plant was planted before tobacco and with what it

was fertilized with; agrotechnical treatments also affect the content of radionuclides already present, as well as the intake and condition of tobacco, the quantity and quality of fertilizers used. In the tobacco industry, tobacco as a plant is harvested, dried and processed into various tobacco products. The most popular ones include: classic cigarettes, tobacco cartridges, clean tobacco for smoking, cigars and chewing tobacco [5-8]. Of those mentioned above, the most popular include classic cigarettes and the currently constantly developing tobacco cartridges, which were supposed to be a healthier replacement for classic cigarettes. Traditional cigarettes themselves have changed over the years, from their appearance to the amount of tobacco to their chemical composition. Tobacco cartridges also vary. The difference between classic cigarettes and tobacco cartridges is the temperature and reaction. The tobacco in classic cigarettes is burnt at a temperature of 700 to 900 °C. However, tobacco in tobacco inserts is heated in dedicated heaters to approximately 350 $^{o}$C, there are various heating systems, heating blades, induction and others. The element that connects both cases is the presence of $^{210}$Po in tobacco, which is found in both tobacco smoke and aerosol. The match of the chemical procedure in this case is very important due to the diverse properties of the product, small amounts of sample, the presence of a tracer and the ability to obtain thin sources from deposition process [9-13]. The aim of the study was to select the conditions of sampling preparation, digestion and deposition of $^{208}$Po on silver disc. Several steps were carried out to gain the procedure with the highest radiochemical efficiency.

**Experimental:** At first, packages of tobacco cartridges of various types, heated and unheated, were collected. The first stage was to weigh the tobacco mass on a paper weighing scale. In the first tests, tobacco from 1 tobacco cartridges was used as the mass of one sample, but it was found that the measurement time was long and the sample mass was increased to 2 tobacco cartridges. Due to the different packages, the tobacco sticks were different weights. The tobacco packing in the cartridge was different. For example, in the case of Neo tobacco inserts, the tobacco is in the form of sawdust, and its weight is greater than the tobacco in one Heets tobacco insert, which was in compressed form. The next step was to add the tracer, $^{208}$Po. Initially, it was added in an amount of approx. 0.1 g, but this amount was reduced, gradually reducing it, and obtaining a more economical amount of marker that gives the same effects when used. The next stage was to create appropriate conditions for digestion process. Various proportions of concentrated acids were used. In the first approach, 8 cm$^3$ of concentrated nitric acid and 2 cm$^3$ of concentrated hydrochloric acid were used for each digestion vessel. In the second approach, the proportions were changed to 6cm$^3$ of concentrated nitric acid and 3 cm$^3$ of concentrated hydrochloric acid. In the third attempt, the previous proportions were maintained, but 1cm$^3$ of hydrogen peroxide was added. Also only concentrated nitric acid in an amount of 8 cm$^3$ with the addition of 2 cm$^3$ of hydrogen peroxide were used. The next step was to select the appropriate parameters in the digestion process, which was performed in a microwave digestion system from Anton Paar. Digestion consisted of several stages, optimization consisted of testing various parameters in terms of temperature microwave power, pressure and time. The selected power ranged from 300 W to 1400 W. Pressure from 45 to 60 bar. The temperature did not exceed 260 $^{o}$C, and the time was modified depending on the given stage. Then, after the digestion process was complete, the samples were individually transferred to the container using

1mol· $dm^{-3}$ of nitric acid and centrifuged. After these, the solution was concentrated under lamps. After evaporation, the 2 mol·$dm^{-3}$ hydrochloric acid was added. The amount of this acid varied, from 30 to 40 $cm^3$. To establish the deposition of $^{210}$Po, 40% hydroxylamine hydrochloride solution and 25% sodium tricitrate solution were prepared. However, it was noticed that during deposition, the beakers with the tested solution turned yellow. The proportions were changed from 2 $cm^3$ to 3 $cm^3$ of 25% sodium tricitrate solution and during deposition, an additional 1$cm^3$ of 40% hydroxylamine hydrochloride solution was added. No major changes were noticed, so the above solutions were changed to ascorbic acid and 0.5 mol·$dm^{-3}$ hydrochloric acid in an amount of 10 $cm^3$. The last stage was the measurement in the alpha spectrometer with PIPS detector (ang. *Planar Passivated Implanted Silicon*).

**Results:** After optimization, the most suitable methodology was selected to determine $^{210}$Po in tobacco products at each stage. Two tobacco cartridges ranging from 0.35 to 0.55 g were left as the sample mass. The amount of $^{208}$Po tracer added was around 0.1 Bq. Preparing the environment for digestion involves using 8 $cm^3$ of concentrated nitric acid and 2 $cm^3$ of hydrogen peroxide. Also the mixture with concentrated HCl and $HNO_3$ can be used. The final parameters in the digestion process (Table 1), power ranged from 500 to 1400 W, the pressure did not exceed 45 bar, and the time, especially of the last stage, power hold, was extended. The temperature does not exceed 260 $^oC$, and the cooling was at 55 $^oC$. In the concentration process, an amount of 30 $cm^3$ of 2 mol·$dm^{-3}$ HCl was used. For deposition, 3 $cm^3$ of 40% hydroxylamine hydrochloride solution, 2 $cm^3$ of 25% sodium tricitrate solution and 6 $cm^3$ of 0.5 mol·$dm^{-3}$ hydrochloric acid were used. Ascorbic acid, added even in the amount of 1 drop, discolored the yellow solution, however, during deposition, carbon was deposited on the silver, covering the deposited $^{210}$Po and blocking visibility and measurement. The measurement time was reduced due to the increase in the mass of tobacco in the sample and the analysis of the presence of significant amounts of $^{210}$Po in tobacco products.

**Table 1.** Microwave digestion parameters.

| Steps | Power [W] | Time [min.] |
|---|---|---|
| Power ramp | 500 | 5 |
| Power hold | 500 | 5 |
| Power ramp | 1400 | 12 |
| Power hold | 1400 | 30 |
| Cooling | 0 | - |

**Conclusions:** Tobacco as a plant has many varieties, and tobacco products often contain a mixture of different types of tobacco of different origins. Optimizing the methodology is an essential element to obtain the best possible results with such great diversity. The methodology presented above seems to be the best for tobacco cartridges. Tobacco products on the market and in the industry are constantly evolving, so it is possible to modify them later to new products or improve small imperfections in the current procedure.

**Acknowledgements:** This work was partially supported by research subvention supported by the Polish Ministry of Education and Science Grant Number 16.16.210.476.

## References:

1. B. Skwarzec, A. Boryło, J. Wieczorek, K. Lanczewska, Journal of Environmental Radioactivity, 268-269 (2023) 123.
2. V. Zagà, Ch. Lygidakis, Polonium and Cancer, Encyclopedia of Metalloproteins, 2013, 1753-1760.
3. G. Romańczyk, A. Boryło, Journal of Environmental Radioactivity, 167 (2017) 70.
4. J.C. Mora, B. Robles, J.A. Corbacho, C. Gascó, M.J. Gázquez, Journal of Environmental Radioactivity, 102 (2011) 520.
5. A.E.M. Khater, Journal of Environmental Radioactivity, 71 (2004) 33.
6. S. Cankurt, A.U. Görgün, Ecotoxicology and Environmental Safety, 197 (2020) 110603.
7. A. Chariton, Medicinal uses of tobacco in history, Journal of the Royal Society of Medicine, 97 (2004) 292.
8. Technical library - fisher's science, M. Dominikiewicz, Tobacco - its cultivation and production – third edition, 1926.
9. D. Hoffmann, I. Hoffmann, Journal Toxicological Environmental Health, 50 (1997) 307.
10. J.P. Schaller, Regulatory Toxicology and Pharmacology, 81 (2016) 27.
11. R.R. Baker, Nature, 247 (1974) 405.
12. K. Bekki, S. Uchiyama, Y. Inaba, A. Ushiyama, Environmental Health and Preventive Medicine, 26 (2021) 89.
13. M. Meišutovič-Akhtarieva, Chemosphere, 223 (2019) 474.

# SYNTHESIS AND SPECTRAL ANALYSIS OF NEW DAPSON SQUARAMIDES

**M.V. QUYNH NGUHEN, A.K. PRZYBYŁ**, Adam Mickiewicz University, Faculty of Chemistry, Uniwersytetu Poznańskiego St. 8, Poznań, Poland.

**Abstract:** The presented project is mainly focused on the development of an efficient and effective method for obtaining new derivatives of cytisine with squaric acid and dapsone. The new obtained compounds are mainly monosquaramides. However, during the reaction of diethyl squarate with dapson the minor by-product, which is a bifunctional squarimide has been obtained. These compounds are expected to show good activity in bioassays, as the 3 molecules used, due to their biological activity, and proven therapeutic activity, have found application in the pharmaceutical industry.

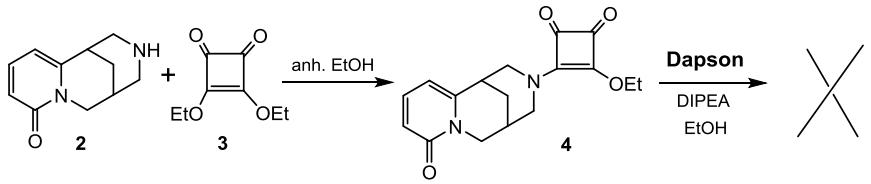
**Introduction:** The popularity of Dapson (**1**, Fig.1) began during World War II in 1940, when this compound became a key part of leprosy therapy [**1**]. Dapsone (1) has a broad spectrum of antibiotic activity, including being active against Plasmodium and Pneumocystis jirovecii. Hence, it is used in the treatment of pneumonia caused by bacteria *Pneumocystis carinii*, and *Toxoplasma encephalitis*, especially in immunocompromised patients [2,3]. In addition, it has found use in both the prevention and treatment of malaria [4]. What's more, during the last pandemic time, Dapsone showed a beneficial effect on patients with COVID-19, improving oxygenation and thus leading to better survival [5]. Dapsone exhibits anti-inflammatory activity [6], which involves inhibiting the production of reactive oxidation species, thereby reducing the neutrophil-mediated inflammatory response and decreasing the effect of eosinophil peroxidase on mast cells [7].

Squaric acid and its derivatives have already found applications in the pharmaceutical industry, it has been found to exhibit antiparasitic, antibacterial, cytotoxic and antiviral properties. In addition, some of the derivatives have been found to exhibit properties of good drug carriers [8], especially carrier in the production of a vaccines against shigellosis (dysentery, caused by Shigella bacilli) [9]. Although its efficacy has so far been tested and confirmed in mice, further studies are planned and it is believed that in the future it will be possible to produce vaccines based on quartic acid for certain diseases, including the aforementioned dysentery as well as cholera. Subsequent studies have shown the feasibility of squaramides as potential drugs in the treatment of malaria. This squaramid base was prepared with the already used drugs clindamycin, chloroquine and mortiamide D. Most of the new squaramid derivatives obtained proved to be more pharmacologically active than the protoplasts, especially the chloroquine-containing compounds [10].

Another bioactive compound of this project is that was planned to be conjugated with Dapson molecule is (-)-cytisine. This alkaloid and its derivatives interact with nicotinic-acetylcholine receptors and have thus found use as model compounds to help understand the action of nACh receptors, as well as active substances in the treatment of nicotine addiction [11].

**Experimental:** (-)-Cytisine (**1**) was isolated from the seeds of golden chain (or golden rain) tree (*Laburnum anagyroides*) [12,13]. Compound purification and preliminary MS analyses were performed using a CombiFlash Rf+ Purion (Teledyne ISCO). ESI mass spectra were obtained on a Waters/Micromass (Manchester, UK) ZQ mass spectrometer (MassLynx V4.0). The sample solutions were prepared in methanol or in methanol–water. The concentration of the analyzed probes was 3.6 d 10_5 M (1:1 ratio), which is typical of ESI, unless indicated otherwise.
The sample solutions were infused into the ESI source using a Harvard pump; the flow-rate was 20 μL/min unless indicated otherwise. The ESI source potentials were as follows: capillary 3 kV, lens 0.5 kV, extractor 4 V and cone voltage 30 V. The source temperature was 120 °C and the desolvation temperature was 300 °C. Nitrogen was used as the nebulizing and desolvating gas at flow-rates of 1000 and 300 l/h, respectively. The FT-IR spectra of the compound were recorded in KBr tablets on an IFS 113v FT-IR spectrophotometer (Bruker, Karlsruhe) equipped with a DTGS detector.

**Results:** The modifications of squaric acid are not difficult and, in most cases, do not require drastic temperature and pressure conditions or the use of catalysts. Thus, a potential modification on an industrial scale should be fast and relatively cheap. In addition, the synthesized compounds are characterized by relatively high persistence and stability. This is related, among other things, to the high acidity of the molecule and to the inductive effect of the oxygen atoms and the unsaturated bond, which leads to the stabilization of the resonant ionic form of the compound. In the square acid dianion, the negative charges are uniformly delocalized between all oxygen atoms [8]. And indeed, the first step of the reaction yielded a monodiamide (Fig.1), which was so stable that the subsequent step of synthesizing the squaramide with Dapsone (1) did not yield the expected result, and this despite the use of DIPEA and heating for several hours/days (Scheme 1).




**Scheme 1.** Synthesis of a new squaramide with cytisine.

Thus, another approach to obtain a bifunctional squaramide, was to first synthesize a mono-substituted squaramide with dapsone (Scheme 2). In this case, a new compound **4** was synthesized as the main product (Fig.2), but by-product **6** was also synthesized. After ESI-MS and FT-IR analysis (Fig.3, characteristic bands for ν C=N in the 2190 $cm^{-1}$ range), it was found that compound **6** is a Schiff base.

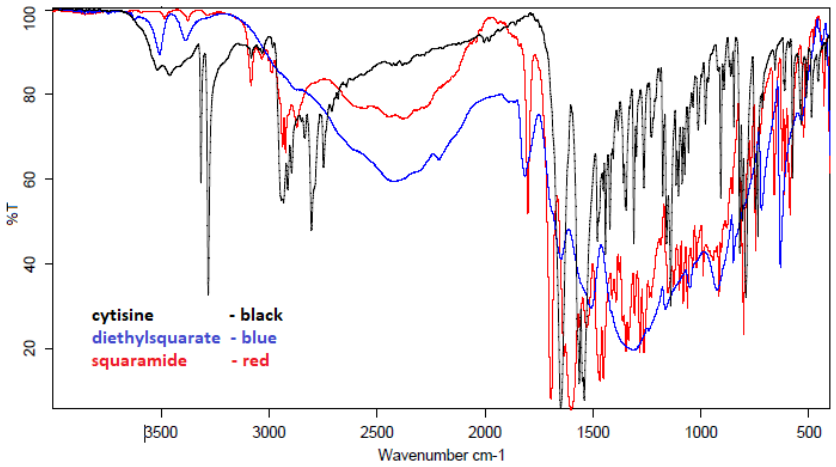
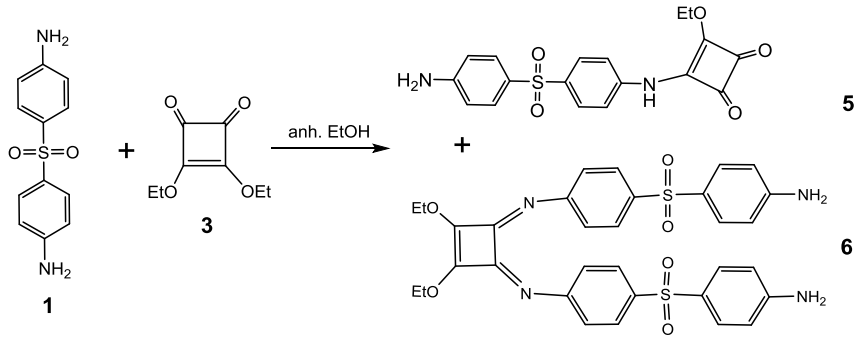



**Fig.1.** The overlaped IR spectra of cytisine (black), diethylsquarate (blue), and the new squaramide (red).




Scheme 2. Synthesis of a new dapsone squaramides **5** and **6**.

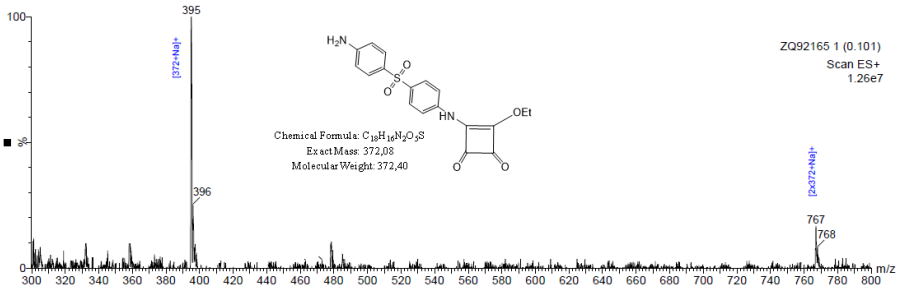



**Fig.2.** The ESI-MS spectrum of new Dapson squaramide (**5**, black).

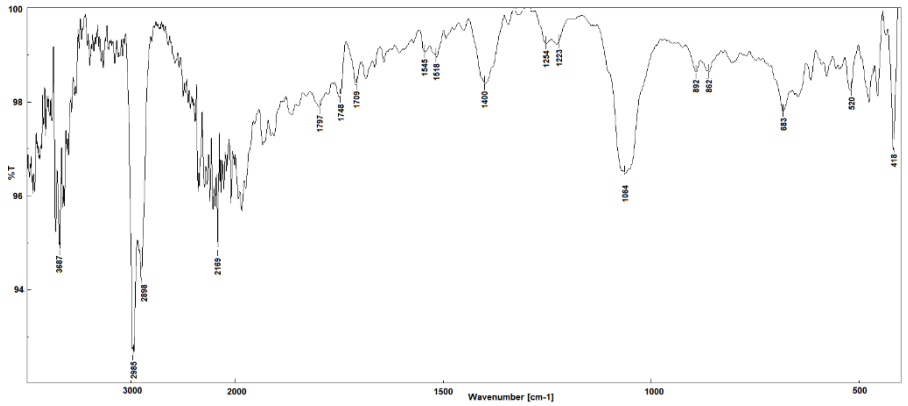



**Fig.3.** The FT-IR spectrum of new Dapson squaramide (**2**, black).

**Conclusions:** The presented data confirm the obtaining of new monosquaramides of cytisine (4) and with Dapson (**5**). Moreover, on the basis of the spectral analysis of ESI-MS (m/z 630) and FT-IR of the minor product the formula of a new bifuctional squaramide (**6**) has been proposed. FT-IR spectrum of the measured compounds (**6**) shows the disappearance of the stretching vibration band characteristic for the carbonyl group and the appearance of the strong bands of imine bands (base Schiffa) at ν -C=N at 2169 $cm^{-1}$. In the next stages of this project, it is planned to obtain bifunctional squaramide substituted with cytisine and Dapson, and then carry out he bioactivity tests of the obtained new squaramide conjugates.

**Acknowledgement:** to the Botanical Garden of the Adam Mickiewicz University in Poznań for the seeds of *Laburnum anagyroides* Medik.

## References:

1. R.H. Gelber, Antimicrobial Agents and Chemotherapy, 42 (1998) 3334.
2. C.E. Corallo, J. Coutsouvelis, S. Morgan, O. Morrissey, S. Avery, Drug Metabolism and Personalized Therapy, 35 (2020) doi: 10.1515/dmpt-2019-0018.
3. M. Opravil, Clinical Infectious Diseases, 20 (1995) 531.
4. B.J. Brabin, T.A. Eggelte, M. Parise, F. Verhoeff, Drug Safety, 27 (2004) 633.
5. B.A. Kanwar, A. Khattak, J. Balentine, J.H. Lee, R.E. Kast, Vaccines, 10 (2022) 195.
6. S.M. Debol, M. J. Herron, R.D. Nelson, Journal of Leukocyte Biology, 62 (1997) 827.
7. M. Khalilzadeh, M. Shayan, S. Jourian, M. Rahimi, M. Sheibani, A.R. Dehpour, Naunyn Schmiedebergs Archives of Pharmacology, 395 (2022) 1509.
8. J. Chasák, V. Šlachtová, M. Urban, L. Brulíková, European Journal of Medicinal Chemistry, 209 (2021) 112872.
9. M. Kelly, Mandlik A, R.C. Charles, S. Verma, S.B. Calderwood, D.T. Leung, R. Biswas, K. Islam, M. Kamruzzaman, F. Chowdhury, F. Khanam, W.F. Vann, A.I. Khan, T.R. Bhuiyan, F. Qadri, A.R. Vortherms, R. Kaminski, P. Kováč, P. Xu, E.T. Ryan, Vaccine 41 (2023) 4967.
10. T. Tremblay, C. Bergeron, D. Gagnon, Ch. Bérubé, N. Voyer, D. Richard, D. Giguèr; ACS Medicinal Chemistry Letters, 14 (2023) 217.
11. C.L. Morales-Perez, C.M. Noviello, R.E. Hibbs, Nature, 538 (2016) 411.
12. E. Marriere, J. Rouden, V. Tadino, M.-C. Lasne, Organic Letter, 8 (2000) 1121.
13. A.K. Przybył, M. Kubicki, Journal of Molecular Structure, 985 (2011) 157.

# A COMPREHENSIVE COMPARISON OF THE SPECTROSCOPIC PROPERTIES OF HETERONUCLEAR *N,O*-DONOR SCHIFF BASE COMPLEXES

**D. OSYPIUK, B. CRISTÓVÃO, A. BARTYZEL**, Maria Curie-Sklodowska University, Faculty of Chemistry, Institute of Chemical Sciences, Department of General and Coordination Chemistry and Crystallography, Maria Curie-Sklodowska Sq. 2, 20-031 Lublin, Poland.

**Abstract:** In the reaction of *N,N'*-bis(2,3-dihydroxybenzylidene)propylene-1,3-diamine ($H_4L$) with methanolic solutions of bis(benzonitrile)palladium(II) chloride or copper(II) acetate and lanthanide(III) nitrate(V) the new complexes with the general formula $[LnPd_2(H_2L)_2(NO_3)](NO_3)Cl{\cdot}mCH_3OH{\cdot}nH_2O$ (where: Ln = Pr (1), Sm (2), Gd (3); m = 3, n = 3 (1, 3) and m = 2, n = 4 (2)) or $[Cu_2Ln(H_2L)(HL)(NO_3)_2]{\cdot}MeOH$ (Ln = Ho (4), Er (5)) were synthesized. The compounds were characterized by elemental analysis, FTIR spectroscopy, TG, DSC, and TG-FTIR analysis. All donor atoms of the salen type ligand $N_2O_4$ are involved in the coordination of the *3d/4d* and *4f* metal ions. The coordination environment around each Pd(II) metal center adopts a distorted square-planar geometry while the coordination sphere of Cu(II) ions is a distorted square-pyramidal. The complexes are stable at room temperature and their thermal decomposition in the air proceeds stepwise.

**Introduction:** Schiff bases, due to their diverse structure and different physical and chemical properties are the subject of much scientific research. They readily form mono- and multi-nuclear complexes with transition metal ions. In the complex crystals, the 3*d/4d* and 4*f* metal centers are linked by two phenoxo oxygen atoms of the Schiff base ligands. The physical and biological properties of complexes depend on many factors, including: the kind and amount of the substituents in the structure of the *N,O*-donor ligands, the kind of metal and counter ions, the conditions of synthesis [1-2]. A review of the literature shows that 3*d*-4*f* complexes with Schiff bases are very popular due to their spectroscopic, thermal, luminescence as well as magnetic properties [3-14]. As a continuation of investigation on salen type Schiff base complexes herein, we report spectral and thermal properties of heteronuclear *3d/4d* and *4f* complexes.

**Experimental:** *N,N'*-bis(2,3-dihydroxybenzylidene)-1,3-diaminopropane $H_4L$ was synthesized by a condensation reaction between 1,3-diaminopropane (5 mmol) and 2,3-dihydroxybenzaldehyde (10 mmol) in methanol (50 ml) under reflux conditions (Fig.1). The yellow mixture was stirred for about 30 minutes. The obtained precipitate was filtrated and dried in the air.

All heteronuclear complexes 1–5 were synthesized in the same manner described below. To the stirred solution of the *N,N'*-bis(2,3-dihydroxybenzylidene)-1,3-diaminopropane (0.4 mmol) in methanol (40 mL) dropwise solutions of bis(benzonitrile)palladium(II) chloride (0.4 mmol) or copper(II) acetate (0.4 mmol) in methanol (10 mL) were added to produce a light brown or green coloured mixture that was stirred for about 30 minutes at 45 ºC.

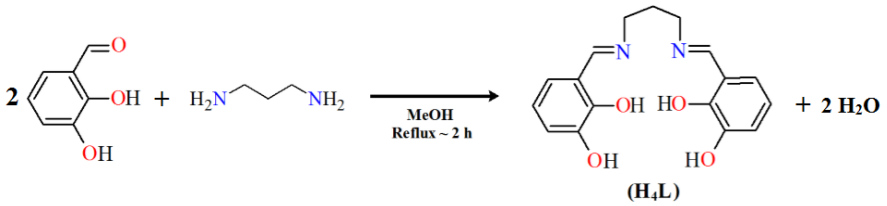



**Fig.1.** Scheme of *N,N*'-bis(2,3-dihydroxybenzylidene)-1,3-diaminopropane ($H_4L$) synthesis.

Next, the freshly prepared solution of $Ln(NO_3)_3$ (0.2 mmol) in methanol (5 mL) was added with constant stirring (Fig.2). The resulting mixture was stirred for another 30 min, filtered and left undisturbed at about 4 ºC for several days, affording good quality crystals.

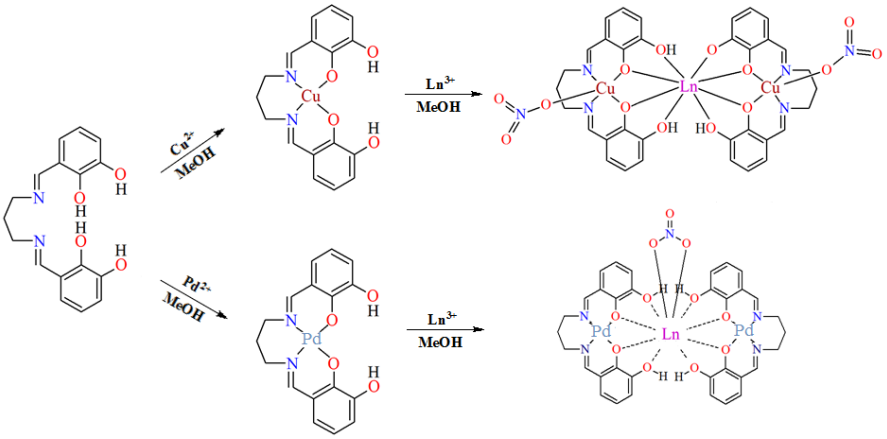



**Fig.2.** Scheme of the synthesis of heteronuclear complexes.

The contents of carbon, hydrogen and nitrogen were determined by elemental analysis using a CHN 2400 Perkin-Elmer analyzer. The amounts of Cu(II), Pd(II) and Ln(III) were established by the X-ray fluorescence XRF method with the use of a spectrophotometer of X-ray fluorescence with energy dispersion EDXRF-1510 (Canberra-Packard). The FTIR spectra of the complexes and the free Schiff base were recorded in the range of 4000–350 $cm^{-1}$ using an M-80 Perking-Elmer spectrometer. The samples were prepared as KBr discs. The thermal stability and decomposition of the complexes were studied in air using a Setsys 16/18 (Setaram) TG, DTG and DSC instrument. The experiments were carried out under air flow rate of 20 mL $min^{-1}$ in the range of 297–1273 K at a heating rate of 10 K $min^{-1}$. The samples were heated in $Al_2O_3$ crucibles. The TG–FTIR measurements of heteronuclear complexes were performed to identify their gaseous decomposition products on the Q5000 TA apparatus coupled with the Nicolet 6700 spectrophotometer. The experiments were carried out under a dynamic nitrogen atmosphere in flowing nitrogen of 20 mL $min^{-1}$ in open platinum crucibles. Complexes were heated up to 1073 K at a heating rate of 20 K $min^{-1}$. The gaseous

decomposition products were analyzed over the range of 4000–400 $cm^{-1}$ using the Nicolet 6700 spectrophotometer.

**Results:** The FTIR spectra of the complexes 1–5 were compared with the spectrum of the free Schiff base ($H_4L$) to obtain information about the binding mode of the ligand to a metal ions. The strong and sharp band due to the azomethine group *ν*(C=N) of the free ligand at 1640 $cm^{-1}$ is shifted to 1612 $cm^{-1}$ in 1–3 and to a strong absorption band at 1618 $cm^{-1}$ for 4 and 1616 $cm^{-1}$ for 5 which indicates the coordination of Cu(II)/Pd(II) centers *via* nitrogen atoms. Additionally, the strong phenolic stretching vibration *ν*(C-O) presents at 1236 $cm^{-1}$ in the FTIR spectrum of the free Schiff base is moved to lower frequencies (1220–1216 $cm^{-1}$) in the FTIR spectra of compounds, which indicating that oxygen atoms coordinate with metal ions. A broad absorption bands in the 3000–3400 $cm^{-1}$ region can be attributed to the O–H stretching vibrations and confirmed the presence of crystallization water and methanol molecules in the crystal structure of complexes.
The TG/DTG/DSC techniques were used to study the thermal properties of complexes 1–5 in the air atmosphere (Fig.3).

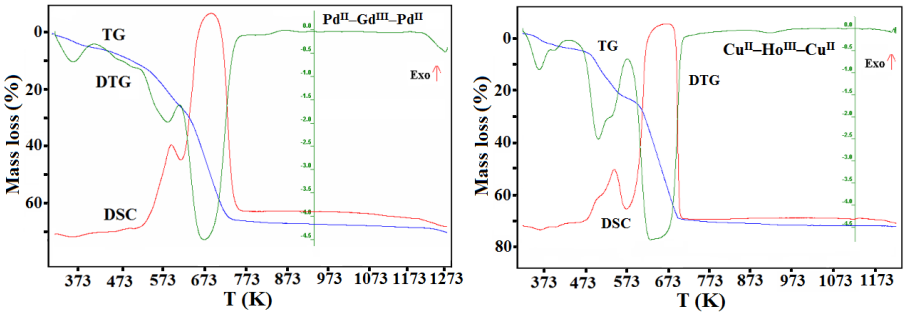



**Fig.3.** TG, DTG and DCS curves of 3 and 4 in air.

The $Pd^{II}$–$Ln^{III}$–$Pd^{II}$ 1–3 and $Cu^{II}$–$Ln^{III}$–$Cu^{II}$ 4, 5 complexes are stable at room temperature. For compounds 1–3, the first weight loss occurs up to 305 K, which is assigned to the elimination of molecules of water and methanol. For complexes 4 and 5 this process starts at a higher temperature (343 K) which shows that they are more thermally stable. The presence of solvent molecules is also confirmed by TG-FTIR analysis (Fig.4). In the FTIR spectra, the characteristic bands for water and methanol appear at 4000–3600 and 1850–1400 $cm^{-1}$. The combustion of the organic ligand is accompanied by a significant exothermic effect, as seen in the DSC curves. The main gaseous products resulting from thermal degradation of the complexes in inert atmosphere during heating to 1073 K are carbon mono- and dioxide as well as hydrocarbons. The final products of the heteronuclear complex decomposition are presumably a mixture of respective oxides: PdO or CuO and suitable lanthanide oxygen.

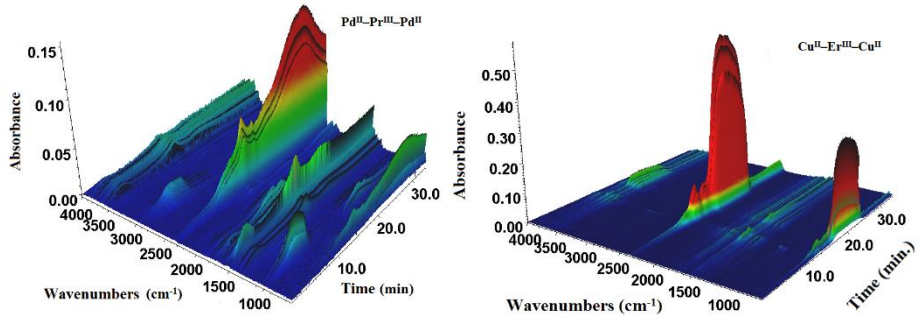



**Fig.4.** TG-FTIR spectra of gaseous products involved of the complexes 1 and 5 decomposition.

**Conclusions:** Depending on the type of ion used for the synthesis, cationic $Pd^{II}$–$Ln^{III}$–$Pd^{II}$ or neutral $Cu^{II}$–$Ln^{III}$–$Cu^{II}$ compounds were obtained. All complexes crystallize as solvates containing different amounts of methanol and/or water molecules. In the crystals of complexes the metal(II) ions are located in $N_2O_2$ and Ln(III) in $O_2O_2$ cavities. The *3d/4d* and *4f* metal ions are connected by two phenoxy oxygen atoms of the deprotonated Schiff base ligand. All complexes are stable at room temperature. Compounds $Cu^{II}$–$Ho^{III}$/$Er^{III}$–$Cu^{II}$ are more thermally stable, which may be related to the presence of different central ions.

## References:

1. L. Jiang, Y. Liu, X. Liu, J. Tian, S. Yan, Journal of the Chemical Society, Dalton transactions, 46 (2017) 12558.
2. X. Yang, R.A. Jones, S. Huang, Coordination Chemistry Reviews, 173 (2014) 63.
3. M. Jesmin, M.M. Ali, J.A. Khanam, The Thai Journal of Pharmaceutical Sciences, 34 (2010) 20.
4. J. Blake, V.A. Cherepanov, A.A. Dunlop, C.M. Grant, P.E.Y. Milne, J.M. Rawson, R.E.P. Winpenny, Journal of the Chemical Society, Dalton transactions, 14 (1994) 2719.
5. A. Jones, V.H. Grassian, S.C. Larsen, Journal of Catalysis, 234 (2005) 401.
6. N. Sharma, T. Spillecke, L. Koo, C. Ansari, K.U. Tripathi, S. Caneschi, A. Klingeler, R. Rajaraman, G. Shanmugam, Inorganic Chemistry 61 (2022) 5572.
7. P. Mahapatra, S. Ghosh, N. Koizumi, T. Kanetomo, T. Ishida, M. Drew, A. Ghosh, Journal of the Chemical Society, Dalton transactions, 46 (2017) 12095.
8. S. Ghosh, C.J.S. Gómez García J.M. Clemente-Juan A. Ghosh, Magnetochemistry, 123 (2016) 2.
9. A. Dey, P. Bag, P. Kalita, V. Chandrasekhar, Coordination Chemistry Reviews, 432 (2021) 213707.
10. K. Liua, W. Shia, P. Chenga, Coordination Chemistry Reviews, 74 (2015) 289.
11. G.A. Zhang, Org. Biomolecular Chemistry, 10 (2012) 2534.
12. J.H. Lee, S.Y. Im, S.W. Lee, Inorganica Chimica Acta, 474 (2018) 89.
13. D. Kori, Y. Dote, M. Koikawa, Y. Yamada, Polyhedron 170 (2019) 612.
14. A. Apostol, I. Mihalache, T. Mocanu, O. Tutunaru, C. Pachiu, R. Gavrila, C. Maxim, M. Andruh, Journal of Applied Organometallic Chemistry, 35 (2021) e6126.

# ANALYSIS OF SELECTED PROPERTIES OF COPPER(II) AND ZINC HOMONUCLEAR COMPLEXES

**D. OSYPIUK, B. CRISTÓVÃO, A. BARTYZEL**, Maria Curie-Sklodowska University, Faculty of Chemistry, Institute of Chemical Sciences, Department of General and Coordination Chemistry and Crystallography, Maria Curie-Sklodowska Sq. 2, 20-031 Lublin, Poland.

**Abstract:** The homonuclear complexes ($C_{19}H_{19.5}Br_2CuN_2O_6$, $C_{23}H_{32}Br_2Cu_2N_2O_{11}$, $Cu_4C_{46}H_{60}N_4O_{14}$, $Cu_4C_{48}H_{68}N_4O_{18}$, $Zn_2C_{21}H_{25}N_2O_{6.5}$, $Zn_3C_{62}H_{54}N_4O_8$, $ZnC_{29}H_{26}N_2O_3$, $ZnC_{30}H_{28}N_3O_{4.5}$, $Zn_2C_{31}H_{26}N_2O_7$) including in the structure polidentate Schiff bases (with $N_2O_2$, $N_3O_4$, $N_2O_5$ or $N_2O_3$ coordination sites) are crystalline compounds, stable at room temperature. The results of FTIR spectroscopy indicate that azomethine nitrogen and phenoxide oxygen atoms of the N,O-donor ligands take part in the coordination of $Cu^{II}/Zn^{II}$ ions. The presence of solvents (methanol and/or water) in the structure of complexes is confirmed by FTIR and thermal analysis (TG/DSC, TG-FTIR techniques). The decomposition of the Cu(II) and Zn complexes in air/nitrogen atmosphere is a multi-step process.

**Introduction:** The synthesis of innovative mononuclear and multinuclear complexes with different compositions and properties is the subject of coordination chemistry research. The choice of a suitable ligand is one of the most important factors to consider when designing a complex. An interesting group of ligands is Schiff bases (Fig.1) because of their structural diversity and ability to react with different ions in different ways [1, 2].

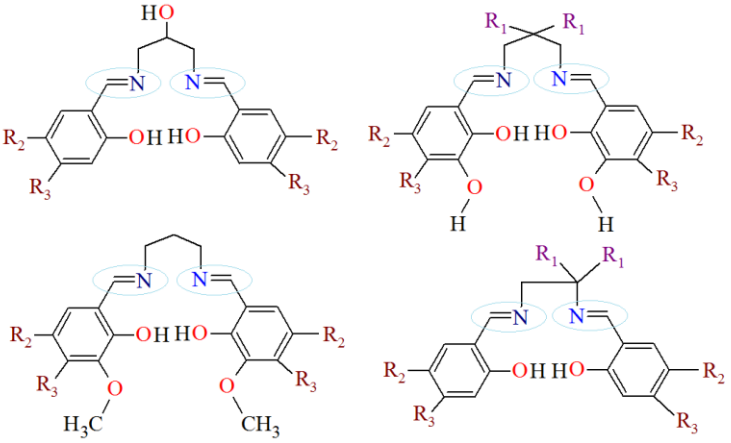



**Fig.1.** Examples of Schiff base with marked an azomethine group.

Schiff bases with salen-type structures, obtained by the condensation reaction of salicylaldehyde or its derivatives with diamines, are commonly used as ligands. The presence of additional functional groups in the structure of the used reagents results in ligands having 4, 5, 6 and more coordination sites. These ligands are able to form a wide variety of $Cu^{II}$ and $Zn^{II}$ complexes, some of which exhibit catalytic, antioxidant, antibacterial, antiviral activity as well as unique optical properties [3-5]. Herein, we report studies of the spectral and thermal properties of $Cu^{II}$ and $Zn^{II}$ complexes with Schiff bases (differed in the amount and kind of substituents in the benzene ring).

**Experimental:** All reagents and solvents were used without further purification and purchased from commercial sources.
The Schiff base ligands were synthesized using a similar method described in previous papers [6–10]. The synthesis of complexes was performed in methanol solution with a ratio of metal ion to the Schiff base 1:1 or 2:1. An appropriate amount of copper(II) or zinc acetate dissolved in methanol was added to the hot methanol solution of an appropriate Schiff base and stirred. The mixture containing $Cu^{II}$ complexes was filtered after 0.5/1 h and allowed to slowly evaporate at low/ambient temperature. In the case of $Zn^{II}$ compounds, the mixture containing the precipitates was refluxed for 0.5 h. The solid products were then filtered off and washed several times with methanol.
The contents of carbon, hydrogen and nitrogen were determined by elemental analysis using a CHN 2400 Perkin-Elmer analyzer. The amounts of metals were established by X-ray fluorescence method with the use of the X-ray fluorescence with energy dispersion EDXRF-1510 (Canberra-Packard). The FTIR spectra of complexes and free Schiff bases were recorded over the range of 4000–350 $cm^{-1}$ using an M-80 Perking-Elmer spectrometer or on a Nicolet 6700 FTIR using the ATR technique (with a resolution of 4 $cm^{-1}$ for 16 scans in the range of 4000 $cm^{-1}$ and 540 $cm^{-1}$). The thermal properties of the complexes were studied in air utilising a Setsys 16/18 (Setaram) TG, DTG and DSC instrument. The experiments were carried out at an air flow rate of 20 mL $min^{-1}$ in the range of 30–700/800 °C at a heating rate of 10 °C $min^{-1}$. The samples were heated in $Al_2O_3$ crucibles. To identify the gaseous decomposition products of the samples, TG–FTIR analysis was performed on a Q5000 TA apparatus coupled to a Nicolet 6700 spectrophotometer. The experiments were carried out under a dynamic nitrogen atmosphere in flowing nitrogen at 20 mL $min^{-1}$ in open platinum crucibles. The complexes were heated up to 700 °C at a heating rate of 20 °C $min^{-1}$. The gaseous decomposition products were analyzed in the range of 4000–400 $cm^{-1}$ using the Nicolet 6700 spectrophotometer.

**Results:** Comparing the FTIR spectra of the $C_{19}H_{19.5}Br_2CuN_2O_6$, $C_{23}H_{32}Br_2Cu_2N_2O_{11}$, $Cu_4C_{46}H_{60}N_4O_{14}$, $Cu_4C_{48}H_{68}N_4O_{18}$, $Zn_2C_{21}H_{25}N_2O_{6.5}$, $Zn_3C_{62}H_{54}N_4O_8$, $ZnC_{29}H_{26}N_2O_3$, $ZnC_{30}H_{28}N_3O_{4.5}$, $Zn_2C_{31}H_{26}N_2O_7$ coordination compounds with those of free Schiff bases (Table 1), it can be seen that the position of some peaks changes during the complexation process. In the spectra of the N,O-donor ligands strong sharp absorption bands present in the range 1644–1589 $cm^{-1}$ can be assigned for the imine stretching frequency $\nu$(C=N). In the spectra of the complexes, this band is shifted towards lower or higher wavelengths, which indicates the coordination of $Cu^{II}$ and $Zn^{II}$ ions *via* azomethine nitrogen atoms. The stretching vibrations $\nu$(C-O) are shifted to lower wavenumbers during the complexation process, confirming the coordination of the

metal(II) ions by oxygen atoms of the deprotonated phenol groups. In the FTIR spectra of the polynuclear complexes the new strong bands are presented at 1574–1531 $cm^{-1}$ and 1439–1409 $cm^{-1}$, respectively which are assigned to the asymmetric $\nu_{as}$(OCO) and symmetric $\nu_s$(OCO) stretching vibrations of the carboxylate group of the acetate ions [7,10,11].

**Table 1.** Selected infrared absorption bands of the Schiff base ligands and complexes ($cm^{-1}$).

| Compound | $\nu$(O–H) | $\nu$(C=N) | $\nu_{as}$(OCO) | $\nu_{as}$(OCO) |
|---|---|---|---|---|
| $C_{19}H_{20}Br_2N_2O_5$ | | 1644 | – | – |
| $C_{19}H_{19.5}Br_2CuN_2O_6$ | 3452 | 1624 | – | – |
| $C_{23}H_{32}Br_2Cu_2N_2O_{11}$ | 3432 | 1632 | 1564 | 1424 |
| $C_{19}H_{24}N_2O_4$ | 2760 | 1608 | – | – |
| $Cu_4C_{46}H_{60}N_4O_{14}$ | 3490 | 1601 | 1532 | 1417 |
| $Cu_4C_{48}H_{68}N_4O_{18}$ | 3180 | 1600 | 1531 | 1409 |
| $Zn_2C_{21}H_{25}N_2O_{6.5}$ | 3206 | 1625 | 1573 | 1439 |
| $C_{29}H_{26}N_2O_2$ | 2561 | 1606 | – | – |
| $Zn_3C_{62}H_{54}N_4O_8$ | – | 1598 | 1571 | 1435 |
| $C_{29}H_{26}N_2O_2$ | 25556 | 1604 | – | – |
| $ZnC_{29}H_{26}N_2O_3$ | 3288 | 1593 | – | – |
| $C_{30}H_{29}N_3O_4$ | 2513 | 1601 | – | – |
| $ZnC_{30}H_{28}N_3O_{4.5}$ | 3566 | 1609 | – | – |
| $C_{29}H_{28}N_2O_6$ | 2560 | 1589 | – | – |
| $Zn_2C_{31}H_{26}N_2O_7$ | 3527 | 1617 | 1574 | 1435 |

A medium or weak broad bands with a maximum in the range 3612–3144 $cm^{-1}$ can be attributed to the OH stretching vibrations, $\nu$(O–H) of solvent molecules (water and/or methanol), as well as to non-bonding Schiff base hydroxyl groups.

The TG/DTG/DSC and TG-FTIR techniques were used to study the thermal properties of homonuclear complexes in the air atmosphere (Fig. 2).

The $Cu^{II}$ and $Zn^{II}$ complexes are stable at room temperature. In the first heating step, the solvates lose methanol and/or water molecules. This process is confirmed by the recorded FTIR spectra of the emitted gases. Further heating leads to decomposition of the complexes. Most compounds are subject to multi-step degradation. The formed intermediate products are unstable and immediately undergo further degradation and combustion, which is accompanied by a significant exothermic effect. The main gaseous products resulting from thermal degradation are: $H_2O$, $CO_2$, CO, and $NH_3$. Depending on the complex, the final products of thermal decomposition are CuO or ZnO.

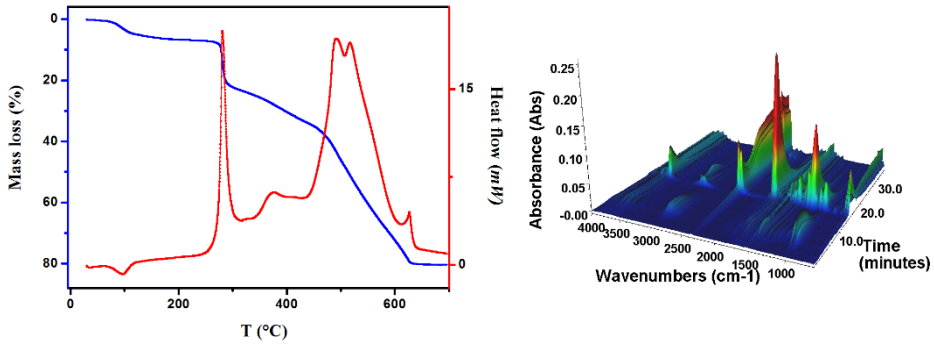



**Fig.2.** TG/DSC and TG/FTIR curves for complex $C_{23}H_{32}Br_2Cu_2N_2O_{11}$.

**Conclusions:** All $Cu^{II}$ complexes are mononuclear or multinuclear compounds crystallizing as solvates with varying amounts of water and/or methanol molecules. $Zn^{II}$ complexes are also synthesized as mononuclear or multinuclear compounds, which are solvent-free or contain water molecules in the structure. $Cu^{II}$ complexes have a solubility in methanol than the $Zn^{II}$ compounds. All complexes are stable at room temperature. The solvated complexes undergo a dehydration process. Desolvated samples of $Zn^{II}$ compounds are more thermally stable compared to $Cu^{II}$ compounds. For example, the decomposition process of the $Zn^{II}$ complex with the same Schiff base starts about 100 °C higher than that of the corresponding $Cu^{II}$ complexes. The thermal stability of the solvent-free compound is also reduced by the number of metal centers and the presence of the additional bridging ligand (acetate ion).

**References:**

1. C.R. Groom, I.J. Bruno, M.P. Lightfoot, S.C. Ward, Acta Crystallographica B, 72 (2016) 171.
2. K. Liua, W. Shia, P. Chenga, Coordination Chemistry Reviews, 290 (2015) 74.
3. C. Shiju, D. Arish, S. Kumaresan, Journal of Molecular Structure, 1221 (2020) 128770.
4. Y. Dong, R. Fan, W. Chen, H. Zhang, Y. Song, X. Du, P. Wang, L. Wei, Y. Yang, Dalton Transactions, 46 (2017) 1266.
5. A.N. Gusev, M.A. Kiskin, E.V. Braga, M. Chapran, G. Wiosna-Salyga, G.V. Baryshnikov, V.A. Minaeva, B. F. Minaev, K. Ivaniuk, P. Stakhira, H. Ågren, W. Linert, The Journal of Physical Chemistry C, 123 (2019) 11850.
6. D. Osypiuk, B. Cristóvão, A. Bartyzel, Crystals, 10 (2020) 1004.
7. D. Osypiuk, A. Bartyzel, B. Cristóvão, Journal of Molecular Structure, 1294 (2023) 136337.
8. M. Dolai, T. Mistri, A. Panja, M. Ali, Inorganica Chimica Acta, 399 (2013) 95.
9. A. Bartyzel, Journal of Thermal Analysis and Calorimetry,127 (2017) 2133.
10. D. Osypiuk, B. Cristovao, L. Mazur, Journal of Molecular Structure, 1261 (2022) 132924.
11. K. Nakamoto, John Wiley & Sons, Inc., Hoboken, New Jersey, 2008.

# REMOVAL OF FLUORIDE IONS FROM AMMONIUM SULPHATE(VI) SOLUTIONS BY ION EXCHANGE RESIN

**A. ZDUNEK[1], D. KOŁODYŃSKA[2], K. BOROWIK[1]**, [1]Fertilizer Research Group, Łukasiewicz Research Network-New Chemical Syntheses Institute, Tysiąclecia Państwa Polskiego Ave. 13A, 24-110 Puławy, Poland, [2]Maria Curie-Sklodowska University, Faculty of Chemistry, Institute of Chemical Sciences, Department of Inorganic Chemistry, M. Curie-Sklodowska Sq. 3, 20-031 Lublin, Poland.

**Abstract:** Studies on fluoride ions removal from ammonium sulphate(VI) solutions using a cation exchange resin modified with $Ca^{2+}$, $Mg^{2+}$, $Fe^{3+}$ and $Al^{3+}$ ions are presented. Experiments were carried out in a batch system, using model solutions of ammonium sulphate(VI) with the concentration of 10-40% (m/m) containing $NH_4F$ as a source of fluoride ions. All of them were also carried out for the aqueous solutions containing fluoride ions to evaluate the effects of the ammonium sulphate(VI) presence on the fluoride removal efficiency. After preliminary tests of fluoride ions removal using each type of modified cation exchange resin, to further detailed studies of the effects of contact time, dose, initial fluoride ions concentration and temperature, the $Al^{3+}$ form was selected. It was noted that the fluoride ions removal from ammonium sulphate(VI) solutions revealed good agreement especially with the Temkin adsorption model, while for the aqueous solutions the compatibility was poor for all adsorption models analyzed.

**Introduction:** The issue of fluoride ions removal usually applies to drinking water as well as industrial wastewater. In the case of industrial solutions, they are usually very complex system. One of the industrial processes that generate solutions contaminated with fluoride ions is flue gases desulphurization process by wet ammonia method (Walther method) [1]. In Poland it is employed by Grupa Azoty, Zakłady Azotowe PUŁAWY S.A. This method enables obtaining of ammonium sulphate(VI) (AS) both in crystalline form and as a saturated solution. AS is a mineral fertilizer containing nitrogen and sulphur - important nutrients for plants. The fluoride ions presence results in corrosive effects on desulphurization and fertilizer production facilities. Reducing the content of fluoride ions in the post-absorption solutions would improve the operating conditions of desulphurization plants and enable the obtained desulphurization products to be used in the production of mineral fertilizers.
Of many methods of fluoride ion removing from solutions described in the literature, one way is to use of ion exchange resins. Weak and strong base anion exchanger [2], chelating ion exchange resin [3], and cation exchange resins modified with multivalent ions as: $La^{3+}$, $Ce^{4+}$, $Y^{3+}$, $Fe^{3+}$, $Al^{3+}$, $Zr^{4+}$ [4,5] are used to remove of fluoride ions. Since the presence of sulphate(VI) anions is the factor that strongly and negatively affects fluoride ions removal efficiency, the use of a modified cation exchange resin seems to be the most favourable for ammonium sulphate(VI) solutions.

**Experimental:** Experiments of fluoride ions removal from ammonium sulphate(VI) solutions were carried out using a cation exchange resin with the trade name of Lewatit MonoPlus SP-112. It is a strongly acidic, macroporous cation exchange resin based on

a styrene-divinylbenzene copolymer, with sulfonic acid as the functional group, supplied in the $Na^+$ form [6]. To obtain a modified form of this resin with cations such as $Ca^{2+}$, $Mg^{2+}$, $Fe^{3+}$ and $Al^{3+}$, it was contacted with solutions of its chloride salts of analytical grade, with concentrations of metal cations corresponding to the resin's theoretical ion exchange capacity. After mixing these solutions for the same time on a magnetic stirrer with the same dose of resin, the modified cationite was separated from the solution and, after rinsing with distilled water, allowed to dry freely under ambient temperature conditions. Since the results of preliminary tests showed that the largest efficiency of fluoride ions removal was obtained for the $Al^{3+}$ ion- modified resin, further detailed studies were carried out only with this form of resin.
Lewatit MonoPlus SP-112 in the form of $Al^{3+}$ was subjected to a study of the effects of various parameters on fluoride ions removal efficiency from both aqueous and from ammonium sulphate(VI) solutions. The contact time, dose, initial fluoride ions concentration and temperature were analyzed. All experiments were carried out for both aqueous solutions containing fluoride ions in the form of $NH_4F$ and ammonium sulphate(VI) solutions with the concentration of 10, 20, 30 and 40% (m/m). All tests were carried out in the fluoride solutions in the amount of 50 mL placed in the PE flasks with caps. They were placed on a multi-position magnetic stirrer to achieve the same mixing conditions (speed of 550 rpm). After carrying out the tests under the assumed conditions, the final concentration of fluoride ions in the tested solutions was determined, using the direct potentiometric method. The fluoride selective electrode of the Monokrystaly 09–37 type (made of lanthanum fluoride single crystal) was used as the indicating electrode combined with the AgCl electrode as the reference one. The TISAB III buffer was used. All experiments were done in triplicate and the presented results are the mean values. Based on the initial fluoride ions concentration in the tested solutions and the values obtained after contact with doses of resin, the percentage removal of fluoride was calculated. On the basis of the average value of fluoride removal efficiency, the ability of modified resin used for fluoride removal $q_e$ ($mg \cdot g^{-1}$) was defined, in the presence and absence of ammonium sulphate(VI). Based on the results of the effect of contact time, the kinetics of fluoride ions binding was characterized by fitting them to the kinetic models of PFO, PSO and IPD. The effect of resin dose depending on the initial fluoride ions concentration value of 0.05 $g \cdot cm^{-3}$, 0.5 $g \cdot cm^{-3}$ and 1.0 $g \cdot cm^{-3}$ was also studied. For better understanding the nature of fluoride ions interactions with the resin, the obtained experimental values of fluoride removal efficiency were fitted to the adsorption equations of the most common adsorption models, i.e. Langmuir, Freundlich, Temkin and Dubinin-Radushkievich isotherm. The effect of temperature in the range of 298-353 K was also investigated.

**Results:** The data presented in Table 1 show that the greatest increase in the fluoride removal efficiency was obtained for the modified cation exchange resin in the form of $Ca^{2+}$ and $Al^{3+}$. Modification with $Al^{3+}$ ions allowed to achieve nearly 90% fluoride removal efficiency, and even larger, already at the lowest resin dose of 0.5 $g \cdot cm^{-3}$. In the case of the $Ca^{2+}$ ion-modified resin, a dose of 2.0 $g \cdot cm^{-3}$ was required to achieve more than 80% fluoride removal efficiency. For the resin modified with $Mg^{2+}$ and $Fe^{3+}$ ions, their effectiveness turned out to be much lower. For all of them, fluoride removal efficiency was larger from ammonium sulphate(VI) solutions than from

aqueous solutions. Therefore, the resin modified with $Al^{3+}$ ions was used for further detailed studies.

**Table 1.** Reduction of fluoride ion content in $NH_4F$-$H_2O$ and $NH_4F$-$(NH_4)_2SO_4$ model solutions containing $F^-$ ions at a concentration of 0.5 g/dm$^3$, obtained using Lewatit MonoPlus SP-112 ionite in the form of $Ca^{2+}$, $Mg^{2+}$, $Fe^{3+}$ and $Al^{3+}$, at different doses, with a contact time of 60 minutes.

| Modified form of resin | Dose [g·50 cm$^{-3}$] | Efficiency of $F^-$ removal [%] | | | | |
|---|---|---|---|---|---|---|
| | | $NH_4F$ −$H_2O$ | $NH_4F$ −10% (m/m) AS | $NH_4F$ −20% (m/m) AS | $NH_4F$ −30% (m/m) AS | $NH_4F$ −40% (m/m) AS |
| $Ca^{2+}$ | 0.5 | 32.45 | 40.33 | 48.28 | 54.29 | 60.07 |
| | 1 | 41.55 | 51.76 | 58.54 | 66.12 | 71.55 |
| | 2 | 54.55 | 83.12 | 87.60 | 88.77 | 92.64 |
| $Mg^{2+}$ | 0.5 | 0.30 | 5.63 | 10.11 | 13.23 | 19.52 |
| | 1 | 1.14 | 6.73 | 14.38 | 21.27 | 28.75 |
| | 2 | 2.26 | 10.11 | 19.28 | 25.36 | 31.18 |
| $Fe^{3+}$ | 0.5 | 5.91 | 14.13 | 14.52 | 14.66 | 14.89 |
| | 1 | 5.98 | 19.51 | 20.17 | 20.86 | 22.16 |
| | 2 | 14.13 | 21.63 | 22.24 | 25.12 | 28.75 |
| $Al^{3+}$ | 0.5 | 96.01 | 94.06 | 93.99 | 90.87 | 85.89 |
| | 1 | 96.17 | 97.64 | 97.78 | 98.26 | 98.78 |
| | 2 | 96.12 | 98.79 | 99.06 | 99.55 | 99.64 |

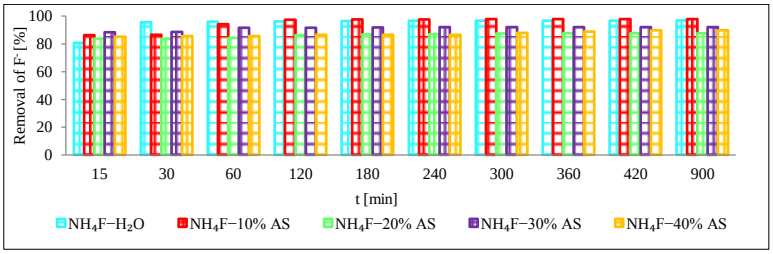



**Fig.1**. Effect of contact time on the fluoride ions removal efficiency from $NH_4F$-$H_2O$ and $NH_4F$-$(NH_4)_2SO_4$ solutions using Lewatit MonoPlus SP-112 $Al^{3+}$ resin (fluoride ions concentration: 0.5 g·dm$^{-3}$, resin dose: 0.5 g·50 cm$^{-3}$, stirring speed: 550 rpm, temperature: 298 K).

Dose effect studies have shown that, depending on the initial fluoride ions concentration of 0.05 g·cm$^{-3}$, 0.5 g·cm$^{-3}$ and 1.0 g·dm$^{-3}$, it is possible to achieve a large degree of fluoride ions removal (Fig.1) when the dose is appropriately matched, and the optimal dose is 0.2 g·50 cm$^{-3}$, 0.5 g·50 cm$^{-3}$ and 1.0 g·cm$^{-3}$, respectively. It can be also observed that with the increasing initial fluoride ions concentration the efficiency of fluoride ions removal from aqueous solution grew when a resin dose of 0.5-1.0 was used.

Analysis of the sorption capacity as a function of equilibrium concentration, for the range of the initial concentrations of fluoride ions of 0.05-1.0 g·dm$^{-3}$, revealed good agreement of experimental data with the theoretical assumptions of the adsorption models under consideration for ammonium sulphate(VI) solutions, while for the aqueous solutions the match was negligible (the values of the correlation coefficient $R^2$ were

below 0.6). Of all the adsorption models under consideration, the best fit, based on $R^2$ as well as agreement between theoretical and experimental values of adsorption capacity, was obtained for the Temkin adsorption model. The adsorption capacity for fluoride ions was about 70 mg·g$^{-1}$, regardless of the concentration of ammonium sulphate(VI).

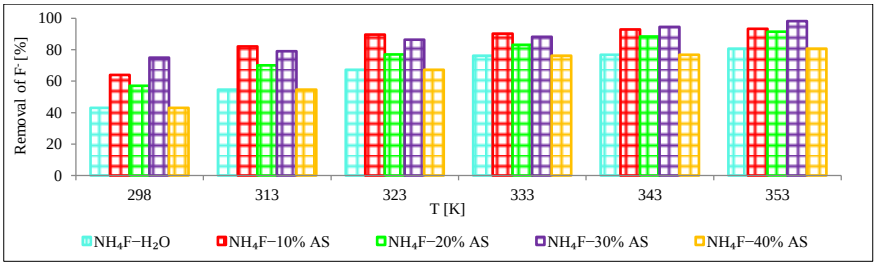



**Fig.2.** Effect of temperature on the fluoride ions removal efficiency from $NH_4F$-$H_2O$ and $NH_4F$-$(NH_4)_2SO_4$ solutions using Lewatit MonoPlus SP-112 $Al^{3+}$ resin (fluoride ions concentration: 0.5 g·dm$^{-3}$, resin dose: 0.5 g·50 cm$^{-3}$, stirring speed: 550 rpm, contact time 30 min).

As temperature increased, an increase in fluoride ions removal efficiency was observed for both aqueous and ammonium sulphate(VI) solutions (Fig.2). Namely, in the temperature range of 298-353 K, the efficiency increased from 43% to 81% for $NH_4F$-$H_2O$ and 43% to 81% for $NH_4F$-$(NH_4)_2SO_4$ (40% (m/m)).

**Conclusions:** Lewatit MonoPLus SP-112 modified with $Al^{3+}$ ions revealed significantly better fluoride ions removal efficiency than in the form of $Ca^{2+}$, $Mg^{2+}$ and $Fe^{3+}$. The results of studies on the effects of contact time, resin dose, initial fluoride ions concentration and temperature showed that this way of the ionite modification enables to achieve a very effective material for fluoride ions removal. Significant efficiency in fluoride ions removal under such conditions as the ammonium sulphate(VI) presence at concentration of 40% (m/m), large concentration of $F^-$ ions (much larger than in drinking water) and a temperature of 350 K make Lewatit MonoPLus SP-112 modified with $Al^{3+}$ ions appear to be a favuorable material for reducing the fluoride ions concentration in post-absorption solutions, generated in the desulphurization process by wet ammonia method.

## References:

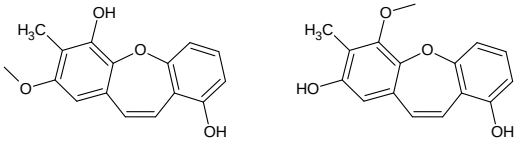
1.Marsulex Environmental Technologies, Ammonium Sulfate WFGD Technology. Overview for general industry information, 2007. https://pdf4pro.com/view/ammonium-sulfate-wfgd-technology-overview-5c400.html (12.02.2020).
2. D. Różycka, M. Grobelny, Przemysł Chemiczny, 84 (2005) 520 (in Polish).
3. D.B. Bhatt, P.R. Bhatt, H.H. Prasad, K.M. Popat, P.S. Indian Journal of Chemical Technology, 11 (2004) 299.
4. F. Luo, K. Inoue, Solvent Extraction and Ion Exchange, 22 (2004) 305.
5. H. Paudyal, K. Inoue, H. Kawakita, K. Ohto, H. Kamata, S. Alam, Journal of Material Cycles and Waste Management, 20 (2018) 975.
6. https://lanxess.com/en-US/Products-and-Brrands/Products (28.03.2024).

# SPOSÓB OTRZYMYWANIA POCHODNYCH AMINOWYCH DIHYDRODIBENZO[*b,f*]OKSEPIN

**P. TOBIASZ[1], M. KOŹBIAŁ[1], F. BORYS[1,2], H. KRAWCZYK[1]**, [1]Politechnika Warszawska, Wydział Chemiczny, Katedra Chemii Organicznej, S. Noakowskiego 3, 00-664 Warszawa, [2]Polska Akademia Nauk, Instytut Biologii Doświadczalnej im. Marcelego Nenckiego PAN, L. Pasteura 3, 02-093 Warszawa.

**Abstrakt:** W niniejszej pracy przedstawiono wyniki badań otrzymywania aminowych pochodnych dihydrodibenzo[*b,f*]oksepiny. Reakcje prowadzone były przy użyciu Pd/C oraz monohydratu hydrazyny $N_2H_4 \cdot H_2O$. Jako rozpuszczalnik stosowano etanol.

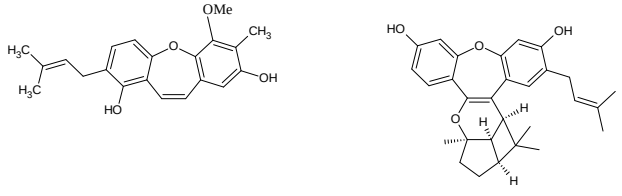
**Wprowadzenie:** Dibenzo[*b,f*]oksepiny charakteryzują się interesującymi właściwościami biomedycznymi, a także są szeroko rozpowszechnione w naturze. Stanowią one analogi stilbenu, w których dwa pierścienie aromatyczne łączą się ze sobą mostkiem winylowym i atomem tlenu.
Dibenzo[*b,f*]oksepiny wykazują korzystne właściwości biomedyczne, które często korelują z właściwościami pochodnych stilbenu. Przykładami dibenzo[*b,*f]oksepin są występujące w naturze - pacharyna **(1)** oraz bauchiniastatyna **(2)** (rys.1).




**(1)** **(2)**

**Rys.1.** Struktura pacharinu (1) oraz bauhiniastatinu (2).

Związki te po raz pierwszy zostały wyizolowane z rośliny o nazwie *Bauhinia purpurea*. Rośliny z tego rodzaju stosowane są np. w niekonwencjonalnym leczeniu raka w Indiach i Afryce. Cząsteczki te charakteryzują się tym, że znacząco zatrzymują rozrost komórek nowotworowych [1], [2]. Wyżej wymienione molekuły strukturalnie przypominają bauhinoxepin B **(3)** oraz artocarpol a **(4)**, które z kolei wykazują właściwości przeciwgrzybicze i przeciwzapalne (rys.2) [1].



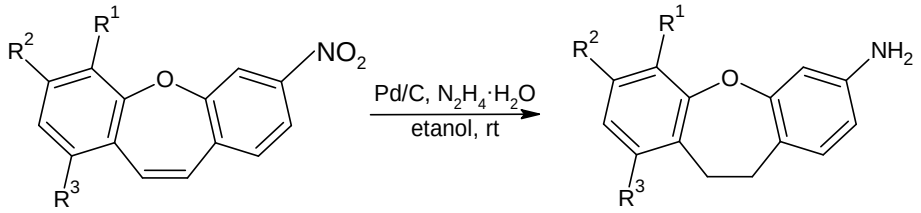

**(3)** **(4)**

**Rys.2.** Struktura bauhinoxepinu B (3) oraz artocarpolu a (4).

Inne dibenzo[*b*,*f*]oksepiny wykazują właściwości antypsychotyczne [1,3,4], przeciwzapalne [1,5] czy też przeciwdepresyjne [1,6].

**Część eksperymentalna:** W kolbie dwuszyjnej o pojemności 25 ml umieszczono element mieszający, 1 mmol odpowiedniej pochodnej dibenzo[*b*,*f*]oksepiny oraz 4 mmole Pd/C 10 wt. %. Całość zaopatrzono w chłodnicę zwrotną i ogrzewano w temperaturze wrzenia rozpuszczalnika. Po ogrzaniu do układu wkroplono powoli 3 mmol monohydratu hydrazyny, po czym reakcję prowadzono przez następne 30 minut. Po tym czasie mieszaninę poreakcyjną przesączono na celicie, przemywając dwukrotnie 1 ml etanolu. Przesącz trzymano w -15$^{o}$C przez 24 h. Otrzymany osad przesączono pod zmniejszonym ciśnieniem otrzymując czysty związek.

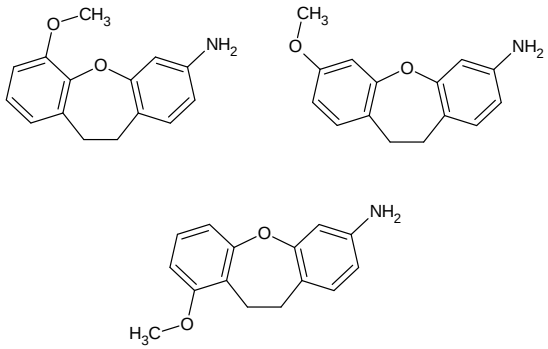
**Wyniki:** Celem przedstawionej pracy było otrzymanie aminowych pochodnych dihydrodibenzo[*b*,*f*]oksepiny. Jako substratów użyto odpowiednie nitrowe pochodne dibenzo[*b*,*f*]oksepiny. Reakcję redukcji prowadzono w obecności Pd/C oraz $N_2H_4 \cdot H_2O$ jako katalizatora (rys.3).




(1) $R_1 = OCH_3$, $R_2$, $R_3 = H$
(2) $R_2 = OCH_3$, $R_1$, $R_3 = H$
(3) $R_3 = OCH_3$, $R_1$, $R_2 = H$

**Rys.3.** Schemat syntezy prowadzący do otrzymania różnych aminowych pochodnych dihydrodibenzo[*b*,*f*]oksepiny.

W wyniku tej reakcji otrzymano 3 różne aminowe pochodne dihydrodibenzo[*b*,*f*]oksepiny zawierające grupy metoksylowe w różnych pozycjach (rys.4).



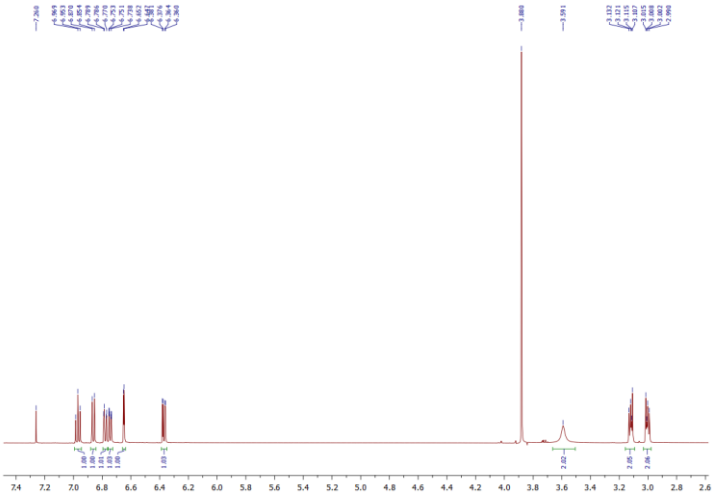
**Rys.4.** Struktura otrzymanych aminowych pochodnych dihydrodibenzo[*b,f*]oksepiny.

Wydajności otrzymywania poszczególnych związków zostały umieszczone w poniższej tabeli. Warto zauważyć, że w wrunkach reakcji, jednocześnie redukcji ulega podwójne wiązanie i grupa nitrowa.

**Tabela 1.** Wydajności otrzymywania aminowych pochodnych dihydrodibenzo[*b,f*]oksepiny.

| Związek | Wydajność |
|---|---|
| 1a | 79% |
| 1b | 69% |
| 1c | 66% |

Poniżej przedstawiono także przykładowe widmo $^{1}$H NMR (rys.5) potwierdzające budowę związku 1a.



**Rys.5.** Widmo $^{1}$H NMR związku 1a.

**Wnioski:** W wyniku reakcji redukcji nitrowych pochodnych dibenzo[*b,f*]oksepiny w obecności Pd/C oraz monohydratu hydrazyny powstają nowe aminowe pochodne dihydrodibenzo[*b,f*]oksepiny. Powstałe związki nie zawierają wiązania podwójnego

pomiędzy pierścieniami aromatycznymi. Otrzymane połączenia posiadają grupę aminową, która w przyszłości może zostać wykorzystana do syntezy związków azowych zawierających szkielet dihydrodibenzo[*b*,*f*]oksepiny.

Projekt został sfinansowany ze środków z grantu NChem3 z programu (IDUB), oraz ze środków budżetowych na naukę w latach 2019-2023, jako projekt badawczy w ramach programu „Diamentowy Grant" – projekt nr DI2018 015448 oraz ze wsparcia finansowego z projektu IDUB (program Stypendium Plus).

**Literatura:**

1. Y. L. Choi, H. S. Lim, H. J. Lim, J. N. Heo, Organic Letters, 14 (2012) 5102.
2. G. R. Pettit, A. Numata, C. Iwamoto, Y. Usami, T. Yamada, H. Ohishi, G. M. Cragg, Journal of Natural Products, 69 (2006) 323.
3. J. Fernández, J. M. Alonso, J. I. Andrés, J. M. Cid, A. Diaz, L. Iturrino, P. Gil, A. Megens, V. K. Sipido, A. A. Trabanco, Journal of Medicinal Chemistry, 48 (2005) 1709.
4. A. A. Trabanco, J. M. Alonso, J. M. Cid, L. M. Font, A. Megens, II Farm., 60 (2005) 241.
5. Y. Nagai, A. Irie, H. Nakamura, K. Hino, H. Uno, H. Nishimura, Journal of Medicinal Chemistry, 25 (1982) 1065.
6. H. H. Ong, J. A. Profitt, V. B. Anderson, T. C. Spaulding, J. C. Wilker, H. M. Geyer, H. Kruse, Journal of Medicinal Chemistry, 23 (1980) 494.

# ANTIOXIDANT ACTIVITY OF BEE BREAD AND DRONE BROOD HOMOGENATE IN LIPID PEROXIDATION PROCESS AND FERRIC(II) CHELATING ASSAY

**R. SAWCZUK, N. GRODZKA, J. KARPIŃSKA**, University of Białystok, Faculty of Chemistry, Department of Analytical and Inorganic Chemistry, K. Ciołkowskiego 1K, 15-245 Białystok, Poland.

**Abstract:** Bee bee bread and drone brood homogenate are little-known products of beekeeping with a complex chemical composition. This work presents the results assessing the antioxidant activity of the mentioned materials in the processes of chelating ferric(II) ions and lipid peroxidation and compares them with the activity of α-tocopherol, gallic acid, ascorbic acid and trolox. Lyophilisates of drone brood homogenate (LDBH) showed high activity in the metal cheating process and inhibition of the initial and final stages of lipid peroxidation. The activity of the bee bread samples was half of that compared to the activity of LDBH in chelation of ferric (II) ions; moreover, in the protocols assessing the impact on lipid oxidation, the bee bread samples showed pro-oxidant activity.

**Introduction:** Bee products are widely used in medicine, various fields of industry and as food products [1]. The products of apiary management that have been most thoroughly examined by scientists include honey, propolis, wax, bee pollen and royal jelly. Little information can be found in scientific sources about drone brood homogenate (DBH) and bee bread (BB). Bee bread is characterized by a complex chemical composition, which includes proteins, free amino acids, sugars, organic acids including lactic acid, lipids and fatty acids, cellulose, minerals, vitamins and polyphenols [2]. Drone brood is a little-known product of apiary management with a complex chemical composition, depending on the stage of its development [3]. The conducted research has shown that the lyophilized drone brood homogenate (LDBH) contains proteins, carbohydrates, lipids and B group vitamins, as well as macro- and microelements. Drone brood, in addition to the nutrients mentioned above, contains small amounts of steroid hormones: testosterone, progesterone, estradiol and prolactin [4].

The nutritional potential of many bee products has been documented in scientific research. One of the parameters determining the value of a given food product is antioxidant activity. There are many analytical methods for determining this parameter. The most commonly used techniques include spectrophotometric, electrochemical and chromatographic techniques [5].

The aim of the research described in the article was to determine the antioxidant activity in the process of lipid peroxidation and ferric(II) ion chelation of BB and LDBH samples at various stages of development: larvae, prepupae and pupae. To assess the antioxidant activity in the initial stage of lipid oxidation, the FTC method (**F**erric **T**hio**C**yanate method) was used, which uses spectrophotometric monitoring of the reaction of primary oxidation products, such as lipid peroxides, with $Fe^{2+}$ [6]. To assess the effect of preventing lipid oxidation processes in their final stage, the TBARS method (**T**hio**B**arbituric **A**cid **R**eactive **S**ubstances method) was used, based on

spectrophotometric measurement of the colored reaction product of secondary lipid oxidation products with 2-thiobarbituric acid [7]. The assessment of antioxidant activity in the metal ion chelation process was based on the spectrophotometric assessment of the reaction of ferric(II) ions with ferrozine [8].

**Experimental:** The antioxidant activity of 36 samples of LDBH collected at various stages of development and 12 samples of BB were analyzed. Extracts were prepared as follows: 2 mL solvent (acidified 80% aqueous ethanol solution (pH 4.6) or 96% ethanol) was added to a 200 mg weigh of lyophilisate or bee bread. The sample was exposed to ultrasounds for 30 min. Afterwards, the obtained suspension was centrifuged for 7 min. at a speed of 4000 rpm. The obtained supernatant was collected into 10 mL tubes, then the solvent was evaporated under a stream of nitrogen. The dry extract was weighed and dissolved in the appropriate amount of the solvent. Antioxidant activity of tested extracts was compared to activity of a well-known antioxidants: ascorbic and gallic acids, trolox and α-tocopherol.

Assessment of ferric (II) ion chelation activity (FICA): To assess the ability to chelate ferric(II) ions, 80% acidified (pH 4.6) ethanol-water extracts of BB and LDBH at a concentration of 2.5 mg/mL were used. 50 μL of the tested extract, 50 μL of a 2 mM $FeCl_2$ solution and 100 μL of a 5 mM ferrozine solution in 70% ethanol were added to 1.8 mL of a 70% aqueous ethanol solution. The prepared sample was vortexed and incubated in the dark for 10 minutes. Then, the absorbance of the solution was read at a wavelength of 562 nm against a blank sample, which was the reaction mixture without the addition of the extract.

Determination of the antioxidant activity of selected samples in the lipid peroxidation process: Samples tested by the FTC and TBARS methods were prepared as follows: 4 mL of the tested LDBH/BB sample with a concentration of 1 mg/mL in 96% ethanol, 4.1 mL of a 2.5% ethanol solution of linoleic acid, 8 mL of phosphate buffer (pH 7) were mixed with 3.9 mL of deionized water. The solutions prepared in this way were incubated at 40 °C in the dark for 7 days.

Assessment of inhibition of the initial stage of peroxidation using Ferric(II) thiocyanide (FTC method): To assess the antioxidant effect of the extracts in the initial process of lipid peroxidation using the FTC method, 100 μL of the incubated solution was taken and mixed with 7.5 mL of 75% ethanol, 100 μL of 30% $NH_4SCN$ solution and 100 μL of 0.02M $FeCl_2$. The resulting mixture was shaken and after 3 minutes the absorbance of the solution was read at a wavelength of 500 nm against the reference being the reaction mixture without the addition of the tested extracts.

Assessment of the impact of the tested extracts on the formation of secondary lipid peroxidation products (TBARS method): To assess the antioxidant effect of the extracts in the final stage of the lipid peroxidation process using the TBARS method, 1 mL of the incubated solution was taken, 2 mL of a 20% trichloroacetic acid solution and 2 mL of a 0.67% 2-thiobarbituric acid solution were added. The mixture was heated for 10 minutes in a boiling water bath, then cooled to room temperature and centrifuged for 20 minutes, after which the absorbance of the solution was measured at a wavelength of 532 nm against the reference being the reaction mixture without the addition of the tested extracts.

**Results:** Table 1 summarizes the results of antioxidant activity of extracts of BB and LDBH at various stages of development on tested assays.

**Table 1.** Comparison of the results of activity of BB and LDBH extracts on chelation of ferric(II) ions and inhibition of products of the initial and final stage of lipid peroxidation.

| Assay | Parameter | LDBH larvae | LDBH prepupae | LDBH pupae | Bee Bread |
|---|---|---|---|---|---|
| FICA | | % of inhibition $Fe^{2+}$ activity | | | |
| | Mean (mediane) | 40.3 (38.2) | 35.8 (35.3) | 35.0 (30.7) | 19.9 (17.8) |
| | Min.-Max. | 21.4-67.3 | 5.6-72.7 | 15.7-55.5 | 5.9-46.8 |
| FTC | | % of lipid peroxides inhibition | | | |
| | Mean (mediane) | 63.3 (61,1) | 44.9 (42.3) | 51.5 (52.4) | -19.2 (-22.4) |
| | Min.-Max. | 45.9-83.1 | 5.4-64.9 | 38.1-63.8 | -48.5-23.8 |
| TBARS | | % of TBARS inhibition | | | |
| | Mean (mediane) | 34.7 (28.8) | 32.6 (35.6) | 41.0 (39.8) | -30.2 (-23.9) |
| | Min.-Max. | 5.1-60.7 | -29.9-55.9 | 6.5-63.0 | -76.8-16.1 |

Table 2 includes the values of the percentage of chelation of $Fe^{2+}$ ions, inhibition of the formation of lipid peroxides and products of the final stage of lipid peroxidation for α-tocopherol, ascorbic and gallic acid and trolox.

**Table 2.** Summary of the effects of chelation of ferric(II) ions, inhibition of products of the initial and final stage of lipid peroxidation by the tested antioxidants.

| | FICA [25 μg/cm$^3$] | FTC [50 μg/cm$^3$ [a]; 25 μg/ cm$^3$ [b]] | TBARS [50 μg/cm$^3$ [a]; 25 μg/cm$^3$ [b]] |
|---|---|---|---|
| α-Tocopherol[a] | 3.9 | 33.3 | 24.6 |
| Ascorbic acid[a] | 2.0 | 27.4 | 7.6 |
| Gallic acid[a] | 7.2 | 53.7 | 28.0 |
| Trolox[b] | 5.6 | 89.4 | 41.5 |

**Conclusions:** The lowest ability to chelating ferric(II) ions was demonstrated by bee bread samples (average 19.92%), while the highest value was obtained by by samples of freeze-dried larvae of DBH (40.30%). Lyophilisates of pupal and prepupal homogenates were characterized by similar ferric(II) ion binding activity - 34.99% and 35.82%, respectively. Bee bread and LDBH extracts showed much higher (5 to 20 times) chelating activity than the analyzed antioxidants. The antioxidant activity of the tested extracts in the process of lipid peroxidation showed that bee bread was characterized by pro-oxidant activity both in the initial and final stages of this process (on average -19.15% and -30.18% for the FTC and TBARS methods, respectively). LDBH extracts were characterized by relatively similar lipid oxidation inhibitory potential, with extracts from drone prepupae showing the lowest antioxidant potential in the FTC and TBARS protocols (approx. 45% and 33%, respectively). In relation to the activity of the tested antioxidants, LDBH extracts showed similar or higher (except for trolox) activity in inhibiting the formation of peroxides in the first stage of peroxidation. The values obtained in the assessment of the inhibitory effect of the samples on the formation of final products of lipid peroxidation are higher or equal to the activity of all tested antioxidants.

To sum up, the tested LDBH and BB extracts are characterized by significant antioxidant potential in the process of chelating ferric (II) ions. Lyophilisates of drone brood homogenate inhibit the formation of products of both the initial and final stages of lipid

oxidation, unlike of bee bread. The research carried out allows us to expand knowledge about the antioxidant properties of bee bread. There are few publications in the scientific literature regarding drone brood homogenate, so the experiments described above provide valuable information about this unknown, although endowed with nutritional potential, bee product.

**References:**

1. R. Krell, Value-added products of beekeeping, FAO Agricultural services bulletin 124, Italy 1996.
2. M. Kieliszek, K. Piwowarek, A.M. Kot, S. Błażejak, A. Chlebowska-Śmigiel, I. Wolska, Trends in Food Science & Technology, 71 (2018) 170.
3. R. Sawczuk, J. Karpinska, W. Miltyk, Journal of Ethnopharmacology, 245 (2019) e111581.
4. S. Bogdanov, 2017. Bee Product Science: Royal jelly, Bee brood: Composition, health, medicine: a review, z www.bee-hexagon.net/files/file/filE/Health/RJBookReview.pdf.
5. A.M. Pisoschi, G.P. Negulescu, Biochemistry & Analytical Biochemistry, 1 (2012) 1.
6. M.A. Ghani, C. Barril, D.R. Bedgood, P.D. Prenzler, Antioxidants, 8 (2019) 366.
7. M.A. Ghani, C. Barril, D.R. Bedgood, P.D. Prenzler, Food Chemistry, 230 (2017) 195.
8. D. Kusztal, C. Mielczarek, Bromatologia i Chemia Toksykologiczna, 44 (2011) 1097.

**SPIS AUTORÓW**

**A**
Abdrakhmanova A. 241
Akimzhanova K. 238
Anđić M. 383
Antoniuk A. 322
Atanaskovic M. 369

**B**
Banaszek T. 12
Baran J. 178
Barczak M. 387
Bartoszewicz M. 187
Bartyzel A. 20, 403, 407
Bazan-Woźniak A. 40, 45
Bąk J. 98, 36
Białek A. 234, 335
Bielecka G. 32
Bieniek M. 116
Bińczak A. 244
Bok-Badura J. 113, 391
Bolińska M.I. 191
Borowik K. 411
Borys F. 16, 415
Bryazun A. 293
Buyan Y. 293

**C**
Chabros A. 199
Charmas B. 66
Choińska R. 120, 298
Chrzanowska A. 28
Ciosmak K. 211
Cristóvão B. 403, 407
Czech B. 74, 78
Czerwiński J. 288, 290
Czyżewska U. 187

**D**
Daumova G. 260
Dawidek K. 207, 211, 215
Dąbrowska A. 298
Djokic A. 369
Djokic L. 369
Dowbysz A. 322
Drabik J. 86
Drewniak M. 124, 199, 331
Drozd A. 178, 182

**E**
Emmons-Burzyńska M. 347

**F**
Fekner Z. 227
Fiałek M. 144, 148
Fila D. 54, 58
Fiołka M.J. 139
Florkowski G. 227
Fornal E. 355, 358
Franus W. 327
Froelich A. 12

**G**
Gac W. 373
Gajewska M. 109
Gazda L. 130
Gęca I. 164, 168
Gęca M. 94
Gładysz-Płaska A. 109
Goliszek M. 124, 199, 203
Golonko A. 317
Gołębiewska E. 116, 120, 307
Goncharuk O. 284
Gorylewski D. 171, 174
Górnik S. 256
Grabarczyk M. 148
Grabias-Blicharz E. 109
Grodzka N. 419
Groszek M. 230
Gruba M. 227, 234, 235
Gryzińska A. 207, 211, 215
Grządka E. 327
Gustaw S. 98

**H**
Hordyjewicz-Baran Z. 362
Hovorova K. 256
Hryniewicka M. 195
Hubicki Z. 54, 58, 101, 105

**I**
Idrisheva Z. 260

**J**
Jadach B. 12
Jakóbik-Kolon A. 113, 391
Janusz P. 338
Jedynak K. 66, 70
Jędrzejczak E. 347
Jiménez V.M. 227
Józefaciuk G. 62
Józwicka W. 338
Józwicki M. 338

**K**
Kaczmarczyk A. 82, 86
Kaczmarczyk M. 387
Kalinowska A. 343
Kalinowska M. 116, 120
Kapelewska J. 187
Kapusta O. 387
Karpińska J. 187, 419
Karpińska-Wlizło K. 373
Kaźmierczak B. 82, 86
Keller 171, 174
Kiczor A. 338
Klekotka U. 187
Kluczyński P. 347
Kolenda G. 120
Kołodyńska D. 36
Kołodyńska D. 54, 62, 98, 182, 411
Kondracka M. 178, 234, 335
Konkol M. 227, 234, 335
Korol W. 32, 377
Korolczuk M. 164
Koronkiewicz K. 116, 120
Kosińska-Pezda M. 331
Kotowska U. 191
Kowalczyk N. 303, 307
Kowalski R. 234, 335
Kowalski R. 335
Koźbiał M. 415
Krawczyk H. 16, 415
Krgović N. 381, 385
Krupa Z. 366
Krystkowiak E. 223
Krystkowicz M. 120
Krzyszowska A. 362
Kuczko W. 12
Kustovska A. 293
Kuzmanenko H. 124, 130

**L**
Lassak A. 178
Lenik J. 156, 160
Lewandowski W. 298, 317

Lewtak K. 139
Lipke A. 109
Litwiniuk Ł. 256

**Ł**
Łyszczek R. 230
Łyszczek R. 244

**M**
Maciejewska M. 219
Maciołek U. 124, 130, 134, 327, 331
Majdan M. 109
Martinović M. 385
Matusiak J. 327
Matysiak J. 265, 271
Mendyk E. 130
Mergo P. 338
Michałek T. 252
Miętus J. 16
Mirković S. 383
Misiołek K. 279
Młynarczyk K. 207
Molenda J. 86
Morawska K. 160
Moric I. 369
Mudrić J. 381, 385
Mussabayeva B. 238
Muszyński P. 271
Myka A. 244

**N**
Nalewajko-Sieliwoniuk E. 343
Nešić I. 383
Nieściór H. 32
Nikolaichuk H. 355, 358
Nizioł J. 366
Nosach L. 28, 284
Nosal-Wiercińska A. 152
Nowicka A. 331
Nowicka B. 12
Nowicki P. 90, 94

**O**
Ochab M. 168
Okholina T. 124, 130
Orzeł J. 124, 130
Osmałek T. 12
Ostasz A. 230
Ostolska I. 260
Osypiuk D. 403, 407

**P**
Padarz J. 109
Paientko V. 293
Paluch D. 40
Paluch M. 182
Pańczuk-Figura I. 134
Paw B. 265
Pawlak A. 152
Pawlak B. 227
Petrović A. 383
Piekutin J. 191
Pietrzak R. 40, 45
Pinchuk O. 293
Piotrowska-Niczyporuk A. 187
Plenis A. 20, 24
Podkościelna B. 49, 203, 207, 211
Przybył A.K. 399
Puszka A. 207, 211

**Q**
Quynh Nguhen M.V. 399

**R**
Radulski P. 82, 86
Regel-Rosocka M. 347, 351
Rogulska M. 219
Rojek B. 20, 24
Rubaj J. 32
Ruman T. 366
Rusek Ł. 248
Rzelewska-Piekut M. 351

**S**
Sabitova A. 238, 241
Sagan-Szendzielorz B. 113, 391
Samsonowicz M. 322
Sandybaev E. 260
Sawczuk R. 419
Senerovic L. 369
Sidorska B. 139
Skibicki J. 120
Skrzetuszewski M. 256
Skrzypek A. 265
Skrzypiec K. 130, 203, 238
Skubiszewska-Zięba J. 70
Skwarek E. 28, 260, 279, 284, 293
Skwarek P. 279, 284
Słowik G. 373
Smułek W. 351
Sofińska-Chmiel W. 124, 130, 134, 139, 199, 338
Sokołowski A. 74, 78
Stachowicz W. 351
Staniec K. 171, 174
Stankovic N. 369
Susdorf A. 16
Szarłowicz K. 395
Szklaruk A. 317
Szybowicz M. 12

**Ś**
Świderski G. 303, 307
Świsłocka R. 298, 311, 317

**T**
Tadić V.M. 381, 383, 385
Tarasiuk B. 49, 207
Tasić Kostov M. 381
Tobiasz P. 16, 415
Tokarska K. 90
Tomczak D. 12
Tomović M. 383
Tyniecka G. 307
Tyszczuk-Rotko K. 171, 174
Tyśkiewicz K. 227, 234, 335
Tyśkiewicz R. 234

**U**
Urban T. 90

**V**
Verspreet J. 227

**W**
Walczyński S. 377
Wardak C. 144, 156, 160
Wardak M. 144, 148, 160
Wasilewski T. 362
Watros A. 178
Wawruch A. 58
Wawrzaszek B. 66
Wawrzkiewicz M. 49
Wawszczak A. 62
Wichniarek R. 12

Wiejak R. 234, 335
Wiśniewska M. 90, 94, 260
Wojciechowski K. 16
Wojnicki M. 252
Wojtyłko M. 12
Wolski R. 45
Wołowicz A. 105
Wójcik G. 101
Wójcik S. 395
Wrzesińska K. 288, 290
Wydrych J. 139
Wysocka I. 343
Wysokowski M. 347
Wziątek A. 227, 234, 335

**Z**

Zajkowski M. 256
Zawadzki W. 373
Zdaniewicz I. 16
Zdunek A. 411
Ziniewicz A. 116
Ziniewicz A.I. 311
Zinkowska K. 101

**Ž**

Žugić A. 381, 383, 385

**Exhibitors, sponsors and supporters:**



PATRONAT HONOROWY
JAROSŁAW STAWIARSKI
MARSZAŁEK
WOJEWÓDZTWA LUBELSKIEGO

PATRONAT HONOROWY
WOJEWODA LUBELSKI
KRYSZTOF KOMORSKI



PATRONAT HONOROWY



PREZYDENT MIASTA LUBLIN
KRZYSZTOF ŻUK




































































CENTRUM PRASOWE
UMCS

# Analytical Laboratory

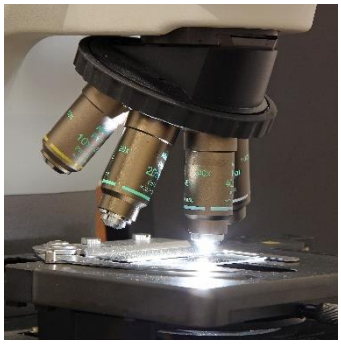
Accreditation certificate
No. AB 1548

https://www.umcs.pl/pl/lab.htm

Institute of Chemical Sciences
Faculty of Chemistry
Maria Curie-Sklodowska University
3 Maria Curie-Skłodowskiej Square
20-031 Lublin



XRF fluorescence
X-ray diffraction
Atomic force microscopy
Optical microscopy
Optical profilometry
XPS spectroscopy

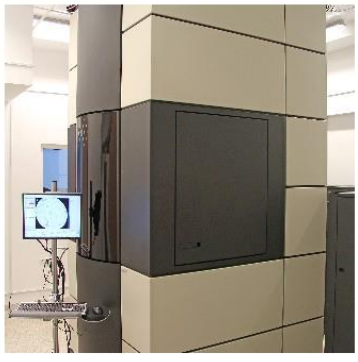








Infrared spectroscopy
Raman spectroscopy
Adsorption and chemisorption
Transmission electron microscopy
Scanning electron microscopy



Maintenance of the equipment in the Analytical Laboratory is co-financed by the INFRASTARt project

Rzeczpospolita Polska

UMCS

NCBR Narodowe Centrum Badań i Rozwoju

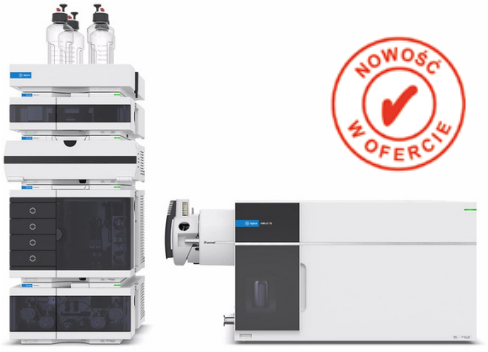
Altium

Agilent | Authorized Distributor

## Jesteśmy liderem w dostarczaniu i wdrażaniu nowoczesnych rozwiązań z branży Analizy Instrumentalnej, Diagnostyki Molekularnej i Genomiki.

Oferujemy chromatografy, spektrometry mas, spektrometry atomowe, spektrofotometry i inne urządzenia wykorzystywane w analizie instrumentalnej oraz akcesoria laboratoryjne. Posiadamy także własne Laboratorium Aplikacyjne, które wraz z dedykowanym zespołem inżynierów aplikacyjnych, stanowi wsparcie merytoryczne dla naszych Klientów.

Dysponujemy wykwalifikowanym zespołem ponad 30 inżynierów serwisu, którzy na terenie całego kraju dbają o sprawność instrumentów i ciągłość badawczą.




Potrójny kwadrupol LC/MS 6495D
w połączeniu z 1290 Infinity II LC Agilent Technologies



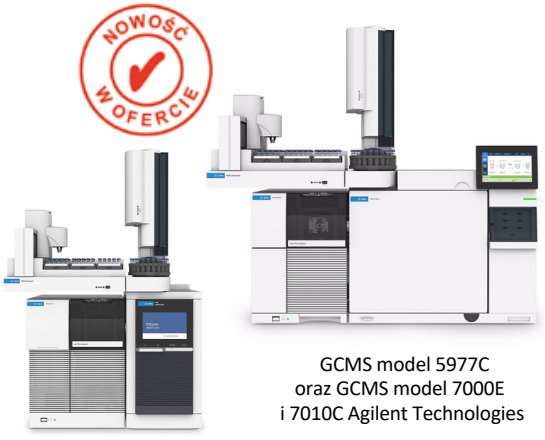

Revident LCMS Q-TOF Agilent Technologies



Analizatory węgla organicznego (TOC)
Sievers M9 firmy Veolia



Optyczny Spektrometr Emisyjny
5900 SVDV ICP-OES Agilent Technologies



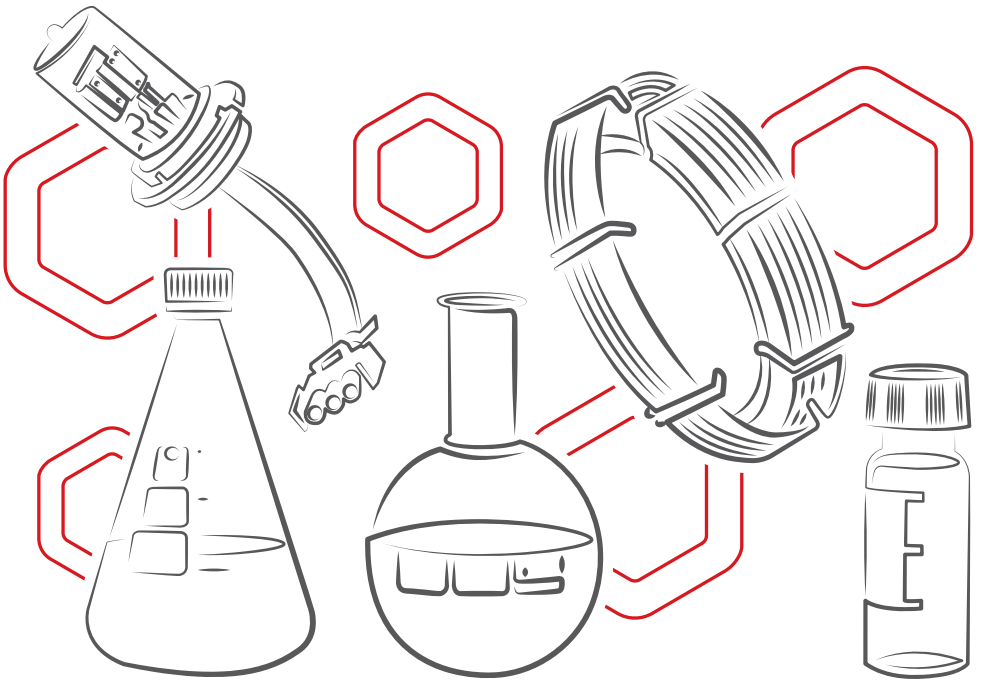

GCMS model 5977C
oraz GCMS model 7000E
i 7010C Agilent Technologies

**Altium International Sp. z o.o.**
ul. Puławska 303, 02-785 Warszawa,
telefon: (+48) 22 549 14 00, e-mail: klient@perlan.com.pl
www.perlan.com.pl | www.altium.net

Altium

Agilent | Authorized Distributor

# Akcesoria laboratoryjne



- Akcesoria Chromatograficzne
- Akcesoria Spektroskopowe
- BIO Kolumny i Odczynniki
- Wzorce i Materiały Odniesienia
- Przygotowanie Próbki
- Drobny Sprzęt Laboratoryjny
- Szkło Laboratoryjne i Miarowe
- Wsparcie Merytoryczne i Aplikacyjne

**Altium International Sp. z o.o.**
ul. Puławska 303, 02-785 Warszawa,
telefon: (+48) 22 549 14 00, e-mail: klient@perlan.com.pl
www.perlan.com.pl | www.altium.net

**NOWOŚĆ!**
**Intuicyjna wyszukiwarka materiałów eksploatacyjnych Agilent Technologies**

www.explore.agilent.com/essentialsupplies

TWÓJ PARTNER W LABORATORIUM

## *Selwa Sp. z o.o. jest autoryzowanym przedstawicielem firm:*

- **SCION Instruments** ***scioninstruments.com***

Chromatografy gazowe, cieczowe spadkobiercy światowego lidera firmy Varian w tej dziedzinie:
- niezawodne chromatografy gazowe nowej generacji serii 8300/8500
- zaawansowane chromatografy gazowe ze spektrometrami masowymi SQ (8700) i TQ (8900)
- chromatografy cieczowe serii 6000-LC w róznych konfiguracjach
- systemy do przygotowania próbek headspace HT-3 i Versa (wcześniej Teledyne Tekmar)
- serie analizatorów do analizy próbek środowiskowych, petrochemicznych itp.
- wszystkie niezbędne akcesoria, części oraz kolumny do chromatografii gazowej i cieczowej
- oprogramowanie sterujące chromatografami cieczowymi i gazowymi większości marek na świecie charakteryzujące się łatwością obsługi oraz nieograniczonym zakresem możliwości obróbki danych

- **Nanalysis Corporation** ***nanalysis.com***

Nastołowe, wszechstronne spektrometry rezonansu magnetycznego dostępne pod ręką w każdym laboratorium. Spektrometry dostępne w dwóch wersjach 60MHz i 100MHz i każda w opcji ekonomicznej i profesjonalnej. Pomiary izotopów 1H, 7Li, 11B, 13C, 19F, 31P. Praca z standardowymi rurkami 5mm wykorzystywanymi dotychczas w stacjonarnych spektrometrach NMR. Urządzenia ze stałym magnesem bez konieczności chłodzenia kriogenicznego. Wyposażone w prosty, dotykowy interfejs.

- **F-DGSi** ***f-dgs.selwa-lab.pl***

Generatory gazów czystych i ultraczystych do wytwarzania gazów w dowolnym miejscu:
- generatory wodoru - czystość do 99,9999%, maksymalne ciśnienie do 12 bar
- generatory azotu - czystość do 99,995%, maksymalne ciśnienie do 8 bar
- generatory czystego i ultraczystego powietrza
- zintegrowane stacje dostarczające wodor, azot, powietrze

- **LabTech Srl** ***www.labtechsrl.com***

Podstawowe wyposażenie każdego laboratorium:
- wysokiej jakości wyparki próżniowe pionowe i diagonalne
- niezawodne mieszadła magnetyczne z grzaniem
- płyty grzewcze oraz bloki do mineralizacji próbek
- cyrkulatory i łaźnie wodne o szerokim zakresie zastosowania

**www.selwa-lab.pl**
**biuro@selwa-lab.pl**
**tel. 0048 22 29 25 106 do 107**
**fax. 0048 22 29 25 108**
**Selwa Sp. z o.o.**
**ul. Stefana Batorego 18/108**
**02-591Warszawa**




ISBN 978-83-227-9805-8